Springer Proceedings in Mathematics & Statistics

Jan Awrejcewicz *Editor*

Dynamical Systems: Theoretical and Experimental Analysis

Łódź, Poland, December 7–10, 2015

Springer

Springer Proceedings in Mathematics & Statistics

Volume 182

Springer Proceedings in Mathematics & Statistics

This book series features volumes composed of selected contributions from workshops and conferences in all areas of current research in mathematics and statistics, including operation research and optimization. In addition to an overall evaluation of the interest, scientific quality, and timeliness of each proposal at the hands of the publisher, individual contributions are all refereed to the high quality standards of leading journals in the field. Thus, this series provides the research community with well-edited, authoritative reports on developments in the most exciting areas of mathematical and statistical research today.

More information about this series at http://www.springer.com/series/10533

Jan Awrejcewicz
Editor

Dynamical Systems: Theoretical and Experimental Analysis

Łódź, Poland, December 7–10, 2015

Springer

Editor
Jan Awrejcewicz
Department of Automation, Biomechanics
and Mechatronics
Łódź University of Technology
Łódź, Poland

ISSN 2194-1009 ISSN 2194-1017 (electronic)
Springer Proceedings in Mathematics & Statistics
ISBN 978-3-319-42407-1 ISBN 978-3-319-42408-8 (eBook)
DOI 10.1007/978-3-319-42408-8

Library of Congress Control Number: 2016945766

Mathematics Subject Classification (2010): 82-xx, 70-xx, 74-xx

© Springer International Publishing Switzerland 2016
This work is subject to copyright. All rights are reserved by the Publisher, whether the whole or part of the material is concerned, specifically the rights of translation, reprinting, reuse of illustrations, recitation, broadcasting, reproduction on microfilms or in any other physical way, and transmission or information storage and retrieval, electronic adaptation, computer software, or by similar or dissimilar methodology now known or hereafter developed.
The use of general descriptive names, registered names, trademarks, service marks, etc. in this publication does not imply, even in the absence of a specific statement, that such names are exempt from the relevant protective laws and regulations and therefore free for general use.
The publisher, the authors and the editors are safe to assume that the advice and information in this book are believed to be true and accurate at the date of publication. Neither the publisher nor the authors or the editors give a warranty, express or implied, with respect to the material contained herein or for any errors or omissions that may have been made.

Printed on acid-free paper

This Springer imprint is published by Springer Nature
The registered company is Springer International Publishing AG Switzerland

Preface

The international conference, "Dynamical Systems—Theory and Applications" (DSTA), held during 7–10 December 2015 in Lodz (Poland), has been the 13th edition of a conference series with a 23-year history. This scientific meeting organized by the Department of Automation, Biomechanics and Mechatronics of the Lodz University of Technology aims at providing a common platform for the exchange of new ideas and results of recent research and the scientific and technological advances of the field as well as modern dynamical system achievements. The scope of the conference covered the following topics: bifurcations and chaos, control in dynamical systems, asymptotic methods in nonlinear dynamics, stability of dynamical systems, lumped and continuous systems vibrations, original numerical methods of vibration analysis, non-smooth systems, dynamics in life sciences and bioengineering, engineering systems and differential equations, and mathematical approaches to dynamical systems.

All topics discussed in this book were covered by participants of the last edition of the DSTA conference. However, only a small part of different approaches and understandings of dynamical systems is presented in this book. In what follows, a brief description of results of theoretical, numerical and experimental investigations conducted by researchers representing different fields of science is given. While at the first sight they seem to be very diverse, they all are linked by the common factor, i.e. dynamical systems.

Chapter "Bifurcation and Stability at Finite and Infinite Degrees of Freedom" deals with problems of bifurcation and stability while modelling mechanical systems having finite and infinite degrees of freedom. Spectra of linear operators, Lyapunov–Schmidt and Centre Manifolds reduction are employed, among others.

The problem of reduction of low-frequency acoustical resonances inside a bounded space with an acoustical source is solved by Błażejewski (Chap. "Reduction of Low Frequency Acoustical Resonances Inside Bounded Space Using Eigenvalue Problem Solutions and Topology Optimization") using eigenvalue problem solutions matched with topology optimization.

Chapter "Analysis of the Macro Fiber Composite Characteristics for Energy Harvesting Efficiency" is aimed at an analysis of the macro-fiber composite characteristics for energy harvesting efficiency. Maximization of the root mean square of output electrical power is illustrated, and a composition of the system dynamics at optimized load resistance levels is carried out. The proposed approach is simulated with the use of the finite elements method and then experimentally validated.

Bučinskas et al. (Chap. "Research of Modified Mechanical Sensor of Atomic Force Microscope") present the method resulting in speed increase in nano-scale surface scanning by adding nonlinear force to lever of mechanical sensor. Comparison of the results of both original and modified atomic force microscope scans is also discussed.

Nonlinear dynamics of the car driving system with a sequential manual transmission is investigated in Chap. "Nonlinear Dynamics of the Car Driving System with a Sequential Manual Transmission". A complex computational model of a car sequential gearbox is constructed and the study of the nonlinear behavior of the whole driving system has been performed.

Dynamics of von Kármán plates under multiplicative white noise loading is analysed in Chap. "Random Attractors for Von Karman Plates Subjected to Multiplicative White Noise Loadings". The existence of random attractors is proved using the estimation of the system energy function.

Chmielewski et al. (Chap. "The Use of Fuzzy Logic in the Control of an Inverted Pendulum") describe the fuzzy logic control of an inverted pendulum. The problem is reduced to a study of a system with two degrees of freedom by means of force extortion of the corresponding carriage displacement.

Drąg (Chap. "Artificial Neural Network for Stabilization of the Flexible Rope Submerged in Sea Water") has employed an artificial neural network for the stabilization of a flexible rope submerged in the seawater. The influence of the sea environment, the vessel velocity and the lumped mass of the rope end is studied.

Chapter "Analysis of Non-autonomous Linear ODE Systems in Bifurcation Problems via Lie Group Geometric Numerical Integrators" aims at a bifurcation analysis using the Lie group geometric numerical integrators. In particular, the importance of the Magnus method in studying certain paradigmatic bifurcation problems is addressed.

Chapter "Transient Vibrations of a Simply Supported Viscoelastic Beam of a Fractional Derivative Type Under the Transient Motion of the Supports" deals with transient vibrations of a simply supported viscoelastic beam under the transient motion of the supports. Both the Riemann–Liouville fractional derivative and the fractional Green's functions are applied and shown that the proposed procedure widens the classical methods aimed at damping modelling of structural elements.

Gapiński and Koruba (Chap. "Analysis of Reachability Areas of a Manoeuvring Air Target by a Modified Maritime Missile-Artillery System ZU-23-2MRE") have analysed the reachability areas of maneouvering air targets achieved by a modified maritime missile-artillery system. In particular, the starting zone and the zone of destination for the particular air-defence fire unit are determined.

In Chap. "Angular Velocity and Intensity Change of the Basic Vectors of Position Vector Tangent Space of a Material System Kinetic Point—Four Examples" the angular velocity and the intensity of basic vectors change of position vector tangent space of a material system kinetic point are studied.

In Chap. "Dynamics of Impacts and Collisions of the Rolling Balls" the theory of dynamics of impacts and collisions of rolling balls are introduced, including various balls configurations. Different ball rolling traces before/after each type of impact/collision are illustrated, and kinematic parameters of impact and corresponding translational and angular velocities are presented.

Approximated analytical solutions to the Jerk equationsare derived in Chap. "Approximate Analytical Solutions to Jerk Equations". The obtained third-order nonlinear differential equations can govern structures performing rotational and translational motions of robots and machine tools.

A simple model of the Chandler wobble is studied from a point of view of stochastic and deterministic dynamics in Chap. "Chandler Wobble: Stochastic and Deterministic Dynamics". The investigations refer to the Earth's torqeless precession with a period of about fourteen months.

Chapter "Impact of Varying Excitation Frequency on the Behaviour of 2-DoF Mechanical System with Stick-Slip Vibrations" presents results of investigation of a varying excitation frequency on the behaviour of two degree-of-freedom system with stick-slip vibrations. A mathematical model of a block-on-belt system with normal force intensification mechanism and the model of a DC motor with worm gear are studied with a special attention paid to the bifurcation phenomena.

In Chap. "An Analysis of the 1/2 Superharmonic Contact Resonance" nonlinear normal contact vibrations of two bodies are studied. Many interesting nonlinear phenomena including loss of contact, multistability, period doubling bifurcations as well as the superharmonic contact resonances are illustrated and discussed.

The optimal variational method is employed in Chap. "The Oscillator with Linear and Cubic Elastic Restoring Force and Quadratic Damping" to study dynamics of simple oscillators with linear and cubic elastic restoring force and quadratic damping. Excellent agreement between analytical and numerical results is obtained.

The wave-based control to suppress vibrations during re-positioning of a flexible robotic arm on a planetary rover in a Martian environment is employed in Chap. "Wave-Based Control of a Mass-Restricted Robotic Arm For a Planetary Rover". The applied controller has performed well in limiting the effects of the flexibility during manoeuvres and in resisting vibrations caused by impacts.

Soft suppression of traveling localized vibrations in medium-length thin sandwich-like cylindrical shells containing magnetorheological layers is investigated in Chap. "Soft Suppression of Traveling Localized Vibrations in Medium-Length Thin Sandwich-Like Cylindrical Shells Containing Magnetorheological Layers via Nonstationary Magnetic Field". The derived differential equations with coefficients depending on the magnetic field are studied, and the asymptotic solution to the initial boundary value problem isproposed. How the application of time-dependent magnetic fields yields a soft suppression of the running waves is demonstrated.

Chapter "The Vehicle Tire Model Based on Energy Flow" is focused on modelling a tire–ground interaction dynamics based on free energy flow between three layers including a flexible tire, a tire–ground system with friction and the ground. Simulation results obtained with the employment of MATLAB/Simulink are compared with real test data.

Młyńczak et al. (Chap. "Research on Dynamics of Shunting Locomotive During Movement on Marshalling Yard by Using Prototype of Remote Control Unit") have presented a remote monitoring system using mobile devices for monitoring of the train driver and the locomotive motion dynamics during manoeuvres. The authors have applied an accelerometer and GPS systems to measure linear accelerations and velocities of the locomotive.

In Chap. "Durability Tests Acceleration Performed on Machine Components Using Electromagnetic Shakers" the possibility of shortening the durability tests using shakers and standard-defined load power spectral density is illustrated and discussed. The investigations are carried out through modification of the kurtosis, skewness and standard deviations of the applied loading.

Chapter "Identification of Impulse Force at Electrodes' Cleaning Process in Electrostatic Precipitators (ESP)" presents a proposal of an identification procedure of impulse force at electrodes cleaning process in electrostatic precipitators by means of measurements of vibrations and computer simulations. The analysis consisted of a repeated series of acceleration measurements at several tens of points of the collecting electrodes.

A new model of energy harvester based on a simple portal frame structure under saturation phenomenon is presented in Chap. "Using Saturation Phenomenon to Improve Energy Harvesting in a Portal Frame Platform with Passive Control by a Pendulum". Optimization of power harvesting and stabilization of chaotic motion to a given periodic orbit are achieved using the average power output and bifurcation diagrams. In addition, control sensitivity to parametric errors in damping and stiffness of the portal frame is implemented.

Štefek et al. (Chap. "Differential Drive Robot: Spline-Based Design of Circular Path") have discussed basic principles of control of a robot with differential drive and its application to design a circular path. The obtained results are verified in a simulator.

In Chap. "Multiple Solutions and Corresponding Power Output of Nonlinear Piezoelectric Energy Harvester" dynamics of a nonlinear flexible beam with a piezoelectric layer and magnetic tip mass subjected to harmonic excitation is studied. The introduced magnets define the system multistability, including a tristable configuration. It is shown that the constructed resonant curves and basins of attractors can help in choosing the optimal system parameters.

Chapter "On the Dynamics of the Rigid Body Lying on the Vibrating Table with the Use of Special Approximations of the Resulting Friction Forces" reports simulations and dynamics investigation of a rigid body lying on a vibrating table. The authors have employed a special approximation of the integral friction models based on the Padé approximants and their generalizations to attempt shaping and control of the body dynamics.

A system of two material points that interact by elastic forces due to the Hooke's law accompanied by their motion restricted to certain curves lying on a plane is studied in Chap. "Analysis of a Constrained Two-Body Problem". Conditions of linear stability are defined and a few particular periodic solutions are identified.

Warczek et al. have analysed forces generated in a shock absorber at conditions similar to the excitation caused by road roughness in Chap. "Analysis of the Forces Generated in the Shock Absorber for Conditions Similar to the Excitation Caused by Road Roughness". Defined random signals are supplied as the input functions which correspond to the real spectral density of road inequalities.

Chapter "A Pendulum Driven by a Crank-Shaft-Slider Mechanism and a DC Motor—Mathematical Modeling, Parameter Identification, and Experimental Validation of Bifurcational Dynamics" reports a continuation of numerical and experimental investigations of a system consisting of a single pendulum with the joint horizontally driven using a chainset (crankset) and a DC motor. The carried out series of experiments has given accurate estimation of the model parameters.

Bio-inspired tactile sensors for contour detection using a FEM-based approach are proposed in Chap. "Bio-Inspired Tactile Sensors For Contour Detection Using an Fem Based Approach". The work is focused on mechanoreceptors built as models of mystacial vibrissae located in the snout region of various mammals, such as mice, cats and rats.

Chapter "Kinematics and Dynamics of the Drum Cutting Units" is aimed at determination of the relationships between the basic parameters and the construction features of cutting drums. The obtained dependencies can be applied to construct a new prototype of a drum of cutting assemblies.

I hope that this book will provide the readers with both the response to their problems and the inspiration for further research.

I greatly appreciate the help of the Springer Editor, Elizabeth Leow, in publishing the presented chapters recommended by the Scientific Committee of DSTA 2015 after the standard review procedure. I would also like to thank all the referees for their help in reviewing the manuscript.

Finally, I would like to acknowledge that Chapters. "Impact of Varying Excitation Frequency on the Behaviour of 2-DoF Mechanical System With Stick-Slip Vibrations", "The Oscillator with Linear and Cubic Elastic Restoring Force and Quadratic Damping", "Analysis of the Forces Generated in the Shock Absorber for Conditions Similar to the Excitation Caused by Road Roughness" and "Kinematics and Dynamics of the Drum Cutting Units" have been supported by the Polish National Science Centre, MAESTRO 2, No. 2012/04/A/ST8/00738.

Łódź, Poland Jan Awrejcewicz

Contents

Bifurcation and Stability at Finite and Infinite Degrees of Freedom

Péter B. Béda

Abstract Conventionally problems of finite and infinite degrees of freedom (DOF) are separated in mechanics. The main reason is that different types of mathematical tools are used to study them. For finite DOF systems algebraic equations or systems of ordinary differential equations are used, while at infinite DOF cases vector and tensor fields and sets of partial differential equations should be used. However, the idea and main steps of stability analysis are the same. In both types of systems stability investigation can be done by calculating the spectrum of a linear operator. This operator is an algebraic operator (matrix) for finite DOF and a differential operator for infinite DOF. In nonlinear stability analysis a bifurcation equation should be derived. For finite DOF the general way is to use center manifold reduction while at infinite DOF Lyapunov–Schmit reduction should be performed. The paper aims to find unity in the dynamics of finite and infinite DOF systems. We show how the steps of stability investigation relate to each other in finite and infinite DOF cases. The presentation will explain how the linear operator can be defined and studied for continua, or how Lyapunov–Schmidt reduction can be used for studying oscillations of finite DOF systems.

1 Systems with Finite Degrees of Freedom

For systems with finite degrees of freedom like particles, systems of particles, rigid bodies, or systems of rigid bodies the equations of motion are systems of second order ordinary differential equations (ODE). We can use Newton's axioms or analytical mechanics, physical or general coordinates. For stability analysis such system is transformed into a system of first order ODEs

$$\dot{x} = f(x,t) \quad x \in R^n, t \in R \tag{1}$$

P.B. Béda (✉)
Department of Vehicle Elements and Vehicle-Structure Analysis, Budapest University of Technology and Economics, Műegyetem rkp. 3., Budapest H-1111, Hungary
e-mail: bedap@kme.bme.hu

© Springer International Publishing Switzerland 2016

J. Awrejcewicz (ed.), *Dynamical Systems: Theoretical and Experimental Analysis*, Springer Proceedings in Mathematics & Statistics 182, DOI 10.1007/978-3-319-42408-8_1

When the left hand side of (1) does not depend on time, a system of autonomous equations is obtained, like scleronom systems of analytical mechanics. Equilibrium can be found when

$$0 = f(x)$$

is solved to x. Let us denote such solution by x_0. Then by substituting $x = x_0 + y$ we have

$$F(y) = f(x(y)) \quad \text{and} \quad F(0) = 0.$$

The stability analysis of solution x_0 can be performed by studying the stability of the zero solution. Firstly, we should linearize

$$A = \left[\frac{\partial F}{\partial y_i}\right]_{y_i=0} \tag{2}$$

and study the eigenvalues of A. When zero is a hyperbolic equilibrium of A it is either stable or unstable depending on the real parts of the eigenvalues. When zero is non-hyperbolic we may find bifurcation. Generally, bifurcation analysis is done by using center manifold [1]. For a given non-hyperbolic equilibrium it is an invariant manifold of the considered differential equation which is tangent at the equilibrium point to the eigenspace of the neutrally stable eigenvalues. As the local dynamic behavior transverse to the center manifold is relatively simple, the potentially complicated asymptotic behaviors of the full system are captured by the flows restricted to the center manifolds. The combination of this theory with the normal form approach was used extensively to study parameterized dynamical systems exhibiting bifurcations. The center manifold provides, in this case, a means of systematically reducing the dimension of the state spaces which need to be considered when analyzing bifurcations of a given type. In fact, after determining the center manifold, the analysis of these parameterized dynamical systems is based only on the restriction of the original system on the center manifold whose stability properties are the same as the ones of the full order system.

In Hopf bifurcation center manifold has two dimensions and in bifurcation analysis is often approximated by its tangent plane. The a restriction to center manifold can be performed by a projection to this plane (see Fig. 1). This procedure results an approximate bifurcation equation, the study of which shows the sub- or supercritical nature.

In continuum mechanics the set of basic equations contain partial differential equations (PDE). There are three groups of equations: the equations of motion

$$\rho \dot{v} = \sigma \nabla, \quad \sigma = \sigma^T \tag{3}$$

the kinematic equation

$$\dot{\varepsilon} = \frac{1}{2}(v\nabla + \nabla v) \tag{4}$$

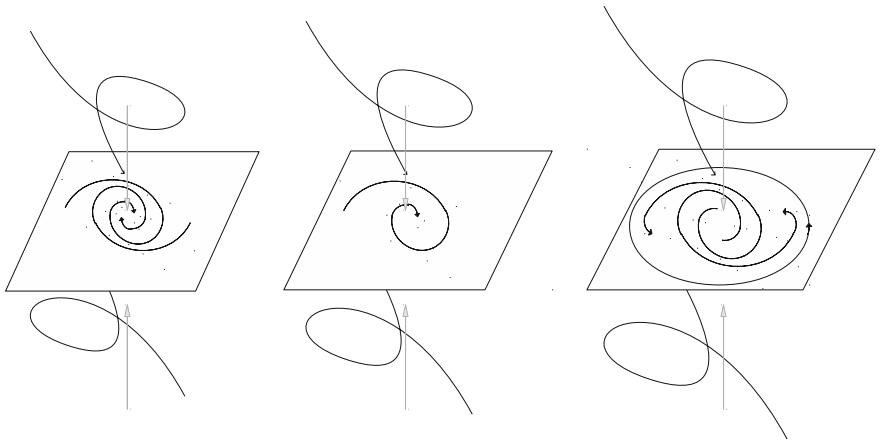

Fig. 1 Center manifold reduction at Hopf bifurcation

and the constitutive equation in a general form

$$g(\varepsilon, \sigma, \dot{\varepsilon}, \dot{\sigma}, \ldots) = 0. \tag{5}$$

All variables are tensor or vector fields like velocity vector v, stress σ, strain and strain rate tensors $\varepsilon, \dot{\varepsilon}$. In stability investigations we concentrate on a state of the solid body $v_0, \varepsilon_0, \sigma_0$, which is a fixed point of system (3)–(5). First, for the local study introduce small perturbations

$$\tilde{v} = v - v_0,\ \tilde{\varepsilon} = \varepsilon - \varepsilon_0,\ \tilde{\sigma} = \sigma - \sigma_0.$$

Then the constitutive equation should be linearized at $v_0, \varepsilon_0, \sigma_0$ to

$$\dot{\tilde{\sigma}} = -(g_4)^{-1} g_1 \tilde{\varepsilon} - (g_4)^{-1} g_2 \tilde{\sigma} - (g_4)^{-1} g_3 \dot{\tilde{\varepsilon}}, \tag{6}$$

where

$$g_1 = \left.\frac{\partial g}{\partial \varepsilon}\right|_{(v_0,\varepsilon_0,\sigma_0)}, g_2 = \left.\frac{\partial g}{\partial \sigma}\right|_{(v_0,\varepsilon_0,\sigma_0)}, g_3 = \left.\frac{\partial g}{\partial \dot{\varepsilon}}\right|_{(v_0,\varepsilon_0,\sigma_0)}, g_4 = \left.\frac{\partial g}{\partial \dot{\sigma}}\right|_{(v_0,\varepsilon_0,\sigma_0)}$$

and we assume that g_4 is invertible. Formally we define a dynamical system from (3)–(5) for the perturbation fields $\tilde{v}, \tilde{\varepsilon}, \tilde{\sigma}$. Equations (3) and (4) imply

$$\dot{\tilde{v}} = \frac{1}{\rho} \tilde{\sigma} \nabla, \tag{7}$$

$$\dot{\tilde{\varepsilon}} = \frac{1}{2} (\tilde{v} \nabla + \nabla \tilde{v}). \tag{8}$$

Introduce operator F acting on the perturbation field by

$$F(\tilde{v},\tilde{\varepsilon},\tilde{\sigma}) = \begin{pmatrix} \frac{1}{\rho}\tilde{\sigma}\nabla \\ \frac{1}{2}(\tilde{v}\nabla + \nabla\tilde{v}) \\ -(g_4)^{-1}g_1\tilde{\varepsilon} - (g_4)^{-1}g_2\tilde{\sigma} - (g_4)^{-1}g_3(\tilde{v}\nabla + \nabla\tilde{v}) \end{pmatrix}. \tag{9}$$

Then the dynamical system for local stability analysis reads

$$\frac{d}{dt}\begin{bmatrix} \tilde{v} \\ \tilde{\varepsilon} \\ \tilde{\sigma} \end{bmatrix} = F(\tilde{v},\tilde{\varepsilon},\tilde{\sigma}). \tag{10}$$

While $v_0, \varepsilon_0, \sigma_0$ is fixed point, $F(0,0,0) = 0$ and the stability analysis of such point can be performed by studying the spectrum of F. Now we should do the same as in previous part with operator (2), but instead of a linear algebraic operator A we have a differential operator (9) acting on the perturbation field $\tilde{v}, \tilde{\varepsilon}, \tilde{\sigma}$ satisfying appropriate boundary conditions.

2 Transformation to the Velocity Field

For the sake of simplicity operator F is transformed to the velocity field. Firstly, from (6) we have

$$\ddot{\tilde{\sigma}}\nabla = -(g_4)^{-1}g_1\ddot{\tilde{\varepsilon}}\nabla - (g_4)^{-1}g_2\dot{\tilde{\sigma}}\nabla - (g_4)^{-1}g_3\ddot{\tilde{\varepsilon}}\nabla \tag{11}$$

then from (7) we get

$$\rho\tilde{v}^{\cdots} = -(g_4)^{-1}g_1\frac{1}{2}(\tilde{v}\nabla + \nabla\tilde{v})\nabla - (g_4)^{-1}g_2\rho\ddot{\tilde{v}} - (g_4)^{-1}g_3\frac{1}{2}(\dot{\tilde{v}}\nabla + \nabla\dot{\tilde{v}})\nabla. \tag{12}$$

With simplifying notations for the linear operators

$$G^1\tilde{v} = -(g_4)^{-1}g_1\frac{1}{2\rho}(\tilde{v}\nabla + \nabla\tilde{v})\nabla,$$

$$G^2\dot{\tilde{v}} = -(g_4)^{-1}g_3\frac{1}{2\rho}(\dot{\tilde{v}}\nabla + \nabla\dot{\tilde{v}})\nabla,$$

$$G^3\ddot{\tilde{v}} = -(g_4)^{-1}g_2\frac{1}{2\rho}\ddot{\tilde{v}}$$

from (12) the system of basic equations for the perturbation velocity field reads

$$w^{\cdots} = G^1w + G^2\dot{w} + G^3\ddot{w}, \tag{13}$$

where $w = \tilde{v}$ is used for the perturbation velocity field. Formally, Eq. (13) can be transformed into a first order system

$$\begin{aligned} \dot{y}_\varphi &= y_\beta, \\ \dot{y}_\beta &= y_\psi, \\ \dot{y}_\psi &= G^1 y_\varphi + G^2 y_\beta + G^3 y_\psi \end{aligned} \tag{14}$$

in new variables

$$y_1 = w_1, \ldots, y_3 = w_3, y_4 = \dot{w}_1, \ldots, y_6 = \dot{w}_3 y_7 = \ddot{w}_1, \ldots, y_9 = \ddot{w}_3$$

and by using indices

$$\varphi = 1, 2, 3, \ \beta = 4, 5, 6, \ \psi = 7, 8, 9.$$

Now the operator defining stability properties reads

$$\hat{G}(y_\varphi, y_\beta, y_\psi) = (y_\beta, y_\psi, G^1 y_\varphi + G^2 y_\beta + G^3 y_\psi).$$

Operator $\hat{G}$ plays the role of algebraic operator A for stability analysis of systems with infinite degrees of freedom. When all the eigenvalues of it are on the left hand side of the complex plane, state $v_0, \varepsilon_0, \sigma_0$ is stable. When at least one of them has positive real part, it is unstable. To study the eigenvalue distribution we can look at the characteristic equation

$$\lambda^3 y_\varphi - \lambda^2 G^3 y_\varphi - \lambda G^2 y_\varphi - G^1 y_\varphi = 0. \tag{15}$$

State $v_0, \varepsilon_0, \sigma_0$ is stable, if for all solutions of (15) $\mathrm{Re}\lambda_i < 0$, $(i = 1, 2, 3, \ldots)$. A generic type of loss of stability happens, when either a single real eigenvalue (static bifurcation: SB) or a pair of conjugate complex eigenvalues (dynamic bifurcation: DB) crosses the imaginary axis of the complex plane:

SB: $\mathrm{Re}\lambda_k = 0$, for some k, or

DB: $\mathrm{Re}\lambda_{k1} = 0$ and $\mathrm{Re}\lambda_{k2} = 0$, where λ_{k1} and λ_{k2} are conjugate complex eigenvalues while for all the other eigenvalues $\mathrm{Re}\lambda_i < 0$.

For the two cases necessary conditions can easily be found. For a static bifurcation the existence of zero eigenvalue $\lambda_k = 0$ is required. From (15) the (SB) condition is

$$G^1 y_\varphi = 0. \tag{16}$$

At dynamic bifurcation the necessary condition is the existence of pure imaginary eigenvalues $\lambda_{k1} = i\omega$. Then from (15)

$$-\omega^2 G^3 y_\varphi - G^1 y_\varphi = 0,$$

thus the (DB) condition reads

$$G^3(G^2 y_\varphi) + G^1 y_\varphi = 0. \tag{17}$$

Both conditions (16) and (17) require to solve a boundary value problem for a system of partial differential equations and it is generally a quite complicated problem in itself. There is no much hope to find analytical results.

One possibility is to do numerical analysis, the other is to restrict the type of perturbations to the so-called periodic perturbation case. When periodic perturbations are used we assume that

$$y_\varphi = u(t) \exp\left(i \sum_{p=1}^{3} n_p x_p \right), \tag{18}$$

where n_p denote the coordinates of the unit normal vector and x_p are physical coordinates as usual. Functions (18) are harmonic and satisfy homogeneous boundary conditions. One important point is the presence of the unit normal vector. There are studies, which concentrate on the search for critical directions, where loss of stability happens. These works are published for determining shear band orientation at material instability problems [2, 3].

3 Lyapunov–Schmidt Reduction

At static bifurcations the number of the stationary solutions of a differential equation changes at quasi-static variation of the so called bifurcation parameter. Types of solutions of a differential equation, such as a fixed point, relative equilibrium, or a periodic orbit can be found by determining the zeros of an appropriate map F, like the one on the right hand side of (10). Then Lyapunov–Schmidt procedure should be applied. Such reduction results in the so-called bifurcation equations, a finite set of equations, equivalent to the original problem. In application of Lyapunov–Schmidt method for static bifurcation we start from an equation for a nonlinear mapping

$$G(u, \lambda) = 0$$

between two Hilbert spaces ($H \to K$). Assume that the linear part A of G is a so-called Fredholm operator, then $H = N(A) \oplus R(A^*)$, where $N(A)$ denotes the kernel of A and $R(A^*)$ denotes the range of its adjoint operator and $N(A)$ and $N(A^*)$ of finite dimensions. Now a projection P is introduced ($P : K \to R(A)$) to get two equations

$$\begin{aligned} PG(u, \lambda_c) &= 0, \\ (I - P)G(u, \lambda_c) &= 0, \end{aligned} \tag{19}$$

where I denotes identity operator. Then u is decomposed

$$u = u_c + u_s,$$

where $u_c \in N(A)$ and $u_s \in R(A^*)$ and is substituted into the first equation of (19)

$$PG(u_c + u_s, \lambda_c) = 0. \tag{20}$$

Because of the construction (20) can be solved to

$$u_s = h(u_c, \lambda_c).$$

When this solution is substituted into the second equation of (19) the bifurcation equation

$$(I - P)G(u_c + h(u_c, \lambda_c), \lambda_c) = 0 \tag{21}$$

is obtained. It is a set of $\dim N(A^*)$ equations for $\dim N(A)$ unknowns. For example in case of a self-adjoint operator with one dimensional nontrivial kernel (21) is a single equation for one variable and is created by projecting into the nontrivial kernel [4].

Lyapunov–Schmidt reduction is a very effective method to investigate the phenomenon of Hopf bifurcation, which concerns the birth of a periodic solution from an equilibrium solution through a local oscillatory instability. Here the equation under consideration includes time derivative. Instead of G

$$\frac{d}{dt}u + Lu$$

and its adjoint

$$-\frac{d}{dt}u + Lu$$

should be used, and the nontrivial kernel is of two dimensions [5].

4 Static Bifurcation Analysis for a Solid Continuum

In this part static bifurcation analysis of a stationary state will be performed. Then

$$\dot{y}_\varphi = \dot{y}_\beta = \dot{y}_\psi = 0.$$

Assume that nonlinear constitutive equation is selected and such nonlinearity results in (nonlinear) term $\hat{N}(y_\varphi, y_\psi)$. Now Eq. (14) implies

$$G^1 y_\varphi + N(y_\varphi) = 0. \tag{22}$$

Assume that operator G^1 depends on (loading) parameter μ and use notation G^1_μ. Additionally, we assume that at $\mu = 0$ operator undergoes a static bifurcation with a critical eigenvector y^0_φ, that is,

$$G^1_{\mu=0} y^0_\varphi = 0. \tag{23}$$

Define operator

$$\tilde{G}^1_\mu y_\varphi := G^1_\mu y_\varphi - G^1_{\mu=0} y_\varphi$$

for functions y^0. Then (22) has the form

$$(\tilde{G}^1_\mu + G^1_{\mu=0}) y_\varphi + N(y_\varphi) = 0. \tag{24}$$

In static bifurcation calculations the nontrivial solutions y^b_0 appearing in a sufficiently small neighborhood of state $v_0, \varepsilon_0, \sigma_0$ is searched for as

$$y_\varphi (= y^b_\varphi) = q y^0_\varphi,$$

where q is a small real number. When it is substituted into (24)

$$\tilde{G}^1_\mu y^0_\varphi + N(q y^0_\varphi) = 0 \tag{25}$$

is obtained, because of (21). Denote $\langle ., . \rangle$ the scalar product in the space of functions y_φ. Now (25) should be projected to function y^0_φ and then

$$q \langle y^0_\varphi, \tilde{G}^1_\mu y^0_\varphi \rangle + \langle y^0_\varphi, N(q y^0_\varphi) \rangle = 0 \tag{26}$$

results a nonlinear algebraic equation for q called the bifurcation equation. For $|q| \ll 1$ Eq. (26) can be approximated as its power series expansion at $q = 0$ and from its lowest order terms q can be expressed as a function of the bifurcation parameter μ

$$q = q(\mu). \tag{27}$$

In such a way in a small neighborhood of the bifurcation point the appearing nontrivial solution can be approximated as

$$y^b_\varphi = q(\mu) y^0_\varphi, \tag{28}$$

When stability of the bifurcated nontrivial solution is asked, nontrivial stationary state $v^b_0, \varepsilon^b_0, \sigma^b_0$ can be determined by using (28). Then its perturbations should be studied by substituting (28) into (14). The type of the bifurcation can be studied by using a bifurcation equation similar to (26).

5 A Uniaxial Example at Nonlinear Material

In uniaxial case all the variables v, ε, σ are scalar functions and the only coordinate is x. Then equation of motion is

$$\rho \dot{v} = \frac{\partial \sigma}{\partial x} \tag{29}$$

and the kinematic equation has the form

$$\dot{\varepsilon} = \frac{\partial v}{\partial x}. \tag{30}$$

Assume that the constitutive equation has the rate form [6]

$$\dot{\sigma} = c_1 \dot{\varepsilon} + c_2 \ddot{\varepsilon} - c_3 \frac{\partial^2 \dot{\varepsilon}}{\partial x^2} - c_3 \frac{\partial \dot{\varepsilon}}{\partial x} \dot{\varepsilon}, \tag{31}$$

where c_1, c_2, c_3, c_4 material parameters have piecewise positive constant values. Take the derivative of (31) with respect to x

$$\frac{\partial \dot{\sigma}}{\partial x} = c_1 \frac{\partial \dot{\varepsilon}}{\partial x} + c_2 \frac{\partial \ddot{\varepsilon}}{\partial x} - c_3 \frac{\partial^3 \dot{\varepsilon}}{\partial x^3} - c_4 \left(\frac{\partial^2 \dot{\varepsilon}}{\partial x^2} \dot{\varepsilon} + \frac{\partial \dot{\varepsilon}}{\partial x} \frac{\partial \dot{\varepsilon}}{\partial x} \right). \tag{32}$$

Equations (29)–(31) can be used to obtain an equation of motion for the velocity

$$\rho \ddot{v} = c_1 \frac{\partial^2 v}{\partial x^2} + c_2 \frac{\partial^2 \dot{v}}{\partial x^2} - c_3 \frac{\partial^4 v}{\partial x^4} - c_4 \left(\frac{\partial^3 v}{\partial x^3} \frac{\partial v}{\partial x} + \frac{\partial^2 v}{\partial x^2} \frac{\partial^2 v}{\partial x^2} \right). \tag{33}$$

Denote the state the stability of which is studied by (scalar) v^0. By adding small perturbation $\acute{v}$ for a local stability investigation $v = v^0 + \acute{v}$ should be substituted into (33)

$$\begin{aligned} \rho \ddot{v}^0 + \rho \ddot{\acute{v}} = c_1 \frac{\partial^2 v^0}{\partial x^2} + c_2 \frac{\partial^2 \dot{v}^0}{\partial x^2} - c_3 \frac{\partial^4 v^0}{\partial x^4} \\ - c_4 \left(\frac{\partial^3 v^0}{\partial x^3} \frac{\partial v^0}{\partial x} + \frac{\partial^2 v^0}{\partial x^2} \frac{\partial^2 v^0}{\partial x^2} \right) + c_1 \frac{\partial^2 \acute{v}}{\partial x^2} + c_2 \frac{\partial^2 \dot{\acute{v}}}{\partial x^2} \\ - c_3 \frac{\partial^4 \acute{v}}{\partial x^4} - c_4 \left(\frac{\partial^3 \acute{v}}{\partial x^3} \frac{\partial \acute{v}}{\partial x} + \frac{\partial^2 \acute{v}}{\partial x^2} \frac{\partial^2 \acute{v}}{\partial x^2} \right. \\ \left. + \frac{\partial^3 v^0}{\partial x^3} \frac{\partial \acute{v}}{\partial x} + \frac{\partial^3 \acute{v}}{\partial x^3} \frac{\partial v^0}{\partial x} + \frac{\partial^2 v^0}{\partial x^2} \frac{\partial^2 \acute{v}}{\partial x^2} \right). \end{aligned} \tag{34}$$

While v^0 is a solution of (33) and a homogeneous stationary state is studied

$$v^0 = 0, \quad \frac{\partial v^0}{\partial x} = 0, \ldots .$$

Equation (34) is simplified to

$$\rho\ddot{v} = c_1\frac{\partial^2 v}{\partial x^2} + c_2\frac{\partial^2 \dot{v}}{\partial x^2} - c_3\frac{\partial^4 v}{\partial x^4} - c_4\left(\frac{\partial^3 v}{\partial x^3}\frac{\partial v}{\partial x} + \frac{\partial^2 v}{\partial x^2}\frac{\partial^2 v}{\partial x^2}\right). \tag{35}$$

The linear part of (35) is

$$\rho\ddot{v} = \left(c_1\frac{\partial^2}{\partial x^2} - c_3\frac{\partial^4}{\partial x^4}\right)v + c_2\frac{\partial^2 \dot{v}}{\partial x^2}. \tag{36}$$

By using new variables $y_1 = v$ and $y_2 = \dot{v}$ (36) can be written into a system of two equations

$$\begin{aligned}\dot{y}_1 &= y_2,\\ \dot{y}_2 &= \left(c_1\frac{\partial^2}{\partial x^2} - c_3\frac{\partial^4}{\partial x^4}\right)y_1 + c_2\frac{\partial^2 y_2}{\partial x^2}.\end{aligned} \tag{37}$$

The characteristic equation of (37) is

$$\lambda^2 y_1 - \lambda\frac{c_2}{\rho}\frac{\partial^2}{\partial x^2}y_1 - \left(c_1\frac{\partial^2}{\partial x^2} - c_3\frac{\partial^4}{\partial x^4}\right)y_1 = 0.$$

For homogeneous boundary conditions at $x = 0$ and $x = \ell_0$ the eigenfunctions are

$$y_1 = \exp(i\alpha_k x),$$

where

$$\alpha_k = \frac{k\pi}{\ell_0}, \quad k = 1, 2, \ldots. \tag{38}$$

The eigenvalues are

$$\lambda_{k12} = \frac{-\frac{c_2}{\rho}\alpha_k^2 \pm \sqrt{\frac{c_2^2}{\rho^2}\alpha_k^4 - 4\alpha_k^2\left(\frac{c_3}{\rho}\alpha_k^2 + \frac{c_1}{\rho}\right)}}{2}.$$

When $c_2 > 0$ and $(c_3\alpha_k^2 + c_1) > 0$ state v^0 is stable. When

$$(c_3\alpha_k^2 + c_1) = 0, \tag{39}$$

there exists a zero eigenvalue, thus the system undergoes a static bifurcation. From (39) a critical α_{k*} can be defined

$$\alpha_{k*} = \sqrt{-\frac{c_1}{c_3}}. \tag{40}$$

In (40) c_1 denotes tangent stiffness of the stress–strain diagram of the standard tensile test. During the test its value starts from large positive number (the Young modulus) and decreases to negative values at the softening region. Looking at (38) and (40) we find that instability may appear in the softening region at $k = 1$, thus the critical value of α_{k*} appears at some c_{10} in the softening zone

$$\alpha_{kr} = \sqrt{-\frac{c_{10}}{c_3}} = \frac{\pi}{\ell_0},$$

where static bifurcation happens, and the critical eigenfunction to the 0 eigenvalue is

$$y_1 = \exp\left(ix\sqrt{-\frac{c_{10}}{c_3}}\right). \tag{41}$$

Let us introduce bifurcation parameter μ then in a small neighborhood of c_{10}

$$c_1 = c_{10} - \mu.$$

By substituting into (35) we have

$$\begin{aligned}\rho\ddot{v}^{\cdot} = &\left(c_{10}\frac{\partial^2}{\partial x^2} - c_3\frac{\partial^4}{\partial x^4}\right)v^{\cdot} - \mu\frac{\partial^2}{\partial x^2}v^{\cdot} \\ &+ c_2\frac{\partial^2\dot{v}^{\cdot}}{\partial x^2} - c_4\left(\frac{\partial^3 v^{\cdot}}{\partial x^3}\frac{\partial v^{\cdot}}{\partial x} + \left(\frac{\partial^2 v^{\cdot}}{\partial x^2}\right)^2\right).\end{aligned} \tag{42}$$

For static bifurcation we consider equilibrium solution. Then from (42)

$$\left(c_{10}\frac{\partial^2}{\partial x^2} - c_3\frac{\partial^4}{\partial x^4}\right)v^{\cdot} - \mu\frac{\partial^2}{\partial x^2}v^{\cdot} - c_4\left(\frac{\partial^3 v^{\cdot}}{\partial x^3}\frac{\partial v^{\cdot}}{\partial x} + \left(\frac{\partial^2 v^{\cdot}}{\partial x^2}\right)^2\right) = 0. \tag{43}$$

As we have seen before, the linear part of (43) is singular at $\mu = 0$ and the critical eigenvalues are (41). Then the real basic vector of the critical null space is

$$v'^0 := (y^0_{\varphi} =)\sin(\alpha_{kr}x).$$

By introducing real variable q, ($|q| \ll 1$) the bifurcated (nontrivial) solutions of (43) are searched for as

$$v'^b := (y^b_{\varphi} =)q\sin(\alpha_{kr}x). \tag{44}$$

When (44) is substituted into (43), the first term is zero and by projecting into the critical null space defined by eigenfunctions v'^0

$$g(q,\mu) = \int_0^{t_0} \left(-\mu \frac{\partial^2}{\partial x^2} q \sin(\alpha_{kr} x) - c_4 \left(\frac{\partial^3 q \sin(\alpha_{kr} x)}{\partial x^3} \frac{\partial q \sin(\alpha_{kr} x)}{\partial x} + \left(\frac{\partial^2 q \sin(\alpha_{kr} x)}{\partial x^2} \right)^2 \right) \sin(\alpha_{kr} x) \right) dx.$$

Having evaluated all of the integrals the approximate bifurcation function reads

$$g(q,\mu) = q \left(-\frac{\mu}{2} + \frac{2\pi}{3\ell_0^2} c_1 q \right),$$

thus instead of (43) we may use the bifurcation equation

$$q \left(-\frac{\mu}{2} + \frac{2\pi}{3\ell_0^2} c_4 q \right) = 0. \tag{45}$$

The solutions of (45) are: the trivial one $q \equiv 0$ and for nontrivial (bifurcated) solution

$$\frac{3\ell_0^2}{4\pi c_4}.$$

Here a transcritical bifurcation is detected (see Fig. 2).

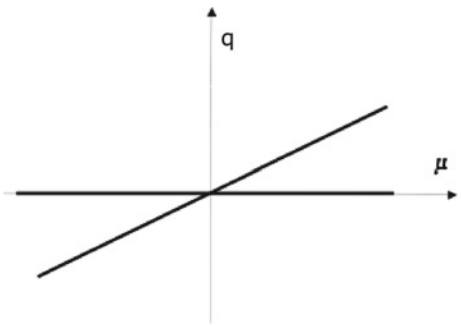

Fig. 2 Transcritical bifurcation diagram

6 Conclusions

In applications center manifold reduction is performed by a projection into a line or a plane for Hopf bifurcation of the Euclidian space depending on the dimension of the kernel of an algebraic operator. Quite similarly in Lyapunov–Schmidt method projection should be done for infinite DOF, but now Hilbert spaces and its subspaces are used. However, the dimension of the kernel plays similar role and low dimensional kernels result nice and simple expressions for bifurcation analysis.

References

1. Marsden, J.E., McCracken, M.: The Hopf Bifurcation and its Applications. Springer, New York (1976)
2. Szabó, L.: On the eigenvalues of the fourth-order constitutive tensor and loss of strong ellipticity in elastoplasticity. Int. J. of Plasticity, **13**, 809–835 (1997)
3. Rice, J.R.: The localization of plastic deformation. In: Koiter, W.T. (ed.) Theoretical and Applied Mechanics, pp. 207–220. North-Holland Publ. Amsterdam (1976)
4. Troger, H., Steindl, A.: Nonlinear Stability and Bifurcation Theory, An Introduction for Scientists and Engineers. Springer-Verlag, Wien, New York (1990)
5. Golubitsky, M., Schaeffer, D.G.: Singularities and Groups in Bifurcation Theory. Springer, New York (1985)
6. Zbib, H.M., Aifantis, E.C.: On the structure and width of shear bands in finite elastoplastic deformations. In: Anisotropy and Localization of Plastic Deformations, pp. 99–103. Elsevier, New York (1991)

Reduction of Low Frequency Acoustical Resonances Inside Bounded Space Using Eigenvalue Problem Solutions and Topology Optimization

Andrzej Błażejewski

Abstract The chapter deals with the problem of a space with an acoustical source, which forms a field of some values. All apply to an acoustic field characterized by an acoustic pressure p. In the low-frequency range and high values of boundary impedance, the modal approach is successfully applied. In this case, the field variation in all points of space is described by a specific time-dependent variable $w(t)$. The field shape is related to eigenfunctions $\Psi(r)$, which are the solution of the eigenvalue problem. Eventually, the acoustic pressure distribution $p(r, t)$ is defined by a sum over a set of a space's eigenfunctions $\Psi(r)$ and time components $w(t)$. Each $w(t)$ contains the source factor Q, which is an integral of the strength source multiplied by the related eigenfunction values in points where the source is located. Thereafter, if the integration is calculated over a region, where the value of the eigenfunction Ψ_m is zero, the source factor Q is zero as well. Considering the above, the aim of this research is to obtain the space where as many points as possible exist, where eigenfunction Ψ_m values are equal to zero, for as many eigenfrequency ω_m as possible. In order to find the specific configuration of the topology, an optimization problem is formulated. The eigenfunctions are considered as design variables. A minimum of multiobjective functions, based on eigenvalue problem solutions is searched. As the result of the optimization, the shape of space and point locations is obtained. The specified point is a possible source location, which guarantees reduction of resonances in a particular frequency range.

1 Introduction

This chapter deals with the problem of reduction of acoustic resonances that may occur when a source is placed inside the domain. This kind of problem appears in room acoustics, where locations of the source inside the enclosure are preferable, to avoid the situation when speech becomes unintelligible or unclear. In the case of devices, an improper location makes their work more oppressive. According to the

A. Błażejewski (✉)
Koszalin University of Technology, Śniadeckich 2, 75-453 Koszalin, Poland
e-mail: andrzej.blazejewski@tu.koszalin.pl

© Springer International Publishing Switzerland 2016

J. Awrejcewicz (ed.), *Dynamical Systems: Theoretical and Experimental Analysis*, Springer Proceedings in Mathematics & Statistics 182, DOI 10.1007/978-3-319-42408-8_2

aim of the room acoustics research, the best acoustic properties of the room are the most common problem in the area of interest [9]. Some works deal with the room size and determination of the room ratio, in particular, the optimal enclosure ratio and shape, which make rooms suitable for music listening or conference rooms audience friendly [19]. More generally, the rooms' shapes and irregularity influence reverberation time and time decay of particular modes, which is investigated in the works of [6, 8, 23]. The problem of the best geometry of the room, in order to create the best acoustic properties, is solved by Cox, D'Antonio, and Avis [4]. It is achieved by optimization methods exclusively for a simple enclosure at a low frequency. Another group of the investigations is generally focused on a modification of existing boundary conditions. In practice it is investigating a proper distribution of absorbing material in the room. Dühring, Jensen, and Sigmund designed the rooms by using topology optimization. Their work shows how to reduce a noise by choosing the best configuration of a reflecting material in the design domain without changing its size [5]. In their paper there is also the review of how other researchers achieve improvement of speech intelligibility by an absorbing material distribution in the room. This method reduces the amplitude response from the loudspeaker and time reverberation. The space/enclosure boundary modification by locating specific acoustic structures, in the form of resonators or wall shaping, is another method that can be applied to affect the acoustic field [27]. Boundary shaping and distributing reflecting and/or absorbing materials, together with optimization methods (i.e., topology optimization) are applied by other authors in the case of small devices design [10, 25]. The values that describe the acoustic field are considered separately in the area of interest. The first is acoustic pressure, as the scalar value is commonly used. Because of the ease measurements of sound pressure, this quantity is suitable in many cases. The intensity is the vector quantity which is more complicated to measure [22], but gives the energetic assessment of the acoustic problem. Pan analyzes the enclosed spaces from the energetic point of view and modal approach [16–18]. These works show that intensity prediction by using the mode model needs mode coupling consideration. At the same time in their work, Franzoni and Bliss [7], show this problem. Simultaneously, the existence of the intensity vortices and a set of vortex modes with eigenfrequencies, which form a harmonic series, predicted by Waterhouse [26], are confirmed. The numerical studies based on the mode model, which is presented by Meissner, show those properties of the intensity field [11]. In this work, the active and reactive components of intensity inside an L-shaped room are investigated. His previous and following works [13] indicate that vortices of active intensity are strongly related to zeros of eigenfunctions. This feature is applied in this chapter as a criterion of resonance reduction, which appears in closed space. In the case of optimization, or generally in a control of the acoustic field inside an enclosure, many factors should be considered, including area of boundaries, their configuration, location, the acoustic properties of the cover materials, and sound/noise source position. Genetic algorithms (GAs) successfully calculate the minimum of objective functions, considering a large number of design variables, such as room surfaces with their acoustic impedance [2, 3]. The authors show how to minimize the level of acoustic pressure inside the whole enclosure, using properties of modal amplitudes (time components

in modal expansion in steady states of an acoustic pressure) by applying a specific configuration of a boundary condition. The configuration is found without changing the size of the enclosure. This chapter deals with the problem of reduction, or more generally control, of the acoustic field. It is realized considering two aspects. On the one hand the source, which is located inside the domain on the specific location, may generate lower values of acoustic pressure than sources that occupy other places. However, those areas are dependent on the domain shape. Those features are introduced in the optimization criteria.

2 The Modal Approach to Acoustic Field Description in a Bounded Space

An acoustic field in an enclosure is a specific case of acoustic wave propagation. The sound source generates an acoustic signal, which is usually partly absorbed and reflected by boundaries. If the source is permanently active the acoustic energy absorbed on the boundaries is equalized in the short term by the energy from the source. After the transient period, the steady-state acoustic field dominating in an enclosure is attained. In order to describe the acoustic field distribution inside a room, the modal approach can be applied under several restrictions [15]. One of them is a low-frequency range of signals generated by a source, which is limited by the Schroeder frequency [20, 21]. This kind of signal guarantees the sparsely distributed acoustic modes, and in the case of high impedance on boundaries, mode uncoupling can be applied. The modal approach assumes that the acoustic field distribution inside an enclosure is dependent on its normal modes (eigenfunctions). The modes are obtained by the solution of the Helmholtz equation for a domain bounded by perfectly rigid walls. It is defined by Neumann's boundary condition equal to zero. After that, eigenfunctions $\Psi_m(r)$, in all enclosure points with coordinates $r(x, y, z)$, together with eigenfrequencies ω_m are determined. Applying eigenfunction $\Psi_m(r)$ in the modal expansion leads to the sum in the form:

$$p(r,t) = \sum_{m=0}^{\infty} w_m(t)\Psi_m(r), \tag{1}$$

where orthogonality and normalization of eigenfunctions are required [12]. Additionally, low frequencies and a narrow band of excitation allow reducing an infinite sum to a finite number N of factors. The first factor in modal expansion, the time components $w(t)$, describe acoustic pressure variation in time, during increasing and decreasing sound, when a source starts and becomes mute. In a steady-state field condition, $w(t)$ represents the magnitude of acoustic pressure in a particular point of the domain. If the sum 1 describes the acoustic field inside the room with a source, it satisfies the linear, inhomogeneous wave equation and the specific boundary conditions. Most often, the conditions are determined by the acoustic impedance. Modal expansion is introduced in the following wave equation [14],

$$-\nabla^2 p(r,t) + \frac{1}{c^2}\frac{\partial^2 p(r,t)}{\partial t^2} = f(r,t), \tag{2}$$

where c is the sound velocity in air and function f defines the source power or outflow. Both the function, $p(r,t)$, and each eigenfunction $\Psi_n(r)$, satisfy the Green theorem. Finally it leads to the solution represented by a set of ordinary differential equations of time components $w_n(t)$. Denoting upper dots as time derivates and omitting independent variables r and t, the equations take the form:

$$\ddot{w}_n + \omega_n w_n + (\rho c^2 \int_S \frac{\Psi_n^2}{Z} dS)\dot{w}_n = -\frac{c^2}{\sqrt{V}} \int_V f \Psi_n dV. \tag{3}$$

Equation 3 shows a form of a second-order linear differential equation with constant coefficients, in the case where the mod coupling is neglected. Coefficient ρ represents a density of medium inside the volume V, bounded by surface S characterized by acoustic impedance Z. The general solutions are presented in [1]. If a source is harmonic and described by the function f in the form $f = q(r)e^{j\omega t}$, the solutions can be obtained after some algebraic calculations. The amplitude of harmonic time components $w_n(t)$ is given by formulae:

$$w_{n\omega} = \frac{Q_n}{(\omega_n^2 - \omega^2) + 2j\alpha_n\omega} \quad \text{and} \quad w_{0\omega} = -\frac{Q_0}{2j\alpha_0\omega - \omega^2}, \tag{4}$$

where index $n\omega$ means a solution for a particular frequency, 0ω a time component, which is the solution of Eq. 3 in the case $\omega_n = 0$; that is, eigenvalue $\lambda_n = \sqrt{\frac{\omega_n^2}{c^2}} = 0$. The coefficients α and Q are defined by the integrals:

$$\alpha_n = \frac{1}{2}\rho c^2 \int_S \frac{\Psi_n^2}{Z} dS \quad \text{and} \quad Q_n = -\frac{c^2}{\sqrt{V}} \int_V q \Psi_n dV, \tag{5}$$

Generally coefficients α and $Q5$ are described in Eq. 3: damping in the system caused by the impedance Z of the boundaries S and a source component. The source component in each equation is an integral of a specific eigenfunction multiplied by a source magnitude $q(r)$ in points, where the source is located. Outside the source location the integral becomes zero. If eigenfunction Ψ_n in the source location has values close to zero, the whole source component in Eq. 5 and consequently related time component $w_{n\omega}$ in Eq. 4 have minimal absolute values. Moreover, in the case of harmonic source, the time components for eigenfrequencies ω_n, significantly different from ω, tend to zero. Consequently, the solution of the wave equation 2 in the form of sum 1, which contains time components 4, gets minimum.

Therefore, the question arises about a space geometry configuration with the interior region, where an active source without regard for damping in the acoustic system and the strength of a source guarantee minimal values of acoustic pressure for particular frequencies.

3 Optimization Problem

In view of these aspects, the optimization problem is formulated. The result of the optimization is a shape of the enclosure and the interior area, where points of eigenfunctions with value equal to zero or close to zero are located. In the case of arbitrary shapes of the enclosure those points are in different locations for different eigenfunctions. There are shapes of closed spaces that own this feature. One of them is a circle in a two-dimensional or sphere in a three-dimensional domain. In their centers are the points, where many eigenfunctions have zero values. Therefore, the enclosure is searched among N different shapes of different k dimensions. These dimensions are considered as design variables, called X_k and $k \in \mathcal{N}_1$. Each set of design variables $\{X_k\}$ is related to a set of eigenfunctions of the exact shape of the enclosure. Thereby, some following set $\{\Psi_0, \Psi_1, \Psi_2, \ldots \Psi_n, \ldots \Psi_m\}_N \equiv \{\Psi_n\}_N \equiv \{X_k\}_N$ of potential solutions is considered, where m represents the limit of the number of following functions considered for each shape. The expected solution is the enclosure, where many zero points are located, as close to each other as possible. It means that two configurations are possible: first, when the zero points for eigenfunctions coincide with others and create one spot, and second, when the zero points for some eigenfunctions overlie an area of enclosure. There are three criteria $C1$, $C2$, and $C3$ that express the above cases:

$$C1 = \left| r_i^* | \Psi_n(r_i^*) = 0, n \in \langle 0, m \rangle \in \mathcal{N}_0, i \in \mathcal{N}_1 \right| \rightarrow max \tag{6}$$

$$C2 = \left| \omega_n^* | \Psi_n(r_j^*) = 0, n \in \langle 0, m \rangle \in \mathcal{N}_0, j \in \mathcal{N}_1 \right| \rightarrow max \tag{7}$$

$$C3 = \sum_{i=1}^{C_1} \sqrt{r_0 - r_i^*} \rightarrow min \tag{8}$$

In Eq. 8 r_0 is a coordinate of an assumed source location inside the enclosure. In the case of an arbitrary enclosure, some eigenfunctions are possible that have very small values (but with not many zero points) in the whole space, whereas others are characterized by significant variation from negatives to positives. The first are preferable in the case of reduction of acoustic pressure. Therefore, it is a suitable approach to look for not zeros but some minimal values. It is proposed to concern 1 % of the mean of all absolute values of all eigenfunctions in the considered range $\langle 0, N \rangle$ as a reference, instead of zero. It generates modification in (6) and (7) $\Psi_n(r_{i,j}) = 0.01 \cdot mean(\{\Psi_n\}_N)$. On the basis of the criteria the multicriteria objective function (F_{obj}) is created in the form:

$$\min_{\{\Psi_n\}_N} F_{obj}(\{\Psi_n\}_N) = [-C1, -C2, C3]^T \tag{9}$$
$$subject \quad to:$$
$$\wedge \quad X_{1min} < X_1 < X_{1max}$$
$$\wedge \quad \cdots$$
$$\wedge \quad X_{kmin} < X_k < X_{kmax}$$

3.1 Solution for an Example 2D Problem

The genetic algorithm is implemented in order to find solutions. The GA uses procedures of nondominated selection of solutions, so-called Pareto solutions. During the selection, which process repeats iteratively, the fitness values of F_{obj} are calculated. The fitness values determine the potential solutions. In each iteration, the chosen set of solutions, in a so-called Pareto set, is compared by GA and nondominated individuals are chosen. Here, the fitness values are calculated, using the modified criteria $C1$ and $C2$, which are taken as negatives and values of criterion $C3$ is taken directly, bearing in mind that GA searches the minimum. As an example the shape represented by a two-dimensional object shown in Fig. 1 is optimized. The optimized object is created as a union of three squares (the big one and two small on the sides) and a circle. The four characteristic dimensions, which vary during the optimization, are indicated as design variables X_k defining $\{\Psi_n\}_N$. There are: X_1, side of the big square; X_2, X_3, sides of the small squares; and X_4, radius of the circle. The constraints are defined as $X_{1min} = 10$, $X_{1max} = 12$, $X_{2min} = 5$, $X_{2max} = 6$, $X_{3min} = 5$, $X_{3max} = 6$, $X_{4min} = 4$, and $X_{4max} = 6$. Additionally, the point indicated in criterion $C3$ with coordinates $r_0(0, 0)$ is chosen. Two shapes determined by dimensions related to optimization constraints, the solutions, that is, the points distributed

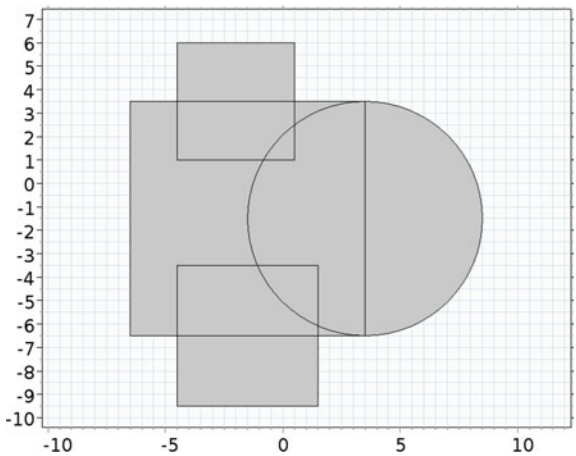

Fig. 1 The design variables: X_1—side of the big *square*, X_2, X_3—sides of the smalls *squares* and X_4—radius of the *circle*

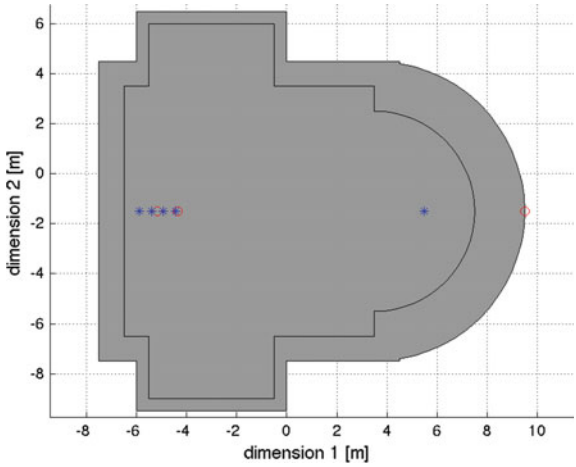

Fig. 2 Points distribution inside examined object in the case of design variable $\{X_k max\}$ and criteria values $C1 = -3, C2 = -48, C3 = 19.5902$ (*circles* o), and criteria values $C1 = -5, C2 = -47, C3 = 27.2038$ (*asterisks* $*$)

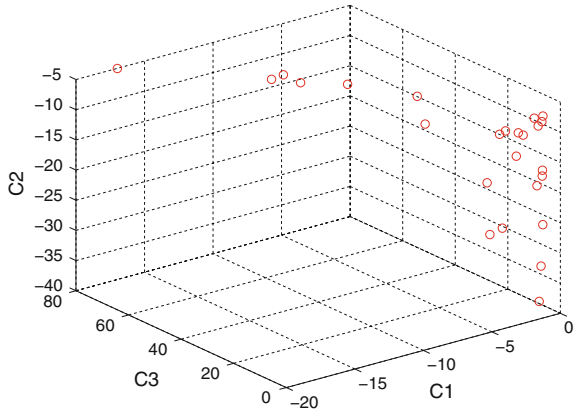

Fig. 3 Pareto optimal solutions found by genetic algorithm in case of 10 Iteration for 30 Individuals in Pareto set

inside the objects, satisfying modified criteria values, are shown in Fig. 2. It seen in this figure, that in both cases the points are located far from point r_0. As mentioned in the previous section, these points can be considered as the area, where a located sound source shall be damped in the range of frequencies $\omega \to \omega_n^*$. The GA after 10 iterations, during each of them comparing the Pareto set $N = 30$ indicates Pareto optimal solutions shown in Fig. 3. Values of criteria are shown on the proper axes. These points lie on a 2-dimensional hyperplane in 3-dimensional criteria space. These three criteria, according to Eq. 9, are related to a set of design variables X_k, which describe a particular space. In order to give the background for the general optimization solution, in Figs. 4, 5 and 6 some of the chosen spaces related to the specific criteria values from an optimal set are shown. In the Fig. 4 there is a space, where at the point shown is the place where an emitted signal is strongly damped for 17 frequencies equal to proper eigenfrequecies. Figure 5 indicates the space with the closest point to the point $(0, 0)$. But at this point the number of damped frequen-

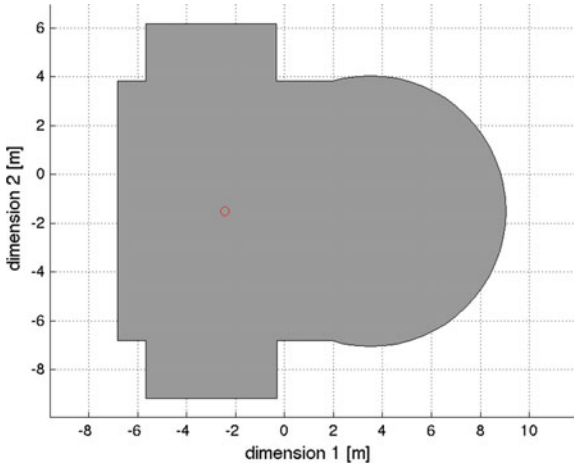

Fig. 4 The space related to the optimal solution found in the case of minimal value of criterion $C2 = -17$ ($C1 = -1; C3 = 2.8774$). The *circle* o, indicates the point, where 17 different frequencies are damped

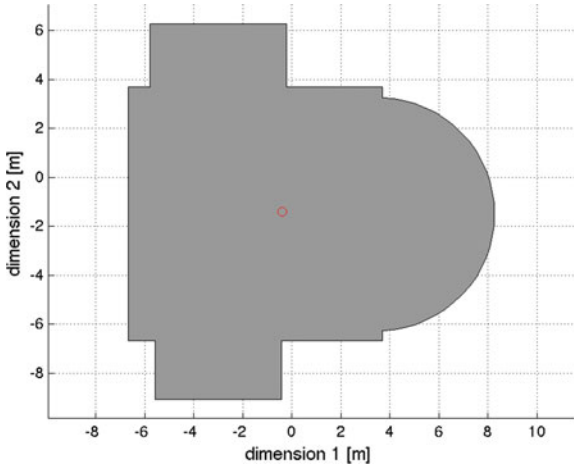

Fig. 5 The space related to the optimal solution found in the case of minimal value of criterion $C3 = 1.4954$ ($C1 = -1; C2 = -7$). The *circle* o, indicates the point the closest to point (0, 0) where 7 different frequencies are damped

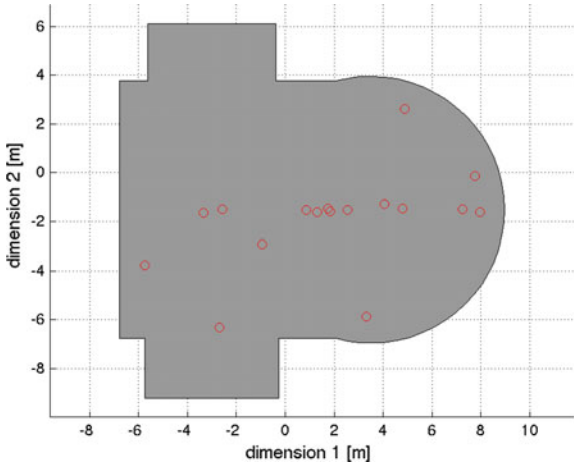

Fig. 6 The space related to the optimal solution found in the case of minimal value of criterion $C1 = -38$ ($C2 = -1; C3 = 79.9091$). The *circles* o, indicate the points where only one frequency is damped

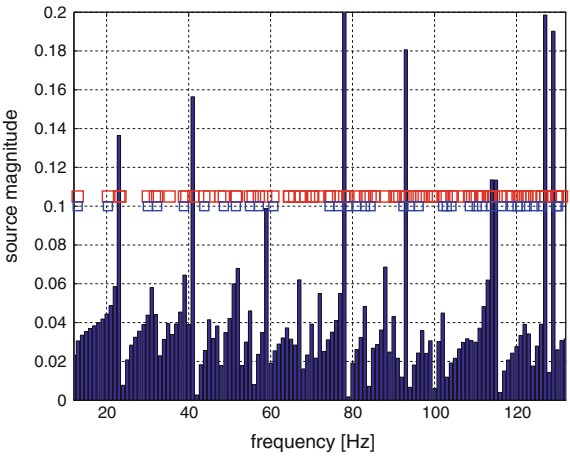

Fig. 7 The magnitude of the source at the point, found by optimization. *Red square* symbols indicate eigenfrequencies of the space. *Blue square* symbols indicate the eignfrequencies, which does not excite resonance, for the source at this point

cies equals 7. Subsequently Fig. 6 presents the space with the maximal number of points, which are found and fulfill the optimization criteria. Thirty-eight points are indicated, where only one frequency is damped.

4 Conlusions

The results presented are related to the work by [11, 13] that deals with the problem from energetic aspects. It is stated there that the vortex of acoustic intensity is characterized by zero pressure at its center. The null pressure is reached when all eigenfunctions get a zero value at the vortex center: the completely reduced acoustic pressure is in the case when all eigenfunctions get zero values in a particular point. As was stated, it is nearly impossible in reality. Therefore, the optimal solution is search and it is stated that it is possible to find the space where there are the point(s) which guarantee that the source located at these point(s) does not excite the acoustic resonance in the chosen frequency range. The field is generated by the point sound source, which by the pressure or volume impact of some magnitude influences the acoustic field. The character of the created field is well described when the modal approach is used to solve the problem in a low-frequency range and weak sound damping. The modal amplitudes (time components) can be reduced or "literally vanished" if the sound source is located in a proper point(s) inside the space. The example shows how to find the maximal field reduction for a specific source location, by "optimal shaping" the space. In this case two main approaches can be distinguished to gain a limited area with points, where the sound source is damped in a wide frequency range or many points, where the source with small dimension is damped at many possible locations, but in a narrow frequency range for each. This feature is shown for the analyzed example space. At some point, found by using optimization, the source is

damped in a significant way. The simulation data in Fig. 7 illustrate this property. The square red symbols in this figure indicate eigenfrequencies of this space. The harmonic source of these or very close frequencies may excite acoustic resonance. Square blue symbols indicate the eigenfrequencies that do not excite resonances for the source at this point.

References

1. Błażejewski A.: Modal approach application and significance analysis inside bounded space in a steady state acoustic field condition. International Journal of Dynamics and Control **3** 50–57 (2015)
2. Błażejewski, A. Krzyżyński, T.: Application of genetic algorithms in multi-objective optimization in room acoustics. Logistyka **6**, 281–289 (2010)
3. Błażejewski, A. Krzyżyński, T.: Multi-objective optimization of the acoustic impedance distribution for room steady state sound field condition. in: Cempel C., Dobry W. (eds.) Vibration in Physical Systems 24 pp. 57–62 (2010)
4. Cox, T.J. D'Antonio, P. A. M.: Room sizing and optimization at low frequencies. Journal of the Audio Engineering Society **52(6)**, 640–651 (2004)
5. Dühring, M.B. Jensen, J. S. Sigmund O.: Acoustic design by topology optimization. Journal of Sound and Vibration **317**, 557–575 (2008)
6. Easwaran V, Craggs, A.: An application of acoustic finite element models to finding the reverberation times of irregular rooms. Acta Acustica united with Acustica **82**, 54–64 (1996)
7. Franzoni, L.P. Bliss, D.: A discussion of modal uncoupling and an approximate closed-formsolution for weakly coupled systems with application to acoustics. Journal of the Acoustical Society of America **103**, 1923–1932 (1998)
8. Gerretsen, E.: Estimation methods for sound levels and reverberation time in a room with irregular shape or absorption distribution. Acta Acustica united with Acustica **92**, 797–806 (2006)
9. Kutruff, H.: *Room Acoustics, fifth edition*. Taylor & Francis Group, New York (2009)
10. Luo, J. Gea, H. Optimal stiffener design for interior sound reduction using a topology optimization based approach. Journal of Vibration and Acoustics **125**, 267–273 (2003)
11. Meissner, M.: Analytical and numerical study of acoustic intensity field in irregularly shaped room. Applied Acoustics **74**, 661–668 (2013)
12. Meissner, M.: Influence of wall absorption on low-frequency dependence of reverberation time in room of irregular shape. Applied Acoustics **69**, 583–590 (2008)
13. Meissner, M.: Numerical investigation of acoustic field in enclosures: Evaluation of active and reactive components of sound intensity. Journal of Sound and Vibration **338**, 154–168 (2015)
14. Morse, P.M., B. R. Sound waves in rooms. Reviews of Modern Physics **16**, 69–150 (1994)
15. Morse, P.M., I. K.: Theoretical acoustics. Mc Graw-Hill, New York (1968)
16. Pan, J.: A note on the prediction of sound intensity. Journal of the Acoustical Society of America **93**, 1641–1644 (1993)
17. Pan, J.: A second note on the prediction of sound intensity. Journal of the Acoustical Society of America **97**, 691–694 (1995)
18. Pan, J.: A third note on the prediction of sound intensity. Journal of the Acoustical Society of America **105**, 560–562 (1999)
19. Rayna, A.L. Sancho, J.: Technical note: the influence of a room shape on speech intelligibility in rooms with varying ambient noise levels. Noise Control Engineering Journal **31**, 173–179 (1988)
20. Schroeder, M.: Reverberation: Theory and measurement. Journal of the Acoustical Society of America. Proceedings Wallace Clement Sabine Centennial Symposium (1994)

21. Schroeder, M.: The ,, Schroeder frequency" revisited. Journal of the Acoustical Society of America **99(5)**, 3240–3241 (1996)
22. Schultz, T.J. Smith, P. M. Malme, C.I.: Measurement of acoustic intensity in reactive sound field. Journal of the Acoustical Society of America **57** 1263–1268 (1975)
23. Sum, K. Pan, J.: Geometrical perturbation of an inclined wall on decay times of acoustic modes in a trapezoidal cavity with an impedance surface. Journal of the Acoustical Society of America **120**, 3730–3743 (2006)
24. Vito, A.: Thesis title Thesis title Thesis title Thesis title Thesis title. PhD thesis, University/School. A sentence about the Supervisor (2015)
25. Wadbro, E. Berggren, M.: Topology optimization of an acoustic horn. Computer Methods in Applied Mechanics and Engineering **196** 420–436 (2006)
26. Waterhouse, R.: Vortex modes in rooms. Journal of the Acoustical Society of America **82**, 1782–1791 (1987)
27. Zhu, X. Zhu, Z. C. Cheng, J.: Using optimized surface modifications to improve low frequency response in a room. Applied Acoustics **65**, 841–860 (2004)

Analysis of the Macro Fiber Composite Characteristics for Energy Harvesting Efficiency

Marek Borowiec, Marcin Bocheński, Jarosław Gawryluk and Michał Augustyniak

Abstract In recent years the energy harvesting has a wide development, especially due to increasing demand on the self-powered devices. The research of converting mechanical energy into suitable electrical is intensity develop. The efficiency of energy harvesting systems is usually as crucial purpose of many works. It depends on various input condition parameters. One of them is a load resistance of an electrical subsystem. A loaded piezoelectric by resistor has a significant influence on the dynamics of the mechanical system. It provides optimization of an output electric power, especially while mechanical system vibrating in resonance zone. In present paper the composite cantilever beam is analysed, with attached the piezoelectric Macro Fiber Composite actuator (M-8503-P1). The applied beam consists of ten prepreg M12 layers, oriented to the beam length in accordance with $[+45/-45/+45/-45/0]_S$. The influence of different load resistances on the system response is reported by both the output beam amplitude—frequency and output power—frequency characteristics of the piezoelectric actuator. The goal of the work is maximising the root mean square of output electrical power and comparison the system behaviours at optimised load resistance levels, while vibrating at resonance zones. The results are simulated by finite element method and also validated by experimental tests.

M. Borowiec (✉) · M. Bocheński · J. Gawryluk
Department of Applied Mechanics, Lublin University of Technology,
Nadbystrzycka 36 St., 20-618 Lublin, Poland
e-mail: m.borowiec@pollub.pl

M. Bocheński
e-mail: m.bochenski@pollub.pl

J. Gawryluk
e-mail: j.gawryluk@pollub.pl

M. Augustyniak
Faculty of Electrical Engineering and Computer Science,
Department of Electrical Drive Systems and Machines, Lublin University of Technology,
Nadbystrzycka 38A St., 20-618 Lublin, Poland
e-mail: michal.augustyniak@induster.com.pl

© Springer International Publishing Switzerland 2016

J. Awrejcewicz (ed.), *Dynamical Systems: Theoretical and Experimental Analysis*, Springer Proceedings in Mathematics & Statistics 182, DOI 10.1007/978-3-319-42408-8_3

1 Introduction

The self-powered microsystems become more popular in many applications, this entails efforts in field of energy harvesting investigation. In field of wireless sensors, watches, biomedical implants or military monitoring devices it is many new challenges [1–3]. Additionally, the small devices are able to powering by an ambient vibration sources [4, 5]. Unfortunately, an expecting energy harvesting efficiency appears around the damaging resonance zones. A challenge is to find a way of avoiding the harmful conditions by simultaneously broaden smooth a resonance response out, in the literature there are papers reporting the way of such problems [6, 7]. The mechanical stiffness of the system has a crucial influence on the system behaviour. In the papers [8–10] are considered such problems, where a piezoelement plays a role of controller's actuator for composite beam system.

In the present paper, in the Sect. 2 the modelling of *MFC* composite has been described in the finite element method environment. The numerical analysis approaches has been provided in Sect. 3, where the response of the beam system are reported for loaded (shorted) and unloaded (open) of piezoelement. In Sects. 4 and 5 the experimental validation of the numerical results have been developed. For keeping the system around the excitation in resonance vibration zones, simultaneously save it by damaging the beam composite with appropriate elasticity was selected. This permitted to focused the tests on searching the optimal load resistances for the sake of maximal output power. Finally in Sect. 6 the conclusions of numerical model validation and the energy harvesting efficiency of the system in the experiment have been reported.

2 Numerical Model

For modelling the *MFC* element at the first step of numerical approach, the finite element model of piezoelectric actuator has been assumed and prepared. In this study the parameters of Macro Fiber Composite (*MFC*) M-8514-P1 has been applied. This is a piezoelectric actuator of d_{33} effect type. The numerical simulations were performed with the commercial system Abaqus, where the phenomena of electromechanical coupling in technical cases were modelled. The active element has been modelled in Abaqus package by the type of solid continuum elements C3D20RE, i.e. 20-nodal second order elements with reduced integration. It has three translational degrees of freedom at each node and one extra degree of freedom associated with the piezoelectric properties. Numerical model of the *MFC* element has been verified by two tests given in manufacturer's documentation—free strain tests and blocking force test. More information of modelling the piezoelectric elements by means of supplementary orthotropic bodies is presented in the paper [11]. A very good compatibility between numerical results and characteristic as given by manufacturer was obtained. A verified piezoelectric coefficient $d_{33} = 91 \times 10^{-9}$ m/V has been used in simulations.

The combination of composite beam with the piezoelectric element was realized by defining interactions as "TIE", it resulted in linking the degrees of freedom of nodes in contact on the appropriate surfaces of the model. The finite element model of the structure is presented in Fig. 1.

The finite element model of the composite beam has been made using continuum shell finite elements *SC*8*R* with reduced integration. The applied beam consisted of ten glass-epoxy unidirectional composite prepreg TVR 380 600 M12 26 % R-glass material layers with thickness 0.255 mm oriented to the beam length in accordance with $[+45/-45/+45/-45/0]_S$. Individual layers of the laminate has been made according to Layup-ply technique, and is presented in Fig. 2. The mechanical boundary conditions of the numerical model were realized at the first beam edge by restraining nodes fixed two translational (x and y) and one rotational degrees of freedom. The kinematic excitation was assumed in vertical z direction. Numerical model of the beam has been defined as a lamina type one. In numerical simulations the following data provided by the manufacturer of the composite have been used: tensile moduli $E_1 = 56$ GPa, $E_2 = 16$ GPa, shear moduli $G_{12} = 4.05$ GPa,

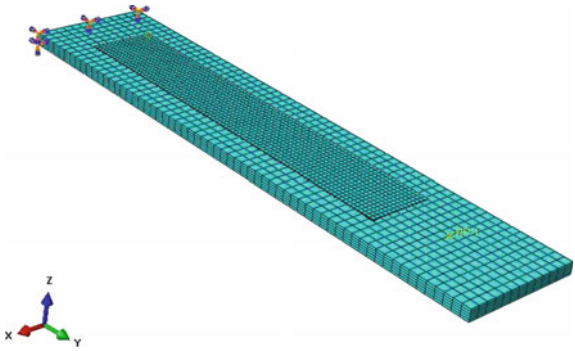

Fig. 1 The *FEM* model of the analysed object

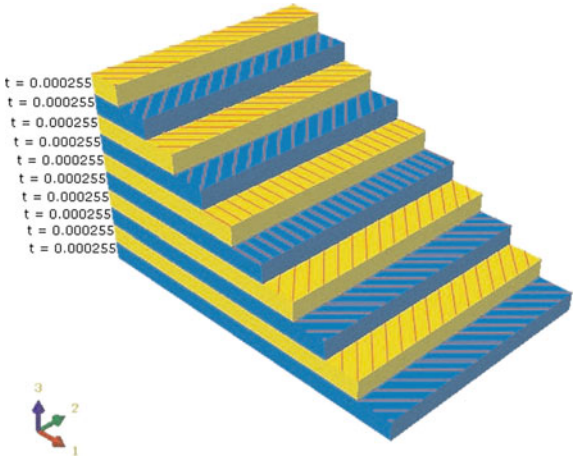

Fig. 2 Composite stacking sequence: $[+45/-45/+45/-45/0]_S$

$G_{13} = G_{23} = 4\,\text{GPa}$, Poisson's ratio $v_{12} = 0.4$ and density $\rho = 2038\,\text{kg/m}^3$. Elastic and ferroelectric properties of piezoelectric element was taken from the manufacturer catalogue: Young's moduli $E_1 = E_2 = 15.857\,\text{GPa}$, $E_3 = 30.336\,\text{GPa}$, Kirchhoff's moduli $G_{12} = G_{13} = G_{23} = 5.515\,\text{GPa}$ and Poisson's ratios $v_{12} = v_{13} = v_{23} = 0.31$, density $\rho = 5440\,\text{kg/m}^3$ and dielectric constant $\xi = 8 \times 10^{-9}\,\text{F/m}$.

3 FEM Analysis and Results

In this section the modal analysis has been reported. In the finite element method simulations the Lanczos algorithm [12] was used in order to determine the natural frequencies and corresponding modes of free vibrations for two load cases. The first one was an open system, where on the one surface the applied voltages potential equalled 0 V but other surface had no applied voltage potential (it corresponds $R = \infty$). The next was a shorted system, where on both surfaces of the *MCF* element the applied potential equalled 0 V (it corresponds $R = 0$). The first two bending modes are taken into consideration. The determined mode shapes are shown in Fig. 3a, b.

The natural frequencies for both cases was presented in Table 1. Comparison of the results showed that for the open system and the shorted one, the increase in natural frequencies was very small, about 4 %. In order to determine the piezoelectric effect of the beam with *MFC*, dynamical analysis was performed. In the finite element method (*FEM*) simulations, the steady-state approach method was used [11]. The influence of opened and shorted piezoelement on the dynamic response was shown in Fig. 4a, b for the first and the second resonance zone, respectively. Comparing the system responses at shorted electrical circuit ($R = 0$) and at open one ($R = \infty$), it is visible simultaneously the resonance point moved to the left as well as a reducing the vibration amplitudes. Such behaviour of the system reveals the

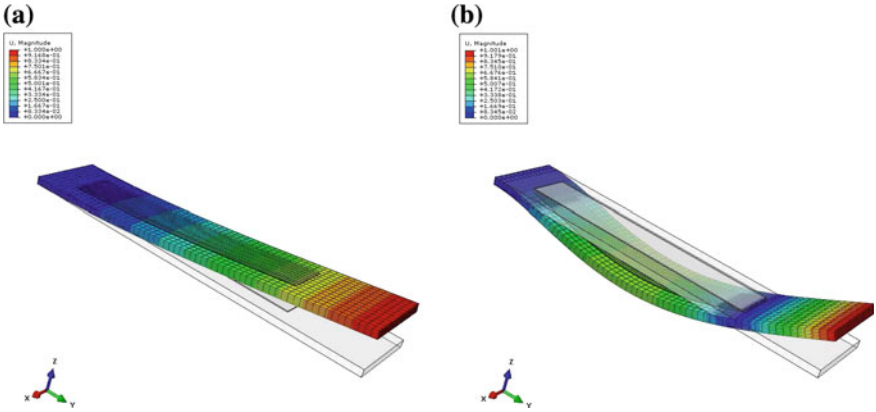

Fig. 3 The first (**a**) and the second (**b**) bending natural mode shapes

Table 1 Natural frequencies from numerical analysis

Mode	Frequency (Hz) at $R = 0$	Frequency (Hz) at $R = \infty$	Difference (%)
1	80.97	84.5	4.18
2	508.85	533.79	4.67

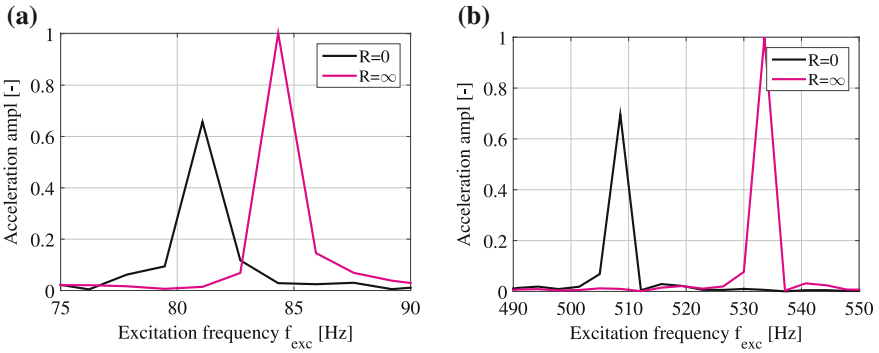

Fig. 4 The influence of the piezoelectric effect for the first (**a**) and the second (**b**) resonance zone on the system response, respectively. The values of the plots are normalised by the maximum value of acceleration amplitude at the open electrodes of each case

piezoelement changes the stiffness of the beam while it is off or on. The numerical results provided, the dynamics of the *MFC* system can be controlled by included load subsystem.

4 Experimental Set-Up

The laboratory experiments have been performed using electromagnetic shaker system TIRAvib 50101 presented in Fig. 5, which reproduced environmental conditions over a required frequency band. The applied shaker was controlled by LMS Test-Lab software, which provided the sinusoidal input excitation signal of the analysed structure during vibration tests. The harmonic signal matched prescribed acceleration level at 1**g** or 2**g**, and swept through a defined range of frequencies, particularly around the resonance zones. The influence of different electrical conditions on the system response is observed by the beam amplitude–frequency characteristics. For energy harvesting acquisition data, the digital signal processing (DSP) module and conditioning system have been applied (Fig. 5). These devices measure the voltage V and current I as well as control the load tuning of the Macro Fiber Composite (*MFC*) actuator, which is connected to the composite cantilever beam. The measuring circuit scheme of the *MFC* system is presented in Fig. 6. The output current

Fig. 5 The equipment of measuring stand

measurement of piezoelectric circuit was realized by voltage measuring on resistor R_P and amplified by Analogue Device AD620. Finally the signal was introduced to the acquisition card with DSP module.

5 Experimental Results

At the beginning of the experimental measurements, the first and the second resonance zones at 1**g** and 2**g** level of excitation have been estimated. It has been done by open *MFC* circuit ($R = \infty$). It provided the frequencies at the first mode in case of 1**g**—$f_{exc}(1g) = 83.7$ Hz, and in case of 2**g**—$f_{exc}(2g) = 84$ Hz, and at the second mode in case of 1**g**—$f_{exc}(1g) = 557.8$ Hz, in case of 2**g**—$f_{exc}(2g) = 556.2$ Hz, respectively.

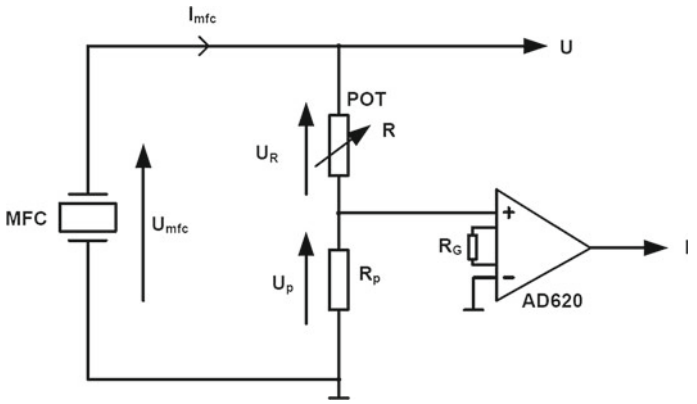

Fig. 6 The measuring circuit scheme of the *MFC* system

In the next step, the measurements of root mean square of power P_{RMS} via load resistance R for found resonance frequencies have been done (Fig. 7). It provided the optimal values of resistance R_{opt} for analysed modes. In the first resonance zone, one can note an insignificant influence of excitation amplitude on R_{opt} value. It corresponds 320 and 300 kΩ in case of 1**g** and 2**g**, and in the second resonance zone it equals 77 and 66 kΩ, respectively. It affirmed that in the second resonance zone, the influence of excitation amplitude on R_{opt} is significant in compare to the previous case.

In the next stage of the experiment the influence of the load resistance R on the response amplitude and harvested power of *MFC* element has been analysed. It has done at both excitation amplitude levels around both resonance zones. The three values of load resistances R have been chosen, an optimal values and two around the optimal. Additionally, the vibration of the beam has been tested at extreme values of the R. It means at shorted and open electrodes of the piezoelement. However

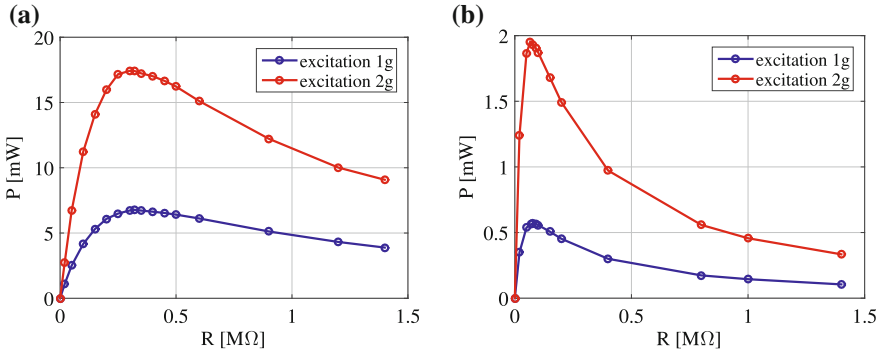

Fig. 7 The influence of the load resistance R on the power P energy harvesting in case of the first (**a**) and the second (**b**) mode, respectively

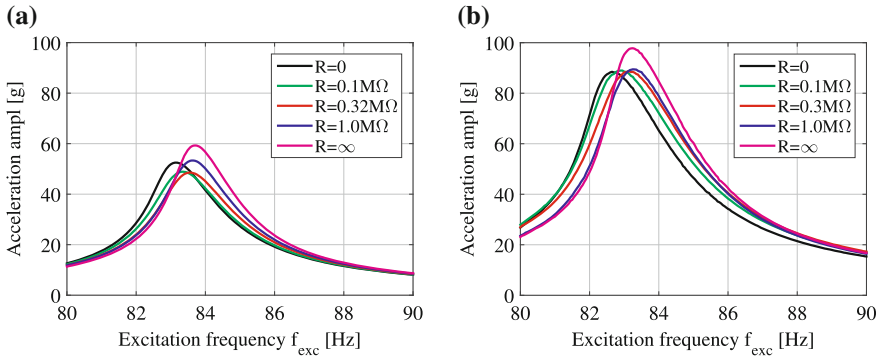

Fig. 8 The response acceleration amplitude of the system at 1**g**, (**a**) and 2**g**, (**b**) of base excitation in case of the first mode

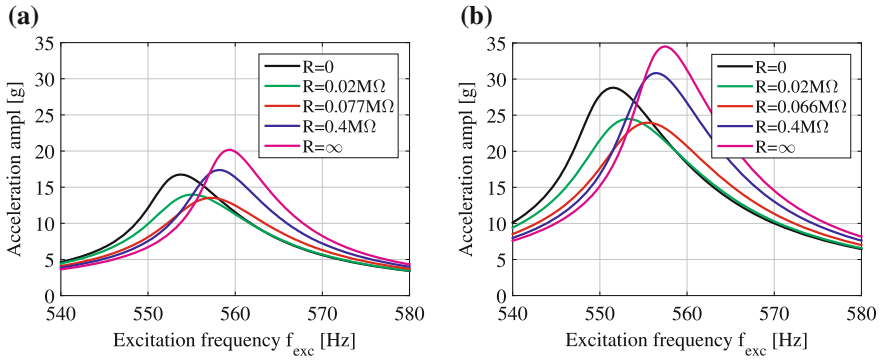

Fig. 9 The response acceleration amplitude of the system at 1**g**, (**a**) and 2**g**, (**b**) of base excitation in case of the second mode

at open electrodes, the *MFC* element stops generated the power. These results are presented in Figs. 8, 9, 10 and 11. According to the *FEM* analysis, one can note decreasing of the system vibration amplitude and moving the peak resonance, while the piezo electrodes were shorted. Analysing the results presented in the Figs. 8 and 9, one can say, that the intermediate load resistances have similar influence on the beam dynamics in all analysed cases of excitations and resonance zones. Taking into account the extreme frequencies of open and shorted system at the excitation 1**g**, the difference was 11 % in the first and 17 % in the second resonance (Figs. 8a, 9a), and at excitation 2**g** it was 9 % in the first and 16 % in the second resonance, respectively (Figs. 8b, 9b—pink and black lines). Note, the most damped vibration of the beam at the fixed external excitation conditions causes the load resistance R closed to the optimal values R_{opt}, even in comparison to the shorted piezoelement case (red line in Figs. 8 and 9). In the first as well as the second resonances, the twofold increasing of the excitation level, leaded dynamical response of the system to the higher values. However in case of the first resonance it increased 46 % but in the second one it

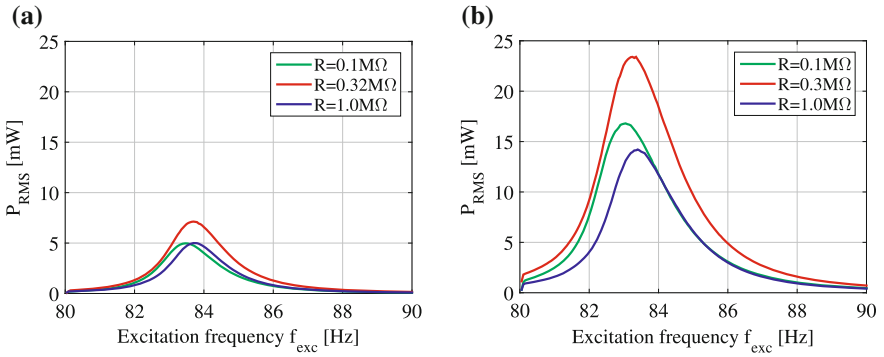

Fig. 10 The root mean square of measured power P_{RMS} of the piezoelectric element via excitation frequency in case of the first cantilever beam resonance, at 1**g**, (**a**) and 2**g**, (**b**) excitation, respectively for chosen load resistances R

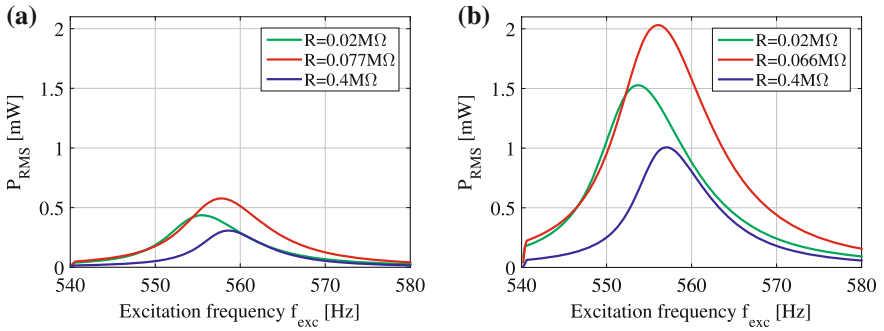

Fig. 11 The root mean square of measured power P_{RMS} of the piezoelectric element via excitation frequency in case of the second cantilever beam resonance, at 1**g**, (**a**) and 2**g**, (**b**) excitation, respectively for chosen load resistances R

was 51 %, respectively. Such increase of the dynamical response shows, the system reveals the nonlinear characteristic.

In the next Figs. 10 and 11, the output power P_{RMS} is reported around the first and the second resonance. The red line presents the power characteristics at optimal load resistance R_{opt}, where the R_{opt} has been estimated on the basis of $P(R)$ characteristics shown in Fig. 7. The change of the R in case of the first resonance has insignificant influence on the top frequency, where an output power reaches a maximum values. But in case of the second resonance that influence is more visible. Increased excitation twice around the first resonance leaded the system to increased around threefold harvested the maximum power P_{RMS} (328 %) (Fig. 10a, b). However in the second resonance, the harvested output power increased three and half times (352 %) (Fig. 11a, b). Moreover, comparing the results of P_{RMS} between the first and the second modes directly, one can notice in the vicinity of the first mode

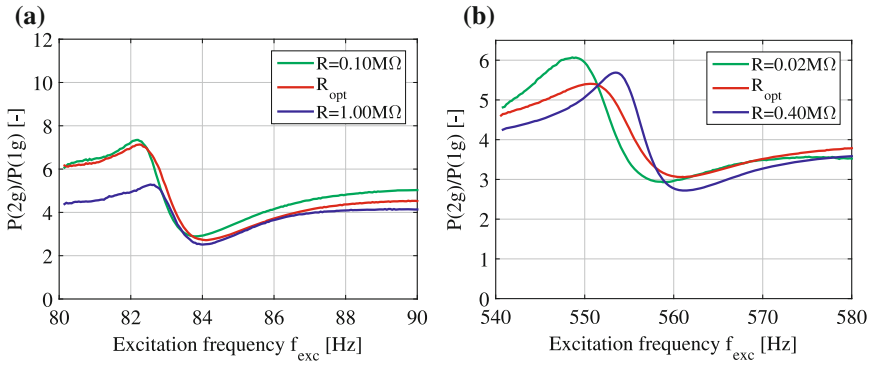

Fig. 12 The ratio of the power P at 2**g**, excitation to the P at 1**g**, excitation in case of the first (**a**) and the second (**b**) cantilever beam resonances, respectively

beam vibrations the output power reaches level of ten times greater than around the second mode beam vibrations for both 1**g** and 2**g** amplitudes excitation.

For precisely analysing the influence of the excitation amplitudes on the output power P increase, the ratio of P has been reporter in Fig. 12a, b to reveal an efficiency of the system around the both resonance zones. It is clearly seeing a great increase of power P which reached even a sevenfold by 82 Hz of excitation frequency in case of the first resonance (Fig. 12a) or a sixfold by $f_{exc} = 549$ Hz in case of the second resonance (Fig. 12b). For excitation frequencies somewhat larger than the resonance one, the power increase due to raised of the excitation amplitude reached the minimum at 3 for both resonance zones. It is around $f_{exc} = 84$ Hz (Fig. 12a) and $f_{exc} = 560$ Hz (Fig. 12b), respectively.

6 Conclusions

The presented results of numerical simulation and experimental measurements revealed a qualitative similarity. The *FEM* analysis gave answer concerned the amplitude response in the relation between shorted and open electrodes of piezoelement. It disclosed an effect of the composite decreasing stiffness while the load resistance had grown up. The influence of the load resistance to the beam stiffness as well as to the generated electrical power P_{RMS} was especially demonstrated in the experimental results. The amplitude–frequency characteristics illustrated the system behaviour against the *MFC* element loaded. There was found an optimal load level R_{opt} while system reached the highest energy harvesting efficiency. It was proved that R_{opt} strongly depends on various condition of mechanical structure of the beam system. Moreover, it was noticed the system generated the maximum power while

the electrical self–impedance of the piezoelement was comparable to the loader impedance. The self–impedance depends mainly on the system capacitance and the excitation frequency.

Acknowledgments This work has been supported by the National Science Centre under the grant Agreement No. DEC-2013/11/D/ST8/03308.

References

1. Torres E, Rincn-Mora G (2009) Electrostatic energy-harvesting and baterry-charrging CMOS systems prototype. IEEE Transactions on Circuit and Systems I, 56(9):1938–1948.
2. Roy W, Keith IF, Chandra N (2009) Energy harvesting and conservation. IEEE Journal of Pervasive Cimputing, 14–7.
3. Priya S, Inman D (2009) Energy harvesting technologies, Springer.
4. Cook-Chennault KA, Thambi N, Sastry AM (2008) Powering MEMS portable devices - a review of non–regenerative and regenerative power supply systems with special emphasis on piezoelectric energy harvesting systems, Smart Material and Structure, vol. 17:043001.
5. Beeby SP, Tudor MJ, White NM (2006) Energy harvesting vibration sources for microsystems applications, Measurement Science and Technology, vol. 17, no. 12:175–195.
6. Borowiec M, Litak G, Friswell MI, Adhikari S (2014) Energy harvesting in a nonlinear cantilever piezoelastic beam system excited by random vertical vibration. International Journal of Structural Stability and Dynamics, 14:1–13.
7. Borowiec M, Litak G, Lenci S (2014) Noise effected energy harvesting in a beam with stopper, International Journal of Structural Stability and Dynamics, vol. 14, no. 8:1440020-1–10
8. Jarzyna W, Augustyniak M, Bocheński M (2010) Active Piezoelectric Structure in Control Systems, Electrotechnical Review, vol. 86, issue 4:252–255.
9. Jarzyna W, Augustyniak M, Warmiński J, Bocheński M (2010) Characteristics and Implementation of Piezoelectric Structures in Active Composite Systems. Electrotechnical Review, 7:320–322.
10. Jarzyna W, Augustyniak M, Bocheński M, et al (2012) PD and LQR controllers applied to vibration damping of an active composite beam. Electrotechnical Review, vol. 88, issue 10B:128–131.
11. Latalski J (2011) Modelling of macro fiber composite piezoelectric active elements in Abaqus system. Maintenance and Reliability 4:72–78.
12. Abaqus 6.14 documentation

Research of Modified Mechanical Sensor of Atomic Force Microscope

Vytautas Bučinskas, Andrius Dzedzickis, Nikolaj Šešok, Ernestas Šutinys and Igor Iljin

Abstract Atomic force microscope (AFM) is a remarkable device for nanoscale surface scanning. Among several positive features, speed of a scanning limits implementation of AFM. This paper proposes method that enables to increase a speed of scanning by modifying some features of mechanical sensor by adding a nonlinear force to lever of a mechanical sensor of AFM. Proposed method is modeled theoretically, using Simulink features by realizing original algorithm, and researched experimentally, using original modification of AFM sensor. Original results are obtained after a research is performed. Finally, comparison of results of original and modified AFM scans is made and corresponding conclusions are drawn.

1 Introduction

Atomic Force Microscopy (AFM) is a form of scanning probe microscopy (SPM) where a small probe is scanned across the sample to obtain information about the sample's surface. The information gathered from the probe's interaction

V. Bučinskas (✉) · A. Dzedzickis · N. Šešok · E. Šutinys · I. Iljin
Vilnius Gediminas Technical University, Basanaviciaus 28, LT03224 Vilnius, Lithuania
e-mail: vytautas.bucinskas@vgtu.lt

A. Dzedzickis
e-mail: andrius.dzedzickis@vgtu.lt

N. Šešok
e-mail: nikolaj.sesok@vgtu.lt

E. Šutinys
e-mail: ernestas.sutinys@vgtu.lt

I. Iljin
e-mail: igor.iljin@vgtu.lt

© Springer International Publishing Switzerland 2016

J. Awrejcewicz (ed.), *Dynamical Systems: Theoretical and Experimental Analysis*, Springer Proceedings in Mathematics & Statistics 182, DOI 10.1007/978-3-319-42408-8_4

with the surface can be as simple as physical topography or as diverse as measurements of the material's physical, magnetic or chemical properties [6]. Data about these properties are collected when the probe is scanned in a raster pattern across the sample to form a map of the measured property relative to the *X*–*Y* position. Thus, the image from AFM shows the variation in the measured property, for example change of surface height over the scanned area. AFM working principle is based on dynamical characteristics of sensitive mechanical system. This system consists of about 200 μm long and 0.5 μm thick cantilever with sharp probe attached at the end. During measurement process, a probe is clamped with initial force to the sample surface. Then scanning starts deflection of cantilevers repeats topography of sample surface. Amplitude of cantilever movements is measured using an optical measurement system. Usually laser is used for this purpose, laser beam is projected on the upper surface of the cantilever close to the tip. Reflected beam by mirror is directed to optical sensor usually four-segment photodiode or camera. Typical system of AFM is schematically shown in Fig. 1.

The main limitation of AFM is its quite low scanning speed, which directly depends on mechanical characteristics of sensor cantilever. If we increase scanning speed, frequency of a cantilever oscillation also increases. Problem is when oscillation frequency approaches the resonant frequency of cantilever, contact between probe and sample surface becomes unstable [4], and as result measurement data becomes inaccurate and unreliable.

Aim of this paper is to deliver solution which will increase AFM scanning speed.

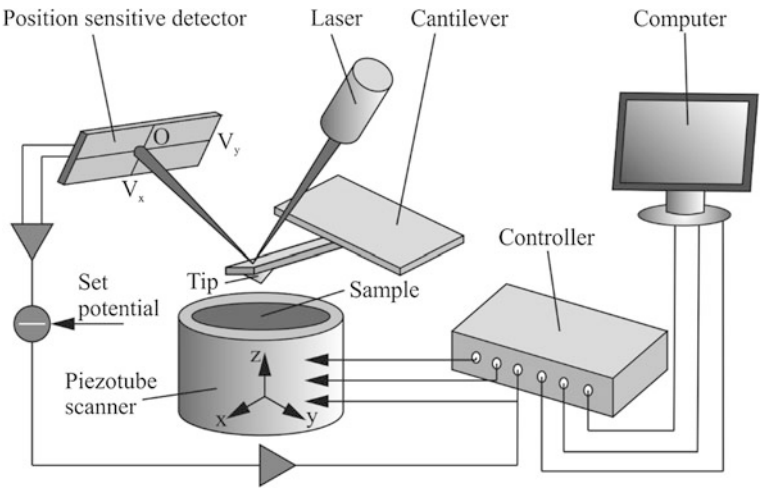

Fig. 1 Structural schematic of AFM microscope sensor

2 Object of Research

For easier understanding of complex AFM structure, all AFM mechanisms relatively can be divided into smaller systems such as scanned sample positioning system, mechanical sensor with scanning tip and measurement system. All systems within AFM are interdependent to each other [4].

Our research focused on mechanical system of AFM sensor. This system consists of about 10-nm long probe, which is attached to a flexible cantilever. Mechanical properties of atomic force microscope cantilever, resonant frequency, and spring constant are most important for AFM technique. High resonant frequency promises fast scan but also the cantilever need to have a small spring constant because of damage-less operation in the contact mode [7].

Many scientists working with various solutions in this direction try to find the best ratio between resonant frequency and stiffness coefficient. One example of possible solutions is presented in [10]. They proposed to improve cantilever characteristics using thin, low-stress zinc oxide (ZnO) film in order to create possibility actuate and sense deflection of cantilever. Main advantages of this improvement in self-sensing tapping mode microscope can work without laser detection system. Tests indicate self-sensing amplitude resolution is good or better than optical detection, with double sensitivity, using the same type of cantilever. Such type of improvements has some limitations. It is limited by unoptimized probe tips, cantilever thicknesses, and stress in the piezoelectric films [10]. Research that is more detailed showed that this improvement gives the best results than AFM works in self-sensing tapping mode. Another popular method of improvement is to design and manufacture cantilever with special geometric shape in order to ensure the necessary dynamic characteristics (resonant frequency or stiffness coefficient). Example of such modification is presented in [7]. Main goal of researches was to create a small atomic force microscopy triangular in shape, cantilever with a length of 7–20 μm, thickness of 0.3 μm and maximum resonant frequency of about 6,6 MHz. Cantilever with such parameters is suitable for high speed scanning. The main drawbacks of such improvement methods are very complex manufacturing process of cantilever. Such small and precise mechanical part cannot be produced without expensive specialized equipment. In addition, production process of cantilevers with individual specific parameters is unprofitable. The method is similar to our idea as described in [5]. Researchers created atomic force microscope (AFM) with direct scanning force modulation. Scanning force is modulated during the scanning process via an external magnetic field that acts directly on the magnetic AFM tip. AFM with such improvement was designed to image the surface of massive samples under various ambient conditions. Main limitation of this improvement is possibility of magnetic field that can have various side effects on sample properties.

Our proposal of AFM sensor improvement is based on the idea to add the model an additional nonlinear stiffness element in order to have possible control dynamic characteristics of the system. This possibility will allow us to change stiffness and

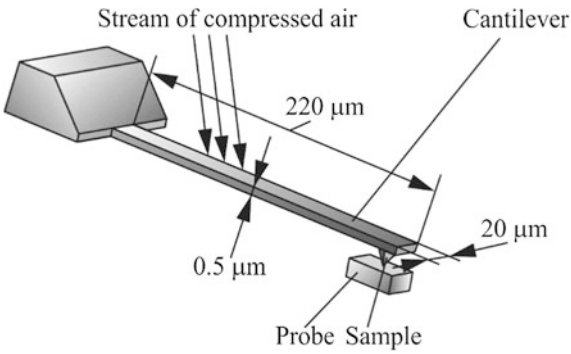

Fig. 2 Structural schematic of improved AFM microscope sensor

resonant frequency of the sensor. This improvement allows to change stiffness of the sensor and shift resonant frequency from the undesired range during scanning process, sensor start vibrate in frequency close to resonant. System stiffness is changed by adding additional controllable force, which acts directly on cantilever surface. Additional force will decrease the probability of contact loss between the probe and sample surface. In case when contact between surface and probe becomes stable, effect of additional stiffness is removed in order to avoid additional friction forces between the probe and sample. Additional force is created using compressed air flow from an installed microscopic air duct. Structure of modified AFM sensor is shown in Fig. 2.

Purpose of our research is to create mathematical and physical model of improved system and to determine the positive effect of our improved system.

3 Mathematical Modeling of Mechanical Structure of Improved AFM Sensor

In order to verify the idea of resonant frequency control using additional stiffness element and to define its influence to the scanning process performance, dynamic model of the mechanical sensor cantilever was developed. The most popular

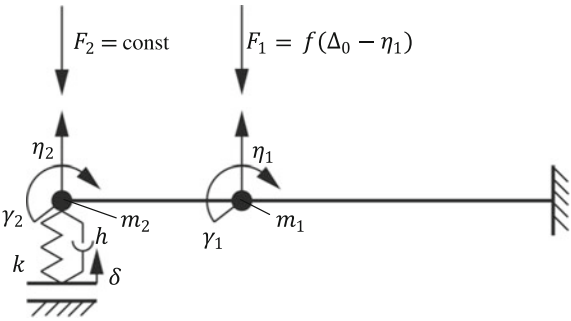

Fig. 3 Dynamical model of improved AFM microscope sensor

modeling techniques used for AFM cantilevers modeling are shown in [2]. Dynamic model of our modified AFM sensor mechanical structure is shown in Fig. 3.

In our model, cantilever of mechanical sensor is represented by a beam with rectangular cross section and this maximally corresponds to real dimensions of modeled object. Model consists from two elastic elements with concentrated mass in the end. Elasticity of each beam is evaluated using cross-sectional parameter EI_{sk}, where E—Young modulus and I_{sk}—moment of inertia of cross section of the beam in respect to horizontal axis. Interaction between the probe and sample surface is modeled, as elastic element with damping; its coefficient of stiffness is k and coefficient of damping is h. Displacement of whole cantilever is described by generalized coordinates η_1, γ_1, η_2, γ_2. Coordinates η_1 represents displacement of point on which is acting additional force, η_2 describes linear movement of tip, and coordinates γ_1 and γ_2 describe rotary movements correspondingly. Roughness of the sample surface, which cinematically excites system oscillations, is described by coordinate δ. Initial clamping force F_2, applied to a cantilever, points to the negative direction of coordinate η_2. Avoidance of contact loss between the probe and surface in the model is ensured by the distance-dependent force F_1.

Mathematical model of linear system part is created using Lagrange equations of second type in the matrix form:

$$[A]\left\{\ddot{q}\right\} + [B]\left\{\dot{q}\right\} + [C]\{q\} = \{Q\} \tag{1}$$

where $[A]$—matrix of inertia forces;

$[B]$—matrix of damping coefficients;

$[C]$—matrix of stiffness coefficients;

$\{q\} = \{\eta_1, \gamma_1, \eta_2, \gamma_2\}^T$—vector of generalized coordinates;

$\{Q\}$—vector of generalized forces.

Nonlinear additional force F_1 depends on many factors, its dependency on distance found by additional research of aerodynamic problem. This dependency is approximated by third-level polynomial for a better mathematical description in the model. Modeling process of nonlinear aerodynamic force is described in detailed in [4].

Our newly developed dynamic model can be divided into three different modules according to the designated function. Simplified structural schematic of our model is presented in Fig. 4.

First module represents effect of nonlinear distance depending aerodynamic force. Second block is a main part of our model, it represents linear part of system. This block is created using Lagrange equations of second type. Similar modeling methods of dynamic systems are represented in [1, 8, 9]. Second block represents behavior of AFM sensor without improvement. Third block is responsible for the control of additional force. It is used to apply the effect of aerodynamic forces, the probability of contact loss between probe and sample appears and remove effect of aerodynamic force then contact is stable.

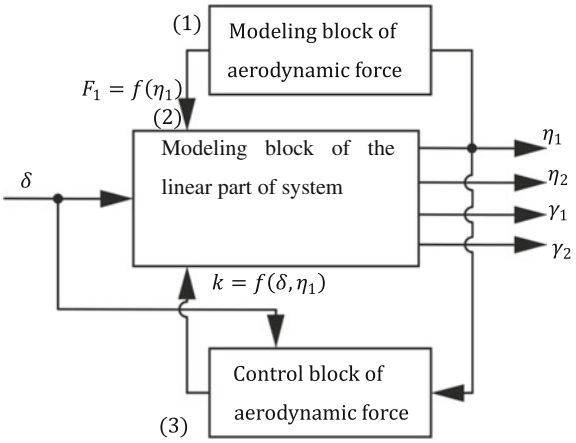

Fig. 4 Simplified structural diagram of mathematical model

Modeling process of improved AFM sensor and the obtained most promising results were presented in detail on the international conference "Mechatronics ideas for industrial applications" in Gdansk, Poland [3, 4].

4 Experimental Research of Improved AFM Sensor, Equipment, and Methodology

Experimental research of AFM sensor was performed in Vilnius in laboratories of Centre for Physical Science and Technology. Our main purpose of initial experimental research was to determine if it is possible to press AFM cantilever with stream of compressed air. Second question, which were interesting for us, was, what size of microscopic air duct should be used, which force we can expect that is created on a cantilever surface and how much pressure of air is needed.

Research was performed using specially created test rig, which consists of optical distance measuring system, special design holder, and standard AFM sensor cantilever.

Distance measuring system was used to measure the displacement of AFM tip in that moment then we effect a cantilever with air stream. In our test rig, we used standard laser measuring system, which is used in many AFMs. Measurement data were recorded using national instruments data acquisition equipment. For measurement system adjustment, calibration, and result processing, we used a software package "LabVIEW 2012".

Special holder for AFM cantilever was manufactured in laboratories of Vilnius Gediminas technical university. In the holder micro air duct was installed, which is 0.2 mm inside diameter. Selection of this size of micro tube was based on experience from the previous research and on theoretical research as described in [4]. This holder is required for precise positioning of cantilever, optical sensor, and air duct.

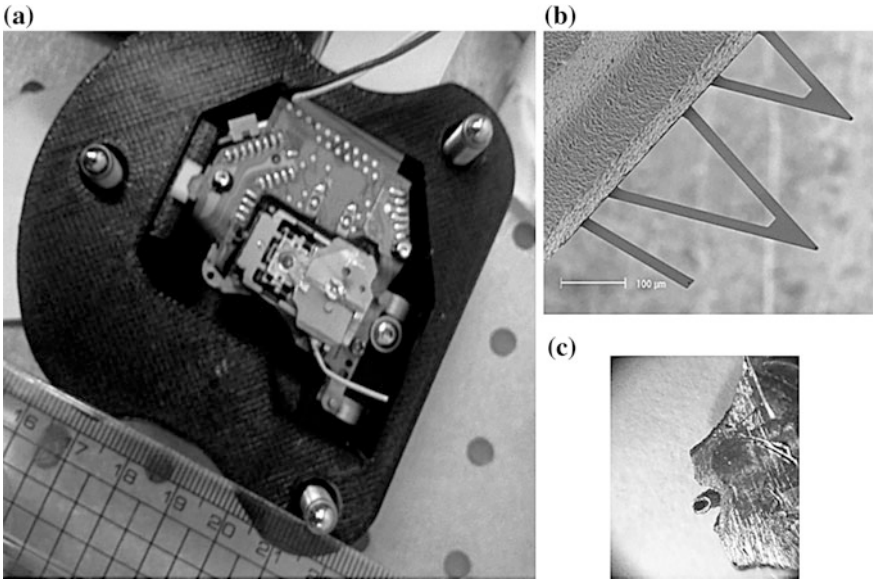

Fig. 5 Test rig of improved AFM microscope sensor: **a** assembled test rig, **b** schematic of triangular cantilever, **c** holder with installed micro air duct

For a research objective, we used AFM probe MLTC-D. Its cantilever has triangular shape of 220 µm long, 20 µm wide, and 0.55 µm thick. Nominal resonant frequency of cantilever is 15 kHz. Test rig and some of its fragments are presented in Fig. 5.

Simultaneously described test rig also developed air supply system used in our experiments. Specially designed compressed air supply system is presented in Fig. 6. Air supply system was created considering facts that compressed air during the experiment will be used only for few minutes and flow rate will be low. Main requirement for air supply system was to ensure supply of clean air with possibility of smooth pressure adjustments in a wide range. In order to avoid air pressure fluctuations in the system, we decided to use compressed air reservoir instead of mini compressor.

Our created system (Fig. 6) consists from three air reservoirs, mechanical pressure regulator and electromagnetic valve. Two balloons (1) of 750 ml capacity connected in parallel acts as main source of compressed air. Air pressure in these balloons can be up to 10 bars. These balloons can be refilled using compressor and special air cleaning filters. Third balloon (3) connected in series using pressure regulator (2), this tank acts as additional filter, which removes pressure fluctuations caused by pressure regulator. It was expected that pressure in tank (3) will be not more than 0.6 bar. Solenoid valve is used to control the output of system, it means to start or stop air supply to micro duct, installed in holder of AFM cantilever. For

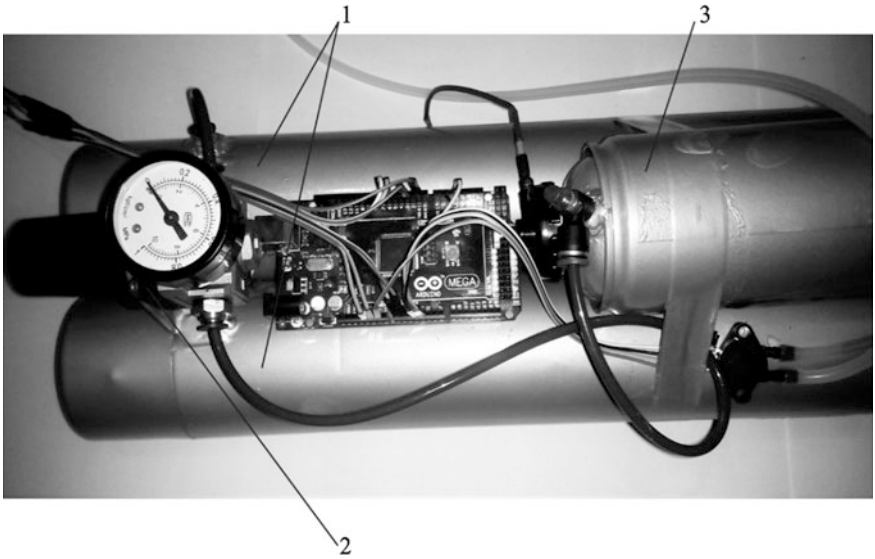

Fig. 6 Compressed air supply system

further research in this system will be added created possibility to control output pressure and flow rate from AFM software.

As it was mentioned earlier, main question, which we want to answer, is if our idea to effect AFM cantilever with air stream working in practice. Therefore, we make experiment by applying some amount of compressed air ant simultaneously measuring displacement of cantilever tip.

Before experiment, laser measuring system was turned on for 20 min to warm up and stabilize. AFM cantilever, air duct and optical sensor were precisely positioned using optical microscope and camera. After that, measurement system was calibrated and adjusted. Then displacement data recording were started, we set output pressure to 0.3 bar and applied air stream for approximately 10 s, when removed for 6 s and applied one more time for 10 s. Experiment was carried out five times in order to avoid side effects.

5 Results of Experimental Research of Improved AFM Sensor

Result of experimental research is shown in Fig. 7. This graph indicates displacement of cantilever tip, of AFM sensor.

Graph presented in Fig. 7 can be divided in three sections. First section in the graph represents process of measurement system calibration and adjustment.

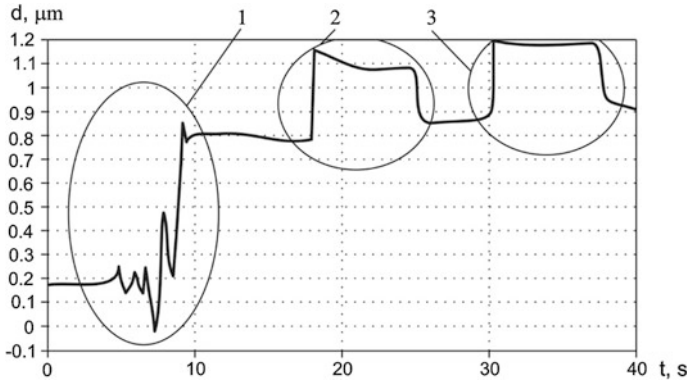

Fig. 7 Displacement amplitude of AFM cantilever tip

Second section represents cantilever response to the applied aerodynamic force. Gentle drift of displacement, which is seen, from graph is caused by pressure adjustment. From this graph, it is seen that aerodynamic force created by air stream with pressure of 0.3 bar, causes AFM probe displacement approximately equal to 0.4 μm. Air stream with pressure of 0.2 bar causes displacement equal to 0.3 μm. Third section shows that if air pressure is constant, cantilever leans remains in this state until force effect is removed and then cantilever goes back to initial position.

Results of this experiment confirm our proposed idea is possible control dynamic characteristics of AFM sensor cantilever. Also from this experiment, we find out that output pressure of air supply system should range from 0 to 0.5 bars. This pressure is much higher than pressure, which was, calculated theoretically [4]. Difference in results between theoretical and practical experiments shows that we have huge loss of pressure in air duct with very small diameters inside.

6 Conclusions

After analyses of the mechanic sensor of AFM were performed, a new idea of increasing scanning speed of microscope without changing design of mechanical system of sensor is proposed.

Performed theoretical research gave us possibility to create mathematical model of improved mechanical system of AFM sensor.

Results obtained from experimental research gave us a lot useful information. Initially, they approved idea that dynamic system of AFM sensor is sensitive to air stream and thus system parameters can be controlled by changing air stream parameters. Such situation will adjust AFM sensor characteristics according to individual sample surface properties and increase scanning speed. Also we find out that air duct diameter 0.2 mm is suitable for our application.

Finally, proposed method and results of initial research of AFM sensor improvement assumed to be prospective and further research in this field will be continued.

References

1. Augustaitis, V.K., Gichan, V., Sheshok, N., Iljin, I. Computer-aided generation of equations and structural diagrams for simulation of linear stationary mechanical dynamic systems. *Mechanika*, 3, 2011, 255–263 p.
2. Dzedzickis, A., Bučinskas, V. Analysis of mechanical structure of Atomic force microscope sensor. *Science - Future of Lithuania,* 6, 2014, 589–594 p.
3. Dzedzickis, A., Bučinskas, V., Šešok, N., Iljin, I., Šutinys, E. Modelling of dynamic system of atomic force microscope. *International conference Mechatronics ideas for industrial applications*, Gdansk university of technology, 2015, 26 p.
4. Dzedzickis, A., Bučinskas, V., Šešok, N., Iljin, I. Modelling of mechanical structure, of atomic force microscope. *11th International Conference Mechatronic Systems and Materials*, 2015, 63–64 p.
5. Florin, E.L., Radmacher, M., Fleck, B., Gaub, H. E. Atomic force microscope with magnetic force modulation. *Review of Scientific Instruments,* 65, 3, 1994.
6. *Handbook of analytical methods for materials.* Materials evaluation and engineering, Inc, Plymouth, 2014.
7. Hosaka, S., Etoh, K., Kikukawa, A., Koyanagi, H. Megahertz silicon atomic force microscopy AFM cantilever and high-speed readout in AFM-based recording. *Journal of Vacuum Science & Technology Microelectronics and Nanometer Structures,* 18, 2000, 94–99 p.
8. Lithuanian patent LT5962 (B), Method and equipment of steel rope quality.
9. PCT application WO2013055196 (A1) “Method and equipment of steel rope quality diagnostics”.
10. Rogers, B., Manning, L., Sulchek, T., Adams, J.D. Improving tapping mode atomic force microscopy with piezoelectric cantilevers. *Ultramicroscopy* 100, 2004, 267–276 p.

Nonlinear Dynamics of the Car Driving System with a Sequential Manual Transmission

Radek Bulín, Michal Hajžman, Štěpán Dyk and Miroslav Byrtus

Abstract Sequential manual transmissions are the most common sources of various contacts and impacts especially in rally cars. Dynamics of such systems can be very interesting and can influence the overall dynamic performance of a whole car. Therefore, it is necessary to have proper tools for dynamical modelling of gearboxes. This paper deals with the modelling and dynamic analysis of a driving system of a real car with a sequential manual transmission. A complex computational model of the sequential gearbox was created and after verification it allows to study nonlinear behaviour of the whole driving system. Parametric studies can be performed in order to investigate various qualitative effects of chosen design elements, etc.

1 Introduction

Car driving systems are very interesting from the viewpoint of its dynamic behaviour that can be related to a gear mesh of wheels, to variable torques during rapidly changing operating conditions or other impacting design elements. Especially, sequential manual transmissions are common sources of impacts and contacts that impose time varying excitation. Design engineers need sufficient computational methodologies and tools in order to predict dynamic behaviour of developing systems. Therefore, this paper is aimed at the modelling methodology and dynamic analysis of a car driving system with a sequential manual transmission.

R. Bulín (✉) · M. Hajžman · Š. Dyk · M. Byrtus
Faculty of Applied Sciences, University of West Bohemia,
Univerzitní 8, Plzeň, Czech Republic
e-mail: rbulin@ntis.zcu.cz

M. Hajžman
e-mail: mhajzman@kme.zcu.cz

Š. Dyk
e-mail: sdyk@ntis.zcu.cz

M. Byrtus
e-mail: mbyrtus@kme.zcu.cz

© Springer International Publishing Switzerland 2016

J. Awrejcewicz (ed.), *Dynamical Systems: Theoretical and Experimental Analysis*, Springer Proceedings in Mathematics & Statistics 182, DOI 10.1007/978-3-319-42408-8_5

General car dynamics including its transmission systems and their effect on vehicle performance are described, e.g. in [7, 10, 14]. Nonlinear dynamics of a car were studied in [9] using a single nonlinear ordinary differential equation. Authors of [3] investigated interesting nonlinear dynamic properties of gear systems in automatic gearbox. Many authors studied synchronization in vehicle transmission systems [1, 11, 13], which is a important dynamic element. A simple driveline model for simulations of dry clutch dynamics was chosen in [16]. Sequential performance is mainly affected by shifting, the event of changing gears. Gear-shift in sports cars was studied in [5], while particular control of shifting was shown in [4, 12].

This paper is divided into two main sections. The general modelling methodology based on multibody dynamics is introduced and the complex computational model of a transmission system with a sequential gearbox for the particular rally car is presented. This model is further used for numerical simulations of shifting and the results are compared with measured results obtained from experiments.

2 Computational Modelling of a Driving System

Theoretical basics suitable for the modelling of studied systems are briefly described in this section. The implementation of a computational model for a particular driving system with a sequential gearbox is then introduced.

2.1 Modelling Methodology

Components of driving systems can be considered as a system of rigid bodies connected by various kinematic couplings (joints) affected by imposed forces and torques and by springs and dampers simulating flexible behaviour of appropriate parts. Such modelling approach is well known as multibody system dynamics. Formulation of equations of motion can be based on various types of coordinates. The method presented in this paper is based on generalized (Cartesian) coordinates and leads to the mathematical model in the form of a set of differential algebraic equations (DAEs). The equations of motion can be derived using the Lagrange's equations (of the mixed type for dependent generalized coordinates $\mathbf{q}$, [17])

$$\frac{\mathrm{d}}{\mathrm{d}t}\left(\frac{\partial E_k}{\partial \dot{\mathbf{q}}}\right) - \frac{\partial E_k}{\partial \mathbf{q}} = \mathbf{Q} - \frac{\partial E_p}{\partial \mathbf{q}} - \frac{\partial R}{\partial \dot{\mathbf{q}}} + \boldsymbol{\Phi}_q^T \boldsymbol{\lambda}, \tag{1}$$

where E_k is the kinetic energy, E_p is the potential energy, R is the Rayleigh's dissipation function, $\mathbf{Q}$ is the vector of generalized forces corresponding to particular generalized coordinates. Holonomic rheonomic constraints between the chosen coordinates can be written using the vector notation

$$\boldsymbol{\Phi}(\mathbf{q},\, t) = \mathbf{0} \tag{2}$$

and for the use in Eq. (1) it must be differentiated to obtain the Jacobian matrix

$$\boldsymbol{\Phi}_q = \frac{\partial \boldsymbol{\Phi}}{\partial \mathbf{q}} = \left[\frac{\partial \boldsymbol{\Phi}_i}{\partial q_j}\right], \quad i = 1,\, 2,\, \ldots,\, m, \quad j = 1,\, 2,\, \ldots,\, n, \tag{3}$$

where m is the number of constraints and n is the number of dependent generalized coordinates. Vector of Lagrange multipliers λ is introduced in Eq. (1).

After the substitution of the particular expressions for the energies and for the generalized forces the equations of motion

$$\mathbf{M}\ddot{\mathbf{q}}(t) - \boldsymbol{\Phi}_q^T \lambda = \mathbf{g}(\mathbf{q},\, \dot{\mathbf{q}},\, t) \tag{4}$$

together with the constraint equations (2) constitute the mathematical model of the constrained multibody system. Matrix $\mathbf{M}$ is the global mass matrix of the multibody system and vector $\mathbf{g}(\mathbf{q},\, \dot{\mathbf{q}},\, t)$ contains centrifugal and Coriolis inertia forces, elastic and damping forces and other externally applied forces including the gravity. The mathematical model (4) is usually transformed into the set of differential algebraic equations of index one

$$\begin{bmatrix} \mathbf{M} & \boldsymbol{\Phi}_q^T \\ \boldsymbol{\Phi}_q & \mathbf{0} \end{bmatrix} \begin{bmatrix} \ddot{\mathbf{q}} \\ -\lambda \end{bmatrix} = \begin{bmatrix} \mathbf{g}(\mathbf{q},\, \dot{\mathbf{q}},\, t) \\ \boldsymbol{\gamma}(\mathbf{q},\, \dot{\mathbf{q}},\, t) \end{bmatrix} \tag{5}$$

by the double differentiation of the constraint equations with respect to time. Vector $\boldsymbol{\gamma}(\mathbf{q},\, \dot{\mathbf{q}},\, t)$ represents the remaining terms after the constraints differentiation. Solution of equations of motion (5) can be based, e.g. on elimination of Lagrange multipliers [8] and further direct integration of the underlying ordinary differential equation.

Effects of contacts and impacts are included in vector $\mathbf{g}(\mathbf{q},\, \dot{\mathbf{q}},\, t)$. In case of interaction of bodies in driving systems, it is necessary to consider elastic and viscous components of contact forces in normal direction and also friction forces in tangential direction. Various models of contact forces were presented in [2]. Alternative treatment of contact problems was shown by authors in [15].

2.2 Model Implementation

The computational model of the particular driving system with a sequential gearbox was built up in MSC.Adams. The model visual representation is shown in Fig. 1. The purpose of the model is to simulate shifting between the third and the fourth gear stage because it is the most common maneuvre during a rally car race.

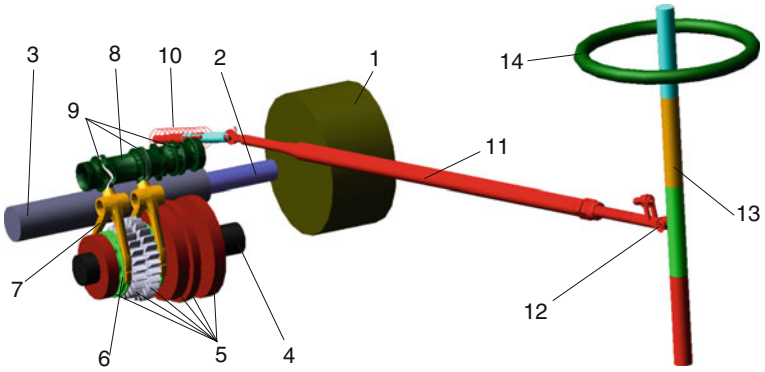

Fig. 1 Geometrical representation of the model of a gearbox and a gear-shifting mechanism

At the input of the driving chain, all the engine parts are modelled using a body with reduced inertia properties (see position 1 in Fig. 1), which include inertia of all relevant rotating parts of the engine. Using torsional elastic coupling of the clutch, body 1 is connected to the inner primary shaft (position 2 in Fig. 1), which goes through the whole body of outer primary shaft (position 3) and at the end, both shafts are coupled by gear coupling.

Body 3—outer primary shaft—includes reduced mass properties of all primary gears. Torque flow is transmitted through the third or the fourth gear stage to the secondary shaft by means of a claw clutch between dog-rings (position 6) and secondary gears (position 5). Gear-shifting is performed by moving a flexible gear-shift lever (position 13) which is connected by a spherical joint to the rod (posotion 11) with a restoring-force spring (position 10). The translational motion of the rod is transformed by gear coupling to the rotation of a selector (position 8) with guide curves (position 9), which translate corresponding forks (position 7) with dog-rings

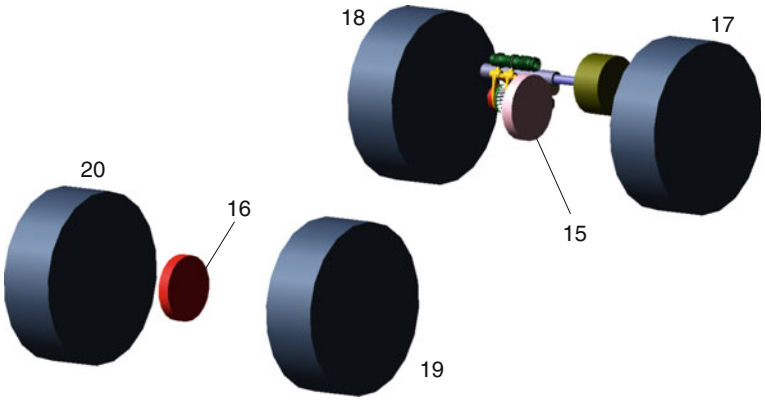

Fig. 2 Geometrical representation of the model of a driving transmission system

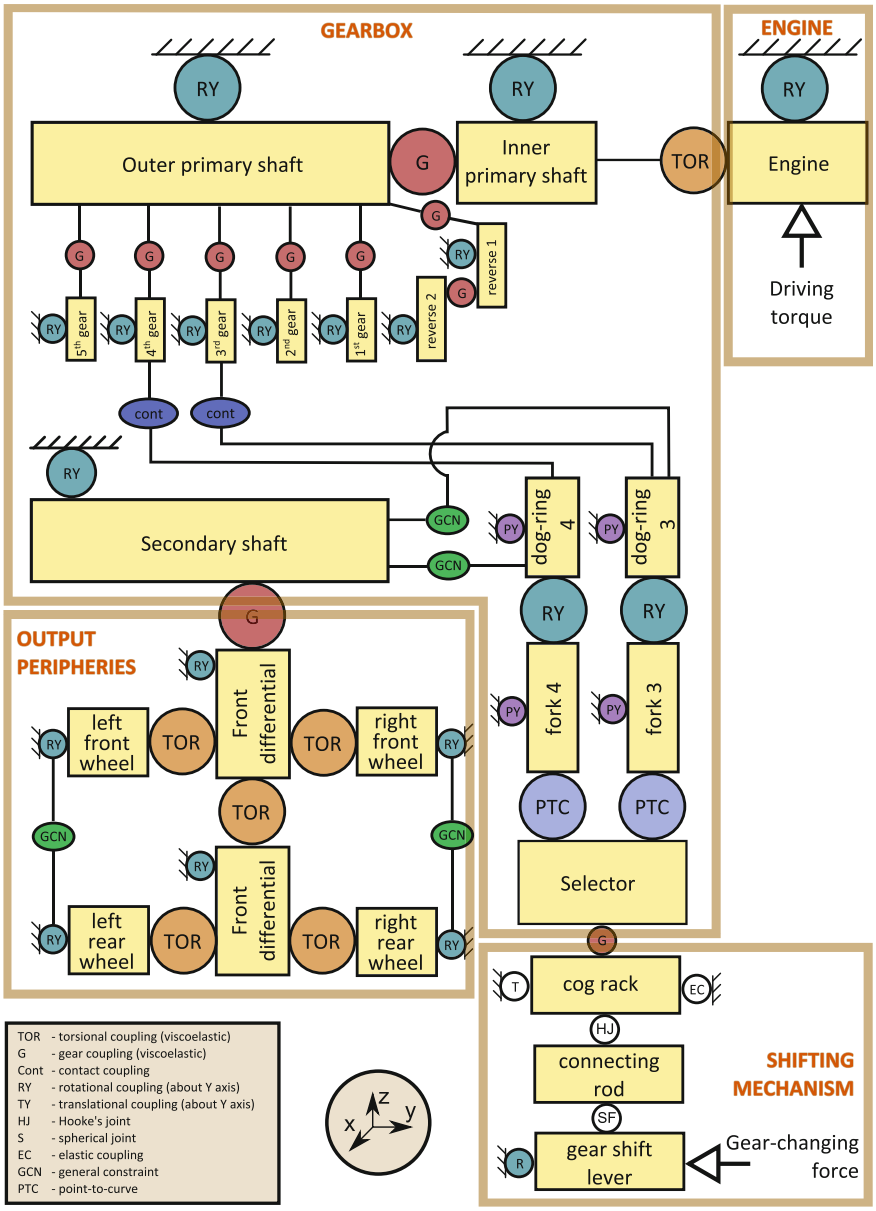

Fig. 3 Kinematical scheme of the whole model

along the axis of the selector. In this manner, the desired gear stage is chosen. At the head of the gear-shift lever, there is a sleeve (poistion 14) elastically connected to the lever, which can simulate conditions at the experimental stand with robot-shifting mechanism.

Several relevant peripheric parts at the output of the gearbox are included, as shown in Fig. 2. At the output, the torque is transmitted to the front differential (position 15 in Fig. 2), which is considered as a single reduced body rotating by angular speed given by corresponding gear ratios. The front differential is coupled with front wheels (position 17) and (position 18) by torsional springs with stiffnesses corresponding to stiffnesses of front half-axes. Simultaneously, the torque is transmitted through a cardan shaft to the rear differential (position 16) and through torsional springs to both rear wheels (position 19) and (position 20).

A kinematical scheme of the whole system model is shown in Fig. 3. Bodies are connected by several types of couplings (rotational, translational, torsional, gear couplings, contact, etc.) and forces as shown in Fig. 3 and the topology of the scheme is given by physical relationships between bodies. Passive mechanical effects such as drag forces [6], tyre passive rolling resistance and damping of couplings affecting the motion are also included in the model.

The simulation begins with given initial conditions corresponding to the situation when the rally car and all the active bodies in the driving chain are in motion at the third gear stage. The shifting is driven by a shifting force acting at the head of the gear-shifting lever. When the force in the shifting rod reaches a given value, the driving torque decreases rapidly and allows the claw clutch to change the gear. After selector's rotation reaches a given rotational angle, the driving torque starts to increase and the claw clutch connects itself at the fourth gear stage.

3 Results and Comparison with the Experiment

The goal of the first simulations was mainly to verify the computational model with the experimental data. It is necessary to note that each gear-shifting is unique during the race, because the operation conditions of whole car are changing. The driver should change gears at a specific engine angular velocity range to obtain maximal power. In addition, experimental data for each driver could be slightly different, because of their strength and driving sense.

Thus to verify the model's experimental data, which correspond with ideal gear change, were chosen. It means that the shifting takes place at an optimal engine angular velocity, while the car is moving on a straight and smooth road. The shifting between the third and the fourth gear was simulated, because it is the most common shifting in a race. Two types of gear-shifting can occur—correct gear-shifting, when the dog-ring properly hits the gear teeth of the claw clutch, and incorrect gear-shifting, when the dog-ring hit the front side of the gear teeth and it bounce off (usually a driver repeats the shifting immediately and the maneuver is correct at the next attempt).

The most important experimental characteristics are engine angular velocity, engine driving torque and shifting force, which is measured by sensor located between the gear-shift lever and the rod. These three parameters are not independent. It is necessary to lower the driving torque (the cut down) for the sake of allowing

the driver to change gears. The cut down of the driving torque starts when a specific shifting force value is achieved and it ends when the selector is rotated by a specific angle. The gear-shift lever input force is in the computational model composed of simple linear functions in order to reflect three stages of the shifting. At first, the input force rises and the whole mechanism gets pre-stressed, then the contact between the third dog-ring and the gear is lost, the dog-ring is released and the selector moves with the fourth dog-ring. The last stage is the contact between the fourth dog-ring and the gear. This model of gear-shift lever input force was chosen in order to simulate the real behaviour of the driver.

The results obtained using the computational model were compared to experimental data. The comparison of computed and experimental data for the ideal case (correct shifting without collision) is shown in Figs. 4, 5 and 6. The parameters are

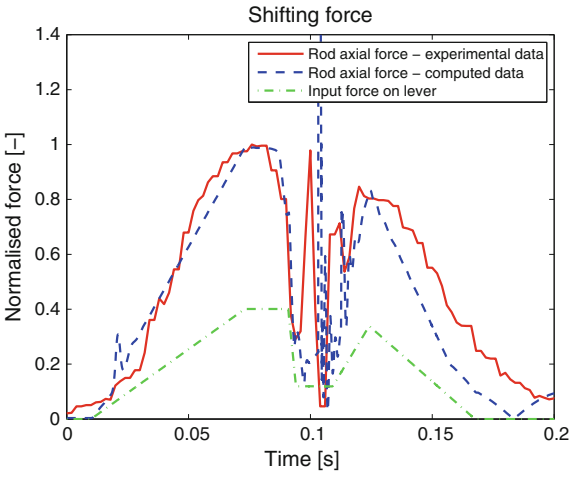

Fig. 4 Comparison of the shifting force with the experimental data

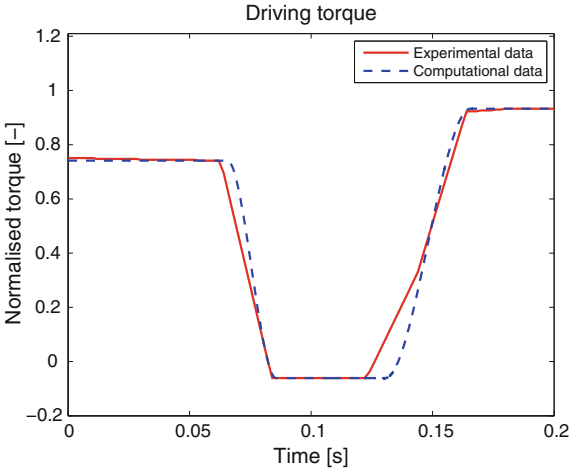

Fig. 5 Comparison of the driving torque with the experimental data

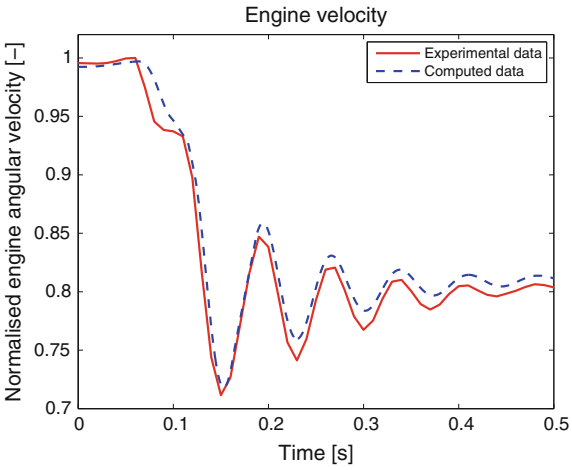

Fig. 6 Comparison of the engine velocity with the experimental data

normalised by the maximal value of corresponding experimental parameter. It can be seen that the presented model of the state-dependent shifting force is in good compliance with the experimental data. The resultant driving torque also corresponds to the experimental data. Finally, almost the same character of engine velocity vibration occurs for the experimental and computed data.

The non-ideal case of shifting (unsuccessful for the first attempt with collision) was also numerically simulated for the sake of evaluating the computational model robustness. The results are compared with the correct shifting in Figs. 7 and 8. The impacts are visible in the time histories of the engine velocity and the shifting force.

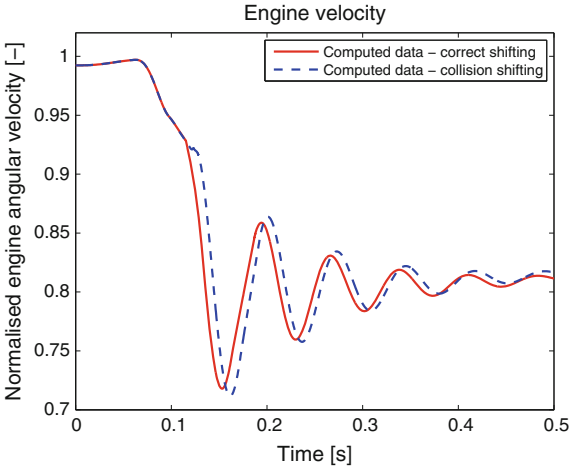

Fig. 7 Comparison of the engine velocity for the cases without and with collision

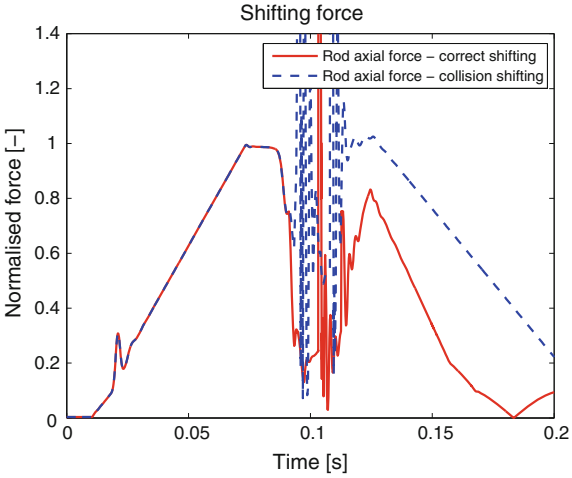

Fig. 8 Comparison of the shifting force for the cases without and with collision

4 Conclusions

The complex methodology for the computational modelling of driving chains in a particular rally car with a manual sequential gearbox was presented in this paper. The methodology of modelling is based on the multibody dynamics approaches. After the implementation of the computational model of a chosen transmission system, several numerical simulations are performed for correct and incorrect shifting. Obtained results are successfully compared with the measured results from experiments. The computational model can be used for various parametric studies in order to optimize a design of transmission elements.

Acknowledgments This publication was supported by the project LO1506 of the Czech Ministry of Education, Youth and Sports.

References

1. Bedmar AP (2013) Synchronization processes and synchronizer mechanisms in manual transmissions. Master thesis. Chalmers University Of Technology, Göteborg
2. Bulín R, Hajžman M (2014) On the Modelling of Contact Forces in the Framework of Rigid Body Dynamics. Manufacturing Technology 14:136–141
3. Chen ZG, Shao YM, Lim TC (2012) Non-linear dynamic simulation of gear response under the idling condition. International Journal of Automotive Technology 13:541–552
4. Deng T, Hu F, Lu R (2015) Research on DCT shifting torque control and a benchmark test. Journal of Mechanical Science and Technology 29:3581–3589
5. Dudnikov A (2006) Estimation procedure of increasing the speed of gear shift in sports cars at the design stage. In: FISITA World Automotive Congress 2006
6. Genta G (1997) Motor vehicle dynamics. World Scientific, Singapore
7. Gillespie TD (1992) Fundamentals of vehicle dynamics. SAE, Warrendale

8. Hajžman M, Polach P (2007) Application of stabilization techniques in the dynamic analysis of multibody systems. Applied and Computational Mechanics 1:479–488
9. Hendrih K, Simonović (2003) Nonlinear phenomena in dynamics of car model. Facta Universitatis, Series Mechanics, Automatic Control and Robotics 3:865–879
10. Jazar RN (2008) Vehicle aynamics: Theory and applications. Springer, New York
11. Khollam SC, Mhaske MS, Belkar SB (2014) A method to optimize brass type single synchronizer ring for manual gearbox. International Journal of Engineering and Advanced Technology 3:93–98
12. Liao C, Zhang J, Zhu H (2004) A study of shift control algorithm without clutch operation for automated manual transmission in the parallel hybrid electric vehicle. In: FISITA World Automotive Congress 2004
13. Lovas L, Play D, Marialigeti J, Rigal JF (2006) Mechanical behaviour simulation for synchromech mechanism improvements. Proc. IMechE Part D: J. Automobile Engineering 220:919–945
14. Milliken WF, Milliken DL (1995) Race car vehicle dynamics. SAE, Warrendale
15. Pfeiffer F, Glocker C (2004) Multibody dynamics with unilateral contacts. Wiley, Weinheim
16. Serrarens A, Dassen M, Steinbach M (2004) Simulation and control of an automotive dry clutch. In: Proceedings of the 2004 American Control Conference, Boston
17. Shabana AA (2001) Computational dynamics, 2nd edn. Wiley, New York

Random Attractors for Von Karman Plates Subjected to Multiplicative White Noise Loadings

Huatao Chen, Dengqing Cao and Jingfei Jiang

Abstract The study on long-time dynamical behaviors of thin plates or panels subjected to random excitations is an important issue. Motivated by problems arising in practical engineering, the dynamics of Von Karman plates without rotational inertia can be described by a partial differential equation driven by multiplicative white noises which can generate a random dynamical system (RDS). According to the estimation of energy function for the vibrations of the plate, it can be proved that there exist random attractors for the corresponding RDS.

1 Introduction

The Von Karman plate equations

$$\rho h U_{tt} - \rho I \Delta U_{tt} + chG(U_t) + \overline{D}\Delta^2 U = F + P + [V(U) + F, U] \tag{1}$$

can be used to describe the nonlinear transversal vibration of elastic plates, where $V(U)$ is the Airy stress function satisfies the following elliptic problem

$$\Delta^2 V = -h^2[U, U] \tag{2}$$

with boundary value $\frac{\partial V}{\partial n} = V = 0$, here n is the outer normal vector, for the physical background, literature [1] may be consulted. Here, it is emphasized that the term $\rho I \Delta U_{tt}$ represents the rotational inertia of the plate, which is proportional to

H. Chen · D. Cao (✉) · J. Jiang
Division of Dynamics and Control, School of Astronautics,
Harbin Institute of Technology, P.O. Box 137 150001, Harbin, China
e-mail: dqcao@hit.edu.cn

H. Chen
e-mail: htchencn@aliyun.com

J. Jiang
e-mail: jjf860623@yeah.net

© Springer International Publishing Switzerland 2016

J. Awrejcewicz (ed.), *Dynamical Systems: Theoretical and Experimental Analysis*, Springer Proceedings in Mathematics & Statistics 182, DOI 10.1007/978-3-319-42408-8_6

the square of the thickness of the plates. the mathematical properties of system (1) and (2) that accounts for the rotational inertia are very different from the one without rotational inertia [2]. Equations of Von Karman plates (1) and (2) are well known in nonlinear elasticity, these equations have attracted a great interesting in mathematician, physicists, and engineers; for more details, one can see the monograph [1, 2] and the references therein.

Let $D \subset \mathbb{R}^2$ be a bounded domain with smooth boundary Γ. This paper is concerned with the asymptotic behavior of the dimensionless Von Karman plates without rotational inertia subjected to multiplicative white noise loadings as following:

$$u_{tt} + \alpha u_t + \Delta^2 u - [v(u) + F_0, u] = p + \sigma u \dot{W} \tag{3a}$$

with the following initial value and clamped boundary

$$t = 0; u = u_0, u_t = u_1 \tag{3b}$$

$$x \in \Gamma : u = \frac{\partial u}{\partial n} = 0 \tag{3c}$$

where $W(t) : \Omega \to \mathbb{R}$ is a one-dimensional two-sided Wiener process on a probability space will be specified later and α that is a positive constant denotes the damping coefficient of the system. $[\cdot, \cdot]$ denotes the Von Karman bracket with the expression:

$$[v, u] = \frac{\partial^2 u}{\partial x_1^2}\frac{\partial^2 v}{\partial x_2^2} + \frac{\partial^2 v}{\partial x_1^2}\frac{\partial^2 u}{\partial x_2^2} - 2\frac{\partial^2 u}{\partial x_1 \partial x_2}\frac{\partial^2 v}{\partial x_1 \partial x_2} \tag{3d}$$

here $v(u)$ is the Airy stress function satisfies the following elliptic problem

$$\Delta^2 v = -[u, u] \tag{3e}$$

$$x \in \Gamma : v = \frac{\partial v}{\partial n} = 0 \tag{3f}$$

It is well known that the long-time behavior of dynamical systems is captured by attractors. Crauel and Flandoli [3, 4] (see also, Schmalfuss [5, 6]) developed the concept of random attractor for random dynamical system [7], which cover some of the most common classes of systems involving randomness and time evolution and proved that the random attractor satisfies most of the properties satisfied by the usual attractor in the theory of deterministic dynamical systems. Many authors have studied random dynamical systems by these notions and methods. Various and wonderful phenomenon about long-time behavior are obtained such as those in [8–13] and the references therein.

The long-time behavior of Von Karman plate equations has been concerned by many authors, One can refer to [2, 14–16] and the references therein, too name but a few. To the best knowledge, there hardly exists results about random attractors for irrotational Von Karman plates subjected to multiplicative white noise loadings. It is

also mentioned that the traditional approach based on "splitting method" is useless to Von Karman plate equation without rotational inertia. For the reason, one can see [2], which produce the difficult to investigate the random attractors for system (3a)–(3f). From the proof of Proposition 3.6, Proposition 3.8 and Theorem 3.11 in [3], it can be obtained that the existence of compact absorbing set is not a necessary condition. Combining the slight modifications on Proposition 3.6 and Theorem 3.11 in [3] with stochastic version of the technique presented in [15] can guarantee the existence of random attractors for system (3a)–(3f).

The rest of this paper is organized as follows. In Sect. 2, some notations and preparation results are given. Utilize the "sharp regularity" of Von Karman bracket and semigroup theory, it is shown that the system (3a)–(3f) can generate RDS in Sect. 3. Section 4 is devoted to the existence of random attractors for the RDS.

2 Preliminaries

In this section, some basic concepts related to RDS and preliminaries that are important for getting the main results are presented. For more details, the reader can refer to [3, 4, 7]. In what follows the $H^s(D)$ denotes the L^2-based Sobolev space of order s and H_0^s is the closure of $C_0^\infty(D)$ in $H^s(D)$. The following notation are also emphasized

$$\|u\| \equiv \|u\|_{L^2(D)}, \|u\|_s \equiv \|u\|_{H_0^s(D)},$$
$$(u,v) \equiv (u,v)_{L^2(D)}, ((u,v)) = (u,v)_{H_0^2(D)}.$$

Let $E = H_0^2(D) \times L^2(D)$ equipped with inner product $(y_1, y_2)_E = ((y_1, y_1)) + (y_2, y_2)$, $\forall (y_1, y_2) \in E$ and norm $\|y\|_E = (y,y)_E^{\frac{1}{2}}$. For other situations, $\|\cdot\|_Y$ represent the norm relevant to Banach space Y.

Let $(X, \|\cdot\|_X)$ be a separable space with Borel σ-algebra $\mathscr{B}(X)$ and $(\Omega, \mathscr{F}, P)$ be a probability space. $\{\theta_t : \Omega \to \Omega, t \in \mathbb{R}\}$ is a family of measure preserving transformations such that $(t,\omega) \to \theta_t\omega$ is measurable, $\theta_0 = \mathrm{id}, \theta_{t+s} = \theta_t \circ \theta_s$ for all $s, t \in \mathbb{R}$. Then the flow θ_t together with the probability space $(\Omega, \mathscr{F}, P, \{\theta_t\}_{t\in\mathbb{R}})$ is called as a metric dynamical system.

Definition 1 A random dynamical system (RDS) on Polish space (X, d) with Borel σ-algebra $\mathscr{B}(X)$ over a metric dynamical system $(\Omega, \mathscr{F}, P, \{\theta_t\}_{t\in\mathbb{R}})$ is a $(\mathscr{B}(\mathbb{R}^+) \times \mathscr{F} \times \mathbb{B}(X), \mathbb{B}(X))$measurable mapping

$$\phi : \mathbb{R}^+ \times \Omega \times X \to X, \quad (t, \omega, x) \mapsto \Phi(t, \omega, x)$$

such that, for $P - a.s.\omega \in \Omega$,

(i) $\phi(0, \omega) = \mathrm{id}$ on X.
(ii) $\phi(t + s, \omega, \cdot) = \phi(t, \theta_s\omega, \cdot) \circ \phi(s, \omega, \cdot)$ for all $s, t \in \mathbb{R}^+$.

A RDS is continuous or differential if $\phi(t,\omega) : X \to X$ is continuous or differential. It is emphasized that RDS $\phi(t,\theta_{-t}\omega)$ can be understood as the solution start from $-t$ to 0.

Definition 2 A set-valued map $D : \Omega \to 2^X$ is said to be a closed (compact) random set, if $D(\omega)$ is closed (compact) for $P-a.s.\omega \in \Omega$ and $\omega \to d(x, D(\omega))$ is $P-a.s.$ measurable for all $x \in X$.

Definition 3 A random set $K(\omega)$ is said to absorb the set $B \subset X$ for a RDS ϕ, if $P-a.s.$ there exists $t_B(\omega)$ such that

$$\phi(t,\theta_{-t}\omega)B \subset K(\omega) \text{ for all } t \geq t_B(\omega)$$

Definition 4 A random set $\mathscr{A}(\omega)$ is called random attractor associated with the RDS ϕ, if $P-a.s.$

(i) $\mathscr{A}(\omega)$ is a random compact set.
(ii) $\mathscr{A}(\omega)$ is invariant, i.e., $\phi(t,\omega)\mathscr{A}(\omega) = \mathscr{A}(\theta_t\omega)$ for all $t \geq 0$
(iii) For all bounded (nonrandom) set $B \subset X$,

$$\lim_{t\to\infty} \text{dist}(\phi(t,\theta_{-t}\omega)B, \mathscr{A}(\omega)) = 0$$

where dist denotes the Hausdorff semidistance:

$$dis(A,B) = \sup_{x\in A}\inf_{y\in B} d(x,y), \quad A, B \subset X$$

The next lemma about "sharp regularity" of Von Karman bracket plays the key role in estimation of the solution for system (3a)–(3f).

Lemma 1 [2] *Assume that D is either smooth-bounded domain or a rectangular, Let Δ^{-2} denotes the inverse of Δ^2 supplied with clamped boundary conditions. Then the bilinear map $(u,w) \mapsto G(u,w) \equiv \Delta^{-2}[u,w]$ is bounded from $H^2(D) \times H^2(D)$ into $W^{2,\infty}(D)$ and the following estimations holds:*

$$\|[u,w]\|_{H^{-2}(D)} \leq C\|u\|_{H^1(D)}\|w\|_{H^2(D)}, \quad u \in H^1(D), w \in H^2(D), \tag{4}$$

$$\|G(u,v)\|_{W^{2,\infty}} \leq C\|u\|_{H^2(D)}\|v\|_{H^2(D)}, \quad u, v \in H^2(D). \tag{5}$$

Consequently,

$$\|[w, G(u,v)]\|_{L^2(D)} \leq C\|u\|_{H^2(D)}\|v\|_{H^2(D)}\|w\|_{H^2(D)}. \tag{6}$$

3 Random Dynamical System

In this section, the existence of RDS for system (3a)–(3f) is discussed. For this purpose, the system (3a)–(3f) should be converted into a deterministic system system with a random parameter.

To this end, the Ornstein–Uhlenbeck process is an useful tool. First, the following probability space $(\Omega, \mathscr{F}, P)$ is given, where

$$\Omega = \{\omega \in \mathscr{C}(\mathbb{R}, \mathbb{R}) : \omega(0) = 0\},$$

$\mathscr{F}$ is the Borel σ-algebra induced by the compact-open topology of Ω, and P the corresponding Wiener measure on $(\Omega, \mathscr{F})$. Define the time shift by

$$\theta_t\omega(\cdot) = \omega(\cdot + t) - \omega(t), \quad \omega \in \Omega, t \in \mathbb{R}.$$

Then $(\Omega, \mathscr{F}, P, \{\theta_t\}_{t\in\mathbb{R}})$ is a metric dynamical system. The Ornstein–Uhlenbeck process $z(\theta_t\omega)$ is the solution of the following Itô equation:

$$dz + \mu z dt = dW, \; z(-\infty) = 0, \tag{7}$$

with the form

$$z(\theta_t\omega) := -\mu \int_{-\infty}^{0} e^{\mu s}(\theta_t\omega)(s)ds, \quad t \in \mathbb{R}.$$

Suppose $F_0 \in W^{2,\infty}(D), p \in L^2(D)$ is time-independent function. It is well known that $\Delta^2 : H_0^2(D) \bigcap L^2(D) \to L^2(D)$, is a self-adjoint, positive, linear operator and its eigenvalues $\{\lambda_i\}_{i\in\mathbb{N}}$ satisfy $0 < \lambda_1 \le \lambda_2 \le \dots$, and $\lambda_m \to \infty$ as $m \to +\infty$. It is convenient to reduce (3a) to Itô form

$$\begin{cases} du = wdt \\ dw = \left(-\Delta^2 u - \alpha w + [v(u) + F_0, u] + p\right) dt + \sigma u dW \\ t = 0; u = u_0, v = u_1 \\ x \in \partial D : u = \frac{\partial u}{\partial n} = 0 \end{cases} \tag{8}$$

Set $\varepsilon = \frac{\alpha\lambda_1}{\alpha^2+3\lambda_1}$, $\varphi_1 = u$, $\varphi_2 = w + \varepsilon u - \sigma u z(\theta_t\omega)$, by (7) and Itô formula,

$$\begin{cases} \dfrac{\partial\varphi_1}{\partial t} = -\varepsilon\varphi_1 + \varphi_2 + \sigma\varphi_1 z(\theta_t\omega) \\ \dfrac{\partial\varphi_2}{\partial t} = (-\Delta^2\varphi_2 + \varepsilon(\alpha - \varepsilon))\varphi_1 + (\varepsilon - \alpha)\varphi_2 \\ \qquad \sigma\left(\mu + 2\varepsilon - \alpha - \sigma z(\theta_t\omega)\right) z(\theta_t\omega)\varphi_1 - \sigma z(\theta_t\omega)\varphi_2 \\ \qquad + [v(\varphi_1) + F_0, \varphi_1] + p \end{cases} \tag{9}$$

Let

$$\varphi = \begin{pmatrix} \varphi_1 \\ \varphi_2 \end{pmatrix}, L = \begin{pmatrix} -\varepsilon I & I \\ -\Delta^2 + \varepsilon(\alpha - \varepsilon) I & \varepsilon - \alpha \end{pmatrix}$$

$$F(\varphi, \theta_t\omega) = \begin{pmatrix} \sigma z(\theta_t\omega)\varphi_1 \\ -\sigma\left(\varphi_2 - \varepsilon\varphi_1 + \sigma\varphi_1 z(\theta_t\omega)\right) z(\theta_t\omega) \end{pmatrix} + \begin{pmatrix} 0 \\ (\mu - \alpha + \varepsilon)\sigma z(\theta_t\omega)\varphi_1 + [v(\varphi_1) + F_0, \varphi_1] \end{pmatrix}$$

Then the system (9) can be written as the following abstract evolution equation:

$$\frac{d\varphi}{dt} = L\varphi + F(\varphi, \theta_t\omega) \tag{10}$$

It follows from [17] that L is the infinitesimal generator of a C_0-semigroup e^{Lt} on E. According to Lemma 1, it is easy to check that $F(\varphi, \theta_t\omega) : E \to E$ is local Lipschitz. With the similar arguments in [17], the mild solution of System (10) is existence and uniqueness. And the solution can be expressed as

$$\varphi(t) = \varphi(t, \omega; \varphi_\tau(\omega)) = e^{L(t-\tau)}\varphi_\tau(\omega) + \int_\tau^t e^{L(t-s)} F(\varphi, \theta_s\omega) ds$$

for any $\varphi_\tau(\omega) \in E$ and $\forall\ \omega \in \Omega$. Then the following theorem holds

Theorem 1 *For any $T > 0$,*

(i) if $\varphi_\tau \in E$, then $\varphi(t) \in C([\tau, \tau + T); H_0^2(D)) \times C([\tau, \tau + T); L^2(D))$.
(ii) $\varphi(t, \theta_\tau; \varphi_\tau(\omega))$ is jointly continuous in t and $\varphi_\tau(\omega)$.

By Theorem 1, the solution mapping

$$\overline{S}_\varepsilon(t, \omega) : \varphi_0(\omega) \to \varphi(t, \omega; \varphi_0(\omega)),\ E \to E \tag{11}$$

generates a RDS. With the analogical arguments in [11], the system (8) also determines a RDS $S(t, \omega) = R(\theta_t\omega)\overline{S}_\omega(t, \varepsilon)R^{-1}(\omega)$, where $R(\theta_t\omega) : (u_0, u_1) \to (u_0, u_1 + \varepsilon u_0 - \sigma u_0 z(\theta_t\omega)$.

4 Random Attractors

In this section, the main results about random attractors for RDS corresponding to system (3a)–(3f) are given.

First, a theorem that give a criterion to the existence of random attractors for a RDS is presented as follow

Theorem 2 *Let ϕ be a RDS on a Polish space (X, d) with Borel σ-algebra $\mathscr{B}$ over the flow $\{\theta_t\}_{t\in\mathbb{R}}$ on a probability space $(\Omega, \mathscr{F}, P)$. Suppose there exists an absorbing set in X, and for any (nonrandom) bound set $B \subset X$, the set $\{\phi(t_n, \theta_{-t_n}\omega)u_n\}_{n=1}^{\infty}$ is relatively compact in X, where $t_n \to +\infty$, and $\{u_n\}_{n=1}^{\infty} \subset B$. Then the set*

$$A(\omega) = \overline{\bigcup_{B\subset X} \Lambda_B(\omega)}$$

is the random attractors for ϕ, where the union is taken over all bounded set $B \subset X$, and $\Lambda_B(\omega)$ is the ω-limit set B given by

$$\Lambda_B(\omega) = \bigcap_{s\geq 0} \overline{\bigcup_{t\geq s} \phi(t, \theta_{-t}\omega)B}$$

Moreover, the random attractor is unique.

Proof The proof is quite similar to the proof of Proposition 3.6 and Theorem 3.11 in [3].

In order to apply Theorem 2 to prove the existence of random attractors, first, it is necessary that the RDS $S(t, \omega)$ owns an absorbing set in E.

Lemma 2 *Suppose $\|F_0\|_{W^{2,\infty}(D)} < \frac{\varepsilon}{4}$, let $\psi \in E$ be a solution of system (10), with initial value $\psi_{-\tau} = (u_0, u_1) \in E$. $\rho(\omega)$ is a random variable. For any bounded (nonrandnom) set $B \subset E$, $P-a.s.$ there exists a $T_B(\omega) > 0$ such that for any $\psi_{-\tau} = (u_0, u_1) \in B, \forall \tau > T_B(\omega)$,*

$$\|\psi(\tau, \theta_{-\tau}\omega; \psi_{-\tau})\|_E \leq \rho(\omega) \tag{12}$$

for large enough μ in (7).

Proof Let φ be a solution of the System (9) with the initial value $\varphi_{-\tau} = (u_0, u_1 + \varepsilon u_0 - \sigma u z(\theta_{-\tau}\omega))^T$. Taking the inner product $(\cdot,\cdot)_E$ of (9) with φ, we have

$$\frac{1}{2}\frac{d}{dt}\left(\|\varphi_1\|_2^2 + \|\varphi_2\|^2\right) = (L\varphi, \varphi)_E + (F(\varphi, \theta_t\omega), \varphi)_E \tag{13}$$

Let $\mathscr{E}(\varphi_1, \varphi_2) = \left(\|\varphi_1\|_{H_0^2}^2 + \|\varphi_2\|_2^2 + \frac{1}{2}\|\Delta v(\varphi_1)\|_2^2\right)$, by the Cauchy–Schwartz inequality, it can be found that

$$\left(\sigma z(\theta_t\omega)\varphi_1, \varphi_1\right)_{H_0^2} \leq |\sigma z(\theta_t\omega)|\|\varphi_1\|_2^2 \leq 2|\sigma z(\theta_t\omega)|\mathscr{E}(\varphi_1, \varphi_2) \tag{14}$$

$$(-\sigma z(\theta_t\omega)\varphi_2, \varphi_2)_2 \leq |\sigma z(\theta_t\omega|\|\varphi\|_2^2 \leq |\sigma z(\theta_t\omega|\mathscr{E}(\varphi_1, \varphi_2) \tag{15}$$

$$\left(\sigma z(\theta_t\omega)\varepsilon\varphi_1, \varphi_2\right)_2 \leq \frac{1}{2\sqrt{\lambda_1}}|\varepsilon\sigma z(\theta_t\omega)|\mathscr{E}(\varphi_1, \varphi_2) \tag{16}$$

with the Properties 1.4.2 in [2], the following relations hold

$$\begin{aligned}\int_D [v,\varphi_1]\varphi_2 dx &= \int_D [(\varphi_1)_t,\varphi_1]v dx + \varepsilon\int_D [\varphi_1,\varphi_1]v dx - \sigma z(\theta_t\omega)\int_D [\varphi_1,\varphi_1]v dx\\ &\le -\frac{1}{2}\int_D (\Delta^2 v)_t v dx - \varepsilon\int_D \Delta^2 v v dx + |\sigma z(\theta_t\omega)|\int_D \Delta^2 v v dx\\ &= -\frac{1}{4}\frac{d}{dt}\|\Delta v\|^2 - \varepsilon\|\Delta v\|^2 + |\sigma z(\theta_t\omega)|\|\Delta v\|^2\end{aligned}$$

and

$$\begin{aligned}\int_D [F,\varphi_1]\varphi_2 dx &\le 4\|F\|_{W^{2,+\infty}}\|\varphi\|_{H_0^2}\|\varphi\|_2\\ &\le 2\|F\|_{W^{2,+\infty}}\left(\|\varphi\|_2^2 + \|\varphi\|^2\right)\end{aligned}$$

then

$$\begin{aligned}\left([v(\varphi_1)+F_0,\varphi_1],\varphi_2\right) \le &-\frac{1}{4}\frac{d}{dt}\|\Delta v\|^2 - \varepsilon\|\Delta v\|^2 + |\sigma z(\theta_t\omega)|\|\Delta v\|^2\\ &+ 2\|F\|_{W^{2,+\infty}}\left(\|\varphi\|_2^2 + \|\varphi\|^2\right)\end{aligned} \tag{17}$$

According Lemma 3 in [11], the relations (13)–(17) and Lemma 3 in [11] imply that, for a large enough μ in (7), the following hold

$$\begin{aligned}\frac{1}{2}\frac{d}{dt}\mathscr{E}(\varphi_1,\varphi_2) \le &-\left(\frac{\varepsilon}{2} - 2\|F\|_{W^{2,+\infty}}\right)\mathscr{E}(\varphi_1,\varphi_2)\\ &+\frac{1}{2\sqrt{\lambda_1}}\left(|\sigma(\mu+2\varepsilon-\alpha)||z(\theta_t\omega)| + |\sigma z(\theta_t\omega)|^2\right)\mathscr{E}(\varphi_1,\varphi_2)\\ &+\frac{1}{2\alpha}\|p\|^2\end{aligned} \tag{18}$$

Let $\varepsilon_0 = \left(\varepsilon - 4\|F\|_{W^{2,+\infty}}\right)$, then, for $\forall t \le 0$,

$$\begin{aligned}\mathscr{E}(\varphi_1,\varphi_2)(0) \le &\, e^{\left(\varepsilon_0 t + \int_t^0 \frac{1}{\sqrt{\lambda_1}}\left(|\sigma(\mu+2\varepsilon-\alpha)||z(\theta_s\omega)| + |\sigma z(\theta_s\omega)|^2\right)ds\right)}\mathscr{E}(\varphi_1,\varphi_2)(t)\\ &+\int_t^0 e^{\left(\varepsilon_0 k + \int_k^0 \frac{1}{\sqrt{\lambda_1}}\left(|\sigma(\mu+2\varepsilon-\alpha)||z(\theta_s\omega)| + |\sigma z(\theta_s\omega)|^2 ds\right)\right)}\frac{1}{2\alpha}\|p\|_2^2 dk\end{aligned}$$

By the relation between φ and ψ,

$$\begin{aligned}&\|(\psi_1,\psi_2)\|_E^2(0) = \|\varphi_1\|_2^2 + \|\varphi_2 - \varepsilon\varphi_1 + \sigma z\varphi_1\|^2(0)\\ \le &\|\varphi_1\|_2^2 + \|\varphi_2\|^2 + \|\varepsilon\varphi_1\| + \|\sigma z\varphi_1\|^2(0)\\ \le &(2+\varepsilon^2+|\sigma z(\omega)|^2)\left(e^{g_1(t)}\mathscr{E}(\varphi_1,\varphi_2)(t) + \int_t^0 \frac{e^{g_2(k)}}{2\alpha}\|p\|_2^2 dk\right)\end{aligned}$$

where

$$g_1(t) = \left(\varepsilon_0 t + \int_t^0 \frac{1}{\sqrt{\lambda_1}} \left(|\sigma(\mu + 2\varepsilon - \alpha)||z(\theta_s\omega)| + |\sigma z(\theta_s\omega)|^2 \right) ds \right)$$

and

$$g_2(k) = \left(\varepsilon_0 k + \int_k^0 \frac{1}{\sqrt{\lambda_1}} \left(|\sigma(\mu + 2\varepsilon - \alpha)||z(\theta_s\omega)| + |\sigma z(\theta_s\omega)|^2 \right) ds \right)$$

By Lemma 1 in [11] and Lemma 1, it can be concluded that for any nonrandom bounded set $B \subset E$ with radius $r(B)$, $P - a.s.$ there exists $T_B(\omega) > 0$ such that for any $\tau > T_B(\omega)$,

$$(e^{g_1}\mathscr{E}(\varphi_1, \varphi_2))(-\tau) < 1$$

then,

$$\|(\psi_1, \psi_2)\|_E^2(0) \leq \rho(\omega)$$

where

$$\rho(\omega) = (2 + \varepsilon^2 + |\sigma z(\omega)|^2) \left(1 + \int_{-\infty}^0 \frac{e^{g_2(k)}}{2\alpha} \|p\|_2^2 dk \right)$$

Thus, the proof completed.

Remark 1 In practical problem, F_0 contains the longitudinal external force. From (18), it can be found that, if the F_0 is too large, then the decay estimation is impracticable, the system may be unstable, This conforms the phenomenon in engineering.

Now, let us turns to concern with the compactness requested in Theorem (2).

Lemma 3 *Assume B is a bounded subset of E. Then for any $\varepsilon > 0$ there exists $T = T_B(\varepsilon, \omega)$ such that*

$$\limsup_{n\to\infty} \sup_{p\in\mathbb{N}} \|S(T, \theta_{-T}\omega)\psi_{n+p} - S(T, \theta_{-T}\omega)\psi_n\|_E \leq \varepsilon \tag{19}$$

where $\{\psi_n\}$ is a sequence in B and $\{S(T, \theta_{-T}\omega)\psi_n\}$ weakly star converges in $L^\infty(0, \infty; E)$).

Proof Let $\varphi_{n+p} = \overline{S}_\varepsilon(t, \theta_{-t}\omega)\varphi_{-t,n+p}, \varphi_n = \overline{S}_\varepsilon(t, \theta_{-t}\omega)\varphi_{-t,n}$ where $\varphi_{-t,n+p} = R(\theta_{-t}\omega)\psi_{n+p}, \varphi_{-t,n} = R(\theta_{-t}\omega)\psi_n$. Similar as the estimation of Lemma 2, properly chose μ, we have

$$
\begin{aligned}
&\frac{1}{2}\frac{d}{dt}\left(\|\varphi_{n+p,1}-\varphi_{n,1}\|_2^2+\|\varphi_{n+p,2}-\varphi_{n,2}\|^2\right)\\
&\quad+\frac{\varepsilon-\|F_0\|_{W^{2,+\infty}}}{2}\left(\|\varphi_{n+p,1}-\varphi_{n,1}\|_2^2+\|\varphi_{n+p,2}-\varphi_{n,2}\|^2\right)\\
&\le k_1(1+\varepsilon)(|z(\theta_t\omega)|+|z(\theta_t\omega)|^2)\left(\|\varphi_{n+p,1}-\varphi_{n,1}\|_2^2+\|\varphi_{n+p,2}-\varphi_{n,2}\|^2\right)\\
&\quad+\left([v(\varphi_{n+p,1}),\varphi_{n+p,1}]-[v(\varphi_{n,1}),\varphi_{n,1}],\varphi_{n+p,2}-\varphi_{n,2}\right)_2 \qquad (20)
\end{aligned}
$$

Set $\delta=\frac{\varepsilon}{2}-\frac{\|F_0\|_{2,+\infty}}{2}$, then

$$
\begin{aligned}
&\frac{1}{2}\left(\|\varphi_{n+p,1}-\varphi_{n,1}\|_2^2+\|\varphi_{n+p,2}-\varphi_{n,2}\|^2\right)(0)\\
&\quad+\delta\int_s^0\left(\|\varphi_{n+p,1}-\varphi_{n,1}\|_2^2+\|\varphi_{n+p,2}-\varphi_{n,2}\|^2\right)(\tau)d\tau\\
&\le\int_s^0\sigma z(\theta_t\omega)\|\varphi_{n+p,1}-\varphi_{n,1}\|_2^2(\tau)d\tau+\int_s^0|\sigma z(\theta_t\omega)|\|\varphi_{n+p,2}-\varphi_{n,2}\|_2^2(\tau)d\tau\\
&\quad+\int_s^0\left|\sigma\left(\mu+2\varepsilon-\alpha-\sigma z(\theta_t\omega)\right)z(\theta_t\omega)\right|(\varphi_{n+p,1}-\varphi_{n,1},\varphi_{n+p,2}-\varphi_{n,2})_2(\tau)d\tau\\
&\quad+\int_s^0\left([v(\varphi_{n+p,1}),\varphi_{n+p,1}]-[v(\varphi_{n,1}),\varphi_{n,1}],\varphi_{n+p,2}-\varphi_{n,2}\right)_2(\tau)d\tau\\
&\quad+\frac{1}{2}\left(\|\varphi_{n+p,1}-\varphi_{n,1}\|_2^2+\|\varphi_{n+p,2}-\varphi_{n,2}\|^2\right)(s) \qquad (21)
\end{aligned}
$$

from which,

$$
\begin{aligned}
&\frac{T}{2}\left(\|\varphi_{n+p,1}-\varphi_{n,1}\|_2^2+\|\varphi_{n+p,2}-\varphi_{n,2}\|_2^2\right)(0)\\
&\le\int_s^0\sigma z(\theta_t\omega)\|\varphi_{n+p,1}-\varphi_{n,1}\|_2^2(\tau)d\tau+\frac{1}{2}\left(\|\varphi_{n+p,1}-\varphi_{n,1}\|_2^2+\|\varphi_{n+p,2}-\varphi_{n,2}\|^2\right)(s)\\
&\quad+\int_s^0\left|\sigma\left(\mu+2\varepsilon-\alpha-\sigma z(\theta_t\omega)\right)z(\theta_t\omega)\right|(\varphi_{n+p,1}-\varphi_{n,1},\varphi_{n+p,2}-\varphi_{n,2})_2(\tau)d\tau\\
&\quad+\int_s^0|\sigma z(\theta_t\omega)|\|\varphi_{n+p,2}-\varphi_{n,2}\|_2^2(\tau)d\tau\\
&\quad+\int_s^0\left([v(\varphi_{n+p,1}),\varphi_{n+p,1}]-[v(\varphi_{n,1}),\varphi_{n,1}],\varphi_{n+p,2}-\varphi_{n,2}\right)_2(\tau)d\tau
\end{aligned}
$$

similar estimations for $\delta\int_s^0\left(\|\varphi_{n+p,1}-\varphi_{n,1}\|_2^2+\|\varphi_{n+p,2}-\varphi_{n,2}\|_2^2\right)(\tau)d\tau$ can also be obtained, then

$$
\begin{aligned}
&\left(\|\varphi_{n+p,1}-\varphi_{n,1}\|_2^2+\|\varphi_{n+p,2}-\varphi_{n,2}\|^2\right)(0)\\
\le&\frac{1}{T}\int_T^0\int_s^0|\sigma z(\theta_t\omega)|\|\varphi_{n+p,1}-\varphi_{n,1}\|_2^2(\tau)d\tau ds+\frac{1}{T}\int_T^0\int_s^0|\sigma z(\theta_t\omega)|^2\|\psi_2-\chi_2\|_2^2(\tau)d\tau ds\\
&+\frac{1}{T}\int_T^0\int_s^0\left|\sigma\left(\mu+2\varepsilon-\alpha-\sigma z(\theta_t\omega)\right)z(\theta_t\omega)\right|^2(\varphi_{n+p,1}-\varphi_{n,1},\varphi_{n+p,2}-\varphi_{n,2})_2(\tau)d\tau ds\\
&+\frac{1}{T}\int_T^0\int_s^0\left([v(\varphi_{n+p,1},\varphi_{n+p,1}]-[v(\varphi_{n,1},\varphi_{n,1}],\varphi_{n+p,2}-\varphi_{n,2}\right)(\tau)d\tau ds\\
&+\frac{\delta}{T}\left[\int_s^0\sigma z(\theta_t\omega)\|\varphi_{n+p,1}-\varphi_{n,1}\|_2^2(\tau)d\tau\right.\\
&+\int_s^0\left|\sigma\left(\mu+2\varepsilon-\alpha-\sigma z(\theta_t\omega)\right)z(\theta_t\omega)\right|(\varphi_{n+p,1}-\varphi_{n,1},\varphi_{n+p,2}-\varphi_{n,2})_2(\tau)d\tau\\
&+\int_s^0|\sigma z(\theta_t\omega)|\varphi_{n+p,2}-\varphi_{n,2}(\tau)d\tau\\
&+\int_s^0\left([v(\varphi_{n+p,1}),\varphi_{n+p,1}]-[v(\varphi_{n+p,1}),\varphi_{n+p,1}],\varphi_{n+p,2}-\varphi_{n,2}\right)_2(\tau)d\tau\\
&\left.+\frac{1}{2}\left(\|\varphi_{n+p,1}-\varphi_{n,1}\|_2^2+\|\varphi_{n+p,2}-\varphi_{n,2}\|^2\right)(s)\right] \qquad (22)
\end{aligned}
$$

It now in the position to adapt the Lemma 4 in [15]. Combine with the Lemma 1 in [11] and the relation between $S(t,\omega)$ and $\overline{S}_\varepsilon(t,\varepsilon)$, this theorem can be proved.

According to Lemma 3, the following results holds

Lemma 4 *For any bounded set $B\subset E$, the set $\{S(t_n)\psi_n\}_{n=1}^\infty$ is relatively compact in E, where $t_n\to\infty$ and $\{\theta_n\}_{n=1}^\infty\subset B$.*

Proof This is the stochastic version of Theorem 2 in [15]. Rely on Kuratowski $\alpha-$measure of noncompactness, the proof is very similar to Proposition 7.1.12 in [2].

By Theorem 2, Lemmas 2–4, the main result can be formulated

Theorem 3 *The RDS associated with* (3a)–(3f) *has a random attractors in E.*

In the present article, the existence of random attractors of the Von Karman plate equation without rotational inertia has been discussed. On the other hand, one of the most interesting properties of attractors for deterministic infinite-dimensional dynamical systems is that these compact sets are in fact finite-dimensional subsets of the original phase space [18], this result reveal the fact that the asymptotic behavior of these systems can be described using a finite number of degrees of freedom. In some cases, the random attractor is finite dimensional also, there exist some approaches to estimate the dimension of random attractors, such as the methods in [19–22]. From the practical view, the numerical result that based on the Approximate Inertial Manifolds for Von Karman plate equation without rotational inertia is also important and meaningful. The authors will pursue this line of research in the near future.

Acknowledgment This research was supported by NSFC (NO.91216106 and NO.11472089)

References

1. Amabili, M.: Nonlinear vibrations and stability of shells and plates. Cambridge University Press, Cambridge (2008).
2. Chueshov, I., Lasiecka, I.: Von Karman Evolution Equations: Well-posedness and Long Time Dynamics. Springer Science & Business Media, Berlin-Heidenburg (2010).
3. Crauel, H., Flandoli, F.: Attractors for random dynamical systems, Prob. Theory and Related Fields. **100**, 365–393 (1994).
4. Crauel, H., Debussche, A., Flandoli, F.: Random attractors, J. Dynam. Differential Equations, **9(2)**, 307–341 (1997).
5. Schmalfuss, B.: Measure attractors and stochastic attractors. Inst. f*ü*r Dynamische Systeme. Fachbereich Mathematik and Informatik, 1995.
6. Arnold, L., Schmalfuss, B.: Fixed points and attractors for random dynamical systems, IUTAM Symposium on Advances in Nonlinear Stochastic Mechanics. Springer Netherlands (1996)
7. Arnold, L.: Random dynamical systems. Springer Science & Business Media, Berlin-Heidenburg (2013).
8. Bates, P., Lu, K., Wang, B.: Random attractors for stochastic Reaction-Diffusion equations on unbounded domains, J. Differ. Equations. **246**, 845–869 (2009).
9. T. Caraballo, T., Langa, J.A., Robinson, J.C.: Stability and random attractors for a reaction-diffusion equation with multiplicative noise. Discrete. Cont. Dyn. **6(4)**, 875–892 (2000).
10. Fan, X.: Random attractor for a damped Sine-Gordon equation with white noise. Pacific J. of Math., **216(1)**, 63–76 (2004).
11. Fan, X.: Attractors for a damped stochastic wave equation of Sine- Gordon type with sublinear multiplicative noise. Stoc. Anal. Appl., **24**, 767–793 (2006).
12. Zhou, S., Yin, F., Ouyang, Z.: Random attractor for damped nonlinear wave equations with white noise. SIAM J. Appl. Dyn. Syst. **4(4)**, 883–903 (2005).
13. Fan, X., Chen, H.: Attractors for the stochastic reaction-diffusion equation driven by linear multiplicative noise with a variable coefficient. J. Math. Anal. Appl. **398(2)**,715–728 (2013).
14. Chueshov, I.: Regularity of solutions and approximate inertial manifolds for von Karman evolution equations. Math. Methods. Appl. Sci. **17(9)**, 667–680 (1994).
15. Khanmamedov, A.K.: Global attractors for von Karman equations with nonlinear interior dissipation. J. Math. Anal. Appl. **318(1)**: 92–101 (2006).
16. Khanmamedov, A.K.: Finite dimensionality of the global attractors for von Karman equations with nonlinear interior dissipation. Nonlinear Anal.-Theor. **66(1)**, 204–213 (2007).
17. Lions, J.L.: Quelques méthodes de résolution des problèmes aux limites non linéaires. Dunod, Paris (1969)
18. Temam, R. Infinite dimensional dynamical systems in mechanics and physics. Springer-Verlag, New York (1997).
19. Crauel, H., Flandoli, F.: Hausdorff dimension of invariant sets for random dynamical systems, J. Dynam. Differ. Equs. **10(3)**, 449–474 (1998).
20. Debussche, A.: On the finite dimensionality of random attractors. Stoc. Anal. Appl. **15(4)**, 473–492 (1997).
21. Debussche, A.: Hausdorff dimension of a random invariant set, J. Math. Pure Appl., **77**, 967–988 (1998).
22. Langa J.A., Robinson, J.C.: Fractal dimension of a random invariant set. J. Math. Pure. Appl. 2006, 85(2): 269–294.

The Use of Fuzzy Logic in the Control of an Inverted Pendulum

Adrian Chmielewski, Robert Gumiński, Paweł Maciąg and Jędrzej Mączak

Abstract Fuzzy logic control is an example of the type of developing the control algorithms using softcomputing, reflecting the imperfections of the real world. The main principle of this type of programming and, therefore, fuzzy logic is to use uncertainty and a part of the truth hidden in the received information in order to achieve the stability and the shortest possible time and simplicity of the implementation. The paper presents an example of using the fuzzy controller in order to maintain proper control of an inverted pendulum. Prepared model of an inverted pendulum pivotally mounted on a carriage represents a nonlinear dynamic object with two degrees of freedom. Control of the system is accomplished by force extortion of the corresponding displacement of the carriage. On the basis of derived equations of motion, the dynamic model of the system in Matlab/Simulink was prepared. At the stage of building a fuzzy controller, they proposed input and output linguistic variables with the respective functions of belonging and base rules. In this paper, the results of a simulation operation of the system of fuzzy logic were presented. Also the advantages and disadvantages of the proposed control method were discussed.

A. Chmielewski (✉) · R. Gumiński · P. Maciąg · J. Mączak
Faculty of Automotive and Construction Machinery Engineering, Institute of Vehicles, Warsaw University of Technology, Narbutta 84, 02–524 Warsaw, Poland
e-mail: a.chmielewski@mechatronika.net.pl

R. Gumiński
e-mail: rgumin@simr.pw.edu.pl

P. Maciąg
e-mail: pawmac47@gmail.com

J. Mączak
e-mail: jma@mechatronika.net.pl

© Springer International Publishing Switzerland 2016

J. Awrejcewicz (ed.), *Dynamical Systems: Theoretical and Experimental Analysis*, Springer Proceedings in Mathematics & Statistics 182, DOI 10.1007/978-3-319-42408-8_7

1 Introduction

Modelling the qualities of physical objects is particularly vital from the cognitive standpoint as well as the predictive perspective [3–5, 12–14]. There are many modelling methods, this article focuses on fuzzy logic. The main use of fuzzy logic is supporting the systems of control, regulation and decision-taking. This is quite a new mathematical problem, because at the first time it was heard of was in the 1960s of the last century. It is based on the theory of fuzzy sets introduced by [20]. In the beginning it was just one of numerous mathematical theories, however, Zadeh's work was promptly built upon by such scientists as Mamdani [9], Sugeno or Yager [17, 18], to create the form enabling its application in industrial technology, house technology and medicine (Angiulli and Versaci [1], (Alhanjouri and Alhaddad [2, 8]. In the case of fuzzy sets, the membership of elements in a set can be partial, i.e. the membership function adopts values from the range [0, 1], unlike in the classical set theory, where an element either belongs or does not belong to the set, which means the membership function adopts values 0 or 1. For this reason, fuzzy logic can be described in simplest terms as multivalent logic, a generalisation of classical logic based on classical set theory [15]. It is worth mentioning that fuzzy logic is based to a large degree on linguistic quantities, i.e. variables, the values of which are words, not numbers. Although words are less precise than numbers, their application is more approximate to human nature. Additionally, each piece of "precise" information expressed by a number is laden with measurement error, thus it is also imprecise. This is why operating with words allows for using tolerance towards the lack of precision of information, due to which costs of the solution can be lowered.

Fuzzy logic is an example of control form using softcomputing [19]. Opposite to traditional programming, softcomputing uses imperfection of the real world. The main principle of the above form of programming, thus of fuzzy logic, too, is using uncertainty and a part of hidden truth in the received information in order to obtain the highest possible execution speed, stability and simplicity of achieving the solution.

A typical scheme of the fuzzy system operation consists of several stages: fuzzification, inference on the basis of rules (implication, aggregation) and defuzzification [16, 6]. Inference takes place on the basis of the principles written for the fuzzy sets. As a consequence, the data fed at the input to the controller undergo fuzzification, i.e. for the existing variable value, a degree of membership in fuzzy sets of linguistic variable is defined. In this step, the functions of membership to individual sets of input variables are used. The rule base includes rules of conduct for the cases which can occur during the process, it is registered in the form of a set of conditional instructions. There are two most frequently used fuzzy models: the Mamdani model [9] and Takagi-Sugeno model [11]. In both models sets of rules are used, in the first, however, the conditional instruction (if-then rule) consequent is a fuzzy set, whereas in the Takagi-Sugeno model—it is a function of

input variables. In the controller presented further in this work, the Mamdani model will be used.

Inferring depends on activating the rules, the conditions of which are fulfilled and on the change of shape of the membership function of the conclusion set, depending on the adopted method, through truncating or scaling. The next step is connecting (aggregation) of sets for every output variable. The last step is defuzzification, i.e. obtaining a specific numerical value on the basis of a fuzzy answer. Most frequently, determining the "*sharp*" value on the basis of the fuzzy set takes place through determining the set's centre of gravity; computing the average from the maxima, choosing the biggest or the smallest of the maxima, the bisection method, etc., are possible, too.

Later in the article, an example of using fuzzy logic in the system controlling the position of an inverted pendulum will be presented. The dynamic model of a mobile carriage with an inverted physical pendulum [7] attached by a joint will be discussed. This system has been described by means of the differentiation equations of the pendulum and carriage motion, which subsequently will be fed to the Matlab–Simulink programme (Matlab Documentation Center [10]). The last step will consist in designing the fuzzy controller maintaining the pendulum in the vertical position.

2 Description of the Model

Figure 1 shows the diagram of the model, with forces acting on the carriage and pendulum marked. Below, the description and values of all the physical quantities necessary for building the dynamic model are presented.

where:

$F\,[N]$—force controlling the carriage,
$N,\ P\,[N]$—horizontal and vertical component of the reaction force in the joint,
$b = 0.1\,[\mathrm{N}\cdot\mathrm{s}/m]$—coefficient of friction for carriage,
$M = 0.4\,[\mathrm{kg}]$—mass of carriage,
$m = 0.1\,[\mathrm{kg}]$—mass of pendulum,
$l = 0.4\,[\mathrm{m}]$—distance from the joint to the pendulum's centre of mass,
$J\,[\mathrm{kg\,m^2}]$—pendulum moment of inertia,
$x\,[m]$—carriage position,
$\Theta\,[\mathrm{rad}]$—pendulum position,
$x_w,\ y_w\ [m]$—position of pendulum's centre of gravity.

The above-mentioned system has two degrees of freedom: horizontal transition of the carriage and the rotation of the pendulum, so the coordinates describing its present state are Θ and x. In order to derive equations, the coordinate system must be adopted. The simplest way of conduct assumes the Cartesian system of coordinates with the abscissa of the same direction as the coordinate x marked in Fig. 1,

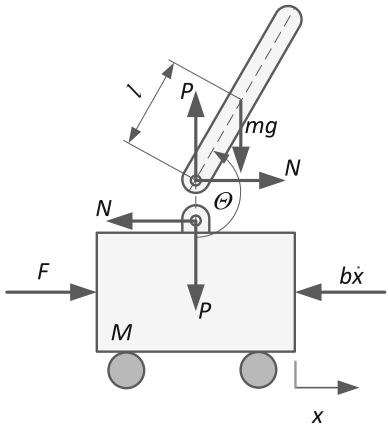

Fig. 1 Illustration of the discussed model of the carriage and inverted pendulum

and with the ordinate perpendicular to the abscissa and oriented upwards. The equation of horizontal forces acting on the carriage takes the form:

$$M\ddot{x} = F - N - b\dot{x} \tag{1}$$

The equations of forces and moments acting on the pendulum are as follows:

$$m\ddot{x_w} = N \tag{2}$$

$$m\ddot{y_w} = P - mg \Rightarrow P = m\left(\ddot{y} + g\right) \tag{3}$$

$$J\ddot{\Theta} = Nlsin(\Theta - 90°) - Plsin(180° - \Theta) = -Nlcos(\Theta) - PLsin(\Theta) \tag{4}$$

Coordinates x_w and y_w can be shown as direct functions of the pendulum deviation Θ:

$$x_w = x + lcos(\Theta - 90°) = x + lsin(\Theta) \tag{5}$$

$$y_w = lsin(\Theta - 90°) = -lcos(\Theta) \tag{6}$$

$$\dot{x_w} = \dot{x} + l\dot{\Theta}\cos(\Theta) \tag{7}$$

$$\dot{y_w} = l\dot{\Theta}\sin(\Theta) \tag{8}$$

$$\ddot{x_w} = \ddot{x} + l\ddot{\Theta}\cos(\Theta) - l\dot{\Theta}^2\sin(\Theta) \tag{9}$$

$$\ddot{y_w} = l\ddot{\Theta}\sin(\Theta) + l\dot{\Theta}^2\cos(\Theta) \tag{10}$$

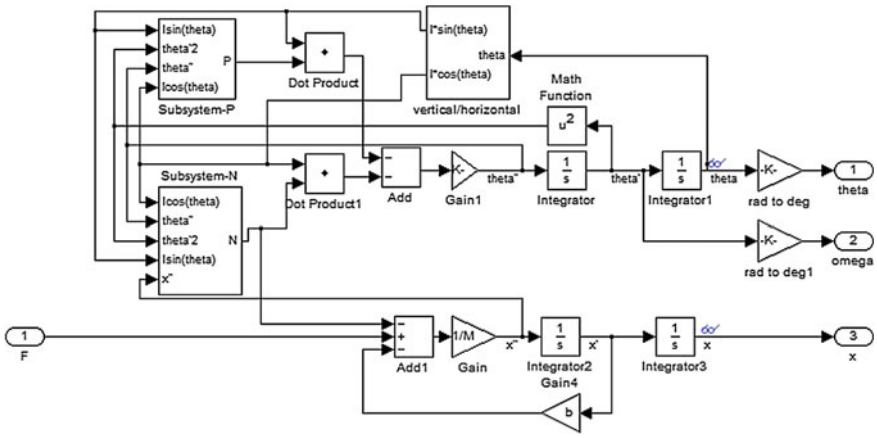

Fig. 2 Diagram of the model of the inverted pendulum on a mobile carriage prepared in the Matlab&Simulink programme

Substituting expressions (9) and (10) to formulae (2) and (3), allows for derivation of equations of unknown values of reactions at a pin (Fig. 1):

$$N = m\left(\ddot{x} + l\ddot{\Theta}\cos(\Theta) - l\dot{\Theta}^2\sin(\Theta)\right) \tag{11}$$

$$P = m\left(g + l\ddot{\Theta}\sin(\Theta) + l\dot{\Theta}^2\cos(\Theta)\right) \tag{12}$$

From this point, forces P and N can be treated as known, therefore, we obtain equations of the model's motion from Eqs. (1) and (4):

$$\ddot{x} = \frac{1}{m}[F - N - b\dot{x}] \tag{13}$$

$$\ddot{\Theta} = \frac{1}{J}[-Nlcos(\Theta) - Plsin(\Theta)] \tag{14}$$

These equations can be fed into the Simulink programme in a simple way in the purpose of building the simulation model of the considered system *(Matlab 2015)*. Figure 2 shows a diagram of the model of the inverted pendulum on a mobile carriage.

3 Description of the Fuzzy Controller

The task of the fuzzy controller presented further on in this chapter will be maintaining the pendulum from the above-mentioned model in the vertical position. The angle of the pendulum deviation is understood as a deviation from the vertical when

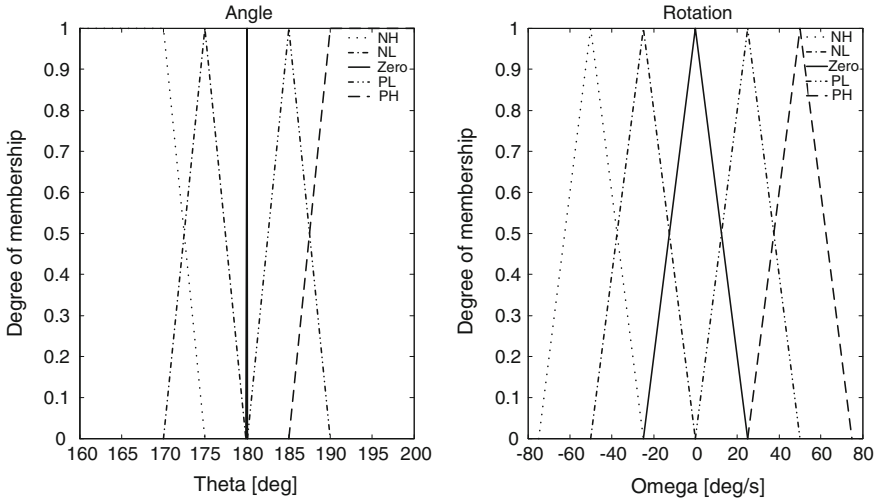

Fig. 3 Membership functions of input variables to the controller of the pendulum position

the pendulum is turned downwards ($\Theta = 0°$), therefore the work area of the pendulum will be oscillating around the value $\Theta = 180°$, i.e. the vertical. The input values of the controller are linguistic variables: *"the angle"* of the pendulum position and *"angular velocity"* of the pendulum.

The membership functions for the input values are shown in Fig. 3. The values of all linguistic variables have been defined as the following sets: negative high (NH), negative low (NL), zero (Zero), positive low (PL), positive high (PH). The membership functions have been defined as triangular functions with the exception of two extremes for the linguistic variable *"the angle"*.

Due to the large number of membership functions in the proximity of the angle analogous to the preset position, it is possible to determine more precisely its position with the help of fuzzy numbers, thus determining more precisely the output value.

The controller's output is the force F applied to the carriage. Similarly as in the case of the input membership functions, the output membership functions take the form of densely distributed fuzzy sets (Fig. 4).

The last element of designing the fuzzy controller is connection of the input fuzzy sets with the output sets by means of rules in the form of the *if-then* conditional instructions. The rule base is shown in Table 1. The rule antecedents (input data) have their representations in rows (*angle*) and columns (*angular velocity*), whereas the consequents have been placed in the matrix cells.

Taking a look at Table 1 enables the observation that using fuzzy logic in controlling is intuitive and versatile. After defining a series of membership functions, the controller's behaviour can be unequivocally described with their help and

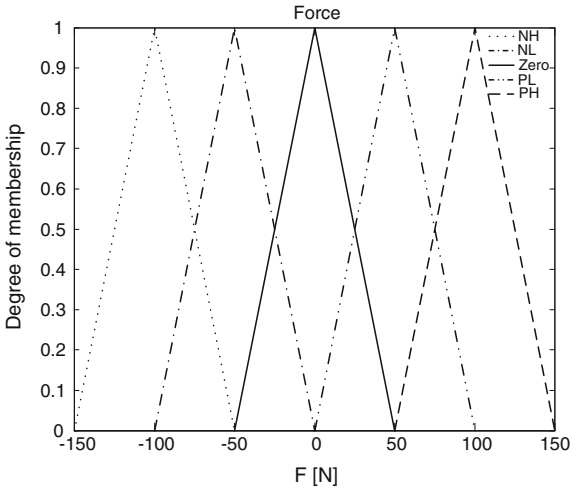

Fig. 4 Membership functions of the output variable from the pendulum position controller

Table 1 Rule bases of the controller responsible for the pendulum position

		Angular velocity				
Angle		UW	UN	Zero	DN	DW
	UW	R1:	R2:	R3:	R4:	R5:
		PH	PH	PH	PL	Zero
	UN	R6:	R7:	R8:	R9:	R10:
		PH	PH	PL	Zero	Zero
	Zero	R11:	R12:	R13:	R14:	R15:
		PL	PL	Zero	NL	NL
	DN	R16:	R17:	R18:	R19:	R20:
		Zero	Zero	NL	NH	NH
	DW	R21:	R22:	R23:	R24:	R25:
		Zero	NL	NH	NH	NH

using the rule base, which is analogous to human intuition: the pendulum drops to the right—push the carriage to the left; the pendulum is in position but about to start falling—push it so that it keeps resting, the pendulum is tilted to the left, but strives towards the equilibrium position—do not do anything, etc.

In the course of constructing the controller, a subjective perception of the issue is taken into consideration, that is why the controller prepared by a different author can have a differently defined fuzzy sets and rules.

Figure 5 shows the model of the object connected with the above-mentioned fuzzy controller. The controlled object is presented in the form of a submodel; a detailed model of an inverted pendulum is shown in Fig. 2.

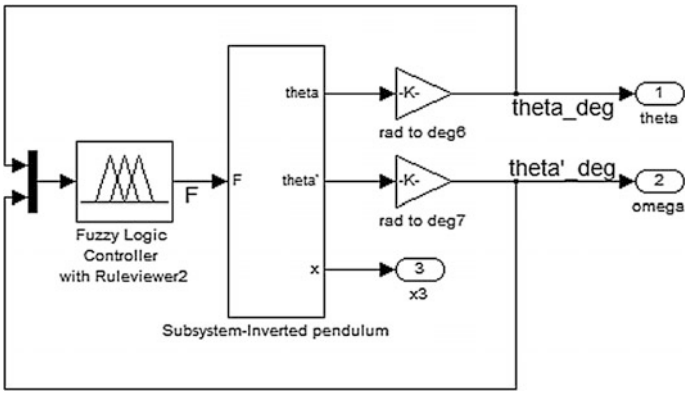

Fig. 5 Diagram of a control system of inverted pendulum

4 Results of Controlling the Inverted Pendulum

In order to evaluate the controller's work, a series of simulations has been performed, with different initial conditions. They have been described at the beginning of each simulation. All simulations have one characteristic in common, constant initial velocity of the carriage. The results are presented below in the form of the charts of the function of the pendulum position, its velocity and force F, i.e. input and output quantities from the controller. Each flow chart is accompanied by a short commentary.

The first simulation has been carried out for the following initial conditions: $\Theta = 160°$, $\dot{\Theta} = 0°/s$. After the simulation was started, as a result of immediate application of force on the carriage (Fig. 6), a sudden increase of angular velocity of the pendulum and a linear angle growth to the required value take place; next, the negative force, which lead the pendulum to the stand-still in the vertical position occurs, causes the decrease in the pendulum velocity. The occurring force values are of impulse character. This results from the fact that fuzzy sets for "*big*" force values were defined for the output variable. The simulations' initial conditions cause activation of the rule No. 3 (Table 1), which produces a fuzzy set "*Positive High*", and after defuzzification—the force equal to approximately 80 N, and, in consequence, an increase in the pendulum angular velocity. Subsequently, the increasing pendulum velocity causes activation of the rule No. 4 (which has a set of forces PL "*Positive Low*" registered in the consequent), and next, of the rule No. 5, which results in acquiring the forces from the "*Zero*" set at the simultaneous decrease in meaning of the third rule, and as a consequence the force value amounts to approximately 0 N.

In the case when the angle adopts the value of approximately 180°, the force adopts negative values, which is related to activation of the rules 14 and 15. It should be also emphasised that the suggested rules and fuzzy sets do not allow for

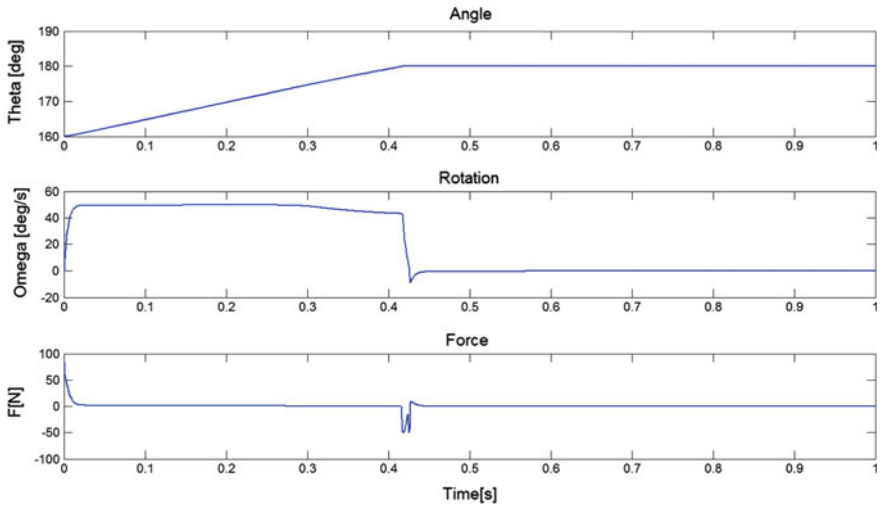

Fig. 6 Curves of angle, angular velocity and force for initial conditions: $\Theta = 160°$, $\dot{\Theta} = 0°/s$

acceleration of the pendulum over 75°/sin spite of big values of forces. The achieved result of decrease in the force value with increase in the angular velocity, and limiting the pendulum angular velocity, prevents occurrence of pendulum oscillations. Defining the fuzzy sets for the linguistic variable "*angular velocity*" within the range (−75, 75) causes negative results, too, i.e. when the pendulum has the speed from outside this range (for example initial conditions), the controlling force will equal zero (for the presented rule base). Limiting the velocity can be imposed also at the object's model but causing limitations in the controller has an advantage in the case of implementation of this algorithm at the real object.

The second simulation was carried out for the initial angle value of $\Theta = 185°$ and angular velocity $\dot{\Theta} = -25°/s$. In the case of this simulation, the pendulum is slightly deviated from the position of equilibrium, but it has a speed value assigned, due to which it seeks the equilibrium position. The input data to the fuzzy system in the form of initial conditions cause activation of the rule No. 17 (Table 1), which has a fuzzy set "*Zero*" registered in the consequent. As a consequence, for nearly 0.2 s the force value is equal to approximately 0 N (Fig. 7); the occurence of a small value of force (~0 N) is caused by a slight decrease in the pendulum angular velocity resulting from the action of the gravitational force (friction at the joint was neglected in the model), which results in activating the rule No. 18. After nearly 0.2 s, the angle value amounts to around 180°, which activates the rule No. 7 causing the occurrence of the force of about 40 N lowering the velocity of the pendulum. The pendulum achieves the predetermined position.

The third simulation was started for the pendulum deviation from the vertical $\Theta = 200°$, and the deviation increases due to the initial velocity $\dot{\Theta} = 30°/s$.

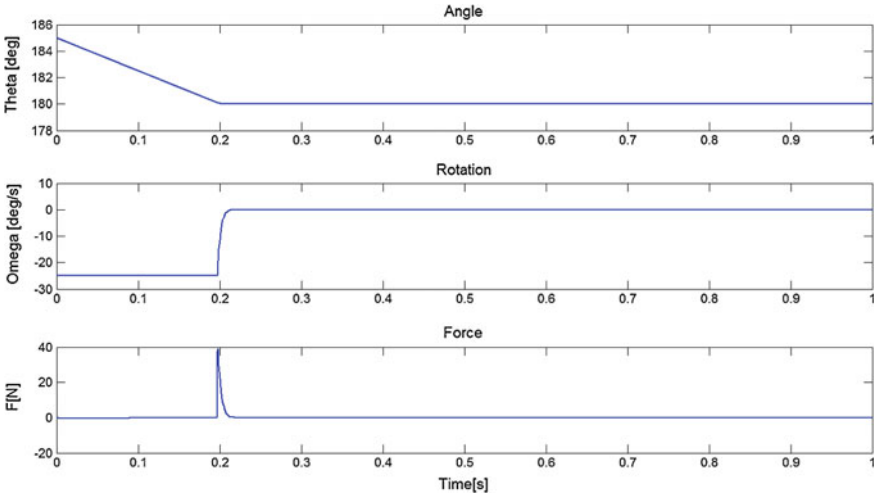

Fig. 7 Curves of angle, angular velocity and force for initial conditions: $\Theta = 185°$, $\dot{\Theta} = -25°/s$

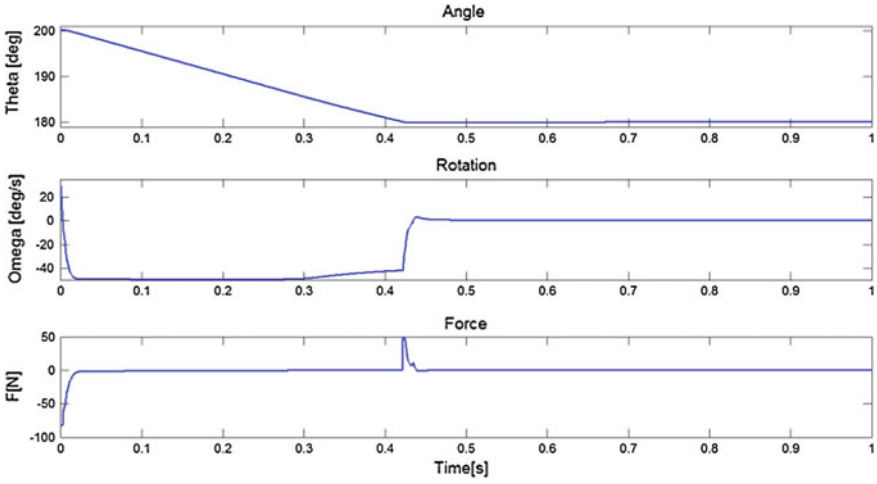

Fig. 8 Curves of angle, angular velocity and force for initial conditions: $\Theta = 200°$, $\dot{\Theta} = 30°/s$

The input signals to the fuzzy control system comply with the rule Nos. 24 and 25, which produce at the output "*Negative High*" the set of forces (Table 1), that is why the force value after starting the simulation amounts to about—83 N (Fig. 8). Operation of this force, increasing after activation of the rules 23 and subsequently 22 and 21, causes in short time the change of the sign of the angular velocity, and the pendulum's return to the preset vertical position. After approximately 0.3 s of

the simulation, the drop in value of the angular velocity (a module) is visible, as a result of a total deactivation of the rule No. 22 (which causes maintaining the force value below zero), and a result of operation of the gravitational force. When the value of the angle approaches 180°, the rules 11 and 12 are activated, reciprocating the force values from the "*Positive Low*" set, and in consequence, the impulse force with the value of about 50 N, and in consequence, maintaining the pendulum in the desired position.

5 Conclusions

The article discusses the general outline of control using a fuzzy logic with an example of application. Operation of the controller has been presented for three simulations with different initial conditions. Clarity and possibility of understanding the controller's operations in different situations enable achieving the effects of regulation depending on the assumed aims.

In the analysis of the obtained simulation results, the effectiveness of the controller operation has not been evaluated; the way of controller's operation during individual phases of bringing the pendulum to the predetermined vertical position has been discussed. However, attention should be paid to proper functioning of the controller while maintaining the pendulum in the predetermined vertical position for any initial conditions from the assumed range.

References

1. Angiulli, G., Versaci M., 2003, Resonant Frequency Evaluation of Microstrip Antennas Using a Neural-Fuzzy Approach, IEEE Trans. Magnetics, 39, 1333–1336.
2. Alhanjouri, M., A. Alhaddad, A., 2014, Optimize Wash Time of Washing Machine Using Fuzzy Logic, Automation, Control and Intelligent Systems, 2(3), 27–32, doi:10.11648/j.acis.20140203.11.
3. Chmielewski A., Gumiński R., Radkowski S., 2015, Chosen Properties of a Dynamic Model of Crankshaft Assembly with Three Degrees of Freedom. 20th In–ternational Conference On Methods and Models in Automation and Robotics (MMAR), IEEE, 1038–1043, ISBN: 978-1-4799-8700.
4. Dybała J., Gałęzia A., 2014, A Novel Method of Gearbox Health Vibration Monitoring Using Empirical Mode Decomposition, in: Dalpiaz G. et al. (Eds.), Advances in Condition Monitoring of Machinery in Non-Stationary Operations, Lecture Notes in Mechanical Engineering, Proceedings of the third International Conference on Condition Monitoring of Machinery in Non-Stationary Operations CMMNO 2013, Springer-Verlag, Berlin Heidelberg, 225–234.
5. Gontarz S., Radkowski S., 2015, Diagnostic Model of Hysteresis for Condition Monitoring of Large Construction Structures, Engineering Asset Management - Systems, Professional Practices and Certification, Springer-Verlag Berlin, Heidelberger Platz 3, D-14197 Berlin, Germany, 611–623, doi:10.1007/978-3-319-09507-3_53.

6. Guney K., Sarikaya N., 2009, Comparison of Mamdani and Sugeno Fuzzy Inference System Models for Resonant Frequency Calculation of Rectangular Microstrip Antennas Progress In Electromagnetics Research B, Vol. 12, 81–104.
7. Halliday D., Resnick R., Walker J., 2012, Podstawy fizyki, część 2 (Fundamentals of Physics, part 2), Wydawnictwo Naukowe PWN, [In Polish].
8. Licata G., 2010, Employing Fuzzy Logic in the Diagnosis of a Clinical Case Health, 2(3), 211–224, doi:10.4236/health.2010.23031.
9. Mamdani E.H., 1974, Application of Fuzzy Algorithms for Control of Simple Dynamic Plant, Proc. IEEE, 121(12), 1585–1588.
10. Matlab Documentation Center [on–line], Massachusetts 2013, World Wide Web: http://ctms.engin.umich.edu/CTMS/index.php?example=InvertedPendulum&section=SimulinkModeling {accessed 28.08.2015}.
11. Piegat A., 1999, Modelowanie i sterowanie rozmyte, (Fuzzy Modeling and Control), Akademicka Oficyna Wydawnicza EXIT, Warszawa, [In Polish].
12. Radkowski S., Jasinski M., 2015, Use of Condition Monitoring in the Proactive Maintenance Strategy. Edited by: Tse, PW; Mathew, J; Wong, K; et al. Conference: 8th World Congress on Engineering Asset Management (WCEAM), Hong Kong, PEOPLES R CHINA, OCT 30–NOV 01, 2013. Book Series: Lecture Notes in Mechanical Engineering, 601–610.
13. Radkowski S., Szulim P., 2014, Analysis of vibration of rotors in unmanned aircraft, Methods Models Autom. Robot. MMAR 2014 19th Int. Conf. On, 748–753.
14. Sauter D., Dubois G., Levrat E., Bremont J., 1993, Fault Diagnosis in Systems Using Fuzzy Logic, In EUFIT' 93, First European Congress on Fuzzy and Intelligent Technologies, Aachen, Germany.
15. Shelah S., 1998, Proper and Improper Forcing, Perspectives in Mathematical Logic, Springer–Verlag, Berlin.
16. Yager R. R., Filev D. P., 1994, Essentials of Fuzzy Modeling and Control, Wiley.
17. Yager, R. R., 2003, Fuzzy Logic Methods in Recommender Systems, Fuzzy Sets and Systems 136, 133–149.
18. Yager, R. R., Filev, D. P., 1993, On the Issue of Defuzzification and Selection Based on a Fuzzy Set, Fuzzy Sets and Systems, 55, 255–272.
19. Zadeh L. A., 1994, Soft Computing and Fuzzy Logic, IEEE Software 11(6), 48–56.
20. Zadeh L. A., 1965, Fuzzy Sets Information and Control, 338–353.

Artificial Neural Network for Stabilization of the Flexible Rope Submerged in Sea Water

Łukasz Drąg

Abstract The paper presents an application of artificial neural network to control the position of the end of the rope. The proposed model allows stabilization of payload at a given depth despite the sea waves and the sea currents. The flexible rope is discretized by means of the one of the modifications of rigid finite element method. For each element of a rope submerged in water, the hydrodynamics forces are taken into account. The MLP and the RBF types of ANN network are considered. Selection of ANN network architecture and calculation of neurons weights has been made in own software. The influence of the sea environment, vessel velocity and lumped mass at the end of the rope on the displacement of the end of the rope is discussed.

1 Introduction

Rapid development of techniques of oil and gas mining from sea and ocean beds has been driven in the last few decades by depletion of on-shore hydrocarbon resources. With appropriate computer modelling, new ways were engineered to extract raw materials from great depths in difficult conditions. Ropes and risers are important offshore rigging components. From the computational point of view, these are slender elements with one-dimensional (length) predominant, subject to large rising movements driven by heave of the sea and ocean currents. Taken into account in their modelling should be the additional dynamic loads from the aquatic environment, such as associated water and hydrodynamic drag forces, which significantly affect the analyzed systems' dynamics. Also, modelling this kind of slender systems gets significantly complicated when they are to be used in control. Control solutions require repeated integration of the motion equations, even for tasks whereby dynamic optimization methods are used.

Ł. Drąg (✉)
Department of Transport and Informatics, University of Bielsko-Biala,
Willowa 2, 43-300 Bielsko-Biala, Poland
e-mail: ldrag@ath.eu

© Springer International Publishing Switzerland 2016

J. Awrejcewicz (ed.), *Dynamical Systems: Theoretical and Experimental Analysis*, Springer Proceedings in Mathematics & Statistics 182, DOI 10.1007/978-3-319-42408-8_8

A solution, with which a mechanical device's operational parameters may be selected without the need for repeated remodelling of its dynamics is an artificial neural network (ANN). With ANN, a numerical simulation's results may be generalized based on a number of input parameters selected for the model. In this paper ANN was used to generalize optimization results obtained from a model of rope dynamics. With the proposed ANN architecture generalized can be the results of numerical simulations, winch drum angle selection to stabilize a load suspended from the rope in the sea wave conditions, with variable parameters of the waves and base vessel movement. The study deals with two types of neural networks: radial basis function (RBF) and multilayer preceptor (MLP). Values obtained from ANN may then be used for control in real time.

2 Model of System

The slender structure modelling in offshore technology deals with complex issues associated with variable configuration of considered systems, large deflections of vulnerable members (elements), and intense aquatic environment impact. One of the many methods used in the dynamic analysis of ropes and risers is the rigid finite element method [4, 5]. In the method's classical approach the rigid finite elements of a spatial arrangement have six degrees of freedom each. Combined, however, they are by elastic-damping elements, which incorporate shear strength (in two directions), longitudinal, flexural (in both directions) and torsional. This approach causes the appearance of high frequency vibration in the dynamic analysis of states digitized with this method. The advantage of this method is, however, the block structure of the mass matrix [4, 7]. On the other hand a modification of this method [1, 7], enables the elimination of high shear and longitudinal stiffness, and provides continuous movements. This makes, however, the mass matrix full, which significantly reduces its numerical performance. A detailed description of the method's classical formulation and its modification can be found in a monograph [7]. It also contains numerous examples of the of method's application in modelling the vibrations of systems with fixed and variable configurations.

The study uses a new modification of the method, which in this author's opinion combine the advantages of its both current formulas without their disadvantages. Thus it allows to eliminate high shear stiffness, and also (if allowed) longitudinal and torsional stiffness without significant changes in the overall algorithm developed for generation of slender system's motion equations. It also retains the block structure of the mass matrix. This is achieved by separating rigid finite elements as in the classical method, and then connecting them by displacement equation of geometric constraints. The new modification of the method has been described in detail in a publication [3].

Due to the high numerical efficiency of the RFE method, modification it is applicable to rope discretization in a dynamic optimization task. The dynamic optimization task reported hereinafter is shown in Fig. 1. It consists in determining

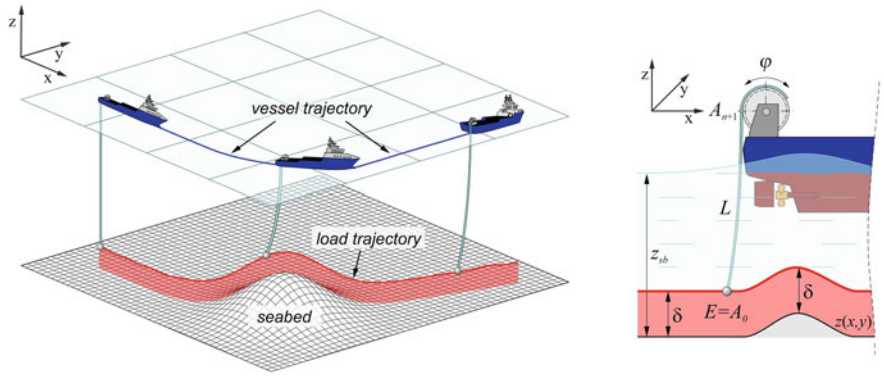

Fig. 1 Selection of angle of rotation of a hoisting winch

the angle of the winch drum rotation $\varphi(t)$, at which the load is at a constant distance from the sea bottom surface.

Motion equations for the whole system are derived from Lagrange equations:

$$\frac{\mathrm{d}}{\mathrm{d}t}\frac{\partial E}{\partial \dot{\mathbf{q}}_i} - \frac{\partial E}{\partial \mathbf{q}_i} + \frac{\partial V^{(g)}}{\partial \mathbf{q}_i} + \frac{\partial V^{(e)}}{\partial \mathbf{q}_i} = \mathbf{Q}_i \text{ for } i = 0, 1, \ldots, n \tag{1}$$

where $E = \sum_{i=0}^{n} E_i$.

Motion equations of the elements $0 \div n$ of the slender member (rope) can be written in the form:

$$\mathbf{A}_i \ddot{\mathbf{q}}_i - \bar{\mathbf{D}}\mathbf{F}_i - \mathbf{D}_i\mathbf{F}_{i+1} = -\frac{\partial V^{(g)}}{\partial \mathbf{q}_i} - \frac{\partial V^{(e)}}{\partial \mathbf{q}_i} + \mathbf{Q}_i = \mathbf{b}_i \tag{2}$$

With entered vectors:

$$\mathbf{q} = \begin{bmatrix} \mathbf{q}_0 \\ \vdots \\ \mathbf{q}_i \\ \vdots \\ \mathbf{q}_n \end{bmatrix} - \text{vector of member's generalized coordinates,} \tag{3}$$

$$\mathbf{F} = \begin{bmatrix} \mathbf{F}_0 \\ \vdots \\ \mathbf{F}_i \\ \vdots \\ \mathbf{F}_n \end{bmatrix} \quad - \text{vector of constraint reaction,} \tag{4}$$

$$\mathbf{Q} = \begin{bmatrix} -\frac{\partial V_0^{(g)}}{\partial \mathbf{q}_0} - \frac{\partial V^{(e)}}{\partial \mathbf{q}_0} \\ \vdots \\ -\frac{\partial V_i^{(g)}}{\partial \mathbf{q}_i} - \frac{\partial V^{(e)}}{\partial \mathbf{q}_i} \\ \vdots \\ -\frac{\partial V_n^{(g)}}{\partial \mathbf{q}_n} - \frac{\partial V^{(e)}}{\partial \mathbf{q}_n} \end{bmatrix} \quad - \text{vector of potential forces,} \tag{5}$$

$$\mathbf{G} = \begin{bmatrix} \mathbf{G}_{-1} \\ \vdots \\ \mathbf{G}_i \\ \vdots \\ \mathbf{G}_{n-1} \end{bmatrix} \quad - \text{vector of right sides of constraint equations,} \tag{6}$$

and matrices:

- mass matrix

$$\mathbf{A} = \begin{bmatrix} \mathbf{A}_0 & \cdots & \mathbf{0} & \cdots & \mathbf{0} \\ \vdots & & \vdots & & \vdots \\ \mathbf{0} & \cdots & \mathbf{A}_i & \cdots & \mathbf{0} \\ \vdots & & \vdots & & \vdots \\ \mathbf{0} & \cdots & \mathbf{0} & \cdots & \mathbf{A}_n \end{bmatrix} \tag{7}$$

- constraint reaction coefficient matrix

$$\mathbf{D} = \begin{bmatrix} \bar{\mathbf{D}} & \mathbf{D}_0 & \mathbf{0} & \cdots & \mathbf{0} & \mathbf{0} & \mathbf{0} & \mathbf{0} & \cdots & \mathbf{0} & \mathbf{0} \\ \vdots & \vdots & \vdots & & \vdots & \vdots & \vdots & \vdots & & \vdots & \vdots \\ \mathbf{0} & \mathbf{0} & \mathbf{0} & \cdots & \mathbf{0} & \bar{\mathbf{D}} & \mathbf{D}_i & \mathbf{0} & \cdots & \mathbf{0} & \mathbf{0} \\ \vdots & \vdots & \vdots & & \vdots & \vdots & \vdots & \vdots & & \vdots & \vdots \\ \mathbf{0} & \mathbf{0} & \mathbf{0} & \cdots & \mathbf{0} & \mathbf{0} & \mathbf{0} & \mathbf{0} & \cdots & \mathbf{0} & \bar{\mathbf{D}} \end{bmatrix} \tag{8}$$

then the motion and constraint equations in acceleration form can be written as:

$$\mathbf{A}\,\ddot{\mathbf{q}} - \mathbf{D}\cdot\mathbf{F} = \mathbf{Q} \tag{9}$$

$$\mathbf{D}^T\,\ddot{\mathbf{q}} = \mathbf{G} \tag{10}$$

Equations (9) and (10) do not contain any force from the aquatic environment impact.

Analysis of the dynamics of slender members (ropes, risers) submerged in water requires including hydrodynamic forces in the model. Therefore, the following forces must be included:

- resistance of the viscous medium which is water,
- inertias, which may include:
  - forces due to water movement (sea currents),
  - forces due to added mass (associate water),
- buoyant force.

Because of the aquatic environment impact, Eqs. (3), (4), (5), (6), (7), (8) and (9) have to be modified. Motion equations of elements now take the form of

$$\mathbf{M}_i\,\ddot{\mathbf{q}}_i - \bar{\mathbf{D}}\mathbf{F}_i - \mathbf{D}_i\mathbf{F}_{i+1} = \mathbf{f}_i \tag{11}$$

where $\mathbf{M}_i = \mathbf{A}_i - \mathbf{M}_{i,a}$,
$\mathbf{f}_i = \mathbf{b}_i + \mathbf{Q}_{\mathrm{w},i} + \mathbf{Q}_{M,i} + \mathbf{Q}^{\mathrm{w}}_{I,i} + \mathbf{Q}^{a}_{I,i}$,
$\mathbf{M}_{i,a}$—matrix of associate water mass,
$\mathbf{Q}_{\mathrm{w},i}$—generalized force due to buoyancy,
$\mathbf{Q}_{M,i}$—generalized force of viscous medium resistance
$\mathbf{Q}^{\mathrm{w}}_{I,i}$—generalized force due to water movement (sea currents)
$\mathbf{Q}^{a}_{I,i}$—generalized force of added mass (associate water).

The constraint equations do not change. In their general form, the slender member motion equations, including the water impact, can thus be written as

$$\mathbf{M}\,\ddot{\mathbf{q}} - \mathbf{D}\mathbf{F} = \mathbf{f} \tag{12}$$

$$\mathbf{D}^T\,\ddot{\mathbf{q}} = \mathbf{G} \tag{13}$$

where $\mathbf{M} = diag\{\mathbf{M}_0, \mathbf{M}_1, \ldots, \mathbf{M}_n\}$ block-diagonal matrix,
$\mathbf{D}, \mathbf{F}$—determined in (3), (4), (5), (6), (7), (8), $\mathbf{f} = \left[\mathbf{f}_0^T, \mathbf{f}_1^T, \ldots, \mathbf{f}_n^T\right]^T$.

The particular (block-diagonal) form should be emphasized for the matrix of inertias (masses) $\mathbf{M}$, and for the constraint reaction matrix $\mathbf{D}$. This allows to use their forms to develop an effective algorithm for integration of Eqs. (12) and (13). Formulation of the constraint equations in the acceleration form, required, however,

supplementing the integration algorithm with a constraints stabilization procedure. The Baumgart method was used in this study.

For the purpose of this study, to solve an optimization task, a model is applied with five degrees of freedom, wherein the generalized coordinates vector is

$$\mathbf{q}_i = \begin{bmatrix} x_{i,1} & x_{i,2} & x_{i,3} & \varphi_{i,3} & \varphi_{i,2} \end{bmatrix}^T \tag{14}$$

The model neglects longitudinal and torsion strains in members, and the coefficients of stiffness reproduce only the member's flexural susceptibility. It is acceptable and justified in analyzing rope and riser dynamics. This allows to extend the step of system motion equations integration.

3 Optimization Task

The study considered a model system consisting of a drive drum and a rope (Fig. 2). Movement of the vessel, on which the rope winch is installed, is known. Provided that drum radius R is small, it is assumed that A_{n+1} coordinates are defined as follows: $x_{A_{n+1}} = \bar{x}_A(t)$, $y_{A_{n+1}} = \bar{y}_A(t)$, $z_{A_{n+1}} = \bar{z}_A(t)$.

Load location height above the sea floor can be adjusted by the winch drum. The drum's rotation changes the length of the line, on which the load is suspended. In the present dynamic optimization task, the course of the drum winch rotation is chosen so that, despite the vessel's horizontal and vertical motion, the load is stabilized at predetermined distance δ from the seabed.

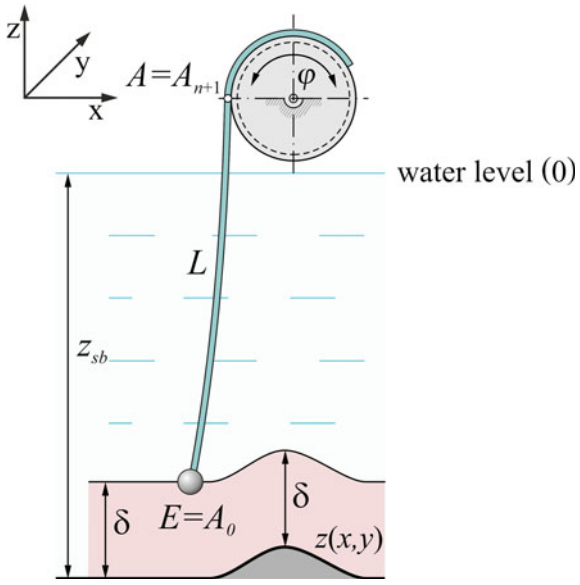

Fig. 2 Model of the system used for dynamic optimisation

In this optimization task, the vertical displacement of point A is neglected. As demonstrated in study [2], the displacements can be compensated by adoption:

$$\varphi = \varphi(\bar{z}_A) + \varphi(\bar{x}_A, \bar{y}_A) \tag{15}$$

where $\varphi(\bar{z}_A) = \frac{\bar{z}_A}{R}$, R—drum winch radius.

The objective function was defined as follows:

$$\Omega = \left[\frac{1}{T} \int_0^T \left(z_{A_0} + z_{sb} - z(x,y) - \delta \right)^2 dt \right]^{\frac{1}{2}} \tag{16}$$

where $z(x, y)$—function describing the seabed topographical features,

z_{sb}—seabed depth for A_O at time $t = 0$, $z_{sb} = -\left(z_{A_0}|_{t=0} - \delta\right)$.

The seabed topographical features are described by following function:

$$z(x,y) = k \exp\left(-\left(\frac{(x - x_0)}{p} \right)^2 - \left(\frac{(y - y_0)}{q} \right)^2 \right) \tag{17}$$

where x_0, y_0, k, p, q—function parameters describing the sea bottom profile.

Calculation of functional Ω requires the integration of motion Eqs. (12) and (13) to determine the function determining $\bar{x}_A(t)$, $\bar{y}_A(t)$. To reduce the issue to nonlinear optimization problem, it was assumed that function $\varphi(t)$ is defined as a third degree spline. Looked for are its values $\varphi_i = \varphi(t_i)$ at equally spaced points in interval $\langle 0; T \rangle$:

$$t_i = i \cdot \frac{T}{p} \quad \text{for} \quad i = 1, \ldots, p, \tag{18}$$

where T—motion simulation time, p—number of sub-intervals in $\langle 0; T \rangle$.

It is assumed that value of $\varphi_0 = \varphi(0) = 0$ is known and results from the initial system configuration. The task of minimizing functional (16) comes down, therefore, to seeking such values $\varphi_1 \div \varphi_p$ being components of vector $\mathbf{f} = \left[\varphi_1, \varphi_2, \ldots, \varphi_p\right]^T$, which satisfy constraints $\varphi_{i,\min} \leq \varphi_i \leq \varphi_{i,\max}$ and minimize functional $\Omega = \Omega(\mathbf{f})$ from (16).

To solve the problem of nonlinear optimization, the creeping simplex method was used. The motion equations were integrated by fourth order Runge–Kutta method with integration step $h = 0.1$ s. It was assumed in the calculations that the optimization process is completed upon a pre-set reduction of the function, or upon completion of a specified number of optimization steps.

4 ANN for Payload Stabilization

Since solving an optimization task with the method presented in the previous section takes few minutes, this method is unsuitable for control in real time. In this study, to approximate the results of dynamic optimization, selection of the angle of rope winding/unwinding on/from winch drum, artificial neural networks were proposed. Considered were sigmoid networks (MLP—*Multilayer Perceptron*) and radial networks (RBF—*Radial Basis Func*tion) [6]. Both types of networks have five input variables (m—lumped mass at the end of rope, v_x,v_y—vessel movement speed in directions x and y, t_x, t_y—delay in vessel movement start in direction of x and y) and one permanent input (bias), and at the output vector p of output signals corresponding to the drum rotation angles φ_i in time t_i (Fig. 3). The learning set and a validation set were setup for data acquired in the dynamic optimization for 405 cases which are combinations of parameters $m \in \langle 0; 1000 \rangle$ kg for five equal distribution points, $v_x, v_y \in \langle 0.75; 1.25 \rangle$ m/s for three points of equal distribution and $t_x, t_y \in \langle 0; 10 \rangle$ s also for three points of equal distribution.

The appropriate network architecture (number of hidden layer neurons) was determined, and the weights were calculated using proprietary software ANN 2.0. The software was developed in Delphi environment and allows calculations a lot of cases divided into multiple threads. The use of multiple processor cores in calculation significantly reduces the time needed to test multiple configurations of neural network. The calculations herein reported refer to neural networks with one hidden layer. The search for the optimal architecture of the network with learning error below permissible error E consisted of increasing the hidden layer neurons, and multiple learning the network for random initial weights.

Multilayer perceptron (MLP) with one-way structure requires iterative learning. For weight calculation ANN 2.0 used an error back-propagation algorithm for random selection of the learning patterns. As the neuron activation function in the

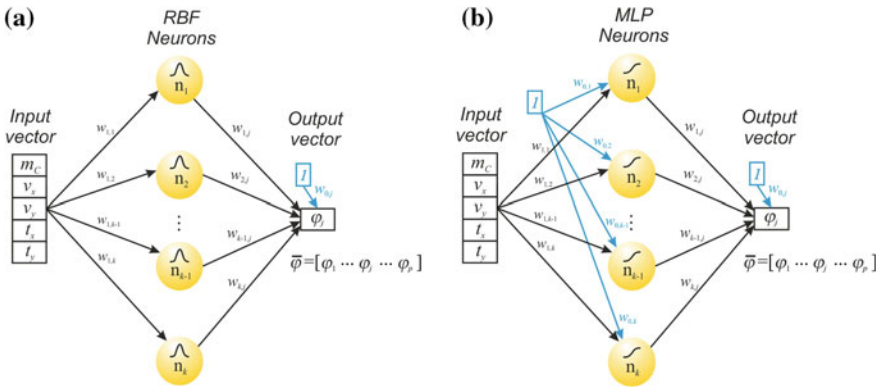

Fig. 3 Structure of the artificial neural networks used for payload stabilization. **a** RBF network. **b** MLP network

hidden and output layers a sigmoid function was adopted. Learning in a RBF network is a two-phase process: In the first phase, a certain number and parameters of centres, radial function, is deployed. Values of the weights connecting radial functions with output neurons will be determined in the second phase. In the case of identical forms of the activation function at outputs, to calculate weights requires the designation of inverse matrix, which is done directly and does not require time-consuming iterative process.

Winch drum rotation angle φ for one neuron at the output depending on the neural network type of was calculated from

$$\varphi^*(m, v_x, v_y, t_x, t_y) = \begin{cases} f\left(\sum_{i=1}^{k} w_i \varphi_i\right) + w_0 & \text{sigmoidal network} \\ \sum_{i=1}^{k} w_i f_i(m, v_x, v_y, t_x, t_y) + w_0 & \text{radial network} \end{cases} \tag{19}$$

where w_i,w_0—weight of neuron i in hidden layer, bias weight

φ—winch drum rotation angle calculated for neuron i in hidden layer

k—number of neurons on hidden layer,

f—activation function.

To evaluate the approximation accuracy, the following indicators were adopted:

$$E = \frac{1}{n \cdot p} \sum_{i=1}^{n} \sum_{j=1}^{p} \left| \varphi_{i,j}^* - \varphi_{i,j} \right| \text{ mean absolute error} \tag{20}$$

$$E_{\max} = \max_{\substack{0 \le i \le n \\ 0 \le j \le p}} \left| \varphi_{i,j}^* - \varphi_{i,j} \right| \text{ maximum absolute error} \tag{21}$$

where n—number of elements in the training set.

$\varphi_{i,j}^*$—angle of winch drum rotation calculated using ANN,

$\varphi_{i,j}$—value from the training set or test set obtained as the dynamic optimization task solution.

Numerical calculations were performed assuming parameters of the rope, water and function describing the shape of the seabed in Table 1.

The total simulation time was $T = 200$ s. The values of decision variables in the optimizing task were calculated for the distribution of simulation time interval $\langle 0; T \rangle$ into $p = 20$ equal sub-intervals. Further herein detailed results are presented of the calculations for three sets of input parameters for the model of dynamics which are also inputs to the neural network:

- $m = 0$ kg, $v_x = 0.75$ m/s, $v_y = 1.25$ m/s, $t_x = 5$ s, $t_y = 0$ s − P1,
- $m = 0$ kg, v_x, $v_y = 1$ m/s, t_x, $t_y = 0$ s − P2,
- $m = 0$ kg, $v_x = 1.25$ m/s, $v_y = 0.75$ m/s, $t_x = 0$ s, $t_y = 5$ s − P3.

Table 1 Rope, water and seabed bottom profile function parameters

Element	Parameter	Unit	Value
Line	Length L	m	400
	Diameter D	m	0.08
	Density ρ	kg/m^3	6500
	Young's modulus E	N/m	$1 \cdot 10^{11}$
	Number of division n	–	20
Water	Density ρ_w	kg/m^3	1025
	C_x' coefficient	–	0.1
	C_y' coefficient	–	1.0
	C_M' coefficient	–	1.9
	Velocity v^W,	m/s	0
	Acceleration a^W,	m/s^2	0
δ	Distance from the seabed	m	5
x_0, y_0, k, p, q	Parameters of the function describing seabed bottom profile	m	50, 20, 10, 20, 20

Positions, velocities and trajectories of point A_{n+1} (vessel) in the directions of axes x and y for input P1 ÷ P3 to the dynamics model shown in Fig. 4 a, b, and c.

Table 2 shows the error values calculated according to (13) depending on the number of neurons in the hidden layer for the two neural network types under consideration.

The average absolute error E of less than 0.05 m for RBF networks was obtained after set of 100 neurons on the hidden layer. In MLP network, a similar learning result was obtained for $n = 70$ neurons. Figure 5 shows the courses of the winch drum rotation angle that stabilizes the load at a predetermined distance from the sea bottom for MLP 5-70-20 and RBF 5-100-20 networks.

Comparison of winch drum rotation angle mapping rates for the both neural network types herein considered shows that better results are obtained when using MLP network. Maximum relative errors for validation data set in MLP 5-70-20 and RBF 5-100-20 networks are $E_{max} = 0.46$ m and $E_{max} = 0.47$ m, respectively.

Figure 6 shows the trajectories of point E (rope end) for data P1 ÷ P3 before the optimization (no control) and with control whereby the drum rotation course was obtained with an artificial neural MLP network with 5-70-20 architecture. In each of the cases analyzed in detail, good results were obtained in load stabilization at a predetermined height above the seabed surface. The maximum rope end displacement from pre-set distance $\delta = 5$ m from the sea bottom does not exceed 0.15 m.

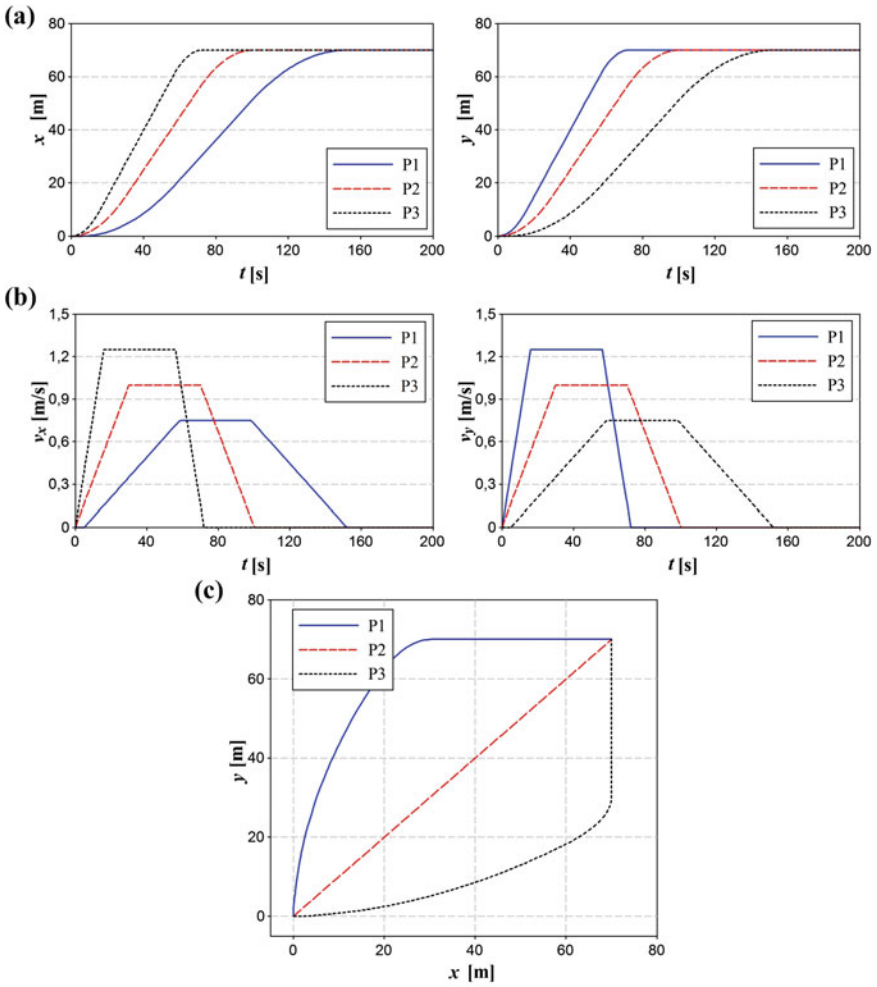

Fig. 4 Vessel movement—point A_{n+1} in x and y directions **a** position, **b** velocity, **c** vessel trajectory (point A_{n+1}) projected on xy plane

Table 2 Errors with respect to number k of the neurons in the hidden layer

RBF 5-x-20	Quantity	Number of k neurons				
		50	75	100	125	150
	E [m]	0.1014	0.0319	0.0345	0.0319	0.0232
	E_{max} [m]	1.2131	0.4553	0.4722	0.4553	0.2980
MLP 5-x-20	Quantity	Number of k neurons				
		10	30	50	70	90
	E [m]	0.0794	0.0478	0.0399	0.0352	0.0273
	E_{max} [m]	1.2110	0.6732	0.5117	0.4624	0.3576

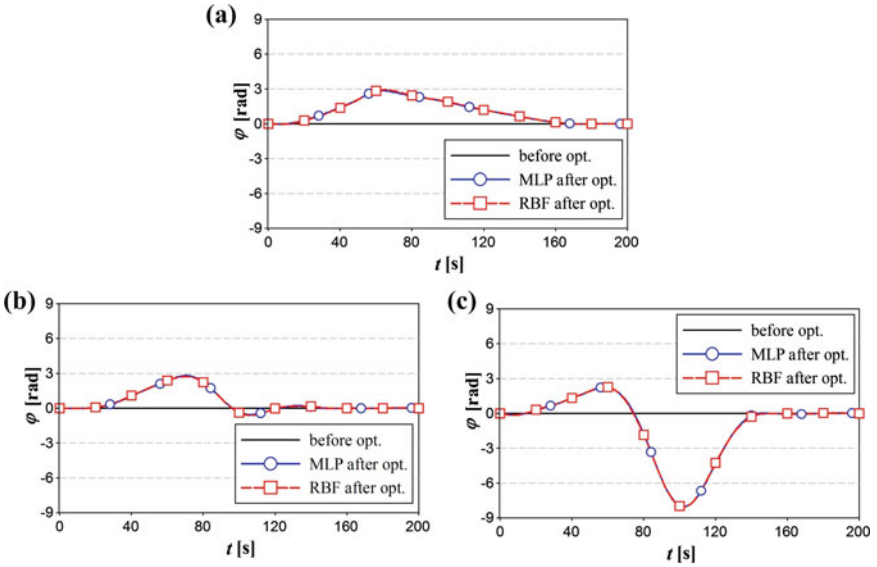

Fig. 5 The course of the hoisting winch drum rotation angle $\varphi(t)$ before and after optimization for data **a** P1, **b** P2, **c** P3 when results are obtained from artificial neural networks

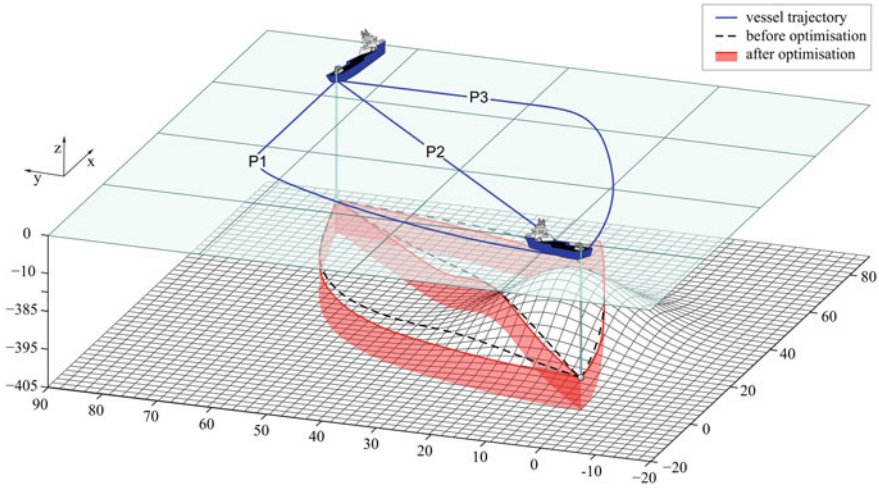

Fig. 6 *E* point trajectory before and after optimization

5 Conclusions

The ANN 2.0 software developed for this study to test and select the optimum MLP and RBF neural network architectures does the job. The paper presents an example application for calculation of course of angle of rope winding/unwinding on/from winch drum to ensure load stabilization of at a pre-set height above the seabed depending on a number of independent parameters. The analyses completed for this study show that drum rotation angle was mapped better in networks with sigmoidal neuron function activation. According to the author, dynamic optimization data would have been better reflected and generalized if the training set was larger. A small change in an input signal has a significant impact on the resulting winch drum rotation angle courses. In addition, generation of a large training set takes a very long time. Therefore, a further step will be to seek and implement solutions that enable fast generation of large training set.

References

1. Adamiec-Wójcik I (2003) Modelling dynamics of multibody systems using homogenous transformations. Rozprawy naukowe Nr 3. Zeszyty Naukowe ATH.
2. Drąg Ł (2015) Model of an artificial neural network for payload positioning in sea waves. Journal of Ocean Engineering, Resubmit.
3. Drąg Ł (2015) Application of dynamic optimisation to the trajectory of a cable-suspended load Nonlinear Dynamics, Resubmit.
4. Kruszewski J, Gawroński W, Wittbrodt E, Najbar F, Grabowski S (1975) Metoda sztywnych elementów skończonych. (The rigid finite element method). Arkady: Warszawa.
5. Kruszewski J, Sawiak S, Wittbrodt E (1999) Metoda sztywnych elementów skończonych w dynamice konstrukcji. (The rigid finite element method for construction dynamics) WNT: Warszawa.
6. Osowski S (2013) Sieci neuronowe do przetwarzania informacji. (Neural networks for information processing). OWPW: Warszawa.
7. Wittbrodt E, Adamiec-Wójcik I, Wojciech S (2006) Dynamics of flexible multibody systems. The rigid finite element method. Springer: Berlin.

Analysis of Non-autonomous Linear ODE Systems in Bifurcation Problems via Lie Group Geometric Numerical Integrators

Pilade Foti, Aguinaldo Fraddosio, Salvatore Marzano and Mario Daniele Piccioni

Abstract A bifurcation analysis developed within the context of the nonlinear theory of elasticity usually leads to the study of systems of second-order ODE's characterized by matrices with varying coefficients. A common practice is that of reducing the governing set of differential equations to a simpler non-autonomous first order linear ODE system. Here, we investigate the potentiality of alternative geometric numerical integrators, based on Lie Group methods, which furnish approximate exponential representations of the matricant of first order linear ODE systems. Within such numerical schemes, the Magnus expansion seems to be very efficient since it features the determination of approximate solutions that preserve at any order of approximation the same qualitative properties of the exact (but unknown) solution and it also exhibits an improved accuracy with respect to other frequently used numerical schemes. As applications of the Magnus method, we study certain paradigmatic bifurcation problems with the major aim of investigating whether solid bodies may support certain instabilities that have common features to some classical hydrodynamic instabilities observed in viscous fluids.

P. Foti (✉) · A. Fraddosio · S. Marzano · M.D. Piccioni
Dipartimento di Scienze dell'Ingegneria Civile e dell'Architettura,
Politecnico di Bari, Bari, Italy
e-mail: pilade.foti@poliba.it

A. Fraddosio
e-mail: aguinaldo.fraddosio@poliba.it

S. Marzano
e-mail: salvatore.marzano@poliba.it

M.D. Piccioni
e-mail: mariodaniele.piccioni@poliba.it

© Springer International Publishing Switzerland 2016

J. Awrejcewicz (ed.), *Dynamical Systems: Theoretical and Experimental Analysis*, Springer Proceedings in Mathematics & Statistics 182, DOI 10.1007/978-3-319-42408-8_9

1 Introduction

The three-dimensional nonlinear theory of elasticity is a classical framework for setting a number of significant bifurcation problems for solids undergoing severe deformations. It usually happens that a bifurcation analysis may lead to the study of systems of second-order ODE's characterized by matrices with varying coefficients, and subject to homogeneous boundary conditions. Then if the structure of the problem permits, it is a common practice to reduce the system of linear second-order ODE's to a simpler non-autonomous first-order linear ODE system. Nevertheless, the resulting differential system may be somewhat complex and only numerically tractable; thus, it is crucial to adopt an adequate strategy for obtaining an accurate numerical solution and, in particular, for determining the bifurcation load and the corresponding bifurcation field.

Approximate expressions of the fundamental matrix (the *matricant*) of non-autonomous linear ODE systems, based either on the multiplicative integral of Volterra or on the truncated Peano expansion, have been recently proposed for bifurcation problems analyzed by means of the Stroh approach within the so-called sextic formalism (see [1, 2]).

Here we investigate the potentiality of alternative numerical methods— based on the Magnus expansion (cf. [3])—which furnish approximate exponential representations of the matricant of first-order linear ODE systems. In particular, the Magnus expansion method seems to be very efficient since it features the determination of approximate solutions that preserve at any order of approximation the same qualitative properties of the exact (but unknown) solution and it also exhibits an improved accuracy with respect to other frequently used numerical schemes.

We recall that the Magnus expansion relies on developing a particular class of the so-called geometric numerical integrators, based on Lie group methods (see [4, 5] for appropriate references). It is well known that a Lie group corresponds to a differential manifold which is endowed with a group structure, and the corresponding Lie algebra, defined as the tangent space to the Lie group at the identity, is a linear space endowed with the matrix commutation operation and the matrix exponential as natural mapping. The role played by the exponential mapping is crucial, because within the context of differential geometry, the matrix exponential maps an element belonging to a matrix Lie algebra into an invertible matrix belonging to its corresponding Lie group. Thus, it is natural to attempt to construct the matricant as a matrix exponential with exponent given by a matrix that belongs to the associated Lie algebra. This represents the basis of the idea developed by Magnus, who further proposed to express the exponent by a matrix series expansion, known as the Magnus expansion.

A very important aspect of this method is that all the terms of the infinite series expansion belong to the same Lie algebra. Thus, any truncation of the Magnus series will also belong to the same Lie algebra, and therefore the exponential map of any truncation will necessarily take part of the corresponding Lie group. This is basically the main reason why an approximated solution obtained by truncating the

Magnus expansion at any order preserves the same qualitative features of the exact solution.

To our knowledge, either use of the Magnus expansion or of more general geometric numerical methods is not widespread in continuum mechanics literature. This basically motivates our interest of investigating the potentiality of such methods for bifurcations problems involving nonlinear elastic solids. As applications of the Magnus method, we study certain paradigmatic bifurcation problems inspired by the analyses developed in [6, 7], with the major aim of investigating whether solid bodies may support certain instabilities that have common features to some classical hydrodynamic instabilities observed in viscous fluids.

In Sect. 2, we briefly illustrate the effectiveness of Lie group geometric numerical integrators with special attention to the Magnus method.

As an application of the Magnus method, in Sect. 3, we investigate the possibility for a Levinson–Burgess compressible isotropic elastic hollow cylinder subject to circular shear to support axially periodic twist-like bifurcation modes similar to the Taylor–Couette axially periodic cellular patterns observed when the flow of a viscous fluid confined in the gap between two rotating concentric cylinders becomes unstable. By considering a class of incremental displacements defined by three unknown scalar functions of the radial coordinate and having an axial periodic structure, we study the related incremental boundary-value problem, which leads to a complex non-autonomous homogeneous system of six first-order linear ODE's with homogeneous boundary conditions. The analysis of the differential problem is performed by a numerical approach based on the Magnus method outlined in Sect. 2, which reveals very effective for the determination of the first singular value of the bifurcating load corresponding to a nontrivial toroidal twist-like solution.

2 Lie Group Geometric Numerical Integrators

A number of problems in scientific and engineering areas require the resolution of systems of differential equations with varying coefficients. Besides some very special cases, for which a fundamental matrix solution is explicitly available, the analysis of the problem usually requires the construction of an approximate representation of the solution of the non-autonomous differential system. In the last decade, recent studies have shown that in many cases the so-called geometric numerical integrators methods may offer better approximation schemes compared to standard numerical integrators.

In this section, we first give a brief overview of geometric numerical integrators and then we deal with the Magnus method as a particular case of geometric numerical integrator based on Lie Group methods.

Geometric numerical integration concerns the development of numerical approximations to the solution of an ODE system with the main goal both of preserving at any order of approximation the qualitative properties of the exact (but unknown) solution and of exhibiting an improved accuracy with respect to other

numerical methods. We consider the bifurcation problem in the following section, we focus our attention to geometric numerical integrators based on the Magnus expansion for the special case of homogeneous *non-autonomous* first order linear ODE systems of the form

$$\mathbf{Y}'(\mathrm{R}) = \mathbf{A}(\mathrm{R})|\mathbf{Y}(\mathrm{R}), \quad \mathrm{R} \geq 0, \quad \mathbf{Y}(0) = \mathbf{I}_{6\times 6}, \tag{1}$$

where the unknown 6×6 matrix $\mathbf{Y}(\mathrm{R})$, usually referred as the matricant of the Cauchy initial-value problem (1), is the 6-dimensional identity matrix when the unique real independent variable is equal to zero.

Generally speaking, these new numerical approaches involve Lie Group methods, which are based on Lie groups and their associated Lie algebras. We recall that a Lie group corresponds to a differential manifold which is endowed with a group structure; the corresponding Lie algebra, defined as the tangent space to the Lie group at the identity, is a linear space endowed with the Lie bracket commutation operation and a natural mapping. Since the unknown matricant of a first order ODE system like (1) must be an invertible 6×6 matrix with variable entries, the setting for finding solutions of (1) is a 6×6 matrix Lie group. In this case, the above general definition of a Lie algebra implies that the 6×6 matrix $\mathbf{A}(\mathrm{R})$ governing (1) is an element of a matrix Lie algebra. Moreover, in this setting the associated matrix Lie algebra is endowed with the matrix commutation law

$$[\mathbf{A}, \mathbf{B}]: = \mathbf{AB} - \mathbf{BA}, \tag{2}$$

where $[\mathbf{A}, \mathbf{B}]$ is commonly called the *matrix commutator*. Finally, for these special matrix Lie groups, the matrix exponential function plays the role of the natural mapping.

We emphasize that in the theory of Lie groups, the role of the exponential mapping is crucial. Indeed, within the context of differential geometry, the matrix exponential maps an element belonging to a matrix Lie algebra into an invertible matrix belonging to its corresponding Lie group; in other words, the exponential mapping allows to recapture the local group structure from the corresponding Lie algebra. Thus, for a first-order ODE system like (1), it is natural to attempt to construct the solution as a matrix exponential with exponent given by a matrix which belongs to the associated Lie algebra. This peculiarity of the exponential mapping probably inspired the idea developed by Magnus [3], who proposed to express the exponent by a matrix series expansion made of infinite terms, each of them belonging to the Lie algebra corresponding to the Lie group of the unknown matricant.

In detail, with reference to the differential problem defined in (1), the Magnus method assumes the matricant to be of exponential form with the exponent given by the following series expansion, called the Magnus expansion:

$$\mathbf{Y}(\mathrm{R}) = \exp[\boldsymbol{\Omega}(\mathrm{R})]\mathbf{Y}(0), \qquad \boldsymbol{\Omega}(0) = \mathbf{O}_{6\mathrm{x}6}, \qquad \boldsymbol{\Omega}(\mathrm{R}) = \sum_{\mathrm{k}=1}^{\infty} \boldsymbol{\Omega}_{\mathrm{k}}(\mathrm{R}). \tag{3}$$

For our purposes, we report here only the first two terms of the series:

$$\boldsymbol{\Omega}_1(\mathrm{R}) = \int_0^{\mathrm{R}} A(\rho_1)\mathrm{d}\rho_1, \qquad \boldsymbol{\Omega}_2(\mathrm{R}) = \frac{1}{2}\int_0^{\mathrm{R}} \mathrm{d}\rho_1 \int_0^{\rho_1} [\mathrm{A}(\rho_1),\ \mathrm{A}(\rho_2)]\mathrm{d}\rho_2, \tag{4}$$

where [. , .] is the matrix commutator (2) and $\mathrm{A}(\cdot)$ is the governing matrix of (1). Notice that each of the remaining terms (here not reported) contains nested matrix commutators of the form (2) involving the matrix operator $\mathrm{A}(\mathrm{R})$. It is worth noting that only if the commutative condition

$$\mathrm{A}(\mathrm{R}_1)\mathrm{A}(\mathrm{R}_2) = \mathrm{A}(\mathrm{R}_2)\mathrm{A}(\mathrm{R}_1) \quad \text{for each } \mathrm{R}_1,\ \mathrm{R}_2 \tag{5}$$

holds, then, in view of (3), (1), and (4), the matricant of (1) takes the exponential form

$$Y(\mathrm{R}) = \exp\left[\int_0^{\mathrm{R}} \mathrm{A}(\rho)\ \mathrm{d}\rho\right], \tag{6}$$

which is analogous to the classical exponential solution for a scalar linear ODE. Clearly, (6) yields the solution of (1) if the entries of the matrix **A** governing (1) are independent of R. Obviously, (5) holds only in special cases because the matrices in general do not commute (this is closely related to the structure of the commutation law (2) which characterizes matrix Lie algebras).

A crucial aspect of the Magnus method related to its pertinence when seeking approximate solutions of differential problems like (1) emerges from the analysis of (3) and (4). By the above discussion, we recall that the matrix $\mathbf{A}(\mathrm{R})$ in (1) belongs to a matrix Lie algebra for all R; thus, in view of (4) we see that any term of the Magnus expansion belongs to the same Lie algebra. This implies that any truncation of the Magnus series will also belong to the same Lie algebra, and therefore the exponential map of any truncation will necessarily stay in the corresponding Lie group. This is basically the main reason why an approximated solution obtained by truncating the Magnus expansion at any order preserves the same qualitative features of the exact solution.

Another major issue concerns the conditions on the matrix $\mathbf{A}(\mathrm{R})$ which guarantee the convergence of the Magnus series. This problem has been studied in [8], where it is shown that a sufficient condition for the local convergence of the Magnus series in a certain interval $[0, \mathrm{R}_2]$ is given by

$$\int_0^{R_2} \|A(R)\|_2 dR < \pi, \tag{7}$$

where the integrand function in (7) is the spectral norm of $\mathbf{A}(R)$, i.e., the square root of the maximum eigenvalue of the product $A(R)^T A(R)$.

The fulfillment of inequality (7) determines the range of the independent variable R for which it is possible to write the solution in the form (3). However, in many applicative cases it happens that the convergence condition (7) does not hold for the whole integration interval $[0, R_2]$. In these cases, as usual for numerical integration methods, it is common dividing the interval $[0, R_2]$ into N subintervals $[R_{i+1}, R_i]$ such that the Magnus series converges in each of them. Given such a subinterval $[R_{i+1}, R_i]$, in view of (3) we may write

$$Y(R_{i+1}) = \exp(\mathbf{\Omega}(R_{i+1}))\ Y(R_i), \tag{8}$$

wherein $\mathbf{\Omega}(R_{i+1})$ is expressed by the infinite Magnus series. Consequently, the matricant of (1) evaluated on the whole domain of interest $[0, R_2]$ takes the form

$$Y(R_2) = \left[\prod_{i=1}^{N} \exp(\mathbf{\Omega}(R_{i+1}))\right]. \tag{9}$$

As it usually occurs when constructing approximate solutions, a crucial issue is that of choosing an appropriate order of truncation for $\mathbf{\Omega}(R_{i+1})$ which guarantees a suitable level of accuracy. To this aim, an efficient procedure may be summarized in the following three steps: first, the series $\mathbf{\Omega}(R_{i+1})$ is truncated at a suitable order in each subinterval wherein the convergence is guaranteed. Then the integrals appearing in each truncated series are approximated by appropriate quadrature rules. Finally, the exponential of the matrix $\mathbf{\Omega}(R_{i+1})$ is evaluated.

3 A Bifurcation Problem for an Elastic Hollow Cylinder Inspired by a Classical Hydrodynamic Instability

In the present section, we study a bifurcation problem set within the context of the nonlinear theory of elasticity. The last part of our analysis contains an explicit application of the Magnus method based on the procedure outlined in the previous section.

We consider a homogeneous, isotropic, compressible, elastic tube which occupies the region

$$\mathcal{C} \equiv \{(\mathrm{R},\, \Theta,\, \mathrm{Z}) | 0 < \mathrm{R}_1 < \mathrm{R} < \mathrm{R}_2,\ \ 0 \leq \Theta < 2\pi,\ \ 0 < \mathrm{Z} < \mathrm{H}\} \tag{10}$$

in its natural reference configuration. $(\mathrm{R}, \Theta, \mathrm{Z})$ denote the cylindrical coordinate of a point $\mathbf{X}$ in a cylindrical coordinate system with orthonormal basis $\{\mathrm{e}_\mathrm{R}, \mathrm{e}_\Theta, \mathrm{e}_\mathrm{Z}\}$. The boundary of $\mathcal{C}$ is divided into two disjoint complementary parts as follows:

$$\begin{aligned} \partial_1\mathcal{C} &\equiv \{(\mathrm{R},\, \Theta,\, \mathrm{Z}) \in \mathcal{C} |\ \mathrm{R} = \mathrm{R}_1 \text{ or } \mathrm{R} = \mathrm{R}_2\}, \\ \partial_2\mathcal{C} &\equiv \{(\mathrm{R},\, \Theta,\, \mathrm{Z}) \in \mathcal{C} | \mathrm{Z} = 0 \text{ or } \mathrm{Z} = \mathrm{H}\}. \end{aligned} \tag{11}$$

A deformation $\mathbf{f}\colon \mathbf{X} \equiv (\mathrm{R},\, \Theta,\, \mathrm{Z}) \in \mathcal{C} \mapsto \mathbf{x} = \mathbf{f}(\mathbf{X}) \equiv (\mathrm{r},\, \theta,\, \mathrm{z}) \in \mathbf{f}(\mathcal{C})$ of $\mathcal{C}$ is assumed to be a smooth function with gradient $\mathbf{F}(\mathbf{X}) \colon = \nabla \mathbf{f}(\mathbf{X})$. Since the tube is elastic and isotropic, the general form of the strain energy function is given by $\mathrm{W}(\mathbf{F}) = \mathrm{W}(\mathrm{I}_\mathbf{B},\ \mathrm{II}_\mathbf{B},\ \mathrm{III}_\mathbf{B})$, where

$$\mathrm{I}_\mathbf{B} = \mathrm{tr}\, \mathbf{B} = \mathbf{F} \cdot \mathbf{F},\ \ \mathrm{II}_\mathbf{B} = \frac{1}{2}\left((\mathrm{tr}\ \mathbf{B})^2 - \mathrm{tr}\ \mathbf{B}^2\right),\ \ \mathrm{III}_\mathbf{B} = \det \mathbf{B} = (\det\ \mathbf{F})^2 \tag{12}$$

are the orthogonal principal invariants of $\mathbf{B} \colon = \mathbf{F}\mathbf{F}^\mathrm{T}$. The Piola stress then takes the form

$$\mathbf{S}(\mathbf{F}) = \mathrm{D}\mathrm{W}(\mathbf{F}) = 2\mathrm{W}_1\ \mathbf{F} + 2\mathrm{W}_2[\mathrm{I}_\mathbf{B}\mathbf{F} - \mathbf{B}\mathbf{F}] + 2\mathrm{W}_3\ \mathrm{III}_\mathbf{B}\, \mathbf{F}^{-\mathrm{T}} \tag{13}$$

with

$$\mathrm{W}_1 := \frac{\partial \mathrm{W}}{\partial \mathrm{I}_\mathbf{B}},\quad \mathrm{W}_2 := \frac{\partial \mathrm{W}}{\partial \mathrm{II}_\mathbf{B}},\quad \mathrm{W}_3 := \frac{\partial \mathrm{W}}{\partial \mathrm{III}_\mathbf{B}}. \tag{14}$$

We assume that the inner cylinder is kept fixed, whereas the outer is subject to a uniform angular displacement $\lambda > 0$ around its axis. On the bases of $\mathcal{C}$, only tangential displacements are admitted. This leads to the following mixed boundary-value problem:

$$\mathrm{Div}\, \mathbf{S}(\mathbf{F}) = \mathbf{0} \quad \text{in } \mathcal{C}, \tag{15}$$

$$\begin{aligned} (\mathbf{f}(\mathbf{X}) - \mathbf{X}) \cdot \mathbf{e}_\mathrm{R} &= \begin{cases} 0 & \text{at } \mathrm{R} = \mathrm{R}_1 \\ \mathrm{R}_2(\cos\lambda - 1) & \text{at } \mathrm{R} = \mathrm{R}_2 \end{cases} \\ (\mathbf{f}(\mathbf{X}) - \mathbf{X}) \cdot \mathbf{e}_\Theta &= \begin{cases} 0 & \text{at } \mathrm{R} = \mathrm{R}_1 \\ \mathrm{R}_2 \sin\lambda & \text{at } \mathrm{R} = \mathrm{R}_2 \end{cases} \qquad \text{on } \partial_1\mathcal{C}, \\ (\mathbf{f}(\mathbf{X}) - \mathbf{X}) \cdot \mathbf{e}_\mathrm{Z} &= 0 \qquad\quad \text{at } \mathrm{R} = \mathrm{R}_1, \mathrm{R}_2 \end{aligned} \tag{16}$$

$$(\mathbf{f}(\mathbf{X}) - \mathbf{X}) \cdot \mathbf{e}_\mathrm{Z} = 0, \quad (\mathbf{S}(\mathbf{F})\, \mathbf{e}_\mathrm{Z}) \times \mathbf{e}_\mathrm{Z} = \mathbf{0} \quad \text{on } \partial_2\mathcal{C}. \tag{17}$$

For the equilibrium problem (15)–(17), we consider the possibility of a circular shear deformation $\tilde{\mathbf{f}}$ defined by

$$r = R, \qquad 0 = \Theta + \omega(R), \qquad z = Z, \tag{18}$$

where ω, the angular displacement field, is assumed to be a smooth function satisfying

$$\omega(R_1) = 0, \qquad \omega(R_2) = \lambda > 0 \qquad \text{on } \partial_1 \mathcal{C}. \tag{19}$$

Consequently, in view of (18) we have

$$\tilde{\mathbf{F}}(R) = \mathbf{I} + R\omega' \, \mathbf{e}_\theta \otimes \mathbf{e}_R, \tag{20}$$

where the prime denotes differentiation with respect to R and $\{\mathbf{e}_r, \mathbf{e}_\theta, \mathbf{e}_z\}$ is the deformed cylindrical orthonormal basis at (r, θ, z). Notice that the circular shear is an isochoric deformation whose principal invariants (12) are given by

$$I_{\tilde{\mathbf{B}}} = II_{\tilde{\mathbf{B}}} = 3 + R^2\omega'^2, \quad III_{\tilde{\mathbf{B}}} = 1. \tag{21}$$

Moreover, (18) trivially satisfies the displacement boundary conditions (16)–(17)$_1$ and, in view of (13) and (20), it is easily seen that also the traction boundary condition (17)$_2$ holds.

It remains to study the equilibrium field Eq. (15). To do this, we consider the Levinson-Burgess strain energy function

$$W(\mathbf{F}) = \frac{1}{2}\mu \left[\begin{array}{l} \alpha(I_{\mathbf{B}} - 3) + (1-\alpha)(J_{\mathbf{B}} - 3) + 2(1-2\alpha)\left(III_{\mathbf{B}}^{1/2} - 1\right) + \\ \left(2\alpha + \dfrac{4\nu - 1}{1 - 2\nu}\right)\left(III_{\mathbf{B}}^{1/2} - 1\right)^2 \end{array} \right], \tag{22}$$

where μ and ν are the referential shear modulus and referential Poisson's ratio, respectively, and $\alpha \in]0, 1[$ is a dimensionless material parameter. Following [9], deformations of the form (18) are allowed only if the following condition on the material parameters holds:

$$\alpha = \frac{3}{4}. \tag{23}$$

Finally, using (19)–(21) and (23), after a nontrivial calculation we obtain from (15) a single ODE, whose solution is given by

$$\omega(R, \lambda) = \lambda \, R_2^2\left(R_1^2 - R^2\right)\left[R^2\left(R_1^2 - R_2^2\right)\right]^{-1}. \tag{24}$$

We now consider the possibility of deformations which bifurcate from the primary equilibrium pure circular shear (18) as the loading parameter (angle) λ increases from 0 (natural state). A condition (*only necessary*) for the occurrence of a local branch of bifurcating solutions at a fixed λ is the existence of a nontrivial

solution of the homogeneous linearized equilibrium problem which corresponds to an adjacent equilibrium state. Such solutions superposed to the primary circular shear must satisfy the adjacent equilibrium equation

$$\operatorname{div}\left(\mathbb{A}\left(\tilde{\mathbf{F}}(r,\lambda)\right)[\operatorname{grad}\mathbf{u}]\right)=\mathbf{0}\quad \text{in } \mathcal{C}\,, \tag{25}$$

and the incremental boundary conditions

$$\mathbf{u}=\mathbf{0}\ \text{ on } \partial_1\mathcal{C}, \tag{26}$$

$$\mathbf{u}\cdot\mathbf{e}_z=0,\quad \mathbb{A}\left(\tilde{\mathbf{F}}(r,\lambda)\right)[\operatorname{grad}\mathbf{u}]\mathbf{e}_z\times\mathbf{e}_z=\mathbf{0}\quad \text{on } \partial_2\mathcal{C}. \tag{27}$$

Here $\mathbf{u}(\mathbf{x})\colon \mathcal{C}\to\mathbb{R}^3$ is an incremental displacement field, "div" and "grad" are the divergence and gradient operators with respect to $\mathbf{x}=\tilde{\mathbf{f}}(\mathbf{X})$, respectively, and $\mathbb{A}$ is the fourth-order *instantaneous* elasticity tensor, given by

$$\mathbb{A}\left(\tilde{\mathbf{F}}(r,\lambda)\right)[\mathbf{H}]:=\mathrm{D}^2\mathrm{W}\left(\tilde{\mathbf{F}}(r,\lambda)\right)\left[\mathbf{H}\ \tilde{\mathbf{F}}(r,\lambda)\right]\ \tilde{\mathbf{F}}^{\mathrm{T}}(r,\lambda),\quad \forall\mathbf{H}\in\mathrm{Lin}. \tag{28}$$

For the constitutive class (22), it follows from (28), (20)–(21), and (23) that

$$\begin{aligned}\mathbb{A}\left(\tilde{\mathbf{F}}(r,\lambda)\right)[\operatorname{grad}\mathbf{u}]=&\frac{\mu}{4}\left((\operatorname{grad}\mathbf{u})^{\mathrm{T}}\tilde{\mathbf{B}}^{-1}+\tilde{\mathbf{B}}^{-1}\left((\operatorname{grad}\mathbf{u})+(\operatorname{grad}\mathbf{u})^{\mathrm{T}}\right)\right)\\&+\frac{3\mu}{4}(\operatorname{grad}\mathbf{u})\tilde{\mathbf{B}}+\frac{2\nu\mu}{1-2\nu}(\mathbf{I}\cdot(\operatorname{grad}\mathbf{u}))\mathbf{I}+\frac{\mu}{2}(\operatorname{grad}\mathbf{u})^{\mathrm{T}}\end{aligned} \tag{29}$$

where $\tilde{\mathbf{B}}$ is given by $(20)_2$. We now restrict our analysis to the class

$$\mathcal{A}:=\left\{\begin{array}{l}\mathbf{u}\equiv(u_r,u_\theta,u_z)\\ u_r=v_1(r)\cos\kappa z,\quad u_\theta=v_2(r)\cos\kappa z,\quad u_z=v_3(r)\sin\kappa z,\\ \kappa=n\dfrac{\pi}{H},\quad n=0,\,1,\,2,..,\quad \mathbf{u}(r_1)=\mathbf{u}(r_2)=\mathbf{0}\end{array}\right\} \tag{30}$$

of periodic bifurcating displacements which are reminiscent of the instability patterns observed in the classical Taylor–Couette shear flow of viscous fluids. Exhaustive analyses of problems related to the one here studied have been developed in [6, 7]. In [6] one may also find stability issues based on [10, 11]. Notice that (30) models the occurrence of an axially periodic cellular pattern in the gap between the inner and outer cylinders (n represents the number of possibly forming cells in the axial direction); in particular, inside each of the n possible forming cells, (30) describes a twist-like displacement perpendicular to the $\mathbf{e}_\theta$-direction of primary annular shear, so that the vector lines of the incremental displacement $\mathbf{u}$ are similar to the streamlines of the twisting Taylor-like effects for fluids.

We easily check from (30) that the displacement incremental boundary condition $(27)_1$ trivially holds, whereas (26) holds provided the smooth scalar functions $v_1(r)$, $v_2(r)$, $v_3(r)$ defined for r in $[R_1,\ R_2]$ are such that

$$\begin{aligned}&\mathbf{v}(r_1) := (v_1(r_1),\ v_2(r_1),\ v_3(r_1)) = \\ &= \mathbf{v}(r_2) := (v_1(r_2),\ v_2(r_2),\ v_3(r_2)) = (0,\ 0,\ 0) \equiv \mathbf{0}.\end{aligned} \tag{31}$$

For what concerns the traction boundary condition $(27)_2$ and the field Eq. (25), we first observe by (30) that

$$\begin{aligned}\operatorname{grad} \mathbf{u} = \cos\kappa z &\begin{pmatrix} v_1' \mathbf{e}_r \otimes \mathbf{e}_r - v_2\ r^{-1} \mathbf{e}_r \otimes \mathbf{e}_\theta + v_2'\ \mathbf{e}_\theta \otimes \mathbf{e}_r \\ + v_1\ r^{-1}\ \mathbf{e}_\theta \otimes \mathbf{e}_\theta + \kappa\ v_3\ \mathbf{e}_z \otimes \mathbf{e}_z \end{pmatrix} \\ &+ \sin\ \kappa\ z\big(-\kappa\, v_1 \mathbf{e}_r \otimes \mathbf{e}_z - \kappa\, v_2 \mathbf{e}_\theta \otimes \mathbf{e}_z + v_3' \mathbf{e}_z \otimes \mathbf{e}_r\big),\end{aligned} \tag{32}$$

and by $(20)_2$ that $\tilde{\mathbf{B}}\, \mathbf{e}_z = \mathbf{e}_z$; thus, in view of (29)–(30), condition $(27)_2$ immediately holds. Finally, by evaluating the divergence of (29) with the aid of $(20)_2$ and (32), after some nontrivial calculation we reduce the partial differential problem (25)–(27) to the following system of three homogeneous second-order ODE's:

$$\begin{cases} \mathbf{P}(r,\ \lambda)\mathbf{v}'' + \Big(\mathbf{P}'(r,\ \lambda) + \mathbf{R}(r,\ \lambda, \kappa) - \mathbf{R}^{\mathrm{T}}(r,\ \boldsymbol{\lambda}, \kappa)\Big)\mathbf{v}' \\ \quad + \Big(\mathbf{R}'(r,\ \lambda, \kappa) + \mathbf{Q}(r,\ \lambda, \kappa)\Big)\mathbf{v} = \mathbf{0}, \qquad r_1 < r < r_2 \\ \mathbf{v}(r_1) = \mathbf{v}(r_2) = \mathbf{0}, \end{cases} \tag{33}$$

where $\mathbf{v} := (v_1,\ v_2,\ v_3)$ (we have omitted the dependence on r) and

$$\mathbf{P}(r,\ \lambda) = \begin{pmatrix} \mu r\left(\frac{2(1-\nu)}{1-2\nu} + \frac{3}{4} r^2 \omega'^2\right) & -\frac{1}{2}\mu r^2 \omega' & 0 \\ -\frac{1}{2}\mu r^2 \omega' & \mu r & 0 \\ 0 & 0 & \mu r \end{pmatrix}$$

$$\mathbf{R}(r,\ \kappa,\ \lambda) = \begin{pmatrix} \mu \frac{2\nu}{1-2\nu} & -\frac{1}{2}\mu r \omega' & \mu r \kappa \frac{2\nu}{1-2\nu} \\ \frac{1}{2}\mu r \omega' & -\mu\left(1 + \frac{1}{4} r^2 \omega'^2\right) & 0 \\ -\mu r \kappa\left(1 + \frac{1}{4} r^2 \omega'^2\right) & \frac{1}{4}\mu r^2 \kappa \omega' & 0 \end{pmatrix}$$

$$\mathbf{Q}(r,\ \kappa,\ \lambda) = \begin{pmatrix} -\mu\left(\dfrac{2(1-\nu)}{1-2\nu} r^{-1} + \dfrac{3}{4} r \omega'^2\right) & -\frac{1}{2}\mu\omega' + \frac{1}{4}\mu r^2 \kappa^2 \omega' & -\mu\kappa \frac{2\nu}{1-2\nu} \\ -\mu r \kappa^2\left(\dfrac{1}{4}\left(1 + r^2 \omega'^2\right) + \dfrac{3}{4}\right) & & \\ -\frac{1}{2}\mu\omega' + \frac{1}{4}\mu r^2 \kappa^2 \omega' & -\mu\left(r\left(\kappa^2 + \omega'^2\right) + r^{-1}\right) & 0 \\ -\mu\kappa \frac{2\nu}{1-2\nu} & 0 & -\mu r \kappa^2 \frac{2(1-\nu)}{1-2\nu} \end{pmatrix} \tag{34}$$

are nonconstant matrices determined by the components of the symmetric fourth-order tensor $\mathbb{A}$ in the coordinate system (r, θ, z). In the following, we drop the dependence of the basic parameters (the inner and outer radii, the height of the tube, the material moduli, and the angle λ) usually assumed as prescribed. We only maintain explicit the dependence on r, in order to emphasize that the linear ODE system is non-autonomous.

It is crucial to observe that for the constitutive class (22) $\mathbf{P}(\mathrm{r})$ is *invertible*. This allows to transform the set of three linear second-order ordinary differential Eqs. (33) into a system of six linear first-order ordinary differential equations, for which well-known existence theorems and procedures for constructing the solutions are available in the literature. With this aim, once introduced the 3×3 matrices

$$\begin{cases} \mathbf{T}: = \mathbf{P}^{-1}(\mathrm{r})\left(\mathbf{R}'(\mathrm{r}) + \mathbf{Q}(\mathrm{r})\right) \\ \mathbf{K}: = \mathbf{P}^{-1}(\mathrm{r})\left(\mathbf{P}'(\mathrm{r}) + \mathbf{R}(\mathrm{r}) - \mathbf{R}^{\mathrm{T}}(\mathrm{r})\right), \end{cases} \tag{35}$$

we rewrite (33) in the form

$$\begin{cases} \mathbf{v}'' = -\mathbf{T}\mathbf{v} - \mathbf{K}\mathbf{v}', \quad \mathrm{r}_1 < \mathrm{r} < \mathrm{r}_2 \\ \mathbf{v}(\mathrm{r}_1) = \mathbf{v}(\mathrm{r}_2) = \mathbf{0}. \end{cases} \tag{36}$$

Then by setting

$$\begin{aligned} \mathbf{y}: &= \begin{Bmatrix} \mathbf{v} \\ \mathbf{v}' \end{Bmatrix}_{6\mathrm{x}1}, \qquad \mathbf{A}: = \begin{pmatrix} \mathbf{O} & \mathbf{I} \\ -\mathbf{T} & -\mathbf{K} \end{pmatrix}_{6\mathrm{x}6}, \\ \mathbf{M}: &= \begin{pmatrix} \mathbf{I} & \mathbf{O} \\ \mathbf{O} & \mathbf{O} \end{pmatrix}_{6\mathrm{x}6}, \qquad \mathbf{N}: = \begin{pmatrix} \mathbf{O} & \mathbf{O} \\ \mathbf{I} & \mathbf{O} \end{pmatrix}_{6\mathrm{x}6}, \end{aligned} \tag{37}$$

we easily see that (36) is equivalent to the linear homogeneous first-order ODE boundary-value problem

$$\begin{cases} y' = \mathbf{A}(\mathrm{r})\mathbf{y} \\ \mathbf{M}\mathbf{y}(\mathrm{r}_1) - \mathbf{N}\mathbf{y}(\mathrm{r}_2) = \begin{Bmatrix} \mathbf{0} \\ \mathbf{0} \end{Bmatrix}_{6\mathrm{x}1} \end{cases} \quad \text{for } \mathrm{r}_1 < \mathrm{r} < \mathrm{r}_2. \tag{38}$$

Now by following elementary results on systems of linear ODE's, we may write a solution of (38) in the form

$$\mathbf{y}(\mathrm{r}) = \mathbf{Y}(\mathrm{r})\mathbf{y}(\mathrm{r}_1) = \mathbf{Y}(\mathrm{r}) \left\{ \begin{array}{c} \mathbf{0} \\ \mathbf{v}'(\mathrm{r}_1) \end{array} \right\}_{6\mathrm{x}1}, \tag{39}$$

where $\mathbf{y}(\mathrm{r}_1)$ is an unknown *constant* vector and

$$\begin{aligned} &\mathbf{Y}(\mathrm{r}) = \begin{pmatrix} \mathbf{U}_1(\mathrm{r}) & \mathbf{U}_2(\mathrm{r}) \\ \mathbf{U}_1'(\mathrm{r}) & \mathbf{U}_2'(\mathrm{r}) \end{pmatrix}_{6\mathrm{x}6}, \det \mathbf{Y}(\mathrm{r}) \neq 0 \quad \text{for} \quad \mathrm{r}_1 < \mathrm{r} < \mathrm{r}_2, \\ &\text{with} \quad \mathbf{Y}(\mathrm{r}_1) = \begin{pmatrix} \mathbf{I} & \mathbf{O} \\ \mathbf{O} & \mathbf{I} \end{pmatrix}_{6\mathrm{x}6}, \end{aligned} \tag{40}$$

is a particular fundamental matrix solution for $(38)_1$, usually called *matricant*. Then, substitution of (39) into $(38)_2$ yields

$$[\mathbf{M}\mathbf{Y}(\mathrm{r}_1) - \mathbf{N}\mathbf{Y}(\mathrm{r}_2)]\mathbf{y}(\mathrm{r}_1) = \left\{ \begin{array}{c} \mathbf{0} \\ \mathbf{0} \end{array} \right\}, \tag{41}$$

which, in view of $(37)_{3-4}$, (40) and (39), is equivalent to the homogeneous system of three algebraic equations

$$\mathbf{U}_2(\mathrm{r}_2)\mathbf{v}'(\mathrm{r}_1) = \mathbf{0} \tag{42}$$

for which nontrivial solution $\mathbf{v}'(\mathrm{r}_1) \neq \mathbf{0}$ are possible if and only if

$$\det \mathbf{U}_2(\mathrm{r}_2) = 0. \tag{43}$$

Finally, a solution of the primary ODE problem (33) can be written in the following form:

$$\mathbf{v}(\mathrm{r}) = \mathbf{U}_2(\mathrm{r})\mathbf{v}'(\mathrm{r}_1), \tag{44}$$

which clearly satisfies the boundary conditions $(34)_2$ (see (41) and (43)).

The above analysis shows that the possibility of determining nontrivial solutions for the bifurcation differential problem (33) is strictly related to the knowledge of the 3x3 matrix $\mathbf{U}_2(\mathrm{r})$, which represents the "north-east" block of the 6×6 matricant (40) of the Cauchy initial-value problem

$$\left\{ \begin{array}{l} \mathbf{Y}'(\mathrm{r}) = \mathbf{A}(\mathrm{r})\mathbf{Y}(\mathrm{r}) \\ \mathbf{Y}(\mathrm{r}_1) = \begin{pmatrix} \mathbf{I} & \mathbf{O} \\ \mathbf{O} & \mathbf{I} \end{pmatrix}_{6\mathrm{x}6} \end{array} \right. \quad \text{for } \mathrm{r}_1 < \mathrm{r} < \mathrm{r}_2. \tag{45}$$

Since (45) has the same structure of the Cauchy initial-value problem (1), we now illustrate a strategy based on the Magnus method for determining the solution of (45) and, in particular, the determination of the critical value λ_{cr} of the primary

angular displacement, that is, the lowest value of the angle λ for which the tube may support (during a loading process) a nontrivial twist-like bifurcation of the form (30) from the fundamental circular shear deformation. The Magnus method is now the key ingredient for approximately determining the matricant of (45), whereas (43) plays the role of bifurcation condition.

Following the steps outlined in the Sect. 2, we first fix the radii R_1 and R_2, the height H, the referential shear modulus μ, and the referential Poisson's ratio ν (recall that $\alpha = 3/4$ by (23)). Then as follows:

- fix the number n of twisting cells in the axial direction starting from $n = 1$;
- fix the value of the loading parameter λ starting from zero;
- compute the matrices (34), which now depend only on r, and then compute $\mathbf{A}(r)$ in (37) by means of (35);
- divide the interval $[R_1, R_2]$ into N subintervals $[r_{i+1},\ r_i]$ such that the Magnus series converges in each of them (see the convergence condition (7));
- employ for simplicity a fourth-order method by truncating the Magnus series $\mathbf{\Omega}(r_{i+1})$ after the second term in each subinterval (see (4)) and by approximating the integrals using a Gauss quadrature rule. This allow us to write

$$\mathbf{\Omega}(r_{i+1}) = \frac{h}{2}\left(\mathbf{A}\left(r_i^{[1]}\right) + \mathbf{A}\left(r_i^{[2]}\right)\right) - \frac{h^2\sqrt{3}}{12}\left[\mathbf{A}\left(r_i^{[1]}\right), \mathbf{A}\left(r_i^{[2]}\right)\right], \tag{46}$$

where

$$r_i^{[1]} = r_i + \left(\tfrac{1}{2} - \tfrac{\sqrt{3}}{6}\right)h, \quad r_i^{[2]} = r_i + \left(\tfrac{1}{2} + \tfrac{\sqrt{3}}{6}\right)h, \text{ with } h = \frac{R_2 - R_1}{N} \tag{47}$$

are two Gauss points in correspondence of which $\mathbf{A}(r)$ and its employed linear approximation agree.

- compute the matrix exponential of $\mathbf{\Omega}(r_{i+1})$ using the function MatrixExp in the software Mathematica;
- evaluate the matricant of (46) at the external radius $r_2 = R_2$ by (8) and (9);
- compute the "north-east" block of the matricant at $r_2 = R_2$, that is the 3x3 matrix $\mathbf{U}_2(r_2)$;
- compute the determinant of $\mathbf{U}_2(r_2)$ and check if the bifurcation condition (43) holds.

Following this procedure, we define λ_{cr}^n as the smallest value of λ which satisfies the bifurcation condition (43) corresponding to the fixed value of n. Of course, when one repeats the above procedure by varying the number of possible axial cells, the corresponding critical load λ_{cr}^n varies. We have performed a large number of computations which show that as n increases, the corresponding λ_{cr}^n determined by (43) decreases until a critical value of n above which (43) definitively does not hold for any λ. In correspondence, a load λ_{cr} corresponding to n_{cr} is determined, and

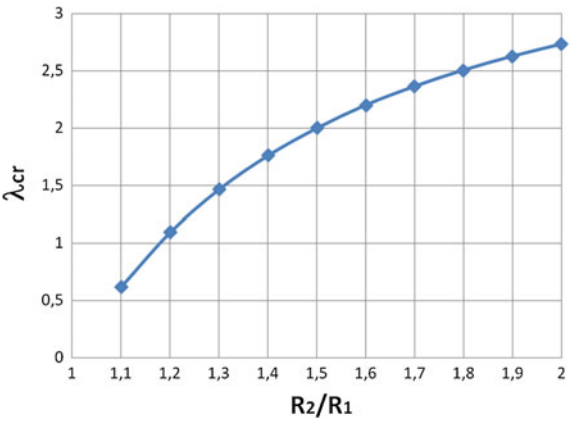

Fig. 1 λ_{cr} versus R_2/R_1, for $\mu = 1$, $\alpha = 3/4$, $\nu = 0.25$, $H/R_1 = 1$

this is the critical value of the circular angle of shear which allows for the occurrence of a nontrivial axial periodic deformation of the form (30).

Figure 1 reports the bifurcation curve for a referential shear modulus $\mu = 1$ MPa, referential Poisson's ratio $\nu = 0.25$, $\alpha = 3/4$, and $H/R_1 = 1$. It shows the critical load λ_{cr} as a function of the ratio R_2/R_1 between the outer and inner radius of the tube. As expected, we observe that twist-like bifurcation may be more easily supported in thin tubes.

Acknowledgments The authors gratefully acknowledge the research projects MIUR-PRIN 2010-2011: "*Dinamica, stabilità e controllo di strutture flessibili*" and MIUR PON-REC: "*MASSIME"—Sistemi di sicurezza meccatronici innovativi (cablati e wireless) per applicazioni ferroviarie, aerospaziali e robotiche*".

References

1. Goriely, A., Vandiver, R., and Destrade, M.. Nonlinear Euler buckling. *Proc. R. Soc. A*, 464 (2008) 3003-3019.
2. Shuvalov, A.L. A sextic formalism for the three-dimensional elastodynamics of cylindrically anisotropic radially inhomogeneous materials. *Proc. R. Soc. Lond.*, 459 (2003) 1611–1639.
3. Magnus, W.. On the exponential solution of differential equations for a linear operator. *Comm. Pure Appl. Math.*, VII (1954) 649–673.
4. Blanes, S., Casas, F., Oteo, J.A., and Ros, J.. The Magnus expansion and some of its applications. *Physics Reports*, 470 (2009) 151–238.
5. Iserles, A., and Norsett, S.P. On the solution of linear differential equations in Lie groups. *Phil. Trans. R. Soc. A*, 357 (1999) 983–1019.
6. Fosdick, R., Foti, P., Fraddosio, A., and Marzano, S. Shear driven planar Couette and Taylor-like instabilities for a class of compressible isotropic elastic solids. *ZAMP*, 61 (2010) 537-554.
7. Fosdick, R., Foti, P., Fraddosio, A., Marzano, S., and Piccioni, M.D. Taylor-like bifurcations for a compressible isotropic elastic tube. *Mathematics and Mechanics of Solids (MMS)*, 19 (2014) 966-987.

8. Moan, P.C., and Niesen, J. Convegence of the Magnus series. *Found. Comput. Math.*, 8 (2008) 291–301, 2008.
9. Haughton, D.M. Circular shearing of compressible elastic cylinders, *Q. Jl. Mech. Appl. Math.*, 46 (1993) 471–486.
10. Fosdick, R., Foti, P., Fraddosio, A., and Piccioni, M.D. A lower bound estimate of the critical load for compressible elastic solids. *Cont. Mech. and Thermodynamics (CMT)*, 22 (2010) 77–97.
11. Fosdick, R., Foti, P., Fraddosio, A., Marzano, S., and Piccioni, M.D. A lower bound estimate of the critical load in bifurcation analysis for incompressible elastic solids. *Mathematics and Mechanics of Solids (MMS)*, 20 (2015) 53–79.

Transient Vibrations of a Simply Supported Viscoelastic Beam of a Fractional Derivative Type Under the Transient Motion of the Supports

Jan Freundlich

Abstract Transient vibrations analysis of a simply supported beam whose viscoelastic properties are expressed in terms of a fractional Kelvin–Voigt model are presented. The Riemann–Liouville fractional derivative of order $0 < \gamma < 1$ is used. The Bernoulli–Euler beam excited by transient motion of the supports is considered. An oscillating function with linearly time-varying frequency is applied as an excitation. The forced-vibration solution of the beam is determined using the mode superposition method. A convolution integral of the fractional Green's function and forcing function is used to achieve the beam response. The Green's function is formulated by two terms. The first term describes damped vibrations around the drifting equilibrium position, while the second term describes the drift of the equilibrium position. The dynamic responses are numerically calculated. A comparison between results obtained using the fractional and integer (classical) viscoelastic material models is presented. In the analysed system, the influence the term describing the drift of the equilibrium position on the beam deflection is relatively low and may be neglected in some cases. The employed procedure widens the methods applied in damping modelling of structural elements.

1 Introduction

A lot of machines, during their use, are started up and stopped down; what causes that machines are subjected to oscillating forces of increasing or decreasing frequency. Moreover, machines often operate above their first or second resonance and therefore must pass through one or more critical speeds when being started up stopped down. Therefore, the problem of determining the maximum amplitudes and stresses in the system due to the forced vibrations during acceleration through resonance is very important. This problem has many applications in engineering

J. Freundlich (✉)
Warsaw University of Technology, Warsaw, Poland
e-mail: jfr@simr.pw.edu.pl

© Springer International Publishing Switzerland 2016

J. Awrejcewicz (ed.), *Dynamical Systems: Theoretical and Experimental Analysis*, Springer Proceedings in Mathematics & Statistics 182, DOI 10.1007/978-3-319-42408-8_10

analysis; some of these applications are vibrations that occur in rotating machinery, bridges or vehicles.

A simply supported beam subjected to transient motion of the supports could be used as a simplified dynamic model of above-mentioned problems. Additionally, viscoelastic material properties could have significant influence on dynamic behaviour of the analysed system. Therefore an appropriate viscoelastic material model ought to be used in dynamic analysis. Fractional derivatives are much often used in modelling viscoelastic material properties [11, 12]. These derivatives, in contrast to integer order derivatives, where the derivative depend only on the local condition of the function, is not local and depends on the time "history" of the function [11, 12]. This property is exploited in processes which depend on the time history of the input (hereditary processes). In particular, the damping properties of viscoelastic material can be modelled using the fractional order derivative and enables us to use smaller number of parameters than using models described by derivatives of the integer order [1]. The fractional models more accurately describe damping properties of variety of materials over wide range of frequencies [1, 2, 5]. The review of publications on the application of fractional calculus in dynamic problems of solids can be found in paper by Rossikhin and Shitikova [15].

Thus, the aim of this work is a comparison of dynamics of beams made of Kelvin–Voigt material described by fractional and integer order differential equations. The comparison is made for a beam under the transient motion of the supports. Moreover, a convolution integral of the fractional Green's function and forcing function is used to achieve the beam response. The Green's function is evaluated using Laplace transform method and use of the closed contour of integration in conjunction with the residue theorem [1, 3, 4, 6, 14]. The proposed approach widens the methods applied in damping modelling of structural elements.

2 Problem Formulation

The equation of motion of the examined beam is derived under the assumption of the Bernoulli–Euler theory, neglecting rotary inertia and shear deformation. Furthermore, the uniform bending stiffness and mass density are assumed. It is assumed that viscoelastic properties of a beam are described by the fractional Kelvin–Voigt model. This model is defined by the following relationship (e.g. [1])

$$\sigma = E\varepsilon(t) + E_{\gamma}^{'}\frac{d^{\gamma}\varepsilon(t)}{dt^{\gamma}} = E\left(\varepsilon + \mu_{\gamma}\frac{d^{\gamma}\varepsilon(t)}{dt^{\gamma}}\right), \tag{1}$$

where, $\mu_{\gamma} = \frac{E_{\gamma}^{'}}{E}$, E is Young modulus of the beam material, $E_{\gamma}^{'}$ is damping coefficient, $\frac{d^{\gamma}}{dt^{\gamma}}$ is the Riemann–Liouville fractional derivative of order γ.

The Riemann–Liouville fractional derivative of order γ is defined by the expression [11, 12]

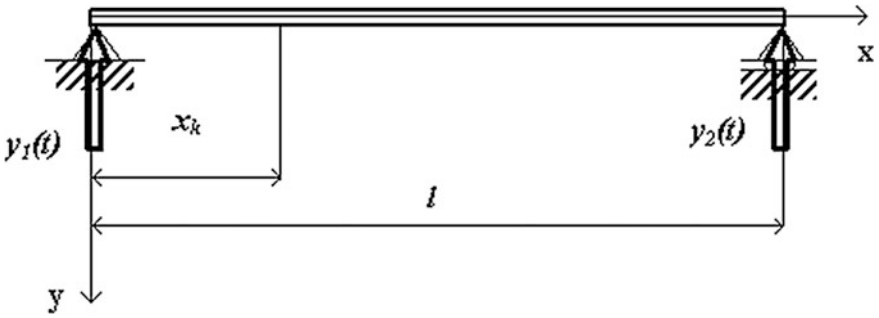

Fig. 1 Schema of the analysed system

$$\frac{d^{\gamma}}{dt^{\gamma}}f(t) \equiv {}_0D_t^{\gamma}f(t) \equiv \frac{1}{\Gamma(m-\gamma)}\frac{d^m}{dt^m}\int_0^t \frac{f(\tau)d\tau}{(t-\tau)^{\gamma+1-m}}, \quad m-1<\gamma\le m. \tag{2}$$

For many real materials, the fractional derivative order is commonly assumed to be in interval $0 < \gamma \le 1$ [1, 5, 8].

In the present research is assumed that the beam is excited only by the supports movement whereas additional loadings do not occur (Fig. 1). Using above assumptions, the governing equation of forced transverse motion of the beam is obtained as shown

$$EJ\left(\frac{\partial^4 y(x,t)}{\partial x^4} + \mu_{\gamma}\frac{d^{\gamma}}{dt^{\gamma}}\left(\frac{\partial^4 y(x,t)}{\partial x^4}\right)\right) + A\rho\frac{\partial^2 y(x,t)}{\partial t^2} = 0, \tag{3}$$

where A is a cross-section area of the beam, J is a moment of inertia of the beam cross-section ρ is material mass density of the beam, $y(x, t)$ is transversal displacement of the neutral beam axis (Fig. 1), t is time, x is a longitudinal coordinate.

The supports excitation is assumed to be a linear time-varying frequency function. The boundary conditions for the analysed beam are assumed as follows:

$$y(0,t) = y_1(t), \;\; y(l,t) = y_2(t), \tag{4}$$

$$\left.\frac{\partial^2 y}{\partial x^2}\right|_{x=0} = \left.\frac{\partial^2 y}{\partial x^2}\right|_{x=l} = 0. \tag{5}$$

Introducing the geometrical relation of the supports movement, the transverse displacement of the neutral axis of the beam can be expressed as

$$y(x,t) = \left(1-\frac{x}{l}\right)y_1(t) + \frac{x}{l}y_2(t) + w(x,t). \tag{6}$$

Substituting Eqs. 4, 5 and 6 into Eq. (3), the equation describing the relative movement of the beam is obtained

$$\frac{\partial^4 w(x,t)}{\partial x^4} + \mu_\gamma \frac{d^\gamma}{dt^\gamma}\left(\frac{\partial^4 w(x,t)}{\partial x^4}\right) + a^2 \frac{\partial^2 w(x,t)}{\partial t^2} = -a^2\left\{\left(1-\frac{x}{l}\right)\ddot{y_1}(t) + \frac{x}{l}\ddot{y_2}(t)\right\}, \tag{7}$$

where $a^2 = \frac{\rho A}{EJ}$.

The solution of Eq. 7 is obtained utilising the mode superposition principle, e.g. [7, 9 13]. The eigenfunctions for a simply supported beam are given by

$$W_n(x) = \sin\frac{n\pi x}{l} \quad n = 1, 2, 3 \ldots. \tag{8}$$

Then, the forced-vibration solution of a beam can be expressed as

$$w(x,t) = \sum_{n=1}^{\infty} \xi_n(t) W_n(x) = \sum_{n=1}^{\infty} \xi_n(t) \sin\frac{n\pi x}{l} \tag{9}$$

and the corresponding derivatives are evaluated below

$$\frac{\partial^4 w(x,t)}{\partial x^4} = \sum_{n=1}^{\infty} W_n^{IV}(x)\xi_n(t), \tag{10}$$

$$\frac{d^\gamma}{dt^\gamma}\left(\frac{\partial^4 w(x,t)}{\partial x^4}\right) = \sum_{n=1}^{\infty} W_n^{IV}(x)\xi_n^\gamma(t), \tag{11}$$

where $\xi_n^\gamma(t) = \frac{d^\gamma}{dt^\gamma}(\xi(t))$, $W_n^{IV}(x) = \frac{d^4 W(x)}{dx^4}$, and

$$\frac{\partial^2 w(x,t)}{\partial t^2} = \sum_{n=1}^{\infty} W_n(x)\ddot{\xi}_n(t), \tag{12}$$

where $\ddot{\xi}(t) = \frac{d^2\xi(t)}{dt^2}$.

The supports movement is assumed as

$$y_1(0,t) = y_{10}\sin(\frac{\varepsilon t^2}{2}),\ y_2(l,t) = y_{20}(\sin\frac{\varepsilon t^2}{2} + \varphi), \tag{13}$$

where y_{10}, y_{20} are displacement amplitudes at the beam edges, φ is a phase angle, ε is angular acceleration.

Substituting Eqs. 10, 11, 12 and 13 into Eq. 7 we get

$$\sum_{n=1}^{\infty}\left[W_n^{IV}\xi_n(t)+\mu_\gamma W_n^{IV}\xi_n^{\gamma}(t)+a^2W\xi_n(t)\right]=-a^2\left\{\left[y_{10}\varepsilon\cdot\cos(\frac{\varepsilon t^2}{2})+\right.\right.$$
$$\left.\left.-y_{10}\varepsilon^2\cdot t^2\sin(\frac{\varepsilon t^2}{2})\right](1-\frac{x}{l})+\left[y_{20}\varepsilon\cdot\cos(\frac{\varepsilon t^2}{2})-y_{20}\varepsilon^2\cdot t^2\sin(\frac{\varepsilon t^2}{2})\right]\frac{x}{l}\right\} \tag{14}$$

Next, integrating over x from 0 to l, and using the orthogonality property of eigenfunctions, after some mathematical transformations, the following relationship is obtained

$$\xi_n(t)+\mu_\gamma\omega_n^2\xi_n^{\gamma}(t)+\omega_n^2\xi_n(t)=\frac{2}{n\pi}\left\{\left[y_{10}\varepsilon\cdot\cos(\frac{\varepsilon t^2}{2})-y_{10}\varepsilon^2\cdot t^2\sin(\frac{\varepsilon t^2}{2})\right]+\right.$$
$$\left.-\left[y_{10}\varepsilon\cdot\cos(\frac{\varepsilon t^2}{2})-y_{10}\varepsilon^2\cdot t^2\sin(\frac{\varepsilon t^2}{2})\right](-1)^n\right\} \tag{15}$$

where $\omega_n=\left(\frac{n\pi}{l}\right)^2\sqrt{\frac{EJ}{\rho A}}$ is the nth natural frequency of the beam.

Assuming zero initial conditions, the solution of Eq. 15 can be expressed as

$$\xi_n(t)=f_0\int_0^t G_n(t-\tau)q_w(\tau)d\tau, \tag{16}$$

where

$$q_w(\tau)=\frac{2}{n\pi}\left\{\left[y_{10}\varepsilon\cdot\cos(\frac{\varepsilon\tau^2}{2})-y_{10}\varepsilon^2\cdot\tau^2\sin(\frac{\varepsilon\tau^2}{2})\right]+\right.$$
$$\left.+\left[y_{10}\varepsilon\cdot\cos(\frac{\varepsilon\tau^2}{2})-y_{10}\varepsilon^2\cdot\tau^2\sin(\frac{\varepsilon\tau^2}{2})\right](-1)^n\right\}, \tag{17}$$

where $G_n(t)$ is the Green's function corresponding to Eq. 15, [12, 14, 15]. This Green's function consists of two terms, namely

$$G_n(t)=K_{1n}(t)+K_{2n}(t). \tag{18}$$

The first term K_{1n} (Eq. 18) represents damped vibrations around the drifting equilibrium position, while the second term K_{2n} describes the drift of the equilibrium position [4, 14]. The term K_{1n} could be calculated from formula given by Beyer and Kempfle [4]

$$K_{1n}(t)=\alpha_n e^{-\sigma_n t}\sin(\Omega_n t+\phi_n), \tag{19}$$

where

$\alpha_n = \frac{2}{\sqrt{\mu_k^2+\nu^2}}$, $\phi_n = \arctan\left(\frac{\mu_k}{\nu}\right)$ $\mu_k = \mathrm{Re}(W'(s_{1,2}))$, $\nu = \mathrm{Im}(W'(s_{1,2}))$, $W(s) = s^2 + \mu_\gamma \omega_n^2 s^\gamma + \omega_n^2$—is the characteristic polynomial of Eq. 15,

$W'(s) = 2s + \gamma\mu_\gamma\omega_n^2 s^{\gamma-1}$—is a derivative of the characteristic polynomial with respect *s*,

$s_{1,2} = -\sigma_n \pm i\Omega_n$—are conjugate complex roots of the characteristic polynomial *W(s)*.

The term K_{2n} could be calculated using formula [4]

$$K_{2n}(t) = \frac{\mu_\gamma \omega_n^2 \sin(\pi\gamma)}{\pi} \int_0^\infty \frac{r^\gamma e^{-rt} dr}{\left[r^2 + \mu_\gamma \omega_n^2 r^\gamma \cos(\pi\gamma) + \omega_n^2\right]^2 + \left[\mu_\gamma \omega_n^2 r^\gamma \sin(\pi\gamma)\right]^2}. \quad (20)$$

In some cases of a vibration analysis, K_{2n} could be neglected in comparison with K_{1n} [10, 14].

In the case of viscoelastic integer order Kelvin–Voigt material model the governing equation of the analysed beam has the following form [9]

$$EJ\left(\frac{\partial^4 y(x,t)}{\partial x^4} + \mu \frac{\partial^5 y(x,t)}{\partial x^4 \partial t}\right) + A\rho \frac{\partial^2 y(x,t)}{\partial t^2} = \frac{2}{n\pi}\left\{\left[y_{10}\varepsilon \cdot \cos\left(\frac{\varepsilon\tau^2}{2}\right) + \right.\right.$$
$$\left.\left. - y_{10}\varepsilon^2 \cdot \tau^2 \sin\left(\frac{\varepsilon\tau^2}{2}\right)\right] + \left[y_{10}\varepsilon \cdot \cos\left(\frac{\varepsilon\tau^2}{2}\right) - y_{10}\varepsilon^2 \cdot \tau^2 \sin\left(\frac{\varepsilon\tau^2}{2}\right)\right](-1)^n\right\}. \quad (21)$$

The solution of the equation could be obtained using similar approach as in the case of the equation with the fractional derivative. For each nth mode, the response could be calculated as follow [9]

$$\xi_n(t) = \frac{f_0}{\omega_{hn}} \int_0^t e^{-h_n(t-\tau)} \sin(\omega_{hn}(t-\tau)) \sin\frac{n\pi g(\tau)}{l} d\tau \quad for\ h_n < \omega_n$$
$$\xi_n(t) = \frac{f_0}{\tilde{\omega}_{hn}} \int_0^t e^{-h_n(t-\tau)} sh(\tilde{\omega}_{hn}(t-\tau)) \sin\frac{n\pi g(\tau)}{l} d\tau \quad for\ h_n > \omega_n, \quad (22)$$

where $h_n = \frac{1}{2}\mu\omega_n^2$, $\omega_{hn} = \sqrt{\omega_n^2 - h_n^2}$, $\tilde{\omega}_{hn} = \sqrt{h_n^2 - \omega_n^2}$.

It should be noted that when $\gamma = 1$ (integer order derivative), component K_{2n} of a fractional Green's function (Eqs. 18 and 20) vanishes. When such system with an integer integer order derivative (Eq. 22) is underdamped (i.e. $\omega_n > h_n$), it could be demonstrated that it is equivalent to a system described by fractional derivative equations (Eq. 15).

3 Calculation Results and Discussion

In the paper, the influence of the order of fractional derivative γ on response of the beam excited by the transient motion of the supports is examined. The achieved formulae, Eqs. 16, 19 and 20, are used to compute responses of the system with the fractional derivative, whereas the responses of the system with the integer derivative are computed using Eq. 22. The computations are performed with the help of the "Mathematica" package.

The calculations are performed for several values of the order of fractional derivative γ, the phase angle $\varphi = \pi/6$, damping coefficient $\mu_\gamma = 2 \times 10^{-3}$ s$^\gamma$, angular acceleration $\varepsilon = 5$ and 10 1/s^2. The analysed beam has a length of 20 m, mass density 7600 kg/m^3, cross-section area 2×10^{-3} m^2, cross-section moment of inertia 3.953×10^{-6} m^4, Young's modulus 2.1×10^5 MPa. In the analysis, vibration amplitude of the beam versus dimensionless time is calculated. The dimensionless time is defined as $\tau = \varepsilon \times t/\omega_1$, where ω_1 is the first natural frequency of the analysed beam (Eq. 15). The beam responses are computed for the point located at $x_k = 10$ m from the left edge of the beam (Fig. 1). In the analysed system, the influence the term describing the drift of the equilibrium position on the beam deflection (Eq. 20) is relatively low in comparison with the term describing oscillations and may be neglected.

The computed beam responses for the case $\varepsilon = 5$ 1/s^2 and several values of the order of the fractional derivative γ are presented in Figs. 2, 3, 4 and 5. It is visible, when the order of the fractional derivative is increased, vibration amplitudes

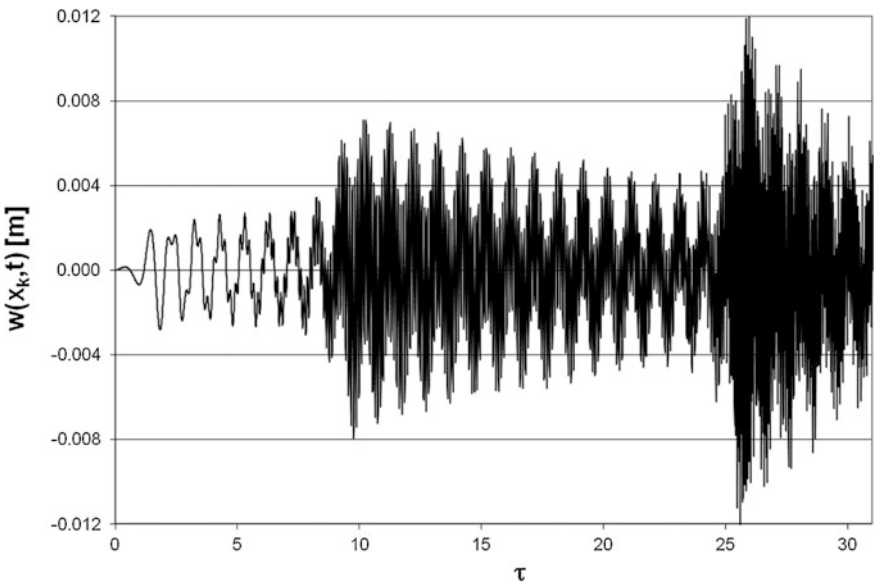

Fig. 2 Beam response for the case $\gamma = 0.25$ and $\varepsilon = 5$ 1/s^2

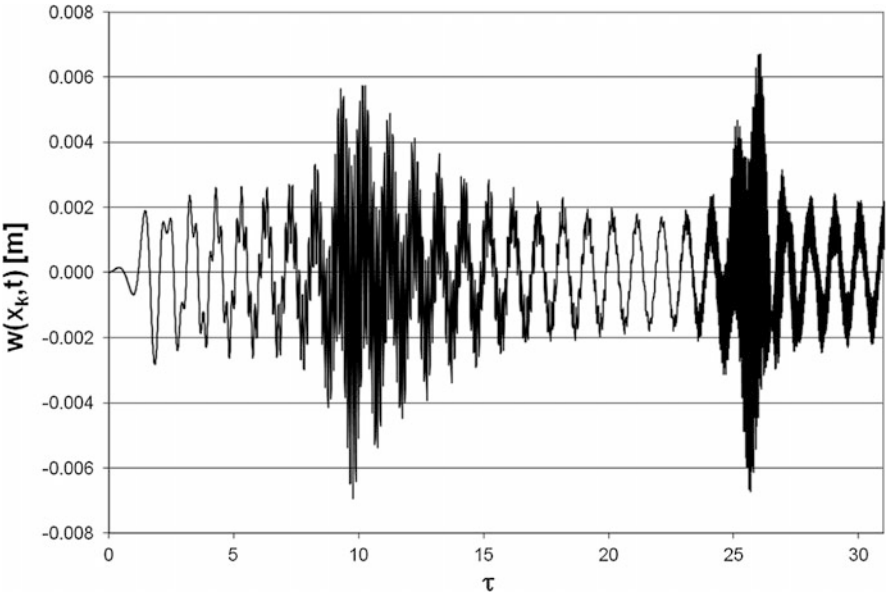

Fig. 3 Beam response for the case $\gamma = 0.50$, $\varepsilon = 5\ 1/s^2$

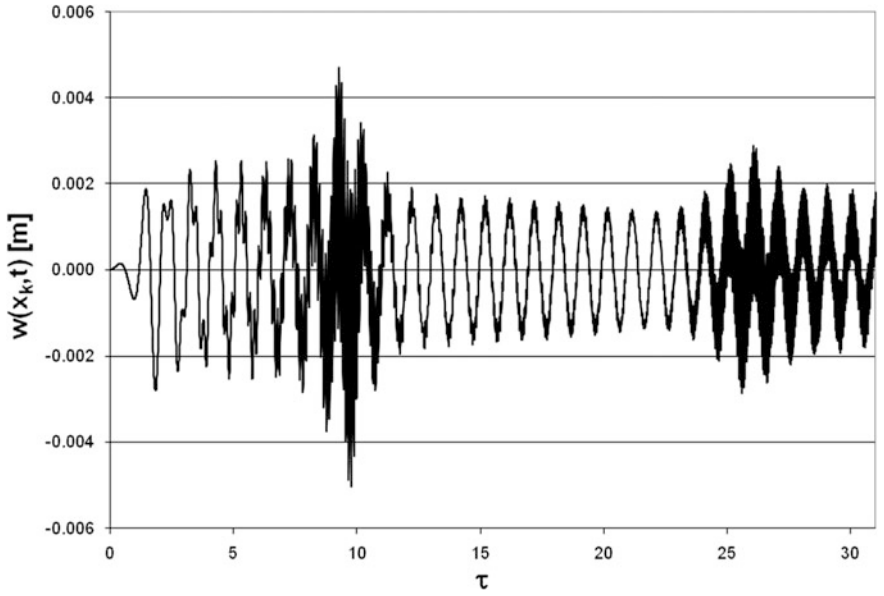

Fig. 4 Beam response for the case $\gamma = 0.75$, $\varepsilon = 5\ 1/s^2$

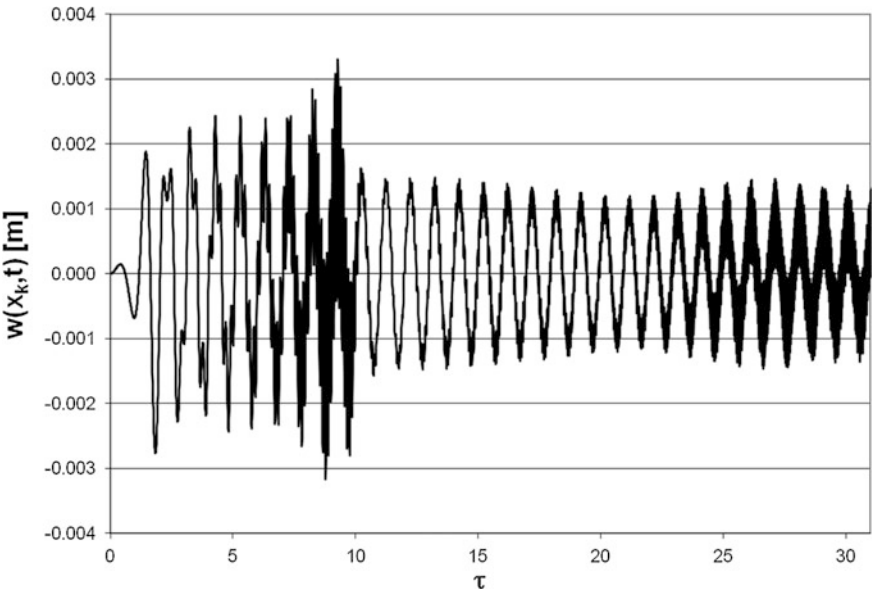

Fig. 5 Beam response for the case $\gamma = 1.0$, $\varepsilon = 5\ 1/s^2$

decrease. In the case of the fractional derivative, vibration amplitudes increase noticeably for values of the dimensionless time $\tau \approx 10$ and 26. These values correspond to the third and fifth vibration modes of the beam. In the case of the order of the fractional derivative $\gamma = 0.25$ and $\gamma = 0.5$, it could be seen that computed vibration amplitudes are greater for the fifth mode of vibration than for the third mode. In contrast, in the case of derivative order $\gamma = 0.75$ and $\gamma = 1.0$ (integer order), vibration amplitudes are greater in the case of third mode than the fifth mode.

Comparison between beam responses obtained for the derivative order $\gamma = 0.25$ and $\gamma = 1.0$ (integer order) is shown in Figs. 6 and 7. In the case of the integer order of derivative, noticeable increase of amplitudes exists only for the third vibration mode (Fig. 5). Furthermore, vibration amplitudes in the case of derivative order $\gamma = 0.25$ are significantly greater than in the case of the integer order derivative (i.e. $\gamma = 1.0$).

Comparing the beam responses for the angular acceleration $\varepsilon = 5\ 1/s^2$ with response for $\varepsilon = 10\ 1/s^2$, for the derivative order $\gamma = 0.25$, it can be seen that the amplitudes are greater for $\varepsilon = 5\ 1/s^2$ than $\varepsilon = 10\ 1/s^2$, whereas the amplitude increase for the fifth mode of vibration is larger than for the third mode in both considered cases.

Comparing the beam responses for different values of derivative order (Figs. 2, 3, 4 and 5), it can be seen that an increase in derivative order causes a decrease in vibration amplitudes. Moreover, in the case of higher values of derivative order, augmentation of vibration amplitudes vanishes for the fifth modal vibration

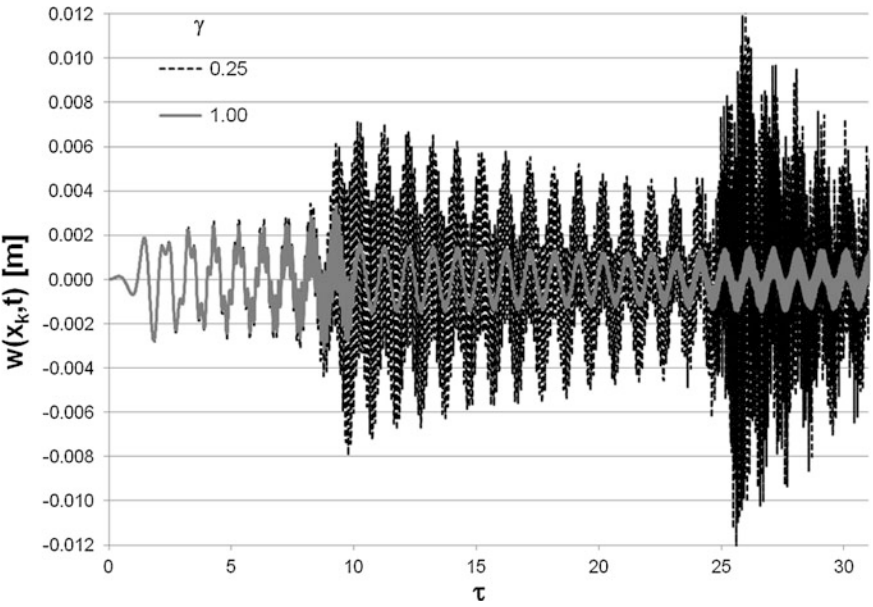

Fig. 6 Comparison between responses for $\gamma = 0.25$ and $\gamma = 1.0$, $\varepsilon = 5$ 1/s^2

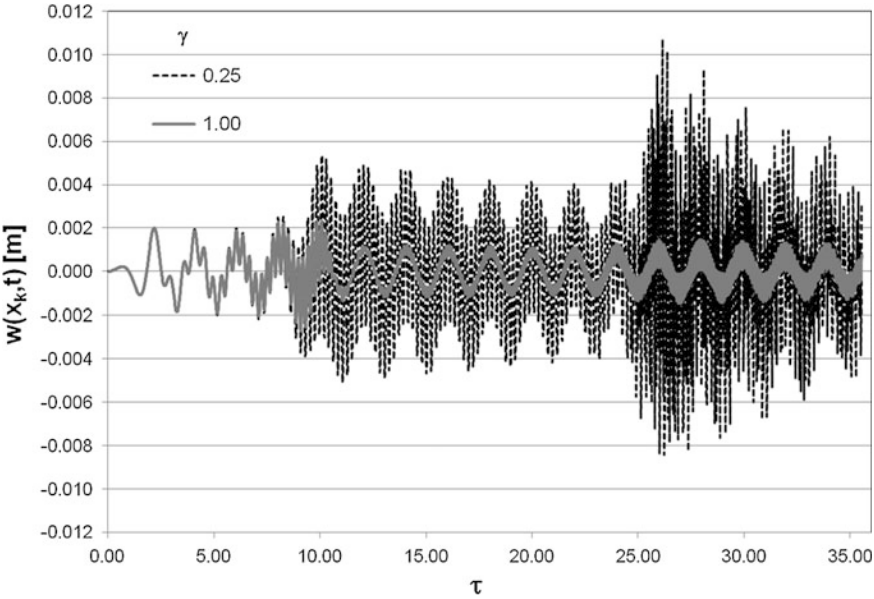

Fig. 7 Comparison between responses for $\gamma = 0.25$ and $\gamma = 1.0$, $\varepsilon = 10$ 1/s^2

frequency of the beam. In the case of the integer order derivative, the amplitude increase for the fifth modal frequency is practically invisible (Figs. 5 and 6).

4 Conclusions

The governing equations of transient vibrations of a simply supported beam whose viscoelastic properties are expressed in terms of the fractional Kelvin–Voigt model are presented. These equations are employed to calculate the transient beam responses to harmonic excitation by movement of the beam supports. The excitation frequency is assumed to be a linearly time-varying increasing function.

Calculated results show that an increase in the derivative order causes a decrease in vibration amplitudes of the beam. Moreover, in the case of the higher values of the derivative order, augmentation of vibration amplitudes vanishes for the fifth modal vibration frequency of the beam. It can be seen, comparing the response obtained for the derivative order $\gamma = 0.25$ with responses for the derivative order $\gamma = 0.75$ and 1.0.

The use of fractional viscoelastic material model expands possibility of selection of appropriate parameters for dynamic analysis of the investigated system.

Experimental studies should be undertaken to determine appropriate parameters of the fractional Kelvin–Voigt model corresponding to the obtained beam response.

References

1. Bagley R.L., Torvik P.J., Fractional Calculus—A Different Approach to the Analysis of Viscoelastically Damped structures, *AIAA Journal*, 21, 5, 741−748 (1983)
2. Bagley R.L., Torvik P.J., A Theoretical Basis for the Application of Fractional Calculus to Viscoelasticity, *Journal of Rheology*, 27, 3, 201−210 (1983)
3. Bagley R. L., Torvik P. J., On The Fractional Calculus Model of Viscoelastic Behavior, *Journal of Rheology*, 30, 1, 133−155 (1986)
4. Beyer H., Kempfle S., Definition of Physically Consistent Damping Laws with Fractional Derivatives *ZAMM*, 75, 8, 623−635 (1995)
5. Caputo M., Mainardi F., A new Dissipation Model Based on Memory Mechanism, *Pure and Applied Geophysics*, 91, 8, 134−147 (1971)
6. Caputo M., Mainardi F., Linear Models of Dissipation in Anelastic Solids, *Rivista del Nuovo Cimento*, 1, 2, 161−198 (1971)
7. Clough R. W., Penzien J., Dynamics of Structures, MacGraw-Hill, New York (1993)
8. Enelund M., Olsson P., Damping Described by Fading Memory Analysis and Application to Fractional Derivative Models, *International Journal of Solids and Structures*, 36, 939−970 (1999)
9. Kaliski S. (Ed.), *Vibrations and waves in solids* (in Polish), Państwowe Wydawnictwo Naukowe, Warszawa (1966)
10. Kempfle S., Schäfer I., Beyer H., Fractional Calculus via Functional Calculus: Theory and application, *Nonlinear Dynamics*, 29, 99−127 (2002)

11. Miller K. S., Ross B., An Introduction to the Fractional Calculus and Fractional Differential Equations, John Willey & Sons Inc., New York (1993)
12. Podlubny I., *Fractional Differential Equations*, Academic Press, San Diego (1999)
13. Rao S., *Mechanical Vibrations*, Prentice Hall, Upper Saddle River (2011)
14. Rossikhin Y. A., Shitikova M. V., Application of fractional derivatives to the analysis of damped vibrations of viscoelastic single mass systems, Acta Mechanica 120, 109−125 (1997)
15. Rossikhin Y. A., Shitikova M. V., Application of Fractional Calculus for dynamic Problems of Solid Mechanics: Novel Trends and Recent Results, *Applied Mechanics Reviews*, 63, 1−51 (2010)

Analysis of Reachability Areas of a Manoeuvring Air Target by a Modified Maritime Missile-Artillery System ZU-23-2MRE

Daniel Gapiński and Zbigniew Koruba

Abstract The paper presents elements of an analysis of reachability areas of manoeuvring air targets achieved by maritime missile-artillery system ZU-23-2MRE. A concept of a modified algorithm of missiles homing of such system is presented. On the basis of tactical and technical data concerning armament of the above-mentioned system and taking into account extremely unfavourable flight parameters of the tracked target, the starting zone and the zone of destruction possible to technical implementation for particular air-defence fire unit were.

1 Introduction

At the current battlefield an enemy has equipment, which creates possibility to perform air combat missions with ever greater precision at ever smaller heights and with increasingly higher speed. Moreover, in recent years unmanned aerial vehicles (UAV) are implemented during exploratory and combat mission more often [5, 13]. The constant development of means of airstrike causes that an operator (shooter-antiaircraft) has ever less time to visually determine the flight parameters. In addition, the process of function personnel training (soldiers responsible for transferring the coordinates of target to aiming devices, soldiers responsible for coordinating target coordinates and transferring them to the above-mentioned soldiers, commanders of battle positions) is complex and requires specific training conditions [7, 8]. Therefore it is important during the process of modernisation of a missile-artillery system ZU-23-2MRE to take into account a possibility of providing it with automatic system, which makes it possible to determine as quickly as possible the reachability zones of an air target for particular air-defence fire units. Precise determination of the above-mentioned zones has a direct influence on the

D. Gapiński (✉) · Z. Koruba
Faculty of Mechatronics and Machinery Design, Kielce University of Technology,
Al. 1000-lecia PP 7, 25-314 Kielce, Poland
e-mail: tu_daniel_kielce@wp.pl

© Springer International Publishing Switzerland 2016

J. Awrejcewicz (ed.), *Dynamical Systems: Theoretical and Experimental Analysis*, Springer Proceedings in Mathematics & Statistics 182, DOI 10.1007/978-3-319-42408-8_11

effectiveness of combating means of airstrike and plays a decisive role in the process of choosing ad adequate air-defence fire unit [6, 9, 10].

2 Tactic and Technical Data

Both, a maritime missile-artillery system ZU-23-2MR presented in the Fig. 1 and its (prototypical) version ZU-23-2MRE in which electrohydraulic drive systems in azimuth and elevation were replaced by electric ones are equipped with two types of air-defence fire units: artillery and missile.

Fig. 1 System ZU-23-2MR [3]

The fire unit that was used is a 23 mm double cannon, cooled with a liquid and marked with a symbol 2A14. The cannons are powered by two magazines containing 200 projectiles. The system is operated by one person. The cannon is adopted to use subcalibre ammunition APDS-T and FAPDS-T, what enables effective destruction of targets within distances up to 2500 m and that fly at an altitude of 1500 m. The true rate of fire of the cannons is 400 shots/min (for each cannon). An average speed of flight for the above-mentioned projectiles amounts to about 1000 m/s. In the case of modernised version, it is advisable to apply automatic system of fire control.

In case of above-mentioned systems, two rocket launchers of anti aircraft short range missiles type "Strzała-2 M" were used as a rocket fire unit. They will be replaced by missiles type "Grom" or its prototypical version "Piorun" in the modernised system. Missiles of such type are intended to combat visually observed air targets, including airplanes, helicopters and other targets that emit infrared

radiation flying on rendezvous courses at the speed up to 400 m/s and pursuit courses up to 360 m/s, and are in the destruction zone with the following parameter limits (parameters for non-manoeuvring targets):

- minimum height of the target—from 10 m
- maximum height of the target—up to 3500 m
- farther striking distance—up to 5500 m
- closer striking distance—from 500 m
- course parameter—up to 2000 m

3 The Concept of an Analysis Algorithm of Reachability Areas of Manoeuvring Air Targets Achieved by Modified System ZU-23-2MRE

The need to automate processes of detecting, tracking and combating means of airstrike forces to create specific procedures and algorithms, which enable as quickly as possible and as precisely as possible to determine flight parameters of means of airstrike and on that basis to conduct analysis of areas of reachability of a target by particular air-defence fire units. Due to the effectiveness as well as tactical and technical parameters at first the reachability zones of a detected target for the infrared homing missiles "Grom" should be determined, and then determine those areas for closer flight zones and for artillery means.

Detecting and tracking the air targets can be performed using optoelectronic head OGSS that scans and tracks [1]. The distance to the target may be determined using a laser rangefinder, controlled on the basis of coordinates designated by OGSS concerning the tracked target. The total scan time of the airspace by the above-mentioned head amounts to 0.102 s, whereas the distance measurement is performed within fractions of a second using a laser rangefinder. The synchronisation of the head and the laser rangefinder enables to determine the flight parameters of a detected target quickly and precisely.

In order to create an algorithm that enables to determine reachability of an air target detected by the missile "Grom", it is necessary to take into account its tactical and technical parameters, delays caused by passage of the missile to full combat readiness as well as limitations associated with to its manoeuvrability. It is also indispensible to take into account a delay necessary for determining flight coordinates of a target performed by OGSS. A delay T_1 during which OGSS on the basis of ten impulses of an initial detection [2] determines the velocity vector of the target and recalculates mathematical algorithm, amounts to 0.4 s. A delay T_2 is a time of reaching operating parameters of "Grom" IR seeker since launch of ground power unit. This unit is to supply with a coolant a device cooling IR seeker and to provide electric power for the system during preparation to launch a missile. A delay T_3 defines time of unlocking IR seeker. Then, the voltage from unlocking

and launching is transferred to arming unit and within a delay T_4 necessary to achieve operating parameters of an on-board power source, the booster engine of a missile is started up. The total delay from the time detecting the target by OGSS till the launch of a missile: $T = T_1 + T_2 + T_3 + T_4$. Approximate time T_{2-4} is presented in [12]. The next value that should be taken into account in the algorithm of assessment of manoeuvring air target by a missile is the so-called maximum angular velocity of line of sight, which in case of missiles type "Grom" should not exceed 12 °/s. In case of exceeding the maximum angular velocity of target line the unlocking and launching unit will not allow to launch a missile, which is caused by its aerodynamic capacity resulting among others from allowable cross-sectional overload of a missile during its flight. In the presented algorithm a limitation of manoeuvre ability of a missile was assumed to such an extent that the cross-sectional overloads, which it causes, shall not exceed 12 g. The next assumption is adopting a minimum distance between a missile and target ($r = 4$ m), for which we consider that its destruction or damage took place.

In the Fig. 2 a coordinate system of targeting characteristic for homing missiles —$x_{Cel}y_{Cel}z_{Cel}$ has been shown. This system with a vector that binds a missile with the target enables determining a position of a missile towards the target. An algorithm of reachability of a manoeuvring air target was derived into the above-mentioned coordinate system. The axis x_{Cel} is directed from the centre of the missile's mass P to the centre of target's mass C. The coordinate system $x_Cy_Cz_C$ is connected with the target, wherein the axis x_C coincide with the velocity vector of the target. The coordinate system $x_Py_Pz_P$ is connected with the missile, whereas the axis x_P coincides with the velocity vector of the missile. The coordinate system $x_Wy_Wz_W$ is a stationary coordinate system, connected with a rocket launcher and is treated as an inertial reference system.

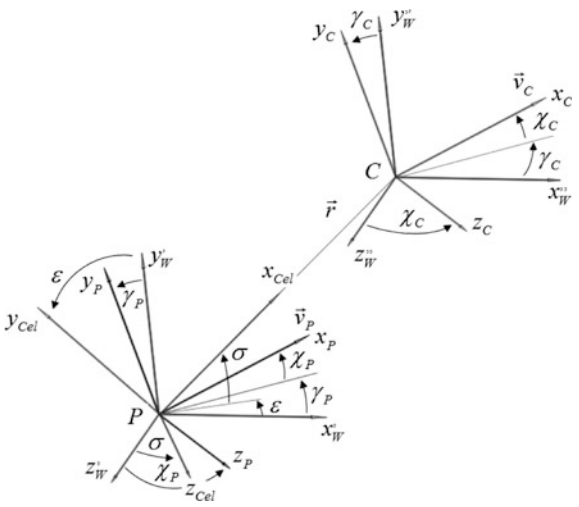

Fig. 2 Adopted coordinate systems

On the basis of the adopted coordinate system, kinematic relations between a missile and a target were introduced [4]:

$$\frac{dr}{dt} = v_C \cdot [\cos(\chi_C) \cdot \cos(\sigma) \cdot \cos(\varepsilon - \gamma_C) + \sin(\chi_C) \cdot \sin(\sigma)] + \\ - \; v_P \cdot [\cos(\chi_P) \cdot \cos(\sigma) \cdot \cos(\varepsilon - \gamma_P) + \sin(\chi_P) \cdot \sin(\sigma)] \tag{1}$$

$$\frac{d\varepsilon}{dt} = \frac{-v_C \cdot \cos(\chi_C) \cdot \sin(\varepsilon - \gamma_C) + v_P \cdot \cos(\chi_P) \cdot \sin(\varepsilon - \gamma_P)}{r \cdot \cos(\sigma)} \tag{2}$$

$$\frac{d\sigma}{dt} = \{ -v_C \cdot [\cos(\chi_C) \cdot \sin(\sigma) \cdot \cos(\varepsilon - \gamma_C) - \sin(\chi_C) \cdot \cos(\sigma)] + \\ + \; v_P [\cos(\chi_P) \cdot \sin(\sigma) \cdot \cos(\varepsilon - \gamma_P) - \sin(\chi_P) \cdot \cos(\sigma)] \} / r \tag{3}$$

where

v_C—target velocity
v_P—missile velocity
γ_P, χ_P—angle of missile flight
γ_C, χ_C—angles of target flight
ε, σ—angles of target observation
r—distance between missile and target

Using Eqs. (1)–(3) we write down a method of missile homing on the target, known in the literature as a method of proportional navigation [11].

$$\frac{\mathrm{d}y_p}{\mathrm{d}t} = a_\gamma \frac{\mathrm{d}\varepsilon}{\mathrm{d}t} \tag{4}$$

$$\frac{\mathrm{d}\chi_p}{\mathrm{d}t} = a_\gamma \frac{\mathrm{d}\sigma}{\mathrm{d}t} \tag{5}$$

The method described by formulas (4) and (5) does not take into account the limits resulting from allowable overloads that can act on manoeuvring missile. It is therefore considerable to take into account the cross-sectional overloads that can be presented as the following kinematic form [4]:

$$n_y = -\frac{v_P}{g} \cdot \dot{\gamma}_P \cdot \cos(\chi_P) - \cos(\gamma_P) \leq n_{yd} \tag{6}$$

$$n_z = \frac{v_P}{g} \cdot \dot{\chi}_P + \sin(\gamma_P) \cdot \sin(\chi_P) \leq n_{zd}, \tag{7}$$

where

g—gravitational acceleration,
n_{yd}—allowable cross-sectional overload acting along the axis,
n_{zd}—allowable cross-sectional overload acting along the axis.

We introduce the so-called coefficients of minimal-time navigation that define the level of manoeuvrability of a missile in order to take into account the allowable overloads in the homing method.

$$a_y = \frac{g \cdot n_{yd}}{v_P} \tag{8}$$

$$a_z = \frac{g \cdot n_{zd}}{v_P} \tag{9}$$

Taking into account the formulas (8) and (9), the homing algorithm is presented as follows:

$$\frac{\gamma_P}{\mathrm{d}t} = a_y \cdot u \tag{10}$$

$$\frac{\chi_P}{\mathrm{d}t} = a_z \cdot v \tag{11}$$

The values "u" and "v" that appear in (10) and (11) are called control signals and are presented as follows:

$$u = \operatorname{sign}\left(\frac{\mathrm{d}\varepsilon}{\mathrm{d}t}\right) \tag{12}$$

$$v = \operatorname{sign}\left(\frac{\mathrm{d}\sigma}{\mathrm{d}t}\right) \tag{13}$$

At the time when the overload of a missile reach the allowable values, algorithm of proportional homing (4), (5) is changed using control signals "u" and "v" to the minimum-time algorithm described by formulas (10) and (11).

4 Study Results

Selected examples of computer simulation of an analysis concerning areas of reachability of manoeuvring air targets by a modernised missile-artillery system ZU-23-2MRE using a modified homing algorithm described by formulas (4), (5), (10) and (11) are presented below.

4.1 Checking a Reachability of Manoeuvring Air Targets by a Missile on Rendezvous Courses (An Attack from a Front Hemisphere)

4.1.1 Simulation of Homing for an Example 1

A simulation conducted for a velocity of target flight $v_C = 300$ m/s. The location of a target towards rocket launcher in the time of its detection by OGSS amounted to $x_W = 2400$ m, $y_W = 500$ m, $z_W = 50$ m. The distance to a target in the time of its detection by OGSS amounted to $r = 2465$ m. The distance to the target at the time of missile launch amounted to $r = 1530$ m (Figs. 3, 4, 5, 6, 7, 8, 9 and 10).

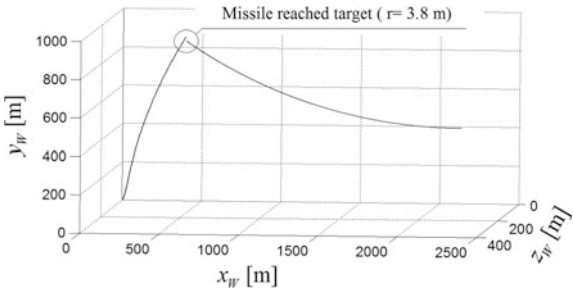

Fig. 3 Flight-path of a target and a missile: *1*—flight-path of a target during a delay "T", *2*—flight-path of a target after missile launch, *3*—flight-path of missile

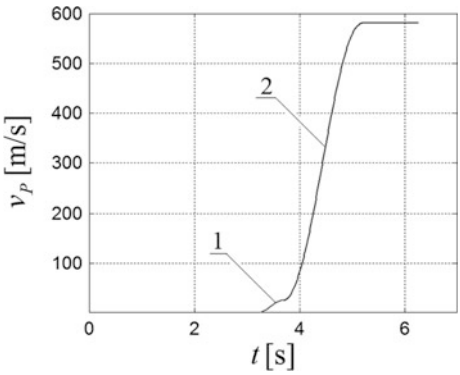

Fig. 4 Missile velocity: *1*—launching velocity, *2*—marching velocity

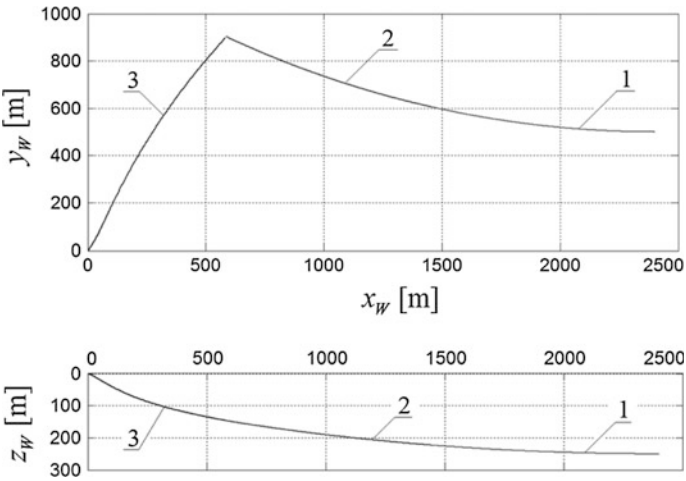

Fig. 5 Flight-path of a target and a missile in vertical and horizontal position: *1*—flight-path of a target during a delay "T", *2*—flight-path of a target after missile launch, *3*—flight-path of missile

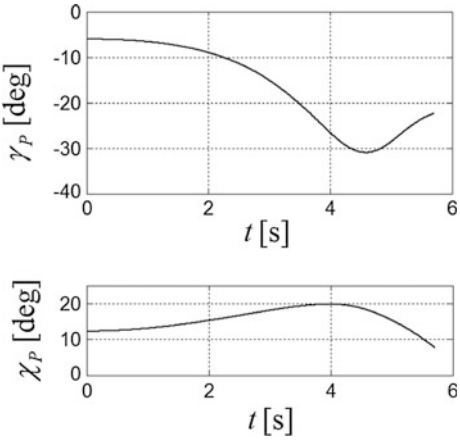

Fig. 6 Change of an angle γ_P and χ_P for trajectories presented in Fig. 5

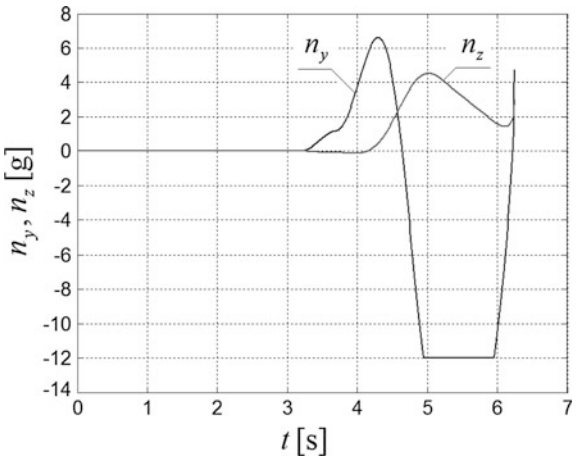

Fig. 7 Cross-sectional overloads of a missile after taking into account a minimum-time algorithm

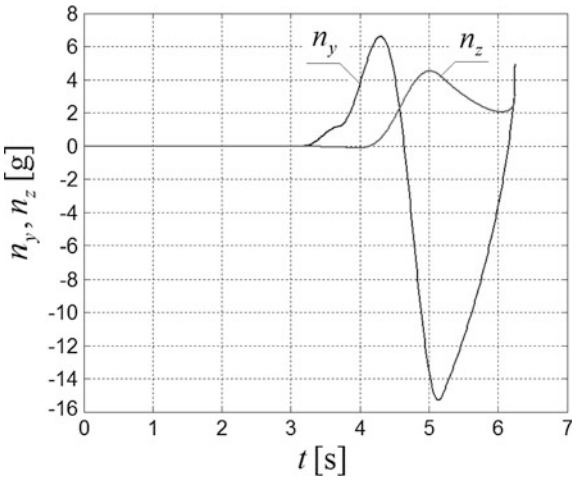

Fig. 8 Cross-sectional overloads without taking into account a minimum-time algorithm

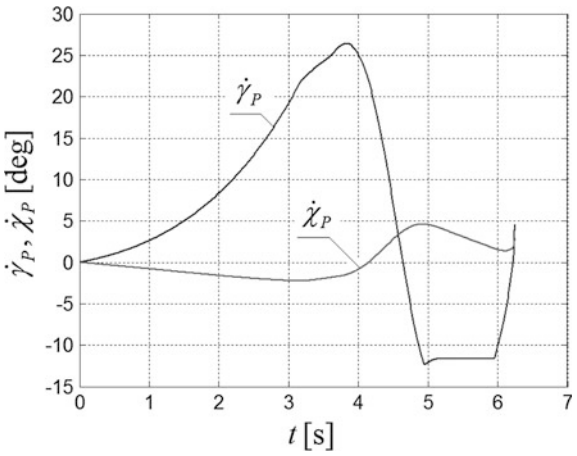

Fig. 9 Angular velocities of a missile after taking into account a minimum-time algorithm

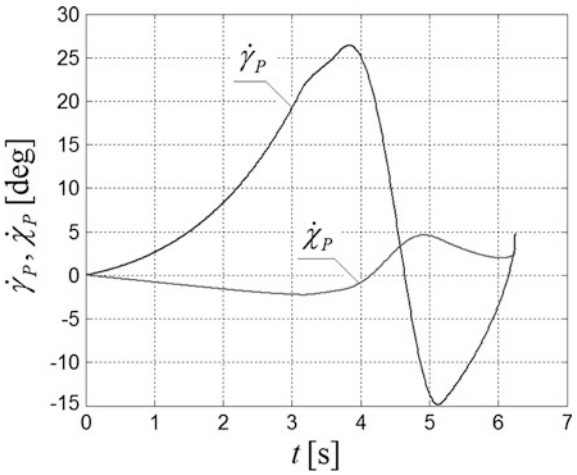

Fig. 10 Angular velocities of a missile without taking into account a minimum-time algorithm

4.1.2 Simulation of Homing for an Example 2

A simulation conducted for a velocity of target flight $v_C = 300$ m/s. The location of a target towards rocket launcher in the time of its detection by OGSS amounted to $x_W = 2260$ m, $y_W = 500$ m, $z_W = 50$ m. The distance to a target in the time of its detection by OGSS amounted to: $r = 2328$ m. The distance to the target at the time of missile launch amounted to $r = 1390$ m (Figs. 11 and 12).

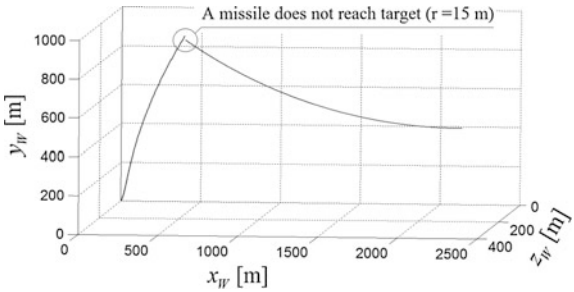

Fig. 11 Flight-path of missile and target crossing the reachability border

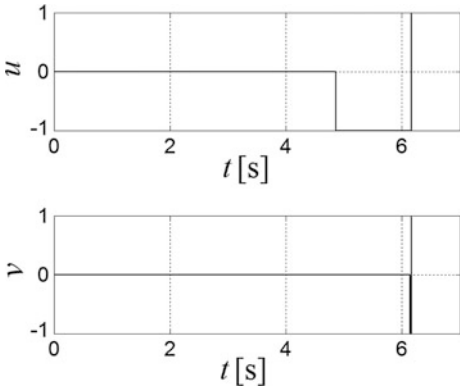

Fig. 12 Signals controlling an algorithm during simulation presented in Fig. 11

4.1.3 Simulation of Homing for an Example 3

A simulation conducted for a velocity of target flight $v_C = 320$ m/s. The location of a target towards rocket launcher in the time of its detection by OGSS amounted to $x_W = -2450$ m, $y_W = 500$ m, $z_W = 0$ m. The distance to a target in the time of its detection by OGSS amounted to $r = 2505$ m. The distance to the target at the time of missile launch amounted to $r = 1523$ m (Figs. 13, 14, 15, 16, 17 and 18).

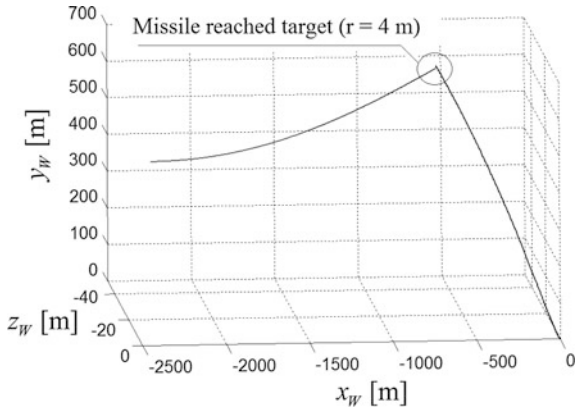

Fig. 13 Flight-path of a target and a missile on rendezvous courses

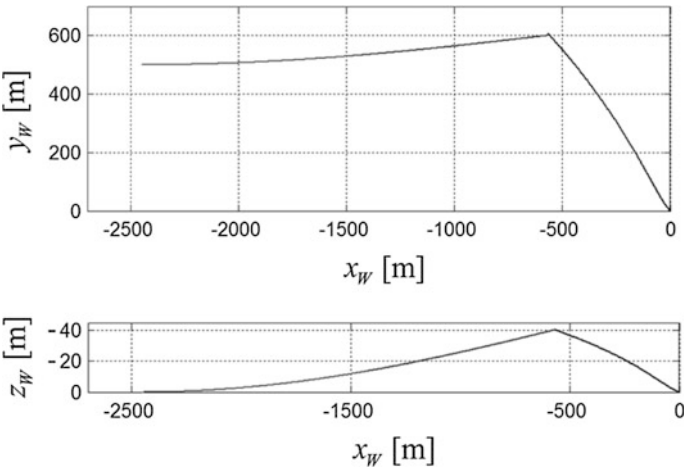

Fig. 14 Flight-path of missile and target from Fig. 13 in vertical and horizontal position

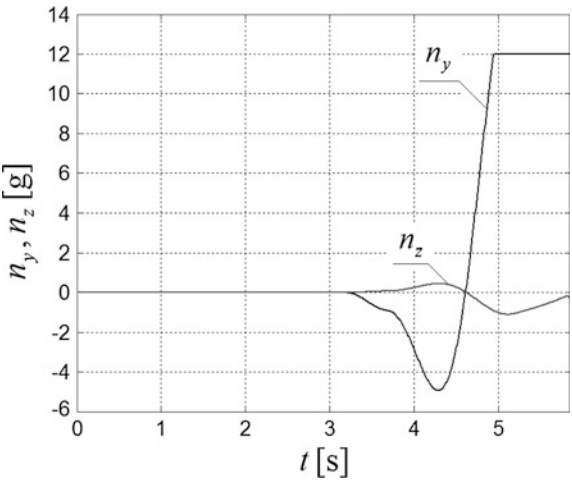

Fig. 15 Cross-sectional overloads of a missile after taking into account a minimum-time algorithm

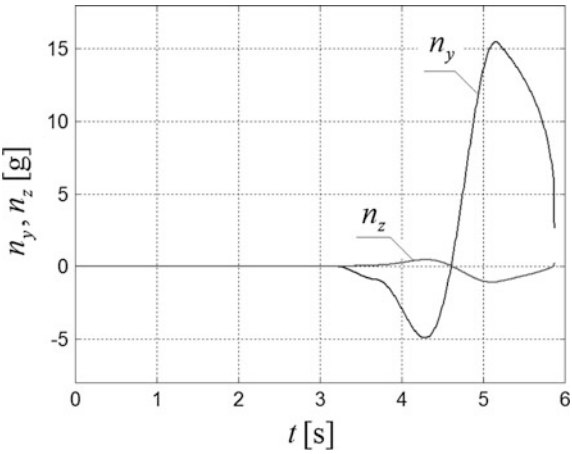

Fig. 16 Cross-sectional overloads of a missile without taking into account a minimum-time algorithm

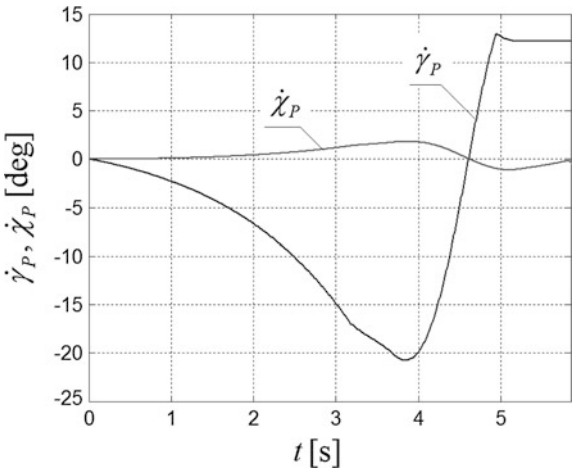

Fig. 17 Angular velocities of a missile after taking into account a minimum-time algorithm

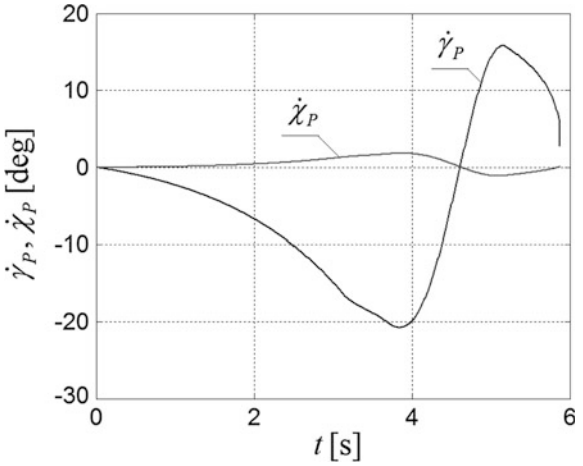

Fig. 18 Angular velocities of a missile without taking into account a minimum-time algorithm

4.1.4 Simulation of Homing for an Example 4

A simulation conducted for a velocity of target flight $v_C = 320$ m/s The location of a target towards rocket launcher in the time of its detection by OGSS amounted to $x_W = -2400$ m, $y_W = 500$ m, $z_W = 50$ m. The distance to a target in the time of its detection by OGSS amounted to $r = 2451$ m. The distance to the target at the time of missile launch amounted to $r = 1476$ m (Figs. 19 and 20).

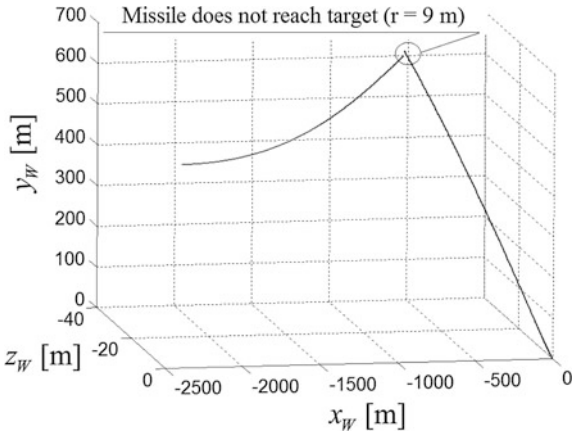

Fig. 19 Flight trajectory of missile and target after crossing the reachability border

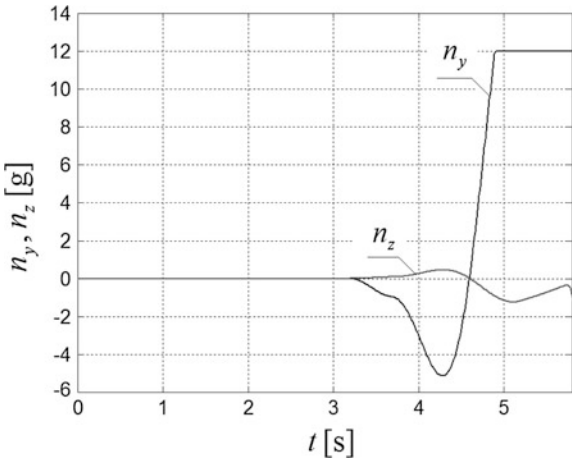

Fig. 20 Cross-sectional overloads of a missile after taking into account a minimum-time algorithm

4.2 Checking a Reachability of Manoeuvring Air Targets by a Missile on Pursuit Courses (An Attack from a Back Hemisphere)

4.2.1 Simulation of Homing for an Example 5

A simulation conducted for a velocity of target flight $v_C = 300$ m/s. The location of a target towards rocket launcher in the time of its detection by OGSS amounted to:

$x_W = 1000$ m, $y_W = 2000$ m, $z_W = 50$ m. The distance to a target in the time of its detection by OGSS amounted to $r = 2236$ m. The distance to the target at the time of missile launch amounted to $r = 2822$ m (Figs. 21, 22, 23 and 24).

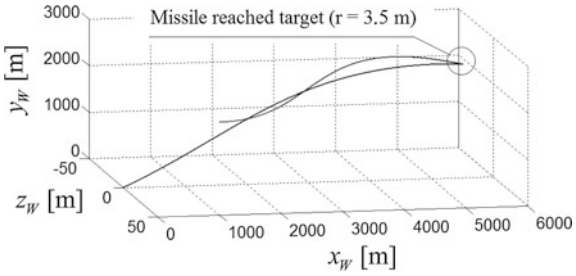

Fig. 21 Flight-path of a target and a missile on a pursuit courses

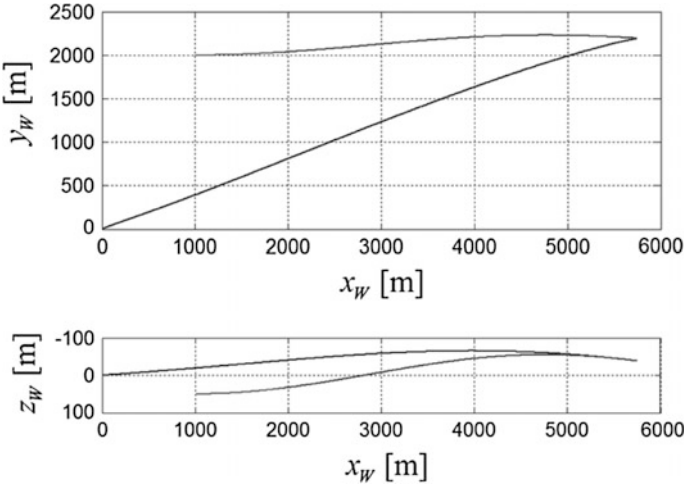

Fig. 22 Flight-path of missile and target from Fig. 21 presented in vertical and horizontal position

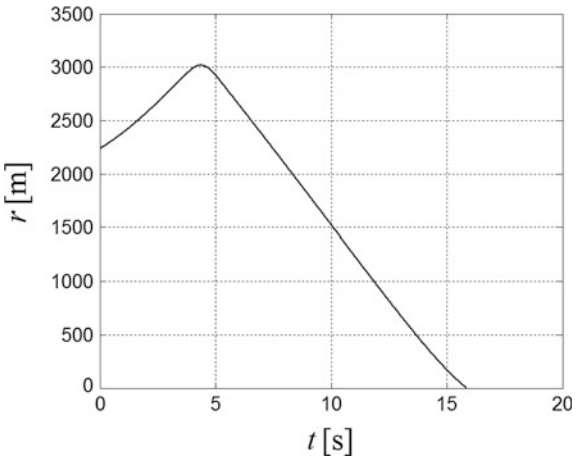

Fig. 23 Change of distance between missile and target for simulation presented in Fig. 21

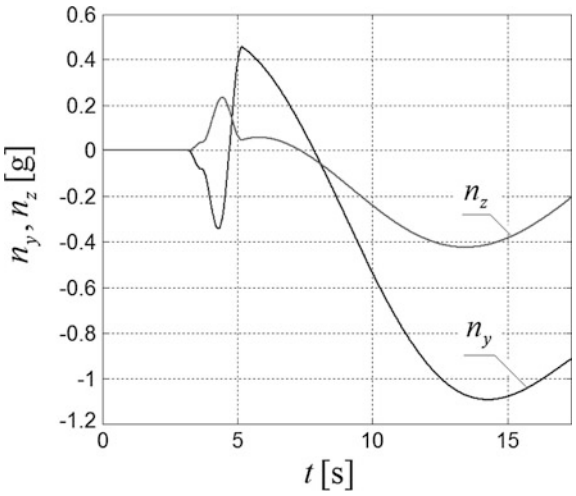

Fig. 24 Cross-sectional overload of a missile during its flight on the basis of trajectory presented in Fig. 21

4.2.2 Simulation of Homing for an Example 6

A simulation conducted for a velocity of target flight $v_C = 300$ m/s. The location of a target towards rocket launcher in the time of its detection by OGSS amounted to $x_W = 1150$ m, $y_W = 2000$ m, $z_W = 50$ m. The distance to a target in the time of its detection by OGSS amounted to $r = 2307$ m. The distance to the target at the time of missile launch amounted to $r = 2928$ m (Figs. 25, 26, 27 and 28).

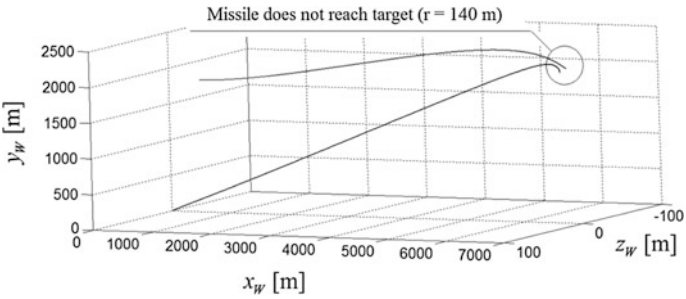

Fig. 25 Flight-path of missile and target after crossing the border of reachability

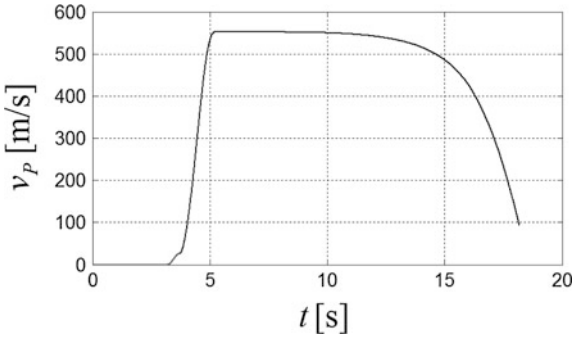

Fig. 26 Missile velocity during its flight on the basis of trajectory presented in Fig. 25

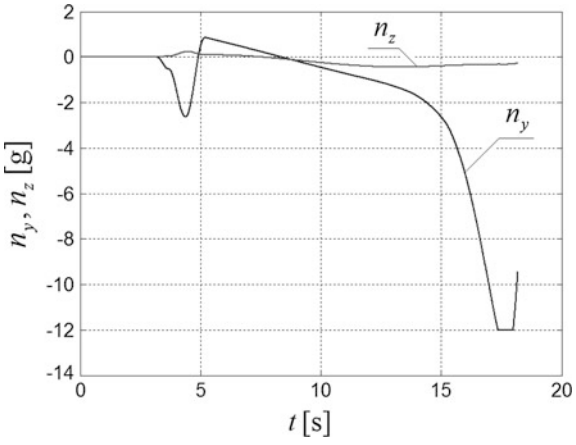

Fig. 27 Cross-sectional overload of a missile during its flight on the basis of trajectory presented in Fig. 25

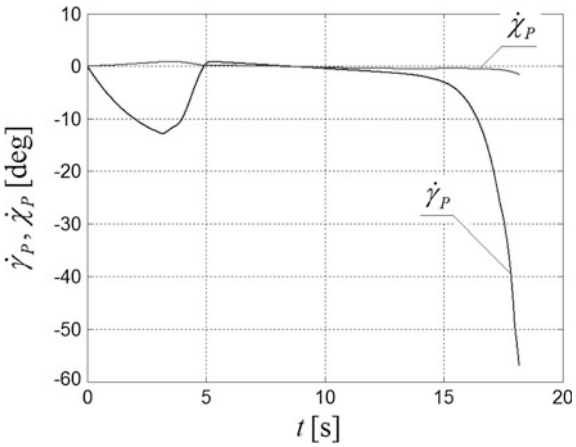

Fig. 28 Angular velocities of a missile during its flight on the basis of trajectory presented in Fig. 25

5 Summary and Conclusion

The results of a simulation show that the developed minimal-time algorithm after taking into account all delays T that influence missile launch and after taking into account the tactical and technical parameters of a modernised ZU-23-2MRE system is able to effectively determine the possibilities of reaching a manoeuvring air target with a satisfactory accuracy for homing conditions. The conducted analysis also revealed that minimum target detecting spheres performed by OGSS for missiles coincide with the destruction zone for artillery fire unit (double cannons 2A14). In case of using the system complementarity of these zones enables effective use of fire in the airspace almost in the whole sector (in the distance from 5500 m from the system). From the research data presented in point 4.1 it can be concluded that the closer border of destruction zone for missile systems during shooting on rendezvous courses is mainly limited by cross-sectional overload. A further border of destruction zone on rendezvous courses will be limited to, above all, a target radiation, for which the homing head of a missiles is still able to detect and track it. The results presented in 4.2 revealed that in case of pursuit courses the closer border of destruction zone will be limited mainly by maximum angular velocity which allows effective tracking the target by the head and cross-sectional missile overload. Further destruction zone border on pursuit courses will be limited mainly by controlled flight range rockets, limited working hours of drive system and the powder pressure battery, as well as meeting the minimum allowable speed missile with the aim of enabling activation of the fuse of a head.

The graphs presented on Figs. 7, 9, 15 and 17 show that the developed algorithm effectively imposes restrictions resulting from the aerodynamic missile capabilities,

shaping the maximum angular velocity of the missile at a level that the cross-sectional overloads does not exceed the limit values.

Due to the fact that the proposed algorithm has no time-consuming complete missile dynamics equations, it can be used for reachability analysis of the so-called air targets at real-time mode. In the results of the study, time constant T_1 includes the delay resulting from the processing carried out by a number of mathematical operations and it has no significant impact on the overall analysis process.

References

1. Gapiński, D., Koruba, Z., Krzysztofik, I.: The model of dynamics and control of modified optical scanning seeker in anti-aircraft rocket missile. Mechanical System and Signal Processing, Vol. 45 (2014), Issue 2, pp 433–447, ISSN 0888-3270
2. Gapiński, D., Krzysztofik, I.: Software selection of air targets detected by the infrared skaning and tracking seeker. Scientific Journal of Polish Naval Academy, Vol. 55 (2014), pp. 39–50, PTMTS, ISSN 0860-889X
3. http://www.zmt.tarnow.pl/pl/oferta/systemy-przeciwlotnicze/23mm-przeciwlotniczy-morski-zestaw-artyleryjsko-rakietowy-zu-23-2mr.html#1
4. Koruba, Z., Osiecki, J.W.: Structure, dynamics and navigation short-range missiles, Kielce University of Technology, script no. 348, ISSN 0239-6386
5. Koruba, Z.: The dynamics and control of the gyroscope on board a flying object, Monographs, Studies, Thesis 25, Kielce University of Technology (2001), PL ISSN 0239-4979
6. Krzysztofik, I.: The Dynamics of the Controlled Observation and Tracking Head Located on a Moving Vehicle. Solid State Phenomena, Vol. 180, pp. 313–322, Trans Tech Publications, Switzerland, ISSN 1012-0394, (2012)
7. Milewski, S., Kobierski, J.W., Chmielewski, M.: Simulators Marine sets of rocket-artillery, Scientific Journal of Polish Naval Academy, ROK LIII nr 3 (190) 2012, ss. 87–100, ISSN 0860-889X
8. Milewski, S., Kobierski, J.W.: Staff training of the marine reconnaissance-fire systems with the use of simulator TR ZU-23-2MR, Mechanics in Aviation, Vol. I, pp. 241–254, PTMTS ISBN 987-83-932107-2-5
9. Palumbo, N. F, Blauwkamp, R. A., Lloyd, J.M.: Basic Principles of Homing Guidance. Jons Hopkins APL Technical Digest, Vol. 29, No. 1, 2010
10. Sonawane, H.R., Mahulikar, S.P.: Effect of Missile Turn Rate on Aircraft Susceptibility to Infrared-Guided Missile. Journal of Aircraft Vol. 50, No. 2, 2013, DOI:10.2514/1.C031902
11. Stefański, K., Grzyb, M.: Comparison of Effectiveness of Antiaircraft Missile Homing Controlled by Rotary Executive System, Problems of Mechatronics. Armament, Aviation, Safety Engineering, Vol. 4, Nr 4(14), Warsaw, 2013, pp. 27–39, ISSN 2081-5891
12. General Staff of the Polish Army – Inspectorate Logistics: Antiaircraft missile Grom-I - technical description and the operating instructions, Warsaw 1996
13. Yanushevsky, R.: Guidance of unmanned aerial vehicles, CRC Press Taylor & Francis Group, U.S. 2011, ISBN 978-1-4398-5095-4

Angular Velocity and Intensity Change of the Basic Vectors of Position Vector Tangent Space of a Material System Kinetic Point—Four Examples

Katica R. (Stevanović) Hedrih

Abstract Chapter starts from author's previous published results about nonlinear transformations of coordinate systems, from affine space to functional-nonlinear curvilinear coordinate system and corresponding geometrical and kinematical invariants along nonlinear transformations of their coordinates from one to other coordinate system. In a curvilinear coordinate system, coordinates of a geometrical or kinematical point are not equal as coordinates of its' corresponding position vector. Expressions of basic vectors of tangent space of kinetic point vector position in generalized curvilinear coordinate systems for the cases of orthogonal curvilinear coordinate systems are derived and four examples are presented. Next, expressions of change of basic vectors of tangent space of kinetic point vector position with time, also, are done. In this chapter, new and original expressions of angular velocity and velocity of dilatations of each of the basic vectors of tangent space of kinetic point vector position, in four orthogonal curvilinear coordinate systems are presented. List of these curvilinear coordinate systems are: three-dimensional elliptical cylindrical curvilinear coordinate system; generalized cylindrical bipolar curvilinear coordinate system; generalized elliptical curvilinear coordinate system, and generalized oblate spheroidal curvilinear coordinate system.

1 Introduction

In author's previously published paper [3–9] difference between linear and nonlinear transformation of coordinates is analyzed and discussed. Also, difference between affine, linear space and nonlinear, functional space with curvilinear coordinate system are pointed out.

K.R. (Stevanović) Hedrih (✉)
Department of Mechanics, Mathematical Institute of Serbian Academy of Science and Arts (SANU), Knez Mihailova 26/III, Belgrde, Serbia
e-mail: khedrih@sbb.rs; khedrih@eunet.rs

K.R. (Stevanović) Hedrih
University of Niš, ul Vojvode Tankosića 3/22, 18000 Niš, Serbia

© Springer International Publishing Switzerland 2016

J. Awrejcewicz (ed.), *Dynamical Systems: Theoretical and Experimental Analysis*, Springer Proceedings in Mathematics & Statistics 182, DOI 10.1007/978-3-319-42408-8_12

In real three-dimensional coordinate system, position vectors of the material–-kinetic points of a material system constrained by geometrical holonomic stationary and nonstationary real constraints (see Refs. [1, 2, 10–13]), are denoted by $\vec{\rho}_{(\alpha)}(q)$, $\alpha=1,2,3,\ldots,N$ and each as functions of generalized coordinated $q^i_{(\alpha)}$, $\alpha=1,2,3,\ldots,N$, $i=1,2,3$, where N is the total number of material system mass particles. Basic vectors of each position vector tangent space are denoted by $\vec{g}_{(\alpha)i}$, $\alpha=1,2,3,\ldots,N$, $i=1,2,3$, and can be expressed in the following form:

$$\vec{g}_{(\alpha)i}=\frac{\partial\vec{\rho}_{(\alpha)}}{\partial q^i_{(\alpha)}},\ \alpha=1,2,3,\ldots,N,\quad i=1,2,3 \tag{1}$$

or in the following form:

$$\vec{g}_{(\alpha)i}=\frac{\partial x_{(\alpha)}\left(q^1_{(\alpha)},q^2_{(\alpha)},q^3_{(\alpha)}\right)}{\partial q^i_{(\alpha)}}\vec{\imath}+\frac{\partial y_{(\alpha)}\left(q^1_{(\alpha)},q^2_{(\alpha)},q^3_{(\alpha)}\right)}{\partial q^i_{(\alpha)}}\vec{\jmath}+\frac{\partial z_{(\alpha)}\left(q^1_{(\alpha)},q^2_{(\alpha)},q^3_{(\alpha)}\right)}{\partial q^i_{(\alpha)}}\vec{k}$$
$$\alpha=1,2,3,\ldots,N,\quad i=1,2,3 \tag{2}$$

Contravariant coordinates of position vectors $\vec{\rho}_{(\alpha)}(q)$, $\alpha=1,2,3,\ldots,N$ of each of material system kinetic points are expressed in published Refs. [3–9].

In Refs. [3–9] the change of basic vectors of position vector tangent space of kinetic point in three-dimensional spaces with curvilinear coordinate system are derived. Without losing generality, let us list expressions for change of basic vectors $\vec{g}_{(\alpha)i}$, $\alpha=1,2,3,\ldots,N$, $i=1,2,3$ of position vector $\vec{\rho}_{(\alpha)}(q)$, $\alpha=1,2,3,\ldots,N$ in three-dimensional tangent space in curvilinear coordinate system for one kinetic point of material system. For that reason, let us present derivatives with respect to time of basic vectors $\vec{g}_{(\alpha)i}$, $\alpha=1,2,3,\ldots,N$, $i=1,2,3$ of position vector tangent space, in the following forms:

$$\begin{aligned}\frac{\mathrm{d}\vec{g}_{(\alpha)1}}{\mathrm{d}t}=&\vec{g}_{(\alpha)1}\left(\Gamma^1_{(\alpha)11}\dot{q}^1_{(\alpha)}+\Gamma^1_{(\alpha)12}\dot{q}^2_{(\alpha)}+\Gamma^1_{(\alpha)13}\dot{q}^3_{(\alpha)}\right)+\\&+\vec{g}_{(\alpha)2}\left(\Gamma^2_{(\alpha)11}\dot{q}^1_{(\alpha)}+\Gamma^2_{(\alpha)12}\dot{q}^2_{(\alpha)}+\Gamma^2_{(\alpha)13}\dot{q}^3_{(\alpha)}\right)+\\&+\vec{g}_{(\alpha)3}\left(\Gamma^3_{(\alpha)11}\dot{q}^1_{(\alpha)}+\Gamma^3_{(\alpha)12}\dot{q}^2_{(\alpha)}+\Gamma^3_{(\alpha)13}\dot{q}^3_{(\alpha)}\right)\end{aligned} \tag{3}$$

$$\begin{aligned}\frac{\mathrm{d}\vec{g}_{(\alpha)2}}{\mathrm{d}t}=&\left(\Gamma^1_{(\alpha)21}\vec{g}_{(\alpha)1}+\Gamma^2_{(\alpha)21}\vec{g}_{(\alpha)2}+\Gamma^3_{(\alpha)21}\vec{g}_{(\alpha)3}\right)\dot{q}^1_{(\alpha)}+\\&+\left(\Gamma^1_{(\alpha)22}\vec{g}_{(\alpha)1}+\Gamma^2_{(\alpha)22}\vec{g}_{(\alpha)2}+\Gamma^3_{(\alpha)22}\vec{g}_{(\alpha)3}\right)\dot{q}^2_{(\alpha)}+\\&+\left(\Gamma^1_{(\alpha)23}\vec{g}_{(\alpha)1}+\Gamma^2_{(\alpha)23}\vec{g}_{(\alpha)2}+\Gamma^3_{(\alpha)23}\vec{g}_{(\alpha)3}\right)\dot{q}^3_{(\alpha)}\end{aligned} \tag{4}$$

$$\begin{aligned}\frac{\mathrm{d}\vec{g}_{(\alpha)3}}{\mathrm{d}t} &= \left(\Gamma^1_{(\alpha)31}\vec{g}_{(\alpha)1} + \Gamma^2_{(\alpha)31}\vec{g}_{(\alpha)2} + \Gamma^3_{(\alpha)31}\vec{g}_{(\alpha)3}\right)\dot{q}^1_{(\alpha)} + \\ &+ \left(\Gamma^1_{(\alpha)32}\vec{g}_{(\alpha)1} + \Gamma^2_{(\alpha)32}\vec{g}_{(\alpha)2} + \Gamma^3_{(\alpha)32}\vec{g}_{(\alpha)3}\right)\dot{q}^2_{(\alpha)} + \\ &+ \left(\Gamma^1_{(\alpha)33}\vec{g}_{(\alpha)1} + \Gamma^2_{(\alpha)33}\vec{g}_{(\alpha)2} + \Gamma^3_{(\alpha)33}\vec{g}_{(\alpha)3}\right)\dot{q}^3_{(\alpha)}\end{aligned} \tag{5}$$

Let us suppose that each position vector tangent space of each kinetic point is three-dimensional and defined in orthogonal curvilinear coordinates $q^i_{(\alpha)}$, $\alpha = 1, 2, 3, \ldots, N$, $i = 1, 2, 3$, then is valid [3–9]

$$\frac{\mathrm{d}\vec{g}_{(\alpha)i}}{\mathrm{d}t} = \overset{*}{\vec{g}}_{(\alpha)i} + \left[\vec{\omega}_{p(\alpha)i}, \vec{g}_{(\alpha)i}\right],\ \alpha = 1, 2, 3, \ldots, N,\ i = 1, 2, 3 \tag{6}$$

Then, on the basis (6), let us separate in expressions (3), (4), and (5) of the corresponding derivatives $\frac{d\vec{g}_{(\alpha)i}}{dt}$, $\alpha = 1, 2, 3, \ldots, N$, $i = 1, 2, 3$, of the basic vectors $\vec{g}_{(\alpha)i}$, $\alpha = 1, 2, 3, \ldots, N$, $i = 1, 2, 3$ of position vector $\vec{\rho}_{(\alpha)}(q)$, $\alpha = 1, 2, 3, \ldots, N$ tangent space terms which correspond to terms of the relative derivatives $\overset{*}{\vec{g}}_{(\alpha)1}$, $\overset{*}{\vec{g}}_{(\alpha)2}$ and $\overset{*}{\vec{g}}_{(\alpha)3}$, $\alpha = 1, 2, 3, \ldots, N$ in the following forms:

$$\begin{aligned}\overset{*}{\vec{g}}_{(\alpha)1} &= \vec{g}_{(\alpha)1}\left(\Gamma^1_{(\alpha)11}\dot{q}^1_{(\alpha)} + \Gamma^1_{(\alpha)12}\dot{q}^2_{(\alpha)} + \Gamma^1_{(\alpha)13}\dot{q}^3_{(\alpha)}\right) \\ \overset{*}{\vec{g}}_{(\alpha)2} &= \vec{g}_{(\alpha)2}\left(\Gamma^2_{(\alpha)21}\dot{q}^1_{(\alpha)} + \Gamma^2_{(\alpha)22}\dot{q}^2_{(\alpha)} + \Gamma^2_{(\alpha)23}\dot{q}^3_{(\alpha)}\right) \\ \overset{*}{\vec{g}}_{(\alpha)3} &= \vec{g}_{(\alpha)3}\left(\Gamma^3_{(\alpha)31}\dot{q}^1_{(\alpha)} + \Gamma^3_{(\alpha)32}\dot{q}^2_{(\alpha)} + \Gamma^3_{(\alpha)33}\dot{q}^3_{(\alpha)}\right),\ \alpha = 1, 2, 3, \ldots, N\end{aligned} \tag{7}$$

These vector terms, $\overset{*}{\vec{g}}_{(\alpha)1}$, $\overset{*}{\vec{g}}_{(\alpha)2}$ and $\overset{*}{\vec{g}}_{(\alpha)3}$, $\alpha = 1, 2, 3, \ldots, N$ defined by expressions (7) represent vectors of relative velocity of basic vectors extensions and is possible to express in scalar forms as relative velocity of magnitude dilatation of each of three basic vectors of each position vector tangent space of each material point in following forms:.

$$\begin{aligned}\varepsilon_{(\alpha)1} &= \frac{\mathrm{d}\left|\vec{g}_{(\alpha)1}\right|}{\left|\vec{g}_{(\alpha)1}\right|\mathrm{d}t} = \left(\Gamma^1_{(\alpha)11}\dot{q}^1_{(\alpha)} + \Gamma^1_{(\alpha)12}\dot{q}^2_{(\alpha)} + \Gamma^1_{(\alpha)13}\dot{q}^3_{(\alpha)}\right) \\ \varepsilon_{(\alpha)2} &= \frac{\mathrm{d}\left|\vec{g}_{(\alpha)2}\right|}{\left|\vec{g}_{(\alpha)2}\right|\mathrm{d}t} = \left(\Gamma^2_{(\alpha)21}\dot{q}^1_{(\alpha)} + \Gamma^2_{(\alpha)22}\dot{q}^2_{(\alpha)} + \Gamma^2_{(\alpha)23}\dot{q}^3_{(\alpha)}\right) \\ \varepsilon_{(\alpha)3} &= \frac{\mathrm{d}\left|\vec{g}_{(\alpha)31}\right|}{\left|\vec{g}_{(\alpha)3}\right|\mathrm{d}t} = \left(\Gamma^3_{(\alpha)31}\dot{q}^1_{(\alpha)} + \Gamma^3_{(\alpha)32}\dot{q}^2_{(\alpha)} + \Gamma^3_{(\alpha)33}\dot{q}^3_{(\alpha)}\right),\ \alpha = 1, 2, 3, \ldots, N\end{aligned} \tag{8}$$

Other terms in each of the expressions (3), (4), and (5) of the corresponding derivatives $\frac{d\vec{g}_{(\alpha)i}}{dt}$, $\alpha=1,2,3,\ldots,N$, $i=1,2,3$, of the basic vectors $\vec{g}_{(\alpha)i}$, $\alpha=1,2,3,\ldots,N$, $i=1,2,3$, of position vector $\vec{\rho}_{(\alpha)}(q)$, $\alpha=1,2,3,\ldots,N$ tangent space are terms which represent the vector expressions of vector product between angular velocity $\vec{\omega}_{p(\alpha)i}$, $\alpha=1,2,3,\ldots,N$, $i=1,2,3$ of corresponding basic vector rotation and same basic vector $\vec{g}_{(\alpha)i}$, $\alpha=1,2,3,\ldots,N$, $i=1,2,3$. From these terms it is easier to express angular velocities of the basic vectors of position vector tangent space during motion of the corresponding kinetic point. These expressions are in the following forms:

$$\begin{aligned}
\left[\vec{\omega}_{p(\alpha)1},\vec{g}_{(\alpha)1}\right] &= \vec{g}_{(\alpha)2}\left(\Gamma^2_{(\alpha)11}\dot{q}^1_{(\alpha)}+\Gamma^2_{(\alpha)12}\dot{q}^2_{(\alpha)}+\Gamma^2_{(\alpha)13}\dot{q}^3_{(\alpha)}\right)+\\
&\quad+\vec{g}_{(\alpha)3}\left(\Gamma^3_{(\alpha)11}\dot{q}^1_{(\alpha)}+\Gamma^3_{(\alpha)12}\dot{q}^2_{(\alpha)}+\Gamma^3_{(\alpha)13}\dot{q}^3_{(\alpha)}\right)\\
\left[\vec{\omega}_{p(\alpha)2},\vec{g}_{(\alpha)2}\right] &= \vec{g}_{(\alpha)1}\left(\Gamma^1_{(\alpha)21}\dot{q}^1_{(\alpha)}+\Gamma^1_{(\alpha)22}\dot{q}^2_{(\alpha)}+\Gamma^1_{(\alpha)23}\dot{q}^3_{(\alpha)}\right)+\\
&\quad+\vec{g}_{(\alpha)3}\left(\Gamma^3_{(\alpha)21}\dot{q}^1_{(\alpha)}+\Gamma^3_{(\alpha)22}\dot{q}^2_{(\alpha)}+\Gamma^3_{(\alpha)23}\dot{q}^3_{(\alpha)}\right)\\
\left[\vec{\omega}_{p(\alpha)3},\vec{g}_{(\alpha)3}\right] &= \vec{g}_{(\alpha)1}\left(\Gamma^1_{(\alpha)31}\dot{q}^1_{(\alpha)}+\Gamma^1_{(\alpha)32}\dot{q}^2_{(\alpha)}+\Gamma^1_{(\alpha)33}\dot{q}^3_{(\alpha)}\right)+\\
&\quad+\vec{g}_{(\alpha)2}\left(\Gamma^2_{(\alpha)31}\dot{q}^1_{(\alpha)}+\Gamma^2_{(\alpha)32}\dot{q}^2_{(\alpha)}+\Gamma^3_{(\alpha)33}\dot{q}^3_{(\alpha)}\right),\ \alpha=1,2,3,\ldots,N
\end{aligned}\tag{9}$$

In previously presented expressions, denotations $\vec{\omega}_{p(\alpha)1}$, $\vec{\omega}_{p(\alpha)2}$ and $\vec{\omega}_{p(\alpha)3}$ present angular velocities of the basic vectors of a position vector tangent space during material point motion. In previous expressions (9), $\Gamma^k_{(\alpha)ij}$, $\alpha=1,2,3,\ldots,N$, $i,j,k=1,2,3$ are Christoffel's symbols of the second kind, and $\Gamma_{(\alpha)ij,k}$, $\alpha=1,2,3,\ldots,N$, $i,j,k=1,2,3$ Christoffel's symbols of the first kind in corresponding curvilinear coordinate system of vector position tangent space of corresponding material kinetic point. These Christoffel's symbol, first and second kind, are expressed by corresponding covariant $g_{(\alpha)ij}(q)$, $\alpha=1,2,3,\ldots,N$, $i,j,k=1,2,3$ or contrvariant $g^{kl}_{(\alpha)}(q)$, $\alpha=1,2,3,\ldots,N$, $i,j,k=1,2,3$ metric tensor of corresponding position vector tangent space, in the following relations [1, 2, 11, 13]:

$$\Gamma_{(\alpha)ij,k}=\frac{1}{2}\left(\frac{\partial g_{(\alpha)ik}}{\partial q^j_{(\alpha)}}+\frac{\partial g_{(\alpha)jk}}{\partial q^i_{(\alpha)}}-\frac{\partial g_{(\alpha)ij}}{\partial q^k_{(\alpha)}}\right),\ \alpha=1,2,3,\ldots,N,\ i,j,k=1,2,3 \tag{10}$$

$$\Gamma^k_{(\alpha)ij}=g^{kl}_{(\alpha)}\Gamma_{(\alpha)ij,l},\ \alpha=1,2,3,\ldots,N,\ i,j,k=1,2,3 \tag{11}$$

$$g_{(\alpha)ik}=\left(\vec{g}_{(\alpha)i},\vec{g}_{(\alpha)k}\right) \tag{12}$$

2 Three-Dimensional Elliptical Cylindrical Curvilinear Coordinate System

For first example, let us determine the change of basic vectors $\vec{g}_{(\alpha)i}\left(\xi_{(\alpha)}, \eta_{(\alpha)}, z_{(\alpha)}\right)$, $\alpha = 1, 2, 3, \ldots, N$, $i = 1, 2, 3$ in three-dimensional elliptical cylindrical curvilinear coordinate system with curvilinear coordinates $\xi_{(\alpha)}, \eta_{(\alpha)}, z_{(\alpha)}$, $\alpha = 1, 2, 3, \ldots, N$ of kinetic point $N_{(\alpha)}$, $\alpha = 1, 2, 3, \ldots, N$ in three-dimensional elliptical cylindrical curvilinear system defined as $N_{(\alpha)}\left(\xi_{(\alpha)}, \eta_{(\alpha)}, z_{(\alpha)}\right)$, $\alpha = 1, 2, 3, \ldots, N$, and with corresponding position by position vector $\vec{\rho}_{(\alpha)}\left(\xi_{(\alpha)}, \eta_{(\alpha)}, z_{(\alpha)}\right)$, $\alpha = 1, 2, 3, \ldots, N$ with cotravariant coordinates $\rho^{i}_{(\alpha)}\left(\xi_{(\alpha)}, \eta_{(\alpha)}, z_{(\alpha)}\right)$, $\alpha = 1, 2, 3, \ldots, N$, $i = 1, 2, 3$. By using previous considerations and derived expressions (see Fig. 1a*) it is valid to write the following expressions, without index (α), and without losing generalities (see Refs. [3–9]) for position vector

$$\begin{aligned} &\vec{\rho}(\xi, \eta, z) = x(\xi, \eta, z)\vec{\imath} + y(\xi, \eta, z)\vec{\jmath} + z(\xi, \eta, z)\vec{k} \\ &\vec{\rho}(\xi, \eta, z) = \vec{\imath} Ch\xi \cos\eta + \vec{\jmath} Sh\xi \sin\eta + z\vec{k} = \rho^{i}(\xi, \eta, z)\vec{g}_{i}(\xi, \eta, z) \end{aligned} \tag{13}$$

and corresponding expressions for covariant basic vectors $\vec{g}_{(\alpha)i}\left(\xi_{(\alpha)}, \eta_{(\alpha)}, z_{(\alpha)}\right)$, $\alpha = 1, 2, 3, \ldots, N$, $i = 1, 2, 3$ of position vector tangent space in three-dimensional three parabolic coordinate system:

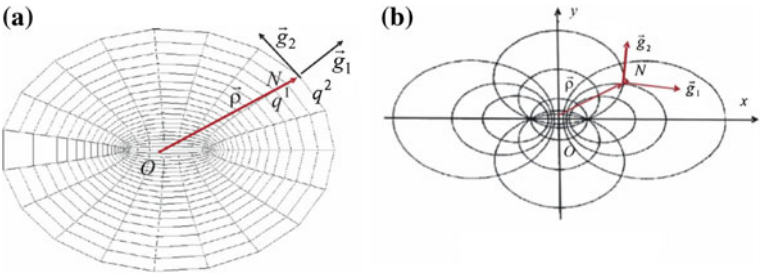

Fig. 1 Presentation of the position vector of a kinetic point in different positions in three-dimensional space, with corresponding basic vectors $\vec{g}_{(\alpha)i}$ of position vector $\vec{\rho}_{(\alpha)}(q)$ tangent space (without index (α) denotation of the order of point); **a*** in elliptic cylindrical coordinate system with orthogonal curvilinear coordinates; **b*** in three-dimensional cylindrical bipolar coordinate system with orthogonal curvilinear coordinates

$$\begin{aligned}
\vec{g}_1 = \vec{g}_\xi &= \frac{\partial \vec{\rho}}{\partial \xi} = \vec{\imath} Sh\xi \cos\eta + \vec{\jmath} Ch\xi \sin\eta \\
\vec{g}_2 = \vec{g}_\eta &= \frac{\partial \vec{\rho}}{\partial \eta} = -\vec{\imath} Ch\xi \sin\eta + \vec{\jmath} Sh\xi \cos\eta \\
\vec{g}_3 = \vec{g}_z &= \frac{\partial \vec{\rho}}{\partial z} = \vec{k}
\end{aligned} \tag{14}$$

Intensities of the basic vectors in el**liptical** cylindrical coordinates are

$$\begin{aligned}
&\left|\vec{g}_1\right| = \left|\vec{g}_\xi\right| = \left|\frac{\partial \vec{\rho}}{\partial \xi}\right| = \sqrt{Sh^2\xi \cos^2\eta + Ch^2\xi \sin^2\eta} \\
&\left|\vec{g}_1\right| = \left|\vec{g}_\xi\right| = \left|\frac{\partial \vec{\rho}}{\partial \xi}\right| = \sqrt{\sin^2\eta + Sh^2\xi} = \sqrt{Ch^2\xi - \cos^2\eta} \\
&\left|\vec{g}_2\right| = \left|\vec{g}_\eta\right| = \left|\frac{\partial \vec{\rho}}{\partial \eta}\right| = \sqrt{\eta^2 + \xi^2} = \sqrt{Ch^2\xi \sin^2\eta + Sh^2\xi \cos^2\eta} \\
&\left|\vec{g}_2\right| = \left|\vec{g}_\eta\right| = \left|\frac{\partial \vec{\rho}}{\partial \eta}\right| = \sqrt{\sin^2\eta + Sh^2\xi} = \sqrt{Ch^2\xi - \cos^2\eta}, \ \left|\vec{g}_3\right| = \left|\vec{g}_z\right| = \left|\frac{\partial \vec{\rho}}{\partial z}\right| = 1
\end{aligned} \tag{15}$$

Metric tensor of position vector tangent space in el**liptical** cylindrical coordinates is

$$g_{ij} = \left(\vec{g}_i, \vec{g}_j\right), \ g = \left(g_{ij}\right) = \begin{pmatrix} \sin^2\eta + Sh^2\xi & 0 & 0 \\ 0 & sin^2\eta + Sh^2\xi & 0 \\ 0 & 0 & 1 \end{pmatrix} \tag{16}$$

Scalar products between each two basic vectors of the position vector tangent space in el**liptical** cylindrical coordinates are $\left(\vec{g}_1, \vec{g}_2\right) = \left(\vec{g}_\xi, \vec{g}_\eta\right) = 0$, $\left(\vec{g}_1, \vec{g}_3\right) = \left(\vec{g}_\xi, \vec{g}_z\right) = 0$ and $\left(\vec{g}_3, \vec{g}_2\right) = \left(\vec{g}_z, \vec{g}_\eta\right) = 0$. Then, we can conclude that these three basic vectors of the position vector tangent space in e**lliptical** cylindrical coordinates are orthogonal.

Unit vectors in directions of the corresponding basic vectors of vector position of a mass particle in el**liptical** cylindrical coordinates are [8–10]

$$\begin{aligned}
\vec{T}_1 = \vec{T}_\xi &= \frac{\vec{g}_\xi}{\left|\vec{g}_\xi\right|} = \frac{1}{\sqrt{\sin^2\eta + Sh^2\xi}} \left(\vec{\imath} Sh\xi \cos\eta + \vec{\jmath} Ch\xi \sin\eta\right) \\
\vec{T}_2 = \vec{T}_\eta &= \frac{\vec{g}_\eta}{\left|\vec{g}_\eta\right|} = \frac{1}{\sqrt{\sin^2\eta + Sh^2\xi}} \left(-\vec{\imath} Ch\xi \sin\eta + \vec{\jmath} Sh\xi \cos\eta\right), \ \vec{T}_3 = \vec{g}_z = \vec{k}
\end{aligned} \tag{17}$$

Corresponding derivatives of covariant basic vectors of position vector tangent space along kinetic point motion, expressed in **elliptical** cylindrical coordinates are

$$\begin{aligned}
\frac{\mathrm{d}\vec{g}_1}{\mathrm{d}t} &= \frac{\mathrm{d}\vec{g}_\xi}{\mathrm{d}t} = \vec{i}(\xi Ch\xi\cos\eta - \dot{\eta}Sh\xi\sin\eta) + \vec{j}(\xi Sh\xi\sin\eta + \dot{\eta}Ch\xi\cos\eta) \\
\frac{\mathrm{d}\vec{g}_2}{\mathrm{d}t} &= \frac{\mathrm{d}\vec{g}_\eta}{\mathrm{d}t} = -\vec{i}(\xi Sh\xi\sin\eta + \dot{\eta}Ch\xi\cos\eta) + \vec{j}(\xi Ch\xi\cos\eta - \dot{\eta}Sh\xi\sin\eta) \\
\frac{\mathrm{d}\vec{g}_3}{\mathrm{d}t} &= \frac{\mathrm{d}\vec{g}_z}{\mathrm{d}t} = 0
\end{aligned} \tag{18}$$

Then, it is necessary, from previous expressions (18) of basic vectors derivatives to separate corresponding terms which correspond to velocities of the basic vectors extensions and rotations. For that reason, expressions (18) are multiplied by unit vectors in direction of basic vectors. After obtaining results and analysis and synthesis obtained results, we can conclude the following:

a* Velocities of basic vector extensions of position vector tangent space in **elliptical** cylindrical coordinate system of orthogonal curvilinear coordinate system, with curvilinear coordinates $\xi_{(\alpha)}$, $\eta_{(\alpha)}$ and $z_{(\alpha)}$ are in following forms:

$$\begin{aligned}
\overset{*}{\vec{g}}_\xi &= \frac{\mathrm{d}|\vec{g}_\xi|}{|\vec{g}_\xi|\mathrm{d}t}\vec{g}_\xi = \frac{1}{\left(\sin^2\eta + Sh^2\xi\right)}\langle \xi Ch\xi Sh\xi + \dot{\eta}\sin\eta\cos\eta\rangle\vec{g}_\xi \\
\overset{*}{\vec{g}}_\eta &= \frac{\mathrm{d}|\vec{g}_\eta|}{|\vec{g}_\eta|\mathrm{d}t}\vec{g}_\eta = \frac{1}{\left(\sin^2\eta + Sh^2\xi\right)}\langle \dot{\xi}Sh\xi Ch\xi + \dot{\eta}\cos\eta\sin\eta\rangle\vec{g}_\eta, \quad \overset{*}{\vec{g}}_z = 0
\end{aligned} \tag{19}$$

b* Angular velocities of the basic vectors rotations of position vector tangent space in **elliptical** cylindrical coordinate system of orthogonal curvilinear coordinate system, are in following forms:

$$\begin{aligned}
\vec{\omega}_{P\xi} &= \frac{1}{\left(\sin^2\eta + Sh^2\xi\right)}\langle -\dot{\xi}\cos\eta\sin\eta + \dot{\eta}Ch\xi Sh\xi\rangle\vec{g}_z \\
\vec{\omega}_{P\eta} &= \frac{1}{\left(\sin^2\eta + Sh^2\xi\right)}\langle -\dot{\xi}\sin\eta\cos\eta + \dot{\eta}Ch\xi Sh\xi\rangle\vec{g}_z, \quad \vec{\omega}_{Pz} = 0
\end{aligned} \tag{20}$$

For the considered case, basic vectors of position vector tangent space in **elliptical** cylindrical coordinate system are orthogonal in each kinetic point position, but change their intensities and orientations, keeping their orthogonality during rotation by angular velocities determined by expressions (20).

Contravariant coordinates $\rho^i_{(\alpha)}\left(\xi_{(\alpha)}, \eta_{(\alpha)}, z_{(\alpha)}\right)$, $\alpha = 1, 2, 3, \ldots, N$, $i = 1, 2, 3$ of kinetic point position vector in **elliptical** cylindrical curvilinear coordinate system defined by basic vectors of position vector tangent space and in coordinate source of fixed pole O, are functions of curvilinear coordinates $\xi_{(\alpha)}, \eta_{(\alpha)}, z_{(\alpha)}$, $\alpha = 1, 2, 3, \ldots, N$.

By using previous expressions of the contravariant coordinates $\rho^i_{(\alpha)}\left(\xi_{(\alpha)}, \eta_{(\alpha)}, z_{(\alpha)}\right)$, $\alpha = 1, 2, 3, \ldots, N$, $i = 1, 2, 3$ of kinetic point position vector in **elliptical** cylindrical curvilinear coordinate system, position vector is possible to present by covariant basic vectors $\vec{g}_{(\alpha)i}$, $\alpha = 1, 2, 3, \ldots, N$, $i = 1, 2, 3$. Then we can write vector position (13) of the mass particle motion in elliptical cylindrical coordinates in the following form:

$$\begin{aligned} &\vec{\rho} = x\vec{\imath} + y\vec{\jmath} + z\vec{k}\rho^1 = \rho^{\xi}\vec{g}_{\xi} + \rho^{\eta}\vec{g}_{\eta} + \rho^{z}\vec{g}_{z} \\ &\vec{\rho} = \frac{1}{\left(\sin^2\eta + Sh^2\xi\right)}\langle \vec{g}_{\xi} Ch\xi Sh\xi - \vec{g}_{\eta}\cos\eta\sin\eta\rangle + z\vec{g}_{z} \end{aligned} \tag{21}$$

3 Generalized Cylindrical Bipolar Curvilinear Coordinate System

Relation between coordinates x, y and z of Descartes coordinate system which is affine space and generalized **cylindrical bipolar** curvilinear coordinates ξ, η and z (see Fig. 1b*) are nonlinear and transformation of the coordinates is generalized nonlinear transformation from affine coordinate system to generalized cylindrical bipolar curvilinear coordinate system which is no affine coordinate system space. These nonlinear relations of coordinate transformation are in the following forms [7]

$$x = \frac{aShv}{Chv - \cos u},\ 0 \le u \le 2\pi,\ y = \frac{a\sin u}{Chv - \cos u},\ -\infty \le v \le +\infty,\ z = z \tag{22}$$

Cylindrical bipolar coordinate system surfaces are $(x - \cot ghy)^2 + y^2 = \frac{a^2}{Sh^2 u}$ are cylinders, $x^2 + (y - actgu)^2 = \frac{a^2}{\sin^2 u}$ are cylinders, and $Z = const$ are planes.

Vector position $\vec{\rho}$ of mass particle $N(x, y, z)$ in Descartes (afine, Cartesian) coordinate system is in the form: $\vec{\rho} = x\vec{\imath} + y\vec{\jmath} + z\vec{k}$ and in new generalized coordinate system with curvilinear coordinates–cylindrical bipolar coordinates u v and z, same vector position of the same mass particle in same position do not have same coordinates as they are bipolar coordinates of the point: $N(u, v, z)$. Coordinates of the vector position, we denote as

$$\vec{\rho}(u, v, z) = \vec{\imath}\frac{aShv}{Chv - \cos u} + \vec{\jmath}\frac{a\sin u}{Chv - \cos u} + z\vec{k} = \rho^i(u, v, z)\vec{g}_i(u, v, z) \tag{23}$$

Basic vectors of the position vector tangent space in cylindrical bipolar coordinates are in the following forms

$$\begin{aligned}\vec{g}_1 = \vec{g}_u &= \frac{\partial\vec{\rho}}{\partial u} = -\vec{\imath}\frac{aShv\sin u}{(Chv-\cos u)^2} + \vec{\jmath}\frac{a(\cos uChv-1)}{(Chv-\cos u)^2} \\ \vec{g}_2 = \vec{g}_v &= \frac{\partial\vec{\rho}}{\partial v} = \vec{\imath}\frac{a(1-Chv\cos u)}{(Chv-\cos u)^2} - \vec{\jmath}\frac{a\sin uShv}{(Chv-\cos u)^2},\ \vec{g}_3 = \vec{g}_z = \frac{\partial\vec{\rho}}{\partial z} = \vec{k}.\end{aligned} \tag{24}$$

Scalar products between each two basic vectors of the position vector tangent space, in cylindrical bipolar coordinates, are equal to zero, and these three basic vectors are orthogonal. Derivative of the first basic vector of the position vector tangent space in bipolar system coordinates

$$\begin{aligned}\frac{\mathrm{d}\vec{g}_1}{\mathrm{d}t} &= \frac{\mathrm{d}\vec{g}_u}{\mathrm{d}t} = \frac{\mathrm{d}}{\mathrm{d}t}\frac{\partial\vec{\rho}}{\partial u} = \\ &= -\vec{\imath}a\frac{\dot{v}(Ch^2v - Chv\cos u - 2Sh^2v)\sin u - \dot{u}\left(Chv\cos u + \cos^2 u - 2\sin^2 u\right)Shv}{(Chv-\cos u)^3} + \\ &+ a\vec{\jmath}\frac{\dot{v}\langle(ChvShv - \cos uShv - 2ChvShv)\cos u - 2Shv\rangle + \dot{u}(2 + \cos uChv - Ch^2v - 2Chv\cos u)\sin u}{(Chv-\cos u)^3}\end{aligned} \tag{25}$$

4 Conclusions

Aim of this paper is to point out difference between linear, affine coordinate systems with staring coordinate lines and functional curved spaces with curvilinear line and also difference between basic vectors in tangent space of a vector position of a kinetic point during moving in space. Basic vectors in functional tangent space of a position vector of the kinetic point changes during the kinetic point motion. The changes of the basic vectors are in change of their intensities and in rotation with corresponding angular velocities.

In author's previously published papers [3–9] expressions for angular velocities and intensity change of basic vectors of position vector tangent space of a material system kinetic point in polar-cylindrical, spherical, parabolic-cylindrical, and three-dimensional-thee-parabolic system of curvilinear orthogonal coordinates are presented.

In Fig. 2, the presentation of the position vector of a kinetic point in different positions in three-dimensional space, with corresponding basic vectors $\vec{g}_{(\alpha)i}$ of position vector $\vec{\rho}_{(\alpha)}(q)$ tangent space (without index (α) denotation of the order of point) in two different functional curvilinear space are presented: in **a*** in elliptical coordinate system with orthogonal curvilinear coordinates and in **b*** in three-dimensional oblate spherical coordinate system with orthogonal curvilinear coordinates. For these cases, also, are derived corresponding expressions for angular velocity and intensity change of basic vectors of position vector tangent space of a material system kinetic point, but no pages for presenting these expressions in these bounded pages.

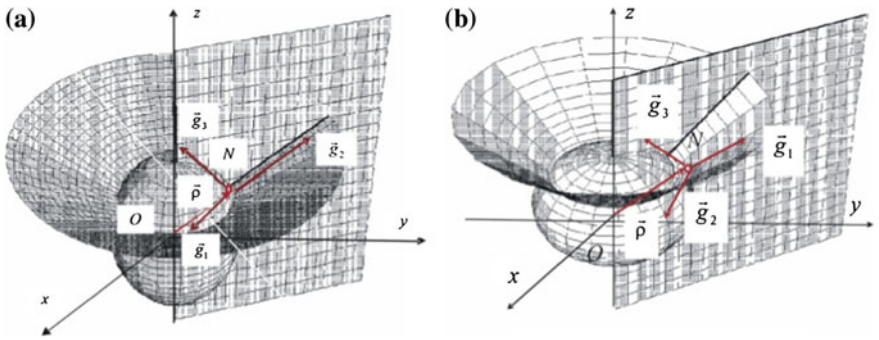

Fig. 2 Presentation of the position vector of a kinetic point in different positions in three-dimensional space, with corresponding basic vectors $\vec{g}_{(\alpha)i}$ of position vector $\vec{\rho}_{(\alpha)}(q)$ tangent space (without index (α) denotation of the order of point); **a*** in elliptical coordinate system with orthogonal curvilinear coordinates; **b*** in three-dimensional oblate spherical coordinate system with orthogonal curvilinear coordinates

Acknowledgments Parts of this research were supported by Ministry of Sciences of Republic Serbia trough Mathematical Institute SANU Belgrade Grant ON174001: "Dynamics of hybrid systems with complex structures; Mechanics of materials.", and Faculty of Mechanical Engineering, University of Niš.

References

1. Andjelić P. T., *Tenzori (Tensor Calculus),* Zavod za izdavanje udžbenika, 1965.
2. Hedrih (Stevanović), K.: *Izabrana poglavlja teorije elastičnosti* (*Selected Chapters form Theory of Elasticity)*, Faculty of Mechanical Engineering, Niš., First Edition 1977, Second Edition 1988, pp. 424. (in Serbian).
3. Hedrih (Stevanović) R. K.: Visibility or appearance of nonlinearity, Tensor, N.S. Vol. 72, No. 1 (2010), pp. 14–33, #3. Tensor Society, Chigasaki, Japan, ISSN 0040-3504.
4. Hedrih (Stevanović) K.: Angular velocities of the basic vectors of the position vectors of a rheonomic system and tangent space extension, (Plenary Lecture), Book of Abstracts, CCMECH-7, 7th International Symposium on Classical and Celestial Mechanics (CCMECH' 2011), October 23–28, 2011, The Russian Academy of Sciences, A. A. Dorodnicyn Computing Centre of RAS, Moscow State University, Moscow State Aviation Institute, and Collegium Mazovia in Siedlce (Poland) pp. 35–39. ISBN 978-83-63169-08-4.
5. Hedrih (Stevanović) K.: Tangent spaces of position vectors and angular velocities of their basic vectors in different coordinate systems, Proceedings of Full Papers, IconSSm 2011, The Third Serbian (28th Yu) Congress on Theoretical and Applied Mechanics, Vlasina lake, Serbia, 5–8 July 2011. M2-07, M1-07, pp. 1181–1193. ISBN 978-86-909973-3-6, COBISS:SR-ID 187662860.
6. Hedrih (Stevanović) K.: Tangent space extension of the position vectors of a discrete rheonomic mechanical system, Professor N. R. Sen Memorial Lecture – Invited Lecture, Abstracts of International Conference on Recent Advances in Mathematical Sciences and Applications (ICRAMSA-2011), December 09–11, 2011, pp. 23–25.

7. Hedrih (Stevanović) K.: Tangent space extension of the position vectors of a discrete rheonomic mechanical system, *Professor N. R. Sen Memorial Lecture,* Bulletin of the Calcutta Mathematical Society Volume 104, No. 2(2012) pp. 81–102. Bull.Cal.Math. 104 (2) 81–102 (2012).
8. Hedrih (Stevanović) K.: Angular velocityand intensity under change of basic vectors of position vector of tangent space of a meterial system kinetic point –Consideration of the difference betwenn linear and nonlinear transformations, To memory of academician Vladimir Metodievich Matrosov (May 8, 1932-April 17,2011) President of Academy of nonlinear Sciences. ***Tensor*, 2014,** Vol. 75, No. 1 pp. 71–93. Tensor Society (Tokyo), c/o Kawaguchi Inst. of Math. Soc., Japan. ISSN 0040-3604.
9. Hedrih (Stevanović) K.: (2015), Velocities of the Basic Vectors of a Tangent Space Of Moving Mass Particle Vector Position In Curvilinear Coordinate Systems, The theoretical and applied mechanics and mathematics, The 3rd International Conference Mechanical Engineering in XXI Century, Proceedings, September 17–18, 2015, NIŠ, Faculty of Mechanical Engineering University of Niš, pp. 449–454. Hard Copy ISBN 978-86-6055-072-1 and CD.
10. Heinbockel J.H.: *Introduction to Tensor Calculus and Continuum Mechanics*, *Department of Mathematics and Statistic Old Dominion University,* Copyright c 1996 by J.H. Heinbockel. All rights reserved. Reproduction and distribution of these notes is allowable provided it is for non-profit purposes only.
11. Rašković D. P.: *Osnovi tenzorskog računa (Basic of tensor Calculus),* Mašinski fakultet Kragujevac, 1974.
12. Rašković D. P.: *Mehanika II- Kinematika (Mehanics II- Kinemtics),* III i dalja izdanja, Zavod za izdavanje udžbenika, 1953, 1966, str. 347.
13. Rašković D. P.: *Teorija elastičnosti (Theory of elasticity),* Naučna knjiga, Beograd. 1985.

Dynamics of Impacts and Collisions of the Rolling Balls

Katica R. (Stevanović) Hedrih

Abstract In the chapter the theory of dynamics of impacts and collisions of the rolling balls is presented for different types of impacts and collisions depending on the balls' configuration in the kinetic state of impacts and collisions. By use of analogy between central impacts or collisions of balls in translator motion and balls' rolling motions before impacts or collisions, corresponding relations between outgoing velocities and outgoing angular velocities of rolling and impact velocities are expressed. Also, change of impact impulse (linear momentum) and moment of impulse (angular momentum) of the balls' rolling motion after and before impacts and collisions are expressed. By use of phenomenological mappings between a set of element dynamics of balls' impact and collisions for central and skew impacts as well as collisions corresponding analogies are identified. Different ball-rolling traces before and after skew impacts and skew collisions as a set of different kinematic elements for each type of impact and collision are discussed and kinematic plans of impacts and corresponding outgoing translator and angular velocities are graphically presented by a series of figures. In conclusion, dynamics of elliptic billiards are presented.

1 Introduction

We start with some words about the competition and the Royal Scientific Society. The Royal Scientific Society, in London, in 1668, announced a competition for the solution of problems of the dynamics of impact and the following now well-known scientists submitted their works to this competition, Wallis (John Wallis,

K.R. (Stevanović) Hedrih (✉)
Department of Mechanics, Mathematical Institute of Serbian Academy of Science and Arts (SANU), Knez Mihailova 26/III, Belgrde, Serbia
e-mail: khedrih@sbb.rs; khedrih@eunet.rs

K.R. (Stevanović) Hedrih
Faculty of Mechanical Engineering, University of Niš, ul Vojvode Tankosića 3/22, 18000 Niš, Serbia

© Springer International Publishing Switzerland 2016

J. Awrejcewicz (ed.), *Dynamical Systems: Theoretical and Experimental Analysis*, Springer Proceedings in Mathematics & Statistics 182, DOI 10.1007/978-3-319-42408-8_13

1616–1703, *Mechanica sive de mote*-1688) and Huygens (Christiaan Huygens, 1629–1695, *De motu corporum ex percusione*).

Using the results of the collision submitted by the Royal Scientific Society learned Willis and Huygens, and given their generalizations, Isaac Newton (1642–1726/7) founded the fundamental basics of the theory of impacts. And before Newton and Huygens and Wallis, others explored the dynamics of impacts. Thus, for example, collision problems are dealt with by Galileo Galilei (1564–1642), who came to the conclusion that the impact force in relation to the pressure force is infinitely large, but it came to the knowledge of the relationship of impact impulse and linear momentum.

Also, this chapter starts with some sentences published by Coriolis (Gaspard-Gustave de Coriolis, 1792–1843), in his book *Mathematical Theory of Billiards Game*:

In connection with the game of billiards … there are various dynamic tasks, whose solutions contain in this event. I think that people who know Theoretical mechanics, and even students of polytechnics, with interest familiarize themselves with explanations of all the original phenomenon that can be observed from the time of movement billiard balls [1–7].

In Fig. 1, upper, the trajectory of a billiard ball rolling along a horizontal plane bounded by a boundary elliptic-cylindrical surface is presented. Also in Fig. 1, lower, a plan of the impact and outgoing angular velocities before and after impacts is presented.

In the world literature, the problem of the impact body on some boundary, as well as collision between two or more bodies is an important research task, but up to now not yet solved in general. It is solved only in particular cases. In Ref. [7] the theoretical part of classical tasks of impact and collision is presented with a part containing new results about mathematical billiards. The content of this book is very useful for introducing the problem of impact especially in presentation of an idea of systems with special one-sided constraints. The basis of the idea about a presentation system with impacts is in introducing a field with conservative and dissipative forces for composition in the system free of one-sided constraints omitted from the system.

In the author's previous coauthored papers [8, 9] collision between two heavy mass particles along a rough circle as well as along curvilinear lines in the dynamics of vibroimpact systems with Coulomb-type friction, numerous new and original results are presented. Also in Refs. [10–12] collision between two heavy rolling balls along a circle in vibroimpact dynamics is investigated.

In this chapter, our results are founded on the results presented in the author's papers [13–16] and also on the unpublished manuscripts containing new original research results on the theory of collision between two rolling balls. We use Petrović's theory presented in two books: *Elements of Mathematical Phenomenology* [17, 18] and *Phenomenological Mappings* [19]. References [17, 18] are not well known because they were published in 1911 in the Serbian language. Only a short presentation [19] of Petrović's theory was published in French. In Refs. [13, 20–25] elements of mathematical phenomenology and phenomenological mapping

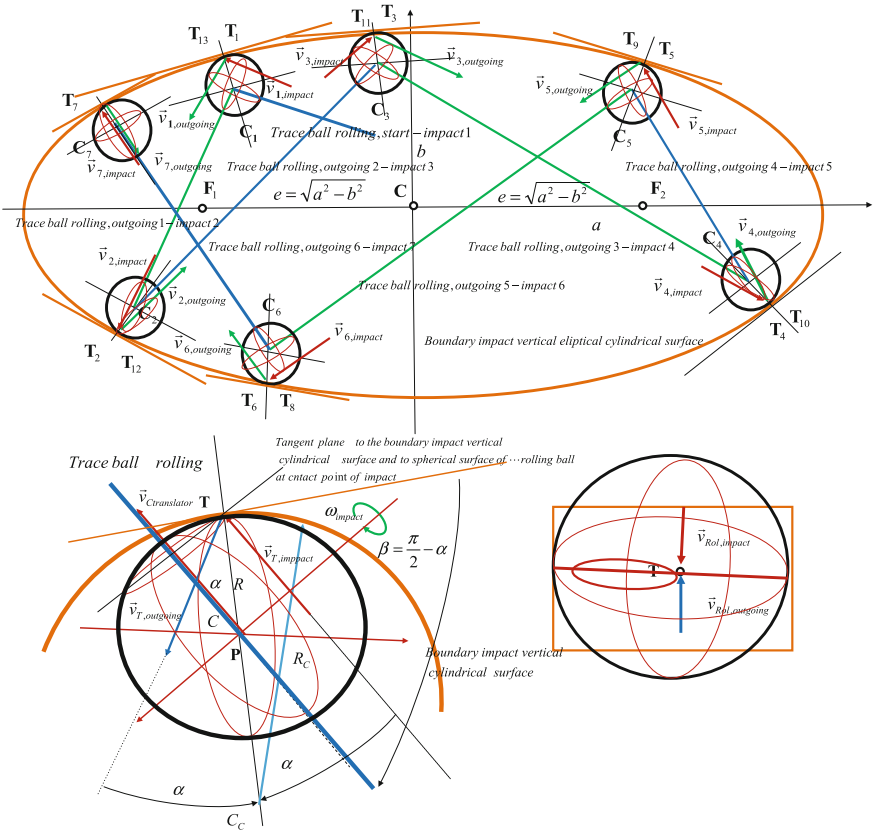

Fig. 1 Trajectory of a billiard ball rolling along a horizontal plane bounded by a boundary elliptic-cylindrical surface with plan of the impact and outgoing angular velocities before and after impacts

presented by the Serbian scientist Mihailo Petrović were applied for solving numerous research tasks and to obtain new original results.

2 Kinematics of Rolling Ball Impact

In this chapter, we begin by analyzing the possible impact points on the rolling ball, which is rolling along a horizontal trace. In the position of ball impact into a boundary vertical cylindrical surface a point is in the contact with the boundary surface. These points at which impacts are possible to be realized are in the biggest circle. In Fig. 2.a*, possible impact points T_0, T_{11}, T_{12}, … of the rolling ball along the horizontal trace to the impacts at the boundary vertical cylindrical surface with

plans of component and resultant impact velocities are presented. These component impact velocities are: translator $\vec{v}_{T0,\text{ translator}}$, $\vec{v}_{T12,\text{ translator}}$, and $\vec{v}_{T13\,\text{translator}}$ and rolling $\vec{v}_{T0,\text{ rolling}}$, $\vec{v}_{T12,\text{ rolling}}$, and $\vec{v}_{T13,\text{ rolling}}$, respectively, of impact points T_0, T_{11}, and T_{12}. Translator components are the same as the translator velocity of the ball mass center $\vec{v}_{C,\text{ rolling}}$ with intensity $v_{C,\text{translator}} = v_{C,\text{ rolling}} = R\omega_{P,\text{ impact}}$, where $\omega_{P,\text{ impact}}$ is the angular velocity of the rolling ball around the momentary axis through the instantaneous pole P. Rolling components $\vec{v}_{T0,\text{ rolling}}$, $\vec{v}_{T12,\text{ rolling}}$, and $\vec{v}_{T13,\text{ rolling}}$ have different intensity depending on the normal distance between the impact point and axis of self-rotation through the ball mass center and all are in the vertical direction. The biggest rolling velocity is in the case of central collision because this distance is equal to the radius of the ball: $v_{T0,\text{rolling}} = R\omega_{C,\text{ impact}} = R\omega_{P,\text{ impact}}$. If we denote by α_i the angle between the ball rolling horizontal trace and normal to the boundary vertical cylindrical surface at possible impact point T_{1i} at the biggest circle on the ball then the ball rolling component velocity is: $v_{T1i,\text{ rolling}} = R\omega_{C,\text{ impact}}\cos\alpha_i = R\omega_{P,\text{ impact}}\cos\alpha_i$. Taking into account that the ball component outgoing velocities, for the case of ideal elastic impacts are equal intensity and ball component impact velocities of the impact point, we can write:

a* for the ball translator outgoing component velocity:

$$v_{C,\text{translatir, autgoing}} = v_{C,\text{rolling, autgoing}} = R\omega_P, \text{impact} = R\omega_{P,\text{outgoing}}.$$

Taking into account that direction of the ball translator outgoing component velocity obtains the direction with angle α_i to the boundary vertical cylindrical surface at the possible impact point we can see that the ball outgoing angular velocity for ideal elastic impact is the same as the impact angular velocity $\omega_{P,\text{ outgoing}} = \omega_{P,\text{ impact}}$. For obtaining the direction of the ball outgoing angular velocity for ideal elastic impact let's analyze the ball rolling component velocities.

b* for ball rolling component velocities:

$$v_{T1i,\text{ rolling, outgoing}} = v_{T1i,\text{ rolling, impact}} = R\omega_{C,\text{ impact}}\cos\alpha_i = R\omega_{P,\text{ impact}}\cos\alpha_i$$

$$v_{1i,\text{rolling, outgoing}} = R\omega_{P,\text{ outgoing}}\cos\alpha_{ii} = R\omega_{C,\text{outgoing}}\cos\alpha_i$$

Taking into account previous analysis of intensity ball outgoing rolling component velocities, which are in vertical directions, but opposite to the corresponding impact component, that direction of the ball outgoing angular velocity obtains direction with angle α_i to the boundary vertical cylindrical surface and also the direction of the ball outgoing trace after impact.

In Fig. 2.b*, the plan of impact and outgoing angular velocities of a rolling ball along horizontal traces before and after impact to the boundary vertical cylindrical surface are presented.

In Fig. 3, an impact point of a rolling ball along the horizontal trace to the boundary vertical cylindrical surface, in the case of skew impact, and with plans of impact and outgoing component velocities and impact angular velocity of the rolling ball are presented.

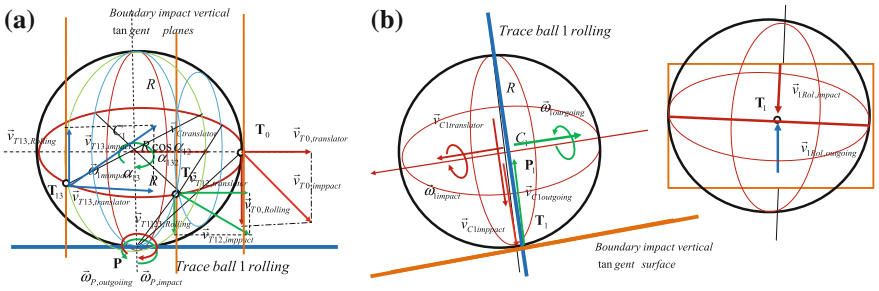

Fig. 2 **a*** Possible impact points of rolling ball along horizontal trace to the boundary vertical cylindrical surface with plans of component and resultant impact velocities. **b*** Plan of impact and outgoing angular velocities of a rolling ball along horizontal trace to the boundary vertical cylindrical surface

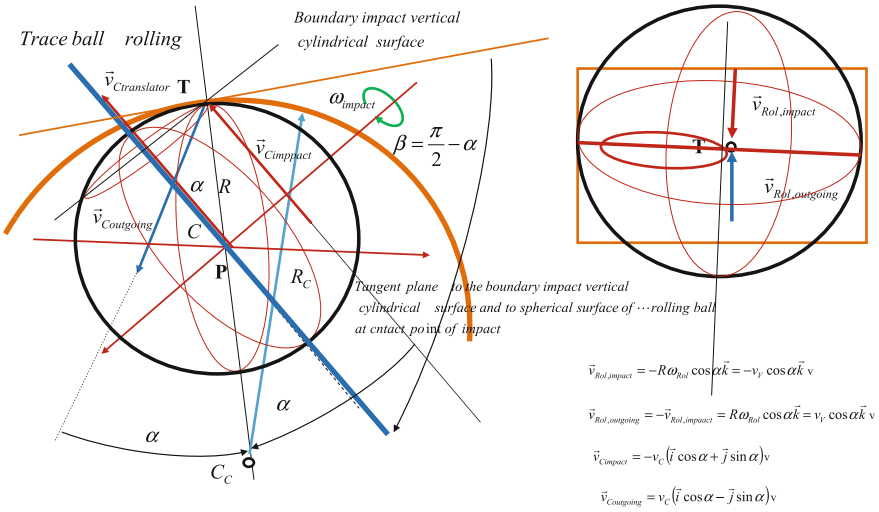

Fig. 3 An impact point of a rolling ball along the horizontal trace to the boundary vertical cylindrical surface, in the case of skew impact, and with plans of impact and outgoing velocities and impact angular velocity of the rolling ball

It may be concluded that is possible to use only rolling ball angular velocities, impact and outgoing for the analysis impact of a rolling ball along the horizontal trace to the boundary vertical cylindrical surface. A conclusion: for the case of the ideal elastic impact a rolling ball along the horizontal trace the boundary vertical cylindrical surface outgoing velocity has the same intensity as the impact angular velocity and the direction of outgoing angular velocity is under the same angle to the normal to the boundary vertical cylindrical surface as the impact angular velocity, and a ball outgoing trace rolling direction is under the same angle as a ball impact trace rolling direction to the normal to boundary vertical cylindrical surface.

3 Kinematics of Collision of Two Rolling Balls

On the basis of the previous analysis of central impact and skew impact of a rolling ball along horizontal traces before and after impact on the boundary vertical cylindrical surface and corresponding analysis of central collision between two rolling balls of the same dimension we can conclude that the tangent plane to the balls in collision at the common point $T_1 = T_2$ corresponds to the tangent plane at the impact point of a rolling ball to the boundary vertical cylindrical surface. Then in kinematic analysis of outgoing angular velocity direction after two rolling balls in collision it is right to conclude that the outgoing angular velocity is in the same or opposite direction depending on the relation between intensities of ball impact angular velocities and other dynamics of ball parameters.

Also, it is possible to conclude that the outgoing balls' rolling traces are orthogonal to a collision of the tangent plane to balls at the point of collision, and the direction of a ball rolling along traces, also depend on the relation between intensities of ball impact angular velocities and other dynamics of ball parameters. Then it is necessary to consider dynamics of rolling balls' collision.

In Fig. 4, the impact-collision point on the rolling balls along horizontal traces to the collision between balls, in the case of skew collision, and with possible plans of impact and outgoing velocities and impact angular velocity of each of the rolling balls, in a possible case of system kinetic parameters, is presented.

For skew collision between two rolling balls along horizontal traces in the same horizontal plane and for a possible relation between the systems' kinetic parameters, when the balls' rolling traces are in opposite directions these traces are under the same angles to the normal to the collision tangent plane as their corresponding impact traces. For other possible system kinetic parameters balls' outgoing traces have the same positions and different directions. These possible cases are necessary for analysis of each case of system kinetic parameters including analysis of dynamics of rolling balls' collision.

This chapter is too short to present all the possible plans of kinematic parameters of two rolling balls in skew collisions.

4 Dynamics of Two Rolling Balls' Collision Along Horizontal Trace

Let's start with the theory of dynamics of collision between two rolling balls of the same radius, and with different mass m_1 and m_2, and different axial mass inertia moments J_{P1} and J_{P2} for the corresponding momentary axis of rotation in rolling along a trace with pre-impact (arrival) angular velocities $\vec{\omega}_{P1,\,\text{impact}} = \vec{\omega}_{P1}(t_0)$ and $\vec{\omega}_{P2,\,\text{impact}} = \vec{\omega}_{P2}(t_0)$. Mass centers C_1 and C_2 of the balls move translatory with pre-impact (arrival) velocities $\vec{v}_{C1.\,\text{impact}} = \vec{v}_{C1}(t_0)$ and $\vec{v}_{C2.\,\text{impact}} = \vec{v}_{C2}(t_0)$. Angular velocities $\vec{\omega}_{P1,\,\text{impact}} = \vec{\omega}_{P1}(t_0)$ and $\vec{\omega}_{P2,\,\text{impact}} = \vec{\omega}_{P2}(t_0)$ we denote as arrival, or

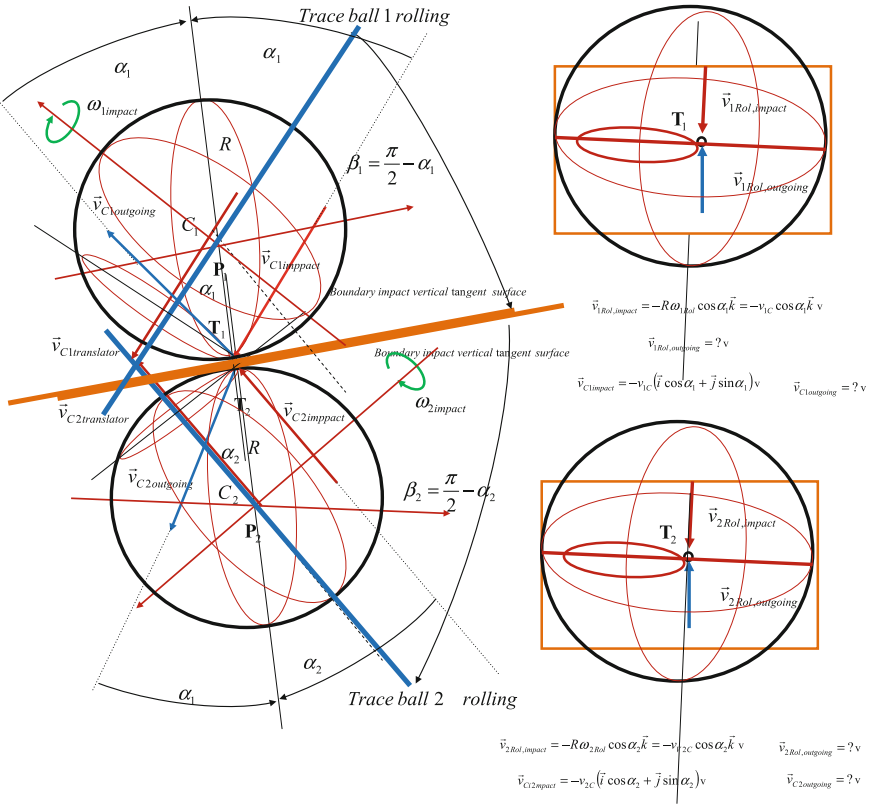

Fig. 4 An impact-collision point of rolling balls along horizontal traces to the collision between balls in the case of skew collision, and with plans of impact and outgoing velocities and impact angular velocity of each of the rolling balls

impact, or pre-impact angular velocities at the moment t_0 (see Figs. 3, 4, and 5). At this moment t_0 of the initial collision between these rolling balls, contact of these two balls is at point T_{12}, in which both balls possess a common tangent plane, plane of contact (touch). In the theory of collision, it is proposed that collision takes a very short period of time $(t_0, t_0 + \tau)$, and that τ tend to zero. After this short period τ bodies, two rolling balls in collision separate and are outgoing by post-impact–outgoing angular velocities $\vec{\omega}_{P1,\,\text{outgoing}} = \vec{\omega}_{P1}(t_0 + \tau)$ and $\vec{\omega}_{P2,\,\text{outgoing}} = \vec{\omega}_{P2}(t_0 + \tau)$. Mass centers C_1 and C_2 of the balls move translatory with post-impact (outgoing) translator velocities $\vec{v}_{C1.\,\text{outgoing}} = \vec{v}_{C1}(t_0 + \tau)$ and $\vec{v}_{C2.\,\text{outgoing}} = \vec{v}_{C2}(t_0 + \tau)$. These translator velocities are each possible to express by the corresponding angular velocity and radius of the corresponding ball.

Taking into account that translator motion of two bodies in central collision is the simplest motion of two bodies, defined by corresponding inertia properties expressed by mass, m_1 and m_2, of each body and also by corresponding translator

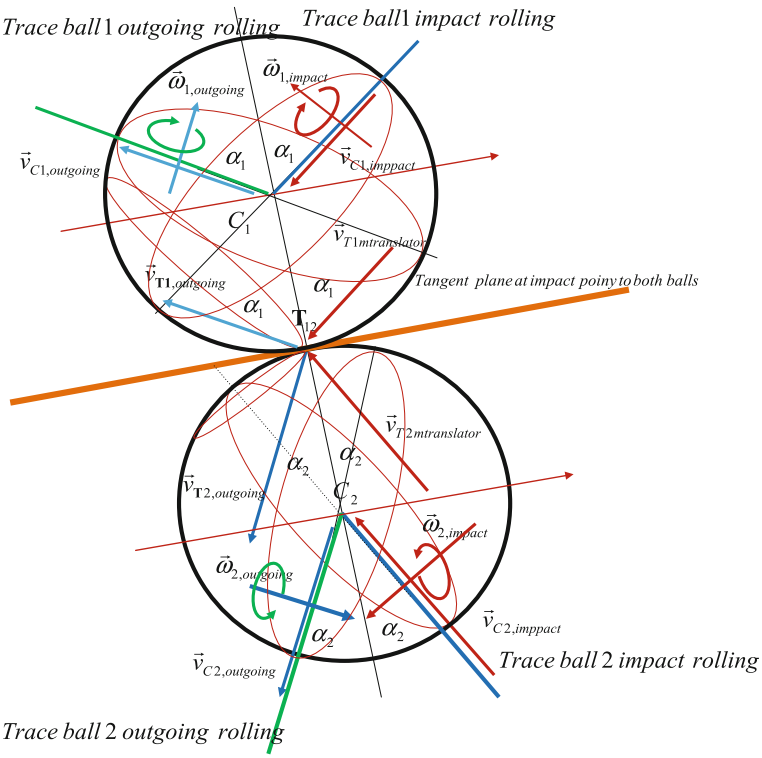

Fig. 5 A common collision point of rolling balls along horizontal traces to the collision between balls in the case of skew collision, and with plans of impact and outgoing velocities and impact and outgoing angular velocity of each of the rolling balls

pre-impact velocity, $\vec{v}_1(t_0)$ and $\vec{v}_2(t_0)$ at the moment before collision and by post-impact–outgoing translator velocities $\vec{v}_1(t_0+\tau)$ and $\vec{v}_2(t_0+\tau)$, it is possible to establish an analogy with collision between two rolling balls. The explanation is in the following form.

Also, rolling balls along a horizontal strength trace is the simplest rotation motion defined only by inertia properties in the axial mass inertia moments J_{P1} and J_{P2} for the corresponding momentary axis of rotation in rolling along the trace with pre-impact (arrival) angular velocities $\vec{\omega}_{P1,\,\text{impact}} = \vec{\omega}_{P1}(t_0)$ and $\vec{\omega}_{P2,\,\text{impact}} = \vec{\omega}_{P2}(t_0)$ and corresponding outgoing post-impact–outgoing angular velocities $\vec{\omega}_{P1,\,\text{outgoing}} = \vec{\omega}_{P1}(t_0+\tau)$ and $\vec{\omega}_{P2,\,\text{outgoing}} = \vec{\omega}_{P2}(t_0+\tau)$.

Using Petrović's theory of elements of mathematical phenomenology and phenomenological mappings [17–19] in parts of qualitative and mathematical analogies, we can indicate a qualitative and mathematical analogy between system translator dynamics and central collision (impact) dynamics of two bodies in translator motion pre-impact and post-impact dynamics phenomena and system

rolling two-ball dynamics and central collision (impact) dynamics of two rolling balls in rolling motion pre-impact and post-impact dynamics phenomena.

On the basis of these indicated qualitative and mathematical analogies it is possible to list analogous kinetic parameters of these systems.

The axial mass inertia moments J_{P1} and J_{P2} for the corresponding momentary axis of rotation in rolling along the trace are analogous to the body masses m_1 and m_2 of two bodies in collision in translatory motion.

Pre-impact (arrival) angular velocities $\vec{\omega}_{P1,\,\text{impact}} = \vec{\omega}_{P1}(t_0)$ and $\vec{\omega}_{P2,\,\text{impact}} = \vec{\omega}_{P2}(t_0)$ of the rolling balls around the corresponding momentary axis are analogous to corresponding translator pre-impact velocity, $\vec{v}_1(t_0)$ and $\vec{v}_2(t_0)$ of two bodies at the moment before collision.

Post-impact–outgoing angular velocities $\vec{\omega}_{P1,\,\text{outgoing}} = \vec{\omega}_{P1}(t_0+\tau)$ and $\vec{\omega}_{P2,\,\text{outgoing}} = \vec{\omega}_{P2}(t_0+\tau)$ of the rolling balls are analogous to corresponding post-impact–outgoing translator velocities $\vec{v}_1(t_0+\tau)$ and $\vec{v}_2(t_0+\tau)$ of two bodies in translator motion to collision.

On the basis of Petrović's theory [17–19] and qualitative and mathematical analogies considered in the previous section, it is possible on the basis of the theorem of conservation of linear momentum (impulse) [26] of impact dynamics of two bodies in translator motion pre-collision and post-collision to formulate an analogous theorem of conservation of angular momentum (moment of impulse) of impact dynamics of two rolling balls' pre-collision and post-collision motion in the relation:

$$J_{P1}\vec{\omega}_{P1}(t_0) + J_{P2}\vec{\omega}_{P2}(t_0) = J_{P1}\vec{\omega}_{P1}(t_0+\tau) + J_{P2}\vec{\omega}_{P2}(t_0+\tau) \tag{1}$$

and analogous with the coefficient of the restitution of rolling balls' collision is in the form:

$$k = \frac{\omega_r(t_0+\tau)}{\omega_r(t_0)} = \frac{\omega_{P2}(t_0+\tau) - \omega_{P1}(t_0+\tau)}{\omega_{P1}(t_0) - \omega_{P2}(t_0)} \tag{2}$$

as the ratio between difference of angular velocities of rolling balls' post-collision and pre-collision kinetic states.

Also, in analogy with expressions of post-collision–outgoing body velocities [26] it is possible to write expressions of post-collision–outgoing rolling balls' angular velocities in the following forms.

$$\omega_{P1}(t_0+\tau) = \frac{(J_{P1} - kJ_{P2})\omega_{P1}(t_0) + (1+k)J_{P2}\omega_{P2}(t_0)}{J_{P1}+J_{P2}}$$

$$\omega_{P1}(t_0+\tau) = \omega_{P1}(t_0) - \frac{1+k}{1+\frac{J_{P1}}{J_{P2}}}(\omega_{P1}(t_0) - \omega_{P2}(t_0)) \tag{3}$$

$$\omega_{P2}(t_0+\tau) = \frac{(J_{P2} - kJ_{P1})\omega_{P2}(t_0) + (1+k)J_{P1}\omega_{P1}(t_0)}{J_{P1}+J_{P2}}$$

$$\omega_{P2}(t_0+\tau)=\omega_{P2}(t_0)+\frac{1+k}{1+\frac{J_{P2}}{J_{P1}}}(\omega_{P1}(t_0)-\omega_{P2}(t_0)) \tag{4}$$

Previous obtained expressions (3)–(4) of post-collision–outgoing rolling balls' angular velocities are new and original results obtained on the basis of Petrović's theory of elements of mathematical phenomenology (see Refs. [17–19]). Previous expressions (4) are possible to obtain and prove by elementary consideration of the two short phases of collision with period local compression and local restitution in the local area of contact point between rolling balls.

5 Conclusion

In Fig. 5, a common collision tangent plane and impact point of rolling balls along horizontal traces to the collision between balls in the case of skew collision, and a possible case of system kinetic parameters and with plans of impact and outgoing velocities and impact and outgoing angular velocity of each of the rolling balls are presented.

In this chapter, the basic kinetic parameters pre- and post-collision between two rolling balls with the same radii and different masses and different balls' axial mass inertia moments for the instantaneous axis of rolling of each balls are presented as new research results. These results present the theoretical basis for large and more studious research on each particular case of two rolling balls' collision in cases with the same as well as different radii of balls.

Derived expressions (3) and (4) for post-collision–outgoing rolling balls' angular velocities for central collision are new and are valid for using and obtaining corresponding expressions of collision-outgoing rolling balls' angular velocities for skew collision of two rolling balls.

Then we have an all-theoretical basis for obtaining all necessary kinetic parameters of dynamics, kinematic and kinetic parameters for generalization of obtained results to kinetics of two rolling balls' collision, in an additional analysis of the position of impact points and impact tangent plane and directions of balls' rolling traces and outgoing angular velocities. These results can possibly be applied to collisions of other axially symmetric bodies with rolling motions in a pre-collision kinetic state.

Acknowledgments Parts of this research were supported by the Ministry of Sciences of Republic Serbia through the Mathematical Institute SANU Belgrade Grant ON174001: "Dynamics of hybrid systems with complex structures; Mechanics of materials," and Faculty of Mechanical Engineering, University of Niš.

References

1. Byrne R.:. Byrne's Advanced Technique in Pool and Billiards. Harcourt Trade. p. 49, 1990. ISBN 0-15-614971-0.
2. Coriolis G.: Théorie mathématique des effets du jeu de billard; suivi des deux celebres memoires publiés en 1832 et 1835 dans le Journal de l'École Polytechnique: Sur le principe des forces vives dans les mouvements relatifs des machines & Sur les équations du mouvement relatif des systèmes de corps (Originally published by Carilian-Goeury, 1835 ed.). Éditions Jacques Gabay, New Edition 1990. ISBN 2-87647-081-0.
3. Coriolis G.: Sur le principe des forces vives dans les mouvements relatifs des machines. J. De l'Ecole royale polytechnique 13: 268–302. 1832.
4. Coriolis G.G.: Sur les équations du mouvement relatif des systèmes de corps. J. De l'Ecole royale polytechnique 15: 144–154, 1835.
5. Hedrih (Stevanović) K.: Dynamics of the elliptic billiards and rolling ball impacts, Proceedings, The 5th International Congress of Serbian Society of Mechanics. Arandjelovac, June 15–17, 2015, pp. 98–98. Published by Serbian Society of Mechanics and Faculty of Technical Sciences Novi Sad, ISBN 978-86-7892-715-7, COBISS.SR-ID 296997639. Plus at USB M2c, pp. 1–4.
6. Hedrih (Stevanović) K.: Elements of geometry, kinematics and dynamics of billiards, April 2015, Lecture at Mechanics Colloquium of Mathematical Institute SANU, http://www.mi.sanu.ac.rs/colloquiums/mechcoll.htm.
7. Козлов В.В., Трешев Д. В.: Билиардì-Генетическое ббедение динамику систем с ударами (Kozlov V.V. and Treshchev D.V.: Billiards - Generate generalization of dynamics with impacts), Издателство Московского университета, 1991. Москва, стр. 192.
8. Hedrih (Stevanović) K., Raičević V., Jović S.: Vibro-impact of a Heavy Mass Particle Moving along a Rough Circle with Two Impact Limiters, ©Freund Publishing House Ltd., International Journal of Nonlinear Sciences & Numerical Simulation 10(11): 1713–1726, 2009.
9. Hedrih (Stevanović) K R., Raičević V., Jović S.: Phase Trajectory Portrait of the Vibro-impact Forced Dynamics of Two Heavy Mass Particles Motions along Rough Circle, Communications in Nonlinear Science and Numerical Simulations, 2011 16 (12): 4745–4755, DOI 10.1016/j.cnsns.2011.05.027.
10. Hedrih (Stevanović) K.: Elements of Geom*etry, Kinematics and Dynamics of Billiards*, Mechanics and C*ontr*ol, The 3rd International Conference Mechanical Engineering in XXI Century, Proceedings, September 17–18, 2015, NIŠ, Faculty of Mechanical Engineering University of Niš, pp. 313–318. Hard Copy ISBN 978-86-6055-072-1 and CD.
11. Hedrih (Stevanović) K.: Dynamics of the elliptic billiards and rolling ball impacts,. Proceedings, The 5th International Congress of Serbian Society of Mechanics. Arandjelovac, June 15–17, 2015, pp. 98–98. Published by Serbian Society of Mechanics and Faculty of Technical Sciences Novi Sad, ISBN 978-86-7892-715-7, COBISS.SR-ID 296997639. Plus at USB M2c, pp. 1–4.
12. Hedrih (Stevanović) K.: Rolling heavy disk along rotating circle with constant angular velocity, *Computer Algebra Systems, in Teaching and Research, Chapter 2. Problems of Classical Mechanics*, Edited by Alexander N. Prokopenya, Mirosław Jakubiak (Eds.), Volume V, pp. 293–304. SiedlceUniversity of Natural Sciences and Humanities, Siedlce 2015, © Copyright Uniwersytet Przyrodniczo-Humanistyczny w Siedlcach, Siedlce 2015, ISSN 2300-7397; ISBN 978-83-7051-779-3.
13. Elements of mathematical phenomenology and phenomenological mapping in non-linear dynamics, Edited by Katica R. (Stevanovic) Hedrih, Ivan Kosenko, Pavel Krasilnikov and Pol D. Spanos, Special Issue of International Journal of Non-Linear, Mechanics, Volume 73, Pages 1–128 (July 2015). http://www.sciencedirect.com.proxy.kobson.nb.rs:2048/science/journal/00207462/73.

14. Hedrih (Stevanovi´c) K.: Elements of mathematical phenomenology in dynamics of multi-body system with fractional order discrete continuum layers, Dedicated to the 100th Anniversary of the Russian Academician Yury Rabotnov, Dedicated to Centennial Jubilee of Russian Academician Yury N. Rabotnov, Special issue of International Journal of Mechanics, 2014, Vol. 8, pp. 339–346, ISSN: 1998-4448.(Paper submitted in January 2014), Journal indexed in SCOPUS (http://www.naun.org/cms.action?id=2828.
15. Hedrih (Stevanović) K.R., (2015), *Elements of mathematical phenomenology: I. Mathematical and qualitative analogies,* Труды МАИ. Выпуск №84, pp. 42 (1–42) www.mai.ru/science/trudy/, http://www.mai.ru/upload/iblock/5f6/hedrih_eng_1.pdf, Эл № ФС77-58560, ISSN: 1727-*6942*.
16. Hedrih (Stevanović) K.R., (2015), *Elements of mathematical phenomenology:II*. Phenomenological approximate mappings, Труды МАИ. Выпуск №84, pp. 29 (1–29) www.mai.ru/science/trudy/, http://www.mai.ru/upload/iblock/5c5/hedrih_eng_2.pdf Эл № ФС77-58560, ISSN: 1727-6942.
17. Petrović, M.: Elementi matematičke fenomenologije (Elements of mathematical phenomenology), Srpska kraljevska akademija, Beograd, 1911. str. 789. http://elibrary.matf.bg.ac.rs/handle/123456789/476?locale-attribute=sr.
18. Petrović M.: Mecanismes communs aux phenomenes disparates, Paris 1921.
19. Petrović M.: Fenomenološko preslikavanje (Phenomenological mapping), Srpska kraljevska akademija, Beograd, 1933, pp. 33. (In Serbian).
20. Hedrih (Stevanović) K.: Philosophy of approach to research of dynamics of billiards, Lecture at Seminar of History and Philosophy of Mathematics and Mechanics, 10 March 2015, Mathematical Institute SANU, Belgrade http://www.mi.sanu.ac.rs/seminars/programs/seminar12.mar2015.htm.
21. Hedrih (Stevanović) K. and Hedrih A. N.: Phenomenological mapping and dynamical absorptions in chain systems with multiple degrees of freedom, *Journal of Vibration and Control* 1077546314525984, first published on March 19, 2014 as doi:10.1177/1077546314525984, ISSN 1077–463. http://jvc.sagepub.com.proxy.kobson.nb.rs:2048/, http://www.sagepub.co.uk/journal.aspx?pid=105701.
22. Hedrih (Stevanović) K. and Tenreiro Machado J.: Discrete fractional order system vibrations, *International Journal Non-Linear Mechanics* 73(2015) 2–11, DOI:10.1016/j.ijnonlinmec.2014.11.009. http://authors.elsevier.com/authorforms/NLM2407/7c32b6b4f19f2471fb24556142da3cd1
23. Hedrih (Stevanović) K. and Simonović J.: Structural analogies on systems of deformable bodies coupled with non-linear layers, *International Journal Non-Linear Mechanic*, 73 (2015) 18–24, DOI:10.1016/j.ijnonlinmec.2014.11.004, http://www.elsevier.com/locate/nlm
24. Hedrih (Stevanovi´c) K.: Elements of mathematical phenomenology in dynamics of multi-body system with fractional order discrete continuum layers, Dedicated to the 100th Anniversary of the Russian Academician Yury Rabotnov, Dedicated to Centennial Jubilee of Russian Academician Yury N. Rabotnov, Special issue of International Journal of Mechanics, 2014, Vol. 8, pp. 339–346, ISSN: 1998-4448.(Paper submitted in January 2014), Journal indexed in SCOPUS (http://www.naun.org/cms.action?id=2828.
25. Katica R. (Stevanović) Hedrih, Central collision of two rolling balls: Theory and examples, (manuscript in review process from 2014, I hope should be appear)
26. Rašković D.P.: Mehanika III-Dinamika (Mechanics III-Dynamics), Naučna knjiga, Beograd, 1965.

Approximate Analytical Solutions to Jerk Equations

Nicolae Herişanu and Vasile Marinca

Abstract Nonlinear third-order differential equations, known as nonlinear jerk equations, involving the third temporal derivative of displacement are considered in this paper. This kind of equations is of much interest in analyzing some structures exhibiting rotating and translating motions such are robots or machine tools, where excessive jerk (defined as the time derivative of the acceleration) lead to accelerated wear in transmissions and bearing elements, noisy operations, and large contouring errors at discontinuities (such as corners) in the machining path. In this paper, we propose a new analytical technique called the Optimal Auxiliary Functions Method (OAFM) to analyze some particular cases of jerk functions involving cubic nonlinearity. Numerical simulations are also developed in order emphasize the accuracy of the obtained results. Several numerical examples show that the proposed procedure is simple and easy to use.

1 Introduction

The nonlinear jerk equations involving the third temporal derivative of displacement have been originally of interest in the field of mechanics, but these kind of equations have found applications in a variety of physical situations. Jerk appears in some structures exhibiting rotating and translating motions, such as robots and machine tools structures. From a practical perspective, excessive jerk arising at some machine tools leads to excitation of vibrations in components in the machine assembly, accelerated wear in the transmission and bearing elements, noisy operations and large contouring errors at discontinuities (such as corners) in the machining path. Also in the case of robots, limiting jerk (defined as the time

N. Herişanu (✉)
University Politehnica Timisoara, Bd. M.Viteazu 1, Timisoara, Romania
e-mail: nicolae.herisanu@upt.ro

V. Marinca
CCTFA, Romanian Academy-Timisoara Branch, Bd. M.Viteazu 1, Timisoara, Romania
e-mail: vasile.marinca@upt.ro

© Springer International Publishing Switzerland 2016

J. Awrejcewicz (ed.), *Dynamical Systems: Theoretical and Experimental Analysis*, Springer Proceedings in Mathematics & Statistics 182, DOI 10.1007/978-3-319-42408-8_14

derivative of the acceleration of the manipulator joints) is very important because high jerk values can wear out of the robot structure, and heavily excite its resonance frequencies. Vibrations induced by non-smooth trajectories can damage the robot actuators, and introduce large errors while the robot is performing tasks such as trajectory tracking. Moreover, low-jerk trajectories can be executed more rapidly and accurately.

Recently, there has been some interest in investigating different types of jerk equations. Gottlieb [1, 2], has found simple forms of the jerk function $\dddot{u} + f(u, \dot{u}, \ddot{u}) = 0$ and has explored the flexibility of applying the method of harmonic balance to achieve analytical approximations of periodic solutions to nonlinear jerk equations. Consequent restrictions on the jerk equations amenable to harmonic balance solution are that only problems which have zero initial acceleration and parity and time-reversal invariant (all terms have the same space parity of reflective behavior under the transformation $u \rightarrow -u$ and time parity of reflective behavior under the transformation $t \rightarrow -t$) can be considered. Wu et al. [3] proposed an improved harmonic balance method for determining accurate expressions of the periodic solutions of nonlinear jerk equations. Ma et al. [4] applied a homotopy approach to the jerk equations. A mixture of methodologies has been employed to study various aspects of nonlinear jerk equations in [5–9].

In this paper, we propose a novel approach, namely, the Optimal Auxiliary Functions Method (OAFM) to analyze some particular cases of jerk functions involving cubic nonlinearity. The accuracy of the analytical results obtained through the proposed approach is proved by numerical simulations developed in order to validate analytical results. Several numerical examples show that the proposed procedure is simple and easy to use.

2 Optimal Auxiliary Functions Method

For convenience of the readers, we consider the nonlinear differential equation:

$$L[u(x)] + g(x) + N[u(x)] = 0, \tag{1}$$

where L is a linear operator, g is a known function and N is a nonlinear operator, x denotes the independent variable, and $u(x)$ is an unknown function. The initial/boundary conditions are:

$$B\left(u(x), \frac{\mathrm{d}u(x)}{\mathrm{d}x}\right) = 0 \tag{2}$$

An exact solution for strongly nonlinear equations of type (1) is frequently hard to be found. To find an approximate solution, we assume that this solution can be expressed in the form:

$$\bar{u}(x, C_i) = u_0(x) + u_1(x, C_i), \quad i = 1, 2, \ldots, s, \tag{3}$$

where the initial and the first approximations will be determined as described in the following. Substituting Eq. (3) into Eq. (1), it results in

$$L(u_0(x)) + L(u_1(x, C_i)) + g(x) + N[u_0(x) + u_1(x), C_i)] = 0 \tag{4}$$

The initial approximation $u_0(x)$ can be obtained from the linear equation

$$\begin{aligned} &L[u_0(x)] + g(x) = 0 \\ &B\left(u_0, \frac{\mathrm{d}u_0}{\mathrm{d}x}\right) = 0 \end{aligned} \tag{5}$$

and the first approximation from equation

$$\begin{aligned} &L[u_1(x, C_i)] + N[u_0(x) + u_1(x, C_i)] = 0 \\ &B\left(u_1, \frac{\mathrm{d}u_1}{\mathrm{d}x}\right) = 0 \end{aligned} \tag{6}$$

The nonlinear term in the last equation is expanded in the form

$$N[u_0(x) + u_1(x, C_i)] = N[u_0(x)] + \sum_{k=1}^{\infty} \frac{u_1^k}{k!} N^{(k)}[u_0(x)] \tag{7}$$

To avoid the difficulties that appear in solving the nonlinear differential Eq. (6) and to accelerate the rapid convergence of the first approximation u_1 and implicitly of the approximate solution $\bar{u}(x)$, instead of the last term arising in Eq. (6), we propose another expression, such that Eq. (6) can be written as

$$\begin{aligned} &L[u_1(x, C_i)] + A_1(u_0(x), u'_0(x), C_i) N[u_0(x)] + A_2\left(u_0(x), u'_0(x), C_j\right) = 0 \\ &B\left(u_1(x), \frac{\mathrm{d}u_1(x)}{\mathrm{d}x}\right) = 0 \end{aligned} \tag{8}$$

where A_1 and A_2 are two arbitrary auxiliary functions depending on the initial approximation $u_0(x)$ and a number of unknown parameters C_i and C_j, $i = 1, 2, \ldots, s$, $j = s + 1, s + 2, \ldots, p$. The auxiliary functions A_1 and A_2 (namely optimal auxiliary functions) are not unique, and are of the same form like u_0. For example, if $u_0(x)$ is a polynomial function, then $A_1(u_0, C_i)$ and $A_2(u_0, C_j)$ are a sum of polynomial functions; if $u_0(x)$ is an exponential function, then A_1 and A_2 are a sum of exponential functions; if $u_0(x)$ is a trigonometric function, then A_1 and A_2 are sums of trigonometric functions, and so on. If $N[u_0(x)] = 0$, then it is clear that u_0 is an exact solution of Eq. (1).

The unknown parameters C_i and C_j can be optimally identified via different methods such as Galerkin method, Ritz method, the least square method,

collocation method, but the preferred one should be minimizing the square residual error: $\int_a^b R^2(x, C_i, C_j)\mathrm{d}x = 0$, where $R(x, C_i, C_j) = L[\bar{u}(x, C_i)] + g(x) + N[\bar{u}(x, C_j)]$, in which the approximate solution $\bar{u}(x)$ is given by Eq. (3), and so on.

By this novel method, the approximate solution is well determined after the identification of the optimal values of the initially unknown convergence-control parameters C_i and C_j. It will be proved that our procedure is a powerful tool for solving nonlinear problems without small or large parameters.

3 OAFM for Jerk Equations

The general form of the Jerk equations is

$$\dddot{u} + \alpha\dot{u}^3 + \beta u^2\dot{u} + \gamma u\dot{u}\ddot{u} + \delta\dot{u}\ddot{u}^2 + \lambda\dot{u} = 0 \tag{9}$$

with the initial conditions

$$u(0) = 0,\ \dot{u}(0) = A,\quad \ddot{u}(0) = 0 \tag{10}$$

where α, β, γ, δ, λ, and A are known constants and the dot denotes derivative with respect to time.

Into Eq. (9), at least one of α, β, γ, and δ should be nonzero. If $\delta = 0$, we require $\gamma \neq -2\alpha$ such that the jerk equations are simply not the time-derivative of an acceleration equation.

If we introduce the independent variable $\tau = \omega t$ and the dependent variable $u = \frac{A}{\omega}x$, then Eqs. (9) and (10) become, respectively:

$$\Omega^2(x''' + \delta A^2 x' x''^2) + \Omega(\alpha A^2 x'^3 + \gamma A^2 x x' x'' + \lambda x') + \beta A^2 x^2 x' = 0 \tag{11}$$

$$x(0) = 0,\quad x'(0) = 1,\quad x''(0) = 0 \tag{12}$$

where prime denotes differentiation with respect to τ and $\Omega = \omega^2$.

For Eq. (11), the linear operator can be written in the form

$$L[x(\tau)] = \Omega^2(x''' + x) \tag{13}$$

with $g(\tau) = 0$, and the corresponding nonlinear operator is

$$N[x(\tau, \Omega)] = \Omega^2(\delta A^2 x' x''^2 - x) + \Omega(\alpha A^2 x'^3 + \gamma A^2 x x' x'' + \lambda x') + \beta A^2 x^2 x' \tag{14}$$

The Eq. (5) becomes

$$x_0''' + x_0 = 0, \quad x_0(0) = x''_0(0) = 0,\ x'_0(0) = 1 \tag{15}$$

and has the solution

$$x_0(\tau) = \sin\tau \tag{16}$$

Substituting Eq. (16) into Eq. (14) we obtain

$$N[x_0(\tau, \Omega)] = M_1 \cos\tau + M_2 \cos 3\tau \tag{17}$$

with

$$\begin{aligned} M_1 &= \left(\frac{1}{4}\delta A^2 - 1\right)\Omega^2 + \left(\lambda + \frac{3\alpha - \gamma}{4}A^2\right)\Omega + \frac{1}{4}\beta A^2 \\ M_2 &= -\frac{1}{4}\delta A^2\Omega^2 + \frac{1}{4}\Omega(\alpha + \gamma)A^2 - \frac{1}{4}\beta A^2 \end{aligned} \tag{18}$$

Equation (8) can be written as

$$\begin{aligned} &\Omega^2(x_1''' + x_1) + A_1(\sin\tau, C_i)(M_1\cos\tau + M_2\cos 3\tau) + A_2(\sin\tau, C_j) = 0, \\ &x_1(0) = x'_1(0) = x''_1(0) = 0, \end{aligned} \tag{19}$$

where the optimal auxiliary functions A_i can be chosen in the forms:

$$\begin{aligned} A_1(\sin\tau, C_i) &= -\Omega^2 C_1 \sin 2\tau; \\ A_2(\sin\tau, C_j) &= -\Omega^2(C_2\sin\tau + C_3\sin 3\tau + C_4\sin 5\tau), \end{aligned} \tag{20}$$

where C_k, $k = 1, 2, 3, 4$ are unknown parameters at this moment. The solution of Eq. (19) is chosen so that it contains no secular terms, which lead to the condition:

$$C_1(M_1 - M_2) + C_2 = 0 \tag{21}$$

The solution of Eq. (19) is given by

$$\begin{aligned} x_1(\tau, C_i) = &\left[\frac{3}{26}(M_1C_1 + C_3) + \frac{5}{124}(M_2C_1 + C_4)\right]\sin\tau - \\ &- \frac{1}{26}(M_1C_1 + C_3)\sin 3\tau - \frac{1}{124}(M_2C_1 + C_4)\sin 5\tau \end{aligned} \tag{22}$$

From Eqs. (16) and (22)and taking into consideration that $\bar{u}(t) = \frac{A}{\omega}\bar{x}(\tau)$, we can get the first-order approximate solution of Eq. (9) in the form

$$\bar{u}(t,C_i)=\frac{A}{\sqrt{\Omega}}\left[\left(1+\frac{3M_1C_1}{26}+\frac{5M_2C_1}{124}+\frac{3C_3}{26}+\frac{5C_4}{124}\right)\sin\sqrt{\Omega}t-\right.$$
$$\left.-\frac{M_1C_1+C_3}{26}\sin 3\sqrt{\Omega}t-\frac{M_2C_1+C_4}{124}\sin 5\sqrt{\Omega}t\right] \tag{23}$$

4 Numerical Examples

Considering the jerk equations containing velocity-cubed and velocity times displacements squared: $\alpha=\beta=1$, $\delta=\gamma=\lambda=0$, Eq. (9) becomes:

$$\dddot{u}+\dot{u}(\dot{u}^2+u^2)=0 \tag{24}$$

with the initial conditions

$$u(0)=0,\quad \dot{u}(0)=A,\quad \ddot{u}(0)=0 \tag{25}$$

Case 4.1 For $A=2$, the parameters C_i and Ω are:

$C_1=-0.000117346$, $C_2=0.000219373$, $C_3=-0.165811985$, $C_4=-0.02975498$, $\Omega=3.206684124$

The first-order approximate periodic solution of Eq. (24) is:

$$\bar{u}(t)=1.094143278\,\sin\sqrt{\Omega}t+0.007124397\,\sin 3\sqrt{\Omega}t+$$
$$+\,2.7033546\times 10^{-4}\sin 5\sqrt{\Omega}t \tag{26}$$

Case 4.2 In this case for $A=10$, we have:

$C_1=1.102734811\times 10^{-8}$, $C_2=1.705419027\times 10^{-5}$, $C_3=-0.367599608$, $C_4=-0.040821072$, $\Omega=72.13317249$

and therefore, the first-order approximate periodic solution of Eq. (24) becomes

$$\bar{u}(t)=1.1255453485\,\sin\sqrt{\Omega}t+0.016646815\,\sin 3\sqrt{\Omega}t+$$
$$+\,0.000387423\,\sin 5\sqrt{\Omega}t \tag{27}$$

To verify the accuracy of the obtained solutions, we have compared the approximate analytical results obtained through OAFM and the numerical integration results. In Figs. 1 and 2 there are compared the present solutions (26) and

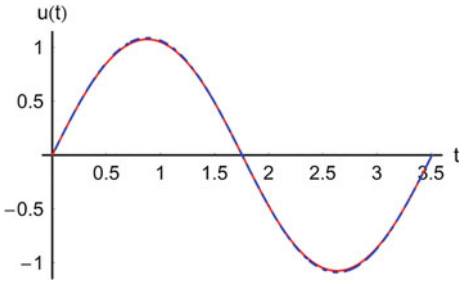

Fig. 1 Comparison between the approximate solution (26) and numerical integration results: —— numerical solution; – – – – approximate solution

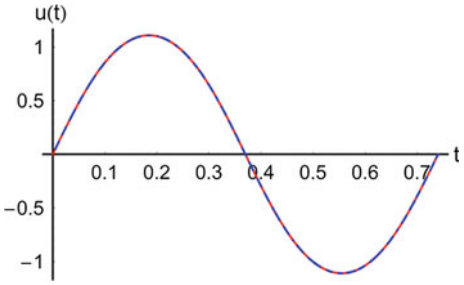

Fig. 2 Comparison between the approximate solution (27) and numerical integration results: —— numerical solution; – – – – approximate solution

Table 1 Error analysis in Case 4.1

t	$u_{\text{R-K}}$	u_{approx}	$\varepsilon = \text{abs}\ (u_{\text{R-K}} - u_{\text{app}})$
T/10	0.647397	0.649905	0.00250
T/9	0.706095	0.709387	0.00329
T/8	0.774124	0.778531	0.00440
T/7	0.852270	0.858271	0.00600
T/6	0.939091	0.947329	0.00823
T/5	1.025365	1.036410	0.01104
T/4	1.074351	1.087289	0.01293
T/3	0.939091	0.947307	0.00821
T/2	-1.85×10^{-8}	-4.84×10^{-5}	0.00004

Table 2 Error analysis in Case 4.2

t	$u_{\text{R-K}}$	u_{approx}	$\varepsilon = \text{abs}(u_{\text{R-K}} - u_{\text{app}})$
T/10	0.677218	0.677384	0.00016
T/9	0.737552	0.737743	0.00019
T/8	0.807137	0.807349	0.00021
T/7	0.886578	0.886803	0.00022
T/6	0.974166	0.974389	0.00022
T/5	1.060446	1.060654	0.00020
T/4	1.109077	1.109285	0.00020
T/3	0.974166	0.974466	0.00029
T/2	1.4×10^{-8}	0.000175	0.00017

(27), respectively, and numerical results obtained by a fourth-order Runge–Kutta method while Tables 1 and 2 present a detailed error analysis.

5 Conclusions

In this work we proposed a reliable technique, namely the Optimal Auxiliary Functions Method (OAFM) that accelerates the rapid convergence of the approximate analytical solution of nonlinear jerk equations.

The proposed procedure is valid even if the nonlinear equation does not contain any small or large parameters. Our construction of the first iteration is different from other traditional approaches especially concerning two optimal auxiliary functions which depend on some initially unknown parameters C_i.

The initially unknown parameters, (called convergence-control parameters), after identifying their optimal values, ensure a fast convergence of the approximate analytical solutions using only one iteration.

The main advantage of the OAFM is the possibility to optimally control and adjust the convergence of the solution through the auxiliary functions.

The obtained approximate analytical solutions are in very good agreement with the numerical integration results, which proves the validity of our method and, on the other hand, proves that this approach is very efficient in practice.

References

1. Gottlieb H.P.W.: Harmonic balance approach to periodic solutions of nonlinear jerk equations, J. Sound Vibr. **271**, 671-683 (2004)
2. Gottlieb H.P.W.: Harmonic balance approach to limit cycles of nonlinear jerk equations, J. Sound Vibr. **297**, 243–250 (2006)
3. Wu B.S., Lim C.W., Sun W.P.: Improved harmonic balance approach to periodic solutions of non-linear equations, Phys. Lett. A **354**, 95–100 (2006)
4. Ma X., Wei L., Guo Z.: He's homotopy perturbation method to periodic solutions of nonlinear jerk equations, J. Sound Vibr. **314**, 217–227 (2008)
5. Ramos J.I.: Approximate methods based on order reduction for the periodic solutions of nonlinear third-order ordinary differential equations, Appl. Math. Comput. **215**, 4304–4319 (2010)
6. Ramos J.I.: Analytical and approximate solutions to autonomous, nonlinear, third-order ordinary differential equations, Nonlinear Anal. Real World Appl. **11**, 1613–1626 (2010)
7. Leung A.Y.T., Guo Z.: Residue harmonic balance approach to limit cycles of non-linear jerk equations, Int. J. Non-Linear Mech. **46**, 898–906 (2011)
8. Ju P., Xue X.: Global residue harmonic balance method to periodic solutions of a class of strongly nonlinear oscillators, Appl. Math. Model. **38**, 6144–6152 (2014)
9. Marinca V., Herisanu N.: The optimal homotopy asymptotic method. Engineering applications, Springer (2015)

Chandler Wobble: Stochastic and Deterministic Dynamics

Alejandro Jenkins

Abstract We propose a model of the Earth's torqueless precession, the "Chandler wobble," as a self-oscillation driven by positive feedback between the wobble and the centrifugal deformation of the portion of the Earth's mass contained in circulating fluids. The wobble may thus run like a heat engine, extracting energy from heat-powered geophysical circulations whose natural periods would otherwise by unrelated to the wobble's observed period of about fourteen months. This can explain, more plausibly than previous models based on stochastic perturbations or forced resonance, how the wobble is maintained against viscous dissipation. The self-oscillation is a deterministic process, but stochastic variations in the magnitude and distribution of the circulations may turn off the positive feedback (a Hopf bifurcation), accounting for the occasional extinctions, followed by random phase jumps, seen in the data. This model may have implications for broader questions about the relation between stochastic and deterministic dynamics in complex systems, and the statistical analysis thereof.

1 Introduction

According to Euler's theory of the free symmetric top, the axis of rotation precesses about the axis of symmetry, unless both happen to align [1]. Applied to the Earth, this implies that the instantaneous North Pole should describe a circle about the axis of symmetry (perpendicular to the Earth's equatorial bulge), causing a periodic change in the latitude of any fixed geographic location (an effect known as "polar motion" or "variation of latitude"). The angular frequency of this free precession is

A. Jenkins (✉)
Escuela de Física, Universidad de Costa Rica, San José 11501-2060, Costa Rica
e-mail: alejandro.jenkins@ucr.ac.cr

A. Jenkins
Academia Nacional de Ciencias, San José 1367-2050, Costa Rica

© Springer International Publishing Switzerland 2016

J. Awrejcewicz (ed.), *Dynamical Systems: Theoretical and Experimental Analysis*, Springer Proceedings in Mathematics & Statistics 182, DOI 10.1007/978-3-319-42408-8_15

$$\omega_{\mathrm{Eu}} = \frac{I_3 - I}{I}\Omega_3, \tag{1}$$

where $I \equiv I_1 = I_2$ and I_3 are the Earth's moments of inertia, and Ω_3 is the component of its angular velocity along the axis of symmetry, which is also the principal axis with moment of inertia I_3. Many textbook treatments of rigid body dynamics cover this effect in detail; see, e.g., [2]. (Some authors refer to the corresponding terrestrial motion as the Earth's "free nutation"; see [3].)

The value of $I/(I_3 - I)$ can be deduced from the periods and amplitudes of the Earth's *forced* precession and nutation, driven by tidal torques [3]. The Eulerian period of the Earth's free precession then comes out to $2\pi/\omega_{\mathrm{Eu}} = 306$ days (about 10 months), but Chandler's careful observations, first published in 1891, established that the actual period is about 14 months [4–6]. This motion is therefore known as the Chandler wobble. A modern estimate [7] of its angular frequency is

$$\omega_{\mathrm{Ch}} = \frac{2\pi}{433.0 \pm 1.1\ (1\sigma)\ \mathrm{days}}. \tag{2}$$

In 1892, Newcomb explained the discrepancy between ω_{Ch} and ω_{Eu} as a consequence of the Earth not being quite rigid [8].

Newcomb also opened a debate, which has raged since, on how the Chandler wobble is maintained against the internal viscosities that would damp it away. Proposed solutions to this puzzle have, for the most part, relied either on stochastic perturbations to the Earth's mass distribution [9, 10], or on marine and atmospheric circulations that might force the wobble near its resonant ω_{Ch} [11–14].

Here we propose a new model of the Chandler wobble as a weakly nonlinear self-oscillation. Unlike a resonator, a self-oscillator maintains periodic motion at the expense of a power source with no corresponding periodicity [15, 16]. A self-oscillation modulates the driving force acting on it, establishing *positive feedback* between it and the external power source. On the many names and guises of self-oscillators, see [16]. One striking instance of such behavior was provided by the swaying of London's Millennium Bridge when it opened in 2000, driven by the synchronized lateral motion of the pedestrians in response to the bridge's own oscillation [17].

In our model, the Chandler wobble is powered by geophysical fluid circulations whose natural periods are unrelated to ω_{Ch}. Due to the centrifugal force of the Earth's rotation, the wobble itself can modulate those circulations. That a dynamical delay in the adjustment of a surrounding flow to a solid's displacement can excite and maintain the solid's vibration is an idea dating back to Airy's conceptualization of the action of the vocal cords [18], based on Willis's pioneering research on the mechanism of the larynx [19]. In the case of the Chandler wobble, variations of the magnitude and geographical distribution of the circulations may turn off the positive feedback. This suggests an explanation of the wobble's extinctions, which occur rarely and are followed by re-excitation with a random phase jump, without obvious connection to major geophysical events [20].

2 Precession and Deformation

Newcomb's simplified treatment in [8] of the Earth's deformability and its connection to the observed ω_{Ch} will lend itself to a physically intuitive formulation of our self-oscillatory model. We therefore begin by summarizing Newcomb's argument. For a full, rigorous treatment of this subject, see [3].

Let $\boldsymbol{\Omega}$ be the Earth's angular velocity and $\hat{\boldsymbol{x}}_3$ be the unit vector along the axis of symmetry, with moment of inertia is I_3. Let I be the value of the moments of inertia along any two axes orthogonal to each other and to $\hat{\boldsymbol{x}}_3$. Since the Earth is flattened at the poles, $I_3 > I$. As shown in Fig. 1, for a rigid Earth the instantaneous North Pole R (the intersection of $\boldsymbol{\Omega}$ with the Earth's surface) would describe a circular trajectory (polhode) around the symmetry pole S (the intersection of $\hat{\boldsymbol{x}}_3$ with the Earth's surface), with angular velocity ω_{Eu} given by Eq. (1).

The centrifugal force generated by the planet's rotation implies that a displacement of R tends to deform the planet by shifting its equatorial bulge, causing S to move toward R. If the Earth were simply fluid, this adjustment would be complete and nearly instantaneous, so that S would always coincide with R and there would be no wobble. For an elastic Earth, the adjustment is partial and the planet may wobble, albeit more slowly than in the rigid case.

Let O be the center of the polhode for the elastic Earth (i.e., the average location of R over a complete period of the wobble) and let us work in a geographic frame of reference, centered at O. As shown in Fig. 2, S describes its own circular trajectory, with fixed

$$k_{\mathrm{w}} = OS/OR \tag{3}$$

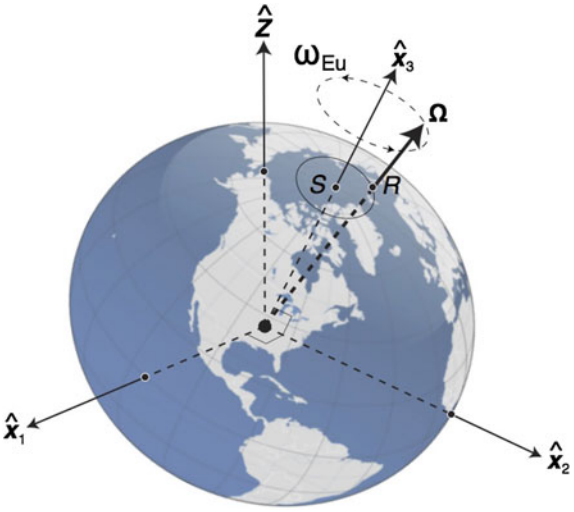

Fig. 1 Free precession of a rigid Earth. The principal axes $\hat{\boldsymbol{x}}_{1,2,3}$ define a non-inertial body frame, $\hat{\boldsymbol{x}}_3$ being the Earth's axis of symmetry. These principal axes move with respect to the inertial space frame (for which only the axis $\hat{\boldsymbol{Z}}$ is shown). S is the symmetry pole and R the instantaneous North Pole. In the body frame, $\boldsymbol{\Omega}$ precesses regularly along the circle SR, with angular velocity ω_{Eu}

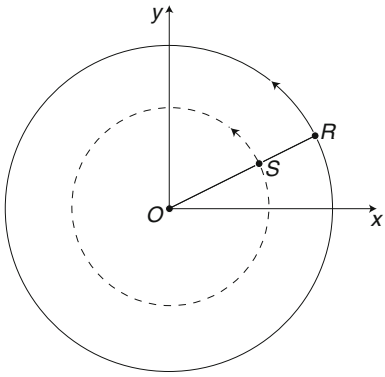

Fig. 2 Free precession of a deformable Earth. R is the instantaneous North pole and S is the symmetry pole. The geographic coordinates (x, y) are centered at O, which corresponds to the average position of R

related to the speed of rotation Ω and to the planet's elastic modulus. The parameter k_w lies between between 0 (rigid case) and 1 (fluid case).

The centrifugal deformation preserves the Earth's ellipticity, leaving I and I_3 unaffected. Newcomb's insight was that the planet's internal forces of cohesion will therefore make $R = (x, y)$ precess instantaneously about $S = (x_S, y_S)$ with the same ω_{Eu} of Eq. (1):

$$\begin{cases} \dot{x} = -\omega_{Eu}\left(y - y_S\right) \\ \dot{y} = \omega_{Eu}\left(x - x_S\right) \end{cases}. \tag{4}$$

By Eq. (3), $x_S = k_w x$ and $y_S = k_w y$, so that Eq. (4) reduces to

$$\ddot{x} + \omega_{Ch}^2 x = \ddot{y} + \omega_{Ch}^2 y = 0, \tag{5}$$

with

$$\omega_{Ch} = \omega_{Eu}\left(1 - k_w\right) \tag{6}$$

the angular velocity of the precession of R around O. The parameter

$$k_w = 1 - \frac{\omega_{Ch}}{\omega_{Eu}} = 1 - \frac{306}{433} = 0.293 \tag{7}$$

measures the Earth's deformability and is consistent with the Love number k_2 computed from the magnitudes of terrestrial and oceanic tides [21, 22].

This simple analysis reveals that the dynamics of a deformable spinning body is subject to a feedback: the displacement of R (the wobble) affects the displacement of S (due to centrifugal deformation), while the displacement of S (the deformation) in turn affects the displacement of R (due to precession). If some of the mass of the planet is in the form of circulating fluids (with their own kinetic energy in the geographic reference frame), we shall see that this feedback can be positive, destabilizing the wobble-less equilibrium.

3 Dissipation and Maintenance

In the body frame (see Fig. 1), we write

$$\boldsymbol{\Omega} = \left(\Omega_1, \Omega_2, \Omega_3\right) \tag{8}$$

with $\Omega_\perp \equiv \sqrt{\Omega_1^2 + \Omega_2^2}$. The magnitude squared of the angular momentum $\boldsymbol{M}$ is therefore

$$M^2 = I^2\Omega_\perp^2 + I_3^2\Omega_3^2. \tag{9}$$

Internal forces keep M fixed, as they produce no net torque. The kinetic energy of rotation is

$$E = \frac{1}{2}\left(I\Omega_\perp^2 + I_3\Omega_3^2\right) = E_0 + \frac{I}{2}\left(1 - \frac{I}{I_3}\right)\Omega_\perp^2, \tag{10}$$

where $E_0 \equiv M^2/2I_3$ is the minimum energy consistent with conservation of M.

Let $\alpha = \arcsin(\Omega_\perp/\Omega)$ be the angle between $\boldsymbol{\Omega}$ and $\hat{\boldsymbol{x}}_3$, in radians. For small α we may express the wobble's energy as

$$E_\mathrm{w} = \frac{I}{2}\left(1 - \frac{I}{I_3}\right)\Omega_\perp^2 \simeq \frac{I}{2}\left(1 - \frac{I}{I_3}\right)\Omega^2\alpha^2. \tag{11}$$

For the Earth this gives $E_\mathrm{w} \sim \alpha^2 \times 10^{27}$ J.

Displacement of the equatorial bulge (and therefore of the symmetry pole S in Fig. 2) induces a small variation in ocean levels, with the same period as the wobble's. Friction as this "pole tide" moves through straits and shallow oceans dissipates E_w. Another source of dissipation is the anelasticity of molten material under the Earth's crust. We would therefore expect the amplitude of the free wobble to decay as

$$\alpha(t) = e^{-t/\tau}\alpha_0 \tag{12}$$

with α_0 set by the Earth's state of rotation at the time $t = 0$ when it solidified, and τ a time constant small compared to the age of the Earth. In terms of the quality factor

$$Q_\mathrm{w} \equiv \frac{\tau\omega_\mathrm{Ch}}{2}, \tag{13}$$

the power that the wobble dissipates is

$$P_\mathrm{w} = \frac{E_\mathrm{w}\,\omega_\mathrm{Ch}}{Q_\mathrm{w}} \sim \frac{\alpha^2}{Q_\mathrm{w}} \times 10^{20}\ \mathrm{W}. \tag{14}$$

The fact that α, averaged over many periods of the wobble, remains of order 10^{-6} indicates that some mechanism injects into it an average power of order $Q_{\mathrm{w}}^{-1} \times 10^8$ W, compensating for the dissipated P_{w} [21, 22].

Stochastic perturbations to the Earth's mass distribution, such as might result from seismic events, could cause random displacements of $\hat{\boldsymbol{x}}_3$, preventing it from becoming aligned with $\boldsymbol{\Omega}$. Jeffreys developed a method for estimating Q_{w} from the data, assuming that the wobble is re-excited stochastically [9]. Jeffreys and others have thus obtained estimates for Q_{w} ranging from 37 to 1,000 [7]. These estimates are not only uncertain, they generally require more dissipation than can be accounted for by known mechanisms of tidal friction and mantle anelasticities [9, 21, 22], while the corresponding P_{w} seems too high to be compensated by seismic activity [23, 24]. Moreover, there is statistical evidence that the Chandler wobble is predominantly a deterministic process [25–27].

Some authors have therefore concluded that the wobble is forced by geophysical fluid circulations [11–14]. In that case the estimates of Q_{w} obtained by Jeffreys's method do not apply (a point stressed in [21], but ignored by some authors). The key difficulty with such models is that a damped and forced linear oscillator ends up moving at the forcing frequency. Even in parametric or nonlinear resonances, the frequency of steady oscillation is usually a rational multiple a/b of the forcing frequency, with integer a and b of low order [2]. In fact, the polar motion has a significant component with a 12 month period, presumably forced by meteorological and other mass transfers connected to the seasons, and this seasonal effect is subtracted to isolate the Chandler wobble [3, 21, 22]. The polar motion's power spectrum is inconsistent with a high-quality oscillation ($Q \gtrsim 300$) being driven by an external power spectrum that is smooth in the vicinity of ω_{Ch} [28]. The observed wobble must therefore be forced by an external power spectrum peaked around the resonant ω_{Ch}, which seems like an implausible coincidence [21, 22].

Moreover, it is well known that in the 1920s the amplitude of the Chandler wobble decreased sharply, only to restart with a phase jump of nearly 180° [21]. A recent analysis finds two other brief extinctions, followed by phase jumps, in the 1850s and 2000s [20]. These irregularities are difficult to explain in stochastic re-excitation or forced resonance models, as they are not associated with obvious geophysical events.

4 Self-oscillation and Intermittence

Consider the portion of the Earth's mass made of circulating fluids. In the body frame of the solid Earth, these circulations carry significant kinetic energy but negligible net angular momentum. Resistance to displacing geographically the mean route of a circulation may be interpreted as an effective rigidity. With respect to the Earth's rotation, we therefore express the total tensor of inertia as

$$I_{ij}^{\mathrm{tot}} = I_{ij} + \varepsilon \tilde{I}_{ij}, \tag{15}$$

with I_{ij} given by the distribution of the mass at rest with respect Earth's solid surface, and $\tilde{I}_{ij}$ by flows whose distribution is expressed in Eulerian coordinates (fixed geographically), rather than in Lagrangian coordinates associated to individual mass elements (see [29]).

The moments of I_{ij} and $\tilde{I}_{ij}$ in Eq. (15) are taken to be of the same order, with ε indicating the small fraction that the circulations contribute to the moments of I_{ij}^{tot}. Euler's equations for the free top may be expressed as

$$\frac{d'\boldsymbol{M}}{dt} + \boldsymbol{\Omega} \times \boldsymbol{M} = 0, \tag{16}$$

where d'/dt measures velocity in the body frame [2]. For $M_i = \sum_j (I_{ij} + \varepsilon \tilde{I}_{ij})\Omega_j$, Eq. (16) implies that the equation of motion for the free precession of $\boldsymbol{\Omega}$ is the weighted superposition of the equations of motion for the precessions separately induced by I_{ij} and $\varepsilon \tilde{I}_{ij}$.

Let S be the symmetry pole for I_{ij}. Let us assume, for simplicity that $\tilde{I}_{ij}$ has its own symmetry pole $\tilde{S}$, as shown in Fig. 3. For an asymmetric $\tilde{I}_{ij}$, we would consider precession about the principal axis of greatest moment of inertia. This precession would not be uniform [2], but our conclusions would be essentially unaffected.

The centrifugal deformation of I_{ij} propagates with the speed of sound in the relevant material, which is very fast compared to the wobble, so that the adjustment of S to the displacement of R is nearly instantaneous [3]. On the other hand, the adjustment of $\tilde{S}$ can show an appreciable delay, caused by the circulating fluids' inertia. For $R = (x, y)$, we therefore take

$$\tilde{S}(t) = \beta\,(x(t-c),\, y(t-c))\,, \tag{17}$$

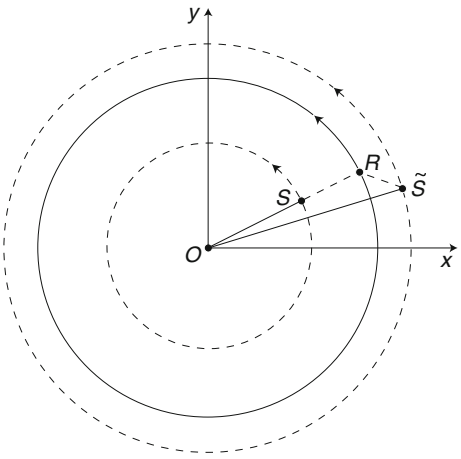

Fig. 3 Torqueless precession of a deformable Earth containing fluid circulations. R is the instantaneous North Pole, S is the symmetry pole of the portion of the mass at rest with respect to the Earth's solid surface, and $\tilde{S}$ is the symmetry pole of the part of the mass in geophysical circulations

where $\beta \equiv O\tilde{S}/OR$ (Fig. 3 is drawn for constant β). The precession of R around $\tilde{S}$ would then be described by

$$\begin{cases} \dot{x}(t) = -\tilde{\omega}_{\mathrm{Eu}} \left[y(t) - \beta y(t-c) \right] \\ \dot{y}(t) = \tilde{\omega}_{\mathrm{Eu}} \left[x(t) - \beta x(t-c) \right] \end{cases}, \tag{18}$$

with $\tilde{\omega}_{\mathrm{Eu}} \equiv \tilde{\Omega}_3(\tilde{I}_3 - \tilde{I})/\tilde{I}$ given by the moments of inertia $\tilde{I}$ and $\tilde{I}_3$ for the tensor $\tilde{I}_{ij}$, and by the component $\tilde{\Omega}_3$ of the angular velocity along the axis of $\tilde{S}$. In terms of x, Eq. (18) corresponds to

$$\ddot{x}(t) = -\tilde{\omega}_{\mathrm{Eu}}^2 \left[x(t) + 2\beta x(t-c) - \beta^2 x(t-2c) \right], \tag{19}$$

and equivalently for y.

Superposing the precession about $\tilde{S}$, given by Eq. (19) and weighed by $\varepsilon \ll 1$, on the precession about S given by Eq. (5), and taking $c \ll \pi/\omega_{\mathrm{Ch}}$ (which lets us approximate $x(t-c) \simeq x(t) - c\dot{x}(t)$ in the full equation of motion) we obtain

$$\ddot{x} + 2c\varepsilon\beta(1-\beta)\tilde{\omega}_{\mathrm{Eu}}^2 \dot{x} + \omega_{\mathrm{Ch}}^2 x = 0. \tag{20}$$

The coefficient of $\dot{x}$ in Eq. (20) is negative when $\beta > 1$, indicating that the wobble *absorbs* energy. As long as

$$\gamma \equiv 2c\varepsilon\beta(\beta-1)\tilde{\omega}_{\mathrm{Eu}}^2 > \omega_{\mathrm{Ch}}/Q_{\mathrm{w}} \tag{21}$$

this effect will dominate over viscous damping, causing R to spiral away from O until nonlinear dissipative effects match the power input, stabilizing the wobble's amplitude. In the theory of ordinary differential equations, this corresponds to approaching a weakly nonlinear limit cycle; see [16]. Note that if the mass associated with $\tilde{S}$ did not have significant kinetic energy in the geographic frame, c would be negligible and it would be impossible to maintain $\beta > 1$.

The parameters ε, β vary with the magnitude and distribution of the geophysical circulations. The anelasticity of $\tilde{I}_{ij}$ implies that centrifugal deformation would tend to make $\beta \to 1$, killing the antidamping in Eq. (20). However, natural changes in circulation patterns may counteract this, maintaining $\beta > 1$ over long periods (recall that $OR \sim 6$ m).

Instead of tending to a limit cycle, the wobble may start to decay if $\tilde{S}$ approaches close enough to the circle OR for the condition of Eq. (21) to fail. Sensitivity to β, determined by the precise geographical distribution of the circulations, implies that extinctions of the wobble need not be associated with major geophysical irregularities. As $OR \to 0$, $\beta \gg 1$ becomes more likely, and we therefore expect the wobble to turn on again, with a random phase jump related to its brief quiescent period. The turning on or off of a self-oscillation as the net linear damping changes sign is known mathematically as "Hopf bifurcation" (see [16]).

The conditions that the delay c in Eq. (17) remain fixed and very small compared to the period of the wobble may be relaxed without qualitatively altering our conclusions. Physically, the point is that the wobble itself induces a modulation of the geophysical circulations, corresponding to the precession of $\tilde{S}$ in Fig. 3. For $\beta > 1$ and $0 < \omega_{\mathrm{Ch}} c < \arccos(1/\beta)$, the resulting force on the solid Earth, described by Eq. (19), *leads* the wobble, thus supplying to it net power (see [30]).

5 Outlook

In the self-oscillatory model offered here, the Chandler wobble is maintained by a positive feedback between the wobble and the centrifugal deformation of the part of the Earth's mass in fluid circulations. The energy to maintain the wobble comes from the flows, which take it in turn from the heat of solar radiation and of the Earth's internal radioactivity. This is a picture of the wobble, not as an unphysical perpetual motion, but as a low-efficiency heat engine, with the geophysical fluids playing the part of the working substance and the solid Earth acting as the piston. That heat engines and motors in general may be conceptualized as self-oscillators that has been stressed in [15, 16].

Evidence of the modulation of the circulations may already have been detected in the atmosphere [11, 13, 14], requiring only reinterpreting that signal as resulting from the wobble's feedback, rather than being an intrinsic property of the circulations. The positive local Lyapunov exponent that [25–27] find in the Chandler wobble data may reflect, not chaos (an aperiodic and strongly nonlinear phenomenon), but rather the linear antidamping of Eq. (20) (which makes the wobble-less equilibrium unstable). The reported variability of this local Lyapunov exponent, and its tendency to increase when the El Niño Southern Oscillation (ENSO) is on its maximum (El Niño) or minimum (La Niña) temperature phase, seem consistent with our model, as ENSO extrema may be associated with stronger atmospheric currents around the equatorial region, and therefore with an increased ϵ in Eq. (15).

This simple model raises issues that may be relevant beyond geophysics. A deterministic self-oscillation turned on and off by stochastic perturbations may lead to behaviors difficult to capture with simple statistical tools. (For a review of how heavy-tailed distributions may emerge when a stochastic parameter triggers repeated dynamical bifurcations, see [31]). This model of the Chandler wobble may therefore offer a case study on the importance of better understanding the relations between stochastic and deterministic dynamics in complex systems.

Acknowledgments The author thanks Eric Alfaro, Jorge Amador, and Paul O'Gorman for discussions on meteorological issues, as well as Howard Georgi and José Gracia-Bondía for encouragement and advice on this project.

References

1. L. Euler, *Theoria motus corporum solidorum seu rigidorum* (A. F. Rose, Rostock & Greifswald, 1765)
2. L. D. Landau, E. M. Lifshitz, *Mechanics*, 3rd edn. (Elsevier, Oxford, 1976)
3. F. Klein, A. Sommerfeld, *The Theory of the Top*, vol. III (Birkhäuser, New York, 2012 [1903])
4. S. C. Chandler, "On the variation of latitude, I", Astron. J. **11** (1891), 59–61
5. S. C. Chandler, "On the variation of latitude, II", Astron. J. **11** (1891), 65–70
6. W. E. Carter, M. S. Carter, "Seth Carlo Chandler, Jr. 1846–1913", in *Biographical Memoirs* **66** (National Academy of Sciences, Washington, D.C., 1995), 44–79
7. C. R. Wilson, R. O. Vicente, "Maximum likelihood estimates of polar motion parameters", in *Variations in Earth Rotation*, eds. D. D. McCarthy and W. E. Carter (American Geophysical Union, Geophysical Monograph Series **59**, 1990), 151–155
8. S. Newcomb, "On the dynamics of the Earth's rotation, with respect to the periodic variations of latitude", Mon. Not. R. Astron. Soc. **52** (1892), 336–341
9. H. Jeffreys, "The variation of latitude", Mon. Not. R. Astron. Soc. **100** (1940), 139–155
10. H. Jeffreys, "The variation of latitude", Mon. Not. R. Astron. Soc. **141** (1968), 255–268
11. H.-P. Plag, "Chandler wobble and pole tide in relation to interannual atmosphere-ocean dynamics", in *Tidal Phenomena* (Springer, Lecture Notes on Earth Sciences **66**, 1997), 183–218
12. R. S. Gross, "The excitation of the Chandler wobble", Geophys. Res. Lett. **27** (2000), 2329–2332
13. Y. Aoyama, I. Naito, "Atmospheric excitation of the Chandler wobble, 1983–1998", J. Geophys. Res. **106** (2001), 8941–8954
14. Y. Aoyama et al., "Atmospheric quasi-14 month fluctuation and excitation of the Chandler wobble", Earth Planets Space **55** (2003), e25–e28
15. A. A. Andronov, A. A. Vitt, S. È. Khaĭkin, *Theory of Oscillators* (Dover, Mineola, 1987 [1966])
16. A. Jenkins, "Self-oscillation", Phys. Rep. **525** (2013), 167–222
17. S. H. Strogatz et al., "Theoretical mechanics: Crowd synchrony on the Millennium Bridge", Nature **403** (2005) 43–44
18. G. B. Airy, "On certain Conditions under which a Perpetual Motion is possible", Trans. Cambridge Phil. Soc. **3** (1830), 369–372
19. R. Willis, "On the Mechanism of the Larynx", Trans. Cambridge Phil. Soc. **4** (1833), 323–352. This work was originally presented in May 1829.
20. Z. Malkin, N. Miller, "Chandler wobble: two more large phase jumps revealed", Earth Planets Space **62** (2010), 943–947
21. K. Lambeck, *The Earth's Variable Rotation* (Cambridge U. P., Cambridge 1980)
22. F. D. Stacey, P. M. Davis, *Physics of the Earth*, 4th edn. (Cambridge U. P., Cambridge, 2008)
23. A. Souriau, "The influence of earthquakes on the polar motion", in *Earth Rotation: Solved and Unsolved Problems*, ed. A. Cazenave (Reidel, Dordrecht, 1986), 229–249
24. B. F. Chao, R. S. Gross, "Changes in the Earth's rotation and low-degree gravitational field induced by earthquakes", Geophys. J. Roy. Astr. S. **91** (1987), 569–596
25. V. Frède, P. Mazzega, "Detectability of deterministic non-linear processes in Earth rotation time-series I. Embedding", Geophys. J. Int. **137** (1999), 551–564
26. V. Frède, P. Mazzega, "Detectability of deterministic non-linear processes in Earth rotation time-series II. Dynamics", Geophys. J. Int. **137** (1999), 565–579
27. V. Frède, P. Mazzega. "A preliminary nonlinear analysis of the Earth's Chandler wobble", Discrete Dyn. Nat. Soc. **4** (2000), 39–53
28. B. B. Mandelbrot, K. McCamy, "On the Secular Pole Motion and the Chandler Wobble", Geophys. J. R. astro. Soc. **21** (1970), 217–232
29. D. J. Tritton, *Physical Fluid Dynamics*, 2nd edn. (Oxford U. P., Oxford, 1998)
30. H. Georgi, *The Physics of Waves* (Prentice Hall, Englewood Cliffs, 1993)
31. D. Volchenkov, T. Krüger, P. Blanchard, "Heavy-tailed Distributions In Some Stochastic Dynamical Models", Discontinuity Nonlinearity Complexity **1** (2012), 1–40

Impact of Varying Excitation Frequency on the Behaviour of 2-DoF Mechanical System with Stick-Slip Vibrations

Wojciech Kunikowski, Paweł Olejnik and Jan Awrejcewicz

Abstract Article shows the influence of varying excitation on dynamics of a 2-DoF mechanical system. The system consists of a vibrating block on a transmission belt driven by a DC motor. Stick-slip frictional effects between the block and the belt introduce significant varying of load affecting the operation of the driving system. Resultant unsteady rotational velocity of the DC motor acts as a time varying excitation for the vibrating system. Behaviour of the analysed system was investigated and compared with its response to a periodic excitation. Mathematical models of the block-on-belt system with normal force intensification mechanism and a DC motor driving system with worm gear have been developed and virtualized. Controlled changes of selected model parameters were made providing interesting results visible on the bifurcation diagrams.

1 Introduction

In many mechanical systems, various oscillatory motions affected by nonlinearities or nonsmoothness caused by backlashes, stick-slip motions, impacts or interactions with a discrete control system can be found. Many publications focus on analysis of complex behaviour exhibited by mechanical systems with nonlinearities [1–10]. Methods of dynamical analysis found their place not only in mechanics, but also in electronics [11], and even in biology [12].

W. Kunikowski (✉) · P. Olejnik · J. Awrejcewicz
Department of Automation, Biomechanics and Mechatronics,
Lodz University of Technology, 1/15 Stefanowski Street, 90-924 Łódź, Poland
e-mail: wojciech.kunikowski@dokt.p.lodz.pl

P. Olejnik
e-mail: pawel.olejnik@p.lodz.pl

J. Awrejcewicz
e-mail: jan.awrejcewicz@p.lodz.pl

© Springer International Publishing Switzerland 2016

J. Awrejcewicz (ed.), *Dynamical Systems: Theoretical and Experimental Analysis*, Springer Proceedings in Mathematics & Statistics 182, DOI 10.1007/978-3-319-42408-8_16

This paper takes a research on the impact of varying excitation on the dynamics of a 2-DoF mechanical system. Two mathematical models are investigated, i.e. with and without the feedback between the oscillating mass and the driving system. Results of our dynamical analysis are presented on bifurcation diagrams.

2 Model of a Mechatronic System

The investigated mechatronic system is depicted in Fig. 1. It consists of three coupled subsystems such as a DC motor, transmission system and the oscillating body with a friction force intensification mechanism realised by a single pendulum (bracket). The DC motor is connected to a worm gear, which transmits the driving torque by a toothed belt to the belt pulley. Velocity of the conveyer belt, which can be deduced from angular velocity of the pulley, plays the role of excitation of the oscillating block mass. Detailed description of the system can be found in [13–16].

Electro-mechanical model of the DC motor follows:

$$i_w L_w = U_{in} - k_e \omega(t) - i_w(t) R_w, \tag{1}$$

$$\dot{\omega}(t) J_{dc} = k_m i_w(t) - M_{load}(t) - b\omega(t) - T_C(\omega(t)), \tag{2}$$

where dot over symbols i and ω denotes the first derivative with respect to time, L_w—winding inductance, R_w—winding resistance, k_e and k_m—electromotive force and motor torque constants, respectively, i_w—winding current, U_{in}—input voltage, ω—angular velocity, J_{dc}—mass moment of inertia of the rotor, b—viscous friction coefficient, M_{load}—time varying load, T_C—Coulomb friction force given by:

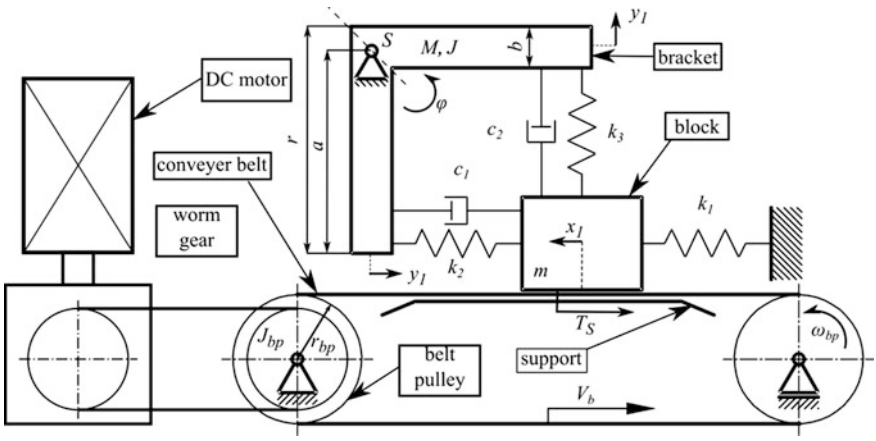

Fig. 1 Model of the investigated mechatronic system

$$T_C(\omega(t)) = \begin{cases} T_{st} & for \quad \omega(t) = 0, \\ -sign(\omega(t))T_{dn} & for \quad \omega(t) \neq 0, \end{cases} \tag{3}$$

where T_{st}—static friction, T_{dn}—dynamic friction.

Equation of motion of the belt pulley is presented in the form:

$$\dot{\omega}_{bp}(t)J_{bp} = M_2 - T_S(t)r_{bp}, \tag{4}$$

where J_{bp}—mass moment of inertia of the pulley, ω_{bp}—pulley's angular velocity, r_{bp}—radius of the pulley, M_2—output torque of the worm gear, T_S—irregularly varying friction force caused by irregular behaviour of mass m.

Equations (5)–(7) constitute the simplified model of the worm gear:

$$M_1 = M_2\eta\rho, \tag{5}$$

$$\omega(t) = \omega_{bp}(t)\rho, \tag{6}$$

$$\dot{\omega}(t) = \dot{\omega}_{bp}(t)\rho, \tag{7}$$

where η—efficiency of the angular velocity transmission system, ρ—a transmission ratio, M_1 and M_2—input and output torques of worm gear.

Substituting Eq. (4) to (5) with regard to (6) yields (8), which describes the total loading torque applied by the transmission system to the DC motor:

$$M_{load} = M_1 = \frac{1}{\eta\rho}\left(\frac{d\omega(t)}{dt}\frac{J_{bp}}{\rho} + T_S(t)r_{bp}\right). \tag{8}$$

Combining Eqs. (2) and (8) leads to Eq. (9), which is an equation of motion of the transmission system reduced to the DC motor's shaft:

$$\frac{d\omega(t)}{dt}\left(J_{bp} + \frac{J_{bp}}{\eta\rho^2}\right) = k_m i_w(t) - \frac{r_{bp}}{\eta\rho}T_S(t) - b\omega(t) - T_C(\omega(t)). \tag{9}$$

Expressions (10)–(17) describe the behaviour of the oscillating body and the friction intensification mechanism realised by the single pendulum. The detailed derivation of aforementioned model can be found in work [17]. Block of mass m is connected to a fixed wall by linear spring k_1 and to a bracket body of mass M(the pendulum) by means of springs k_2 and k_3. The virtual dampers c_1 and c_2 represent some effects of system damping in the bearings and resistance of the air.

Two characteristic phases of movement can be distinguished in the examined system dynamics. The "stick" phase of movement occurs when the block moves with constant velocity equal to V_b—velocity of the conveyer belt. When the static friction reaches its maximum value and does no longer compensate for the resultant force of springs, then the contact between the mass and the moving belt is lost, hence, the "slip" phase of the motion starts. The block of mass m moves then with

accelerated motion in the opposite direction to the belt's motion, until the dynamic friction forces compensate the resultant force of springs and inertia of the sliding body.

The investigated two-degrees-of-freedom mechanical system is described by the two second order differential equations (10) and (11):

$$\ddot{x_1}\, m + \dot{z}_1 c_1 + (k_1 + k_2)x_1 + k_2 y_1 + \frac{k_3 x_1}{r}\left(y_1 + \frac{x_1^2}{2r}\right) = -T_S, \tag{10}$$

$$\ddot{y_1}\frac{J}{r^2} + \dot{z}_1 c_1 + \dot{y}_1 c_2 + k_2 z_1 + k_3\left(y_1 + \frac{x_1^2}{2r}\right) + Mg\lambda_r = -\frac{Q}{r}, \tag{11}$$

where g—gravity constant, Q—resistance torque in the pivot point S

$$\lambda_r = \frac{\sqrt{2}l}{2r}\left(1 + \frac{y_1}{r} - \frac{y_1^2}{2r^2} - \frac{y_1^3}{6r^3}\right), \tag{12}$$

where $l = (3\sqrt{2}/4)r$ is the distance between the centre of rotation and the centre of gravity of the rotating bracket of mass M.

Parameter z_1 and its first derivative represent an internal state variables expressed as follows:

$$z_1 = x_1 + y_1, \tag{13}$$

$$\dot{z}_1 = \dot{x}_1 + \dot{y}_1. \tag{14}$$

On that basis, the friction force in the frictional contact of the block-on-belt model follows as below:

$$T_S = \mu(V_{rel})mg\left(1 + \frac{M}{m}\lambda_r - \frac{k_3}{mg}\left(y_1 + \frac{x_1^2}{2r}\right) - \frac{c_2}{mg}\dot{y}_1\right). \tag{15}$$

The experimentally verified friction coefficient dependent on the relative velocity is proposed [17]:

$$\mu(V_{rel}) = \frac{\mu_0}{1 + \gamma|V_{rel}|}\left(1 + \frac{\beta}{\cosh \alpha V_{rel}}\right)\tanh \alpha V_{rel}, \tag{16}$$

$$V_{rel} = \dot{x}_1 - V_b, \tag{17}$$

where α, β and γ are the friction law parameters controlling the shape of curve given by Eq. (16), and $V_b = \omega_{bp} r_{bp}$ is the velocity of the conveyer belt.

3 Simulation Results

Mathematical modelling presented in previous section was realised in NI LabVIEW supported by the Control Design and Simulation Module. Two versions of aforementioned model were tested. In first case, constant value of rotational speed of the belt pulley was assumed, and the equations describing the simplified DC motor and transmission system's dynamics were omitted. In second case, the full model allows to investigate the influence of feedback on the system's dynamics was tested.

To measure differences between the simplified and full model, their responses to changes in parameter k_3 were investigated. The parameter was changed from 80 to 100 [N/m] with a step of 0.01. For each value of k_3, the simulation took 40 s but measurements were started after 15 s to avoid transitional dynamics.

Figures 2, 3, 4, 5, 6 and 7 show the bifurcation diagrams of the displacement of block of mass m when its motion exhibits "slip" to "stick" transitions. It was assumed, that a point of Poincaré map appears when the acceleration $\ddot{x_1}$ crosses 0 from above.

Figures 8, 9, 10, 11, 12 and 13 also show other bifurcation diagrams of the displacement of mass m. In this case, the condition of acquiring the point for the Poincaré map was an angular position of the pulley. After full rotation of the pulley, a point for the bifurcation diagram was captured. If all the apparent lines on the diagram intersect, the position of the block is identical after each turn of the pulley. This method has allowed to search for some points at which synchronisation between movement of the block and the pulley's angular rotation occurred.

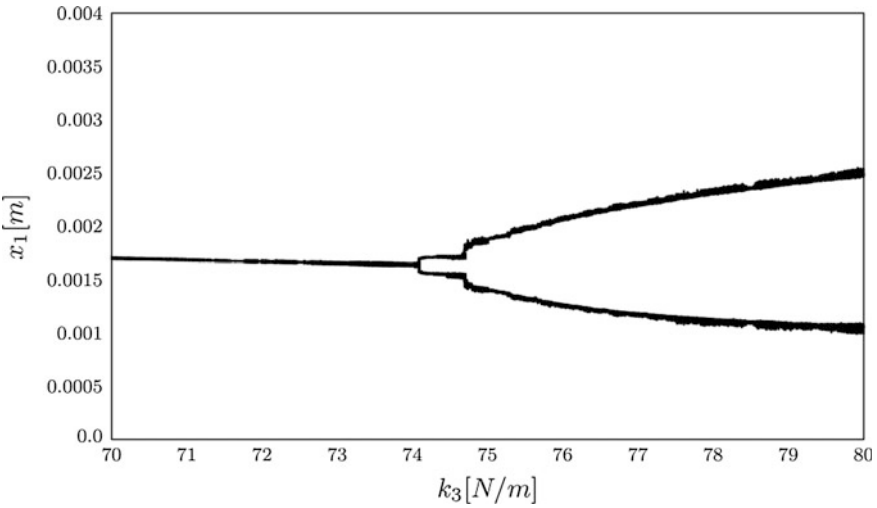

Fig. 2 Bifurcation diagram of simplified model with respect to the parameter k_3 ranging from 70 to 80

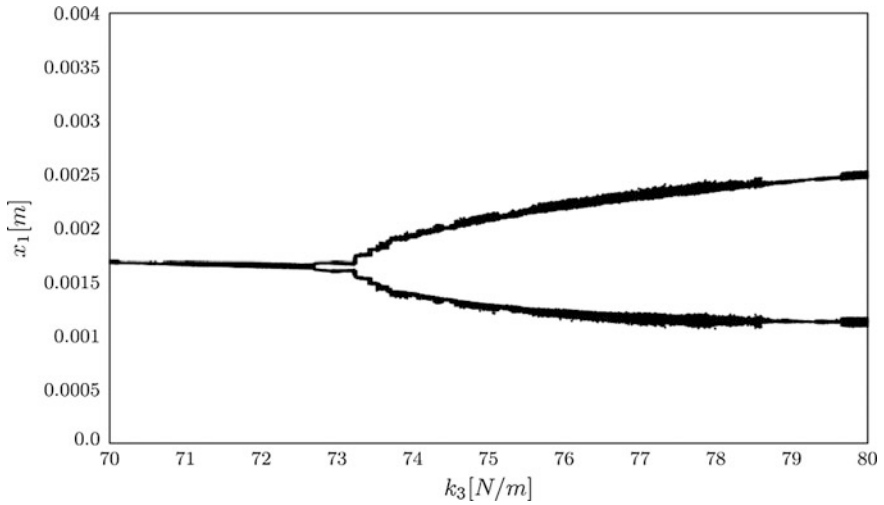

Fig. 3 Bifurcation diagram of full model with respect to the parameter k_3 ranging from 70 to 80

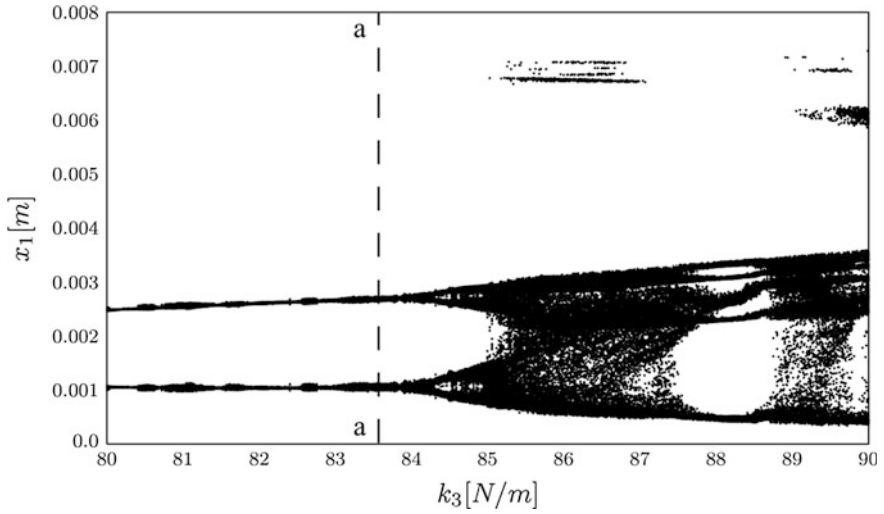

Fig. 4 Bifurcation diagram of simplified model with respect to the parameter k_3 ranging from 80 to 90. *Dashed line* "a–a" marks the synchronisation point

It can be observed that both models respond with a pitchfork bifurcations to the change of the bifurcation parameter. Basic difference is seen in the value of k_3 at which period doubling is observed. Full model dynamics experiences the bifurcation point a bit earlier.

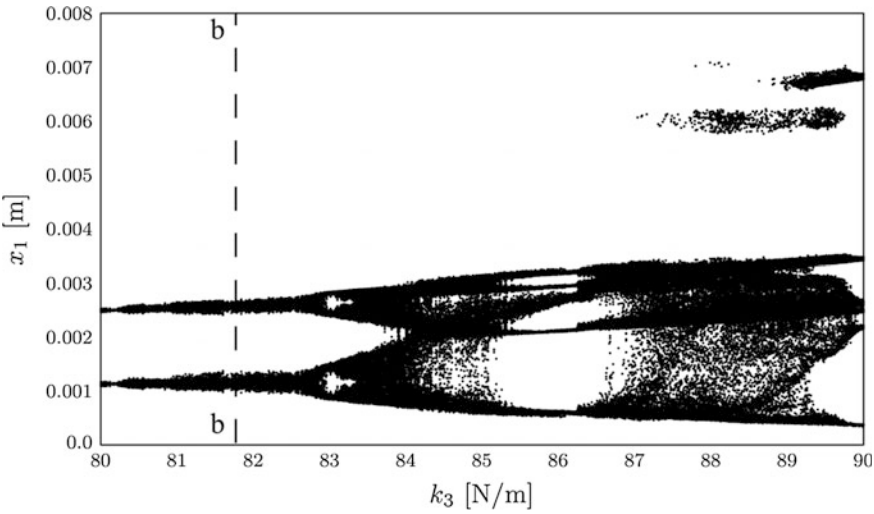

Fig. 5 Bifurcation diagram of full model with respect to the parameter k_3 from ranging 80 to 90. *Dashed line* "b–b" marks the synchronisation point

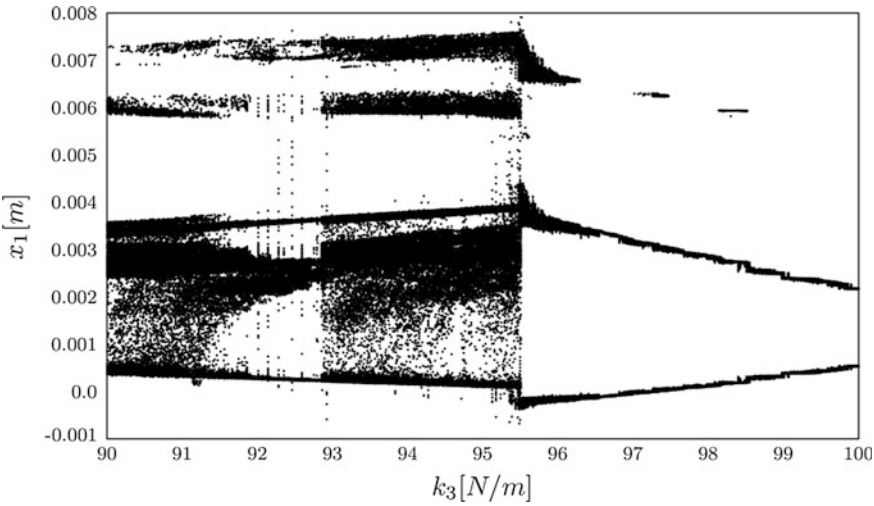

Fig. 6 Bifurcation diagram of simplified model with respect to the parameter k_3 ranging from 90 to 100

Similar situation can be observed for the next range of the bifurcation parameter. Both models demonstrate the same types and order of changes in their dynamics. Once again, the only difference between the two models can be found in the values of bifurcation parameter for each type of change in the dynamics.

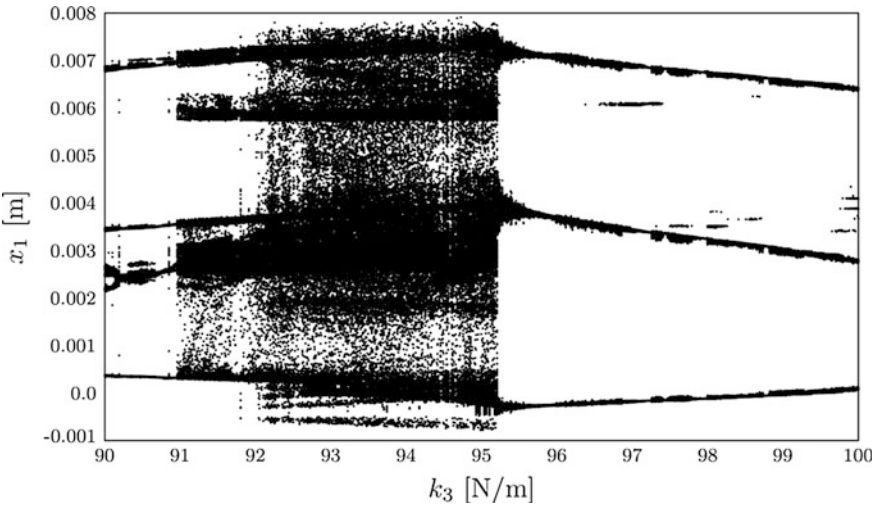

Fig. 7 Bifurcation diagram of full model with respect to the parameter k_3 ranging from 90 to 100

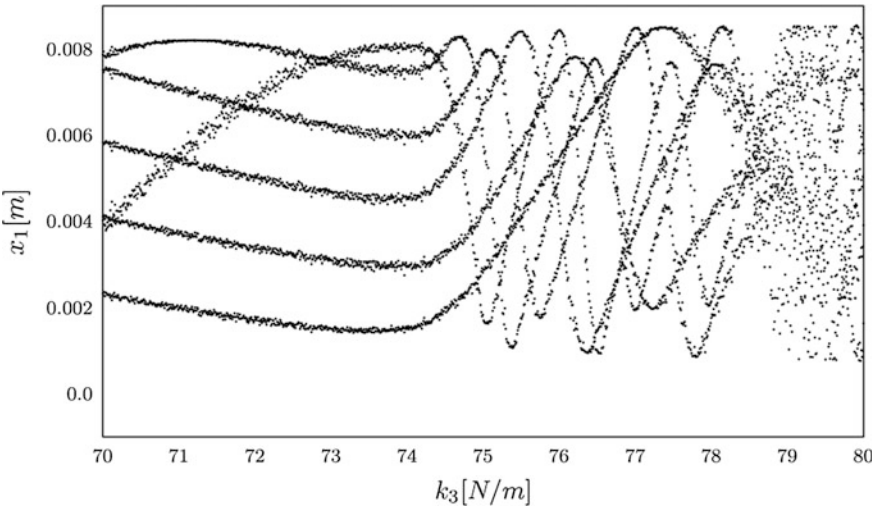

Fig. 8 Bifurcation diagram of simplified model with respect to the parameter k_3 ranging from 70 to 80

For this range of bifurcation parameter, the impact of the feedback between the oscillating mass and the drive system is clearly visible. The full model indicates a much longer interval of chaotic motion with a bigger spread of possible stick-phase points. Interestingly enough both models demonstrate an outgoing transition from chaos for nearly the same value of the bifurcation parameter $k_3 \approx 95.3$ [N/m].

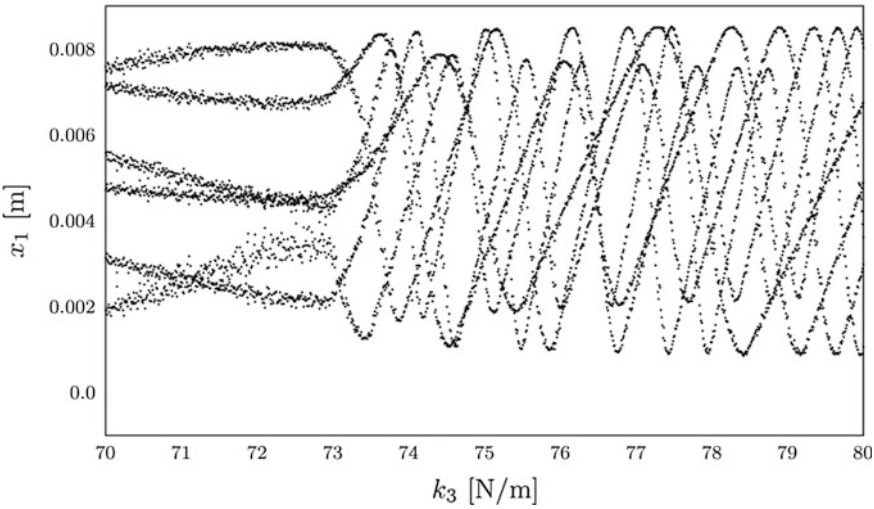

Fig. 9 Bifurcation diagram of full model with respect to the parameter k_3 ranging from 70 to 80

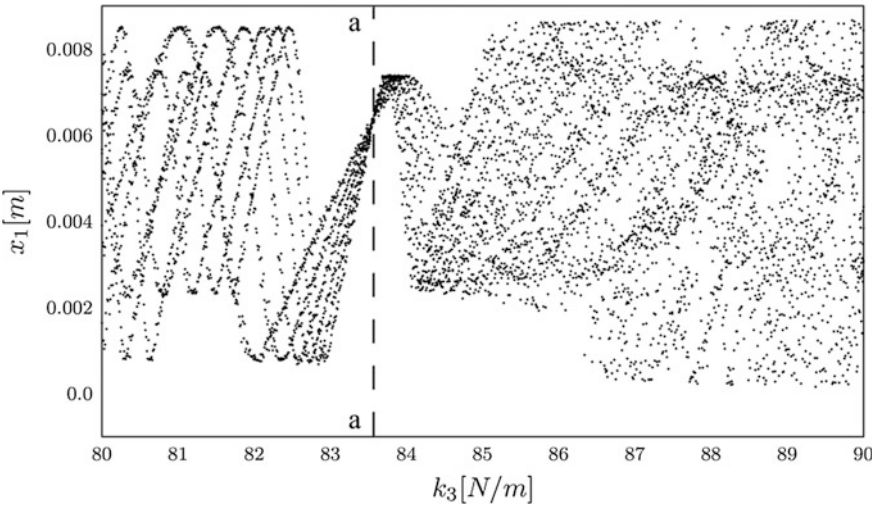

Fig. 10 Bifurcation diagram of simplified model with respect to the parameter k_3 ranging from 70 to 80. *Dashed line* "a–a" marks the synchronisation point

Here, in Figs. 8 and 9, the change in frequency of oscillations of the presented bifurcation branches can be observed right after the point, at which the pitchfork bifurcations occur.

Whenever the lines seen in Figs. 10 and 11 meet each other, we can speak about the synchronisation of displacements of the pulley and the block. It can be observed

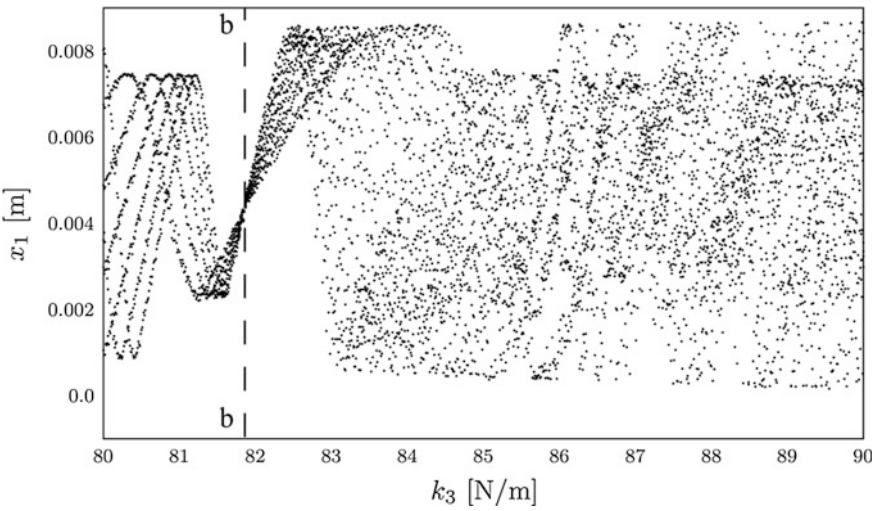

Fig. 11 Bifurcation diagram of full model with respect to the parameter k_3 ranging from 80 to 90. *Dashed line* "b–b" marks the synchronisation point

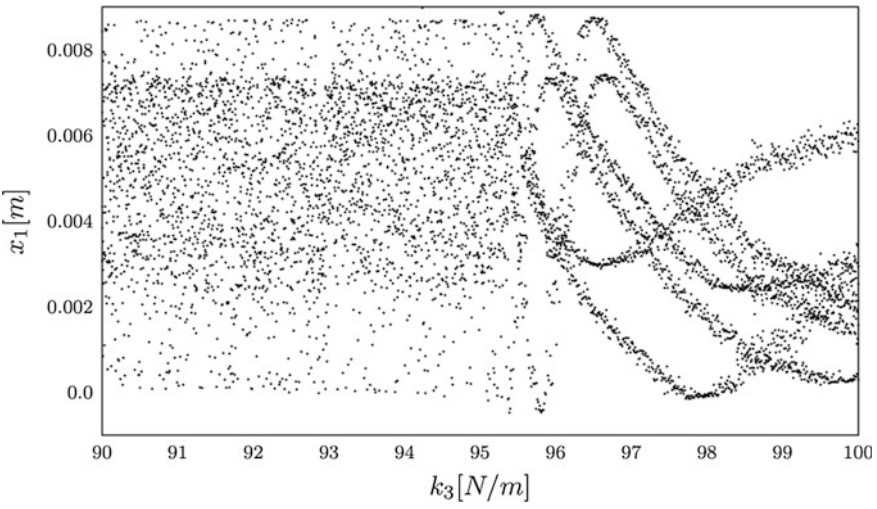

Fig. 12 Bifurcation diagram of simplified model with respect to the parameter k_3 ranging from 90 to 100

that transition into chaos also can be determined. The range of bifurcation parameter for which no lines can be distinguished closely resemble the periods of chaotic movement. An outgoing transition from chaos is also clearly visible in Figs. 12 and 13.

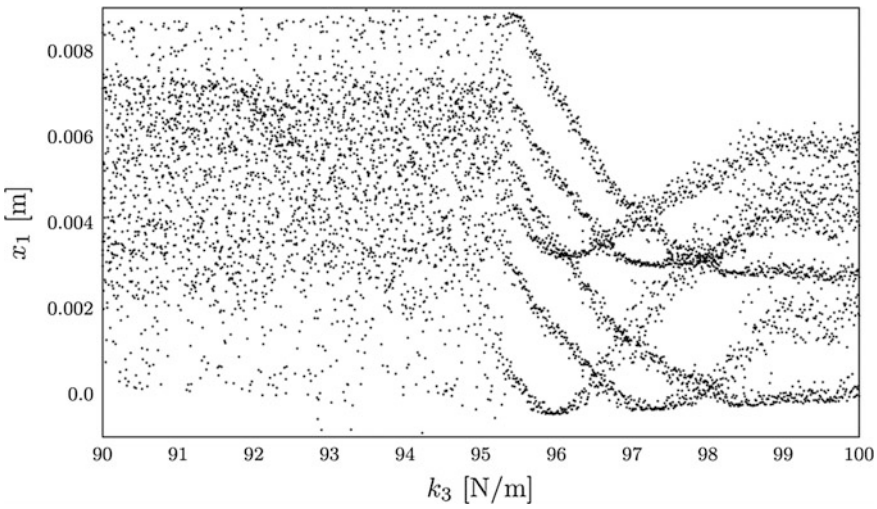

Fig. 13 Bifurcation diagram of full model with respect to the parameter k_3 ranging from 90 to 100

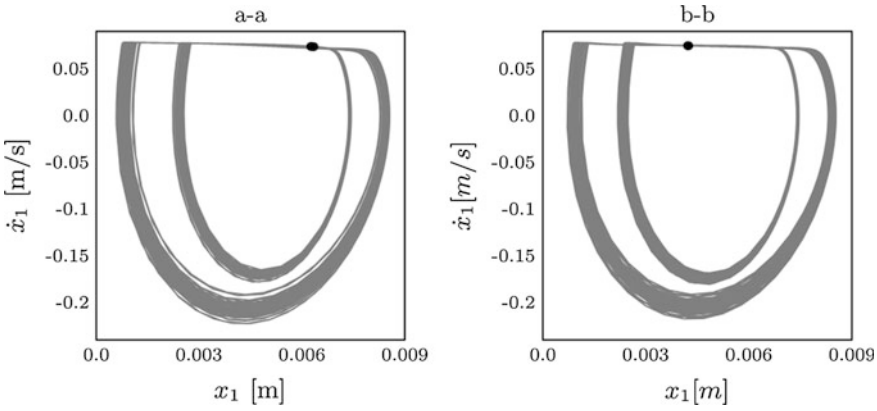

Fig. 14 Phase-space diagrams for the synchronisation points marked by *lines* "a–a" and "b–b" in Figs. 4, 5, 10 and 11

Figures 4, 5, 6 and 7 contain a number of measurements that do not represent the stick-phase points. Due to the nature of numeric simulations, conditions $V_{rel} = V_b$ and $\ddot{x_1} = 0$ are met only by defining a "window" for the values V_b and 0. Acceleration $\ddot{x_1}$ crosses 0 on a rising edge randomly during the stick phase of the motion. This is clearly visible in Figs. 4 and 5. For $x_1 > 0.005$, random clusters of point can be observed, which continue to occur on next two figures. It should be assumed that points above the threshold are not correctly estimated and do not represent any changes in dynamics of the motion.

In Fig. 14, a phase-space diagrams for the bifurcation parameter determined by the cross-sections “a–a” and “b–b” are presented. Black dots mark the points of Poincaré map while using the second method of generating of the presented bifurcation diagrams. As can be observed, all black dots overlap satisfactorily. They are acquired after each full rotation of the belt pulley. Therefore, a single point on the Poincaré map indicates synchronisation of dynamics of both coupled systems.

4 Conclusions

Influence of time varying excitation on the dynamics of 2-DoF mechanical system was tested. As can be observed, both investigated models behave similarly and return comparable changes in their dynamical behaviour. The only distinguishable differences are seen in the bigger spread of points on the Poincaré map in a case of the full model and visibly different values of bifurcation parameter when some changes occur.

The second method of generating bifurcation diagrams delivers interesting results. Six different curves can be noticed in Figs. 8 and 9. After appearance of first pitchfork type bifurcation their “frequency” increases. This clearly indicates a change in dynamics of the system, but does not allow for distinguishing the type of movement. The same scenario can be witnessed for transition into chaos. In that case, no longer any curves are observable. The main advantage of this approach of generating bifurcation diagrams is the ability to clearly indicate the points when a synchronisation of dynamics of the mass vibrating on the transmission belt and the belt pulley occurs. The synchronisation takes place when all of the curves coincide in single point.

Acknowledgments The work has been supported by the Polish National Science Centre, MAESTRO 2, No. 2012/04/A/ST8/00738.

References

1. Alzate, R., di Bernardo, M., Montanaro, U., Santini, S., Experimental and numerical verification of bifurcations and chaos in cam-follower impacting systems, Nonlinear Dynamics 50, 2007, pp 409–429.
2. Luo, G.W., Period-doubling bifurcations and routes to chaos of the vibratory systems contacting stops, Physics Letters A 323, 2004, pp 210–217.
3. Mann, B.P., Bayly, P.V., Davies, M.A., Halley, J.E., Limit cycles, bifurcations, and accuracy of the milling process, Journal of Sound and Vibration 277, 2004, pp 31–48.
4. Oberst, S., Lai, J.C.S., Numerical study of friction-induced pad-mode instability in disc brake squeal, Proceedings of 20th International Congress on Acoustics, ICA 2010, 23–27 August 2010, Sydney, Australia, 12 p.

5. Piiroinen, P.T., Virgin, L.N., Champneys, A.R., Chaos and Period-Adding: Experimental and Numerical Verification of the Grazing Bifurcation, Journal of Nonlinear Science, Vol. 14, 2004, pp. 383–404.
6. Saha, A., Bhattacharya, B., Wahi, P., A comparative study on the control of friction-driven oscillations by time-delayed feedback, Nonlinear Dynamics 60(1), 2010, pp 15–37.
7. Saha, A., Wiercigroch, M., Jankowski, K., Wahi, P., Stefański, A., Investigation of two different friction models from the perspective of friction-induced vibrations, Tribology International 90, 2015, pp 185–197.
8. Vahid, O., Eslaminasab, N., Golnaraghi, M.F., Friction-induced vibration in lead screw systems: Mathematical modeling and experimental studies, Journal of Vibration and Acoustics 131(2), 2009, 10 p, doi:10.1115/1.3025837.
9. Wang, X.J., Han, W.X., Cui, X., Li, S.Z., Du, C.Z., "Research on the motor friction model of electro-hydraulic servo system", Key Engineering Materials 579–580, 2013, pp. 594–597.
10. Zimmermann, K., Zeidis, I., Behn, C., Mechanics of Terrestrial Locomotion: With a Focus on Non-pedal Motion Systems, Springer, Berlin, Heidelberg, 2009.
11. Ueta, T., Tamura, A., Bifurcation analysis of a simple 3D oscillator and chaos synchronization of its coupled systems, Chaos, Solitons & Fractals 45, 2012, pp 1460–1468.
12. Misra, J.C., Mitra, A., Instabilities in single-species and host-parasite systems: Period-doubling bifurcations and chaos, Computers and Mathematics with Applications 52, 2006, pp 525–538.
13. Awrejcewicz, J., Olejnik, P., Friction pair modeling by 2-dof system: numerical and experimental investigations, Int. J. Bif. & Chaos, 15(6), 2005, pp 1931–1944.
14. Awrejcewicz, J., Olejnik, P., Occurrence of stick-slip phenomenon, Journal of Theoretical and Applied Mechanics, 45(1), 2007, pp 33–40.
15. Awrejcewicz, J., Olejnik, P., Numerical and experimental investigations of simple nonlinear system modeling a girling duo-servo brake mechanism, International Design Engineering Technical Conferences and Computers and Information in Engineering Conference ASME (DETC), September 2–6, 2003, Chicago, USA, pp 1491–1497.
16. Kunikowski, W., Awrejcewicz, J., Olejnik, P., Efficiency of a PLC-based PI controller in stabilization of a rotational motion affected by the chaotic disturbances, Dynamical Systems–Applications, Eds. J. Awrejcewicz, M. Kaźmierczak, P. Olejnik, J. Mrozowski, Publishing House of Lodz University of Technology, 2013, pp 173–184.
17. Pilipchuk, V., Olejnik, P., Awrejcewicz, J., Transient friction-induced vibrations in a 2-DOF model of brakes, Journal of Sound and Vibration, Elsevier, 344, 2015, pp 297–312.

An Analysis of the 1/2 Superharmonic Contact Resonance

Robert Kostek

Abstract This paper presents a study of non-linear normal contact vibrations, excited by an external harmonic force, in a system containing two bodies being in a planar contact; the system models, for instance the positioning systems. The contact vibrations are associated with strongly non-linear phenomena like: asymmetry of vibrations, loss of contact, bending resonance peak, multistability, period-doubling bifurcations, chaotic vibrations, chaotic transient; which are observed for the ½ superharmonic resonance. The main aim of this article is presentation evolution of the ½ superharmonic contact resonance under various excitation amplitudes. These vibrations change from periodic to chaotic motion, and then the ½ superharmonic resonance divides into two separate parts.

1 Introduction

Contact phenomena, which take place between solid bodies, influence behaviour of many mechanical systems, thus certain models of contact are applied for instance in: finite element method (FEM), discrete element method (DEM), and multibody systems (MBS) [3]. Contact phenomena influence for example stiffens of machines, which refers particularly to precision machines; because guideways are the most flexible in normal direction under low contact pressure. The contact deflections can be even larger than the distortion of machine parts, hence certain machine parts can be modelled as rigid bodies [8]. In this case, springs and dampers model contact interfaces. Characteristic of rough contact loaded in the normal direction is non-linear and progressive, thus the contact vibrations are non-linear and asymmetrical. Most of the articles describing contact resonances are focused on the primary resonance, whereas some describe the superharmonic contact resonances [1, 4–6, 9, 11, 12]. In spite of the fact that many articles present study of contact

R. Kostek (✉)
Faculty of Mechanical Engineering, University of Technology and Life Sciences in Bydgoszcz, 7 Al. Prof. S.Kaliskiego, 85-796 Bydgoszcz, Poland
e-mail: robertkostek@o2.pl

© Springer International Publishing Switzerland 2016

J. Awrejcewicz (ed.), *Dynamical Systems: Theoretical and Experimental Analysis*, Springer Proceedings in Mathematics & Statistics 182, DOI 10.1007/978-3-319-42408-8_17

vibrations, the evolution of the ½ superharmonic contact resonance from periodic to chaotic vibrations is not described in literature known to author. In consequence, process of dividing of the ½ superharmonic resonance to two separate parts is not well described. Thus, these two phenomena are described in this article.

2 Mathematical Model

The system contains two rigid bodies being in a planar contact; which are the slider resting on the massive slideway (fixed base) (Fig. 1a). Whereas, the planar contact of rough surfaces is modelled with non-linear springs and dampers, which represent interacting roughness asperities (Fig. 1b). After homogenisation contact is modelled with one non-linear spring and damper (Fig. 1c). In consequence, the studied model can be considered mass–spring–damper system, which has one degree of freedom in normal direction. Therefore, normal contact vibrations can be studied. The displacement of the slider y is determined in the coordinate Y with respect to the sideway. The coordinate is pointing downward, and its origin is fixed on the level where the contact deflection δ begins (Fig. 1c, d). The static contact deflection due to the weight of the slider is the equilibrium position $\delta_0 = y_0$, which is an important parameter.

Four forces act on the slider, they are: the terrestrial gravity force Q, spring force F_s, damping force F_d, and exciting harmonic force P. The forces are described by the following equations:

$$Q = M\,g, \tag{1}$$

$$\text{if } (y>0) \text{ then } F_s = -S\,c_n y^{m2};\ \delta = y;\ \text{else } F_s = 0;\ \delta = 0; \tag{2}$$

$$\text{if } (y>0) \text{ then } F_d = -S\,h_n \dot{y}\,y^{l};\ \text{else } F_d = 0; \tag{3}$$

$$P = P_a \cos(2\pi f_e t), \tag{4}$$

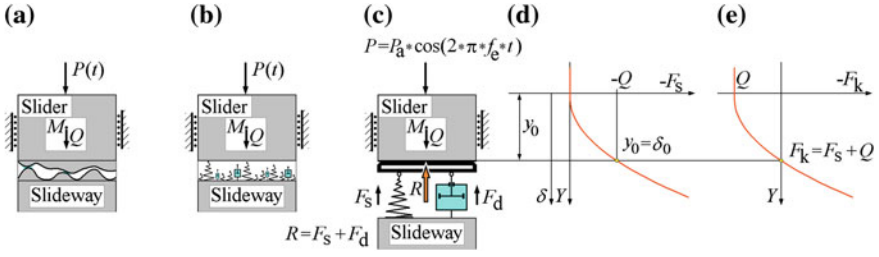

Fig. 1 Scheme of the studied dynamical system (**a**), and its physical models (**b**, **c**), characteristic of the spring force F_s (**d**), characteristic of the conservative force F_k (**e**)

where Q denotes the terrestrial gravity force, M—the mass of the slider $M = 0.2106$ kg, g—is the acceleration of gravity $g = 9.81$ m/s^2, F_s—the spring force, F_d—is the damping force, S—the nominal (apparent) contact area, δ—the normal contact deflection, whereas c_n, m_2, h_n, and l are parameters of the contact interface, P—the exciting harmonic force, P_a—amplitude of the exciting force, f_e—frequency of excitation, t—denotes time, and $\dot{y}$—the first time derivative $\dot{y} = dx/dt$. The contact parameters used to simulation have been identified from experimental results obtained for a planar rough surfaces contact; $S = 0.0009$ m^2, $c_n = 4.52\text{E}16$ N/m^4, $m_2 = 2$, $h_n = 3.5\text{E}11$ Ns/m^4, $l = 1$.

Sum of the spring force F_s and the damping force F_d is the contact force $R = F_s + F_d$ (Fig. 1c) [2]; whereas, sum of the spring force F_s and the terrestrial gravity force Q is the conservative force $F_k = F_s + Q$ (Fig. 1e). Graph of the conservative force is non-linear and asymmetrical, because graph of the spring force is non-linear and asymmetrical (Fig. 1d, e). Hence, normal contact vibrations are non-linear and asymmetrical. These vibrations are described by the following non-linear differential equation:

$$\ddot{y} = (Q + F_s(y) + F_d(y, \dot{y}) + P(t))/\mathrm{M}, \tag{5}$$

where $\ddot{y}$ is acceleration—$\ddot{y} = d^2x/dt^2$. This equation was solved with direct numerical methods, because the contact force R is non-linear.

During contact vibrations loss of contact ($y < 0$) can be observed. At this period the contact force R does not act on the slider, thus the exact solution can be found. This provides an opportunity to reduce time of computations and numerical errors, because the exact solution can be used. Whereas, the second period of contact vibrations is the period of contact between these two bodies ($y > 0$). If the contact force R is linear, then the exact solution can be found as well, otherwise numerical methods are used. This switching between contact and non-contact can be problem, which is described below. The time history of acceleration is a continuous function, but higher-order derivatives of acceleration are discontinuous functions. Thus the Runge effect can be observed for numerical methods based on higher degree polynomials. The first solution is to use low order methods, which are not sensitive to the Runge effect, for example direct Newmark methods. In this case, time step should be very small to obtain small numerical error. The second solution is to use direct methods based on Hermite polynomials. These methods are less computationally expensive than the fourth-order classical Runge–Kutta method. Moreover, are not sensitive to the Runge effect, because Hermite polynomials are not sensitive to this effect. The third method is to find the time instance when $y = 0$. The direct method based on Taylor series and methods based on Hermite polynomials can be used to find this time instance. Then the time step can be changed or divided into two smaller steps, to precisely separate contact and non-contact periods and solutions. This approach provides an opportunity to avoid problems associated with discontinuous derivatives and obtain small numerical error.

3 Evolution of the ½ Super Harmonic Resonance

If amplitude of the exciting force tends to zero, then contact resonance is linear; otherwise, phenomena typical for non-linear vibrations appears. First, the natural frequency of this system decreases with increase of vibration amplitude, thus the primary resonance peak bends to lower frequencies; which in turn introduces bistability. Then, apart from the primary resonance, the superharmonic resonances are excited. Amplitude of the ½ superharmonic resonance is growing, and its peak bends; which introduces multistability. After that, others superharmonic resonances are excited, and their peaks bends. Finally, the ½ superharmonic resonance is divided into two separate parts, which is described in this article (Fig. 2).

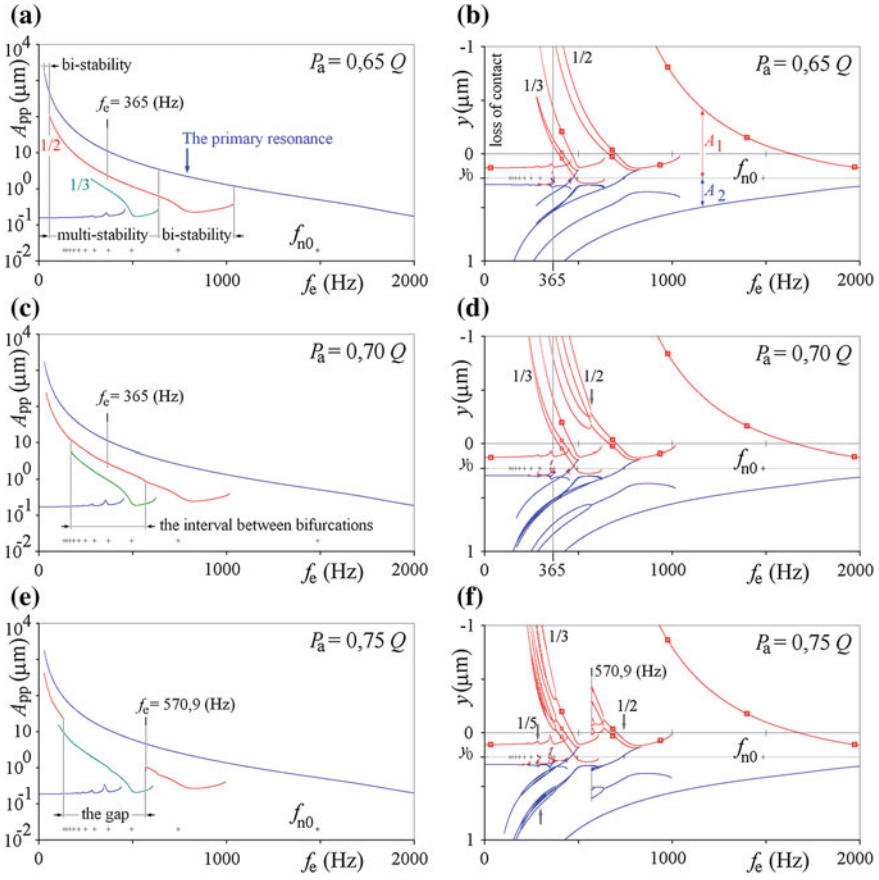

Fig. 2 Graphs of the contact resonances; peak-to-peak amplitude $A_{pp} = y_{max}$-y_{min}, against the frequency of excitation f_e (**a**, **c**, **e**); plus signs (+) represent resonant frequencies $f_e \approx f_{n0}/m$ (Eq. 6). And local extrema of time histories against the frequency of excitation f_e; (square, *red* line—minima, *blue* line—maxima) (**b**, **d**, **f**) [6]

If, frequency of the mth harmonic is near the natural frequency then its amplitude is amplified, which reveals nature of superharmonic resonances [13]. Hence the resonant frequencies are described by the following formula:

$$f_e \approx f_{n0}/m, \tag{6}$$

where: f_e—is excitation frequency, which excite the $1/m$ superharmonic resonance, f_{n0}—the natural frequency, whereas m—a natural number. Consequently, the ½ superharmonic resonance is excited near half of the natural frequency, and amplitude of the second harmonic is amplified.

The primary resonance and superharmonic resonances are depicted in Fig. 2. These figures present evolution of the contact resonances due to increase of the excitation amplitude. The contact resonances can be depicted in various ways. The first way is to present peak-to-peak amplitude in a logarithmic scale versus excitation frequency f_e (Fig. 2a, c, e); this provides an opportunity to present large amplitudes of resonances, bistability and multistability. Whereas the second method is to present local extrema of time histories versus excitation frequency f_e (Fig. 2b, d, f); which provides an opportunity to present: bistability, multistability, bifurcations, loss of contact, and asymerty of vibration. Two various amplitudes of vibrations—up A_1 and down A_2—from the equilibrium position are presented in Fig. 2b. This shows that a notion of amplitude should be precisely defined for non-linear vibrations.

For the excitation amplitude being $P_a = 0.65Q$, peaks of the primary and two superharmonic resonances bend, thus bistability and multistability are visible in Fig. 2a, b. Let analyse vibrations of the ½ superharmonic resonance excited with frequency being $f_e = 365$ Hz. Four extrema are observed over one vibration period in Fig. 3a, thus four curves represent the ½ superharmonic resonance in Fig. 2b. These vibrations are asymmetrical to the equilibrium position y_0, and loss of contact is visible. Furthermore, these vibrations are multi-harmonic, hence phase portrait has sophisticated shape (Fig. 3b). Besides the orbit point circumnavigates the origin twice. Which reveal complex nature of these vibrations. Period of this vibrations equals excitation period, hence Poincaré section contains one point (Fig. 3b).

Next, for the excitation amplitude being $P_a = 0.70Q$ two opposing period-doubling bifurcations appear at the ½ superharmonic resonance. They create a loop in Fig. 6b, which is called incomplete period-doubling cascade [13]. One of these bifurcations is visible in Fig. 2d, whereas second is not, because vibration amplitude is large. The interval between these two bifurcations is depicted in Fig. 2c. Eight lines represent this resonance within interval between these two bifurcations in Fig. 2d, because period of vibration is doubled, and eight extrema are observed over one vibration period (see Fig. 4a). Accordingly, the orbit point circumnavigates the origin four times over one vibration period, a subharmonic frequency appears ($f_e/2$), and Poincaré section contains two points (see Fig. 4b). Which show complex nature of contact vibrations.

After that, for the excitation amplitude being $P_a = 0.75Q$, farther increase of vibration amplitude is observed, hence more superharmonic resonances are visible

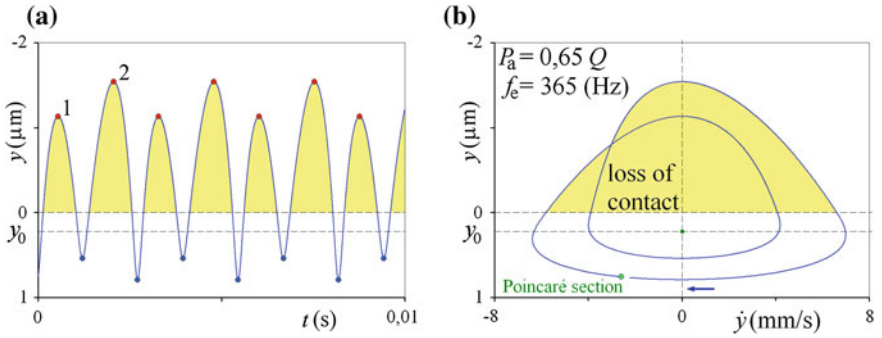

Fig. 3 Time history of displacement (**a**), and phase portrait with Poincaré section (**b**), of the ½ superharmonic resonance vibrations, excited by a harmonic force of the parameters—$P_a = 0.65Q$, $f_e = 365$ Hz; two local minima are observed over one vibration period

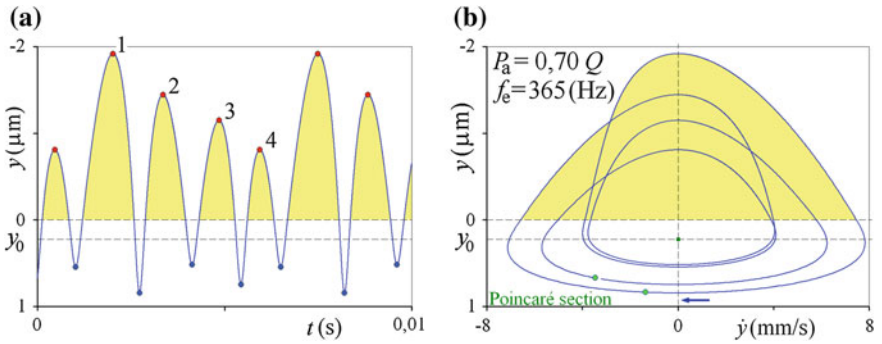

Fig. 4 Time history of displacement (**a**), and phase portrait with Poincaré section (**b**), of the ½ superharmonic resonance vibrations after first period-doubling bifurcation, excited by a harmonic force of the parameters—$P_a = 0.70Q$, $f_e = 365$ Hz; four local minima are observed over one vibration period

in Fig. 2f. Besides, incomplete period-doubling cascade is observed at the 1/3 superharmonic resonance, which is separate issue. Moreover, two opposing cascades of bifurcations leading to chaos appear at the ½ superharmonic resonance (Figs. 2e, f and 9). These cascades divide the branch of ½ superharmonic resonance into two separate parts, hence special procedure should be used to find this part near 100 Hz. A farther increase of the excitation amplitude makes this gap between these two parts of the ½ superharmonic resonance larger [7].

The evolution of the ½ superharmonic resonance from periodic to chaotic vibrations, is studied below. The evolution is depicted in a bifurcation diagram (Fig. 5a), which presents a cascade of bifurcations leading to chaos. This bifurcation diagram is obtained at a constant frequency of excitation, being $f_e = 365$ Hz, and for various amplitudes of the excitation force. Certain amplitudes of excitations are indicated in the diagrams with vertical lines.

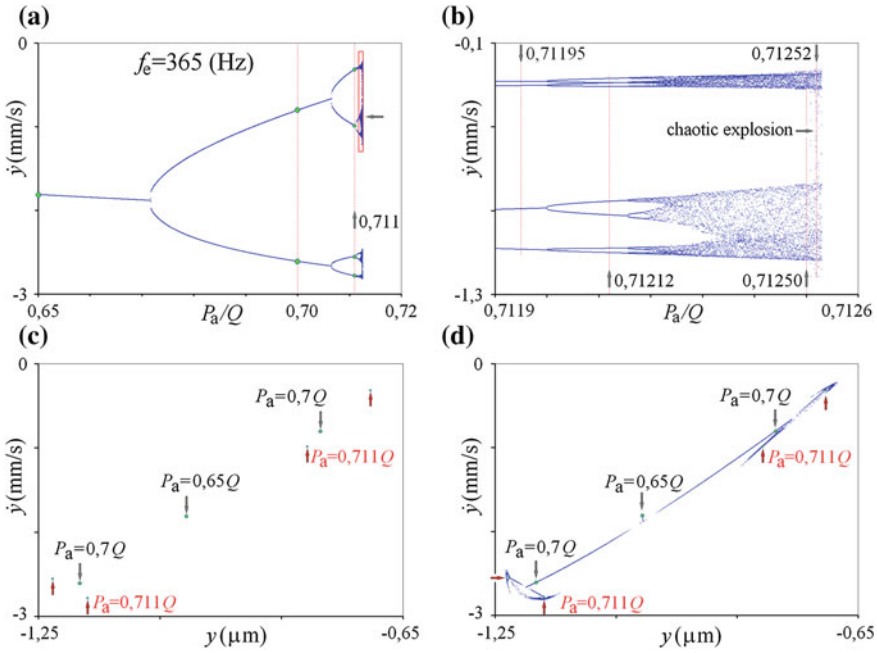

Fig. 5 Bifurcation diagram (**a**, **b**) and Poincaré sections (**c**, **d**) obtained for the ½ superharmonic resonance, excited at constant frequency of excitation f_e = 365 Hz

First, periodic vibrations, which period equals the excitation period, are observed for an excitation amplitude being $P_a = 0.65Q$ (Fig. 3). Thus, a single line represents these vibrations in Fig. 5a, and Poincaré section contains one point (Figs. 3b and 5c). Then, the first period-doubling bifurcation appears; hence, for an amplitude of excitation being $P_a = 0.70Q$ the vibration period is doubled. Consequently two curves represent these vibrations in Fig. 5a, and Poincaré section contains two points (Figs. 4b and 5c). Next, the vibration period is doubled once again. And therefore, for an amplitude of excitation being $P_a = 0.711Q$, the vibration period is four times longer than the excitation period, four curves represent these vibrations in Fig. 5a, and Poincaré section contains four points (Fig. 5c). The following bifurcations are difficult to find in Fig. 5a, thus the structure bounded by the box is magnified in Fig. 5b. Then, for the excitation amplitude being $P_a = 0.71195Q$, the period of vibrations is eight times longer than the period of excitation, which is a result of a next period-doubling bifurcation. After that, for an amplitude of excitation being $P_a = 0.71212Q$, the period of vibrations is 16 times longer than the period of excitation (Fig. 5b). Accordingly, the period-doubling cascade makes the period of vibrations longer and longer. Last, chaotic vibrations are obtained for the excitation amplitude being $P_a = 0.7125Q$. And finally, a chaotic explosion is visible [13]; hence, for the excitation amplitude being $P_a = 0.71252Q$, points between these two branches are visible in Fig. 5b. Summarising this, the presented

description clearly shows the consecutive stages of evolution from periodic vibrations, in which the period equals the period of excitation, through stable vibrations, which period is 2, 4, 8 and 16 (2^1, 2^2,…) times longer than the excitation period, to chaotic vibrations. The evolution from periodic to chaotic vibrations is depicted in Fig. 5d as well. This figure shows consecutive Poincaré sections.

The presented description should be complemented by bifurcation diagrams obtained for any constant excitation amplitude and various excitation frequencies (Figs. 6, 7 and 9); they can be considered cross sections. These diagrams show an influence of the excitation frequency, and the following excitation amplitudes, on vibrations of the ½ superharmonic resonance. These diagrams are integral to and with the diagram presented in Fig. 5, thus excitation frequency $f_e = 365$ Hz is indicated in these diagrams with vertical line. First, vibrations excited by the external force of an amplitude being $P_a = 0.65Q$ are studied. The vibrations are periodic, and their period equals the period of excitation (see Fig. 3). Hence, a single line represents these vibrations in Fig. 6a. These vibrations are presented in Fig. 2a, b as well. Then, vibrations excited by the external force of an amplitude being $P_a = 0.70Q$ are analysed. The two opposing period-doubling bifurcations, which generate a closed loop (a bubble), are visible in Fig. 6b. This is the so-called incomplete period-doubling cascade. Hence, between these two opposing bifurcations, the period of vibrations is doubled (Figs. 4 and 5a). One of the period-doubling bifurcations is visible in Fig. 2d. Next, the further evolution of the incomplete period-doubling cascade is visible in Fig. 6c, d, e. The observed periods of vibrations equal the period of excitation, or are two, four, eight or sixteen times longer than the period of excitation. The period of vibrations, which are excited at a frequency of excitation being $f_e = 365$ Hz, and for an excitation amplitude being $P_a = 0.711Q$, is four times longer than the period of excitation (Fig. 6c); thus four curves are visible. In the same way, the period of vibrations, excited at the same frequency of excitation, but for an excitation amplitude being $P_a = 0.71195Q$, becomes eight times longer than the period of excitation (Fig. 6d). Then, the period of vibrations, excited by the external force, of the frequency $f_e = 365$ Hz and amplitude $P_a = 0.71212Q$, is 16 times longer than the period of excitation (Fig. 6e). Accordingly, a number of loops and opposing period-doubling bifurcations are visible in Fig. 6b, c, d, e. The numbers of loops and period-doubling bifurcations become larger with an increase of the excitation amplitude. Therefore, shapes of the incomplete period-doubling cascades become more complex (Fig. 6b, c, d, e).

After that, two opposing period-doubling cascades leading to chaos are visible in Fig. 6f. Therefore, the vibrations excited by the external force, of the frequency $f_e = 365$ Hz and amplitude $P_a = 0.7125Q$, are chaotic (Fig. 5b). Chaotic vibrations are not periodic, they are sensitive to initial conditions, and are difficult to predict (the butterfly effect). In this case, the "chaotic part" of these vibrations is small, compared with the amplitude of vibrations, which is a characteristic feature. It is called "noisy periodicity" [13]. For this excitation amplitude, a sweeping signal

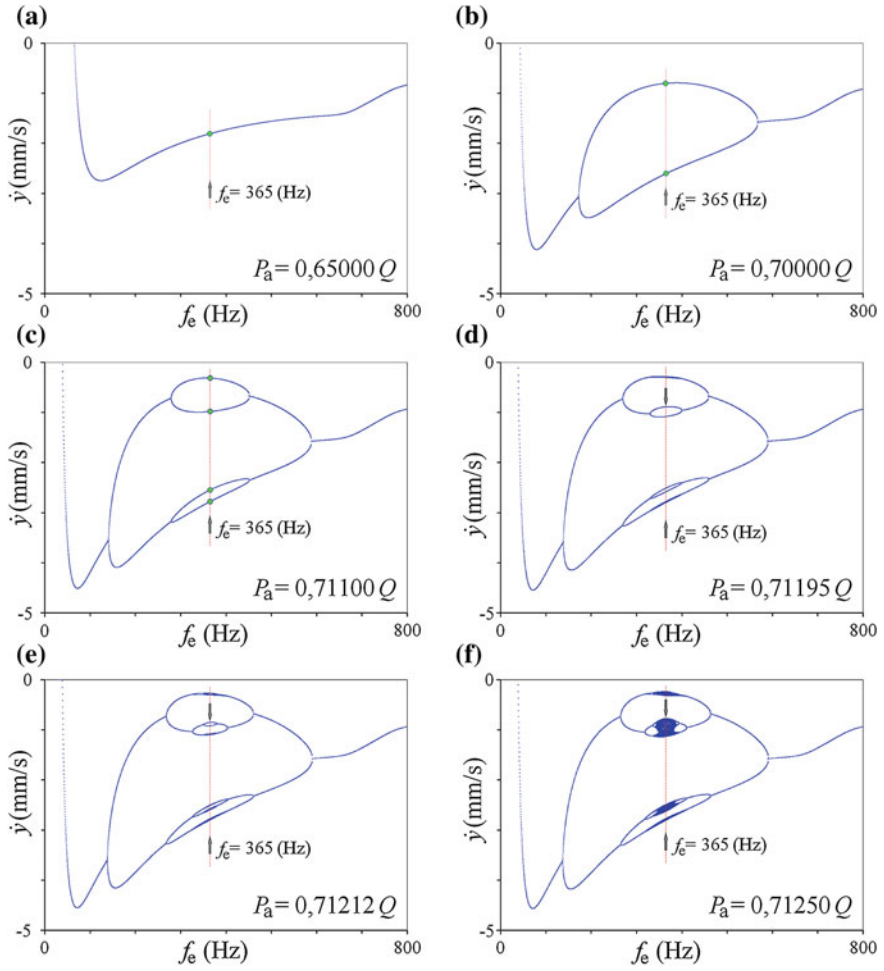

Fig. 6 The bifurcation diagrams of the ½ superharmonic resonance; evolution from periodic vibrations which period equals excitation period (**a**), via incomplete period-doubling cascades (**b**–**e**), to two opposing period-doubling cascades leading to chaos (**f**)

gives an opportunity to go from periodic vibrations, through the chaotic vibrations, again to the periodic vibrations. That means, that the ½ superharmonic resonance is not divided into two parts.

Finally, vibrations excited by the external force of an amplitude being $P_a = 0.71252Q$, are studied (Fig. 7). Their bifurcation diagram depicted in Fig. 7a is similar to one previously presented in Fig. 6f. However these parts, where chaotic vibrations appear, are various, because points are observed between the branches of bifurcations in Fig. 7 (chaotic explosion). These points are observed in Fig. 5b as well. The structure bounded by the box in Fig. 7a is magnified in Fig. 7b, which

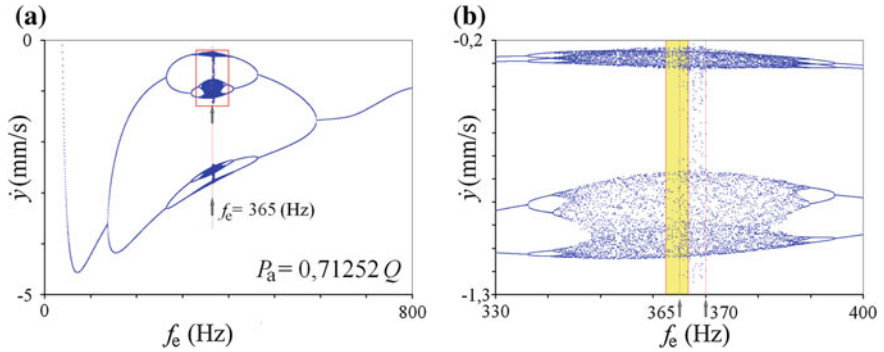

Fig. 7 Bifurcation diagram of the ½ superharmonic resonance; two opposing period-doubling cascades leading to chaos, obtained at a constant amplitude of excitation $P_a = 0.71252$ (**a**), magnification of the structure bounded by the box (**b**)

provides valid information. Two opposing period-doubling cascades leading to chaos are visible near the left and right edges of this diagram, whereas in the middle part chaotic vibrations appear. In this case, the ½ superharmonic resonance is divided into separate parts. Hence, a sweeping signal gives an opportunity to calculate solutions, except these in the middle part, marked in yellow. Because in this area, at certain excitation frequencies, the ½ superharmonic resonance does not exist, its attractor is destroyed; therefore, other vibrations are excited. In consequence, the separate solutions corresponding to the ½ superharmonic resonance have been found, with a special numerical procedure.

The chaotic vibrations excited by the external force, of the frequency $f_e = 370$ Hz and amplitude $P_a = 0.71252$Q are depicted in Figs. 7b and 8. In contrast to the periodic vibrations their phase portrait is not a closed loop, it has a shape of a "ribbon" (see the red line in Fig. 8a). The "chaotic part" of these vibrations is small, compared with the amplitude of vibrations; thus the Poincaré section is relatively small compared with the phase portrait (see the blue (black) points in Fig. 8a). The Poincaré section has a complex shape, which first seems to be two curves; but after magnification these two "lines" contains a few more "lines" (see Fig. 8b). The further magnifications of the structures bounded by the boxes (Fig. 8b, c, d) reveal that, the Poincaré section is self-similar. The self-similarity is the basis for the definition of fractal structures, which leads to conclusion, that the studied vibrations are chaotic. Moreover, the attractor is "leaky", therefore after thousands of excitation periods "by chance", the orbit point leaves this non-attracting chaotic set; thus, other vibrations are excited. This phenomenon is the so-called chaotic transient. The chaotic transient is a result of a boundary crisis, which destroy chaotic attractors. More information about these phenomena has been described in literature, see e.g. [10].

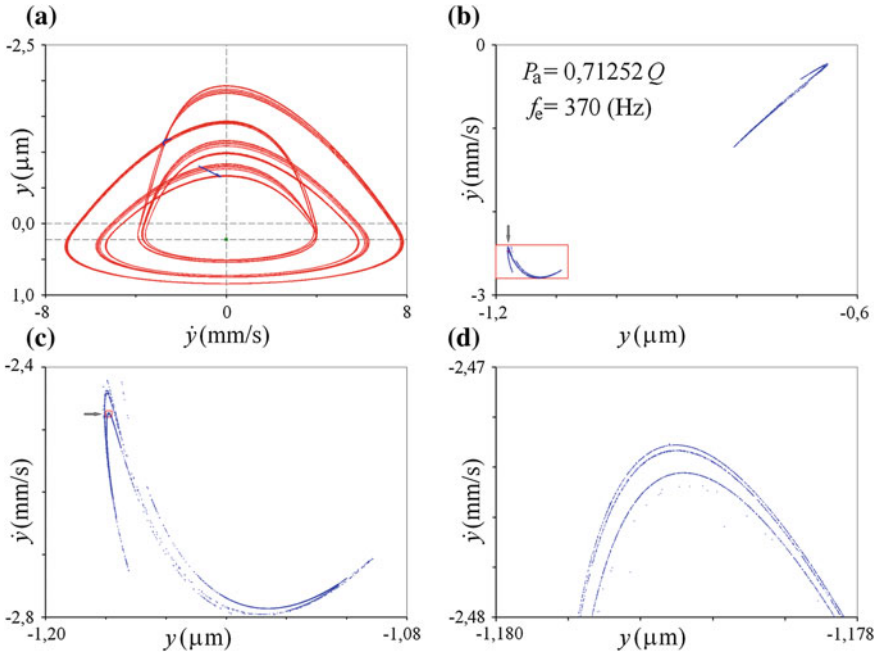

Fig. 8 Phase portrait (*red line* (*grey*)) (**a**), and Poincaré section (*blue* points (*black*)) (**a**, **b**, **c**, **d**), of chaotic vibrations of the ½ superharmonic resonance, excited by a harmonic force of the parameters—P_a = 0.71252Q, f_e = 370 Hz; sequence of magnifications of the structure bounded by boxes (**c**, **d**)

The last stage, of the studied evolution is a complete separation of these two parts of the ½ superharmonic resonance. This can be observed for the excitation amplitude being $P_a = 0.75Q$ (Figs. 2e, f and 9). The gap between these two parts of the resonance is so large, that the bifurcation diagram is presented in two Fig. 9a, b. The bifurcation diagrams present two opposing period-doubling cascades leading to chaos. The structures bounded by the boxes are magnified in Fig. 9c, d, which provide valid information. The chaotic explosion is visible in Fig. 9c, while in Fig. 9d the explosion is not observed. The cascade of bifurcation presented in Fig. 9b is visible in Fig. 2f too.

The vibrations excited at the excitation frequency $f_e = 570.9$ Hz and amplitude $P_a = 0.75Q$ are chaotic (Figs. 2f and 9d), hence, their Poincaré section is self-similar. First, the section seems to be four curves (Fig. 10a); whereas the further magnifications of the structures bounded by the boxes (Fig. 10b, c, d) reveal that, the "lines" contain more and more "lines". Moreover, this attractor is not "leaky"; therefore the orbit point does not leave this attractor, and more points are depicted.

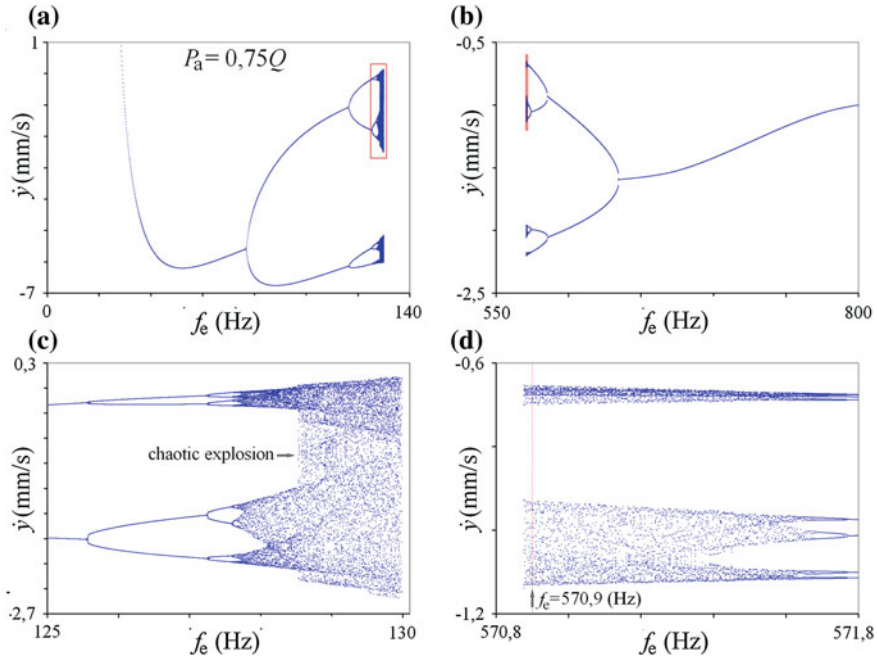

Fig. 9 Bifurcation diagrams (**a**, **b**) of the ½ superharmonic resonance, obtained at constant amplitude of excitation $P_a = 0.75Q$; magnifications of the structures bounded by boxes (**c**, **d**)

It should be mentioned that a Poincaré section is a section of the three-dimensional phase stream $(y, \dot{y}, t)$ obtained for the same phases of excitation force. Whereas a phase portrait is a projection of the three-dimensional phase stream, on two-dimensional space $(y, \dot{y})$. Then, bifurcation diagram contains a number of one-dimensional of the Poincaré sections.

Summarising, in this section phenomena coupled with strongly non-linear vibrations have been presented. They are incomplete period-doubling cascade, period-doubling cascade leading to chaos, chaotic vibrations, chaotic transients, and self-similarity of a Poincaré section, all of which show a complexity of contact vibrations and contact dynamics.

4 Conclusions

The contact flexibility influences dynamics precision machines, which refers for example to machine tools. Usually linear model of contact is used, hence non-linear effect are neglected. The following non-linear phenomena were found: asymmetry of vibrations, “gapping”, multi-harmonic motion, superharmonic resonances,

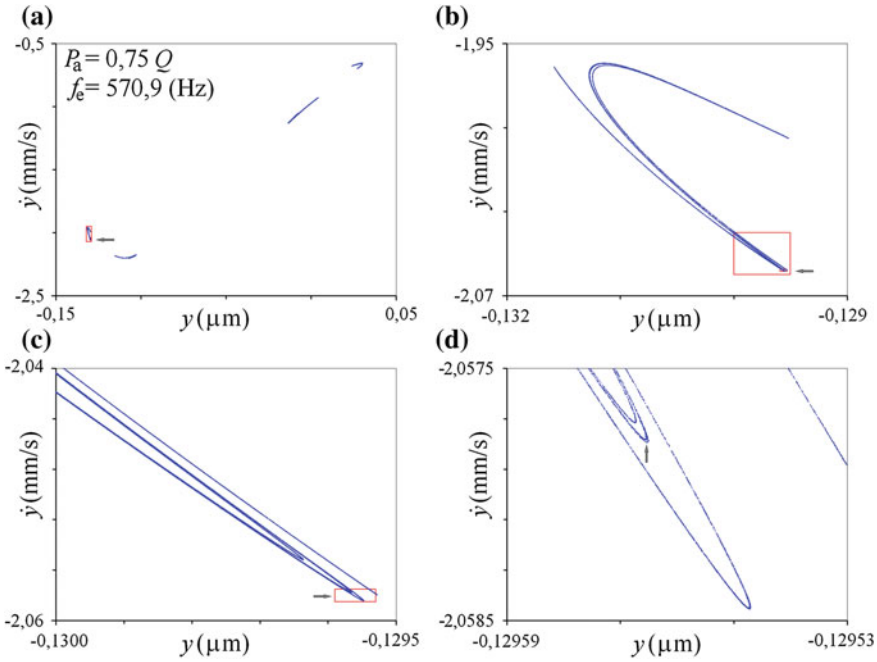

Fig. 10 Poincaré section (**a**) of chaotic vibrations of the ½ superharmonic resonance excited by a harmonic force of the parameters—$P_a = 0.75Q$, $f_e = 570.9$ Hz; sequence of magnifications of the structure bounded by boxes (**b**, **c**, **d**)

bending resonance peaks, multistability, incomplete period-doubling cascade, period-doubling cascades leading to chaos, chaotic motion, and chaotic transient, which reveals complex nature of normal contact vibrations. As is evident, non-linear models of contact, and non-linear dynamics should be used to analyse machine tools vibrations, and reduce machining errors. Moreover, non-linear models of contact can be implemented in control systems, to reduce machine tools vibrations. The contact resonances should be studied under a wide range of excitation signals to understand their evolution. This article is mainly focused on the evolution of the ½ superharmonic resonance due to increase of the excitation force amplitude. First, periodic vibrations are excited. Then, chaotic vibrations are observed. And finally, branch of the ½ superharmonic resonance is divided into two separate parts. Which summarises in short evolution of the ½ superharmonic resonance.

References

1. Grudziński, K., Kostek, R., An analysis of nonlinear normal contact microvibrations excited by a harmonic force, Nonlinear Dynamics 50, 2007, pp 809–815
2. Hunt, K.H., Crossley, F.R.E., Coefficient of restitution interpreted as damping in vibroimpact, ASME Journal of Applied Mechanics 42, 1975, pp 440–445
3. Kostek, R., The modelling of loading, unloading and reloading of the elastic-plastic contact of rough surfaces, JTAM 50, 2012, pp 509–530
4. Kostek, R., Analysis of the primary and the superharmonic contact resonances – Part 1, JTAM 51, 2013, pp 475–486
5. Kostek, R., An analysis of the primary and the superharmonic contact resonances – Part 2, JTAM 51, 2013, pp 687–696
6. Kostek, R., An analysis of the primary and the superharmonic contact resonances – Part 3, JTAM 51, 2013, pp 799–812
7. Kostek, R., https://www.youtube.com/watch?v=cNRU-TUXCao, 30 November 2012
8. Marchelek, K., Dynamika obrabiarek, WNT, Warszawa, 1974
9. Moradi, H., Bakhtiari-Nejad, F., Movahhedy, M.R., Ahmadian, M.T., Nonlinear behaviour of the regenerative chatter in turning process with a worn tool: Forced oscillation and stability analysis, Mechanism and Machine Theory 45, 2010, pp 1050–1066
10. Nusse, H.E., Yorke, J.A., Dynamics: Numerical Explorations, Springer, 1997
11. Perret-Liaudet, J., Superharmonic resonance of order two on a sphere-plane contact, Comptes Rendus de l'Académie des Sciences - Series IIB 326, 1998, pp 787–792
12. Perret-Liaudet, J., Rigad, E., Superharmonic resonance of order 2 for an impacting Hertzian contact oscillator: Theory and experiments, ASME Journal of Computational and Nonlinear Dynamics 2, 2007, pp 190–196
13. Thompson, J.M.T., Stewart, H.B., Nonlinear Dynamics and Chaos, Wiley, 2002

The Oscillator with Linear and Cubic Elastic Restoring Force and Quadratic Damping

V. Marinca and N. Herişanu

Abstract A novel analytic approximate technique, namely optimal variational method (OVM), is employed to propose an approach to solve some nonconservative nonlinear oscillators. Different from perturbation methods, the validity of the OVM is independent on whether or not there exist small physical parameters in the considered nonlinear equations. This procedure offers a promising approach by constructing a generalized Lagrangian and a generalized Hamiltonian for nonlinear oscillators. An excellent agreement has been found between the analytical results obtained by the proposed method and numerical integration results.

1 Introduction

The entire conventional theory of Lagrangian representation in the space of the generalized coordinates of conservative Newtonian systems subject to holonomic constrains is based on the often tacit assumption that constrains are frictionless. But in practice, holonomic constrains are realized by mechanical means. Therefore, the presence of frictional forces is inevitable whenever holonomic constrains occur and in turn, a Lagrangian representation that does not reflect this dissipative nature commonly is considered a first approximation of the system. For computing a Lagrangian for dynamical systems with more general Newtonian forces are nowadays applicable only to systems with force derivable from a potential function (basically conservative systems). But conservative systems do not exist in our

V. Marinca · N. Herişanu (✉)
University Politehnica Timişoara, Bd.Mihai Viteazu, Nr.1,
300222 Timişoara, Romania
e-mail: nicolae.herisanu@upt.ro

V. Marinca
e-mail: vasile.marinca@upt.ro

V. Marinca · N. Herişanu
Center for Advanced and Fundamental Technical Research, Romanian Academy,
Timisoara Branch, Bd. M.Viteazu, Nr.24, 300223 Timişoara, Romania

© Springer International Publishing Switzerland 2016

J. Awrejcewicz (ed.), *Dynamical Systems: Theoretical and Experimental Analysis*, Springer Proceedings in Mathematics & Statistics 182, DOI 10.1007/978-3-319-42408-8_18

Newtonian environment. In consequence, Lagrangian representation of conservative Newtonian systems is in general only a crude approximation of physical reality. The problem of the existence of a Lagrangian or Hamiltonian can be studied today with a variety of modern and sophisticated mathematical tools which include the use of functional analysis, prolongation theory, and differential geometry. This question is called as "Inverse problem in Newtonian Mechanics" and consists in the identifications of the methods for the construction of a Lagrangian or Hamiltonian from given equation of motion [1–3].

The aim of this paper is to construct approximations to periodic solutions and frequencies of nonlinear oscillators with linear and cubic elastic restoring force and quadratic damping. These oscillators are examples of nonconservative dynamical systems. Such systems with linear and cubic elastic restoring force and quadratic damping appropriately describe those real systems for which the damping of the oscillations is produced by a turbulent liquid flow inside the damper. A typical example of an oscillator with quadratic damping is the suspension of a vehicle equipped with hydraulic shock absorbers. Suspensions with nonlinear elastic and damping characteristics are frequently utilized, because nonlinearity limits displacements and velocity reduces the extreme values of the acceleration and leads to a more uniform dynamic loading of the suspensions. The damping nonlinearity is usually achieved by using hydraulic or hydropneumatic shock absorbers. If v is the velocity of the sprung mass, for small values of v, the flow of the oil in the shock absorber is laminar and the damping characteristic is linear. As v increases, the flow becomes turbulent and the characteristic takes a parabolic form. When the velocity reaches a certain "critical" value, the pressure inside the shock absorber becomes large enough to bring about the opening of the relief valves, and this modifies the further dependence of the damping force on velocity [4]. Quadratic damping is a subject of interest for many scientists [5–9].

In this paper we consider a nonlinear oscillator with linear and cubic elastic restoring force and quadratic damping in the form

$$\ddot{u} + u + \alpha \dot{u}^2 + \beta u^3 = 0 \tag{1}$$

subject to initial conditions

$$u(0) = A, \quad \dot{u}(0) = 0 \tag{2}$$

where dot denotes derivative with respect to time and α, β, A are known constants, $A > 0$.

In the last few decades, considerable work has been invested in developing new methods for analytical and numerical solutions of strongly nonlinear oscillators, but it is still difficult to obtain convergent results in cases of strong nonlinearity. There is a great need for effective algorithms to avoid shortcomings of some traditional techniques. In this way, recently, many new approaches have been proposed for determining periodic solutions and frequencies to nonlinear oscillators by using a mixture of methodologies [10–20].

In what follows, we construct approximations to periodic solutions and frequencies of nonlinear oscillators by applying the optimal variational method. The most significant features of this new approach are the optimal control of the convergence of approximations and its excellent accuracy. Different from other methods, the validity of the OVM is independent on whether or not there exist small parameters in the considered nonlinear equations. Our procedure is very effective and this work demonstrates the validity and great potential of the OVM.

2 Basic Formulation of the OVM

In order to develop an application of the OVM, we consider the following differential equation of the nonlinear oscillations

$$f(t, u, \dot{u}, \ddot{u}) = 0 \tag{3}$$

with the initial conditions

$$u(0) = A, \quad \dot{u}(0) = 0, \; A > 0 \tag{4}$$

where f is a nonlinear function. In our procedure, f does not need to contain a small parameter.

Variational principle can be easily established if there exists a functional called the action functional or action for short:

$$J = \int_0^{T/2} L(t, u, \dot{u}) dt \tag{5}$$

where T is the period of the nonlinear oscillator, $T = 2\pi/\Omega$, and Ω is the frequency of the system (3), which admits as extremals the solutions of Eqs. (3) and (4) and L is the generalized Lagrangian of the system (3). On physical grounds, the primary significance of this principle rests on the fact that the acting forces of Newtonian system (3) need not necessarily be derivable from a potential.

We assume that the solutions of Eq. (3) can be expressed in the form

$$u(t) = C_1 + C_2 \cos \Omega t + C_3 \cos 2\Omega t + \cdots + C_{s+1} \cos s\Omega t \tag{6}$$

where $C_i, i = 1,2,\ldots,s + 1$ are arbitrary parameters at this moment and s is a positive integer number.

Substituting Eq. (6) into Eq. (5), it results in

$$J(C_1, C_2, \ldots, C_{s+1}, \Omega) = \int_0^{T/2} R(t, C_1, C_2, \ldots, C_{s+1}, \Omega)dt \tag{7}$$

where

$$\begin{aligned} &R(t, C_1, C_2, \ldots, C_{s+1}, \Omega) = \\ &= L(t, u(t, C_1, C_2, \ldots, C_{s+1}, \Omega), \dot{u}(t, C_1, C_2, \ldots, C_{s+1}, \Omega))dt \end{aligned} \tag{8}$$

is the residual.

Equation (7) can be rewritten in the form

$$J(C_1, C_2, \ldots, C_{s+1}, \Omega) = \int_0^{\pi} R(x, C_1, C_2, \ldots, C_{s+1}, \Omega)dx \tag{9}$$

Applying the Ritz method, we require

$$\frac{\partial J}{\partial C_1} = \frac{\partial J}{\partial C_2} = \cdots = \frac{\partial J}{\partial C_{s+1}} = \frac{\partial J}{\partial \Omega} = 0 \tag{10}$$

From Eqs. (10) and initial conditions (4) which become

$$C_1 + C_2 + \cdots + C_{s+1} = A \tag{11}$$

we can obtain optimally the parameters C_i, $i = 1,2,\ldots,s + 1$ and the frequency Ω.

We remark that expression (6) is not unique. We can alternatively choose another expression of the solution in the form

$$u(t) = C_1^{'} \cos \Omega t + C_2^{'} \cos 2\Omega t + C_3^{'} \cos 3\Omega t + \cdots \tag{12}$$

or, if the function f from Eq. (3) is an odd function:

$$u(t) = C_1^{''} \cos \Omega t + C_2^{''} \cos 3\Omega t + C_3^{''} \cos 5\Omega t + \cdots \tag{13}$$

and so on, where $C_i^{'}$ and $C_j^{''}$ are the convergence control parameters. With these parameters known, the approximate solution is well determined.

Another possibility to determine the optimal values of these parameters C_i is to solve the system

$$R(x_1, C_1, \ldots, C_{s+1}, \Omega) = R(x_2, C_1, \ldots, C_{s+1}, \Omega) = \cdots = \\ = R(x_{s+2}, C_1, \ldots, C_{s+1}, \Omega) = 0 \tag{14}$$

where $R(x, C_i, \Omega)$ is the residual given by Eq. (8) and $x_i \in (0, \pi)$, i = 1,2,…,s + 2.

The parameters C_i and the frequency Ω can be determined by the least square method, the Galerkin method, the collocation method and so on [10], [18], [19].

The Hamiltonian of Eq. (3) can be expressed in the form

$$H(t, u, \dot{u}) = p\dot{u} - L(t, u, \dot{u}) \tag{15}$$

where p is the generalized momenta

$$p = \frac{\partial L}{\partial \dot{u}} \tag{16}$$

If the Lagrangian is independent of time, then also the Hamiltonian is independent of time and results that

$$H(t, u(t, C_i, \Omega), \dot{u}(t, C_i, \Omega)) = H(t_0, \mathrm{u}(\mathrm{t}_0), \dot{u}(\mathrm{t}_0)) = \text{constant} \tag{17}$$

where t_0 is a fixed value of t such that $t_0 \in [0, \pi/\Omega]$.

On the other hand, the parameters C_i, i = 1,2,…,s + *1* and Ω from Eq. (17) can be determined from the conditions

$$H(t_1, u(t_1, C_i, \Omega), \dot{u}(t_1, C_i, \Omega)) = H(t_2, u(t_2, C_i, \Omega), \dot{u}(t_2, C_i, \Omega)) = \cdots \\ = H(t_{s+2}, u(t_{s+2}, C_i, \Omega), \dot{u}(t_{s+2}, C_i, \Omega)) = \text{constant} \tag{18}$$

3 The Oscillator with Linear and Cubic Elastic Restoring Force and Quadratic Damping

The system described by Eqs. (1) and (2) is a nonconservative system, but we try to determine a generalized Lagrangian L in the form

$$L(t, u, \dot{u}) = e^{F(u)}[X(u) + Y(\dot{u})] + \int G(u) e^{F(u)} du \tag{19}$$

where F, X, Y, and G are unknown functions. The expression (19) is not unique, because it is well known that the generalized Lagrangian L is not unique. Our problem consists in studying the conditions under which there exist the Lagrangian given by Eq. (19) such that Lagrange's equation in L coincide with

$$-\frac{d}{dt}\left(\frac{\partial L}{\partial \dot{u}}\right)+\frac{\partial L}{\partial u}=h(t,u,\dot{u})\left(\ddot{u}+u+\alpha\dot{u}^2+\beta u^3\right) \tag{20}$$

where $h(t,u,\dot{u})$ is an arbitrary function such that $h(t,u,\dot{u})\neq 0$. It is clear that the Eq. (1) and the equation

$$h(t,u,\dot{u})\left(\ddot{u}+u+\alpha\dot{u}^2+\beta u^3\right)=0 \tag{21}$$

have the same solutions, because $h(t,u,\dot{u})\neq 0$.

From Eq. (19), we can write

$$\frac{d}{dt}\left(\frac{\partial L}{\partial \dot{u}}\right)=\left[\ddot{u}\frac{d^2Y(\dot{u})}{d\dot{u}^2}+\dot{u}\frac{dY(\dot{u})}{d\dot{x}}\frac{dF(x)}{dx}\right]e^{F(u)} \tag{22}$$

$$\frac{dL}{du}=\left[\frac{dF(u)}{du}(X(u)+Y(\dot{u}))+\frac{dX(u)}{du}+G(u)\right]e^{F(u)} \tag{23}$$

Substituting Eqs. (22) and (23) into Eq. (20) we have

$$\begin{aligned}&\left[\ddot{u}\frac{d^2Y(\dot{u})}{d\dot{u}^2}+\dot{u}\frac{dY(\dot{u})}{d\dot{u}}\frac{dF(u)}{du}-\frac{dF(u)}{du}(X(u)+Y(\dot{u}))-\right.\\&\left.-\frac{dX(u)}{du}-G(u)\right]e^{F(u)}=\left(\ddot{u}+u+\alpha\dot{u}^2+\beta u^3\right)h(t,u,\dot{u})\end{aligned} \tag{24}$$

If we choose

$$h(t,u,\dot{u})=e^{F(u)}\neq 0 \tag{25}$$

$$\frac{d^2Y(\dot{u})}{d\dot{u}^2}=1 \tag{26}$$

then, from Eq. (26) we deduce that

$$Y(\dot{u})=\frac{1}{2}\dot{u}^2+C_1\dot{u}+C_2 \tag{27}$$

For simplification, we choose $C_1=C_2=0$ into Eq. (27), then substituting Eqs. (25) and (27) into Eq. (24) it follows that

$$\ddot{u}+\frac{1}{2}\dot{u}^2\frac{dF(u)}{du}-X(u)\frac{dF(u)}{du}-\frac{dX(u)}{du}-G(u)=\ddot{u}+u+\alpha\dot{u}^2+\beta u^3 \tag{28}$$

Into Eq. (28) we choose

$$\frac{dF(u)}{du} = 2\alpha \tag{29}$$

$$X(u) = -\frac{\beta}{2\alpha}u^3 \tag{30}$$

From Eqs. (28), (29) and (30) we obtain

$$G(u) = -u + \frac{3\beta}{2\alpha}u^2 \tag{31}$$

$$F(u) = 2\alpha u \tag{32}$$

The Lagrangian L given by Eq. (19) can be obtained from Eqs. (27), (30), (31) and by integrating the last term in Eq. (19). In this way, we can write the generalized Lagrangian in the form

$$L(u,\dot{u}) = e^{2\alpha u}\left[\frac{\dot{u}^2}{2} + \beta\left(-\frac{u^3}{2\alpha} + \frac{3u^2}{4\alpha^2} - \frac{3u}{4\alpha^3} + \frac{3}{8\alpha^4}\right) - \frac{u}{2\alpha} + \frac{1}{4\alpha^2}\right] \tag{33}$$

The generalized momenta becomes

$$p = \frac{\partial L}{\partial \dot{u}} = \dot{u}e^{2\alpha u} \tag{34}$$

The generalized Hamiltonian given by Eq. (15) can be written

$$H(u,\dot{u}) = e^{2\alpha x}\left[\frac{\dot{u}^2}{2} + \beta\left(\frac{u^3}{2\alpha} - \frac{3u^2}{4\alpha^2} + \frac{3u}{4\alpha^3} - \frac{3}{8\alpha^4}\right) + \frac{u}{2\alpha} - \frac{1}{4\alpha^2}\right] \tag{35}$$

The generalized Lagrangian given by Eq. (33) and therefore the generalized Hamiltonian given by Eq. (35) are independent of time, and therefore from Eqs. (35), (17) and (4) we obtain

$$\begin{aligned} e^{2\alpha u}\left[\frac{\dot{u}^2}{2} + \beta\left(\frac{u^3}{2\alpha} - \frac{3u^2}{4\alpha^2} + \frac{3u}{4\alpha^3} - \frac{3}{8\alpha^4}\right) + \frac{u}{2\alpha} - \frac{1}{4\alpha^2}\right] &= \text{constant} = \\ = e^{2\alpha A}\left[\beta\left(\frac{A^3}{2\alpha} - \frac{3A^2}{4\alpha^2} + \frac{3A}{4\alpha^3} - \frac{3}{8\alpha^4}\right) + \frac{A}{2\alpha} - \frac{1}{4\alpha^2}\right] & \end{aligned} \tag{36}$$

We rewrite Eq. (36) in the form

$$R(u(t),\dot{u}(t))=e^{2\alpha(u-A)}\left[\frac{\dot{u}^2}{2}+\beta\left(\frac{u^3}{2\alpha}-\frac{3u^2}{4\alpha^2}+\frac{3u}{4\alpha^3}-\frac{3}{8\alpha^4}\right)+\frac{u}{2\alpha}-\right.$$
$$\left.-\frac{1}{4\alpha^2}\right]-\beta\left(\frac{A^3}{2\alpha}-\frac{3A^2}{4\alpha^2}+\frac{3A}{4\alpha^3}-\frac{3}{8\alpha^4}\right)-\frac{A}{2\alpha}+\frac{1}{2\alpha^2}=0 \tag{37}$$

Equations (1) and (37) are equivalent because they have the same solutions. For Eq. (37) we suppose that the solution (6) has the form (s = 5)

$$u(t)=C_1+C_2\cos\Omega t+C_3\cos 2\Omega t+C_4\cos 3\Omega t+$$
$$+C_5\cos 4\Omega t+C_6\cos 5\Omega t \tag{38}$$

The action functional (5) is very difficult to solve with the solution (38), but in this case we use Eq. (37). Substituting Eq. (38) into Eq. (37), we obtain

$$R(\tau,C_1,C_2,\ldots,C_6,\Omega)=0 \tag{39}$$

where $\tau=\Omega t$.

4 Numerical Examples

In order to show the validity of the OVM, Eq. (39) has been numerically solved for the case $\alpha = 1/2$, $\beta = 1$ and $A = 1$. Making collocation in 7 points for Eq. (39), we obtain

$$C_1=-0.19619;\ C_2=1.41281;\ C_3=-0.308496;\ C_4=0.119584;$$
$$C_5=-0.0363356;\ C_6=0.00856476;\ \Omega=1.50999723$$

and therefore the solution (38) becomes

$$u(t)=-0.19619+1.41281\cos\Omega t-0.308496\cos 2\Omega t+$$
$$+0.119584\cos 3\Omega t-0.0363356\cos 4\Omega t+0.00856476\cos 5\Omega t \tag{40}$$

Figure 1 shows the comparison between the present solution and the numerical integration results obtained using a fourth-order Runge–Kutta scheme.

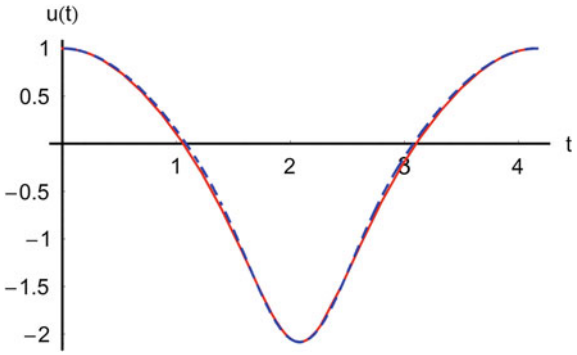

Fig. 1 Comparison between the approximate solution given by Eq. (40) and numerical solution of Eq. (1): – – – – approximate solution; ——— numerical integration results

5 Conclusions

In this paper, an efficient variational approach, called the optimal variational method (OVM) is employed to propose a new analytic approximate solution for some nonlinear oscillators with linear and cubic elastic restoring force and quadratic damping.

Our construction of the variational approach is different from the classical variational approach especially referring to the involvement of some initially unknown parameters C_1, C_2, …, which ensure a fast convergence of the solution. Also, the generalized Lagrangian and the generalized Hamiltonian are given in a proper manner. It should be underlined that the form of the generalized Lagrangian (19) is currently not found in the literature. Moreover, the arbitrary function h from (20) and the equivalence of the Lagrangians are completing a new approach to Lagrangian function and variational principle.

Our procedure is valid even if the nonlinear equations do not contain any small or large parameters. The OVM provides us with a simple and rigorous way to control and adjust the convergence of a solution through the parameters C_i which are optimally determined. This version of variational approach proves to be very rapid, effective, and accurate. We proved this comparing the solution obtained by the proposed method with the solutions obtained via numerical integration using a fourth-order Runge–Kutta scheme. Actually, the capital strength of the OVM is its fast convergence to the exact solution, which proves that this method is very efficient in practice.

References

1. Santilli R.M.: Foundations of theoretical mechanics I. The inverse problem in Newtonian mechanics, Springer, Berlin (1984)
2. Obădeanu V., Marinca V.: The inverse problem in analytical mechanics, West Publishing House, Timişoara (1992)

3. Obădeanu V. Marinca V: On the inverse problem in Newtonian mechanics Tensor N.S **48** 30–35 (1989)
4. Dincă F., Teodosiu C.: Nonlinear and random vibrations, Academic Press, New York (1973)
5. Cveticanin L.: Oscillator with strong quadratic damping force, *Pub. Inst. Math*. **85** 119–130 (2009)
6. Pakdemirli M.: A comparison of two perturbation methods for vibrations of systems with quadratic and cubic nonlinearities, Mech. Res. Commun. **21** 203–208 (1994)
7. Kovacic I., Rakaric Z.: Study of oscillators with non-negative real-power restoring force and quadratic damping Nonlin. Dyn. **64** 293–304 (2011)
8. Ji J., Yu L., Chert Y.: Amplitude modulated motions in a two degree-of-freedom system with quadratic nonlinearities under parametric excitation: experimental investigation, Mech. Res. Commun. **26** 499–505 (1999)
9. Starosvetsky Y., Gendelman O.V.: Vibration absorption in systems with a nonlinear energy sink: Nonlinear damping, J. Sound Vibr. **324** 916–939 (2009)
10. Herişanu N., Marinca V.: Optimal homotopy perturbation method for a non-conservative dynamical system of a rotating electrical machine, Zeit. fur Naturfors. A **8–9** 509-516 (2012)
11. Beléndez A., Méndez D.I., Fernández E., Marini S., Pascual I.: An explicit approximate solution to the Duffing-harmonic oscillator by a cubication method *Phys. Lett. A* **373** 2805–2809 (2009)
12. Mickens R.E., Oyedeji K.: Comments on the general dynamics of the nonlinear oscillator J. Sound Vibr. **330**, 4196 (2011)
13. Wu B.S., Lim C.W., Li P.S.: A generalization of the Senator–Bapat method for certain strongly nonlinear oscillators Phys. Lett. A **341** 164–169 (2005)
14. Pakdemirli M., Karahan M.M.F., Boyacı H.: Forced vibrations of strongly nonlinear systems with multiple scales Lindstedt Poincare method Math. Comput. Appl. **16** 879–889 (2011)
15. Pilipchuk V., Olejnik P., Awrejcewicz J.: Transient friction-induced vibrations in a 2-DOF model of brakes, J. Sound Vibr. **344**, 297–312 (2015)
16. Natsiavas S., Paraskevopoulos E.: A set of ordinary differential equations of motion for constrained mechanical systems, Nonlinear Dyn **79** 1911–1938 (2015)
17. Chen Y.M., Liu J.K.: A modified Mickens iteration procedure for nonlinear oscillators J. Sound Vibr. **314** 465–473 (2008)
18. Herisanu N., Marinca V.: An iteration procedure with application to van der Pol oscillator, Int. J. Nonlinear Sci. Numer. Simulation **10** 353–361 (2009)
19. Marinca V., Herisanu N.: The Optimal Homotopy Asymptotic Method. Engineering Applications, Springer (2015)
20. Lee K.C.: Energy Methods in Dynamics, Springer Berlin Heidelberg (2014)

Wave-Based Control of a Mass-Restricted Robotic Arm for a Planetary Rover

David J. McKeown and William J. O'Connor

Abstract Here wave-based control is applied to suppress vibrations during repositioning of a flexible robotic arm on a planetary rover in a Martian environment. Typically, such a robotic arm has very low power and mass budgets, implying significant flexibility, with static and dynamic consequences. Meeting precision performance specifications then becomes challenging and active vibration control is required. The example of the DExtrous LIghtweight Arms for exploratioN (DELIAN) arm is the focus of this paper. DELIAN is a general purpose arm, currently in development by SELEX ES for the European Space Agency (ESA). For active vibration control, a wave-based controller is used: a strategy formulated specifically for flexible mechanical systems. It considers actuator motion as launching and absorbing mechanical waves into and from the system. Absorbing the returning wave provides effective, active vibration damping while simultaneously moving the system to the target displacement. It is robust to both actuator performance and modelling errors, very stable, and easy to implement. The controller was found to perform well in limiting the effect of the flexibility during manoeuvres and also when rejecting vibrations due to impacts.

1 Introduction

Robotic arms play an important role in space, from large arms deployed in microgravity environments, such as the Canadarm upon the ISS, to smaller arms on planetary rovers. Typically, the arm specification has very low power and mass budgets, and the lighter the structure the more flexible it becomes. This elasticity has consequences for both the dynamics and the static deflections. Meeting the precision performance specifications then becomes challenging and a strategy for active control of the vibrations is required.

D.J. McKeown (✉) · W.J. O'Connor
School of Mechanical and Materials Engineering, University College Dublin,
Belfield, Dublin 4, Ireland
e-mail: david.mckeown@ucd.ie

© Springer International Publishing Switzerland 2016

J. Awrejcewicz (ed.), *Dynamical Systems: Theoretical and Experimental Analysis*, Springer Proceedings in Mathematics & Statistics 182, DOI 10.1007/978-3-319-42408-8_19

In this paper we take the example of the DExtrous LIghtweight Arms for exploratioN (DELIAN) arm. DELIAN is a general purpose arm, currently in development by SELEX ES for the European Space Agency (ESA). Its design allows for many configurations for different operating scenarios. Here we consider the scenario of a planetary rover vehicle with an arm designed to pick up and place scientific instruments, but where the arm mass is tightly constrained. The combination of arm length and payload mass gives this implementation the lowest natural frequencies and therefore the greatest need for active vibration damping. Another configuration envisages using the arm for surface drilling, with a tool attached at the end effector, which would also give rise to system vibrations.

To provide active control of the vibrations, a wave-based controller is designed and implemented. Wave-Based Control (WBC) is a control strategy formulated specifically for the control of flexible mechanical systems [1]. It is based on the idea of considering actuator motion as launching and absorbing mechanical waves into and from the system.

2 Robotic Arm Model

The DELIAN Arm, for the chosen scenario, is a 4 DOF robotic arm. A simplified computer-generated model is shown in Fig. 1. It has four revolute joints each capable of controlled rotation about a single axis. The first joint, located nearest the base, below limb 1, controls the yaw of the arm, while the other three motor joints control the pitch of its associated limb.

Figure 1 shows the arm in a compact "stowed up" configuration required for transit. When in use it deploys into a long reach arm. The Denavit–Hartenberg parameters describing the arm in this stowed configuration are shown in Table 1.

The limbs are made of a light, high-strength, titanium alloy (Ti-6Al-4 V) with a circular ring cross section. The geometry of the limbs is given in Table 2 and the mass budget for the joints and limbs is given in Table 3.

The arm is designed to sustain loads due to gravity in an environment representative of Mars ($g_{\text{mars}} = 3.711$ m/s^2) and to be capable of applying a 10 N vertical force at the tip.

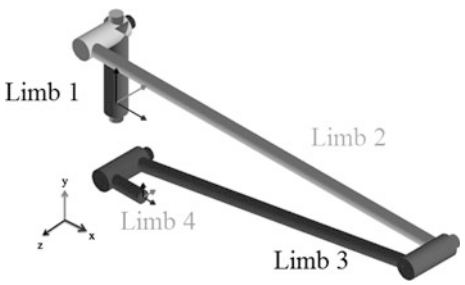

Fig. 1 DELIAN arm consisting of a base (below limb 1), two long flexible limbs and end effector, connected together with 4 flexible motor joints

Table 1 Denavit-Hartenberg parameters for DELIAN arm in curled up configuration shown in Fig. 1

Joint #	a[m]	α[deg]	d[m]	q_{inital}[deg]	q_{min}[deg]	q_{max}[deg]
1	0	90	0.18	0	−170	+170
2	1.0	0	0.08	0	−170	+170
3	0.8	0	0.08	−170	−170	+170
4	0	−90	0.076	170	−170	+170

Table 2 Dimensions of DELIAN limbs

	Length [mm]	External Dia. [mm]	Thickness [mm]
Limb 1	893	37	1
Limb 2	708	34	1

Table 3 Mass budget DELIAN arm

	Mass (kg)
Motor Joint 1	0.438
Motor Joint 2	1.038
Motor Joint 3	0.585
Motor Joint 4	0.585
Base	0.15
Limb 1	0.461
Limb 2	0.338
Harness (incl. P/L)	0.61
Total	4.205

In addition to the rigid body dynamics, two sources of flexibility need to be considered and modelled: the compliance of the motor joints and the structural flexibility of the limbs themselves.

2.1 Motor Joint Flexibility

The four joints are actuated by four low-power brushless motors, each connected with one planetary gear and one harmonic drive, with an overall transmission ratio ranging from 8400 to 18840 designed to supply the torque necessary to hold and manoeuvre the arm. A preliminary analysis of an experimental setup to measure the motor joint parameters is presented in [2].

Each motor joint can provide a maximum torque of 28 mNm, and has a position sensor resolution of 1 arcmin at the output shaft. The maximum rotational speed is 10 deg/s and the deadband for output shaft motion transmission is 1 arcmin.

Table 4 Stiffness of DELIAN arm joints

Joint #	Torsional stiffness [Nm/rad]	Transversal stiffness [Nm/rad]
1	4000	8000
2	20000	30000
3	8000	12000
4	8000	12000

The motor joint flexibility is modelled by torsional and transversal springs. The stiffness values are summarized in Table 4.

In this study it is assumed that each motor is already equipped with its own, angular position sub-controller, which takes an angular position reference as input. These sub-controllers are assumed to give an ideal response, causing each joint to move perfectly to follow its reference input, ignoring the errors at the output shaft due to the flexibility. The flexibility effects are then handled by wave-based control acting at a higher level, to adjust the inputs to the sub-controllers using the wave-inspired strategy, in a way described below. WBC can therefore be considered a supervisory control strategy, or an outer loop, around the inner loop comprising the standard, actuator sub-controllers which are blind to the flexibility effects. In the results below, the response without the WBC is described as "open loop", which should therefore be understood as arm motion control without provision for simultaneous active vibration damping.

2.2 Limb Flexibility

The equivalent cantilever beam stiffness of the mains limbs is shown in Table 5 and can be calculated using the material and geometry data given in Tables 2 and 3.

To obtain the results shown in Sect. 5 the limbs are modelled in ADAMS multibody software using discrete flexible link elements. Each limb is split into 6 discrete rigid bodies of hollow circular cross section connected by beam force elements, which model the flexibility using the constitutive law described in [3, 4].

The material and geometry properties determine the masses and moments of inertia of the arms, and a small damping ratio of 1.0E-005 was chosen.

2.3 Modal Frequencies

The DELIAN arm is capable of a wide range of configurations, each requiring a different set of motor joints holding torques. The modal frequencies also change

Table 5 Stiffness of DELIAN arm limbs

	Cantilever beam stiffness [N/m]
Limb 1	8.7905e + 003
Limb 2	1.3588e + 003

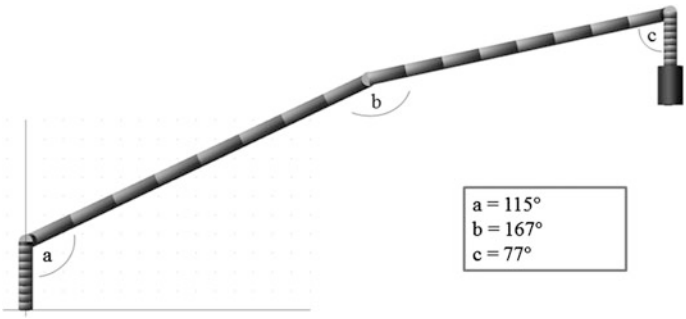

Fig. 2 ADAMS model of DELIAN arm in the default deployed configuration

Table 6 Ten lowest modal frequencies of the DELIAN arm in the default deployed configuration (Fig. 3)

Mode #	Frequency (Hz)	Damping ratio
1	1.40	2.65E-05
2	1.83	5.37E-05
3	10.58	2.53E-04
4	17.44	5.22E-04
5	30.81	8.84E-04
6	38.87	6.61E-04
7	73.83	2.13E-03
8	109.02	3.35E-03
9	147.84	4.52E-03
10	174.88	4.98E-03

with each configuration. Here we chose a default starting configuration for all simulations, as shown in Fig. 2. It represents a challenging configuration with the arm almost fully extended, requiring a large holding torque at Joint a. Table 6 shows the 10 lowest modal frequencies of the arm in this configuration (payload mass 6 kg). The lowest is 1.4 Hz, significantly lower than when the arm is stowed (4.7 Hz).

3 Active Vibration Control

As explained, the DELIAN Arm has four independent joints, each containing an actuator to reposition the arm. The motion of any actuator will induce vibrations throughout the system due to the flexibility in both the joints and the limbs. The challenge is how to get the actuators to move the limbs to a new configuration while simultaneously controlling the vibrations which quickly spread throughout the whole system.

Here we present a wave-based control strategy to actively absorb these vibrations. A brief overview of wave-based control will be given here. A more detailed account can be found in [1].

3.1 Wave-Based Control Background

The theory of wave-based control is based upon the separation of motion into notional incoming and outgoing waves at the interface between the actuator and the flexible system. Moving the actuator launches a wave (in this case a displacement wave) into the system. Simultaneously a return wave component can be calculated at the interface, using a measure of angular displacement or torque. The return wave can be thought of as vibrations that have passed through the system and have been reflected at points within the system, to arrive back, sooner or later, at the actuator. The summation of the launch and return wave, at any location, gives the real motion of the system exactly.

A wave-based controller can be designed which will absorb the return wave on arrival back to the actuator. This avoids reflecting it back into the system, where it would have the effect of maintaining the vibration. In other words, the actuator acts as an active vibration damper, even while simultaneously launching any desired displacement wave into the system. At steady state, in the absence of external disturbances, the net displacement of the actuator associated with absorbing the return wave will equal the net final displacement of the launch wave. Furthermore all vibrations will have been removed from the system by this absorbing action. We now outline how these waves can be calculated.

Consider the 1-D, lumped, uniform, flexible system shown in Fig. 3, which shows a notional right travelling "launch wave", denoted Ai(s) at the ith mass, and a left travelling "return wave" denoted Bi(s), with the actual displacement of each mass, $X_i(s)$ being the sum of the two waves, or $X_i(s) = \mathrm{A_i}(s) + \mathrm{B_i}(s)$. The waves travel through the system such that $A_{i+1} = G(s)\ A_i$ and $\mathrm{B_i} = G(s)\ B_{i+1}$, where

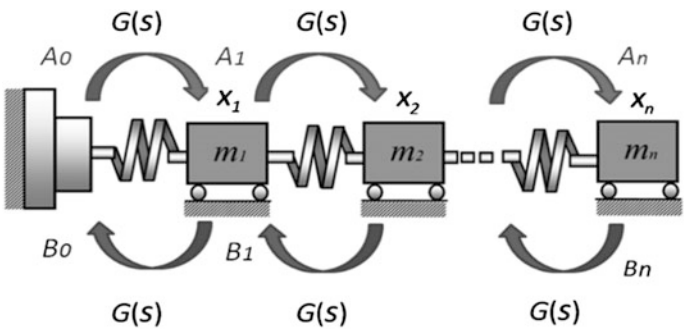

Fig. 3 1-D *n*-mass lumped flexible system

$G(s)$ is called the Wave Transfer Function (WTF) which models the dispersive wave motion through the system.

The WTF is the transfer function between the motion of any mass and that of the next mass in a uniform lumped flexible system that is assumed to extend uniformly to infinity. The full derivation of the WTF can be found in [1] and is given by

$$G(s) = 1 + \frac{1}{2}(s/\omega)^2 - (s/\omega)\sqrt{1 + (s/2\omega)^2} \tag{1}$$

where $\omega = \sqrt{(k/m)}$ and m and k correspond to the masses the spring stiffness of the uniform lumped infinite system. Taking the inverse Laplace transform of (1) gives

$$g(t) = 2\left(\frac{J_1(2\omega t)}{\omega t^2} - \frac{J_0(2\omega t)}{t}\right). \tag{2}$$

where J_n is an nth order Bessel function of the first kind. For control purposes, $G(s)$ can be sufficiently well approximated by a simple second order transfer function

$$G(s) = \frac{\omega_G^2}{s^2 + \omega_G s + \omega_G^2} \tag{3}$$

with characterizing frequency $\omega_G = \sqrt{2k/m}$. The launch wave can be set to any profile desired, with a final value equal to half the required displacement. The simplest choice is half the reference displacement profile

$$A_0(s) = 1/2R(s). \tag{4}$$

The return wave at the actuator $B_0(s)$, which is motion returning from the flexible system towards the actuator, as seen at the actuator, can be expressed in terms of expressions in $G(s)$, the actuator displacement, $X_0(s)$, and a measured displacement of the first mass, $X_1(s)$, as

$$B_0(s) = \left[\frac{G(s)^2}{G(s)^2 - 1}\right] X_0(s) - \left[\frac{G(s)}{G(s)^2 - 1}\right] X_1(s). \tag{5}$$

As shown in the next section, rather than $X_1(s)$, the measured variable to determine $B_0(s)$ could alternatively be chosen as the torque close to the actuator, with a small modification of the standard WBC theory.

The summary introduction to WBC above assumes a uniform, lumped system. It transpires that when the system is not uniform, or has more distributed (continuous) dynamics, similar control strategies continue to work remarkably well. For a discussion of this phenomenon, see [5].

4 Implementation

To implement WBC on the DELIAN arm, each of the motors joints has a separate wave-based control system, acting almost independently. Any dynamic coupling between the axes can be regarded as mutual disturbances, coming from one controlled axis to another. For rest-to-rest motion any such disturbances are transient.

The motion of the waves throughout the arm can be visualised in a similar manner to that shown in Fig. 3 by imagining the dynamics of the arm reduced to rotation springs modelling the flexibility in the motor joints and flexible beams modelling the arms.

The control challenge is to calculate and absorb the return wave component, and add it to the launch wave, to give the required input angular displacement to achieve the target (reference) motion while also controlling the multiple, complex system vibrations.

To achieve this the actuator displacement, X_0, is set as the sum of a set launch wave of half the reference, $R(s)$, plus the measured return wave, allowing for simultaneous launching and absorbing. Thus

$$X_0(s) = A_0(s) + B_0(s) = 1/2\,R(s) + B_0(s) \tag{6}$$

To calculate the return wave WBC requires the measurement of two independent variables at the actuator-system interfaces. Because the beam deflections are likely to be small and difficult to measure, the torque close to the motor joint, or the torque provided by the motor itself, provides a more practical measurand. This measurement can be obtained using a strain gauge setup as suggested in Fig. 4.

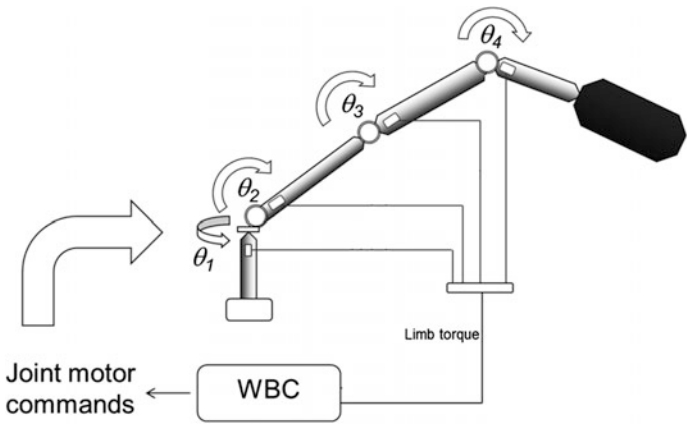

Fig. 4 The DELIAN arm has 4 inputs which control the angular displacements of the joints. Measurement of the torque close the motor joints is used to calculate the return wave component of the motion

The return wave $B(s)$ can be determined using a modification of the standard WTF given by Eq. (1), called a "crossover wave transfer functions", or xWTFs, first presented in [6]. These perform a similar job to the standard WTF, but are reformulated to provide a transfer function, G_{D2T}, whose input is an angular displacement and whose output is a torque, and G_{T2D} with a torque input and angular displacement output.

The return wave at the actuator, $B_0(s)$, is then given by

$$B_0(s) = \left[\frac{G_{D2T}G_{T2D}}{G_{D2T}G_{T2D}-1}\right]\theta_0 - \left[\frac{G_{T2D}}{G_{D2T}G_{T2D}-1}\right]\tau_0 \tag{7}$$

where G_{D2T} and G_{T2D} are related to the standard WTF $G(s)$ by

$$G_{D2T} = k(G-1) \tag{8}$$

$$G_{T2D} = \frac{G}{k(G-1)} \tag{9}$$

and where θ_0 and τ_0 are the angular displacement and torque at the actuator interface. The variable k is the same stiffness value used in tuning $G(s)$. As is the case with the standard WTFs there is one tunable parameter, a frequency, $\omega_G = \sqrt{2k/m}$, used in defining G_{D2T} and G_{T2D}, the exact value of which is not critical. For a given reference input, this frequency can be tuned to give a more gentle response, or a more rapid response at the cost of greater stress on the system during the manoeuvre and a small increase in overshoot. For all results in Sect. 5 below, ω_g was set to the lowest modal frequency in the deployed configuration (8.79 rad/s).

The launch wave is set to half the requested angular displacements, $\theta_{\text{ref}}(s)$, of the joint.

$$A_0(s) = 1/2\,\theta_{ref}(s) \tag{10}$$

A schematic of the wave-based controller is shown in Fig. 5 for Joint 2, the same configuration is used for all four motor joints.

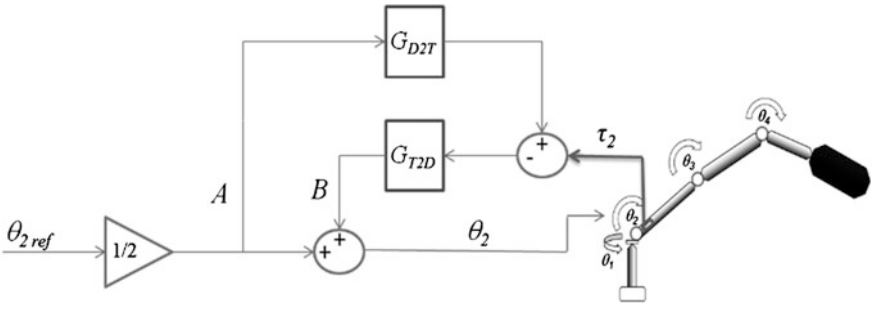

Fig. 5 Wave-based controller for joint 2. The actuator motion is made up from half the desired reference input and the calculated return wave

4.1 Gravitational Strain

As already explained, in the absence of external disturbances, at steady state the net displacement associated with absorbing the return wave will equal the net displacement of the launch wave. When, however, there are variations in the gravitational strain during manoeuvres, they will appear to the controller as an externally excited waves (or disturbances). Rather than resisting them, the controller will move to absorb them, leading to position errors. Furthermore, these (unlaunched) returning waves will typically endure, so the continuing absorption process will cause the system to drift from the target displacement. To overcome this, any DC offset in the measured value of the torque is removed, and a high-pass filter (1 Hz) is used to remove any DC drift from the measured torque, ensuring the (vibratory) torque returns to zero when the vibrations have died out.

5 Results

In the simulation results in this section the plant was a nonlinear ADAMS model of the DELIAN arm, using the parameters given in Sect. 2, while the controller was implemented in Simulink.

5.1 Flexibility Levels and Sources

The motion of any of the four actuators will cause the entire system to vibrate. To analyse the typical levels of vibration in the system due to its own motion, without active vibration control, a series of simulations were run. Each joint was rotated through 60° from the deployed configuration (Sect. 2.3) and the displacement and angle of the tip were recorded, as were the torques in all the joints. The reference angular displacements were all set to ramp up over time, at 10 deg/s.

A sample result for motor joint 2 is shown in Fig. 6. Most excitation happens at the start and end, with the vibrations settling to lower values during the manoeuvre itself. The maximum vibration amplitudes for similar manoeuvres using the other joints is summarized in Table 7. The largest vibrations occur when manoeuvres involve joint 1 or joint 2 or when all the joints are moved together and stop simultaneously.

Flexibility arises in both the motor joints and the robot limbs. To establish which contributes most to the vibrations, another model was created in which the flexibility was removed from the motor joints. Figure 7 shows 10 deg/s ramp input of 60° at joint 2 for both models. It is clear that, with the rigid joints, the vibration amplitude is not significantly less, strongly suggesting that the main source of the vibrations is the flexibility of the limbs themselves and not that of the motors and

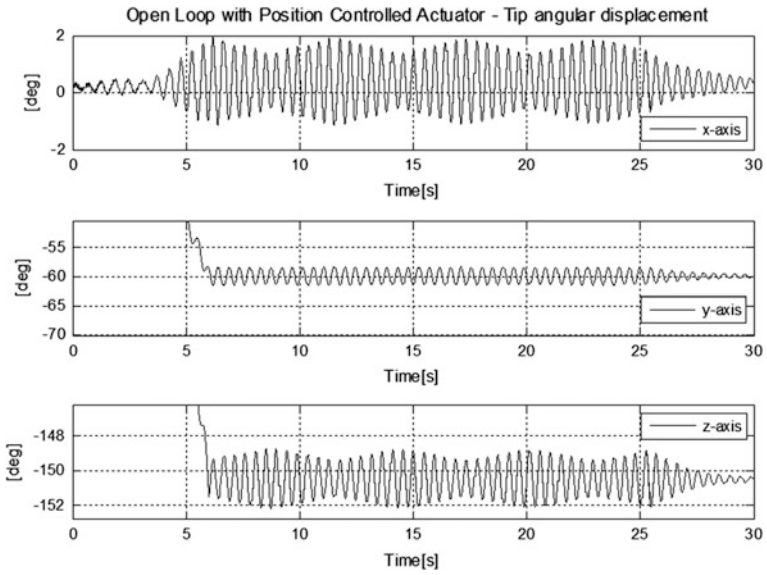

Fig. 6 Angular displacement of tip during a 60° rotation of joint 2 (rotation about z-axis) at 1 deg/s (from the default deployed configuration)

Table 7 Maximum deflection of tip during a 60° manoeuvre, individually for the four motor joints and all joints together

	Joint 1	Joint 2	Joint 3	Joint 4	All joints
Angular (deg)	1.65	1.03	0.5	0.1	1.7
Deflection (mm)	35.2	20.15	6.55	1.9	24.25

joints. Removing the flexibility from the joints does, however, cause an increase the lowest modal frequency of the system from 1.4 Hz to 1.8 Hz. This frequency change can also be noticed in Fig. 7.

6 Wave-Based Control

In this section we will focus on the benefits of using wave-based control when repositioning the arm. Wave-based control was implemented as described in Sect. 4 and a series of simulations carried out. Figures 8 and 9 show the displacement and angular displacement of the tip for 60° rotation (maximum joint rotation speed of 10 deg/s) of Joint 2 using wave-based control to absorb the vibrations. When compared with the "open loop" case, as presented in Sect. 5.1, the vibrations are

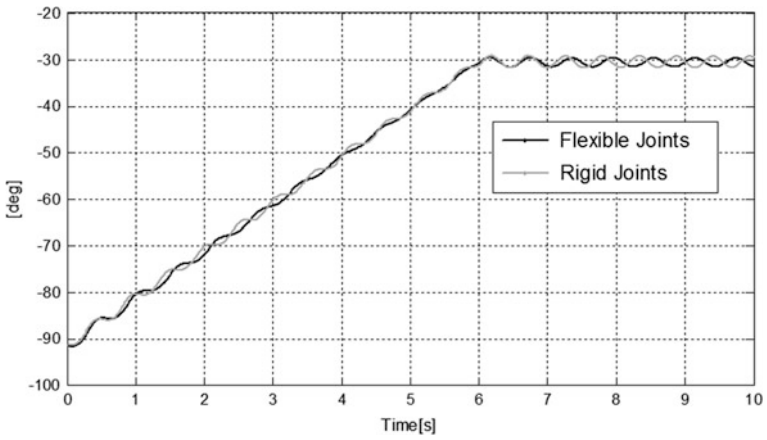

Fig. 7 Angular displacement of tip during a 60° rotation of joint 2 (rotation about z-axis) at 10 deg/s (from the default deployed configuration). *Black line* shows the nominal case and *gray line* when the joint flexibility has been removed

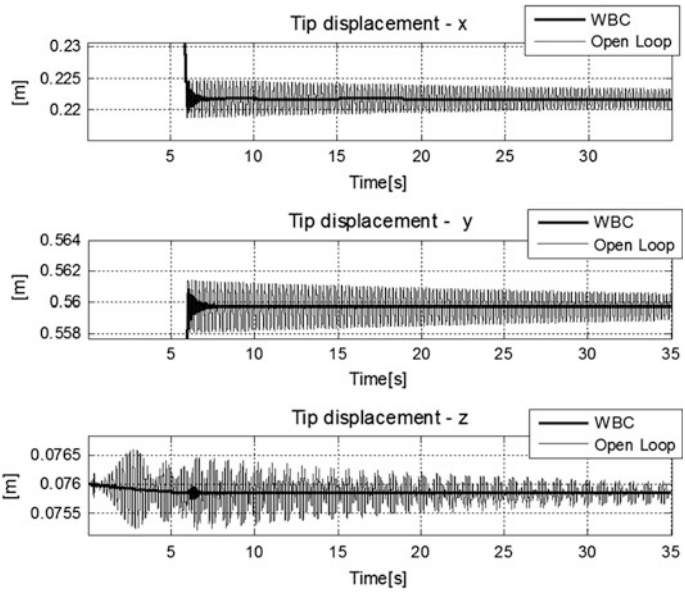

Fig. 8 Tip displacement resulting from a 60° rotation of motor joint 2. Vibrations are absorbed quickly on all axes using wave-based control

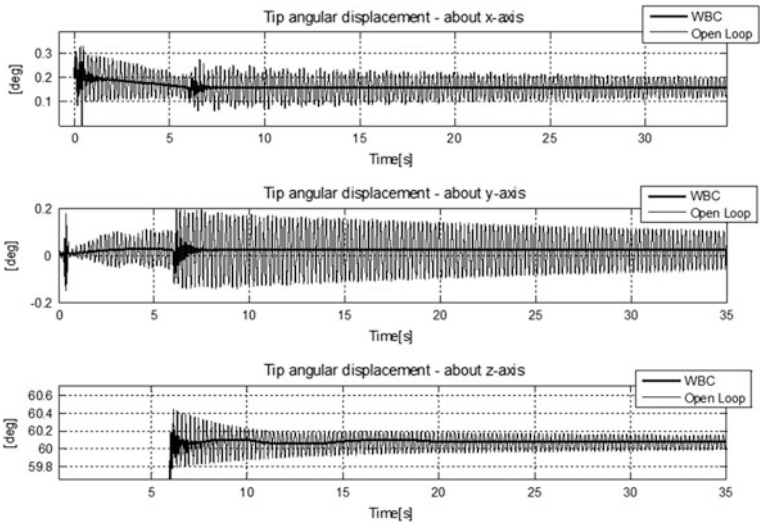

Fig. 9 Tip angular displacement resulting from a 60° rotation of joint 2. Vibrations are absorbed quickly on all axes using wave-based control

smaller in amplitude and quickly decay. These results are representative of manoeuvres using any combination of the motor joints.

The motor torque during the manoeuvre is shown in Fig. 10 and it can be seen that the torque profile is much smoother and the peak torque reduced.

6.1 Impacts

The level of vibration excited by the motor joints can be reduced if the motors move more slowly. When reduction of manoeuvre time is not a priority this is a sensible solution. But it can create a mistaken confidence that the flexibility will not have detrimental effects on the dynamic performance and practical operation. During normal operations there are various ways arm vibrations could be excited by external effects, such as contact, impact, stick-slip, digging or drilling, especially when these cause sudden increases or decreases in the external load. Also, if the arm is mounted on a rover vehicle which itself is moving, this in turn will cause significant vibrations of the arm. WBC can be used to quickly absorb these vibrations, settle the system and maintain precision. Figures 11 and 12 show the response under WBC when an impact force of 100 N is applied to the tip of the arm in the *y*-direction for 1 s and then removed.

The amplitudes of vibrations are much larger than those excited internally during repositioning, but, perhaps more seriously, they endure for a very long time with very slow decay rates. With WBC, however, the vibrations are quickly reduced to negligible levels, while maintaining the position control.

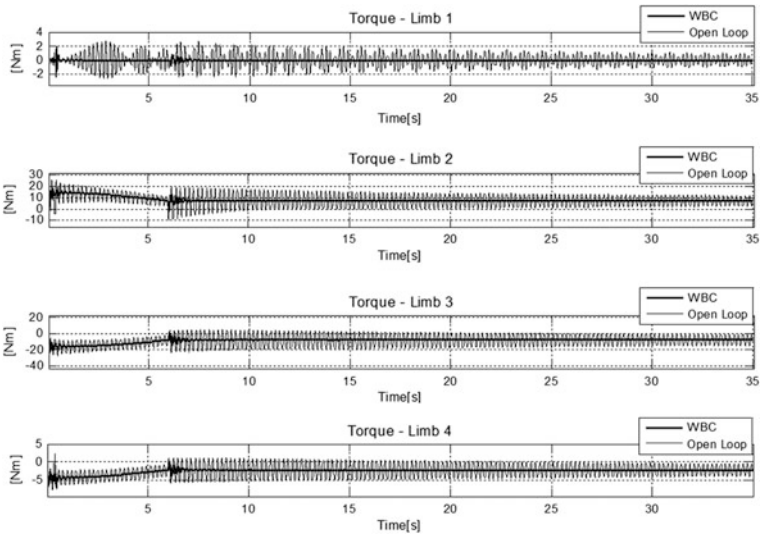

Fig. 10 Torque at the four motor joints during a 60° rotation of joint 2. Wave-based control provides a smoother manoeuvre with a lower peak torque

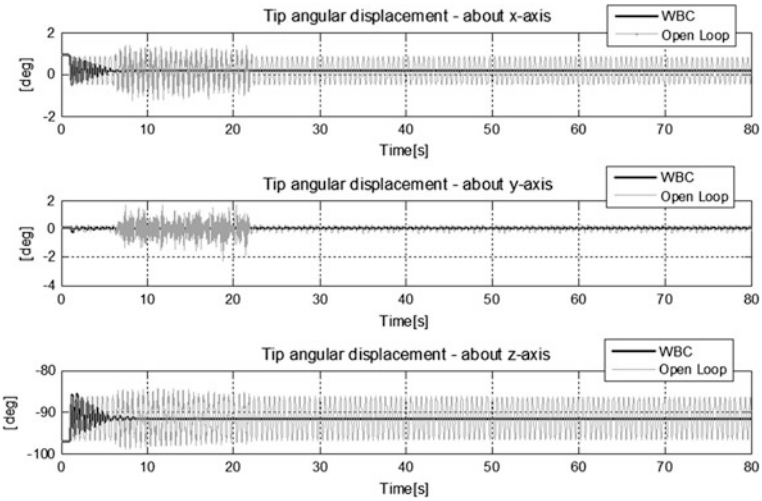

Fig. 11 Tip angular displacement in response to a 100 N force (y-axis) applied for 1 s to the tip and then left to vibrate freely

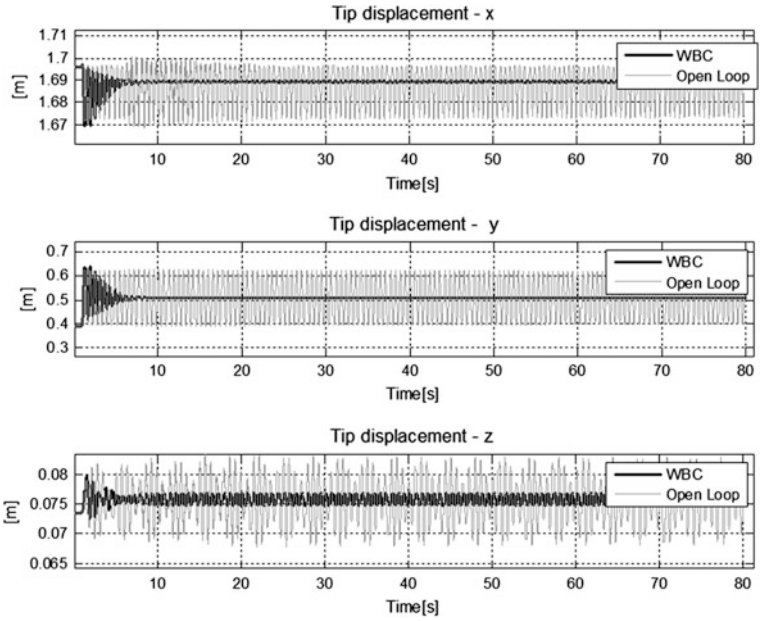

Fig. 12 Tip displacement in response to a 100 N force (y-axis) applied for 1 s to the tip and then removed

7 Conclusion

Wave-based control has proved effective in simultaneously combining position control and active vibration damping for the DELIAN Arm. It is also effective in absorbing vibrations due to external effects, including impact, returning the arm quickly to the pre-impact configuration.

The added performance requires only a measure of the torque in the motor joint, or close to joint, and has the benefit of not requiring a detailed system model, which can be complex, time varying and nonlinear. The control system can be shown to be easily tuned and is robust to system changes.

The internally excited vibrations, due to arm manoeuvres, could be managed by decreasing the maximum rate of the inputs, at the expense of longer manoeuvre times. In practice, however, a flexible robot arm will not move in isolation from its environment. It is likely to experience vibrations due to external interactions. WBC has been shown to provide a dramatic and rapid reduction of such vibrations for both these problems, while maintaining good position control. It thus achieves a seamless combination of the two control challenges: position control and active vibration damping.

The main source of the overall flexibility in the DELIAN arm comes from the elasticity of the arms rather than from the nonrigid behaviour of the joints. In

designing the arm to be lighter or longer the challenges posed by this flexibility becomes greater and the need for active vibration control becomes much greater.

Because of very low power budgets, the low motor torques and slow slew rates are likely to be features of planetary rovers. By contrast, robotic arms on satellites in Earth orbit are likely to require more rapid slewing rates, so that the need to combine position control and active vibration damping, even for self-excited vibrations, is likely to become greater. And of course, like rover arms, such robotic arms would also be subject to externally excited vibrations when executing tasks involving interaction with the environment, so active vibration damping via actuator motion would also be very important in such applications.

Acknowledgments This research was carried out under a programme of, and funded by, the European Space Agency.

References

1. W. J. O'Connor, "Wave-based analysis and control of lump-modeled flexible robots," *IEEE Transactions on Robotics,* vol. 23, pp. 342–352, Apr 2007.
2. L. Bascetta, G. Ferretti, F. Fossati, G. Magnani, A. Rusconi, and B. Scaglioni, "Modelling, identification and control of a flexible lightweight robot for space applications," in *IAA Conference on Dynamics and Control of Space Systems* Roma, Italy, 2014.
3. R. J. Roark, W. C. Young, R. G. Budynas, and A. M. Sadegh, *Roark's formulas for stress and strain*, 8th ed. New York: McGraw-Hill, 2012.
4. J. S. Przemieniecki, *Theory of matrix structural analysis*. New York: Dover, 1985.
5. W. J. O'Connor, F. R. de la Flor, D. J. McKeown, and V. Feliu, "Wave-based control of non-linear flexible mechanical systems," *Nonlinear Dynamics,* vol. 57, pp. 113–123, Jul 2009.
6. W. J. O'Connor and A. Fumagalli, "Refined Wave-Based Control Applied to Nonlinear, Bending, and Slewing Flexible Systems," *Journal of Applied Mechanics-Transactions of the Asme,* vol. 76, Jul 2009.

Soft Suppression of Traveling Localized Vibrations in Medium-Length Thin Sandwich-Like Cylindrical Shells Containing Magnetorheological Layers via Nonstationary Magnetic Field

Gennadi Mikhasev, Ihnat Mlechka and Holm Altenbach

Abstract A medium length thin laminated cylindrical shell composed by embedding magnetorheological elastomers (MREs) between elastic layers is the subject of this investigation. Physical properties of MREs are assumed to be functions of the magnetic field induction. Differential equations with complex coefficients depending upon the magnetic field and based on experimental data for MREs are used as the governing ones. The shell is subjected to perturbations in their surface so that the initial displacements and velocities are localized in a neighborhood of some generatrix. The problem is to study the response of the MRE-based shell to the initial localized perturbations and the applied time-dependent magnetic field. The asymptotic solution of the initial boundary value problem for the governing equations is constructed by superimposing families of localized bending waves running in the circumferential direction. It is shown that applying the time-dependent magnetic field result in soft suppression of running waves.

1 Introduction

Due to their superior mechanical properties multilayered thin shells have a wide range of applications in numerous engineering structures, such as airborne or spaceborne vehicles, underwater objects, cars, etc. [17, 18]. Undesirable vibrations often impedes the effective operation of these structures. And so, it is very important to

G. Mikhasev (✉) · I. Mlechka
Belarusian State University, Nezavisimosti Avenue 4, 220030 Minsk, Belarus
e-mail: mikhasev@bsu.by

I. Mlechka
e-mail: ignat.mlechka@gmail.com

H. Altenbach
Otto-von-Guericke-Universität Magdeburg,
Universitätsplatz 2, 39106 Magdeburg, Germany
e-mail: holm.altenbach@ovgu.de

© Springer International Publishing Switzerland 2016

J. Awrejcewicz (ed.), *Dynamical Systems: Theoretical and Experimental Analysis*, Springer Proceedings in Mathematics & Statistics 182, DOI 10.1007/978-3-319-42408-8_20

provide vibration damping to achieve a required dynamical perfection of operating thin-walled structures.

Applying materials with different physical properties one can design sandwich-like or laminated structures fulfilling up-to-date requirements, such as high stiffness, good buckling resistance, and noiselessness. New multifunctional composite materials with active and adaptive properties (so-called smart materials) open new possibilities [3, 6] to solve the urgent problem on vibroprotection of thin-walled laminated structures. Some of these smart materials are magnetorheological elastomers (MREs). They consist of magnetizable particles, such as iron, molded in either rubbery polymers or deformed inorganic polymer matrices [4]. The optimum concentrations of the iron particles, carrier viscous liquid, and polymer determine shear modulus, viscosity, and response time of smart MREs. Above properties can vary almost instantaneously when subjected to magnetic field [4, 5]. It is expected that MREs embedded between elastic layers may provide for a sandwich a wide range of viscoelastic properties which may be controlled rapidly by applying magnetic field and, in such a way, be used to control and/or efficiently suppress vibrations.

Although there are numerous studies that have been devoted to the exploration of the mechanical and rheological properties of magnetorheological media and elastomers (see, e.g., [1, 2, 4, 8, 24]), very few literature is available on the dynamic simulation of thin-walled laminated structures with magnetosensitive embedded cores or layers. The majority of available papers relates to three-layered beams with the magnetorheological (MR) core. Considerable contribution to fundamental investigations of MRE-based sandwich beams has been done by Zhou et al. [25–27]. They have observed that the change of the dynamic properties of the sandwich beam is mainly caused by the change of shear modulus of MRE. Free and forced vibrations of a three-layered beam with MRE core and outer aluminium layers at different levels of magnetic field were analyzed in Ref. [9]. As shown in this study, for the assumed parameters of the MRE-based beam the optimal intensity of magnetic field (about 350 mT) provides the best suppression of vibrations.

As concerns studies on the dynamic analysis of sandwich-like or multilayered shells with embedded sensitive core or layers, there are only a few available papers. In [23], an analytical model has been developed and adopted to the discrete finite element method to investigate the vibration and damping characteristics of a three-layered orthotropic cylindrical shell with electrorheological core and outer constraining layers. Free vibrations of thin laminated circular cylinders with homogeneous MR layers under different levels of applied magnetic field were investigated in [15]. A shown in this paper, the applied magnetic filed may have a significant effect on the vibration characteristics of thin MRE-based sandwich cylinders. And the recent study [16] has revealed that applying constant magnetic field may result in strong distortion of eigenmodes corresponding to the lowest frequencies. In particular, if a circular cylindrical sandwich containing a strongly polarized MR core is subjected to the action of a uniform stationary magnetic field whose force lines have different angles with the magnetizable particles alignment in the MRE, then its eigenmodes corresponding to the lowest frequencies turn out to be localized near some lines where the reduced shear modulus gets its extremum.

Probably, the first attempts to examine the response of MRE-based thin-walled structures to the action of time-dependent magnetic field have been undertaken in reference [9]. In this paper, authors have shown that the pulsed signal of external magnetic field may results in exciting nonstationary high-frequency vibrations of the adaptive beam containing MR core. In other words, the MRE-based sandwich structure, subjected to the impulse action of magnetic field, experiences the parametric impact. In our opinion, soft suppression of vibrations in a thin-walled structure is more preferable, and so, more comprehensive investigations are needed to further examine the time-dependent magnetic field effect on dynamic response of laminated shells containing MR layers.

The aim of this paper is to show that the application of varying magnetic field may be used with success in order to obtain soft suppression of nonstationary vibrations in thin laminated shells with the magnetic field induced viscoelastic properties. The subject of our study is running localized vibrations called wave packets (WPs) [11]. Localized vibrations may be generated in the shell by some transient forces applied along a line or point on the shell surface. Similar vibrations may also appear [12] as a result of the parametric excitation of a shell with variable geometric parameters (e.g., a curvature, a thickness or a generatrix length) and/or experiencing nonuniform loading. The nonhomogeneity of both the geometric parameters [10, 14, 20] and viscoelastic properties (for instance, in a polarized MRE [16]) may cause the localization of free vibrations and unsteady wave process [11, 13] in a vicinity of the so-called weakest generatrix on the shell surface. Vibrations localized in small region of a structure is extremely undesirable and destructive because they are the cause of the noise radiation and results in concentration of dangerous stresses.

2 Laminated MRE-Based Structure

Let us consider a medium length thin laminated cylindrical shell consisting of N transversely isotropic layers (see Fig. 1). The thickness, density, Young's modulus, and Poisson's ratio for the nth layer are denoted by h_n, ρ_n, E_n and ν_n, respectively, where $n = 1, 2, \ldots, N$, and N is an odd number. The middle surface of any fixed layer is taken as the original surface. A coordinate system α_1, α_2 as illustrated in Fig. 1 is chosen in such a way that the first quadratic form of the original surface has the form $I = R^2\left(\mathrm{d}s^2 + \mathrm{d}\varphi^2\right)$. The shell is assumed to be not circular with the curvature radius of the original surface $R_2 = Rk(\varphi)$. Here, s and φ are the dimensionless coordinate and angle, respectively, and R is the characteristic size of the shell which is introduced as the maximum value of R_2. The shell is bounded by the two not necessarily plane edges $L_1(\varphi) \leq \alpha_1 \leq L_2(\varphi)$.

Layers with the odd numbers are made of elastic material which is not affected by external magnetic field, with the parameters E_k and the shear moduli G_k being real constants. And layers having the even numbers are fabricated from a viscoelastic MRE whose mechanical and rheological properties depend on the applied magnetic

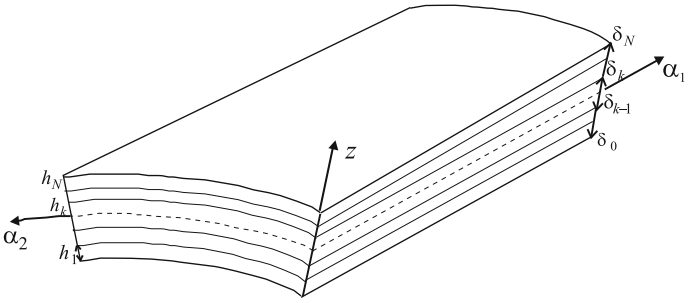

Fig. 1 Laminated cylindrical shell with a curvilinear coordinate system

field. For these layers, the above parameters are assumed to be complex and dependent of B: [8, 9]:

$$E_n = E_n'(B) + iE_n''(B),\ G_n = G_n'(B) + iG_n''(B), \quad i = \sqrt{-1}. \tag{1}$$

From all variety of available MREs, we consider elastomer consisting of a deformed polymer matrix and magnetic particles embedded in this matrix. The procedure of manufacturing these MREs, their composition and a percentage of components are shortly described in references [8, 9, 16]. The properties of the given elastomers show a dependence on the manufacturing technology and operative conditions. In particular, the complex shear modulus $G_{MR} = G'_{MR} + \mathrm{i}G''_{MR}$ is strongly influenced by a magnetic field induction, frequency of an external excitation and an amplitude of deformations as well. For the MRE under consideration, these properties [9] at small (linear) deformations and high frequency (more than 10 Hz) are displayed in Fig. 2. The dissipative properties of a smart viscoelastic material is characterized by the parameter $\tan\delta = G''_{MR}/G'_{MR}$. It is seen that our material possesses

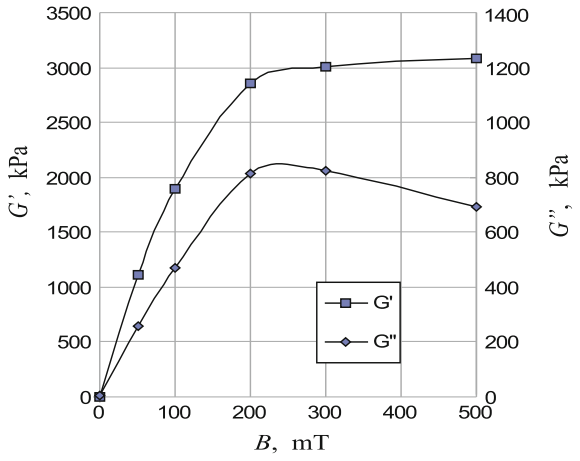

Fig. 2 Dependence of the real and imaginary parts of the MRE shear modulus versus the magnetic field induction

the highest damping capability at about $B = 200$ mT. In the interval $0 \le B < 200$ mT, the data presented in Fig. 2 correlate with the supposition in [22] about the linear dependence of the imaginary part of the shear modulus of the MR material on the magnetic field induction.

In what follows, we will study running low-frequency bending vibrations with a large number of waves in the circumferential direction. For similar stress–strain state the tangential displacements are substantially smaller then displacements in the radial direction [14]. In the frame of the suggested model the adaptive layer may be considered as transversally isotropic that means $E_{MR} = 2(1 + \nu_{MR})G_{MR}$, where E_{MR} is the complex elastic modulus and ν_{MR} is the Poisson's ratio of MRE. Assuming small strains, for many elastomeric materials the real constant ν_{MR} is assumed to be less than 0.4 [21]. In our study $\nu_{MR} = 0.4$.

The data presented in Fig. 2 will be used to predict suppression of running localized vibrations in the MRE-based shell via magnetic field.

3 Governing Equations

The variant of the equivalent single layer (ESL) models developed by Grigoliuk and Kulikov [7] will be used here. This model is completely based on the introduction of the generalized kinematic hypothesis of Timoshenko for the whole laminated packet. Survey articles and monographs devoted to ESL theories are, e.g., [17–19].

On basis of the generalized kinematic hypothesis of Timoshenko, Grigoliuk, and Kulikov [7] have derived a system of five differential equations for elastic laminated cylindrical shells with constant and real moduli E_n, G_n. Recently, this system has been generalized [15] for more common case when some of layers are viscoelastic with complex E_k, G_k dependent on the magnetic field induction. We do not write these equations out here because of inconvenience. However, if vibrations are accompanied by formation of a large number of waves although in one direction at the shell surface, these equations are essentially simplified.

Let δ_k be the distance between the original surface and the upper bound of the nth layer, $h = \sum_{n=1}^{N} h_n$ is the total thickness of the shell (see Fig. 1), w is the normal displacements of points on the original surface, and χ is the displacement function coupled to w by the formula $w = \left(1 - h^2/\beta\Delta\right)\chi$. Then the simplified equations by Grigoliuk and Kulikov [7] read:

$$\begin{aligned} &\frac{Eh^3\eta_3}{12(1-\nu^2)}\left(1 - \frac{\theta h^2}{\beta}\Delta\right)\Delta^2\chi + \frac{1}{R_2(\alpha_2)}\frac{\partial^2\Phi}{\partial\alpha_1^2} + \rho h\frac{\partial^2}{\partial t^2}\left(1 - \frac{h^2}{\beta}\Delta\right)\chi = 0, \\ &\Delta^2\Phi - \frac{Eh}{R_2(\alpha_2)}\frac{\partial^2}{\partial\alpha_1^2}\left(1 - \frac{h^2}{\beta}\Delta\right)\chi = 0. \end{aligned} \tag{2}$$

Here, $\Delta = \partial^2/\partial\alpha_1^2 + \partial^2/\partial\alpha_2^2$ is the Laplace operator in the curvilinear coordinates α_1, α_2, and χ and Φ are the displacement and stress functions, respectively. In Eq. (2),

t is time, E, ν, ρ are the reduced modulus of elasticity, Poisson's ratio and density respectively, and the last parameters η_3, θ, β characterize the reduced shear stiffness of the laminated shell. All the reduced parameters appearing in Eq. (2) are calculated as follows:

$$
\begin{gathered}
\nu = \sum_{k=1}^{N} \frac{E_k h_k \nu_k}{1-\nu_k^2} \left(\sum_{k=1}^{N} \frac{E_k h_k}{1-\nu_k^2} \right)^{-1}, \quad E = \frac{1-\nu^2}{h} \sum_{k=1}^{N} \frac{E_k h_k}{1-\nu_k^2}, \quad \rho = \sum_{k=1}^{N} \rho_k \xi_k, \\
\beta = \frac{12(1-\nu^2)}{Eh\eta_1} q_{44}, \quad q_{44} = \frac{\left[\sum\limits_{k=1}^{N} \left(\lambda_k - \frac{\lambda_{k0}^2}{\lambda_{kk}} \right) \right]^2}{\sum\limits_{k=1}^{N} \left(\lambda_k - \frac{\lambda_{k0}^2}{\lambda_{kk}} \right) G_k^{-1}} + \sum_{k=1}^{N} \frac{\lambda_{k0}^2}{\lambda_{kk}} G_k, \\
\lambda_{kk} = \int\limits_{\delta_{k-1}}^{\delta_k} f_0^2(z) dz, \quad \lambda_{kn} = \int\limits_{\delta_{k-1}}^{\delta_k} f_k(z) f_n(z) dz, \quad \theta = 1 - \eta_2^2/(\eta_1 \eta_3), \\
\eta_1 = \sum_{k=1}^{N} \xi_k^{-1} \pi_{1k} \gamma_k - 3c_{12}^2, \quad \eta_2 = \sum_{k=1}^{N} \xi_k^{-1} \pi_{2k} \gamma_k - 3c_{12} c_{13}, \\
\eta_3 = 4 \sum_{k=1}^{N} (\xi_k^2 + 3\zeta_{k-1}\zeta_k) \gamma_k - 3c_{13}^2, \quad h\xi_k = h_k, \quad h\zeta_n = \delta_n \, (n = 0, \, k), \\
\frac{1}{12} h^2 \pi_{1k} = \int\limits_{\delta_{k-1}}^{\delta_k} g^2(z) \, dz, \qquad \frac{1}{12} h^2 \pi_{2k} = \int\limits_{\delta_{k-1}}^{\delta_k} z \, g(z) \, dz, \quad \frac{1}{12} h^2 \pi_{3k} = \int\limits_{\delta_{k-1}}^{\delta_k} g(z) \, dz, \\
c_{13} = \sum_{k=1}^{N} (\zeta_{k-1} + \zeta_k) \gamma_k, \quad c_{12} = \sum_{k=1}^{N} \xi_k^{-1} \pi_{3k} \gamma_k, \; \gamma_k = \frac{E_k h_k}{1-\nu_k^2} \left(\sum_{k=1}^{N} \frac{E_k h_k}{1-\nu_k^2} \right)^{-1}, \\
f_0(z) = \frac{1}{h^2} (z - \delta_0)(\delta_N - z), \quad f_n(z) = \frac{1}{h_n^2} (z - \delta_{n-1})(\delta_n - z).
\end{gathered}
\tag{3}
$$

As opposed to the classical shell theory based on the Kirchhoff-Love hypotheses, Eq. (3) take into account shear deformations.

From all variants of boundary conditions derived in [7] we consider the conditions for simply supported edges with a diaphragm of an infinite rigidity which inhibit to relative shears of layers along the shell edge [7]:

$$
\chi = \Delta\chi = \Delta^2\chi = \Phi = \Delta\Phi = 0 \quad \text{at} \quad \alpha_1 = L_1(\varphi), L_2(\varphi). \tag{4}
$$

4 Setting the Problem

Let the shell be sufficiently thin so that $h_* = h/R$ is a quantity of the order ~0.01 or less. We introduce a small parameter $\varepsilon^8 = h_*^2 \eta_{3r}^{(0)} / \{12[1 - (\nu_r^{(0)})^2]\}$. Here and below, the superscript (0) means that an appropriate parameter is calculated at $B = 0$, and $z_r = \Re z$ is the real part of a parameter z.

Equation (2) contain four basic parameters E, η_3, θ, β which are complex and depend on the induction B. As shown in paper [16], their impact on damping of the MRE-based laminated shell strongly depends on the correlation between moduli E_n and thicknesses h_n of elastic and adaptive viscoelastic layers. Following reference [16], we assume that all layers which are not affected by external magnetic field are made of the ABS plastic SD-0170 with parameters $E_{pl} = 1.5 \times 10^9$ Pa, $\nu_{pl} = 0.4$, $\rho_{pl} = 1.04 \times 10^3$ kg/m^3, and the total thickness of the MR layers is not less then 70 % from the total thickness h of the whole sandwich. Calculations performed in paper [16] for similar shells have permitted to get the following asymptotic estimations:

$$\nu = \nu_r^{(0)}(1 + \varepsilon^4 \delta\nu), \quad \theta_r \sim \varepsilon^3, \quad \theta_i \sim \varepsilon^4, \quad \eta_3 = \eta_{3r}^{(0)}(1 + \varepsilon^2 \delta\eta_3),$$

$$\eta_{3r}^{(0)} = \pi^{-4}\eta_r^{(0)}[1 - (\nu_r^{(0)})^2], \quad E_r = E_r^{(0)} d, \quad \frac{E_i}{E_r^{(0)}} \sim \varepsilon^4, \quad \frac{K}{\pi^2} = \varepsilon^2 \kappa = \varepsilon^2(\kappa_0 + \mathrm{i}\varepsilon\kappa_1)$$

at $\varepsilon \to 0$, where $K = \pi^2 h_*^2/\beta$, and $z_i = \Im z$ is the imaginary part of z.

Let us introduce the dimensionless magnitudes $\chi^*, \boldsymbol{\Phi}^*$ and time τ as follows:

$$\chi = \varepsilon^{-4} R \chi^*(s, \varphi, t), \quad \boldsymbol{\Phi} = E_r^{(0)} h R^2 \boldsymbol{\Phi}^*(s, \varphi, t), \quad t = \varepsilon^{-3} t_c \tau, \tag{5}$$

where $t_c = \sqrt{\rho R^2 / E_r^{(0)}}$ is the characteristic time. Then Eq. (2) may be rewritten in the dimensionless form:

$$\begin{aligned} &\varepsilon^4 d(B) \Delta^2 \chi^* + k(\varphi) \frac{\partial^2 \boldsymbol{\Phi}^*}{\partial s^2} + \varepsilon^2 \frac{\partial^2}{\partial \tau^2}[1 - \varepsilon^2 \kappa(B) \Delta] \chi^* = 0, \\ &\varepsilon^4 \Delta^2 \boldsymbol{\Phi}^* - d(B) k(\varphi) \frac{\partial^2}{\partial s^2}[1 - \varepsilon^2 \kappa(B) \Delta] \chi^* = 0, \end{aligned} \tag{6}$$

and the corresponding boundary conditions read

$$\chi^* = \Delta\chi^* = \Delta^2 \chi^* = \boldsymbol{\Phi}^* = \Delta\boldsymbol{\Phi}^* = 0, \quad \text{at} \quad s = s_1(\varphi), s_2(\varphi). \tag{7}$$

In Eq. (6), $d(B), \kappa(B)$ are the functions of the magnetic field induction B. When deriving Eqs. (6) from (2), we have omitted the operator $\Delta^3 \chi$ because of smallness of the coefficient $K\theta$ and disregarded by very small dimensionless parameters $\varepsilon^4 \delta\nu, \varepsilon^2 \delta\eta_3, E_i/E_r^{(0)}$.

Let us consider the following initial conditions for the displacement function χ^*:

$$\begin{aligned} &\chi^*|_{\tau=0} = \chi_0 \exp[\mathrm{i}\varepsilon^{-1} S_0(\varepsilon)], \ \dot{\chi}^*|_{\tau=0} = \mathrm{i}\varepsilon^{-1} v_0 \exp[\mathrm{i}\varepsilon^{-1} S_0(\varepsilon)], \\ &S_0(\varphi) = a_0 \varphi + \tfrac{1}{2} b_0 \varphi^2, \quad \mathrm{i} = \sqrt{-1}, \quad a_0 > 0, \quad \Im b_0 > 0, \end{aligned} \tag{8}$$

$$a_0, |b_0|, |\chi_0|, |v_0|, |\partial\chi_0/\partial s|, |\partial v_0/\partial s| = O(1) \quad \text{when} \quad \varepsilon \to 0, \tag{9}$$

where $\chi_0(s, \varphi, \varepsilon), v_0(s, \varphi, \varepsilon)$ are complex-valued functions satisfying (7).

The real and imaginary parts of functions (8), with account taken of the inequality in (8), define the two initial wave packets localized near the generatrix $\varphi = 0$ on the shell surface. These functions may be considered as approximations of the initial perturbations being the result of some transient forces applied along the line $\varphi = 0$. It should be also noted that under some conditions for parameters a_0, b_0, functions (8) coincide with the eigenmodes localized in a vicinity of the so-called weakest generatrix at the surface of a shell with variable geometric parameters [14]. So, availability of an oblique edge or/and variable radius of curvature may result in localization of both free and parametric vibrations which are approximated by functions like (8).

The problem is to construct a solution of the initial boundary value problem (6)–(8) and analyze the influence of the magnetic field on the amplitude of running WPs on conditions that the induction $B(\tau)$ is a slowly growing function of τ.

5 Asymptotic Approach

Let

$$y_j(s,\varphi) = \sin\frac{\pi j[s - s_1(\varphi)]}{l(\varphi)} \quad \text{and} \quad \lambda_j = \frac{\pi^4 j^4}{l^4(\varphi)}, \quad j = 1, 2, 3, \ldots \tag{10}$$

be an infinite system of eigenfunctions and eigenvalues, respectively, of the boundary value problem:

$$\frac{\mathrm{d}^4 y}{\mathrm{d}s^4} - \lambda y = 0, \tag{11}$$

$$y = y'' = 0 \quad \text{at} \quad s = s_1(\varphi), s = s_2(\varphi), \tag{12}$$

where $l(\varphi) = s_2(\varphi) - s_1(\varphi)$.

Because the functions $\chi_0(s,\varphi), v_0(s,\varphi)$ appearing in (8) satisfy the boundary conditions (7), they can be expanded in terms of the eigenfunctions $y_j(s,\varphi)$ into uniformly convergent series in some section $\varphi_1 \le \varphi \le \varphi_2$:

$$\begin{aligned} \chi_0 &= \textstyle\sum_{j=1}^{\infty} \chi_j^\circ(\varphi,\varepsilon) y_j(s,\varphi), \quad \chi_j^\circ = \int_{s_1(\varphi)}^{s_2(\varphi)} \chi_0(s,\varphi,\varepsilon) y_j(s,\varphi)\mathrm{d}s, \\ v_0 &= \textstyle\sum_{j=1}^{\infty} v_j^\circ(\varphi,\varepsilon) y_j(s,\varphi), \quad v_j^\circ = \int_{s_1(\varphi)}^{s_2(\varphi)} v_0(s,\varphi,\varepsilon) y_j(s,\varphi)\mathrm{d}s. \end{aligned} \tag{13}$$

It is assumed that χ_j°, v_j° are polynomials of $\varepsilon^{-1/2}$ whose coefficients are regular functions of ε. Then they may be represented by the series [13]

$$\begin{aligned} \chi_j^\circ &= \textstyle\sum_{i=0}^{\infty} \varepsilon^{i/2} \chi_{ji}^\circ(\zeta), \quad \chi_{ji}^\circ(\zeta) = \sum_{k=0}^{M_{ji}} c_{jik}^\circ \zeta^k, \\ v_j^\circ &= \textstyle\sum_{i=0}^{\infty} \varepsilon^{i/2} v_{ji}^\circ(\zeta), \quad v_{ji}^\circ(\zeta) = \sum_{k=0}^{M_{ji}} d_{jik}^\circ \zeta^k \end{aligned} \tag{14}$$

where $\zeta = \varepsilon^{-1/2}\varphi$, and $c_{jik}^\circ, d_{jik}^\circ = O(1)$.

Due to linearity of the initial boundary value problem (6)–(9), its solution may be presented in the form

$$\chi^* = \sum_{j=1}^{\infty} \chi_j^*(s, \varphi, \tau, \varepsilon), \quad \boldsymbol{\Phi}^* = \sum_{j=1}^{\infty} \boldsymbol{\Phi}_j^*(s, \varphi, \tau, \varepsilon), \tag{15}$$

where $\chi_j^*, \boldsymbol{\Phi}_j^*$ are the required functions localized in a neighborhood of moving generatrix $\varphi = q_j(\tau)$. Here $q_j(t)$ is a twice differentiable function such that $q_j(0) = 0$. The pair of functions $\chi_j^*, \boldsymbol{\Phi}_j^*$ is called [11, 13] the jth wave packet (WP) with the center at $\varphi = q_j(\tau)$.

Let us hold any number j fixed and study the behavior of the jth WP. It is convenient to go over to a local coordinate system $\varphi = q_j(\tau) + \varepsilon^{1/2}\xi_j$ associated with the moving center $\varphi = q_j(\tau)$. In the new coordinate system equations (6) read

$$\begin{aligned}
&d(B)\left(\varepsilon^2 \frac{\partial^4 \chi_j^*}{\partial \xi_j^4} + 2\varepsilon^3 \frac{\partial^4 \chi_j^*}{\partial \xi_j^2 \partial s^2} + \varepsilon^4 \frac{\partial^4 \chi_j^*}{\partial s^4}\right) + k(\varphi)\frac{\partial^2 \boldsymbol{\Phi}_j^*}{\partial s^2} + \left(\varepsilon^2 \frac{\partial^2}{\partial \tau^2} - 2\varepsilon^{3/2}\dot{q}_j \frac{\partial^2}{\partial \xi_j \partial \tau}\right.\\
&\left. + 2\varepsilon \dot{q}_j^2 \frac{\partial^2}{\partial \xi_j^2} - \varepsilon^{3/2}\ddot{q}_j \frac{\partial}{\partial \xi_j}\right)\left[\chi_j^* - \kappa(B)\left(\varepsilon \frac{\partial^2 \chi_j^*}{\partial \xi_j^2} + \varepsilon^2 \frac{\partial^2 \chi_j^*}{\partial s_j^2}\right)\right] = 0,\\
&\varepsilon^2 \frac{\partial^4 \boldsymbol{\Phi}_j^*}{\partial \xi_j^4} + 2\varepsilon^3 \frac{\partial^4 \boldsymbol{\Phi}_j^*}{\partial \xi_j^2 \partial s^2} + \varepsilon^4 \frac{\partial^4 \boldsymbol{\Phi}_j^*}{\partial s^4} - d(B)k(\varphi)\frac{\partial^2}{\partial s^2}\left[\chi_j^* - \kappa(B)\left(\varepsilon \frac{\partial^2 \chi_j^*}{\partial \xi_j^2} + \varepsilon^2 \frac{\partial^2 \chi_j^*}{\partial s_j^2}\right)\right] = 0,
\end{aligned} \tag{16}$$

where $\kappa = \kappa_0(B) + \mathrm{i}\kappa_1(B)$, and the function $k(\varphi)$ is expanded into a series in a neighborhood of the center $\varphi = q_j(\tau)$:

$$k(\varphi) = k[q(t)] + \varepsilon^{1/2}k'[q(t)]\xi_j + \frac{1}{2}\varepsilon k''[q(\tau)]q_j^2 + \cdots \tag{17}$$

Here and in what follows, the dot $(\cdot)$ and prime $(')$ denote differentiation with respect to dimensionless time τ and angle φ, respectively.

The initial conditions for jth WP take the form

$$\begin{aligned}
\chi_j^*|_{\tau=0} &= \chi_j^\circ(\varphi, \varepsilon) y_j(s, \varphi) \exp\left[\mathrm{i}\varepsilon^{-1} S_0(\varphi)\right],\\
\dot{\chi}_j^*|_{\tau=0} &= \mathrm{i}\varepsilon^{-1} v_j^\circ(\varphi, \varepsilon) y_j(s, \varphi) \exp\left[\mathrm{i}\varepsilon^{-1} S_0(\varphi)\right].
\end{aligned} \tag{18}$$

The dynamic stress state of the shell consists of the basic stress state and the dynamic edge effect integrals describing the shell behavior in a small neighborhood of each edge. To study the basic state on each edge, one only needs to satisfy two basic conditions. Apart from terms of the order ε^2 these conditions for the jth WP have the form

$$\chi_j^* = \boldsymbol{\Phi}_j^* = 0 \quad \text{at} \quad s = s_1(\varphi), s_2(\varphi). \tag{19}$$

We note that the functions s_1, s_2, y_j should be also expended into series in a vicinity of the center $\varphi = q_j(\tau)$.

In what follows, we omit the subscript j. For instance, the notations χ_j^*, χ_j°, $y_j, \chi_{ji}^\circ, \xi_j, c_{jik}^\circ$ are replaced by $\chi^*, \chi^\circ, y, \chi_i^\circ, \xi, c_{ik}^\circ$, respectively.

Following references [11, 13], the solution of the initial boundary value problem (16), (18), (19) may be constructed in the form of the following series:

$$\begin{aligned} &\chi^* = \sum_{\varsigma=0}^{\infty} \varepsilon^{\varsigma/2} \chi_\varsigma \exp\left(\mathrm{i}\varepsilon^{-1} S\right), \ \boldsymbol{\Phi}^* = \sum_{\varsigma=0}^{\infty} \varepsilon^{\varsigma/2} \boldsymbol{\Phi}_\varsigma \exp\left(\mathrm{i}\varepsilon^{-1} S\right), \\ &S = \int_0^\tau \omega(\tilde{\tau})\mathrm{d}\tilde{\tau} + \varepsilon^{1/2} p(\tau)\xi + \tfrac{1}{2}\varepsilon b(\tau)\xi^2, \end{aligned} \tag{20}$$

where $\Im b(\tau) > 0$ for any time $\tau > 0$, $\chi_\varsigma(s, \xi, \tau), \boldsymbol{\Phi}_\varsigma(s, \xi, \tau)$ are polynomials in ξ with complex coefficients depending on τ and s, $|\omega(\tau)|$ is the momentary frequency of vibrations in a neighborhood of the moving center $\varphi = q(t)$, $p(\tau)$ is the variable wave parameter, and $b(\tau)$ defines the width of the jth WP, the inequality $\Im b(\tau) > 0$ guaranteeing attenuation of wave amplitudes within the WP.

As seen, functions (20) approximate running transitional localized vibrations in the shell. In the case when $q = 0$, and $\omega, p, b, \chi_\varsigma$ and $\boldsymbol{\Phi}_\varsigma$ are independent of time τ, expansions (20) are degenerated into the stationary WP describing free localized vibrations of elastic [20] or viscoelastic [10] cylindrical shells in a vicinity of the fixed (weakest) generatrix.

To define all required functions appearing in ansatz (20), one needs to substitute them into governing equations and boundary conditions as well. The substitution of expansions (20) into Eq. (16) results in the sequence of differential equations

$$\sum_{j=0}^{\varsigma} \mathbf{L}_j \chi_{\varsigma-j} = 0, \quad \varsigma = 0, 1, 2, \ldots \tag{21}$$

where

$$\mathbf{L}_0 z = \frac{k^2(q) d(B)[1 + \kappa_0(B)p^2]}{p^4} \frac{\partial^4 z}{\partial s^4} + \left\{p^4 - [1 + \kappa_0(B)p^2](\omega - \dot{q}p)^2\right\} z, \tag{22}$$

$$\begin{aligned} &\mathbf{L}_1 = \left(b\mathbf{L}_p + \mathbf{L}_q + \dot{p}\mathbf{L}_\omega\right)\xi - \mathrm{i}\mathbf{L}_p \tfrac{\partial}{\partial \xi}, \\ &\mathbf{L}_2 = \left(b^2\mathbf{L}_{pp} + 2b\mathbf{L}_{pq} + \mathbf{L}_{qq} + \dot{p}^2\mathbf{L}_{\omega\omega} + 2\dot{p}\mathbf{L}_{\omega q}\right. \\ &\left. + 2\dot{p}b\mathbf{L}_{\omega p} + \dot{b}\mathbf{L}_\omega\right)\xi^2 - \tfrac{1}{2}\mathbf{L}_{pp}\tfrac{\partial^2}{\partial \xi^2} - \mathrm{i}\left(b\mathbf{L}_{pp} + \mathbf{L}_{pq} + \dot{p}\mathbf{L}_{\omega p}\right)\xi\tfrac{\partial}{\partial \xi} - \\ &\mathrm{i}\mathbf{L}_\omega \tfrac{\partial}{\partial t} - \mathrm{i}\left(\tfrac{1}{2}b\mathbf{L}_{pp} + \tfrac{1}{2}\dot{\omega}\mathbf{L}_{\omega\omega} + \dot{p}\mathbf{L}_{\omega p} + \tfrac{1}{2}\mathbf{L}_{pq} + +\ddot{q}p + \mathbf{N}\right), \ldots, \end{aligned} \tag{23}$$

$$\mathbf{N} = \frac{\mathrm{i}\kappa_1(B) d(B) p^6(\tau)}{1 + \kappa_0(B)p^2(\tau)}. \tag{24}$$

In Eq. (23), the subscripts p, q, ω denote differentiation with respect to the corresponding variables p, q, ω. Operators L_ς for $\varsigma \geq 3$ are not written out here because of its awkwardness and may be found in book [14].

The functions $\boldsymbol{\Phi}_\varsigma$ may be found step by step from a sequence of inhomogeneous equations and expressed in terms of the functions χ_ς.

The substitution of (20) into the basic boundary conditions lead to the sequence of the boundary conditions written in terms of the functions χ_ς:

$$\chi_0 = 0, \qquad \frac{\mathrm{d}^2\chi_0}{\mathrm{d}s^2} = 0, \quad \text{at} \quad s = s_i[q(t)]; \tag{25}$$

$$\chi_1 + \xi s_i' \frac{\partial \chi_0}{\partial s} = 0, \quad \frac{\partial^2 \chi_1}{\partial s^2} + \xi s_i' \frac{\partial^3 \chi_0}{\partial s^3} = 0, \quad \text{at} \quad s = s_i[q(t)]; \quad \ldots \tag{26}$$

The sequence of one-dimensional boundary value problems (21)–(26) serves for determination of required functions appearing in ansatz (20). The procedure for their sequential finding is given in references [11, 13, 14]. Omitting its details, we give only the principle equations.

In the zeroth order approximation ($\varsigma = 0$), one has the homogeneous ordinary differential equation (21) with the homogeneous boundary conditions (25). Its solution may be presented in the form

$$\chi_0(s, \xi) = P_0(\xi, \tau) y[s, q(\tau)], \tag{27}$$

where $P_0(\xi, \tau)$ is an unknown polynomial in ξ. Substituting Eqs. (27) into (21) at $\varsigma = 0$ yields the relation

$$\omega = \dot{q}(\tau) p(\tau) - H^{\pm}[p(\tau), q(\tau), \tau] \tag{28}$$

coupling the momentary frequency $\omega(\tau)$ to the wave parameter $p(\tau)$ and the grope velocity $v(\tau) = \dot{q}(\tau)$ of the jth WP, where

$$H^{\pm}(p, q, \tau) = \pm \sqrt{d[B(\tau)] \left\{ \frac{p^4}{1 + \kappa_0[B(\tau)] p^2} + \frac{\lambda(q) k^2(q)}{p^4} \right\}} \tag{29}$$

are Hamilton functions.

The signs $\pm$ in Eq. (28) indicate the availability of two branches (positive and negative) of the solutions corresponding to the functions $H^{\pm}$. These signs are omitted in what follows, and all further constructions are fulfilled for the function H^{+}.

In the first order approximation (at $\varsigma = 1$), one has the nonhomogeneous differential equation (21) with the nonhomogeneous boundary conditions (26). The compatibility condition for this nonhomogeneous boundary value problem results in the two Hamiltonian systems

$$\dot{q} = \frac{\partial H}{\partial p}, \quad \dot{p} = -\frac{\partial H}{\partial q} \quad \text{and} \quad \dot{q} = -\frac{\partial H}{\partial p}, \quad \dot{p} = +\frac{\partial H}{\partial q} \tag{30}$$

corresponding to the positive and negative branches of the solution, respectively. Here and below, $H = H^+$.

The comparison of Eqs. (18) and (20) gives the initial conditions for Eq. (30):

$$p(0) = a^\circ, \quad q(0) = 0. \tag{31}$$

Finally, the compatibility condition for the nonhomogeneous boundary value problem (21), (26) arising in the second order approximation ($\varsigma = 2$) yields the differential equation

$$(\xi^2 \mathbf{D}_b - 2\mathbf{D}_{\xi t})P_0 = 0, \tag{32}$$

where

$$\begin{aligned}
&\mathbf{D}_b = \dot{b} + H_{pp}b^2 + 2H_{pq}b + H_{qq}, \quad \mathbf{D}_{\xi t} = \hat{h}_0 \tfrac{\partial^2}{\partial \xi^2} + \hat{h}_1 \xi \tfrac{\partial}{\partial \xi} + \hat{h}_2 \tfrac{\partial}{\partial t} + \hat{h}_3, \\
&\hat{h}_0(t) = \tfrac{1}{2}H_{pp}, \quad \hat{h}_1(t) = \mathrm{i}(bH_{pp} + H_{pq}), \quad \hat{h}_2 = \mathrm{i}, \\
&\hat{h}_3(t) = \tfrac{\mathrm{i}}{2H}\left\{ bHH_{pp} - \dot{\omega} - 2H_q H_p + \ddot{q}p + \tfrac{1}{\eta}\int_{s_1}^{s_2} \mathbf{L}_\omega \dot{y} y \mathrm{d}s + \Gamma \right\}, \\
&\Gamma(t) = -\tfrac{2k(\tau)k'(\tau)d(B)[2+\kappa_0(B)p^2(\tau)]\lambda[q(\tau)]}{p^5(\tau)} - \tfrac{d(B)\kappa_1(B)p^6(\tau)}{1+\kappa_0(B)p^2(\tau)}.
\end{aligned} \tag{33}$$

Equation (32) has a solution of polynomial form if and only if the function $b(\tau)$ satisfies the Riccati equation

$$\dot{b} + H_{pp}b^2 + 2H_{pq}b + H_{qq} = 0. \tag{34}$$

The comparison of Eqs. (18) and (20) gives the initial condition

$$b(0) = b^\circ. \tag{35}$$

Then (32) is reduced to the following equation

$$\mathbf{D}_{\xi t}P_0 \equiv \hat{h}_0 \frac{\partial^2 P_0}{\partial \xi^2} + \hat{h}_1 \xi \frac{\partial P_0}{\partial \xi} + \hat{h}_2 \frac{\partial P_0}{\partial \tau} + \hat{h}_3 P_0 = 0 \tag{36}$$

called the amplitude one.

A solution of (36) may be presented in the following form [13]:

$$P_0 = \Theta_m(\tau)\mathscr{H}_m(x), \tag{37}$$

where $\mathscr{H}_m(x)$ is the Hermite polynomials in x of the mth degree, and

$$x = \rho(\tau)\xi, \quad \rho(\tau) = \frac{\exp\left[-\int \frac{\hat{h}_1(\tau)\mathrm{d}\tau}{\hat{h}_2(\tau)}\right]}{\sqrt{4\int \frac{\hat{h}_0(\tau)}{\hat{h}_2(\tau)} \exp\left[-2\int \frac{\hat{h}_1(\tau)\mathrm{d}\tau}{\hat{h}_2(\tau)}\right]\mathrm{d}\tau}},$$
$$\Theta_m(\tau) = \frac{\left\{4\int(\hat{h}_0/\hat{h}_2)\exp\left[-2\int(\hat{h}_1/\hat{h}_2)\mathrm{d}\tau\right]\mathrm{d}\tau\right\}^{m/2}}{\exp\left[\int(\hat{h}_3/\hat{h}_2)\mathrm{d}\tau\right]}. \tag{38}$$

It is evident that the polynomial

$$P_0(\xi, \tau; c_m) = \sum_{m=0}^{M} c_m \Theta_m(\tau) \mathscr{H}_m[\rho(\tau)\xi] \tag{39}$$

of the Mth degree is also the solution of the amplitude equation (36), where c_m are arbitrary constants found from the initial conditions.

The function

$$\chi^* = \left[\chi_0(s, \xi, \tau) + O\left(\varepsilon^{1/2}\right)\right] \exp\left[\mathrm{i}\varepsilon^{-1} S(s, \xi, \tau; \varepsilon)\right] \tag{40}$$

found from the first three approximations is the main term in expansion (20).

The derived above Hamiltonian functions as well as other principal equations take into account the dependence of viscoelastic properties of MR materials on the induction B of the magnetic field. Thus, applying the external magnetic field, one can control running localized vibrations in the MRE-based sandwich. Furthermore, slowly increasing the magnetic field, we can softly suppress unsteady vibrations.

6 Examples

Let us consider examples illustrating the damping capacity of MREs imbedded between elastic layers in laminated cylindrical shells.

Example 1. At first, we consider the simplest case when all geometrical parameters, the curvature and the generatrix length, are constants. Here, $k \equiv 1, s_1 = 0, s_2 = l$ and the Hamilton function for jth WP is simplified:

$$H(p, \tau) = \pm\sqrt{d[B(t)]\left\{\frac{p^4}{1 + \kappa_0[B(t)]p^2} + \frac{\pi^4 j^4}{l^4 p^4}\right\}}. \tag{41}$$

Then all principle equations admit solutions in the explicit form:

$$p^{\pm} = a_0,\ q^{\pm}(\tau) = \int_0^{\tau} H_p^{\pm} \mathrm{d}\tau,\ \omega^{\pm}(\tau) = p^{\pm} H_p^{\pm} - H^{\pm},\ b^{\pm}(\tau) = \frac{b_0}{1 + b_0 \int_0^{\tau} H_{pp}^{\pm} \mathrm{d}\tau},$$
$$\chi_0^{\pm}(\tau) = c^{\pm} \sqrt{\frac{b^{\pm}}{H^{\pm}} \exp\left\{ a_0^6 \int_0^{\tau} \frac{\hat{d}[B(\tau)]\kappa_1[B(\tau)]}{H^{\pm}\left\{1 + a_0^2 \kappa_0[B(\tau)]\right\}} \mathrm{d}\tau \right\}}. \tag{42}$$

If the magnetic field is stationary (B is constant), then the momentary frequencies $|\omega^{\pm}|$ for both WPs are constants; if not, then $|\omega^{\pm}(\tau)|$ are dependent of time. The functions $\mathfrak{I}b^{\pm}(\tau)$ characterize a size of the shell area enveloped in vibrations, and $\chi_0^{\pm}(\tau)$ define the amplitudes of these unsteady vibrations. We have performed calculations of $\omega = |\omega^{\pm}(\tau)|$, $\mathfrak{I}b = \mathfrak{I}b^{\pm}(\tau)$, $|\chi_0| = |\chi_0^{\pm}(\tau)|$ versus dimensionless time τ for the three-layered sandwich with the external layers made of ABS plastic SD-0170 and internal core fabricated of MRE with geometric parameters $R = 0.4$ m, $L = 1.5$ m, $h_1 = h_3 = 0.5$ mm, $h_2 = 11$ mm for the two different cases: (a) at the zero level of magnetic field ($B = 0$); (b) when the induction $B(\tau) = c\tau$ is the linear function of dimensionless time at $c = 5, 10$ mT. The following parameters were considered as the initial ones: $a_0 = 2.5, b_0 = \mathrm{i}, \chi_1^{\circ} = 1, v_1^{\circ} = 0$ and $\chi_j^{\circ} = v_j^{\circ} = 0$ at $j > 1$. Figure 3 shows that for the accepted parameters and case (b) the momentary frequency $\omega(\tau)|$ is the decreasing function of time. As seen from Fig. 4, the width of the 1*st* running WP increases in time for both cases, (a) and (b), that means that the WP spreads in the circumferential direction. But the speed of this spreading depends weakly on whether the magnetic field is stationary or time-dependent. As concerns the wave amplitudes (see Fig. 5), they demonstrate a very strong dependence on the viscoelastic properties of MREs which are affected by the applied magnetic field. The curve corresponding to $c = 0$ mT shows the capability of the MRE to damp traveling vibrations in the sandwich without magnetic field. The other two curves bring out clearly that this capability becomes stronger under the action of growing magnetic field. So, when comparing amplitudes at the fixed moment $\tau = 2.4$, one can see that the maximum amplitude $|\chi_0|$ for $c = 5$ mT and $c = 10$ mT are 3-and 6-times less, respectively, than that for $c = 0$ mT.

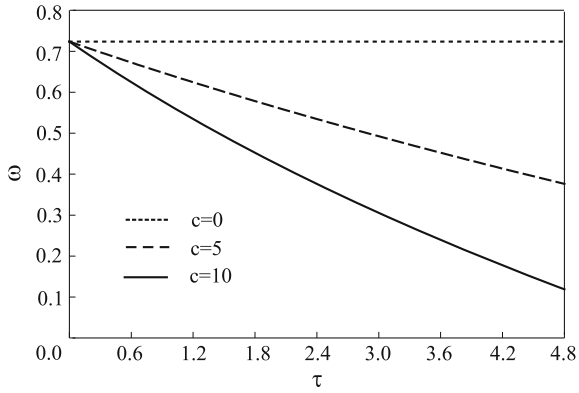

Fig. 3 The dimensionless momentary frequency $\omega = |\omega^{\pm}(\tau)|$ versus dimensionless time for different $c = 0, 5, 10$ mT

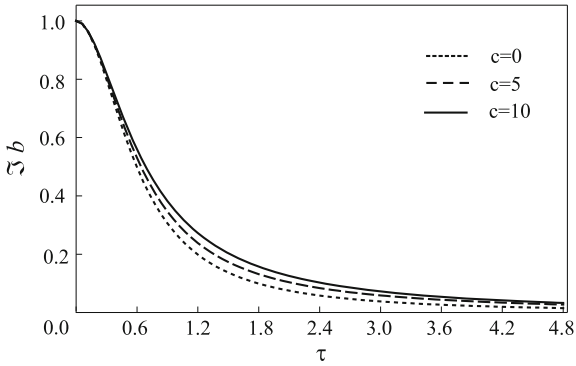

Fig. 4 The parameter $\Im b = \Im b^{\pm}(\tau)$ versus dimensionless time for different $c = 0, 5, 10$ mT

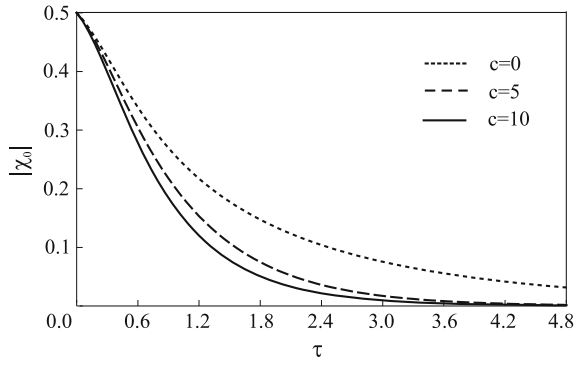

Fig. 5 The maximum amplitude $|\chi_0|$ versus dimensionless time for different $c = 0, 5, 10$ mT

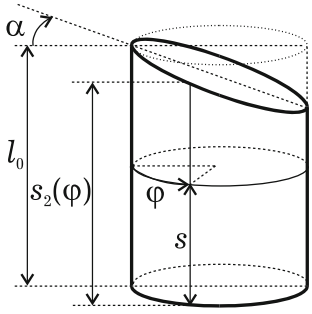

Fig. 6 The middle surface of a circular laminated cylindrical shell with slanted edge

Example 2. Now we consider a circular laminated cylindrical shell with a slanted edge as shown in Fig. 6.

Here

$$k = 1, \quad s_1 = 0, \quad s_2(\varphi) = l_0 + (\cos\varphi - 1)\tan\beta.$$

Then the eigenmodes corresponding to low-frequency vibrations will be localized in a neighborhood of the longest generatrix $\varphi = 0$ which is called the weakest one [14, 20]. Indeed, let the parameters $q = 0, p = a_0$ satisfy the system of equations

$$H_p = 0, \quad H_q = 0, \tag{43}$$

and $b = b_0$ is the solution of the quadratic equation

$$H_{pp} b^2 + 2H_{pq} b + H_{qq} = 0 \tag{44}$$

at the zero level of magnetic field ($B = 0$). In Eq. (44), the derivatives H_{pp}, H_{pq}, H_{qq} are calculated at $q = 0, p = a_0$. Then, up to amplitudes $\chi_j^\circ, \mathrm{i}\varepsilon^{-1} v_j^\circ$, the initial WP (18) with the number j is the eigenmode [14, 20] localized in a vicinity of the longest generatrix $\varphi = 0$.

Now, let $B(\tau)$ be a slowly growing function of time such that $B(0) = 0$. We set the problem to study the influence of applied nonstationary magnetic field on this eigenmode at $\tau > 0$. Because any initial perturbations may be expanded in terms of eigenmodes, this problem will illustrate the possibility of soft suppression of vibrations excited near the weakest line in the MRE-based sandwich via the time-dependent magnetic field.

Figures 7, 8, 9, 10 and 11 show the dependence of $p^+, q^+, \omega^+, \mathfrak{I} b^+, |\mathfrak{R} \chi_0^+|, |\mathfrak{I} \chi_0^-|$ on dimensionless time τ for the three-layered sandwich of the radius $R = 0.4$ m

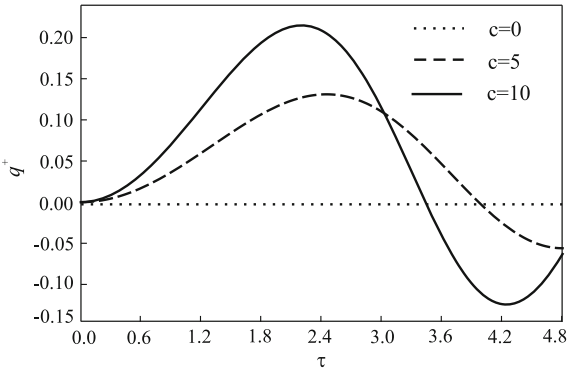

Fig. 7 The center $\varphi = q^+ = 0$ of the initial WP (at $c = 0$ mT) and the center $\varphi = q^+$ of the 1st positive WP versus dimensionless time τ at different rates of growing of the magnetic field induction ($c = 5, 10$ mT)

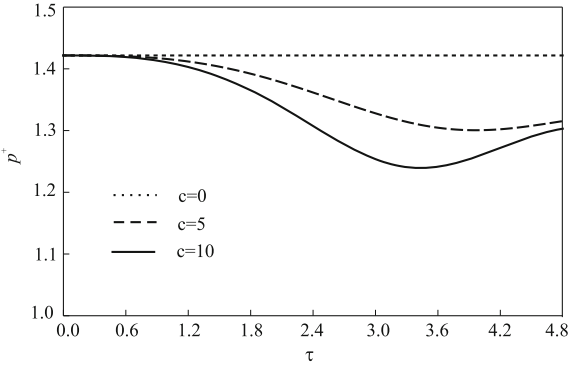

Fig. 8 The wave parameter $p^+ = a_0 \approx 1.41$ of the initial WP (at $c = 0$ mT) and parameter p^+ of the 1st positive WP versus dimensionless time τ at different rates of growing of the magnetic field induction ($c = 5, 10$ mT)

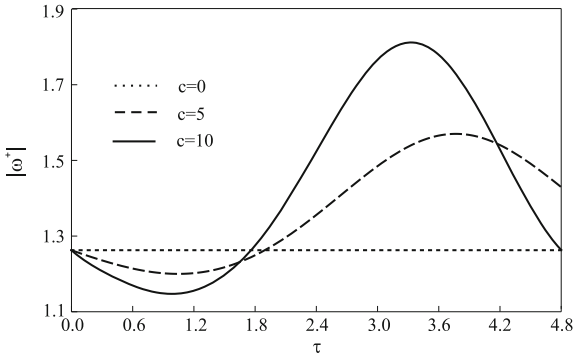

Fig. 9 The natural frequency $|\omega^+| = \omega_0 \approx 1.25$ of the initial WP (at $c = 0$ mT) and the momentary frequency $|\omega^+|$ of the 1st positive WP versus dimensionless time τ at different rates of growing of the magnetic field induction ($c = 5, 10$ mT)

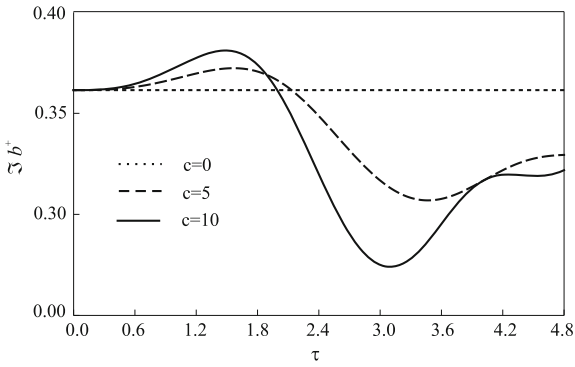

Fig. 10 The parameter $\mathfrak{I}b^+ = \mathfrak{I}b_0 \approx 0.36$ for the initial WP and parameter $\mathfrak{I}b^+$ for the 1st positive WP versus dimensionless time at different rates of growing of the magnetic field induction ($c = 5, 10$ mT)

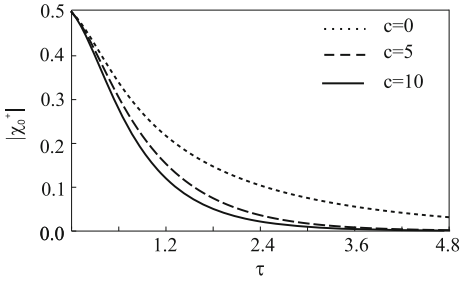

Fig. 11 The $|\chi_0^+|$ for the 1st positive WP versus dimensionless time at $c = 0$ and different rates of growing of the magnetic field induction ($c = 5, 10$ mT)

and length $L = 0.8$ m under the action of growing induction $B = c\tau$ at different $c = 0, 5, 10$ mT. The external elastic layers and the internal viscoelastic core were assumed to be made of the same material as in the previous example. The thicknesses of the elastic layers were taken to be equal to $h_1 = h_3 = 0.5$ mm, and the thickness of the MRE core was $h_2 = 11$ mm. The calculations were performed for the 1*st* positive WP (at $j = 1$) with the initial amplitudes $\chi_1^\circ = 1$, $v_1^\circ = 0$ in (18). Due to the symmetry of the shell and the initial WP with regard to the plane $\varphi = 0$, the curves for all functions corresponding to the negative WP are the same as in Figs. 7, 8, 9, 10 and 11.

In all Figs. 7, 8, 9, 10 and 11, the straight dotted lines correspond to the eigenform localized in a neighborhood of the longest generatrix $\varphi = 0$. Thus, if a magnetic field is absent ($c = 0$ mT), the initial WP coinciding with one of eigenmodes stays motionless, with the wave number p^+, eigenfrequency ω^+ and parameter b^+ being constants for any point of time. Whereas, the maximum amplitude of free vibrations (see Fig. 11) is the decreasing function of the dimensionless time τ. This damping is a consequence of viscoelastic properties of the MRE core at the zeroth induction of magnetic field.

Interesting effects are observed when the magnetic field is applied. After its turning on, the eigenmode (initial WP) is spitted into two WPs, positive and negative ones, traveling in the opposite directions (see Fig. 7). Figure 7 shows also that the increase of the magnetic field induction $B(\tau)$ results in the multiple refections of the WP from the certain generatrices $\varphi = \varphi_r = q^+(\tau_r)$, these refections being accompanied by slight focusing (see Fig. 10). Herewith, the larger the growth rate of the induction (parameter c, mT) is, the earlier the reflection occurs. So, for $c = 5$ mT the first reflection occurs from the generatrix $\varphi \approx 0.13$ at the point of time $\tau = \tau_r \approx 2.45$, and for $c = 10$ mT, one has $\varphi \approx 0.21$, $\tau_r \approx 2.1$. At $\tau = \tau_0$, the WP center goes back to the initial position at the longest generatrix ($\varphi = 0$). Here, $\tau_0 \approx 4.0$ and $\tau_0 \approx 3.58$ for $c = 5$ mT and $c = 10$ mT, respectively. Figures 8 and 9 demonstrate the manner in which the wave parameter p^+ and the dimensionless momentary frequency $|\omega^+|$ vary with the course of time. It is seen that, in the beginning, the frequency $|\omega^+|$ drops slightly, but then it runs up together with the induction $B(\tau)$. The strong growth of the frequency is explained by increasing the total stiffness for the sandwich at high level of the applied magnetic field.

The important conclusions are followed from the analysis of Fig. 11: increasing the magnetic field induction leads to a soft suppression of running vibrations. For instance, at $c = 10$ mT, the damping decrement is about two times than that without magnetic field (at $c = 0$ mT). At that, the larger the growth rate of the magnetic field is, the faster the damping of running vibrations occurs.

7 Conclusions

The modified governing equations, based on the ESL theory for laminated shells, have been used for the analysis of running localized vibrations in the multilayered cylindrical shells assembled from elastic and viscoelastic layers. The viscoelastic layers were assumed to be made of MREs whose elastic and rheological properties are sensitive to the applied magnetic field. The dynamic response of the MRE-based shell to the initial localized perturbations, on condition that the magnetic field induction was time-varying function, has been predicted by using the asymptotic method. The solution of the initial boundary value problem for the governing equations has been constructed in the form of the superimposition of WPs running in the circumferential direction.

In order to demonstrate the damping capability of MREs, two examples were considered. The first example has showed that under zeroth level of magnetic field, localized vibrations in the cylindrical shell with constant geometrical parameters spread rapidly over the shell surface and decay. The application of increasing magnetic field does not influence essentially the speed of the WPs spreading, but has a noticeable effect on the rate of decay of traveling vibrations.

In the second example, the effect of time-dependent magnetic field on the localized eigenmodes of the circular cylindrical shell with the oblique edge was analyzed. It was revealed that increasing the magnetic field induction results in the splitting of the localized eigenmode into two packets of bending waves traveling in the opposite directions. The unlimited increase of magnetic field leads to very complicated behavior of running WPs, viz., their multiple reflections from more stiff regions (adjacent to the shortest generatrix), slight focusing and very quick decreasing the waves amplitudes. The damping decrement is found to be influenced by the level of magnetic field: the larger the growth rate of the magnetic field induction is, the faster the damping of running vibrations becomes.

The basic conclusions of this study are the following:

- smart materials like MREs may be considered as promising ones for designing thin-walled laminated structures with adaptive viscoelastic properties;
- thin composite laminated shells assembled by embedding MRs between elastic layers turns out to be sensitive to the applied magnetic field, their reduced dissipative properties being strongly influenced by the applied magnetic field;
- slowly varying magnetic field may be used with success in order to ensure soft suppression of nonstationary localized vibrations in thin MRE-based laminated shells.

Acknowledgments The research leading to these results has received funding from the People Programme (Marie Curie Actions) of the European Union's Seventh Framework Programme FP7/2007-2013/under REA grant agreement PIRSES-GA-2013-610547-TAMER.

References

1. Bica, I.: The influence of the magnetic field on the elastic properties of anisotropic magnetorheological elastomers. J. Industr. Eng. Chemist. **18**, 1666–1669 (2012)
2. Boczkowska, A., Awietjan, S.F., Pietrzko, S., Kurzydlowski, K.J.: Mechanical properties of magnetorheological elastomers under shear deformation. Composites: Part B **43**, 636–640 (2012)
3. Deng, H.-X., Gong, X.-L.: Application of magnetorheological elastomer to vibration absorber. Commun. Nonlinear Sci. Numer. Simul. **13**, 1938–1947 (2008)
4. Farshad, M., Benine, A.: Magnetoactive elastomer composites. Polym. Test. **23**, 347–353 (2004)
5. Fuchs, A., Shang, Q., Elkins J., Gordaninejad, F., Evrensel, C.: Development and characterization of magnetorheological elastomers. J. App.l Polym. Sci. **105**, 2497508 (2007)
6. Gibson, R.F.: A review of recent research on mechanics of multifunctional composite materials and structures. Compos. Struct. **92**, 2793–2810 (2010)

7. Grigolyuk, E.I., Kulikov, G.M.: Multilayer Reinforced Shells: Calculation of Pneumatic Tires (in Russian). Mashinostroenie, Moscow (1988)
8. Korobko, E.V, Zhurauski, M.A., Novikova, Z.A., Kuzmin, V.A.: Rheological properties of magnetoelectrorheological fluids with complex disperse phase. J. Phys.: Conf. Ser. **149**, 12–65 (2009)
9. Korobko, E.V, Mikhasev, G.I., Novikova, Z.A., Zurauski, M.A.: On damping vibrations of three-layered beam containing magnetorheological elastomer. J. Intell. Mater. Syst. Struct. **23**(9), 1019–1023 (2012)
10. Mikhasev, G.I.: Low-frequency free vibrations of viscoelastic cylindrical shells. Int. Appl. Mech. 28 (9), 586–590 (1992)
11. Mikhasev, G.I.: Localized families of bending waves in a non-circular cylindrical shell with sloping edges. J. Appl. Math. Mech. **60** 4, 629–637 (1996)
12. Mikhasev, G.I.: Free and parametric vibrations of cylindrical shells under static and periodic axial loads. Technische Mechanik **17**, 209–216 (1997)
13. Mikhasev, G.I.: Localized families of bending waves in a thin medium-length cylindrical shell under pressure. J. Sound Vib. **253**(4), 833–857 (2002)
14. Mikhasev, G.I., Tovstik, P.E.: Localized Vibrations and Waves in Thin Shells. Asymptotic Methods (in Russ.). FIZMATLIT, Moscow (2009)
15. Mikhasev, G.I., Botogova, M.G., Korobko, E.V.: Theory of thin adaptive laminated shells based on magnetorheological materials and its application in problems on vibration suppression. In: Altenbach, H., Eremeyev, V.A. (eds.) Shell-like Structures. Advanced Structured Materials. Volume 15, pp. 727–750. Springer, Berlin (2011)
16. Mikhasev, G.I., Altenbach, H., Korchevskaya, E.A.: On the influence of the magnetic field on the eigenmodes of thin laminated cylindrical shells containing magnetorheological elastomer. Compos. Struct. **113**, 186–196 (2014)
17. Qatu, M.S.: Vibration of laminated shells and plates. Elsevier. San Diego (2004)
18. Qatu, M.S., Sullivan, R.W, Wang, W.: Recent research advances on the dynamic analysis of composite shells: 2000–2009. Compos. Struct. **93**, 14–31 (2010)
19. Reddy, J.N.: Mechanics of laminated composite plates and shells: theory and analysis. 2nd ed. CRC Press, Florida (2003)
20. Tovstik, P.E.: Two-dimensional problems of buckling and vibrations of the shells of zero gaussian curvature. Soviet Phys. Dokl. **28**(7), 593–594 (1983)
21. White, J.L., Choi, D.D.: Polyolefins: processing, structure, development, and properties. Carl Hanser Verlag, Munich (2005)
22. Yalcintas, M., Dai, H.: Vibration suppresion capabilities of magnetorheological materials based adaptive structures. Smart. Mater. Struct. **13**, 1–11 (2004)
23. Yeh, J.-Y.: Vibration and damping analysis of orthotropic cylindrical shells with electrorheological core layer. Aerospace Sci. Technol. **15**, 293–303 (2011)
24. Zhou, G.Y.: Complex shear modulus of a magnetorheological elastomer. Smart. Mater. and Struct. **13**, 1203–1210 (2004)
25. Zhou, G.Y., Wang, Q.: Magnetorheological elastomer-based smart sandwich beams with nonconductive skins. Smart. Mater. Struct. **14**, 1001–1009 (2005)
26. Zhou, G.Y., Wang, Q.: Use of magnetorheological elastomer in an adaptive sandwich beam with conductive skins. Part I: Magnetoelastic loads in conductive skins. Int. J. Solids Struct. **43**, 5386–5402 (2006)
27. Zhou, G.Y., Wang, Q.: Use of magnetorheological elastomer in an adaptive sandwich beam with conductive skins. Part II: Dynamic properties. Int. J. Solids Struct. **43**, 5403–5420 (2006)

The Vehicle Tire Model Based on Energy Flow

Tomasz Mirosław and Zbigniew Żebrowski

Abstract Modeling of cooperation between tire and ground is the most important part of modeling of a vehicle and its drivetrain's operation. In this paper, a short overview of a tire–ground cooperation model is presented. One of the most common models (developed among others by Kutzbach), in which the propelling force is related to the slip with a coefficient μ(s), is not easy to use in computer modeling because of the slip (s) that is an "artificial" value calculated from real speeds of a vehicle and a tire. In a computer model, this function can cause some troubles and it is replaced by a simplified function. In this paper, authors present proposal of a tire-ground cooperation model based on the energy flow through three layers, i.e., the flexible tire, the tire-ground system with friction and the ground as a flexible and deformable material. The force that appears between relatively moving tire and ground surfaces, gives the propelling forces. All layers are modeled in the same way with inertia, friction and elastic forces. It results in a model of displacements and energy loses in each of the layers. In this paper authors present the model created in Matlab/Simulink in a graphical form and some examples of the simulation results in reference to real test results.

The model is a simplified description of reality using simple laws that helps to better understand behavior of an object or a course of process with special attention to the problem that is interesting for the user. Problem may consist in searching for the exact quantitative description of the phenomenon with omitting the essence of physical effects (for example, models based on neuron network or research results) or in describing a principle of operation and focusing on searching for physical effects that influence behavior of the model. The aim of this model is to show

T. Mirosław (✉) · Z. Żebrowski
Faculty of Automotive and Construction Machinery, Institute of Construction Machinery Engineering, Warsaw University of Technology, 84 Narbutta Str, 02-524 Warsaw, Poland
e-mail: tmiroslaw@simr.pw.edu.pl

Z. Żebrowski
e-mail: zzebrowski@simr.pw.edu.pl

© Springer International Publishing Switzerland 2016

J. Awrejcewicz (ed.), *Dynamical Systems: Theoretical and Experimental Analysis*, Springer Proceedings in Mathematics & Statistics 182, DOI 10.1007/978-3-319-42408-8_21

relationships and mutual influence of particular phenomena without looking for its exact parameters. Logical cohesion should be a feature of such a model. In this paper authors present the model based on a theoretical analysis.

1 Introduction

Nowadays, road transport predominates and it is not likely to be squeezed out by any other mean of transport. Even though a wheel has been known, at least, for 5000 years, new designs of wheels and tires are being developed. Man still searches for the model that would help to describe and better understand behavior of a wheeled vehicle on a road. This behavior depends mostly on cooperation between the tire and the road. In a pneumatic tire there are numerous effects connected with tire's design, that affect acting of the forces which allow driving and steering the vehicle [1–5]. The shape and the structure are chosen in such a way that on the defined surfaces it will be possible to obtain the finest grip. Tires, while forced into the pavement, obtain friction coefficient even greater than one for some surfaces. However, the behavior of the tire is influenced by: temperature of the tire and the pavement, type of the pavement including its moisture content and the most important one, i.e., presence of water and loose sand [1]. Hence moving layers between the tire and the road arise. The design of a vehicle influences its behavior: mass distribution, wheel track, toe-in, a way the wheels turn and many others. Despite the fact that many phenomena are known and features' influences on a system can be described, there is some disappointment when it comes to the wheel model that would be coherent and backed up with understandable and coherent analysis. Most of the models are based on empirical experiments and observations, often without logical explanation. Although many authors of models base them on Coulomb's model of friction where the force depends on the relative speed of moving and rubbing against each other bodies, at some point they use the model in which the force occurring between a tire and a pavement depends on slip s [6–8].

$$F(s) = N\,\mu(s)$$

where: F—propelling force,

N—load (weight of a vehicle),
$\mu(s)$—friction coefficient depending on slip

Slip does not have any physical representation—it is not possible to measure it and is defined as a result of a mathematical operation:

$$s = 1 - V/V_t$$

where: V—real velocity of a vehicle,
V_t—theoretical velocity

Man can easily state the problem in case of zero velocity value of a vehicle. Due to this authors of models define separately the slip of a propelled wheel and the slip of a pulled wheel [5, 6, 8–12]. In some models, the definition of the slip changes depending on if a wheel is propelled or braked and then the slip value is in range <−1;0) or (0;1>.

It is also possible to find models that skip (do not describe) the behavior of a vehicle for zero ride velocity value or when a wheel does not rotate.

This is the reason why many diagrams showing these relationships are discontinuous close to the zero slip value. It follows that the behavior of a vehicle is not precisely described at the zero slip value where only a deformation of a tire occurs without sliding of the tire surface on the road and minimum slip results from deformation of thread blocks. This takes place at very low velocities.

Modeling the cooperation between the tire and the ground was one of the difficult issues of automatization of farm tractor's operation [11, 13, 14] and creating its computer model [12, 15, 16] that authors of this paper had to solve. The created model was designed for automatization of farm tractor operation and at first was based on the relationship between the force and the slip, that is widespread it literature. Modeling of the forces and the moments in the farm tractor moving with specified slip of wheels can be found in literature [17]. In this paper authors did not model dynamical behavior of the tractor because it was not in scope of the research. Authors looked for the slip values as solutions of the system of equations in which parameters like load and velocity of the tractor unit were changed.

Continuing that work authors decided to model the forces in dynamic states where change of movement parameters is a product of the forces that acted in the past.

Authors were not able to build the model based on the slip that would discretely change its value. Therefore, a way round the problem needed to be found. In paper [12] author proposed a new model of relationship between propelling force and the slip in that common definition for propelled wheel as well as braked wheel is valid (Figs. 1 and 2).

$$s = 1 - V/Vt$$

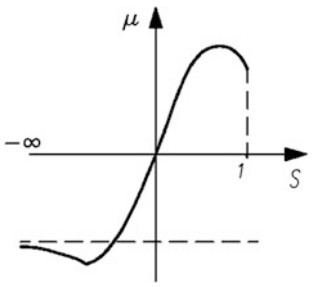

Fig. 1 Diagram of the wheel's slip as a function of the propelling force coefficient [12]

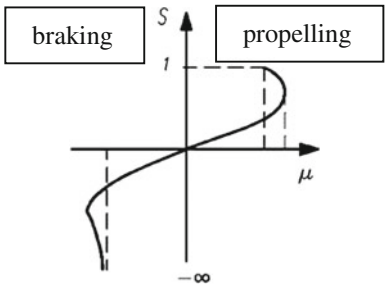

Fig. 2 Diagram of the propelling force coefficient as a function of the wheel's slip [12]

Thus range of the slip for the wheel changes, as said earlier, in the ranges $-\infty < s < 0$ for braking and $0 < s < 1$ for propelling.

Within the scope of the analytical studies the computer model was created using Matlab/Simulink software and some simplifications [18]. First of them was substituting the pull force as a function of the slip, with the pull force as a function of the relative velocity of the tire and the surface of the ground F(dv). Second simplification was using continuous and symmetric, in respect to zero point of coordinate system, function of force resulting from the velocity difference—"the slip velocity".

First, approximation of this function for velocities from zero to dv_k was linear. It reflected a thesis that many authors proposed (ex. [19]) in which without a slip the propelling force cannot exist. Further the force function was described by an exponential function and coherent model was obtained. Results of the simulations were consistent with field studies [10].

A photo from tests of measuring apparatus of the mobile test bench is shown in Fig. 3.

Created model was described precisely in papers [11, 13–16], it was validated during field studies in various conditions. The results of simulations showed surprisingly good consistence despite simplification of relationships.

Fig. 3 Tractor unit URSUS 1204 during testing the measuring apparatus on the deformable pavement

Good consistence of field tests and simulation results (using the above-described simplified model), that was better than for a model based on the force that was dependent on a slip, induced authors to analyze them accurately. In order to do so, phenomena occurring during propelling a vehicle were analyzed (starting at the engine and moving to the wheels) taking into account models that are regarded commonly as correct.

A model is a simplified description of reality using simple laws that helps to better understand behavior of an object or a course of process with special attention to the problem that is interesting for the user. The problem may consist in searching for the exact quantitative description of the phenomenon with omitting the essence of physical effects (for example, models based on neuron network or research results) or in describing principle of operation and focusing on searching for physical effects that influence behavior of the model (or analogical phenomena). The aim of this model may be to show relationships and mutual influence of particular phenomena without looking for its exact parameters. Logical cohesion should be a feature of such a model. In this paper authors present the model based on theoretical analysis. The model was designed as computer model, i.e., it is meant to simulate continuous dynamic process of cooperation between a tire and a ground. It is not meant to determine the forces values and the slips in a specific moment. This is a new class of models that takes advantage of modern computational tools to describe occurring phenomena.

2 Characteristic of the Most Widespread Models of a Wheel

The most popular models that describe cooperation between a tire and a ground are based on the propelling force function depending on a slip [1–4, 8, 10].

One of the most common wheel models was developed by Hanse. This model is called "the magic formula." It is written in form

$$F(s) = \mathrm{d} \cdot \sin\{\mathrm{c} \cdot \arctan[\mathrm{b}(1-\mathrm{e})\mathrm{k} + \mathrm{e} \cdot \arctan(\mathrm{b} \cdot \mathrm{k})]\}$$

where: $F(s)$ is the propelling force that depends on s (slip), b, c, d, and e that represent fitting parameters. Each tire can be characterized by ten to twenty coefficients that are mostly determined in an experimental way.

This formula does not have any logical explanation. The additional disadvantages are difficulties in implementation to a computer model. It requires some special steps for low speed movement.

Another model was developed by Schreiber, Kutzbach [8] who based on other authors like Grecenko, Schuring, and others. They noticed the difficulties with the slip definition and introduced different models for pulled and driven wheel like presented in the paper [3]. Different movement possibilities can be seen in diagram depicted in Fig. 4.

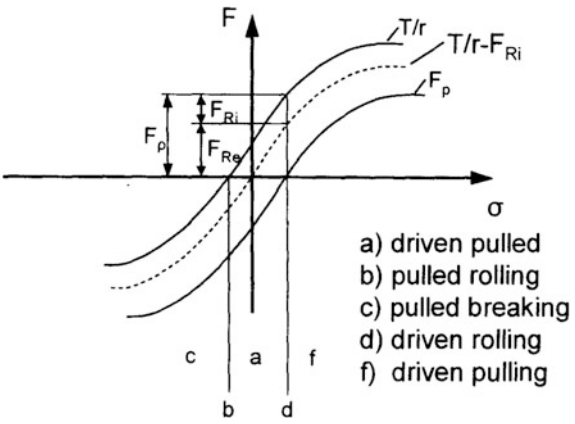

Fig. 4 Gross traction T/r, circumferential force $T/r - F_{ri}$ and net traction F_p in dependence on the slip σ [8]

Such models are very difficult to use in a computer simulation. Basing on the Steinkamof's measurement data, Schreiber and Kutzbach proposed the standardization of tire characteristics [8].

The standardized curve was proposed in the form presented in Fig. 5 [8].

To find out the right curve some coefficients need to be calculated. This model seems to be better for computer simulation especially for the tractors that wheels move at low speed with high slip in the basic operation mode.

But it is still a model based on an experiment not on a modeling the real physical phenomena. The model based on simple physical rules seems to be needed for wide range computer simulation. Of course the measurement data should be used for its parameterization.

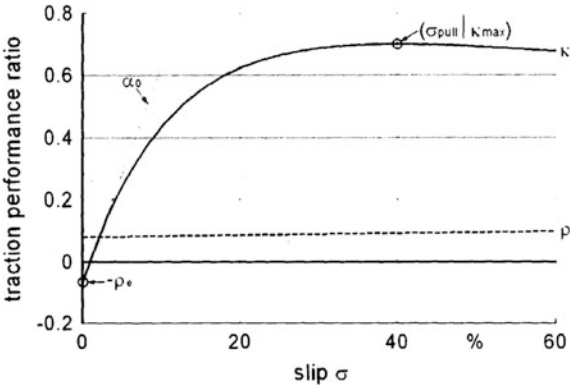

Fig. 5 κ-curve with four characterizing values ρ_e, α_0, κ_{max}, and σ_{pull}

3 Analysis of the Tire's Performance Based on an Energy Flow

Many of the currently used models of tire-pavement cooperation base on field studies that indicate that the propelling force depends on the slip and not on the velocity. This kind of a relationship is inconsistent with intuition regarding modeling where real (measurable) value is expected, e.g., a velocity or an acceleration. Due to this many authors try to explain analytically relationships between the propelling force and the slip.

While searching for the relationship between a vehicle's propelling force and the force interacting between the tire and the pavement, an energy flow between the engine and the ground was analyzed. It was assumed that in steady state the power, that propels a vehicle, flows between the engine and the pavement in both ways [12]. The power transferred between the wheel and the ground can be written as a product of the friction force and the mutual velocity of the rubbing surfaces. This force can be modeled as a resultant of static and viscous friction forces that are a function of the velocity of motion between the tire–ground contact area and the pavement.

Viscous friction force depends on the mutual speed of the two rubbing against each other surfaces, in case of the wheel moving on a pavement, where V is the velocity of a vehicle and V_t is the velocity of the tire–ground contact area, it equals to

$$P = T \cdot (V - V_t)$$

Power P that a vehicle must produce to overcome the friction resistance (equal to the propelling force F) during moving at V velocity equals

$$P = F \cdot V$$

where: F—propelling force, produced in the tire–ground contact area

After comparing both equations following is obtained:

$$F \cdot V = T \cdot (V - V_t)$$

hence $F = T \cdot (V - V_t)/V$

Taking into account that for the zero slip value the static friction occurs with its maximum value (F_{max}) proportional to the weight

$$F = F_{max} = N\,\mu$$

where: N—vehicle load,

μ—traction coefficient (determines grip between the tire and the ground).

Coherent notation of above mentioned relationships needs to be done:

$$F = N\,\mu\,(V - V_t)/V = N\,\mu\,(s)$$

In that case it can be assumed that determining the propelling force as a function of the wheel load and the velocity difference of rubbing against each other surfaces, using the vehicle's energy model (one that takes into consideration the energy flow and its change into elastic energy of elastic elements, kinetic energy of elements and layers through which energy flows in dynamic states) is going to be ideologically consistent with model of the force value dependent on the slip for steady states.

After careful analyzes of the wheel on various pavements it can be stated that there are cases when wheels rotate but a vehicle does not move. Therefore, the rotation resistance must be distinguished from the rolling resistance which is a superposition of translational and rotational motion.

Rotational motion resistance, that also counterbalances a propelling force in a translational motion, is a friction force between wheel and pavement.

Wheel begins to rotate when that force overcomes the rotational motion resistance.

Upon analysis of "the pneumatic wheel" and the forces acting on its axis can be stated that to make it rotate around overturn line c (Fig. 6) the propelling force must unbalance it from static balance state.

It corresponds with a model shown in Fig. 7 that describes rolling resistance moment M_o defined by following equation:

$$M_o = e\ N$$

where: e—offset between point of application of reaction force on wheel from ground and vertical axis of a wheel.

Friction force acts through the tire on the wheel axis. Friction force adds up to load force and the resultant force appears as a vector whose direction and value are the result of totaling up both forces. During propelling the wheel the resultant vector changes its direction from vertical to tilted in front direction. In makes a difference in the load distribution on the pavement and change of shape of the contact area.

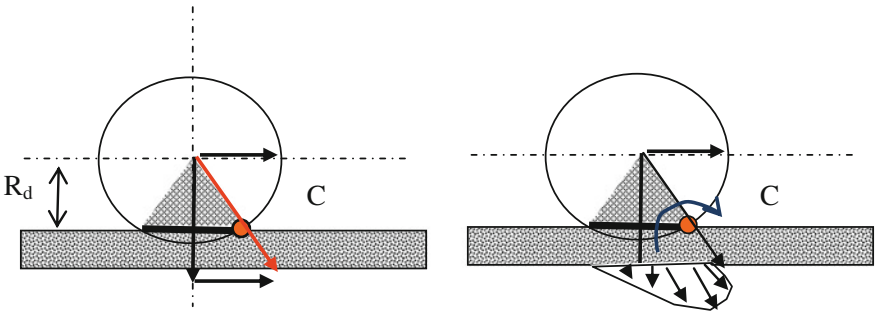

Fig. 6 Schematic diagram of a wheel rolling principle used in the model basing on wheel statics

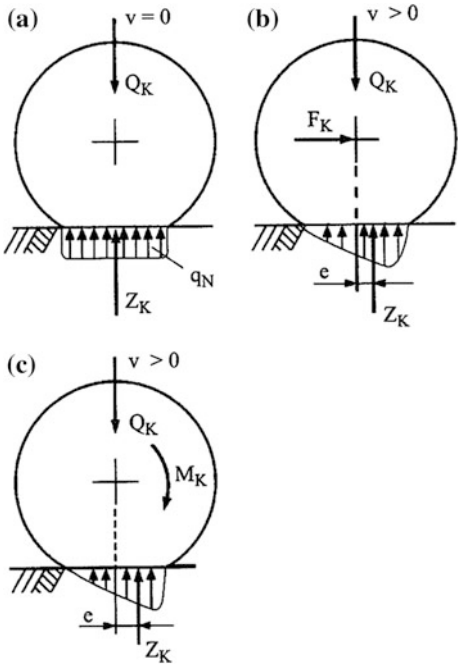

Fig. 7 Wheel pressing on a ground (**a**—motionless wheel, **b**—rolled wheel, **c**—propelled wheel) [9]

When the resultant vector leaves base area, the tire loses its contact and starts to roll (Fig. 6).

Proposed description of the phenomenon is consistent with other models of rolling resistance (ex. [9]) that come from the load force and the offset e of application point of the reaction force on the wheel from a ground (Fig. 7).

The propelling force/moment value that is demanded to cause rolling is called the rolling resistance:

$$F = e\,N/R_d$$

This is the minimum force which can cause motion of a vehicle.

Translational motion velocity of a wheel depends on excess of the propelling force over the rolling resistance and the load of a vehicle.

It means that in dynamic states rotational speed of a wheel and a velocity of rolling can be treated as separate quantities where an angular velocity of a wheel rotation does not influence directly a translational velocity of an axis.

Energy flow from an engine through a wheel to a pavement and back to the vehicle through a wheel is a result of the ground–wheel interaction. Energy flowing through the wheel is accumulated in elastic elements of the tire. Propelling a wheel with a tire on it that is held in contact area causes its tension and compression (see Fig. 8) in function of propelling moment M_k.

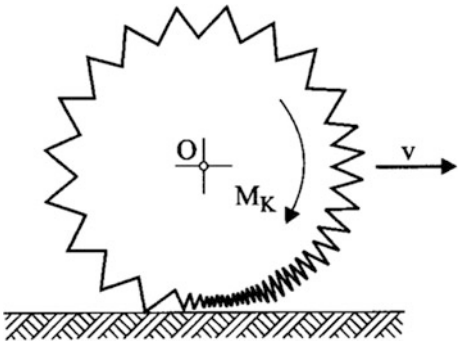

Fig. 8 Circumferential tire deformation [9]

Along with increase of the wheel propelling moment, tensioned part of a wheel grows and compressed part of it contracts. A wheel starts to deform. If it is assumed that the wheel rolls and the forces between pavement and wheel appear, then every part of the tire is submitted to cyclic compressing and tensioning. The tire is modeled as an elastic element with a damper. As a result there are going to occur energy losses and the deformation range is going to depend on a frequency of changes (of angular velocity). When this frequency will be high enough the tire will not be able to keep up with deforming.

It is assumed that thread blocks are the elements through which a tire contacts a pavement, they are an elastic intermediate elements between rotating a wheel and a ground. Thread blocks deform in a tire-ground contact area.

When moment propelling rotational motion of a wheel increases, the moment caused by static friction counteracts this motion not allowing the tire to move on a pavement. When wheel propelling moment is greater than the moment caused by static friction thread blocks begin to move with kinetic friction. Moreover, when the friction force reaches its critical value the rubber starts to wear off, that results in limiting the maximum value of an acting force between thread blocks and a ground. When wearing off a pavement appears, it limits propelling force "under the wheel."

Another factor, that influences wheel rotation and its rolling motion, is a possibility of appearing the moving layers between a tire and an immovable ground. Those layers can have various friction coefficients in between, also they can move. Other issue is taking into consideration existence of deformable and boggy ground, etc. Due to this the model that describes cooperation between the tire and the ground should also consider presence of these moving layers.

4 Multilayer Model of a Wheel–Ground Cooperation

Taking all the above into consideration, the new multilayer (cascade) model of a wheel-ground cooperation was developed. It is based on energy flow and forces acting between individual layers. Model depicted in Fig. 9 consists of four similar

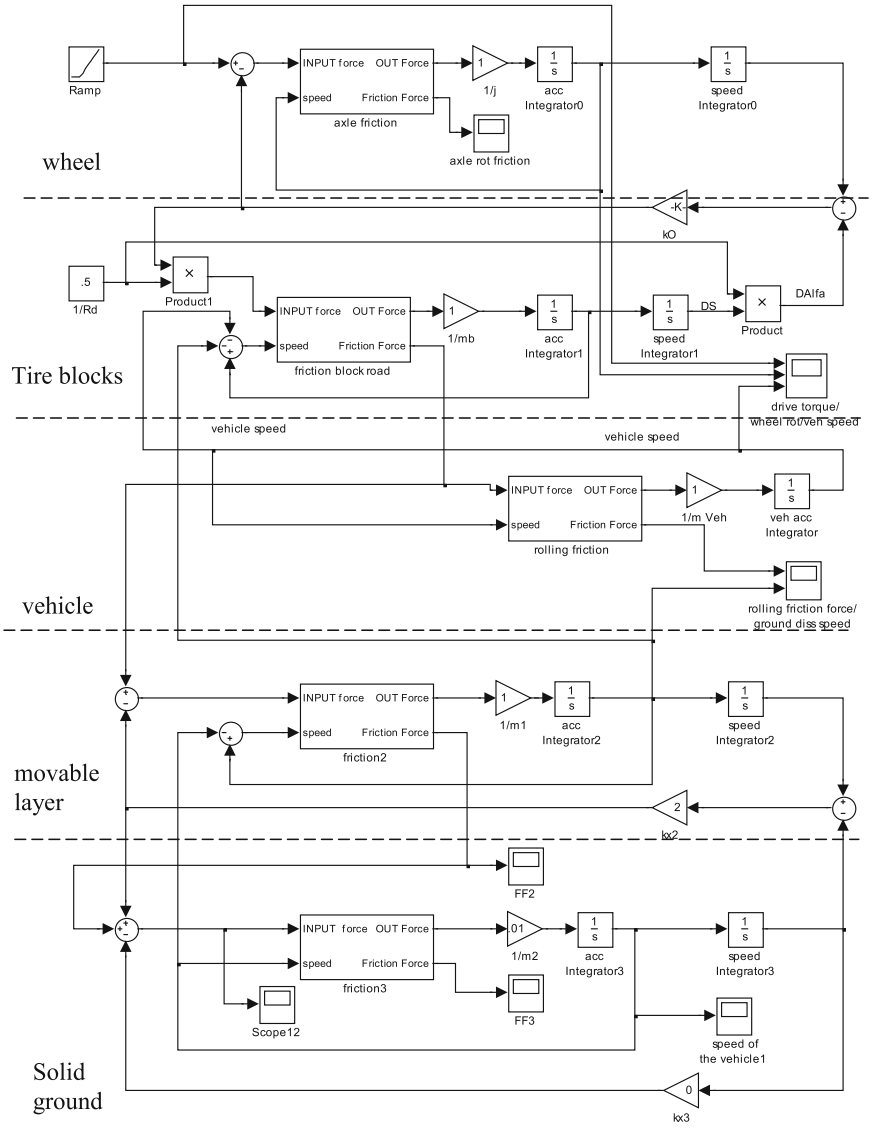

Fig. 9 Model of a wheel–ground cooperation for a vehicle

layers: a wheel, thread blocks, a movable intermediate layer and an immovable ground, also there is a model of a vehicle represented by a mass and an acceleration integrating system that outputs the velocity. All the layers consist of "friction" block whose inputs are: the force (from moment) propelling given layer and the

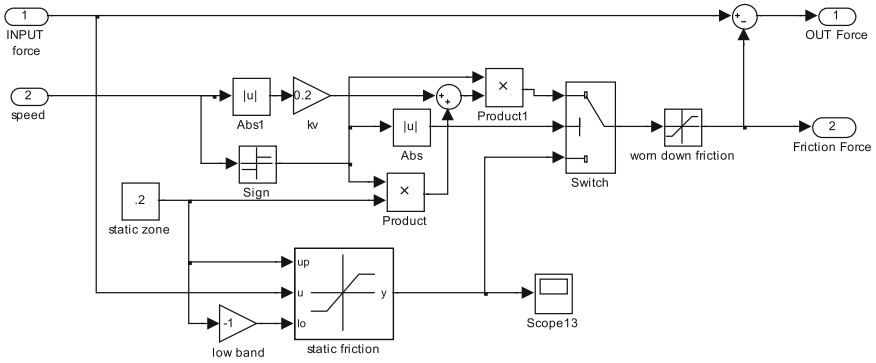

Fig. 10 Friction model

mutual velocity of two cooperating layers. This block's outputs are: the resultant force that propels an element of a given layer, the amplifying system that represents inertia of a given element (its value is a converse of inertia) and the integrating elements that are connected in series. Between a wheel and a thread block occurs a conversion of moments into forces by dividing moments by dynamic radius R_d. In the model multiplication by a converse of dynamic radius ($1/R_d$) was used.

Depending on a layer type the driving force is decreased by the motion resistance of the inner layer. Friction block is depicted in Fig. 10. Input signals are: the driving force and the velocity and output signals are: the friction force and the propelling force. Friction force acts between the adjacent layers and propelling force causes the acceleration of an element of the layer. Friction force value depends on the velocity. For zero velocity value and the input force lower than the maximum static friction, output force equals to the driving force and the propelling force equals to zero. When driving force overcomes the static friction and input velocity equals to zero then the output friction value equals to maximum static friction value and propelling force is the difference value between driving force and friction. When velocity increases and is different from zero then the channel of friction computing switches to the "velocity" channel and is determined according to the T(v) function.

In the presented example it is a linear function that is discontinuous at zero point and symmetric for both signs of input velocity.

Friction block has a maximum value limit. That corresponds to the force when wearing off of an element appears—once grip loss (friction loss) appears.

Presented friction model describes well the rolling resistance that appears in the part of the model describing the vehicle.

In the model depicted in Fig. 9 mutually moving elements can act on each other with elastic forces likewise between a tire and thread blocks. Stopped thread blocks

twist and act on the tire with the force dependent on the position difference between the block end and the block origin (base that is joined with a tire). Elastic force acts on both elements with opposite signs. Other kind of a force is a kinetic friction. For a tire also a kinetic inner friction appears—depending on rotational velocity of a tire–representing cyclic tire stress changes and as a result the energy losses. However, basically the friction depends on the velocity difference between the rubbing against each other surfaces.

Basing on the above mentioned assumptions the model of a wheel–ground cooperation was developed and depicted in Fig. 9.

Elastic force that propels the thread blocks is inserted into the thread blocks block of friction against ground. Output from this block is a result of finding the mutual velocity between the thread block and the pavement. Velocity of a thread block in an absolute coordinate system equals to: the traveling speed of a vehicle minus the velocity of a thread block movement (a thread block moved in opposite direction to a vehicle). Due to this finding the mutual velocity is a result of the operation on three elements. Friction force of the thread block acting against a pavement is the reaction of the propelling force on: a pavement and a vehicle represented in the model by the rolling resistance, the inertia and the integrating system that determines vehicle's speed.

Thread blocks friction force that propels the pavement is added up to the force reacting with the lower layer and is the input to friction block and a block that represent the friction between this layer and layer of the pavement. Output force propels the layer causing its movement. In the example ground layers are linked by an elastic element from which comes the reacting force. Output force from the block of friction with ground layer is added up with the elastic force and acts (propels) on the bottom layer that represents here an immovable ground with some elasticity value.

Presented model shows basic types of interactions, i.e., friction and elastic force of mutual deflection. This model can be extended with more layers.

Simulations tested behavior of the system in which between the thread blocks and the pavement the moving layer appears and how limiting the maximum friction value between layers influences the motion.

Testing the model showed a very good consistence of appearing phenomena during simulation with the observations of reality. In one of the experiments, the wheel was propelled with an increasing driving moment. Simulation results are showed in Figs. 11 and 12.

Along with the drive moment increase the rotational velocity of a wheel increases and with some time delay the vehicle's velocity. Along with velocity the rolling resistance rises as well as the speed of movement of movable ground layer.

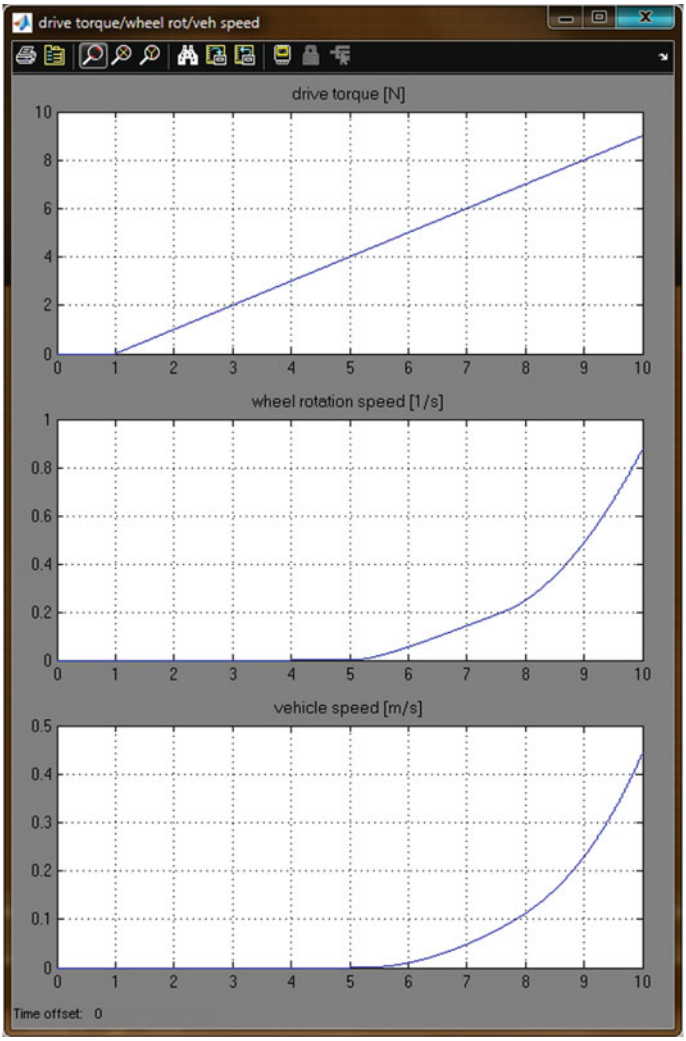

Fig. 11 Diagrams of driving moment, rotational velocity of a wheel and vehicle's driving speed when driving moment increases linearly in time

Interesting behavior of a system that is a response to the discrete value of the wheel propelling moment is shown in Figs. 13 and 14. On these diagrams inertia of accelerating the wheel and the vehicle can be noticed. Also changes in the rolling resistance forces and the velocity of movement of movable layer can be observed.

Presented results are consistent with expectations and it can be stated that the model works correctly.

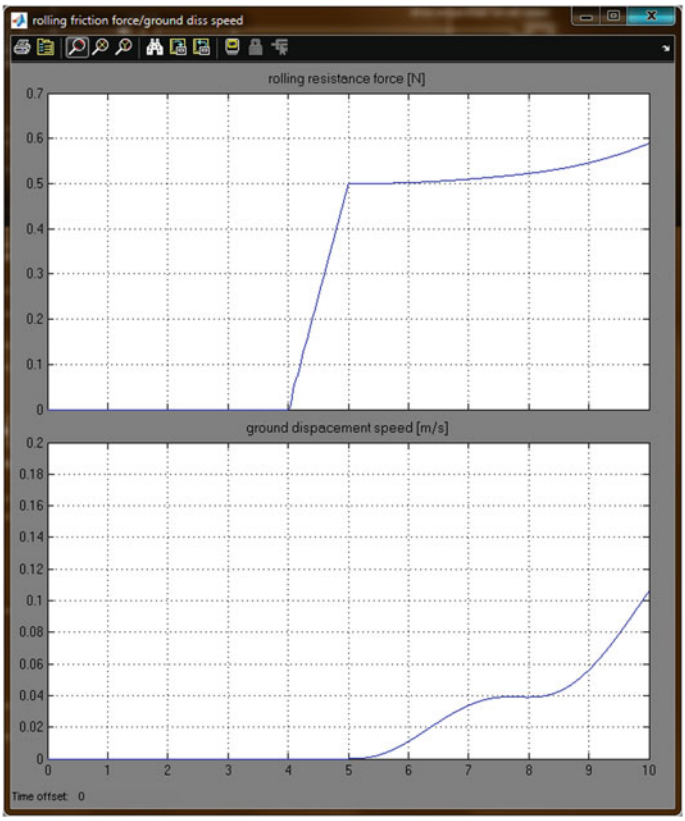

Fig. 12 Diagram of a rolling resistance and a velocity of a moving layer of ground for a linear change in time of driving moment of a wheel

5 Conclusions

During analyzes of the tire behavior and using the farm tractor model, developed for automatization of engaging the front drive based on the slip analysis [13], authors proved that finding the propelling forces basing on the velocity difference between the tire and the pavement is consistent with models based on field studies where this force depends on the slip. One dimensional model (for driving straight ahead) was created; it simulates the deformation of tire, the movement of intermediate layers and the grip loss. This model has a modular layout that allows to increase amount of the layers and to change the features of reacting. The model uses simple principles that describe the inertia systems that are connected in series by the elements that rub against each or the elements that have an elastic connection. Typical model of a friction and appearing the reacting forces was used.

Simulation results are qualitatively consistent with the observations.

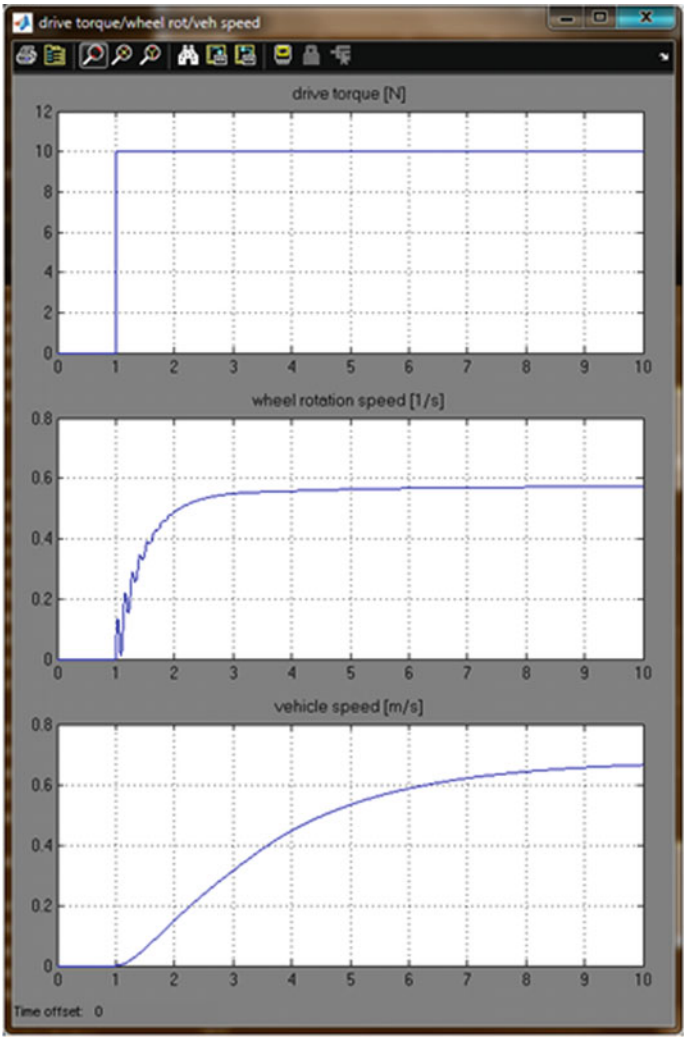

Fig. 13 Diagrams of driving moment, rotational velocity of a wheel and vehicle's driving speed when driving moment increases discrete in time

This is a dynamic model therefore it cannot be used to determine the forces values or the slip values in a specific time moment without continuous analysis.

This model can be easily readjusted to two dimensions what would allow modeling a tire–ground cooperation during making a turn.

While changing model parameters of the individual layers behavior of the system can by modified. Modification can be made on one layer and its parameters that describe this layer's cooperation with the adjacent layers which is consistent with real causes of ongoing phenomena.

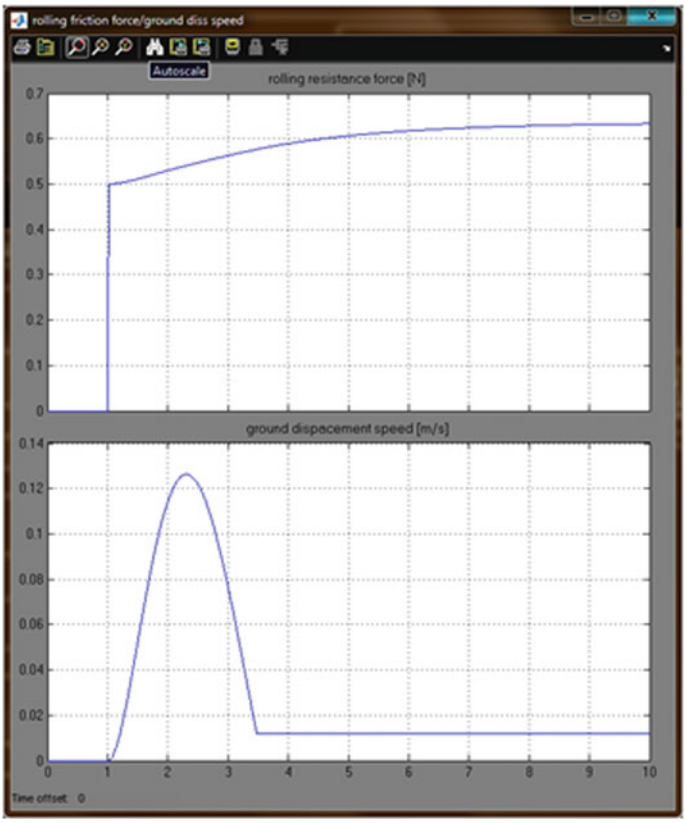

Fig. 14 Diagram of a rolling resistance and a velocity of a moving layer of ground for a discrete change in time of driving moment of a wheel

References

1. Bekker M., 1969.: Introduction to terrain-vehicle systems. Michigan Press, An Arbor, USA.
2. Goriaczkin B.P.: Tieoria kolesa. Sobranie soczinienii. Sielchozgisz, Moskwa 1937.
3. Grečenko A.: Einflüsse auf die Kraftübertragung von Ackerschlepperreifen. Agrartechnische Kolloquium, Hohenheim, 1989.
4. Jakliński L., 1999. Modele oddziaływania koła pneumatycznego na glebę. Prace Naukowe Politechniki Warszawskiej, Seria Mechanika, Zeszyt 175.
5. Kutzbach D., 1982. Ein Beitrag zur Fahrmechanik der Ackerschleppers- -Reifenschlupf, Schleppermasse und Flächenleistung. Grundladen Landtechnik Bd. 32(2).
6. Pacejka H. B, 2004.: Tyre and Vehicle Dynamics. Elsevier Press.
7. Pytka J. Teoretyczno doświadczalne studium układu element jezdny – podłoże odkształcalne. PL Monografie. Lublin 2011.
8. Schreiber M., Kutzbach H. D., 2007. Comparison of different zero-slip definitions and a proposal to standardize tire traction performance. J. Terramechanics 44.
9. Prochowski L., 2004. Mechanika ruchu. Seria Pojazdy Samochodowe, WKiŁ Warszawa.

10. Bakker, E. ; Nyborg, L. ; Hans B. Pacejka H. B.: Tyre modelling for use in vehicle dynamics studies 1987 Jan. Society of Automotive Engineers, Warrendale, PA.
11. Pacejka H. B.: The wheel shimmy phenomenon: A theoretical and experimental investigation with particular reference to the nonlinear problem (Analysis of shimmy in pneumatic tires due to lateral flexibility for stationary and no-stationary conditions), Ph.D. Thesis, Delft University of Technology, Delft, 1966
12. Żebrowski Z.: Metodyka automatyzacji pracy ciągnika kołowego. Prace Naukowe Politechniki Warszawskiej, Mechanika, z. 256. Oficyna Wydawnicza Politechniki Warszawskiej, Warszawa 2013.
13. Pacejka H. B.: Tire and Vehicle Dynamics, Butterworth-Heinemann, Oxford, 2002.
14. Gurkan Erdogan, Tire modelling Lateral and longitudinal Tire Forces April 27, 2009.
15. Mirosław T., Żebrowski Z.: Sterowanie załączaniem i rozłączaniem napędu przedniego ciągników kołowych. Przegląd Mechaniczny 1'01.
16. Mirosław T., Żebrowski Z.: "Modelling and Simulation of Tractor Differential Mech-anism.; „ Mechanical Review" (Przeglad Mechaniczny) 6'2013.
17. Żebrowski Z., Żebrowski J., Kolator B.: Metodyka badań trakcyjnych opon napędowych pojazdów terenowych. III Międzynarodowa Konferencja Naukowo-Techniczna nt. „Rozwój i kierunki badań samojezdnych żurawi hydraulicznych", PIMB Warszawa 22 ÷ 24 październik 1997.
18. Matlab 2004 – User Handbook. MathWorks, Natick, USA.
19. Renius K.T.: Traktoren: Technik und ihre Anwendung. Aufb. – München: BLV Verlagsgesellschaft. Frankfurt (Mein) 1987.

Research on Dynamics of Shunting Locomotive During Movement on Marshalling Yard by Using Prototype of Remote Control Unit

Jakub Młyńczak, Rafał Burdzik and Ireneusz Celiński

Abstract The paper refers to presentation on 13th International Conference on Dynamical Systems Theory and Applications. The discussion of such wide group of scientists allowed to extend the paper and presents some new results. The processes conducted on marshalling yard generate a lot of movement with many direction and speed changes which generate different dynamic forces. In the course of shunting of train, there are large range of activities performed that enable observation of multiple dynamic phenomena under relatively advantageous conditions. Thus the main focus of the research was to test possibilities of developed remote measurement system. Also algorithm of analysis was developed and implemented as software into control unit. The paper discussed both the concept and the application of a simple method of remote supervision of shunting runs using mobile devices enabling observation and recording of chosen dynamic parameters of a rail vehicle. The paper presents result of linear accelerations of vibration in 3 axes and speed occurring in the course of the shunting locomotive's operation and also current physical position and altitude above sea level. Such a simple measuring system allows for monitoring of basic physical parameters of shunting operations performed by the shunting engine driver.

J. Młyńczak · I. Celiński
Faculty of Transport, Department of Transport Systems and Traffic Engineering, Silesian University of Technology, Krasinskiego, 8, 40-019 Katowice, Poland
e-mail: jakub.mlynczak@polsl.pl

I. Celiński
e-mail: ireneusz.celinski@polsl.pl

R. Burdzik (✉)
Faculty of Transport, Silesian University of Technology, Krasińskiego, 8, 40-019 Katowice, Poland
e-mail: rafal.burdzik@polsl.pl

© Springer International Publishing Switzerland 2016

J. Awrejcewicz (ed.), *Dynamical Systems: Theoretical and Experimental Analysis*, Springer Proceedings in Mathematics & Statistics 182, DOI 10.1007/978-3-319-42408-8_22

1 Introduction

Railway transport is considered as main competitor for road transport. Due to the sustainable development, it should be considered as main supplementary mode of transport, especially for load handling. Thus there are many innovations in railway transport and new scientific and research scope has become open again. Problems of dynamics of rail vehicles are addressed in a vast number of scientific studies on account of the extensive impact of dynamic phenomena on such aspects as safety, technical reliability, efficiency of processes, and comfort [1]. For example, novel research on evaluation of the braking process through analysis of the braking vibration during braking to stop with a permanent analysis of temporal signals of vibration acceleration in the frequency domain. The paper [2] presents method for estimating the braking process one value of the diagnostic parameter of the vibration signal generated by the disc braking level set during braking. Another scope of research is focused on ground-borne vibrations in the built environment generated by a large number of excitation mechanisms. One of these is traffic-induced vibration. The latter railway vibration is generated by parametric excitation due to the discrete supports of the rails, transient excitation due to rail joints and wheel flats and the excitation due to wheel and rail roughness and track unevenness [3]. It is natural for vehicles to induce vibration when it runs on a traffic structure, which affect the riding comfort and the safety, but also cause the vibration of the ambient ground near the traffic line. These phenomena are especially important for high-speed railways, where the vibrations induced by trains are intermittent, while the time of passing each train's passage is relative short. The paper [3] describes that the standard vibration level of the Shinkansen train-induced vibrations is of a trapezoid form, with the lasting duration being 4–7 s under the train speed of 200–300 km/h. However, owing to its heavy traffic volume, such vibrations take place in every 5–10 min, thus the influence is considerable. It is described how important are duration, intensity and train vehicle speed for the exposure to such vibration [4].

The obstacles one encounters while modelling and observing dynamic phenomena in rail vehicles are due to limitations of accessibility, external conditions and dimensions. Therefore, the research assumption adopted was the observation of dynamics of a locomotive in the course of shunting. One of the most important aspects of operation of a railway station comprises shunting activity. Principal goals of such activity are mainly marshalling and setting of train sets. In the course of shunting, there is often a necessity of changing the number of cars or cars are being reset and admitted at different technical points of a station (for cargo handling). Such a large range of activities enable observation of multiple dynamic phenomena under relatively advantageous conditions. Moreover, when properly performed, shunting activity is a prerequisite of efficient railway traffic management. Besides general regulations typical of the given railway line, shunting activity is performed in accordance with shunting rules and regulations established for the given

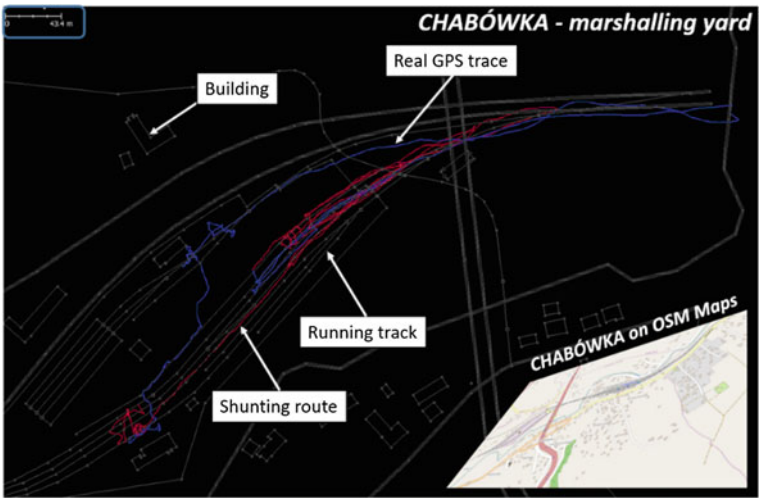

Fig. 1 Shunting runs studied, plotted against a plan of the testing workshop. *Source* OSM/JSOM

technical point. While conducting this type of activity, what proves decisive of its characteristics is often the type of the means of transport being marshalled and the cargo being transported.

It was assumed to investigate both the concept and the application of a simple method of remote monitoring of shunting runs using mobile devices enabling observation and recording of chosen dynamic parameters of a rail vehicle. In the course of the studies, a diesel locomotive was used, being one of the most popular means of cargo transport (SM42 series). The plan of the railway station–testing workshop, with the blue line designating the GPS trace of the locomotive studied while performing shunting activity has been depicted in Fig. 1.

2 Methodology

The research methodology was adopted to preliminary research limited by time and the availability of infrastructure. Assumptions of the method proposed are as follows: mobility, simplicity of operation, short time of installation of measuring apparatus, synchronisation of time and location (GPS positioning). For the sake of these assumptions, own application was developed for mobile unit to replace standard measuring devices. A mobile unit is attached to the driver's cab floor in such a manner that its top part indicates the driving direction while the locomotive is moving ahead during shunting. The sensor vertical axis is perpendicular to the track substructure plane. The mobile unit features an application created by the

authors, dedicated to the platform, which uses the accelerometer system (MEMS) to record linear accelerations in 3 axes occurring in the course of the shunting locomotive's operation (forward and reverse shunting).

For the sake of analysis of dynamics of locomotive also are recorded the running speed and its physical position in space (latitude, longitude). Also a number of other parameters are recorded, including speed, locomotive altitude above sea level, etc. Such a simple measuring system allows for monitoring of basic physical parameters of shunting operations performed by the shunting locomotive driver. In combination with simultaneous measurement of the shunting locomotive position, it enables verification of legitimacy of the manoeuvres performed by the driver and their parameters as well as the degree to which the driver adheres to specific legal regulations and standards. Hence it can be useful for the control unit.

In the measurement process digital data with 100 Hz sampling frequency will be collected. Due to the preliminary analysis of dynamic phenomena this range of frequency is sufficed. In the course of the measurement, basic data related to the locomotive's running characteristics may be sent to the shunting signal box using the SMS protocol. Depending on the data transmission technique applied, the data transferred only concern mean values of the characteristics examined (SMS) of aggregated data (GPRS). In this manner, an additional reverse channel is created while conducting shunting activity (supplementary to the channels used in accordance with the applicable legal regulations, i.e. the visual and the radio one), which accurately enables supervision of the work performed by the shunting locomotive driver based on the characteristics being measured. In the aftermath of the research in question, the authors are planning to use transmission channels to remotely control the driver's work by means of the WiFi and BT protocols. All these parameters allow to consider developed mobile unit for the further development into remote control unit. Figure 2 is a diagram illustrating the research methodology applied in the scope of remote control of shunting activity using a testing locomotive. Also it is a conceptual scheme of the remote control system.

Based on the characteristics acquired by means of a mobile device, data of the locomotive's linear acceleration (each axis) and positioning (as well as a number of other characteristics, such as speed, altitude above sea level) are processed (ca. 100 MB data file in each hour). The data in question are aggregated and/or compressed, and then, using the chosen transmission channel (SMS, GPRS), sent to the shunting signal box. This enables the shunting signal box personnel to acquire accurate knowledge on the locomotive parameters, and owing to the station's radio communication system, they can monitor changes in these parameters. This observation is far more accurate than visual [5–7].

Due to the utilitarian of the research, the methodology and measurement system has been adopted and installed into smartphones. The preliminary tests have been conducted and evaluated with good result. Thus it can be considered as remote control unit.

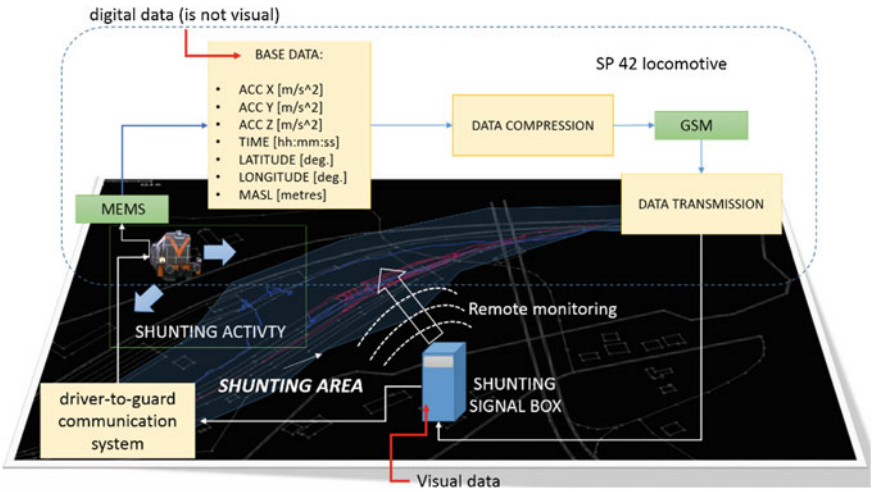

Fig. 2 Schematic concept of the proposed research methodology. *Source* authors' own materials

3 Train Marshalling Process

Shunting operations are defined as intended movements of railway vehicles. The foregoing also applies to other activities related to the said movements, as they are performed on tracks of shunting stations. The operations excluded from those activities are the train entry, exit and passing. Shunting is performed with motor-driven railway vehicles, among others.

The method described in paper [8] and its extension described in previous section mainly applies to this kind of shunting activity, although, on account of its simplicity, it may also be used for the sake of marshalling conducted by means of rail and road tractors or special machinery. The shunting activity is performed in a place referred to as a shunting area. It is a pre-defined (delimited) section of a railway station territory forming an independent set of tracks and machines used for shunting activity by one shunting manager by means of one shunting locomotive. A division into shunting areas and districts (two or more shunting areas) has been introduced in order to enable efficient and safe performance of shunting activity.

One of major parameters of shunting activity is the shunting speed, as specified in Instruction Ir-9 (R34) [9]. Shunting operations are often performed in tracks occupied by rolling stock. It is for that reason that individual shunting operations should be performed with care, maintaining safe running speed, as defined in Instruction Ir-9 [9]. Shunting speeds have been precisely specified in the instruction with reference to different cases of technological activities and incidents. Safety of shunting activity is not only the matter of the rolling stock, but it also concerns the goods transported by rail, and primarily people. Permissible running speed ranges for shunting activity are defined in Instruction Ir-9. While performing shunting

operations, the running speed must not exceed 25 km/h, however, depending on the technology used for shunting and the infrastructure elements involved, the permissible speeds range considerably from 3 km/h up to 40 km/h. For instance, a self-propelled railway vehicle running in the "idle" mode, in certain cases and at selected points of the shunting area, may run with the permissible speed as high as 40 km/h. In an extremely restrictive case, while a shunting locomotive is driving up to the rolling stock, this speed must not exceed 3 km/h. In accordance with the methodology proposed in the article, the shunting signal box receives real-time information on the shunting locomotive position and its actual speed. This enables remote monitoring of correctness of the shunting activity to be performed by shunting brigades, even those operating within particularly vast shunting areas and under diversified weather conditions. Not only is it important from the perspective of shunting safety, but also regarding potential claims of owners/insurers of the goods transported. The method in question allows for documenting the course of shunting activity using highly accurate parameters by way of verifiable measurement. In such a case, each shunting activity is digitised and stored at the appropriate shunting signal box or centrally archived. Moreover, working characteristics of individual shunting brigades may be compared between one another, e.g. in order to calculate bonuses for individual members of brigades in recognition of their effort.

Information on the shunting activity is transferred in real time to the shunting signal box which enables the activity to be adjusted using reverse communication channels from the signal box (mainly radio communications, but video and audio signals as well).

What matters while performing shunting activity is the precise information on locations of shunting vehicles and members of shunting brigades. In accordance with the applicable regulations, vehicles must be equipped with an active bottom headlight whose position corresponds to the driver's station arrangement (left side, right side). This piece of information is particularly is important for shunting brigades. Knowing it, one may determine the side on which the driver is seated as well as the direction in which the shunting locomotive is moving. Assuming that members of shunting brigades have been equipped with appropriate terminals enabling them to acquire information on the locomotive position, the methodology proposed may additionally increase safety of shunting activity. For instance, as the shunting locomotive is approaching, a brigade member may be warned with vibrations or an audible signal [10–13]. Such safeguards are fundamental to shunting activity conducted at large marshalling yards of high throughput as well as when working under difficult atmospheric conditions (fog, heavy rain, etc.). Unfavourable station layout, i.e. considerable slopes or longitudinal profiles with large curvature, should also be considered as a factor imposing implementation of such safety procedures.

4 Dynamics of Shunting Locomotive

The methodology proposed is mainly based on indications of an accelerometer (MEMS) installed inside the locomotive driver's cab those provided by a GPS receiver as well. Such a simple system enables monitoring of the locomotive position and others parameters of its motion as it performs shunting activity (basic 10 parametres). Hence characteristics of dynamics of locomotive can be observed and analysed due to many issues or train traffic management requirements.

The graphical material provided in the article has been developed based on the data recorded while studying the locomotive running along the trace plotted on the test station site plan (Fig. 1).

Figure 3 illustrates linear accelerations measured inside the cabin of the diesel locomotive performing shunting activity. The first chart (a_z) in Fig. 3 marks vertical accelerations. The seconds corresponds to accelerations in the longitudinal axis of the locomotive's motion (a_y), and third in the axis transverse to the direction of the locomotive's movement (a_x), i.e. lateral accelerations. In the Fig. 3 we can see any deviation from the mean values. The amplitude is affected by the state of the: locomotive driver, railway infrastructure, locomotive speed, shunting team, etc.

Each of the characteristics (a_x, a_y, a_z) stems directly from the type and parameters of the actions undertaken by the driver, which may prove variable within a certain range, as well as from the physical position of the locomotive over specific elements of the track infrastructure. To a considerable degree, it also results from the condition of the rolling stock performing the shunting operations and technical characteristics of the locomotive itself. What also affect these characteristics, yet to a

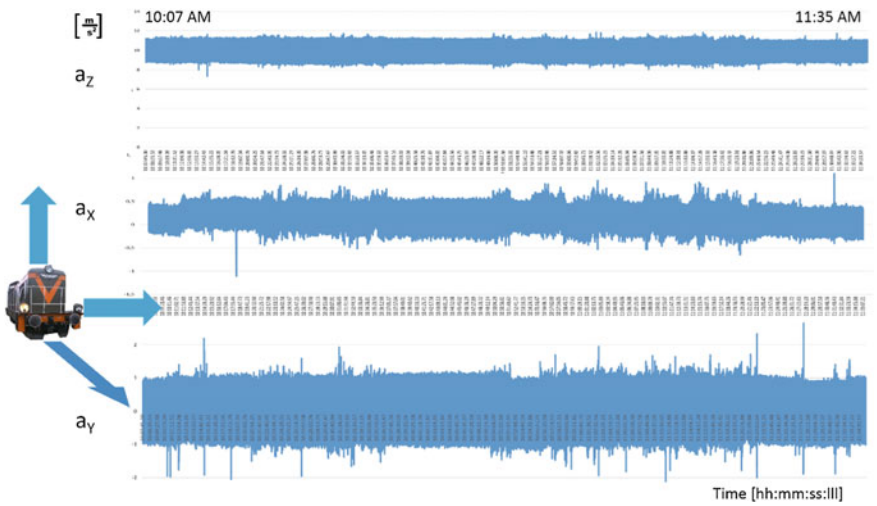

Fig. 3 Accelerations in 3 axes measured within 10:07 AM to 11:35 PM of shunting activity (presented graphs based on 100 MB file data). *Source* authors' own materials

lesser extent, are the weather conditions and other random factors, such as physical condition of the driver performing shunting operations.

Very important parameter of shunting locomotive is speed profile. Figure 4 illustrates the shunting locomotive speed during the test. Apart of standard assessment of the speed adjustment to the shunting operations performed (in correlation with the locomotive location on the station plan), such a graph also makes it possible to assess the efficiency of utilising the shunting locomotive working time. This can allow for increasing efficiency of locomotive working time. Since changes to the running speed illustrated in the graph in Fig. 4 are considerably dynamic, it may also be considered as a premise for optimisation of a schedule of shunting operations for the sake of fuel saving etc.

For the analysis of dynamics of locomotive, the information on current altitude can be useful. The shunting locomotive altitude profile provided in Fig. 5 with reference to the sea level proves particularly helpful for purposes of the running speed control (shunting were carried out in the mountainous area). The track slope exerts a major impact on the locomotive running speeds (particularly at mountain stations, ramp-type shunting stations and those featuring a gravity yard hump). In correlation with the locomotive's traction characteristics as well as its position on the station plan, it enables calibration of the shunting locomotive speed.

According to the method proposed, the remote monitoring of shunting activity is ensured by using the SMS and GPR transmission channels. There are numerous restrictions to the first option, namely those of technical and economic nature. The maximum SMS length is 140 8-bit characters (900 characters owing to the CSMS technology) [9]. The foregoing means that a single SMS may only be used to send information about ca. basic 3 data sets (each in the minimum composition: three values of linear acceleration, value of longitude and latitude) at three pre-defined locations of the shunting station. Therefore, this technology only enables data to be sent in an aggregated form (mean over the time or distance), and only for certain

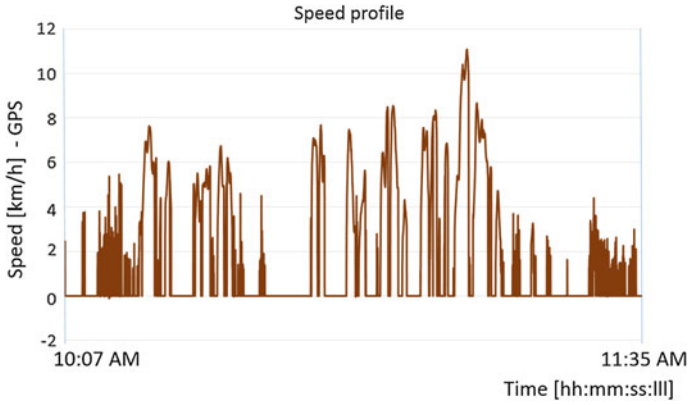

Fig. 4 Shunting locomotive speed profile over all distance (ca. 1.5 h). *Source* authors' own materials

Fig. 5 Profile of the locomotive altitude above sea level, all track. *Source* authors' own materials

sections of long tracks. In practice, it virtually precludes ongoing supervision of a shunting rail vehicle. What seems prospective for the method proposed is the use of communication channels based on the WiFi and BT technologies [10–12]. Nevertheless, when considering the latter case, one should bear in mind the technical (length related) constraints of this method, since not all track systems will allow for this technology to be deployed.

Measurements of acceleration of train enable more advanced analysis. Commonly applied are frequency analysis and time–frequency distribution where possibilities of identification of frequency components are widely described in many papers [13–17]. Authors decided to develop other useful metrics to describe dynamical properties of the driving train. Due to heavy construction of train vehicle and typical solution of suspension system between wheelsets, bogies and cabin or wagon, the current Position of cabin has to be considered as important parameter. Position of cabin (superelevation) is the result of dynamic forces generated and interacting during train movement. Thus, the authors proposed other parameter for evaluation of current position of cabin as resultant horizontal accelerations. It was calculated as inverse tangent function of current longitudinal and transverse accelerations. As the result we obtain resultant angle and information on relation between longitudinal and transverse interactions. The distribution of inverse tangent function has been depicted in Fig. 4. Analysis of Fig. 6 shows clearly different activities of shunting locomotive selected into two sections. First section is much more organised and the second section is more chaotic. It can be interpreted as movement with different speed and directions or shunting processes. The sensitivity of inverse tangent function on locomotive activities has been tested on result of measurement of movement of locomotive in other station, where activities were determined by characteristics of infrastructure and it has been grouped into two shunting sections.

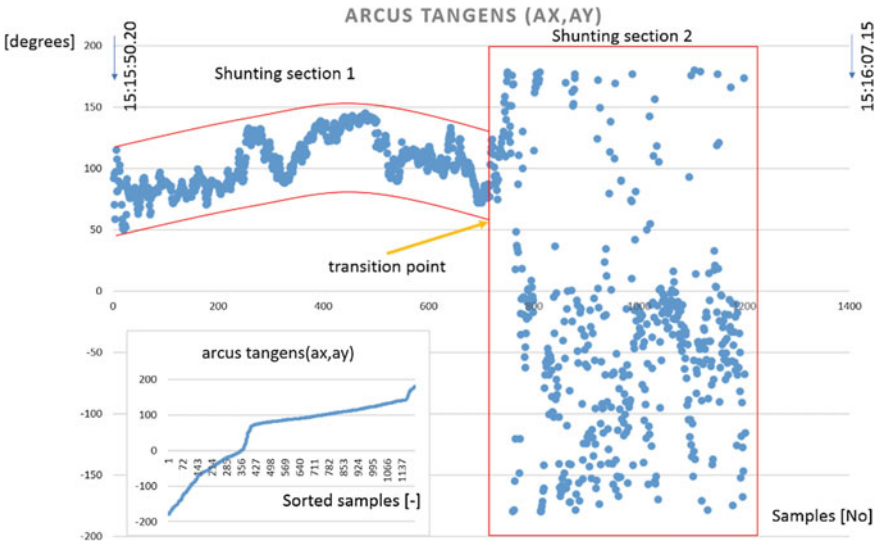

Fig. 6 Distribution of inverse tangent function. *Source* authors' own materials

For the more complex analysis, the inverse tangent function has been collected with acceleration waveforms. It allows to confirm direct relations between resultant angle and acceleration. Figure 7 presents time window correlated with Sect. 2 from inverse tangent distribution.

5 Remote Control Unit

For the purpose of utility of developed methodology and dynamics, monitoring system for shunting activities of locomotive the concept of control unit was proposed. Taking into consideration the above mentioned and properties of shunting activities, it was assumed that the control unit has to be remote for possibilities of operating from distance.

Different communications channels between engine driver and master signal box can be used during the shunting processes. In case where locomotive is working on shunting, the vehicle obligatory is equipped with ERTMS/ETCS level 1 system. Also the rail tracks have ERTMS/ETCS level 1 system. Thus all shunting processes have to be conducted with ERTMS/ETCS level 1 system. In case when ERTMS/ETCS system does not exist or not working, it is allowed to communicate by the radio or verbally. Movements inspector inform verbally or by the radio assistant shunter about methods for shunting processes. The communication channel has to guarantee constant information exchange. Currently commonly used are radio links and visual channel.

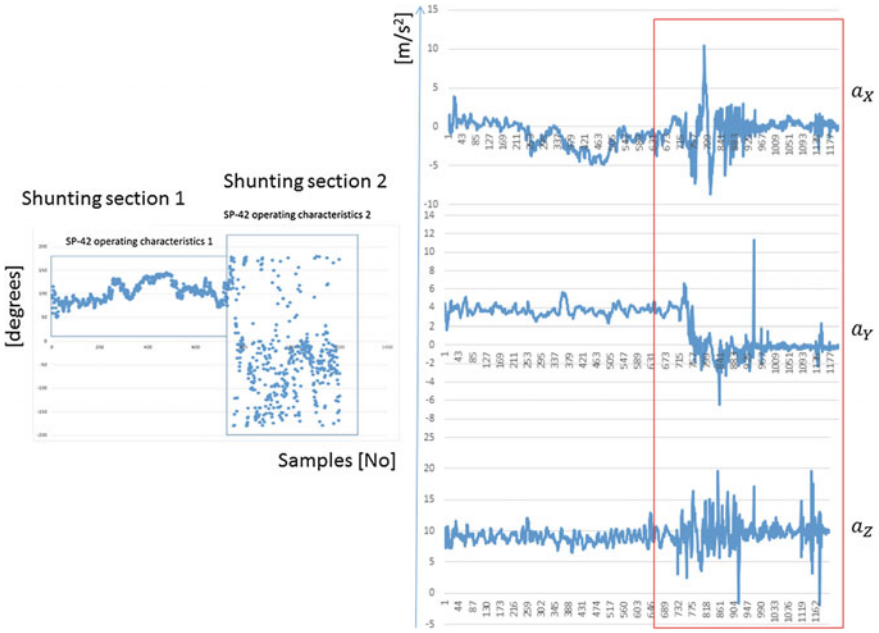

Fig. 7 Correlation of inverse tangent function and acceleration in 3 axis. *Source* authors' own materials

The paper presents concept of support for the communication channel by means of the SMS, WiFi and BT protocols. The advantages and disadvantages of each communication methods [18, 19] have been presented in Fig. 8.

The concept of communication model assumed that radio links method is main channel but some of the limitation or disadvantages can be reduced by the supported method. The main limitation is low information capacity, especially for the current reports of shunting activities. The proposed model allows to send digital information where possibilities of type of information are much bigger and the precision is very good. Thus the information is sending in real time with good precision and high capacity. Hence shunting activities are reported with details, so shunting becomes more safer and efficient. Other advantages of the communication model are two-way communication (receiving and transmitting) and independence due to other two communications channels.

The most important properties of the communication model are possibilities of real-time analysis of the collected data. Thus it can be considered as remote control unit for shunting processes.

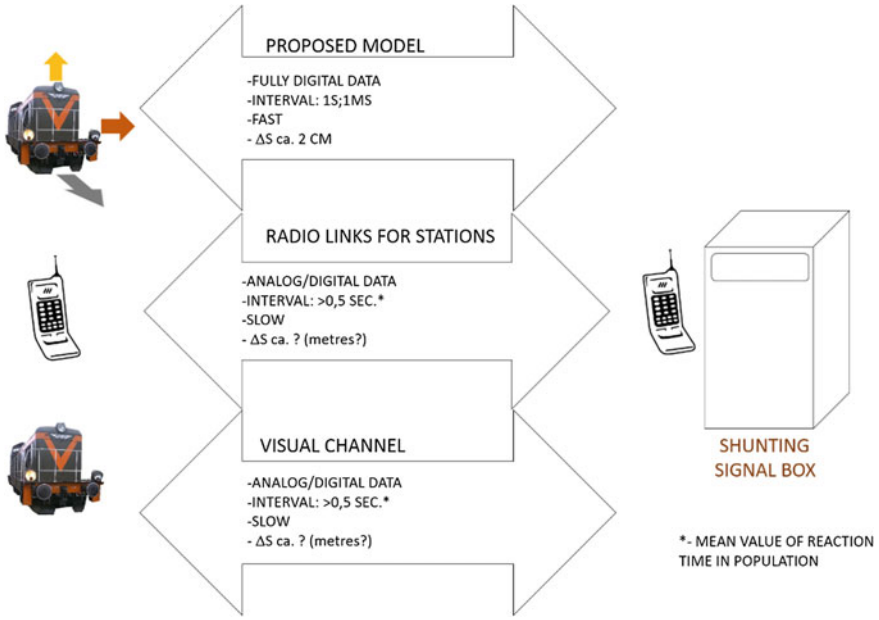

Fig. 8 Comparison of different communication methods. *Source* authors' own materials

6 Conclusions

The results show possibilities of using monitoring of dynamics of locomotive in wide applications. The research method, the mobile application and the procedures for analysing the locomotive's shunting activity at a marshalling yard, are all discussed in this article, which enable assessment whether the locomotive driver's duties are pursued in a correct manner. Within the given shunting area, one can monitor the shunting activity by application of the method in question. Prospectively, such an information channel combined with a reverse channel (radio communications) enables the driver's operations to be corrected. As regards further prospects of application, it may also enable completely automated shunting activity. Thus it can be considered as remote control unit.

The paper describes research method adopted to the limitation of railway procedures and properties of shunting activities. The method proposed offers interesting new opportunities for performance of shunting activity at large marshalling yards, especially in cases when the given shunting run extends on neighbouring switching circuits. The horizontal and vertical acceleration, altitude and speed profiles and current position of shunting locomotive are registered. It allows to collect set of data of current dynamics of locomotive.

Authors proposed other parameter for evaluation of current position of cabin as resultant horizontal accelerations. It was calculated as inverse tangent function of

current longitudinal and transverse accelerations. As a result, we obtain resultant angle and information on relation between longitudinal and transverse interactions. The results obtained are promising.

The paper discusses model of communication between engine driver and master signal box with real-time analysis of the collected data. Thus it can be considered as remote control unit for shunting processes.

Due to the utilitarian of the research the methodology and measurement system has been adopted and installed into smartphones (GPS and MEMS). The preliminary tests have been conducted and evaluated with good result.

This article has provided several illustrations to solutions enabling the data in question to be analysed. The authors have also proposed other options for monitoring parameters of shunting activity as well as technical condition of both facilities and means of transport taking part in shunting. This subject is very multi-facet.

Acknowledgments This article has been developed under externally financed research project DEMONSTRATOR + Supporting scientific research and development works in demonstration scale, the title of the project is Integrated system for support the management of information in passenger railway transportation (no. DEM/1/RT4/2013/0 PASAŻER).

The authors would like to expresses their gratitude towards the Southern Division of PKP CARGO S.A. based in Katowice for enabling them to conduct the studies discussed and requires considerable technical and financial resources to be involved.

References

1. Carman, R., Reyes, C., Glickman, G., Schaeffler M.: Comparison of two metrics for assessing human response to vibration. In B. Schulte-Werning et al. (Eds.): Noise and vibration mitigation for rail transportation systems, 99 pp. 215–221. Springer, Berlin Heidelberg (2008).
2. Sawczuk, W.; Application of selected frequency characteristics of vibration signal for the evaluation of the braking process for railway disc brake. Diagnostyka, 16 (3), pp. 33–38. Olsztyn (2015).
3. Lombaert, G., Degrande, G., Bekaert J.: The Influence of the train speed on vibrations due to high speed trains. In B. Schulte-Werning et al. (Eds.): Noise and vibration mitigation for rail transportation systems, 99 pp. 19–25. Springer, Berlin Heidelberg (2008).
4. Xia, He, Cao, Yanmei, De Roeck Guido, Degrande Geert: Environmental problems of vibrations induced by railway traffic. Front. Archit. Civ. Eng. China, 1(2), pp. 142–152 (2007).
5. Parkinson, B.W.: Global Positioning Systems. American Institute of Aeronautics and Astronautics. (1996).
6. Mendizabal, R. and Berenguer, R. and Melendez, J.: GPS and Galileo, GPS & Galileo: Dual RF Front-end Receiver and Design, Fabrication, and Test. McGraw Hill (2009).
7. Dolecek, R., Cerny, O., Lenoch, V.: The GPS application for the control of the rail vehicle. IEEE, 24th International Conference on Radioelektronika, Bratislava, Slovakia (2014).
8. Młyńczak, J., Burdzik, R., Celiński, I.: Remote monitoring of the train driver along with the locomotive motion dynamics in the course of shunting using mobile devices. In Awrejcewicz, J. et al. (Eds.): Dynamical system Control and stability, pp. 411–422. Łódź (2015).
9. CLOCKWORK, http://www.clockworksms.com/blog/concatenated-sms/; access (10-03-2016).
10. Ross, J.: The book of wirelees.., No Starch Press, CA (2008).
11. Huang, A., Rudolph, L.: Bluetooth for Programmers. MIT Computer Science and Arifficial Inteligence Laboratory, Massachusetts (2005).

12. Lubkowski, P., Laskowski, D., Maslanka, K.: On supporting a reliable performance of monitoring services with a guaranteed quality level in a heterogeneous environment. In: Zamojski, W., Mazurkiewicz, J., Sugier, J., et al. (Eds.): Theory and engineering of complex systems and dependability, Book Series: Advances in Intelligent Systems and Computing, 365 pp. 275–284 (2015).
13. Ir-9 (R-34), Instruction on maneuvers technique. PKP Polskie Linie Kolejowe S.A., Warszawa (2012).
14. Burdzik, R.: Identification of sources, propagation and structure of vibrations affecting men in means of transport based on the example of automotive vehicles. JVE International Ltd., Kaunas (2014).
15. Burdzik, R.; Identification of structure and directional distribution of vibration transferred to car-body from road roughness. Journal of Vibroengineering, 16(1), pp. 324–333. Kaunas (2014).
16. Dabrowski, Z., Zawisza, M.; Investigations of the vibroacoustic signals sensitivity to mechanical defects not recognised by the OBD system in diesel engines. Solid State Phenomena, 180 pp. 194–199 (2014).
17. Listewnik, K., Grzeczka, G., Klaczynski, M., et al.: An on-line diagnostics application for evaluation of machine vibration based on standard ISO 10816–1. Journal of Vibroengineering, 17(8), pp. 4248–4258. Kaunas (2015).
18. Siergiejczyk, M, Rosiński, A.; Selected aspects of the supervision of ICT systems used in the rail transport. Diagnostyka, 16 (2) pp. 67–72. Olsztyn (2015).
19. Dolecek, R., Cerny, O., Novak, J.: Interference in power system for traction drive with PMSM. Przeglad Elektrotechniczny, 88(9A), pp. 204–207 (2012).

Durability Tests Acceleration Performed on Machine Components Using Electromagnetic Shakers

Adam Niesłony, Artur Dziura and Robert Owsiński

Abstract Acceleration of vibration tests to increase utilization of test equipment was performed till now mainly by increasing intensity of excitation. In this paper it was shown possibilities of shortening random vibration tests included in standard MIL-STD 810 G and it was proposed to use existing methods to predict damage in non-Gaussian random vibration tests.

1 Introduction

Environmental tests of designed mechanical structures includes very often dynamic endurance test, during which designed structure is subjected to many different accelerations [1–3]. Those accelerations should represent loading which will occur during whole life of normal operation. Durability of design under cyclic accelerations (vibrations) depends on accelerations itself and their interactions with dynamic properties of tested structure and fatigue properties of tested material. To get right level of accelerations, their spectral behavior during environmental test it have to be known and analyzed time depend acceleration response in whole life of product. However, there are products in which it is hard or not possible at all to determinate such time depended representative loads. This is due to variation of operating conditions or the way how it was used and the most common for both of those factors together. As example here it can be shown aerospace designs or automotive designs. In such a case, random vibration test can be performed to

A. Niesłony (✉) · R. Owsiński
Faculty of Mechanical Engineering, Department of Mechanics and Machine Design, Opole University of Technology, 5 Mikołajczyka Street, 45-271 Opole, Poland
e-mail: a.nieslony@po.opole.pl

R. Owsiński
e-mail: r.owsinski@po.opole.pl

A. Dziura
WABCO Polska Sp.z o.o., 34 Aleksandra Ostrowskiego Street, 53-238 Wrocław, Poland
e-mail: artur.dziura@wabco-auto.com

© Springer International Publishing Switzerland 2016

J. Awrejcewicz (ed.), *Dynamical Systems: Theoretical and Experimental Analysis*, Springer Proceedings in Mathematics & Statistics 182, DOI 10.1007/978-3-319-42408-8_23

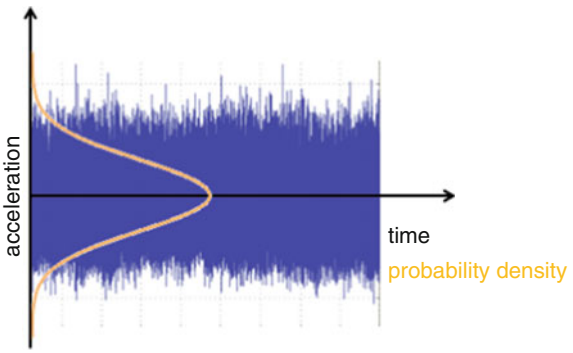

Fig. 1 Acceleration in time and calculated probability density function

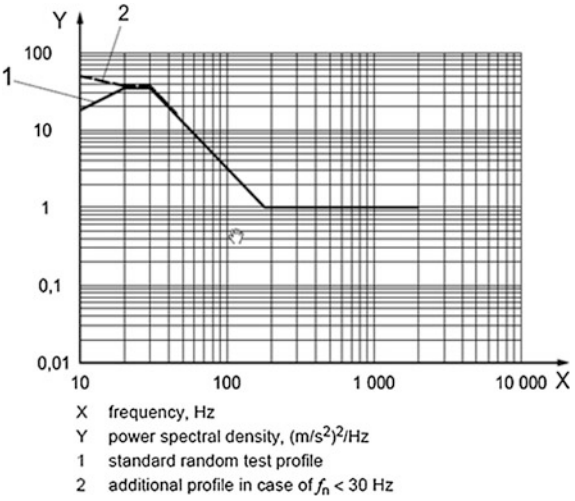

Fig. 2 Power spectral density for random vibration test included in ISO FDIS 16750-3 (2006) Road vehicles —Environmental conditions and testing for electrical and electronic equipment—Part 3: Mechanical loads

verify design. During this test design is shocked with predefined distribution of acceleration according to statistical distribution of instantaneous value of this distribution (most common it is Gaussian distribution). It is also setup acceleration levels for different frequency intervals. Sufficient specification of random vibration test consists information about used probability density function, power spectral density function, which inform about level of acceleration for specific excitation frequency interval, exposition time for those conditions and direction of excitation, which was shown in Figs. 1 and 2.

In practice random vibration tests are performed using so called shakers, which can generate acceleration with specified frequency on specified mass. There are two main groups of such shakers:

- electromechanical (recommended by higher frequency, but for smaller forces),
- hydraulic (recommended to lower frequency, but higher forces and displacements).

The tests typically last several hours and are thus expensive. Because of that interesting feature are procedures which let us shortening the test time by influencing the "damaging portion" of the dynamic endurance test. This can be done through specialized preparation of the loading taking into account fatigue properties of the material.

2 Procedure of Calculating of Fatigue Durability by Random Vibration Loading

Durability of design on random vibration test can be predicted on the numerical calculation way with usage of finite element method. Unfortunately due to simulation efficiently some assumptions have to be introduced:

1. Model have to be linear (due to contact, material nonlinearity, and geometrical nonlinearity);
2. Damping of tested design has to be defined. This will ensure correct dynamic response. Damping has to be constant against loading (acceleration in this case) level.

Those limitations very often lead to difficulties in converged of real tested design behavior with simulated model. That is why it is recommended to use information about a natural frequency of tested design for verification simulation model on early stage of simulation in modal analysis. Modal analysis is first step which from one side gives possibilities of model verification by comparing of natural frequency with observe ones and on the other includes input data to next step: harmonic analysis. Modal analysis allows also to detect mistakes in number of freedom degree (zero frequency of Eigen value and scaled view of shape for each natural frequency). As this analysis is relative fast, this verification has big practical meaning and it is common used. As already was mentioned next step is to perform harmonic analysis of design by using finite element method. Target of this analysis is to get dynamic response of design for unit load acceleration defined in frequency domain. This result is so called amplitude–frequency characteristic in form of stress tensor components and their phase angle, which defines phase shift of response relative to excitation. Frequency range of modal analysis is twice of harmonic analysis.

Results from described harmonic response are in next step reduced to one resultant stress for each considered frequency. For such reduction it can be used common known strength hypothesis (e.g., maximal principal stress, Huber-Mises-Henckey, maximal absolute principal stress, or octahedral plane stress), which does not include in resultant stress information about phase angle included in amplitude–frequency characteristic. There is also criterion, which partially is using this information: Preumont and Piefort criteria. Details for this criterion can be found in much elaboration [4–6]. Such resultant response of

dynamic system is called transfer function [$S(f)$] and it is further used in next steps of life time estimation during random vibration test simulation. Based on transfer function and power spectral density of input signal ($\mathrm{PSD}_{\mathrm{input}}$) it can be calculated power spectral density of stress ($\mathrm{PSD}_{\mathrm{output}}$).

$$\mathrm{PSD}_{\mathrm{output}}(f) = \mathrm{PSD}_{\mathrm{input}}(f) \cdot S(f)^2 \tag{1}$$

Power spectral density of reduced stresses is function which is further used to calculate moments of n-th range based on following equation:

$$m_k = \int_{f1}^{f2} \mathrm{PSD}_{\mathrm{output}}(f) \cdot f^k \mathrm{d}f \tag{2}$$

Moments of power spectral density of reduced stress is needed to calculate statistical values which defines changes of reduced stress and used in fatigue calculation. Based on this in next step expected number of cycles n_i for small stress range $\mathrm{d}S_i$ interval will be calculated

$$n_i = E[P] \cdot T \cdot p(S) \cdot \mathrm{d}S_i \tag{3}$$

where T is exposition on vibration time in second, $p(S)$ is probability of cycle occurrence $E[P]$ is expected number of stress peaks and it depends on moments of $\mathrm{PSD}_{\mathrm{output}}$ in following way

$$E[P] = \sqrt{\frac{m_4}{m_2}} \tag{4}$$

Probability of cycle occurrence with specific amplitude can be estimated based on a lot of methods. In this algorithm probability of cycle occurrence is calculated based on information from power spectral density of reduced stress. Most popular methods for calculation of probability of cycle occurrence are:

Narrow Band approximation: theoretical derivate formula with assumption of low frequency range and Gaussian distribution, which gives probability of cycle occurrence for specific stress range ($\mathrm{d}S$) as Rayleigh distribution. In practice for wide frequency range it gives lifetime estimated in conservative way.

$$p(S) = \frac{S}{4 \cdot m_0} \cdot \exp\left(\frac{-S}{8 \cdot m_0}\right) \tag{5}$$

Dirlik: formula obtained by empirical method based on the weighted sum of the Rayleigh, Gaussian and exponential probability distributions [6–8].

$$p(S) = \frac{\frac{D_1}{Q} \cdot \exp\left(\frac{-Z}{Q}\right) + \frac{D_2 \cdot Z}{R^2} \cdot \exp\left(\frac{-Z^2}{2 \cdot R^2}\right) + D_3 \cdot Z \cdot \exp(\frac{-Z^2}{2})}{2 \cdot \sqrt{m_0}} \tag{6}$$

where:

$$D_1 = \frac{2 \cdot (X_m - \gamma^2)}{1 + \gamma^2} \tag{7}$$

$$D_2 = \frac{1 - \gamma - D_1 + D_1^2}{1 - R} \tag{8}$$

$$D_3 = 1 - D_1 - D_2 \tag{9}$$

$$Z = \frac{S}{2 \cdot \sqrt{m_0}} \tag{10}$$

$$Q = \frac{1.25 \cdot (\gamma - D_3 - D_2 \cdot R)}{D_1} \tag{11}$$

$$X_m = \frac{m_1}{m_0} \sqrt{\frac{m_2}{m_4}} \tag{12}$$

$$R = \frac{\gamma - X_m - D_1^2}{1 - \gamma - D_1 + D_1^2} \tag{13}$$

$$\gamma = \frac{m_2}{\sqrt{m_0 m_4}} \tag{14}$$

Lalanne is proposing to use probability of peaks for Gaussian broadband process in the place of rainflow cycles PDF. Such kind of function was provided by Rice in the form [9]

$$p(S) = \frac{1}{2} \cdot (\exp(\frac{S_a^2}{2 \cdot m_0 \cdot (\gamma - 1)}) \cdot \sqrt{-\frac{\gamma^2 - 1}{2\pi \cdot m_0}} + \frac{\gamma \cdot S_a}{2 \cdot m_0 \cdot \exp\left(\frac{S_a^2}{2 \cdot m_0}\right)} (1 + \operatorname{erf}\left(\frac{\gamma \cdot S_a}{\sqrt{2 \cdot m_0 \cdot (1 - \gamma^2)}}\right)) \tag{15}$$

where:

$$\operatorname{erf} = \frac{2}{\pi} \cdot \int_0^x e^{-t^2} \mathrm{d}t \tag{16}$$

$$x = \frac{\gamma \cdot S_a}{\sqrt{2 \cdot m_0 \cdot (1 - \gamma^2)}} \tag{17}$$

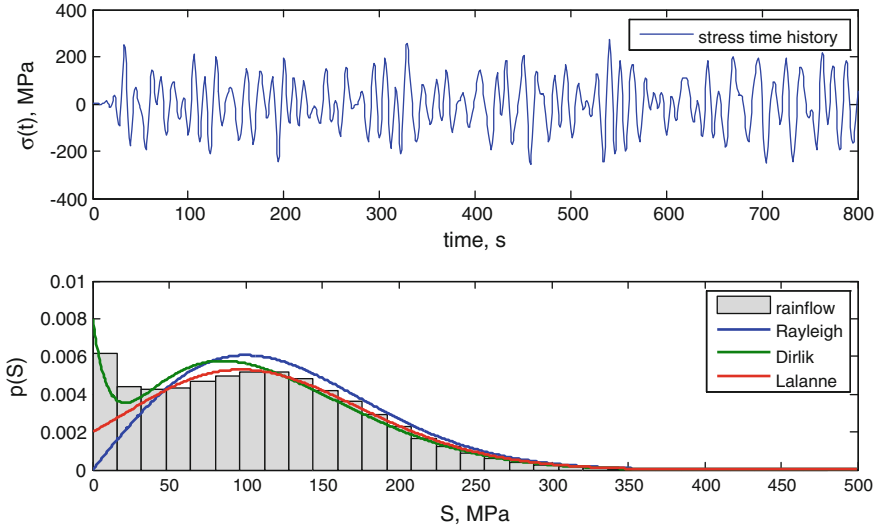

Fig. 3 Example of a stress time history observed on a structure and the PDF of amplitudes counted directly from the stress history using rainflow algorithm compared to PDF's obtained according (5), (6), and (15) from PSD function

By calculating probability density based on Eqs. (5), (6), and (15) see Fig. 3, upper limit of stress amplitudes S is taken as 3.5–5.0 times of standard deviations from stress distribution. Standard deviation can be easy calculated from power spectral density of reduced stress based on following relationship:

$$\mathrm{RMS}_{\mathrm{output}} = \sqrt{m_0} \tag{18}$$

After calculation of cycle number for each given amplitude of reduce stress it have to be calculated number of cycles which is possible to survive by material before crack will occur also for each given amplitude. This is typical exercise for single axial fatigue strength. It can be used for this both, stress life or strain life method. As random vibration test usually are connected with huge number of cycles, so stress life method is more adequate in this case. This method is also less complicated from numerical point of view. It has to be remembered about mean stress correction if it is available, as this can have significant impact on durability.

Last step is to calculate partial damage in each stress amplitude interval and sum of partial damages to total damage. This procedure is called cumulative damage accumulation and most common it is executed by using linear hypothesis of Palmgren-Miner, which can be described by following equation:

$$E[D] = \sum_{i=1}^{i=K} \frac{n_i}{N_i} \tag{19}$$

where n_i is number of cycles which will occur in i-th stress interval ($i = 1,\ldots, K$), N_i is number of cycles possible to survive for i-th stress interval comes from fatigue graph prepared for loading with constant amplitude.

Sum over all intervals of stress amplitudes gives total damage value, which when reach value of 1, crack during test will occur. In Fig. 4 is shown the procedure in the form of process map.

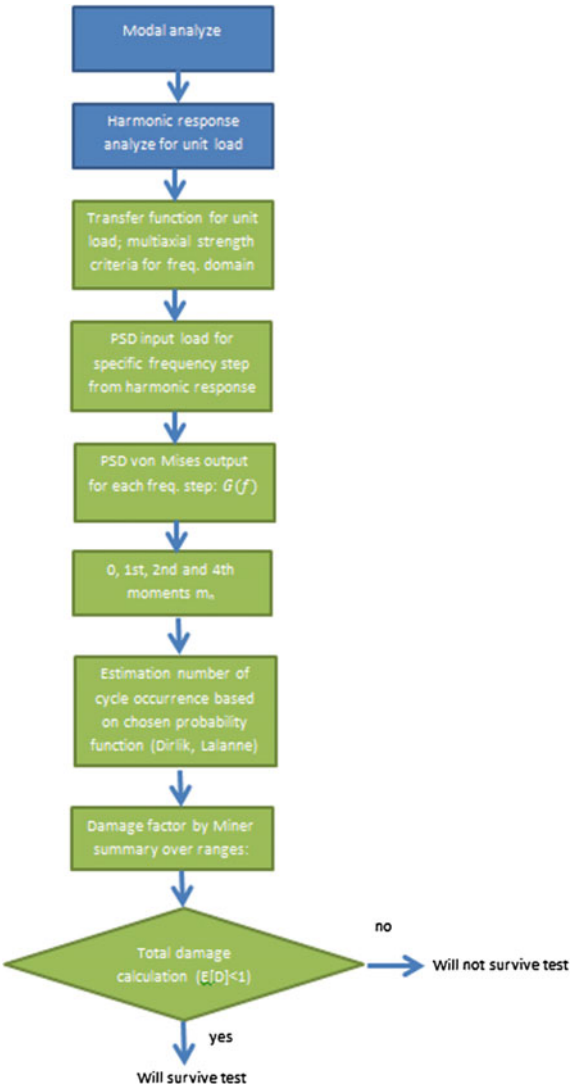

Fig. 4 Process map for durability estimation of random vibration tests

3 Acceleration of Vibration Tests

Vibration tests are expensive and long. Almost each random vibration test is accelerated one as:

- it represents real working conditions, which will take place during life of product (only scaled to test time),
- test time is shortened in comparison to real life of product.

Nevertheless, environmental working conditions of product in the meaning of the working environment and interaction of dynamic loading and response of design are not easy to define. In such a case it is worth to use standard which gives for some group of products time and power spectral density of input acceleration for specific usage or working condition (e.g., standard ISO 16750 part 3). It is often that such input power spectral density are delivered as design requirements as results of real design measurement and experience in design of specific products. Times of exposition during those tests can be even few tens of hours. With reflect to relative high cost of such a test it makes acceleration of random vibration test justified.

3.1 Random Vibration Tests Acceleration Possibilities

Each design respond on a given random loading profile with own specific way. Newer the less there is general rule which says that for higher loading intensity we will get higher stress in design during test. Each cycle is participating in cumulative accumulation of fatigue damage by using Palmgren-Miner rule. Higher amplitude of stress form loading cycle means higher portion of damage in this cycle. By increasing in controlled way this portion of damage we can much faster achieve total damage higher than in test with not changed parameters. There are two main methods of shortening random vibration test:

- by increasing level of acceleration power spectral density on input,
- by usage non-Gaussian distribution of stress–number of cycles with high stress amplitude increase.

Common known method is increase of input acceleration power spectral density level. This method has restrictions due to increased stress level can yield material. As a consequence of this response of design will not be linear any longer, which is not in-line with assumption of calculation algorithm. In such a case—nonlinearity of material and nonlinearity due to change of damping in yield area will occur. Never the less method is used most common. It is also described in standard MIL-810 G method 514.6.

3.1.1 Method of Increasing Loading Level

Fatigue durability calculation algorithms can be split due to valve which represents strength of material on two groups: stress and strain driven. In strain group algorithm most popular fatigue relationship is Manson-Coffin-Basquin [10]. This formula describes in accurate way fatigue material properties in low cycles and high cycle. This formula is shown below:

$$e_t = \frac{\sigma_f^{'}}{E}(2N_f)^b + e_f^{'}(2N_f)^c \tag{20}$$

where e_t is total strain amplitude, $\sigma_f^{'}$ strength coefficient (elastic component), E young modulus, N_f number of cycles to failure, b strength exponent (elastic component), $e_f^{'}$ ductility coefficient (plastic component), c ductility exponent (plastic component). Manson-Coffin-Basquin formula includes elastic part and plastic part. In many cases, especially in high cycle fatigue, amplitude of plastic deformation is negligible small. It is used in many stress analysis. In vibration analysis most commonly it used only elastic part of Manson-Coffin-Basquin equation.

$$S_a = \sigma_f^{'}(2N_f)^b \tag{21}$$

Linear cumulative damage accumulation of Palmgren-Miner and formula of fatigue life in stress method can be transform to form which is used to acceleration of vibration tests proposed in MIL-STD 810 G in method 514.6 annex A.

$$\frac{t_2}{t_1} = \left[\frac{S_1}{S_2}\right]^m \tag{22}$$

where t_1, t_2 are tests time with specified RMS value S_1, S_2, and m is connected with b, strength exponent of elastic component in (21). According to suggestion included in MIL-STD810G value m for random vibration test is 0.8 of b. This standard gives also average value of m as 7.5 and it can variate in range from 5 to 8. In MIL standard it is also given maximal acceleration, which can be determinate by using this method as $\frac{S_1}{S_2} \leq 1.4$.

3.1.2 Method of Changed Probability Density Function of Loading

Another method of random vibration testing acceleration is changing of probability density of loading. It is a common rule that probability density function of loading time domain signal is treated as Gaussian distribution. Gaussian distribution can be defined by following formula:

$$p_g(x)[=\frac{1}{\sigma\sqrt{2\pi}}\exp\left[-\frac{(x-\bar{x})^2}{2\sigma^2}\right] \tag{23}$$

where σ is standard deviation, and $\bar{x}$ is expected value of probability density functions.

$$\bar{x}=\frac{1}{N}\sum_{i=1}^{N}x \tag{24}$$

$$\sigma^2=\frac{1}{N}\sum_{i=1}^{N}[x-\bar{x}]^2 \tag{25}$$

Described method of random vibration test acceleration is changing shape of Gauss curve in this way to increase occurrence of high amplitude cycles. Cycles with high amplitude brings also high portion of damage. We can than expect that this procedure will accelerate test significantly. Modifying of probability distribution of stress cycle occurrence is executed by using statistical parameters such as skewness Sk and kurtosis Ku. Those characteristics can be calculated based on central statistical moments of loading described by following rule:

$$M_n=\frac{1}{N}\sum_{i=1}^{N}[x-\bar{x}]^n \tag{26}$$

Skewness is defined by following statistical moment relationship:

$$\mathrm{Sk}=\frac{M_3}{(M_2)^{1.5}}=\frac{M_3}{\sigma^3} \tag{27}$$

Kurtosis is defined by following statistical moment's relationship

$$\mathrm{Ku}=\frac{M_4}{(M_2)^2}=\frac{M_4}{\sigma^4} \tag{28}$$

For standard Gaussian distribution Sk = 0, Ku = 3. Skewness determinates symmetry relative to expected value and kurtosis determinates flatness of distribution. By changing kurtosis (decreasing of Ku) it can be achieved non-Gaussian distribution with occurrence of high amplitude increased in comparison to Gaussian deformation.

As it is shown in P. Baren elaboration [11] real distribution of probability density function very often is not Gaussian one, so testing of components with using of non-Gaussian distribution is justified. Estimation of damage for non-Gaussian loading distribution can be used for correction of testing time, which does not have possibilities of applying non-Gaussian loading profile to achieve the same damage as damage of non-Gaussian loading by initial exposition time.

Claudio Braccesi et al. [12] propose correction of damage calculated based for Gaussian distribution and correction factor which will include influence of non-Gaussian loading:

$$E[D]_{\mathrm{ng}} = E[D]\lambda_{\mathrm{ng}} \tag{29}$$

where $E[D]_{\mathrm{ng}}$ is damage for non-Gaussian distribution, $E[D]$ is damage calculated for Gaussian distribution and λ_{ng} is correction factor. It can be written following general dependence:

$$\lambda_{\mathrm{ng}} = f(\bar{x}, \sigma, \mathrm{Sk}, \mathrm{Ku}, b), \tag{30}$$

As it is state by authors of this publication expected value $\bar{x}$ can be ignore as it is representation of static condition and it can be consider in other steps of analyze. Standard deviation σ can be calculated form area under stress power spectral density curve, b is material parameter.

Factor λ_{ng} is key elements for estimation of durability on random vibration test with non-Gaussian distribution of loading and it depends on standard deviation σ, skewness Sk, kurtosis Ku, and fatigue strength exponent in stress method b (21).

Winterstein is calculating this factor by using following relationship [13]:

$$\lambda_{\mathrm{ng}} = \left(\frac{\sqrt{\pi}k}{2\Gamma(1+|v_2|)}\right)^b \left(\frac{\Gamma(1+b|v_2|)}{\Gamma\left(1+\frac{b}{2}\right)}\right) \tag{31}$$

where:

$$k = \frac{1}{\sqrt{1+2h_3^{*2}+6h_4^{*2}}} \tag{32}$$

$$v_2 = \sqrt{\frac{4}{\pi}\left(1+h_4+h_4^*\right)-1} \tag{33}$$

and h_4, h_4*, h_3, h_4* depend on skewness Sk and kurtosis Ku in following way:

$$h_4 = \frac{\mathrm{Ku}-3}{24} \tag{34}$$

$$h_4^* = \frac{\sqrt{1+1.5(\mathrm{Ku}-3)}-1}{18} \tag{35}$$

$$h_3 = \frac{\mathrm{Sk}}{6} \tag{36}$$

$$h_3^* = \frac{\mathrm{Sk}}{6(1+6h_4^*)} \tag{37}$$

Also Wang proposed relationship to calculate factor λ_{ng} in following way [14]:

$$\lambda_{ng} = k^b(1 + b(b-1)h_4 + b(b+1)kh_3\frac{\sigma}{S_{ut}} \tag{38}$$

where S_{ut} is ultimate tensile strength.

Authors Braccesi et al. [12] calculated in their elaboration factor λ_{ng} by using following formula:

$$\lambda_{ng} = e^{\frac{\frac{3}{2}}{\pi}\left(\frac{(Ku-3)}{5} - \frac{Sk^2}{4}\right)}. \tag{39}$$

4 Conclusions

Constantly striving to reduce the cost of long environmental tests on electromagnetic actuators led to the shortening procedures for these tests. The most reliable and efficient methods are using both theory of random signals and knowledge of materials fatigue. Following those theories some general limitations are arising:

- PSD of loading cannot be scaled without taking into account the yield limit of the tested material;
- Scaling of whole PSD proportional to the frequency lead up to higher power assumption of tests stands (shakers). More efficient method is to adopt the PSD shape for each test. The disadvantage of this method is the changed PSD shape what is not allowed in some normalized tests;
- It is shown that the directed to higher damage change of the kurtosis gives good results in shortening of the tests duration, however, back calculation to the equivalent Gaussian loading is needed for making the method usable in practice.

References

1. Environmental engineering considerations and laboratory tests MIL-STD-810 G (2008) http://www.everyspec.com
2. Piersol AG, Paez TL, editors. (2010) Harris' Shock and Vibration Handbook. 6. ed. New York, NY: McGraw-Hill
3. Kos VP, Slavič J, Boltežar M (2015) Fatigue Damage for Sweep-Sine and Random Accelerated Vibration Testing. Advances in Mechanical Engineering 7: 1–8. doi:10.1155/2014/340545
4. Preumont A, Piefort V (1994) Predicting Random High-Cycle Fatigue Life With Finite Elements. J Vib Acoust 116: 245–248. doi:10.1115/1.2930420
5. Pitoiset X, Preumont A (2000) Spectral methods for multiaxial random fatigue analysis of metallic structures. International Journal of Fatigue 22: 541–550. doi:10.1016/S0142-1123(00)00038-4

6. Niesłony A (2010) Comparison of Some Selected Multiaxial Fatigue Failure Criteria Dedicated for Spectral Method. J Theor Appl Mech 48: 233–254.
7. Dirlik T (1985) Application of computers in fatigue analysis. Phd, University of Warwick
8. Zalaznik A, Nagode M (2013) Validation of temperature modified Dirlik method. Computational Materials Science 69: 173–179. doi:10.1016/j.commatsci.2012.11.036
9. Christian Lalanne Random Vibration ISBN-13: 978-1848216464
10. Niesłony A, el Dsoki C, Kaufmann H, Krug P (2008) New method for evaluation of the Manson-Coffin-Basquin and Ramberg-Osgood equations with respect to compatibility. International Journal of Fatigue 30: 1967–1977. doi:10.1016/j.ijfatigue.2008.01.012
11. Philip Van Baren The Missing Knob on Your random vibration controller. Sound and vibration Oct 2005.
12. Claudio Braccesi, Filippo Cianetti, Guido Lori, Dario Pioli (2009) The frequency domain approach in virtual fatigue estimation of non-linear systems: The problem of non-Gaussian states of stress, International Journal of Fatigue 31: 766–775
13. Winterstein SR (1988) Nonlinear vibration models for extremes and fatigue. J Eng Mech; 114: 1772–89
14. Wang X, Sun JQ (2005) Effect of Skewness on fatigue life with mean stress correction. J Sound Vib; 282: 1231–7

Identification of Impulse Force at Electrodes' Cleaning Process in Electrostatic Precipitators (ESP)

Andrzej Nowak, Paweł Nowak and Stanisław Wojciech

Abstract In the studies related to simulation of vibrations in collecting electrodes of dry electrostatic precipitators, it is necessary to correctly determine the course of impact force of a beater on an anvil beam to which the plates with deposited particulate matter are attached. The courses of these forces have a direct impact on the effectiveness of rapping particulate matter, and therefore on accelerations causing the detachment of dust particles. The paper presents a procedure, which allows for an approximate determination of the course of impact force, based on the results of vibration measurements and computer simulation, in which a self-developed model of the system was used. The analysis covered repeated series of acceleration measurements at several tens points of the system of collecting electrodes. Acceleration measurements were performed using IPC 356A02 triaxial sensors. A computer model, based on the rigid finite element method (RFEM) allows for the determination of a course of accelerations for a strictly specific course of impact force. Comparing the results (of acceleration) obtained by measurements and calculations, a correct course of the impact force was found. Knowing the correct course of the impact force, it is possible, using only computer simulations, to conduct studies of the influence of geometrical and structural parameters of the system on the effectiveness of rapping particulate matter.

A. Nowak (✉) · P. Nowak · S. Wojciech
Department of Transport and Informatics, University of Bielsko-Biała,
Willowa 2, 43-300 Bielsko-Biała, Poland
e-mail: a.nowak@ath.bielsko.pl

P. Nowak
e-mail: pnowak@ath.bielsko.pl

S. Wojciech
e-mail: swojciech@ath.bielsko.pl

© Springer International Publishing Switzerland 2016

J. Awrejcewicz (ed.), *Dynamical Systems: Theoretical and Experimental Analysis*, Springer Proceedings in Mathematics & Statistics 182, DOI 10.1007/978-3-319-42408-8_24

1 Introduction

Modern dry electrostatic precipitators are large industrial devices, designed for a very precise cleaning of exhaust gases from solid particles. Their effectiveness depends, among others, on the conditions of gas flow, but also on geometrical parameters of the ESP. The reduction of particulate emission using electrostatic precipitators still remains an important and current research problem. The analysis covers both electric fields in the chambers of electrostatic precipitators and flows of exhaust gas through the section of collecting electrodes, including the use of computational fluid dynamics models [1–3]. Conducted studies also include the analysis of the course of dust extraction and the influence of geometrical parameters on the efficiency of electrostatic precipitator [4, 5].

It should be noted that in each dry electrostatic precipitator, two processes are simultaneously conducted, which are seemingly mutually exclusive. The first one is responsible for efficient capture of particulate matter from the gas flow and their collection on surfaces of collecting electrodes. The second one is a process of periodic removal of the deposited particulate matter from these surfaces by inducing their vibrations. The sources of vibrations are rapping systems, generating impulse forces, and their direct measures are values of tangential and normal components of accelerations at the checkpoints. Inadequately selected vibrations may be too small to detach particulate matter from the surface, and then corona discharges and a rapid

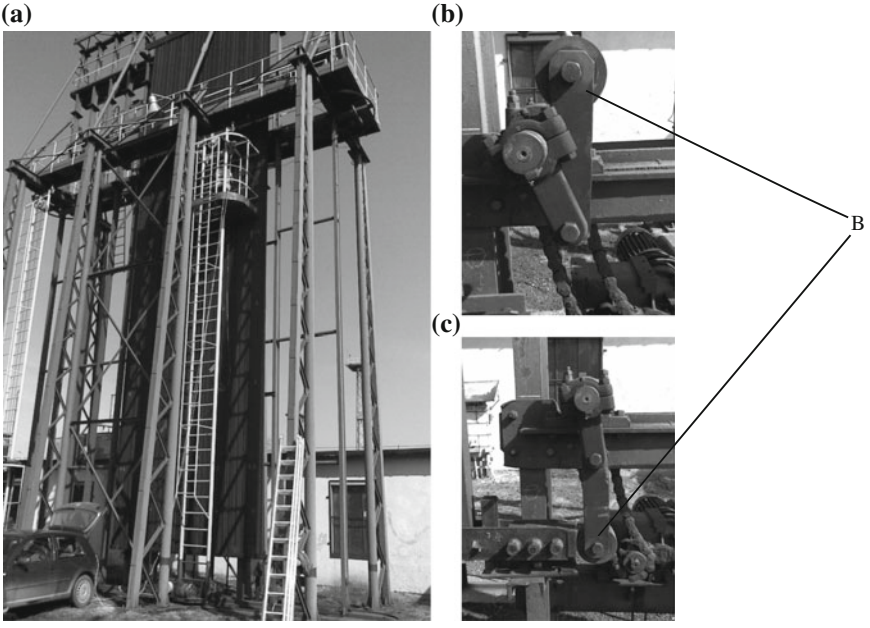

Fig. 1 Test stand: **a** general view, **b** initial and **c** final position of the beater B

drop in the potential of the electric field take place. In turn, if the induced vibrations are too strong, the produced cloud of particulate matter can cause a secondary pollution of gases. In both cases, the efficiency of E operation decreases.

Measurements and related analyses described in this paper constitute one of the validation stages of numerical models, described in [6–9]. Acceleration measurements were performed on a special test stand (Fig. 1a).

The test system comprises nine plates of collecting electrodes (CE), of a length $L = 16$ m, made of sheet metal of a thickness $h = 1.5$ mm, hanging on a common suspension beam (SB) and fastened at the bottom by an anvil beam (AB), terminated with an anvil (A) on the side of the anvil beam (Fig. 2). In the rapping system, a beater (B) having a weight $m = 8$ kg was mounted (Fig. 1b). As the acceleration measurements were performed independently of the measurement of the impulse force, further analyses, especially those used to validate numerical models, required a numerical identification of the course of the impulse force, which could not be measured at that time. In turn, the course of the impulse force $F(t)$ is necessary to determine the load in the modeled system of collecting electrodes.

Therefore, the further part of the paper presents a procedure leading to the determination of the course of the impulse force. For this purpose, it was assumed that the value of the impulse force will change linearly (Fig. 3)—increases from zero to a certain value $F_{\max}$, and then linearly decreases to zero within a predetermined time interval t_F. Based on the test results obtained from one of the manufacturer of electrostatic precipitators it was assumed that $t_F \cong 0.00025$ s.

Therefore, the value of the force impulse equals $S = \frac{1}{2} t_F F_{\max}$. As demonstrated by test calculations, the impact of the increase intensity of the impulse force (Fig. 3, curves 2 and 3) on the obtained acceleration results is small. Thus, a course $F(t)$ corresponding to an isosceles triangle, indicated by a solid line 1 in Fig. 3 was applied in the calculations.

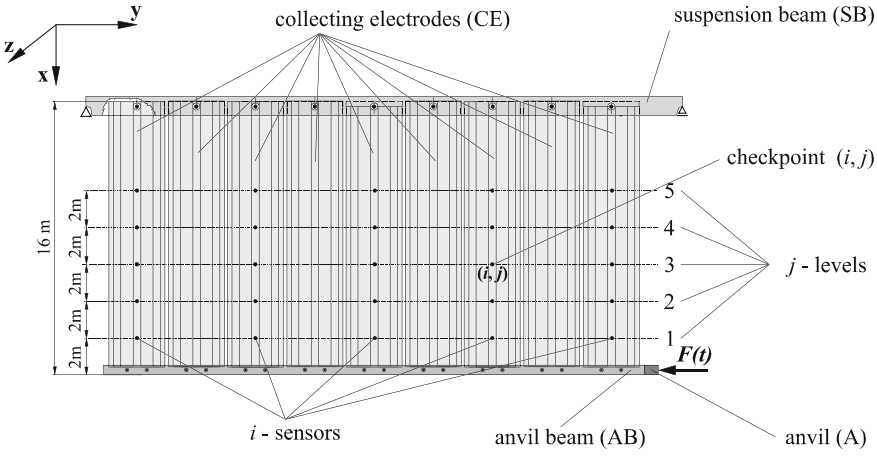

Fig. 2 Configurations of checkpoints

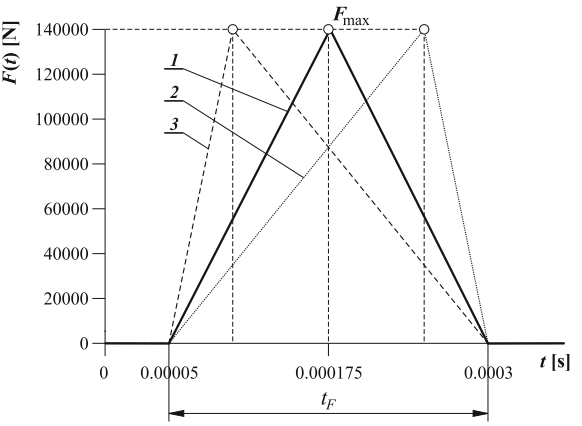

Fig. 3 Exemplary (predicted) course of the impulse force $F(t)$ in time t_F

2 Implementation of Measurements

The formalized algorithm of the procedure, aimed to determine the correct value of the maximum force $F_{\max}$, requires the introduction of symbols. Thus, it is assumed that

I—number of a sensor,
n_i—number of sensors,
j—number of a level,
n_j—number of levels,
k—number of the value of force $F_{\max}$ in the calculations,
n_k—number of adopted equidistant values $F_{\max}^{(k)}$ in the interval $(F^{\min}, F^{\max})$,
m—number of a measurement series at j level,
$n_m^{(j)}$—quantity of measurement series at j level,
$a_{\alpha,k}^{(i,j)}$—acceleration α corresponding to sensor i at level j in calculations for $F_{\max} = F_{\max}^{(k)}$, wherein $a \in \{x, y, z, \tau, t\}$, $a_{x,k}^{(i,j)}$, $a_{y,k}^{(i,j)}$, $a_{z,k}^{(i,j)}$ are acceleration components of the point, obtained directly from the calculations and $a_\tau = \sqrt{a_x^2 + a_y^2}$ and $a_t = \sqrt{a_x^2 + a_y^2 + a_z^2}$,
$\tilde{a}_{\alpha,m}^{(i,j)}$—acceleration α corresponding to sensor i at level j induced by an unknown impulse force in measurements of series m.

The main components of measurement equipment were: a 16-channel recorder TEAC lx110, a portable computer with the LX Navi software, $n_i = 5$ triaxial vibration ICP sensors of 356A02 type, provided by PCB Piezotronics.

In the course of the measurements, the signals were registered at a sampling frequency of 24 kHz (for each channel). Each time a reaction to a single impulse input (impact of a beater) was recorded—this kind of measurement event will be

further referred to as a series. Therefore, a series comprises $3n_i$ courses of accelerations $\tilde{a}_x$, $\tilde{a}_y$, $\tilde{a}_z$ in n_i sensors placed at level j. For each position of sensors (configuration at level j), $n_m^{(j)} = 10$ measurement series was performed. The full system of sensor configuration is presented in Fig. 2. Impacts of the beater were executed when the electric drive switched off (Fig. 1b, c). The sensors were attached to the surface of the electrodes using an adhesive. The processing of the obtained signals was performed using self-developed software and the FlexPro 9.0 package. Figure 4 presents fragments of exemplary courses of accelerations $\tilde{a}_{\alpha,m}^{(i,j)}$, recorded in a single measurement series at one of the levels. Rectangular border (dashed line) indicates a window limiting time interval t_α, being the subject of further analyses.

In the former (design, operational) practice, both among manufacturers of electrostatic precipitators and their business partners, the primary criterion for the

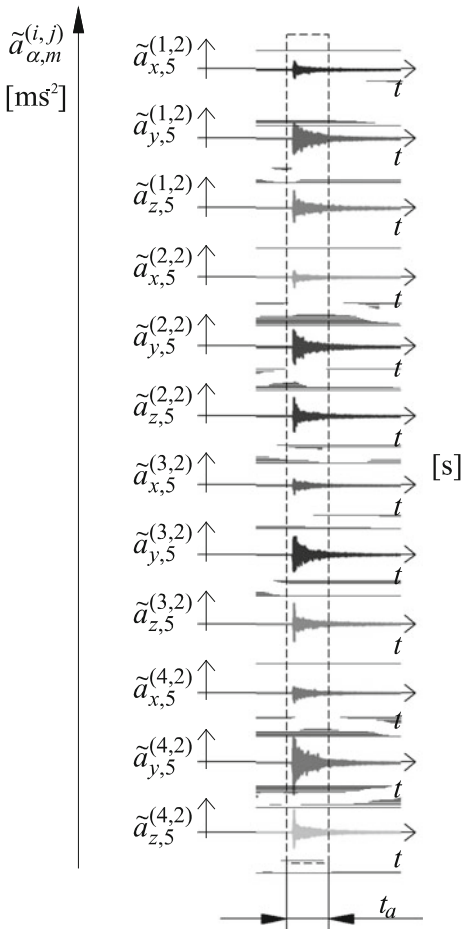

Fig. 4 Exemplary courses of accelerations $\tilde{a}_x, \tilde{a}_y, \tilde{a}_z$ recorded by $n_i = 4$ sensors for $m = 5$ measurement series in $j = 2$ configuration

efficiency evaluation of cleaning collecting electrodes was a comparison of a normal component of acceleration to the surface of the electrode at the measurement point. It was assumed that the rapping system operates correctly, if at each checkpoint of the section, the peak value of this component (i.e., the maximum value for a module) exceeds 100 g (g—gravitational acceleration). This approach was often forced by a class of available measuring equipment. Currently, thanks to the development of measuring techniques, more and more often the values of the remaining components of acceleration and the values of the resultant acceleration are considered, but also the search for totally new measures to evaluate the vibrations is going on. Therefore, the preprocessed signals were used to determine the peak values $\tilde{a}_{\alpha,m}^{(i,j)}$ of the component and resultant accelerations of the checkpoints.

3 Simulations—Numerical Calculations

Previous studies of the authors present models and algorithms allowing for the analysis of vibrations of collecting electrodes using different methods. Papers [9, 10] present a model obtained by the finite element method, paper [9] describes a model using the plate strip method, while in paper [10] a model obtained using a so-called hybrid method is presented. In all these studies, the rigid finite element method was used to discretize the beams. Further, a validation of these models, comparing the results of calculations with the results of the measurements and using the Abaqus commercial package was performed.

The rigid finite element method was also used for modeling the vibrations of the plates of electrostatic precipitators [11]. A detailed description of this method is presented in [12]. The results of model validation and software based on this method were satisfactory as in the case of using the aforementioned methods of

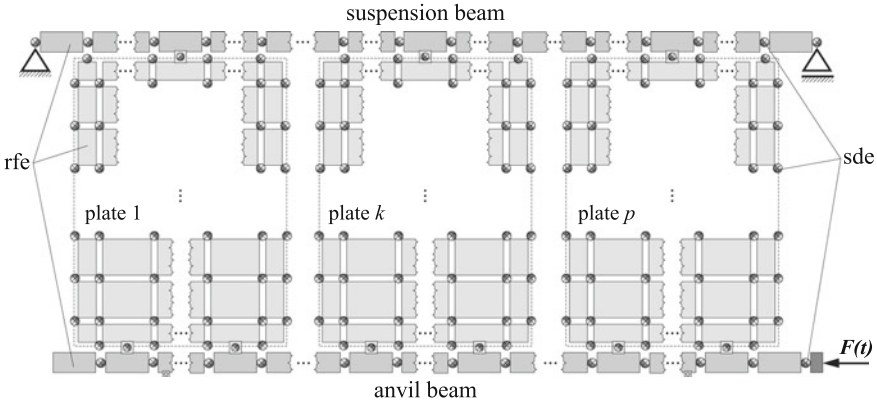

Fig. 5 Diagram of a system discretized using the RFEM method: *rfe* rigid finite element, *sde* spring-damping element

discretization of plates. Figure 5 shows a diagram of a system discretized using the RFEM method.

The equation of motion of the discretized system can be expressed as a system of ordinary second-order differential linear equations in the form

$$\mathbf{M}\,\ddot{\mathbf{q}} + \mathbf{K}\mathbf{q} = \mathbf{f} \tag{1}$$

where

M—diagonal mass matrix,
K—stiffness matrix of constant coefficients,
$\mathbf{f} = \mathbf{f}(F(t))$—input vector,

$$\mathbf{q} = \left[\mathbf{q}_1^{\mathrm{T}}, \ldots, \mathbf{q}_i^{\mathrm{T}}, \ldots, \mathbf{q}_n^{\mathrm{T}}\right]^{\mathrm{T}}; \mathbf{q}_i = \left[x_i, y_i, z_i, \varphi_i, \theta_i, \psi_i\right]^{\mathrm{T}}$$

x_i, y_i, z_i—coordinates of the center of rfe mass,
φ_i, θ_i, ψ_i—small angles of rfe rotations.

M and **K** matrices are matrices with constant coefficients. The advantage of the rfe method is a diagonal matrix **M**. The integration of Eq. (1) was performed using the Newmark method with a constant integration step.

During calculations the peak value of force $F_{\max}^{(k)}$ was changed in the range from $F^{\min} = 45\,\mathrm{kN}$ to $F^{\max} = 110\,\mathrm{kN}$, with an increment $\Delta F = 2.5\,\mathrm{kN}$. Therefore, it was assumed that

$$F_{\max}^{(k)} = F^{\min} + k\frac{F^{\max} - F^{\min}}{n_k}, \text{ for } k = 0, 1, \ldots, 26 = n_k. \tag{2}$$

4 Identification of Force Impulse

Determination of the maximum value of the impulse $F_{\max}^{(k)}$ was based on the results of measurements of accelerations of the components of checkpoints of the collecting electrode system and on the conducted numerical calculations. As a result the values of acceleration components were obtained, which served to determine resultant accelerations $a_{t,k}^{(i,j)}$ and $\tilde{a}_{t,m}^{(i,j)}$. In the study, the determination of force impulse was based on total accelerations $(a_{t,k}^{(i,j)}, \tilde{a}_{t,m}^{(i,j)})$, so on values, which indirectly represent the remaining components of acceleration. Peak values of accelerations obtained based on calculations and based on measurements, denoted as $W_{\max k}^{(i,j)}$ and $\tilde{W}_{\max m}^{(i,j)}$, respectively, were calculated

$$W_{\max k}^{(i,j)} = \max_{0 \le t \le t_a} \left| a_{t,k}^{(i,j)} \right|, \tag{3a}$$

$$\tilde{W}_{\max m}^{(i,j)} = \max_{0 \le t \le t_a} \left| \tilde{a}_{t,m}^{(i,j)} \right|. \tag{3b}$$

where t_a—time of analysis (assuming that $t_a = 0.02$ s).

For each point (i, j), in successive approximations of force $F_{\max}$, thus for different k and for each series m, a relative percentage error $\delta_{k,m}^{(i,j)}$ was calculated

$$\delta_{k,m}^{(i,j)} = \frac{\left| \tilde{W}_{\max m}^{(i,j)} - W_{\max k}^{(i,j)} \right|}{\tilde{W}_{\max m}^{(i,j)}} \cdot 100\,\%. \tag{4}$$

$\delta_{k,m}^{(i,j)}$ values represent differences (in percents) between the values of total accelerations at (i, j) points for different k (value of force $F_{\max}$ assumed for the calculations) and the number of measurement series m. These are basic values which served to select the $F_{\max}$ force.

In order to determine the mean value of error at j level, the following values were calculated:

$$\bar{\delta}_{k,m}^{(j)} = \frac{\sum_{i=1}^{n_i} \delta_{k,m}^{(i,j)}}{n_i}. \tag{5}$$

It allowed for the determination of measurement series $m_k^{(j)}$ for which at the specific level j, the value of mean error $\bar{\delta}_{k,m}^{(j)}$ reached a minimum value for a specific level j and value of impulse force $F_{\max}^{(k)}$ designated as k

$$\bar{\delta}_{\min k}^{(j)} = \min_{1 \le m \le n_m^{(j)}} \bar{\delta}_{k,m}^{(j)}. \tag{6}$$

Table 1 presents the determined numbers of measurement series $m_k^{(j)}$ for $k = 6$, which corresponds to force $F_{\max} = F_{\max}^{(6)} = 60$ kN.

To clearly define the value of force $F_{\max}$, the values expressing a total error (after all levels), corresponding to $F_{\max}^{(k)}$ forces, were determined

Table 1 Selection of measurement series $m_k^{(j)}$ for $k = 6\ F_{\max}^{(k)} = 60$ kN

$F_{max}^{(k)} = 60$ kN					
Level j	1	2	3	4	5
Series m	10	8	6	4	6

Table 2 Resultant relative error $\delta^{(i,j)}_{6,m_6^{(j)}}$ for all checkpoints (i, j)

		i			
	j	1	2	3	4
$W^{(i,j)}_{\max t,6}\ (\mathrm{ms}^{-2})$	1	2165	1997	2476	2961
$\tilde{W}^{(i,j)}_{\max t,10}\ (\mathrm{ms}^{-2})$		1832	2037	2495	3525
$\delta^{(i,j)}_{6,10}\ (\%)$		18.1	1.9	0.7	16.0
$W^{(i,j)}_{\max t,6}\ (\mathrm{ms}^{-2})$	2	2179	2168	2153	3044
$\tilde{W}^{(i,j)}_{\max t,8}\ (\mathrm{ms}^{-2})$		1844	1976	2121	2856
$\delta^{(i,j)}_{6,8}\ (\%)$		18.1	9.7	1.5	6.6
$W^{(i,j)}_{\max t,6}\ (\mathrm{ms}^{-2})$	3	1924	1715	2053	2807
$\tilde{W}^{(i,j)}_{\max t,6}\ (\mathrm{ms}^{-2})$		2225	1695	2265	2798
$\delta^{(i,j)}_{6,6}\ (\%)$		13.5	1.2	9.4	0.3
$W^{(i,j)}_{\max t,6}\ (\mathrm{ms}^{-2})$	4	1223	1218	1496	1892
$\tilde{W}^{(i,j)}_{\max t,4}\ (\mathrm{ms}^{-2})$		1204	1311	1563	2046
$\delta^{(i,j)}_{6,4}\ (\%)$		1.6	7.1	4.3	7.5
$W^{(i,j)}_{\max t,6}\ (\mathrm{ms}^{-2})$	5	1403	1483	1466	1915
$\tilde{W}^{(i,j)}_{\max t,6}\ (\mathrm{ms}^{-2})$		1347	1790	1503	1918
$\delta^{(i,j)}_{6,6}\ (\%)$		4.1	17.2	2.4	0.2

$$\underset{\min k}{\delta} = \frac{\sum_{j=1}^{n_j} \bar{\delta}^{(j)}_{\min k}}{n_j}. \tag{7}$$

In the last step of the procedure $\underset{\min}{k}$ was determined as the value of k, for which $\underset{\min k}{\delta}$ is the lowest. In the case discussed in the present study $\underset{\min}{k} = 6.$ was obtained. Table 2 shows the values $\delta^{(i,j)}_{6,m_6^{(j)}}$. This error ranged from 0.2 to 18.2 % (Table 2).

5 Conclusions

Correct determination of force impulse is necessary to conduct further research using computer simulations. The method for determination of the correct course of impact force presented in this study produces good results and can be used in practice. As a result of the analysis of the measurements and numerical calculations for a beater of a mass of $m = 8\,\text{kg}$, a peak value of force impulse $F_{\max}^{(k)} = 60\,\text{kN}$ was obtained. The relative percentage error $\delta_{k,m}^{(i,j)}$ between the results of measurements and numerical calculations did not exceed a predetermined level of 20 % in any of the checkpoints (i, j) for the total acceleration $a_t^{(i,j)}$. The presented procedure can be easily generalized in a way, which will allow for the selection of any acceleration component or tangential acceleration instead of the total acceleration, as the compatibility criterion (which means the assumption that α equals x, y, z or τ).

References

1. Zhao X, Luo S (2008) A Discussion on the ESP-FF Hybrid Precipitator. 11th International Conference on Electrostatic Precipitation (ICESP XI), Hagzhou, China, 2008, Zhejiang University Press, Springer: 472–474.
2. Long Z, Yao Q, Song Q, Li S (2009) A second-order accurate finite volume method for the computation of electrical conditions inside a wire-plate electrostatic precipitator on unstructured meshes. Journal of Electrostatics 67(4): 597–604.
3. Neimarlija N, Demirdžić I, Muzaferij S (2009) Finite volume method for calculation of electrostatic fields in electrostatic precipitators. Journal of Electrostatics 67(1): 37–47.
4. Talaie MR (2005) Mathematical modeling of wire-duct single-stage electrostatic precipitators. Journal of Hazardous Materials 124(1–3): 44–52.
5. Yang XF, Kang YM, Zhong K (2009) Effects of geometric parameters and electric indexes on the performance of laboratory-scale electrostatic precipitators. Journal of Hazardous Materials 169(1–3): 941–947.
6. Adamiec–Wójcik I, Nowak A, Wojciech S (2009) Dynamic analysis of electrostatic precipitators using finite strip method. In: DSTA 2009 Conference Proceedings, Łódź, Poland, Vol. 2:889–896.
7. Nowak A, Adamiec–Wójcik I (2009) Vibration analysis of collecting electrodes of precipitators by means of the hybrid finite element method. In Conference Proceedings of Multibody Dynamics, ECCOMAS 2009 Thematic Conference, Warsaw, Poland: 214–217.
8. Nowak A, Wojciech S (2004) Optimisation and experimental verification of a dust-removal beater for the electrodes of electrostatic precipitators. Computers and Structures Vol. 82(22): 1785–1792.
9. Adamiec-Wójcik I, Nowak A, Wojciech S (2011) Comparison of methods for vibration analysis of electrostatic precipitators. Acta Mech. Sinica 1(27): 72–79.
10. Adamiec-Wójcik I, Awrejcewicz J, Nowak A, Wojciech S (2014) Vibration Analysis of Collecting Electrodes by means of the Hybrid Finite Element Method. Mathematical Problems in Engineering, doi:10.1155/2014/832918.
11. Adamiec-Wójcik I (2011) Modelling of Systems of Collecting Electrodes of Electrostatic Precipitators by means of the Rigid Finite Element Method. Archive of Mechanical Engineering 58(1): 27–47, doi:10.2478/v10180-011-0002-x.

12. Nowak A, Nowak P, Awrejcewicz J (2015) Influence of position of an anvil beam on vibrations of collecting electrodes. In: DSTA 2015 Conference Proceedings, Łódź, Poland (in print).

Using Saturation Phenomenon to Improve Energy Harvesting in a Portal Frame Platform with Passive Control by a Pendulum

Rodrigo Tumolin Rocha, Jose Manoel Balthazar, Angelo Marcelo Tusset, Vinicius Piccirillo and Jorge Luis Palacios Felix

Abstract A new model of energy harvester based on a simple portal frame structure subjected to saturation phenomenon is presented. Energy is collected via a piezoelectric device whose nonlinearities are considered in the mathematical model. The system is a bistable Duffing oscillator presenting chaotic behaviour. Optimization of power harvesting and stabilization of chaotic motions to a given periodic orbit is obtained analysing the average power output and bifurcation diagrams. Control sensitivity to parametric errors in the damping and stiffness parameters of the portal frame is studied. The proposed passive control technique uses a simple pendulum tuned to the vibrations of the structure to improve energy harvesting. The results show that with the implementation of this control strategy it is possible to eliminate the need for active of semi-active control, usually more complex. The control also provides a way to regulate the energy captured to a desired operating frequency.

R.T. Rocha (✉)
Faculty of Mechanical Engineering, UNESP—Sao Paulo State University,
CP 473, Bauru, SP 17033-360, Brazil
e-mail: digao.rocha@feb.unesp.br

J.M. Balthazar
ITA—Aeronautics Technological Institute, Sao Jose Dos Campos, SP 12228-900, Brazil
e-mail: jmbaltha@ita.br

J.M. Balthazar
UNESP—Sao Paulo State University, CP 473, Bauru, SP 17033-360, Brazil

A.M. Tusset · V. Piccirillo
UTFPR—Federal Technological University of Parana, Ponta Grossa, PR 83016-210, Brazil
e-mail: tusset@utfpr.edu.br

V. Piccirillo
e-mail: piccirillo@utfpr.edu.br

J.L.P. Felix
UFFS—Federal University of Fronteira Sul, Cerro Largo, RS 97900-000, Brazil
e-mail: jorge.felix@uffs.edu.br

© Springer International Publishing Switzerland 2016

J. Awrejcewicz (ed.), *Dynamical Systems: Theoretical and Experimental Analysis*, Springer Proceedings in Mathematics & Statistics 182, DOI 10.1007/978-3-319-42408-8_25

1 Introduction

In recent past years, the search about vibration energy harvesting has been increased substantially. Many of those vibration sources are found in structures that are excited by wind, sea waves, vehicles traffics, i.e. external excitations. One of most promising and studied devices as a means of low power energy harvesting is the piezoelectric material.

The research about these materials begun with some experiments, showing itself a nonlinear material [1]. Recently, a big gamma of works introducing the piezoelectric material as a means of energy transduction has been widely studied, as we see in [2–6]. Specially, the nonlinearities of the piezoelectric material, which was experimentally found, was analytically proposed as an approximation by [7]. The nonlinearities of vibratory energy harvesting were widely exploited by [8].

The vibratory energy harvesting generally contains the piezoelectric material coupled to a structure. Some kind of structures may present particular configurations that may improve the energy harvesting, even provide periodic behaviour. One of the particular exploited configurations is the internal resonance, such as 2:1, between two modes of vibration, so that the system transfers part of the vibration energy available at a certain coordinate to the another one. This is the saturation phenomenon described by many authors, for example, among others [9–11]. The implementation of saturation as control method was proposed and studied by [12–14], among others.

Works involving electromechanical systems have been recently studied by many authors. A model of an energy harvester based on a simple portal frame of a single-degree-of-freedom structure was presented in [15]. The system was considered as a non-ideal system (NIS) due to a full interaction of the structure motion, with the energy source, a DC motor with limited power supply. The nonlinear piezoelectric material was considered in the coupling mathematical model. The system was found to be a bistable Duffing oscillator presenting chaotic behaviour. The structure was controlled using a pendulum as a passive control and improved the energy harvesting of the system.

The passive control using a pendulum was implemented by [16], showing to be a very useful controlled and energy harvesting tune.

In this work, we will explore the passive control using a pendulum coupled in a simple portal frame of two-degrees-of-freedom structure, as studied by [17, 18]. We will show the control and improvement of energy harvesting of the system setting a control parameter of the pendulum.

2 Energy Harvesting Modelling

The energy harvesting model studied in this paper, illustrated in Fig. 1, consists in a portal frame of two-degrees-of-freedom with a piezoelectric material coupled to a column and a linear pendulum coupled to the midspan of the beam, i.e. the pendulum will move according to the symmetric mode movement.

The portal frame consists of two columns clamped in their bases with height h and a horizontal beam pinned to the columns at both ends with length L. Both column and beam have flexural stiffness as a lumped mass system with two-degrees-of-freedom. The coordinate q_1 is related to the horizontal displacement in the sway mode, with natural frequency ω_1, and q_2 to the midspan vertical displacement of the beam in the symmetric mode, with natural frequency ω_2. The linear stiffness of the columns and beam can be evaluated by a Rayleigh-Ritz procedure using cubic trial functions. Geometric nonlinearity is introduced by considering the shortening due to bending of the columns and of the beam.

The linear pendulum is coupled to the mass of the midspan of the beam, consisting of a mass m_3, rotational stiffness k_3 and rotational damping as c_3.

The nonlinear piezoelectric material is coupled to the column as an electric circuit, which is excited by an internal voltage (back-emf) proportional to the mechanical velocity, in order to harvest energy from the vibration of the column. This circuit consists of a resistor R, a produced charge Q and a capacitance C_p of the capacitor. The dimensionless relation of the nonlinearity of the piezoceramic is given by $d(q_1) = \theta(1 + \Theta|q_1|)$ defined by [7], where θ is the linear piezoelectric coefficient and Θ is the nonlinear piezoelectric coefficient.

The mechanical system is based-excited by a harmonic force which has amplitude F_0 and external frequency ω_n. This external force frequency is set near resonance with the symmetric mode. Frequency ω_2 is also set twice the frequency of the sway mode as $2\omega_1 = \omega_2$. These conditions of resonance are necessary to have modal coupling in the nonlinear adopted model. In these conditions, we have the saturation phenomenon.

2.1 Modelling of the Dynamical System

The modelling of the physical model was developed by Lagrange's energy method which uses the Lagrangian function and Euler-Lagrange equation.

Nodal displacements, shown in Fig. 1, are

$$\begin{array}{llll} u_1 = q_1 & u_2 = u_1 + \dfrac{B}{4}v_1^2 & u_3 = u_1 - \dfrac{B}{4}v_1^2 & X_1 = -u_1 + l\sin\phi \\ v_1 = q_2 & v_2 = -\dfrac{A}{2}u_1^2 & v_3 = \dfrac{A}{2}u_1^2 & Y_1 = v_1 + l\cos\phi \end{array} \tag{1}$$

where $A = 6/5h$ and $B = 24/5L$. The stiffness of the beam and column calculated by Rayleigh-Ritz method are, respectively, $k_b = 48EI/L^3$ and $k_c = 3EI/h^3$.

The generalized coordinates considered here are the displacements of the mass at the midspan of the beam M. Using nodal displacements of Eq. (1), the kinetic energy is defined in Eq. (2).

$$T = \frac{1}{2}M\left(\dot{u}_1^2 + \dot{v}_1^2\right) + \frac{1}{2}m\left(2\dot{u}_1^2\right) + \frac{1}{2}m_3\left(\dot{X}_1^2 + \dot{Y}_1^2\right) \tag{2}$$

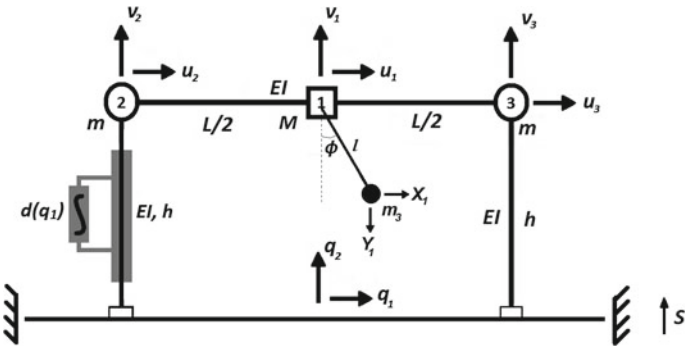

Fig. 1 Physical model of a simple portal frame of two-degrees-of-freedom structure

Introducing the generalized coordinates q_1 and q_2, the kinetic energy becomes to Eq. (3).

$$T = \frac{1}{2}M\left(\dot{q}_1^2 + \dot{q}_2^2\right) + \frac{1}{2}m\left(2\dot{q}_1^2\right) + \frac{1}{2}m_3\left(\dot{q}_1^2 + \dot{q}_2^2 + l^2\dot{\phi}^2 + 2l\dot{\phi}\left(\dot{q}_1\cos\phi + \dot{q}_2\sin\phi\right)\right) \quad (3)$$

The potential energy of the system is given by the strain energy of the structure, the stiffness of the pendulum, the work of the weight of the masses of the beam, columns and pendulum and by the electrical potential part of the piezoelectric circuit with the contribution of the piezoelectric and the capacitor, resulting in Eq. (4).

$$U = \frac{1}{2}k_c\left(u_2^2 + u_3^2\right) + \frac{1}{2}k_b\left(v_1 - \frac{v_2 + v_3}{2}\right)^2 + mg\left(v_2 + v_3\right) + Mgv_1 + \cdots$$
$$m_3gY_1 + \frac{1}{2}k_3\phi^2 - \frac{d(q_1)}{C_p}Q(u_2 + v_2) + \frac{1}{2}\frac{Q^2}{C_p} \quad (4)$$

Substituting Eq. (1) in (4), in terms of the general coordinates q_1, q_2, ϕ and Q, we have the potential energy in Eq. (5).

$$U = \left(k_c - mgA\right)q_1^2 + \frac{1}{2}k_b\left(q_2^2 + Aq_2q_1^2\right) + Mgq_2 + m_3g\left(l\cos\phi - q_2\right) + \cdots$$
$$\frac{1}{2}k_3\phi^2 - \frac{d(q_1)}{C_p}Q\left(q_1 + \frac{B}{4}q_2^2\right) + \frac{1}{2}\frac{Q^2}{C_p} \quad (5)$$

Now, we consider energy dissipation of the system, comprising the structural and pendulum damping defined by Rayleigh function and the resistor of the electrical circuit. Then it follows in Eq. (6).

$$D = \frac{1}{2}c_1\dot{q}_1^2 + \frac{1}{2}c_2\dot{q}_2^2 + \frac{1}{2}c_3\dot{\phi}^2 + \frac{1}{2}R\dot{Q}^2 \quad (6)$$

The harmonic excitation force is given by Eq. (7).

$$S = F_0 \cos(\omega_n t) \tag{7}$$

The Lagrangian function is defined by Eq. (8). Substituting Eqs. (3) and (5) in Eq. (8) we have the Lagrangian of Eq. (9).

$$L(q, \dot{q}, t) = T - U \tag{8}$$

$$L = \begin{array}{c} \frac{1}{2}M\left(\dot{q}_1^2 + \dot{q}_2^2\right) + \frac{1}{2}m\left(2\dot{q}_1^2\right) - \cdots \\ \left[\begin{array}{c} -\frac{1}{2}m_3\left(\dot{q}_1^2 + \dot{q}_2^2 + l^2\dot{\phi}^2 + 2l\dot{\phi}\left(\dot{q}_1\cos\phi + \dot{q}_2\sin\phi\right)\right) + \cdots \\ Mgq_2 + m_3 g\left(l\cos\phi - q_2\right) + \frac{1}{2}k_3\phi^2 - \cdots \\ \frac{d(q_1)}{C_p}Q\left(q_1 + \frac{B}{4}q_2^2\right) + \frac{1}{2}\frac{Q^2}{C_p} \end{array}\right] \end{array} \tag{9}$$

Now, using Euler-Lagrange, Eq. (10), we have the equation of motion of the system that are Eqs. (11), (12), (13) and (14).

$$\frac{d}{dt}\left(\frac{\partial L}{\partial \dot{q}_i}\right) - \frac{\partial L}{\partial q_i} + \frac{\partial D}{\partial \dot{q}_i} = Q_{ext} \qquad i = 1, 4 \tag{10}$$

$$(2m + M + m_3)\ddot{q}_1 + 2(k_c - mgA)q_1 + k_b A q_2 q_1 + c_1\dot{q}_1 = \cdots$$
$$m_3 l\left(\ddot{\phi}\cos\phi - \dot{\phi}^2\sin\phi\right) + \frac{d\left(q_1\right)}{C_p}Q \tag{11}$$

$$(M + m_3)\ddot{q}_2 + k_b q_2 + c_2\dot{q}_2 + (M + m_3)g + \frac{Ak_b}{2}q_1^2 = F_0\cos\omega_n t + \cdots$$
$$m_3 l\left(\ddot{\phi}\cos\phi + \dot{\phi}^2\cos\phi\right) + \frac{d(q_1)}{C_p}\frac{B}{2}Qq_2 \tag{12}$$

$$m_3 l^2\ddot{\phi} + c_3\dot{\phi} + k_3\phi + m_3 l\left[\ddot{q}_1\cos\phi + (\ddot{q}_2 - g)\sin\phi\right] = 0 \tag{13}$$

$$R\dot{Q} - \frac{d(q_1)}{C_p}\left(q_1 + \frac{B}{4}q_2^2\right) + \frac{Q}{C_p} = 0 \tag{14}$$

For a better analysis, a dimensionless process is carried out, resulting the dimensionless equations of motion of the system as follows:

$$x_1'' + \mu_1 x_1' + x_1 + \alpha_1 x_1 x_2 = \gamma_1\left(\phi''\cos\phi - \phi'^2\sin\phi\right) + \theta(1 + \Theta|x_1|)\delta_1 V \tag{15}$$

$$x_2'' + \mu_2 x_2' + \omega_2^2 x_2 + \alpha_2 x_1^2 + G_0 = E_0\cos\Omega\tau + \theta(1 + \Theta|x_1|)\delta_2 V x_2 + \cdots$$
$$\gamma_2\left(\phi''\sin\phi + \phi'^2\cos\phi\right) \tag{16}$$

$$\phi'' + \mu_3\phi' + \omega_3^2\phi + \gamma_3 x'' \cos\phi + (\gamma_4 x_2'' - G_3)\sin\phi = 0 \tag{17}$$

$$V' - \theta(1 + \Theta|x_1|)(\delta_3 x_1 + \delta_4 x_2^2) + \delta_3 V = 0 \tag{18}$$

where dimensionless parameters are

$$\begin{gathered}
x_1 = \frac{q_1}{h} \quad x_2 = \frac{q_2}{h} \quad V = \frac{Q}{q_0} \quad \tau = \omega_1 t \quad \omega_1 = \sqrt{\frac{2(k_c - mgA)}{M_T}} \\
\bar{d}(x_1) = \frac{h}{q_0} d(q_1) \quad \mu_1 = \frac{c_1}{M_T\omega_1} \quad \mu_2 = \frac{c_2}{(M+m_3)\omega_1} \quad G_2 = \frac{g}{\omega_1^2 L} \\
E_0 = \frac{F_0}{(M+m_3)\omega_1^2 L} \quad G_3 = \frac{g}{\omega_1^2 l} \quad e = \frac{1}{m_3} \quad \omega_2 = \frac{1}{\omega_1}\sqrt{\frac{k_b}{(M+m_3)}} \\
\alpha_1 = \frac{Ak_bL}{M_T\omega_1^2} \quad \alpha_2 = \frac{Ak_bh^2}{2(M+m_3)\omega_1^2 L} \quad \Omega = \frac{\omega_n}{\omega_1} \quad \gamma_3 = \frac{h}{L} \quad \gamma_4 = \frac{l}{L} \\
\delta_1 = \frac{q_0^2}{\omega_1^2 h^2 M_T C_p} \quad \delta_2 = \frac{Bq_0^2}{2(M+m_3)\omega_1^2 h C_p} \quad \delta_3 = \frac{1}{RC_p\omega_1} \quad \gamma_1 = \frac{m_3 l}{M_T h} \\
\delta_4 = \frac{BL^2}{4RC_p\omega_1 h} \quad \omega_3 = \frac{1}{\omega_1}\sqrt{\frac{k_3}{m_3}} \quad M_T = (2m + M + m_3) \\
\gamma_2 = \frac{m_3 l}{(M+m_3)L} \quad \mu_3 = \frac{c_3}{m_3 l^2 \omega_1}
\end{gathered} \tag{19}$$

To calculate the harvested power of the system, Eqs. (20) and (21) are given as dimensional and dimensionless harvested power, respectively.

$$P = R\dot{Q}^2 \tag{20}$$

$$P = R_0 V'^2 \tag{21}$$

where $R_0 = R(\omega_1 q_0)^2$.

The average power of the system can be calculated by Eq. (22), as in [7, 15, 17, 18].

$$P_{avg} = \frac{1}{T}\int_0^T P(\tau)d\tau \tag{22}$$

Next, Sect. 3 will discuss numerical simulations with and without the pendulum, considering the nonlinear piezoelectric contribution fixed in $\Theta = 1$.

3 Numerical Simulations Results and Discussions

The numerical simulations realized in this work were performed by MATLAB software. The parameters considered to the numerical simulations are in Table 1. The parameters were adjusted to have saturation phenomenon at the portal frame system, that is, $\omega_2 = 2\omega_1$, and the external force frequency is in resonance with the symmetric mode ($\Omega = \omega_2 + \sigma$), where σ is a detuning factor.

A new control parameter will be considered in order to configure the system with the optimal energy harvesting and behaviour of the system. This new parameter will be defined in Eq. (23).

$$e = \frac{1}{m_3} \tag{23}$$

The parameter "e" will be varied with an acceptable ratio that the pendulum mass (m_3) should not overpass the value of the mass of the midspan of the beam (M). This interval is $0.5 \leq e \leq 100$.

Next, we will present results of numerical simulations considering and not considering the passive control, and in the end, compare the results with each other showing the contribution of the pendulum as a passive controller.

Table 1 Dimensional system parameters

Parameters	Values	Means
g (m/s^2)	9.81	Gravity acceleration
M (kg)	2.00	Beam mass
m (kg)	0.50	Column mass
m_3 (kg)	Vary	Pendulum mass
c_1 (Ns/m)	0.001	Column damping
c_2 (Ns/m)	0.002	Beam damping
c_3 (Ns/rad)	0.061	Pendulum damping
EI (Nm^2)	128	Linear stiffness
k_3 (Nm/rad)	0.403	Torsional pendulum stiffness
L (m)	0.52	Beam length
h (m)	0.36	Column length
l (m)	0.16	Pendulum length
F_0 (N)	40	External excitation amplitude
R (kΩ)	100	Piezoelectric resistance
C_p (μF)	1	Piezoelectric capacitance
ω_n (rad/s)	146.9	External excitation frequency
θ	0.1	Linear piezoelectric coefficient
Θ	1	Nonlinear piezoelectric coefficient

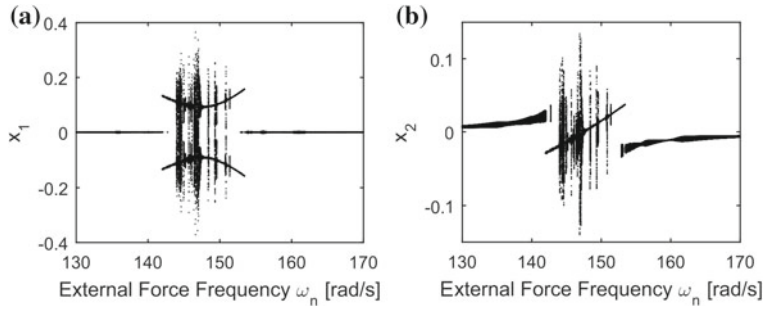

Fig. 2 Bifurcation diagrams of **a** horizontal movement, **b** vertical movement

3.1 Dynamical Analysis of the Portal Frame Structure

In this first subsection, we will show some analysis of behaviour and energy harvesting of the system without the pendulum coupling to show the saturation phenomenon and its advantage to harvest energy. Using the parameters of Table 1, next figures provide some numerical results.

Figure 2a and b show the bifurcation diagrams of the horizontal and vertical movement, respectively, related to the external force frequency. We can see some values of the frequency that the system tends to be chaotic. The interval of the frequency, showed in the bifurcation diagrams, shows the relation of resonance between the vertical movement and the external excitation.

The external force frequency $\omega_n = 146.9$ rad/s (the same as Table 1) will be analyzed in order to compare, because it is in the chaotic area of the bifurcation. Therefore, in next simulations we will consider the external frequency as $\omega_n = 146.9$ rad/s.

Figure 3a and b show the Poincare maps of the horizontal and vertical movement, respectively, in order to analyze the behaviour of the system. We see that the system is chaotic.

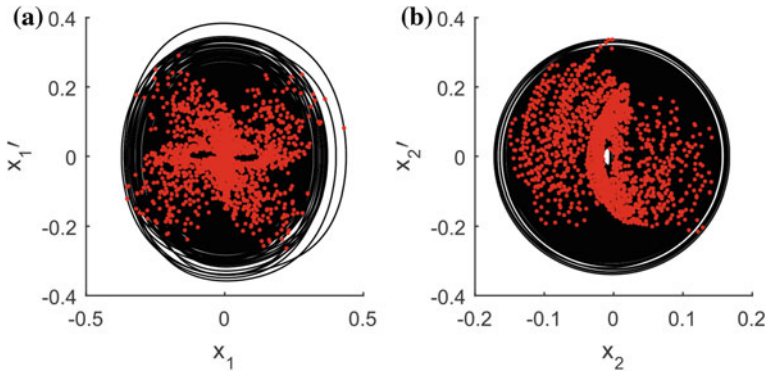

Fig. 3 Phase plane (in *black*) and Poincare maps (*red dots*) of; **a** horizontal movement, **b** vertical movement

Finally, we calculated the average harvested power of the chaotic system, and it is 9.169, approximately.

In the next section, we will show the influence of the pendulum coupled to the mass "M" of the midspan of the beam to the behaviour and energy harvesting of the system.

3.2 *Analysis of the Pendulum Coupled to the Dynamical System*

In this section, we will perform some analysis of behaviour and energy harvesting of the system with the pendulum coupled with the portal frame. To the analysis of the control of the chaotic behaviour, we will set a control parameter by "e". This control parameter is the inverse of the pendulum mass ($e = 1/m_3$), so we can see the influence of the pendulum mass to the behaviour of the system.

To follow the same line as in Sect. 3.1, we will consider the external force frequency as in Table 1 to the next simulations.

First, we built a bifurcation diagram related to the control parameter and we can carry some results. Figure 4a–c show the bifurcation diagram of the horizontal, vertical and pendulum movements. Figure 5 shows the average harvested power related to the control parameter. We see some intervals of "e" that controlled the chaotic behaviour, forcing it to a periodic orbit. This interval is approximately $25 \leq e \leq 68$ (region 1). The average power at region 1 is approximately 4.80. In region 2, $e < 25$, we see a great improvement of the energy harvestings; a peak of 69.02 amount of power. However, the behaviour is most of the time quasiperiodic and sometimes the system presents periodic behaviour. In region 3, $e > 68$, we see the average harvested power increasing slowly from 4.80 to 8.63, approximately, but the behaviour tends to be quasiperiodic all the time. Analyzing the full interval of e, there is no chaotic behaviour anymore.

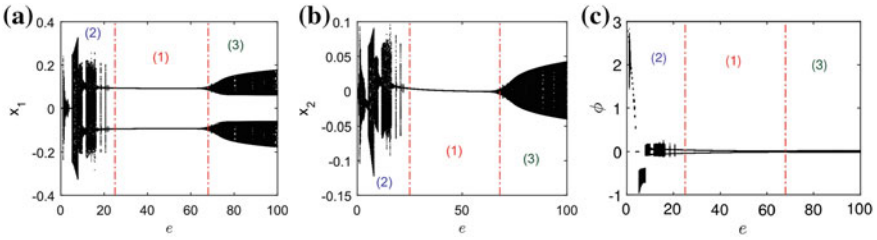

Fig. 4 Bifurcation diagram related to the control parameter "e" of **a** horizontal movement, **b** vertical movement and **c** pendulum movement

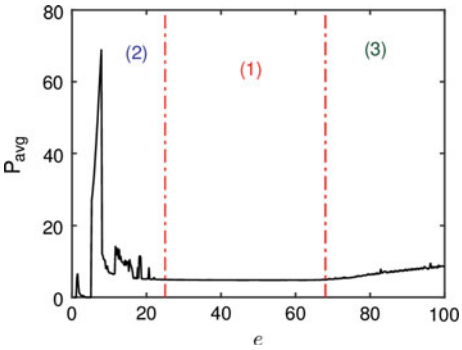

Fig. 5 Parametrical analysis of the control parameter "*e*" related to the average harvested power

4 Conclusions

This work presented the energy harvesting of a simple portal frame of two-degrees-of-freedom structure using a pendulum as a passive control.

The pendulum showed to be very useful as a controller, it eliminated the presence of chaotic behaviour, forcing the system to a periodic orbit and quasiperiodic behaviour. However, it will depend on the value of the parameter control "*e*".

The energy harvesting could be improved. We see in Fig. 5 that some regions of the parametrical analysis have more or less harvested power. In region 1, the system presented periodic behaviour all the time, while in region 2 and 3 most of the time it presented quasiperiodic behaviour. However, the average power goes from 4.80 to 69.02, approximately. It will depend on the value of "*e*".

The advantage of using a passive control is that, it is not necessary that for any electronic component to control the system, as an active control. Therefore, we can tune the energy harvesting to choose a desired parameter control.

Based on the results obtained in this work, we should compare the efficiency between the NES [19], which is a small mass-spring-damping system coupled to a degree-of-freedom of the main structure, and the present pendulum approach.

References

1. Crawley, E. F., & Anderson, E. H. (1990). Detailed models of piezoceramic actuation of beams. Journal of Intelligent Material Systems and Structures, 1(1), 4–25.
2. Erturk, A., & Inman, D.J. (2011). Piezoelectric energy harvesting. John Wiley & Sons.
3. Erturk, A., Hoffmann, J., & Inman, D.J. (2009). A piezomagnetoelastic structure for broadband vibration energy harvesting. Applied Physics Letters, 94(25), 254102.
4. Litak, G., Friswell, M.I., Kwuimy, C.A.K., Adhikari, S., & Borowiec, M. (2012). Energy harvesting by two magnetopiezoelastic oscillators with mistuning. Theoretical and Applied Mechanics Letters, 2(4), 043009.
5. Stephen, N.G. (2006). On energy harvesting from ambient vibration. Journal of sound and vibration, 293(1), 409–425.

6. Priya, S., & Inman, D.J. (Eds.). (2009). Energy harvesting technologies (Vol. 21). New York: Springer.
7. Triplett, A., & Quinn, D.D. (2009). The effect of non-linear piezoelectric coupling on vibration-based energy harvesting. Journal of Intelligent Material Systems and Structures, 20(16), 1959–1967.
8. Daqaq, M.F., Masana, R., Erturk, A., & Quinn, D.D. (2014). On the role of nonlinearities in vibratory energy harvesting: a critical review and discussion. Applied Mechanics Reviews, 66(4), 040801.
9. Mook, D.T., Plaut, R. H., & HaQuang, N. (1985). The influence of an internal resonance on non-linear structural vibrations under subharmonic resonance conditions. Journal of Sound and Vibration, 102(4), 473–492.
10. Nayfeh, A.H., & Mook, D.T. (2008). Nonlinear oscillations. John Wiley & Sons.
11. Nayfeh, A.H. (2000). Nonlinear interactions. Wiley.
12. Pai, P.F., Wen, B., Naser, A.S., & Schulz, M.J. (1998). Structural vibration control using PZT patches and non-linear phenomena. Journal of Sound and Vibration, 215(2), 273–296.
13. Tusset, A.M., Piccirillo, V., Bueno, A.M., Balthazar, J.M., Sado, D., Felix, J.L.P., & da Fonseca, R.M.L.R. (2015). Chaos control and sensitivity analysis of a double pendulum arm excited by an RLC circuit based nonlinear shaker. Journal of Vibration and Control, 1077546314564782.
14. Felix, J.L.P., Balthazar, J.M., & Brasil, R.M. (2005). On saturation control of a non-ideal vibrating portal frame foundation type shear-building. Journal of Vibration and Control, 11(1), 121–136.
15. Iliuk, I., Balthazar, J.M., Tusset, A.M., Piqueira, J.R.C., de Pontes, B.R., Felix, J.L.P., & Bueno, M. (2013). A non-ideal portal frame energy harvester controlled using a pendulum. The European Physical Journal Special Topics, 222(7), 1575–1586.
16. Arbex, H.C., Balthazar, J.M., de Pontes Junior, B.R., da Fonseca, R.M.L.R., Felix, J.L.P., Tusset, A.M., & Bueno, M. (2015). On nonlinear dynamics behavior and control of a new model of a magnetically levitated vibrating system, excited by an unbalanced DC motor of limited power supply. Journal of the Brazilian Society of Mechanical Sciences and Engineering, 37(4), 1139–1150.
17. Balthazar, J.M., Rocha, R.T., Brasil, R.M.F.L., Tusset, A.M., de Pontes, B.R., & Silveira, M. (2014, August). Mode saturation, mode coupling and energy harvesting from ambient vibration in a portal frame structure. In ASME 2014 International Design Engineering Technical Conferences and Computers and Information in Engineering Conference (pp. V008T11A044–V008T11A044). American Society of Mechanical Engineers.
18. Rocha, R.T.; Balthazar, J.M.; Tusset, A.M.; Piccirillo, V.; Felix, J.L.P. & Brasil, R.M.L.R.F. (2015, August). On energy harvesting of a flexible portal frame support exploiting the saturation phenomenon. In: ASME 2015 International Design Engineering Technical Conferences & Computers and Information in Engineering Conference (IDETC/CIE 2015), 2015, Boston, Massachusetts, USA. Proceedings of ASME-IDETC/CIE 2015. NY, USA: ASME. p. 1. (Technical review/presented).
19. Vakakis, A.F., Gendelman, O.V., Bergman, L.A., McFarland, D.M., Kerschen, G., & Lee, Y.S. (2008). Nonlinear targeted energy transfer in mechanical and structural systems (Vol. 156). Springer Science & Business Media.

Differential Drive Robot: Spline-Based Design of Circular Path

Alexandr Štefek, Václav Křivánek, Yves T. Bergeon and Jean Motsch

Abstract When moving a robot, acceleration of the robot varies. This is an important problem, when changes in acceleration are abrupt, all parts of the robot are subjected to these variations. Parts of the robot can bend or damages can appear. When using camera on-board (like RGB-D), you need to put it at a height such that you can see obstacles. Due to acceleration, the camera will swing and you need to stop the robot and wait till the end of oscillations to take the picture. To avoid this problem on a differentially driven robot (two motors), we need to have a constant rotation of the two wheels. Acceleration should be zero and has to be considered as a constraint. For the purpose of this paper, it is assumed that the robot moves on a path of shape of a circular arc. It should be noted that circular arc function does not fit all possible paths, which the robot might be required to take. This results in the need for adaptation of the path design and makes computing an optimal path not only an interesting but also an important problem. For its solution, the following has to be taken into account: physical features of the robot, dynamics of the robot and environments where the robot operates. In later sections of this paper, two possible adaptations are presented and discussed. The first one is based on a modification of a known algorithm, while the second one is authors' own contribution to the problematic. Resulting adaptations of the design are then tested and assessed using simulation.

A. Štefek · V. Křivánek (✉)
University of Defence, Kounicova 65, Brno, Czech Republic
e-mail: vaclav.krivanek@unob.cz

A. Štefek
e-mail: alexandr.stefek@unob.cz

Y.T. Bergeon · J. Motsch
Écoles de Saint-Cyr Coëtquidan, 56381 Guer Cedex, France
e-mail: yves.bergeon@st-cyr.terre-net.defense.gouv.fr

J. Motsch
e-mail: jean.motsch@st-cyr.terre-net.defense.gouv.fr

© Springer International Publishing Switzerland 2016

J. Awrejcewicz (ed.), *Dynamical Systems: Theoretical and Experimental Analysis*, Springer Proceedings in Mathematics & Statistics 182, DOI 10.1007/978-3-319-42408-8_26

1 Introduction

Path planning is a complex problem, which can be either a three-dimensional issue for Unmanned Aerial Vehicles (UAVs) [7, 10] or mostly reduced to two-dimensional space for Unmanned Ground Vehicles (UGVs) [8, 9]. In both cases, it involves meeting physical constraints of unmanned robot (entity), constraints of operating environment and other operational requirements.

Design of the planned paths highly depends on the amount of known information about the operating area. Different techniques are then used according to this area that might be known, unknown or partially known. Physical limitations, operating environment and communication requirements then make the planning even more complex. It is essential to have an on-board processor to design and execute paths and trajectories.

Research into path planning is widely documented in the fields of ground robotics and manipulation systems [16]. There are number of criteria (i.e. nature of applications, operation environment, medium of operation and path constraints) partitioning path planning methods into several categories. These criteria have then resulted in the development of variety of algorithms and techniques. The predominant methods used in ground robotics are

1. the road map method,
2. the cell decomposition method,
3. the potential field method.

A common denominator of all these methods is their purpose. That is, they focus on the generation of routes for a robot to move from a starting point to a finishing point. It is also important to note that these methods rely on an accurate description of the environment. This environment is defined using a map which contains known and unknown obstacles. Finding a path between two points on the map is often simplified by (i) discretizing of the map into small areas called cells or by (ii) converting the map into a continuous field.

Therefore, path planning methods can be classified either as discrete or as continuous methods. A suitable search algorithm is then used to find a path connecting the start and finish points on this simplified map. The road map and cell decomposition methods transform the environment into a discrete map, while the potential field method transforms the map into a continuous function [15]. These methods, which produce a path for a given map or an environment, are also called *global path planners*. These methods also transform the given environment into a searchable database [16].

For simplification purposes, in this article, the global path is considered to be known and set of checkpoints to be given. The issue at hand is then to deal with the crossing from one checkpoint on the planned path to the next, and simultaneously, to build optimal conditions to reach the next following checkpoint. Previous experience shows that the use of odometry and inappropriate algorithm can result in missing the checkpoints on the planned path, as shown in Fig. 7. For the robot to travel through

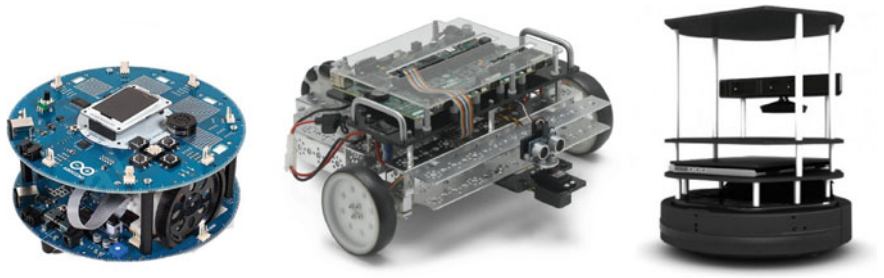

Fig. 1 Three types of differentially driven robots. *Notes* The pictures are not scaled. From *left* to *right* side (*i*) ArduRobot; (*ii*) DaNI; (*iii*) TurtleBot 2

a set of given points, a new algorithm based on *splines* can be used, as described in [5, 11–13, 18].

In order to go a little bit further into the context of this article, some details are to be given about the robots that are to be taken into consideration. Indeed, three types of robot with differential drive were considered for the designing of a general algorithm, as can be see on Fig. 1. The smallest one is an ArduRobot controlled by Arduino. The medium-sized one is a DaNI driven by Single Board RIO by National Instruments. And the biggest one is a TurtleBot 2 managed by ROS (Robot Operating System). These are the robots that will be targeted after simulation methods fully show the potential of our planning method.

The focus of this article is to describe this spline-based algorithm and compare it to the commonly used method—proportional control. This paper is divided into five sections. Following this introductory section, Sect. 2 contains description of differential driven robot control. Section 3 deals with control algorithms alongside the minimum control requirements included in the motor motion dynamics. Section 4 describes the simulation results. And finally, Sect. 5 contains summarized conclusion of the paper and a plan for the future work on the issue.

2 Robot with Differential Drive

2.1 Description of the Problem

Differentially driven robot consists of two wheels mounted on a common axis and controlled by separate motors, as depicted in Fig. 2. It is perhaps the simplest possible design for a ground-contact mobile robot [3, 6]. Its movement is computed by the use of kinematics. Kinematics deals with the relationship between control parameters (relative velocity of the two wheels v_r, v_l) and the behaviour of the system in state space [4, 17].

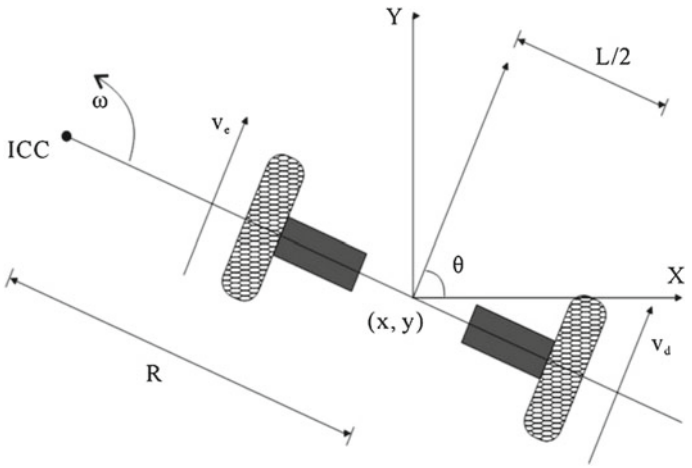

Fig. 2 Differentially driven kinematics

For the robot to rotate around a point, both left and right wheels have to follow a path that moves around the *Instantaneous center of rotation* (ICC) at the same angular rate ω, at each instant in time, and thus

$$\omega\left(R+\frac{l}{2}\right)=v_r,\ \omega\left(R-\frac{l}{2}\right)=v_l. \tag{1}$$

where l is the axis distance between the center of the two wheels, v_l is the left wheel's velocity along the ground, v_r is the right wheel's velocity along the ground and R is the distance of ICC to the midpoint between the two wheels [2]. Note that v_l, v_r, ω and R are all functions of time. At any instant in time, solving for R and ω results in

$$R=\frac{l(v_l+v_r)}{2(v_r-v_l)},\ \omega=\frac{v_r-v_l}{l}. \tag{2}$$

As one can see, commonly used standard form has also been used for the equations above (as an example see [4]). Nevertheless, for practical implementation, the R (radius) variable becomes problematic, when $v_r=v_l$ (R becomes infinity, see Eq. 2, and the robot is moving on a straight line). As a numerical implementation using computer cannot deal with such infinite radius, these cases must be strictly avoided. One way to tackle the problem is by expressing the problem by hand using a different point of view

$$\begin{pmatrix}\dot{x}\\ \dot{y}\\ \dot{\varphi}\end{pmatrix}=\begin{pmatrix}\cos\varphi & 0\\ \sin\varphi & 0\\ 0 & \frac{2}{l}\end{pmatrix}\cdot\begin{pmatrix}v\\ \Delta\end{pmatrix}, \tag{3}$$

where x, y are robot's position coordinates in state space, φ is its orientation, v is its velocity, Δ is half of difference in circumferential velocities of its wheels and l is the distance between the wheels.

Relations between both representations are given by

$$v = \frac{v_r + v_l}{2}, \tag{4}$$

$$\Delta = \frac{v_r - v_l}{2}, \tag{5}$$

$$r = \frac{vl}{2\Delta}, \tag{6}$$

$$\omega = \frac{2\Delta}{l}, \tag{7}$$

where r is radius of rotation for planned path and ω is angular velocity of the whole robot. If robot's direction is straightforward then radius r approaches infinity, ω and Δ are null.

2.2 Usual Approach to Control of Differentially Driven Robot

The usual approach to control of differentially driven robot is done by using angular differences. Figure 3 depicts this situation. After comparing the angles φ, α and $(\alpha - \varphi)$, the differential equation, in this case, takes the following form:

$$\omega = K \cdot \alpha, \tag{8}$$

The real challenge is hidden in fixing an appropriate value for the proportional control coefficient K. For example, in the case of a value of K that is too small, the robot might miss its goal. This type of differential driven robot control is considered as a benchmark for comparison to the new approach presented in the next sections.

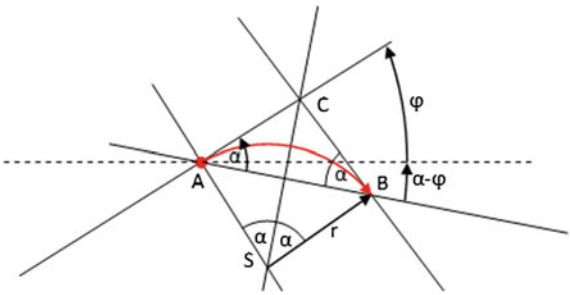

Fig. 3 Relationship between two points on the robot path

3 Derivation of Feedback-Based Control for Circular Path

Unfortunately, there is a problem with the use of the classical control method. The problem being that, if start-ups and slow-downs occur too often, then the whole dimetric-based measurement system can show significant deviation. That is caused by an occurrence of delay between the estimated and the actual time of acceleration and deceleration (speed-ups and slow-downs), which can result in integration of time errors. If it could be assured that the angular velocity of both wheels is kept at a constant level during the whole control process (or at least during its significant part), then the resulting trajectory deviation would be kept to a minimum.

Keeping the motor speeds at constant level can be achieved by using a path trajectory in the shape of a circular arc. If the speeds are kept at constant level, during most of the trajectory segments, then the changes in motor speeds are minimized and the deviation in the measurement system is significantly reduced. To plan adaptive control, during the motion of the robot on the circular arc, it is important to define feedback-based control that constantly handles speeds of both motors on every point of the robot's path. Taking these requirements into account, it is possible to reverse-engineer the feedback-based control by the following method.

Any two points can be connected by an infinite set of different circular arcs. But given that the robot has a certain starting orientation which is in the direction of a tangent line, then there is only one acceptable circular arc to consider, e.g. Fig. 4.

The Fig. 3 describes the robot's position and its relation to position of its goal (the starting and the final orientations of the robot are also considered). When the robot is moving from point A to point B, the relation between distance of points A and B and radius of rotation can be expressed by Eq. 9.

$$\begin{aligned} 2r \sin \alpha &= |AB|, \\ \sin \alpha &= \frac{\frac{1}{2}|AB|}{r}. \end{aligned} \tag{9}$$

Considering Eqs. 6 and 7, we have:

$$\omega = \frac{v}{r} = 2v \frac{\sin \alpha}{|AB|}, \tag{10}$$

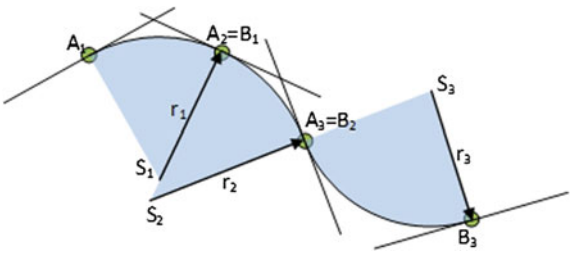

Fig. 4 Robot path compounded by circular segments

and the following set of equations can be easily derived with use of trigonometry

$$\cos(\alpha - \varphi) = \frac{ab_x}{|AB|},$$
$$\sin(\alpha - \varphi) = -\frac{ab_y}{|AB|}, \tag{11}$$
$$\sin(\alpha) = \sin[(\alpha - \varphi) + \varphi] = \cos(\alpha - \varphi) \cdot \sin\varphi + \sin(\alpha - \varphi) \cdot \cos\varphi, \tag{12}$$
$$\sin\alpha = \frac{ab_x \sin\varphi - ab_y \cos\varphi}{|AB|}. \tag{13}$$

Combining Eqs. 10 and 13 gives:

$$\omega = 2v\frac{ab_x \sin\varphi - ab_y \cos\varphi}{|AB|^2}. \tag{14}$$

Compared to Eq. 7, the final form of feedback-based control is

$$\omega = \frac{2\Delta}{l} = 2v\frac{ab_x \sin\varphi - ab_y \cos\varphi}{|AB|^2}, \tag{15}$$

thus:

$$\Delta = vl\frac{ab_x sin\varphi - ab_y cos\varphi}{|AB|^2}. \tag{16}$$

It is interesting to notice that, according to Eqs. 3 and 15, it can be derived that

$$\omega = 2\frac{ab_x\dot{y} - ab_y\dot{x}}{|AB|^2}. \tag{17}$$

Lets be reminded that:

$$\overrightarrow{AB} = (ab_x; ab_y),\ |AB| = \sqrt{(ab_x)^2 + (ab_y)^2}. \tag{18}$$

The final mathematical form of feedback-based control for robot moving on circular path segments is defined by Eqs. 3, 5 and 16. As derived control cannot change the behaviour of the robot, adding K_c coefficient to the equation can play an important role

$$\Delta = K_c vl\frac{ab_x sin\varphi - ab_y cos\varphi}{|AB|^2}. \tag{19}$$

The Eq. 19 then allows running of multiple experiments and fine-tuning a path of a robot on a single line segment. In the next chapter, two approaches are going to be compared to each other. One using this latter form and the other being the former classical one (proportional control for ω).

4 Simulation Results

The comparison in this chapter was done by the use of simulation tools. To be as close to real results as possible, the dynamic of motors was also considered. A dynamic model of motor behaviour had to be modelled, to consider its dynamic characteristic on the robot chassis.

4.1 Motor Dynamics

Because two identical motors are used for one robot chassis, only one transfer function will be defined. The common transfer function for single motor is

$$F(s) = \frac{Y(s)}{U(s)} = \frac{1}{a_2 s^2 + a_1 s + 1}, \tag{20}$$

where $a_2 = T_1 \cdot T_2$, $a_1 = T_1 + T_2$, and T_1, T_2 are time constants. Thus from:

$$a_2 \ddot{y} + a_1 \dot{y} + y = u, \tag{21}$$

we can obtain state differential equations of both motors

$$\dot{x}_{or} = -\frac{1}{a_2} \cdot v_r + \frac{1}{a_2} \cdot v_{sr}, \qquad \dot{v}_r = -\frac{a_1}{a_2} \cdot v_r, \tag{22}$$

$$\dot{x}_{ol} = -\frac{1}{a_2} \cdot v_l + \frac{1}{a_2} \cdot v_{sl}, \qquad \dot{v}_l = -\frac{a_1}{a_2} \cdot v_l. \tag{23}$$

The values T_1 and T_2 have been set to 0.03 s for all simulations. The simulation uses this list of equations: 3, 5, 16, 22 and 23. Motor is modelled here as a complex system where the input is the demanded angular velocity and the output is the real angular velocity.

4.2 Path Comparison

For the purpose of comparison, the parameters have been set to lead to similar trajectories. In Fig. 5 there are five trajectories based on the same originally planned path which is also shown. Trajectory `Robot A0` is purely circular path (K_c is equal to 1), `Robot A1` uses $K_c = 4$, `Robot A2` uses $K_c = 8$. Two trajectories `Robot W1` and `Robot W2` both use the classical approach to motion control but with different increments of coefficient K_c. It is interesting to notice that trajectories `Robot W1` and `Robot A1` are nearly the same as trajectories `Robot W2` and `Robot A2`.

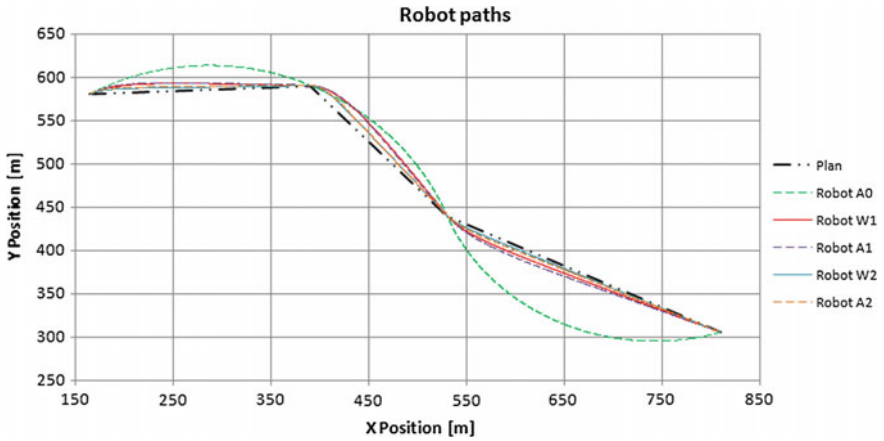

Fig. 5 Robots path, overview of all planned paths for different K and K_c

4.3 Limitation of Centripetal Acceleration

High values of centripetal acceleration can lead to the tipping of the robot. So observing this parameter during robot control becomes very important. For the new approach presented in this paper, it is straightforward to limit the centripetal acceleration to a desired interval by the use of K_c. That can be done because the presented algorithm has a robust stability (comparatively to Fig. 7 where the unstable behaviour of classical approach is depicted for low value of gain K). Figure 6 shows the centripetal acceleration versus time. It should be noted that, for one segment of a path (e.g. from point A to point B), `Robot A0` has constant centripetal acceleration.

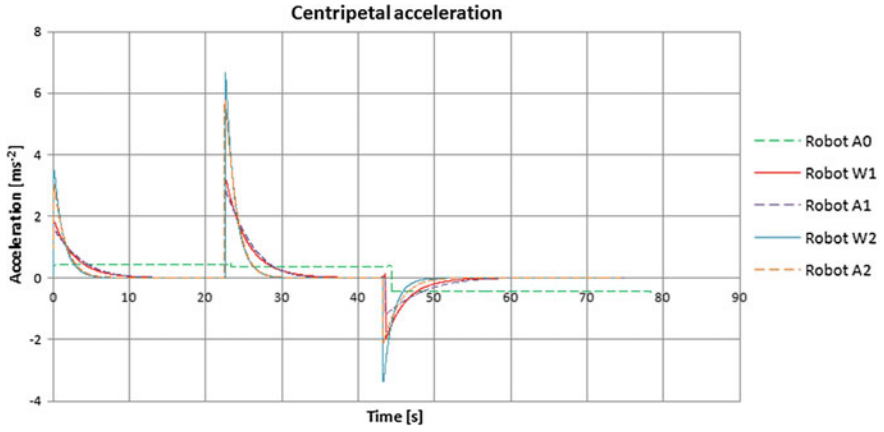

Fig. 6 Centripetal acceleration, detailed view

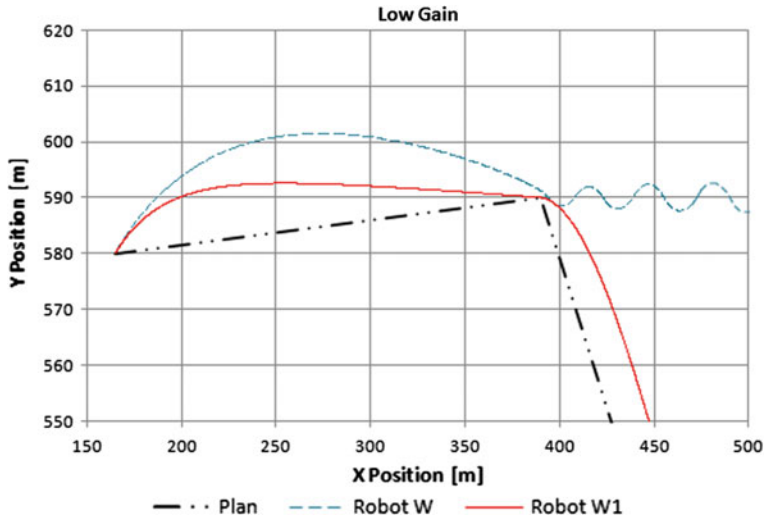

Fig. 7 The example of path for both approaches. Classical approach `Robot W` implies instability around the second check point for low value of gain K

A case when centripetal acceleration was strictly in the interval $\langle -3; 3 \rangle$, was tested. Both filtered and unfiltered paths were compared; difference between both was minimal. It this case centripetal acceleration filtering did not play a significant role. The robot path was nearly the same but the centripetal acceleration was low enough.

5 Conclusion

A new approach to differential robot control was derived, presented and compared to classical proportional approach. This approach can help the robot to move on a single segment of its path with minimal changes to both angular velocities of wheels. Moreover the extended version of control with K_c coefficient can play an important role in the limitation of centripetal acceleration which has a substantial impact on stability of the robot chassis during switching from one path segment to another one.

Possible future work can include on-the-move adaptations of K_c coefficient to find an optimal behaviour and (sub)optimum of fitness function for given robot (see Fig. 1). The issue is to compare real path of different approaches made by differential control robots. A very useful way is to construct a portal as a camera holder to observe the scene with robot. Hence the quality of control process is transformed to machine vision problem [1, 3].

Proposed algorithm can be used not only for UGVs but also for UAVs, which are then going to be able to follow the planned trajectory with minimum changes

caused by dynamic effects of the environment [14]. For the implementation of the algorithm, it is needed to extend the state space to three-dimensional territory.

Acknowledgments The work presented in this article has been supported by the Czech Republic Ministry of Defence (University of Defence development program "Research of sensor and control systems to achieve battlefield information superiority").

References

1. Bergeon, Y.T.: Calculation of the distance covered by a robot thanks to image analysis with a two-robot team. In: International Conference on Military Technologies, ICMT 2011, pp. 849–854. University of Defence (2011). ISBN 978-80-7231-788-2
2. Chitsaz, H., LaValle, S., Balkcom, D.J., Mason, M.T.: Minimum wheel-rotation paths for differential-drive mobile robots. In: Proceedings of International Conference on Robotics and Automation. ICRA 2006, pp. 1616–1623 (2006). 10.1109/ROBOT.2006.1641938. ISSN 1050-4729
3. Doskočl, R., Křivánek, V., Štefek, A., Bergeon, Y., Motsch, J.: Uav assisted landing on moving ugv. In: V. Křivánek (ed.) International Conference on Military Technology, pp. 611–615. Brno (2015). 10.1109/MILTECHS.2015.7153646. ISBN 978-80-7231-976-3
4. Dudek, G., Jenkin, M.: Computational principles of mobile robotics. Cambridge University Press (2000). ISBN 0-521-56876-5
5. Eren, H., Chun Che, F., Evans, J.: Implementation of the spline method for mobile robot path control. In: Proceedings of the 16th IEEE Instrumentation and Measurement Technology Conference. IMTC/99., pp. 739–744 (1999). 10.1109/IMTC.1999.776966. ISSN 1091-5281
6. Hellström, T.: Kinematics equations for differential drive and articulated steering. Tech. rep., Umeå University (2011). ISSN 0348-0542
7. Jan, G.E., Chang, K.Y., Parberry, I.: Optimal path planning for mobile robot navigation. IEEE Transactions on Mechatronics **13**(4), 451–460 (2008). 10.1109/TMECH.2008.2000822. ISSN 1083-4435
8. Lai, S., Wang, K., Qin, H., Cui, J.Q., Chen, B.M.: A robust online path planning approach in cluttered environments for micro rotorcraft drones. Control Theory and Technology **14**(1), 83–96 (2016). 10.1007/s11768-016-6007-8. ISSN 2198-0942
9. Lee, K.S., Ovinis, M., Nagarajan, T., Seulin, R., Morel, O.: Autonomous patrol and surveillance system using unmanned aerial vehicles. In: International Conference on Environment and Electrical Engineering (EEEIC), pp. 1291–1297 (2015). 10.1109/EEEIC.2015.7165356. ISBN 978-1-4799-7992-9
10. Petrov, P.: Modeling and adaptive path control of a differential drive mobile robot. In: Proceedings of the 12^{th} WSEAS international conference on Automatic control, modelling & simulation. ACMOS'10, pp. 403–408. World Scientific and Engineering Academy and Society (WSEAS) (2010). ISBN 978-954-92600-1-4
11. Piazzi, A., Bianco, C., Ronano, M.: η^3 - splines for the smooth path generation of wheeled mobile robots. IEEE Transactions on Robotics **23**(5), 1089–1095 (2007). 10.1109/TRO.2007.903816. ISSN 1552-3098
12. Reister, D.B., Pin, F.G.: Time-optimal trajectories for mobile robots with two independently driven wheels. The International Journal of Robotics Research **13**(1), 38–54 (1994)
13. Reuter, J.: Mobile robots trajectories with continuously differentiable curvature: An optimal control approach. In: International Conference on Intelligent Robots and Systems, pp. 38–43. IEEE (1998). ISBN 0-7803-4465-0
14. Salga, J., Maturkanič, D.: Flight trajectory modelling to increase general aviation safety. Advance in Military Technology **6**(1), 107–120 (2011). ISSN 1802-2308

15. Šeda, M., Pich, V.: Planning smooth trajectories in the plane with obstacles. Cybernetic Letters p. 5 (2008). ISSN 1802-3525
16. Tsourdos, A., White, B., Shanmugavel, M.: Cooperative Path Planning of Unmanned Aerial Vehicles. Wiley-Blackwell (2010). 10.1002/9780470974636. ISBN 978-0-470-74129-0
17. Wan, J., Chen, P.C.Y.: A Robust Nonlinear Control for Differential Mobile Robots and Implementation on Formation Control, chap. 5, pp. 71–94. InTech Open Access Book (2011). 10.5772/13317. ISBN 978-953-307-425-2
18. Zhang, J., Raczkowsky, J., Herp, A.: Emulation of spline curves and its applications in robot motion control. In: IEEE World Congress on Computational Intelligence. Proceedings of the Third IEEE Conference on Fuzzy Systems, pp. 831–836 (1994). 10.1109/FUZZY.1994.343843. ISBN 0-7803-1896-X

Multiple Solutions and Corresponding Power Output of Nonlinear Piezoelectric Energy Harvester

Arkadiusz Syta, Grzegorz Litak, Michael I. Friswell and Marek Borowiec

Abstract Energy harvesting is used for an increasing number of small electronic devices and sensors in various applications. Ambient sources of vibration are exploited to provide low levels of power to devices where battery replacement is difficult. One of the simplest concepts for energy harvesting from mechanical vibrations is based on a linear mechanical resonator combined with a piezoelectric transducer. In this case, mechanical energy scavenged from mechanical stress or strain is transferred to electrical voltage. However, such devices work most efficiently in the vicinity of a resonant frequency and it is difficult to tune them in the presence of variable ambient conditions. On the other hand, nonlinear devices seem to be more effective in such conditions due to the broader frequency spectrum of their response. In this paper, we analyse the dynamics of a nonlinear flexible beam with a piezoelectric layer and a magnetic tip mass under the harmonic excitation. The additional magnets define system multistability, including a tristable configuration. The resonant curves and basins of attraction are predicted and can be helpful in choosing the optimal values of the system parameters.

A. Syta (✉) · G. Litak · M. Borowiec
Faculty of Mechanical Engineering, Lublin University of Technology,
Nadbystrzycka 36, 20-618 Lublin, Poland
e-mail: a.syta@pollub.pl

M. Borowiec
e-mail: m.borowiec@pollub.pl

G. Litak
Department of Process Control, AGH University of Science and Technology,
Mickiewicza 30, 30-059 Cracow, Poland
e-mail: g.litak@pollub.pl

M.I. Friswell
College of Engineering, Swansea University Bay Campus, Fabian Way,
Crymlyn Burrows, Swansea SA1 8EN, UK
e-mail: m.i.friswell@swansea.ac.uk

© Springer International Publishing Switzerland 2016

J. Awrejcewicz (ed.), *Dynamical Systems: Theoretical and Experimental Analysis*, Springer Proceedings in Mathematics & Statistics 182, DOI 10.1007/978-3-319-42408-8_27

1 Introduction

Novel structures for energy harvesting that transform mechanical energy from nonlinear vibrations into voltage have been studied recently to improve the efficiency of the devices [1]. The level of harvested power is dependent on exciting mechanical resonances with higher amplitude. However, nonlinearities can be used to extend the bandwidth of energy harvesters for broadband ambient frequency excitation [1]. Such broadband effects have been investigated by many researchers, including [2–5] which considered monostable potentials. Bistable energy harvesters and their efficiency have been analysed in [6–14], including numerical and experimental investigations of the dynamical response to both low- and high-amplitude harmonic excitations with white or coloured noise. In [15–17] the authors discussed the role of asymmetry in the potential and how it affects the broadband response. Interesting comparisons between the efficiency of monostable and bistable nonlinear energy harvesters can be found in [1, 18, 19]. Achieving high level of harvested power from variable (small and moderate) amplitude ambient vibrations is very difficult since the barrier between two potential wells must be overcome for efficient harvesting. For this reason, the tristable nonlinear energy harvester has been considered recently to improve the sensitivity to low-amplitude ambient vibrations [20–23].

In this paper, we study the dynamical response of a tristable nonlinear energy harvester composed of a vertical beam with a tip magnet with additional inclined magnets under harmonic excitation. We also discuss the geometry of the potential and its influence on the harvested power. This system has shown a number of possible solutions from periodic inter-well motions through non-periodic to periodic outer-well motions with different corresponding power outputs [22]. The main goal of this paper is to analyse the sensitivity to initial conditions with respect to the level of the harvested power using basins of attraction which can help tune values of parameters to improve the efficiency of the system.

2 The Model

The general equations of a multistable energy harvester are [22]

$$\begin{aligned} m\ddot{\tilde{x}} + c\dot{\tilde{x}} + \frac{dU}{d\tilde{x}} - \theta\tilde{v} &= -m\ddot{\tilde{x}}_e \\ C_p\dot{\tilde{v}} + \tilde{v}R_l^{-1} + \theta\dot{\tilde{x}} &= 0, \end{aligned} \tag{1}$$

where m is the equivalent mass, c denotes damping and θ is electromechanical coupling coefficient. C_p is the capacitance of the piezoelectric material, R_l is the load resistance, $\tilde{v}$ is the voltage, while $\tilde{x}$ and $\tilde{x}_e$ denote the tip mass displacement and the base acceleration, respectively. U is the potential energy function defined by

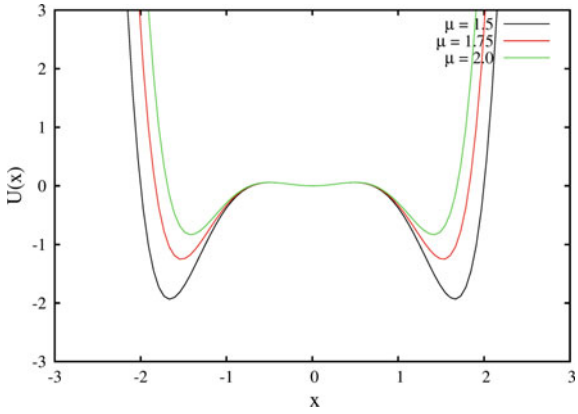

Fig. 1 The tristable potential function of the system (3) for different values of μ

$$U(\tilde{x}) = \frac{1}{2}k_1\tilde{x}^2 + \frac{1}{4}k_2\tilde{x}^4 + \frac{1}{6}k_3\tilde{x}^6. \tag{2}$$

Adjusting the coefficients of the nonlinear restoring force, k_1, k_2 and k_3, one can change type of multistability of the potential. The governing dimensionless electromechanical equations, after substituting the assumed potential function, are

$$\begin{aligned} \dot{x} &= y, \\ \dot{y} &= -\zeta y - x - \lambda x^3 - \mu x^5 + \alpha z + A\cos(\omega\tau), \\ \dot{z} &= -\beta z - \alpha y, \end{aligned} \tag{3}$$

where x corresponds to $\tilde{x}$, y to $\dot{\tilde{x}}$ and z to $\tilde{v}$, respectively. The damping is denoted by ζ, the nonlinear coefficients—λ and μ, the electromechanical coupling—α and the time constant of the piezoelectric dynamics—β. A and ω correspond to the amplitude and the frequency of external forcing. In this paper, we are interested in the case of tristability, which means that the system has five equilibrium points; three of them are stable and two of them are unstable. Such a potential can be obtained by changing two parameters in Eq. (3), namely μ and λ. For $\mu > 0$ and $\lambda < -2\sqrt{\mu}$ the system is a tristable nonlinear energy harvester. Figure 1 compares the potential for different values of μ when $\lambda = -4.5$. We can observe that for fixed λ both the depth and the distance between the symmetric potential wells decreases as μ increases. However, changing μ does not affect the middle potential well. A higher potential barrier requires a higher amplitudes of ambient vibration to switch between the two potential wells.

3 Numerical Simulations

We examine the system response by numerically integrating Eq. 3 using the Runge-Kutta method with the fixed time step $\Delta\tau = \frac{2\pi}{1000\omega}$. The other parameters were fixed to [22] $\alpha = 0.9$, $\beta = 0.5$, $\zeta = 0.03$, and $\lambda = -4.5$. We analysed the system response

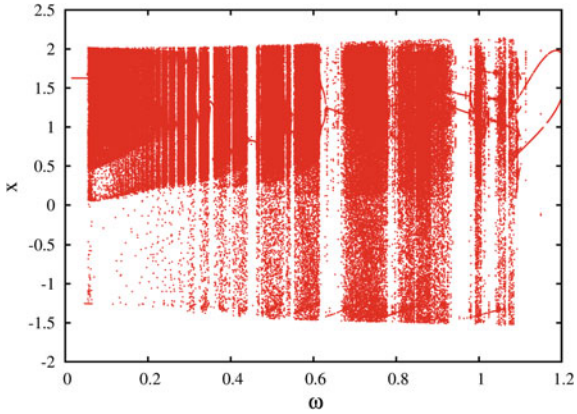

Fig. 2 Bifurcation diagram of the x coordinate, $\mu = 1.75$, $(x_0, y_0) = (0, 0)$

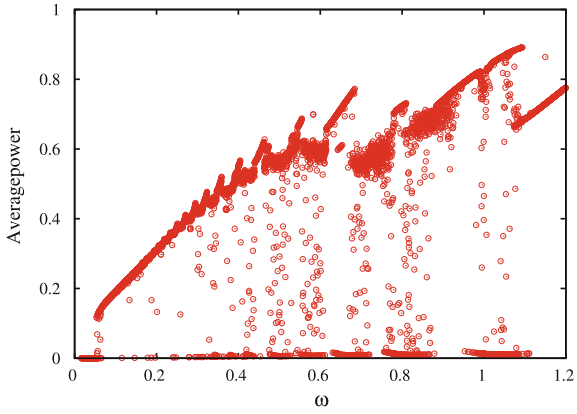

Fig. 3 Bifurcation diagram of the average power $\bar{P} = \frac{1}{n}\sum_{i=1}^{n} z_i^2$. $\mu = 1.75$, $(x_0, y_0) = (0, 0)$

for different amplitudes, A, and frequencies, ω, of the external harmonic excitation. Figure 2 presents the bifurcation diagram of the system response with respect to ω. Figure 2 shows that the right potential well is visited more often than the left potential well. For $\omega < 0.05$ we observe inter-well periodic solutions with low average power output $\bar{P} = 0.0007$. For $\omega > 0.05$ and $\omega < 1.1$ various solutions appear: from period one to period doubling and non-periodic, with different level of corresponding power. High power is generated for $\omega > 1.1$ when period one outer-well solutions appear with $0.62 < \bar{P} < 0.77$ (see Fig. 3). We also analysed the efficiency of the tristable energy harvester at the low excitation frequency $\omega = 0.2$ with respect to the μ parameter in Fig. 4. As expected, higher amplitudes of ambient vibration gives higher power output from the system and a wider range of outer-well solutions. Moreover, the difference between power output obtained for $A = 1.2$–2.2 is more significant than between $A = 2.2$ and 3.2. Figure 5 compares a typical inter-well solution to a typical outer-well solution. The low energy solution is limited to one potential well while the high energy solution overcomes the potential barrier and shows intermittency, i.e. it is trapped in the left or right potential well for some time.

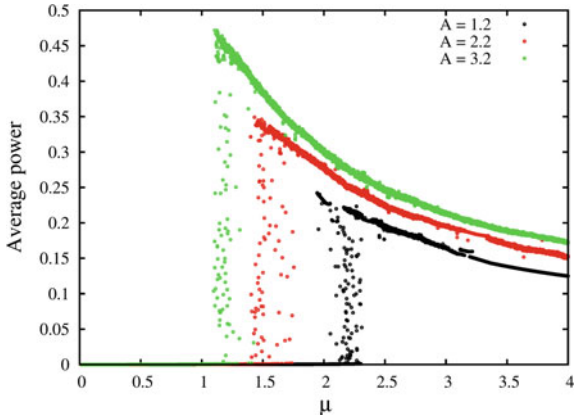

Fig. 4 Resonant curves for different amplitudes of external excitation A. $\mu = 1.75,\ \omega = 0.2$, $(x_0, y_0) = (0, 0)$

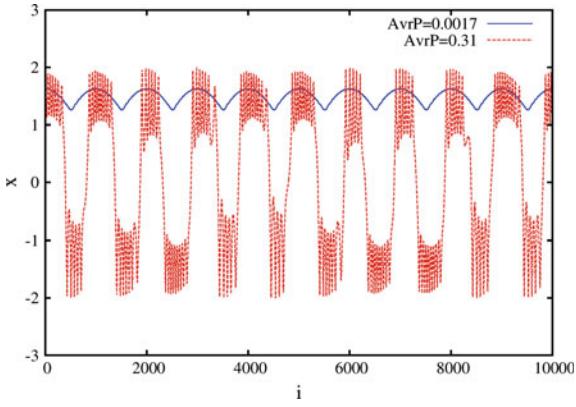

Fig. 5 Time series of the x coordinate and corresponding powers calculated for $\mu = 1.75$ and $(x_0, y_0) = (1.5, 0.0)$ (*blue*) or $(x_0, y_0) = (1.2, 0.5)$ (*red*)

4 Influence of Initial Conditions

The main goal of this paper is to investigate the global efficiency of the tristable energy harvester model for low-frequency ambient vibrations using basins of attraction. This method presents the stability of different solutions by their basins of attraction and borders. First, let us consider solutions for $\mu = 1.5$ with the widest and deepest potential wells (see Fig. 1). Figure 6 shows the basins of attraction and corresponding levels of harvested power calculated for grid of initial conditions $(x_0, y_0) \in [-2, 2] \times [-2, 2]$. In this case we can observe two areas of low energy solutions located in left or right potential well (blue dots) surrounded by high energy solutions (red dots) mixed with low energy solutions (blue dots). Moreover, the borders separating the basins of attraction have a fractal character near the left and right equilibria. The situation changes when one increases μ to 1.75 (Fig. 7). In this case, the volume of the basins defining the single well solutions decreases while number of cross well solutions increases. Moreover, there are still coexisting mixed solutions

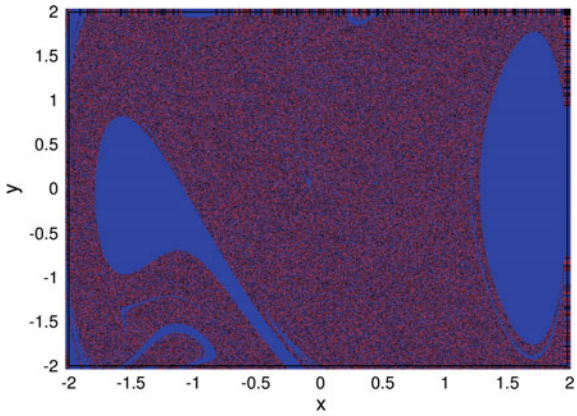

Fig. 6 Basins of attraction calculated for $\mu = 1.5,\ \omega = 0.2$. *Blue colour*—low energy output, *red colour*—high energy output

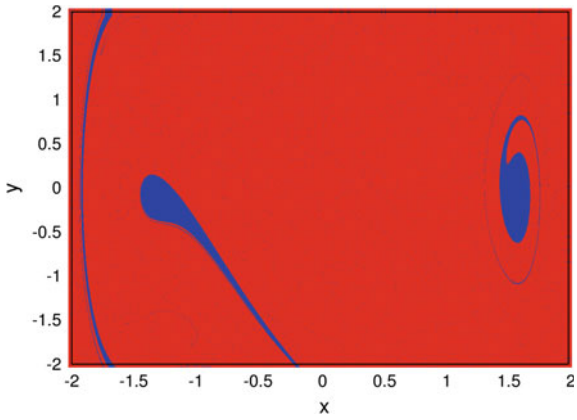

Fig. 7 Basins of attraction calculated for $\mu = 1.75,\ \omega = 0.2$. *Blue colour*—low energy output (see Fig. 5), *red colour*—high energy output (see Fig. 5)

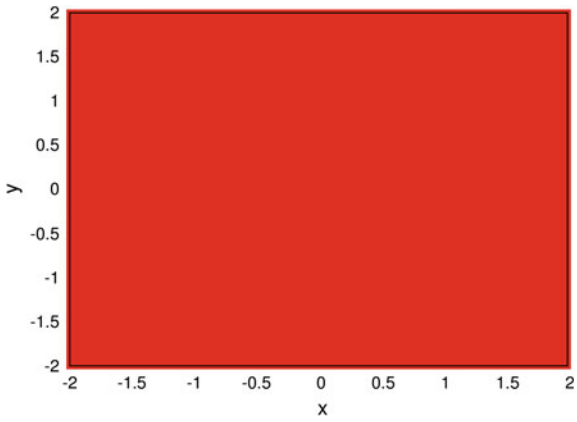

Fig. 8 Basins of attraction calculated for $\mu = 2.0,\ \omega = 0.2$. *Blue colour*—low energy output, *red colour*—high energy output

surrounding the two stable equilibria. Finally, Fig. 8 shows the basins of attraction calculated for $\mu = 2.0$ with the lower barrier separating potential wells. In this case, the low energy solutions disappear and the system is the most efficient.

5 Conclusions

The examined energy harvester exhibited different dynamical responses with periodic and non-periodic solutions. The power output increased significantly when the system changed from the inter-well to the outer-well solution even for a low frequency of the external excitation. The μ parameter is responsible for the shape of the potential and can be tuned to increase the efficiency of the system. A higher value of μ gives shallower potential wells and makes it easier to switch between the two stable equilibria (more harvested power). On the other hand, increasing μ changes the shape of the potential and changes multistability from tristable through bistable to monostable (less harvested power). The corresponding basins of attraction confirmed that the system can be an efficient energy harvester for low frequency ambient vibrations.

Acknowledgments AS gratefully acknowledge the support of the Polish National Science Center under grant DEC-2013/11/D/ST8/03308.

References

1. Daqaq M F and Masana R and Erturk A and Quinn D D (2014) On the role of nonlinearities in vibratory energy harvesting: a critical review and discussion. Applied Mechanics Reviews – Transactions of ASME 66:040801
2. Mann B P and Sims N D (2009) Energy harvesting from the nonlinear oscillations of magnetic levitation. Journal of Sound and Vibrations 319:515–530
3. Ramlan R and Brennan M J and Mace B R and Kovacic I (2010) Potential benefits of a non-linear stiffness in an energy harvesting device. Nonlinear Dynamics 59:545–558
4. Marinkovic B and Koser H (2009) Smart Sand? A Wide Bandwidth Vibration Energy Harvesting Platform. Applied Physics Letters 94:103505
5. Hajati A and Kim S G (2011) Ultra-wide bandwidth piezoelectric energy harvesting. Applied Physics Letters 99:083105
6. Cottone F and Vocca H and Gammaitoni L (2009) Nonlinear Energy Harvesting. Applied Physics Letters 102:080601
7. Erturk A and Hoffmann J and Inman D J (2009) A piezomagnetoelastic structure for broadband vibration energy harvesting. Applied Physics Letters 94:254102
8. Gammaitoni L and Neri I and Vocca H (2009) Nonlinear oscillators for vibration energy harvesting. Applied Physics Letters 94:164102
9. Litak G and Friswell M I and Adhikari S (2010) Magnetopiezoelastic energy harvesting driven by random excitations. Applied Physics Letters 96:214103
10. Erturk A and Inman D J (2011) Broadband piezoelectric power generation on high-energy orbits of the bistable Duffing oscillator with electromechanical coupling. Journal of Sound and Vibrations 330:2339–2353

11. Stanton S C and McGehee C C and Mann B P (2010) Nonlinear dynamics for broadband energy harvesting: Investigation of a bistable piezoelectric inertial generator. Physica D 239:640–653
12. Ferrari M and Ferrari V and Guizetti M and Ando B and Baglio S and Trigona C (2010) Improved energy harvesting from wideband vibrations by nonlinear piezoelectric converters. Sensors and Actuators A: Physical 162:425–431
13. Daqaq M F (2011) Transduction of a bistable inductive generator driven by white and exponentially correlated Gaussian noise. Journal of Sound and Vibrations 330:2554–2564
14. Syta A and Bowen C R and Kim H A and Rysak A and Litak G (2015) Experimental analysis of the dynamical response of energy harvesting devices based on bistable laminated plates. Meccanica 50:1–10
15. He Q F and Daqaq M F (2014) Influence of potential function asymmetries on the performance of nonlinear energy harvesters under white noise. Journal of Sound and Vibrations 332:3479–3489
16. Halvorsen E (2013) Fundamental issues in nonlinear wideband-vibration energy harvesting. Physical Review E 87:042129
17. Harne R L and Wang R L (2014) Influence of potential function asymmetries on the performance of nonlinear energy harvesters under white noise. Journal of Vibration and Acoustics – Transactions of ASME 136:021009
18. Zhao S and Erturk A (2013) On the stochastic excitation of monostable and bistable electroelastic power generators: relative advantages and tradeoffs in a physical system. Applied Physics Letters 102:103902
19. Masana R and Daqaq M F (2011) Relative performance of a vibratory energy harvester in mono-and bi-stable potentials. Journal of Sound and Vibrations 330:6036–6052
20. Kim P and Seok J (2014) A multi-stable energy harvester: Dynamic modeling and bifurcation analysis. Journal of Sound and Vibrations 333:5525–5547
21. Zhou S and Cao J and Inman D J and Lin J and Liu S and Wang Z (2014) Exploitation of a tristable nonlinear oscillator for improving broadband vibration energy harvesting. The European Physical Journal - Applied Physics 67:30902
22. Cao J and Zhou S and Wang W and Lin J (2015) Influence of potential well depth on nonlinear tristable energy harvesting. Applied Physics Letters 106:173903
23. Tekam G T O and Kwuimy C A K and and Woafo P (2015) Analysis of tristable energy harvesting system having fractional order viscoelastic material, Chaos 25:013112

On the Dynamics of the Rigid Body Lying on the Vibrating Table with the Use of Special Approximations of the Resulting Friction Forces

Michał Szewc, Grzegorz Kudra and Jan Awrejcewicz

Abstract This paper is a presentation of the simulation and dynamical behaviour of a rigid body lying on a vibrating table. Shaping and control of the body's dynamical behaviour, by the use of manipulation of parameters of the table oscillations, are presented. This article includes an implementation of the specially prepared mathematical models of friction between table and the moving body as well. The above-mentioned models are based on the integral model assuming the fully developed sliding on the plane contact area with the foundation of any pressure distribution. In order to simplify the calculations and reduce their computational cost, special approximations of the integral models of friction force and moment are proposed. They are based on Padé approximants and their generalizations.

1 Introduction

This article is the extended version of the paper presented during the conference Dynamical Systems Theory and Applications 2015 [10] and most of the content can be found in both papers. The examination of systems with friction forces resulting between contacting bodies is the significant part of theoretical and applied mechanics. It has been investigated by scientists for years forming the separate branch of mechanics called tribology. Theoretical foundations analyzed in tribology focus mostly on stationary or periodical parts of motion. However, in mechanics one can encounter many examples, including the motion of bodies with friction,

M. Szewc (✉) · G. Kudra · J. Awrejcewicz
Department of Automation, Biomechanics and Mechatronics,
Lodz University of Technology, 1/15 Stefanowski Street, 90-924 Łódź, Poland
e-mail: michu.szewc@gmail.com

G. Kudra
e-mail: grzegorz.kudra@p.lodz.pl

J. Awrejcewicz
e-mail: jan.awrejcewicz@p.lodz.pl

© Springer International Publishing Switzerland 2016

J. Awrejcewicz (ed.), *Dynamical Systems: Theoretical and Experimental Analysis*, Springer Proceedings in Mathematics & Statistics 182, DOI 10.1007/978-3-319-42408-8_28

which shows that the transient stages between rolling and sliding can be a crucial part of analysis. The other problem in describing the system consisting of two contacting bodies with the dry friction forces is the normal pressure distribution over the contact area. The above-mentioned difficulties can occur in daily life examples like the dynamics of billiard ball moving on the flat table, curling rocks, bowling ball, Celtic stone, rolling bearing and many others issues related to robotics. Many theoretical studies on such dynamical processes have been developed. In most cases, they are based on simple static models of the static laws of Coulomb dry friction. Systems with Coulomb dry friction can behave interestingly in the instances of transition from sliding to rolling. However, the shape and size of the contact area may be the most important factor, which influence the global dynamics of the body. With the assumption that the flat base is deformed by the contacting body using the Hooke's law, MacMillan [1] described the normal pressure distribution as a linear function. He used the elliptic integrals to describe the friction forces and torque in the case of the circular contact area. Contensou in 1962 [2] has presented the paper in which he assumes fully developed sliding and the classical Coulomb law of frictions forces with the plane circular contact area. Applying the Hertzian contact distribution, Contensou showed the integral model of the resultant contact forces. Basing on the Contensou results, Zhuravlev [3] developed his theory and showed exact analytical functions, which defines the frictions forces and torque and he proposed special approximations on the basis of Padé approximations. Those models are much more suitable for the cases in which the relation between the sliding direction and the resultant friction components is considered. The dynamics of the motion of disk on a flat table was analyzed by Borisov et al. [8]. Kireenkov in [9] has proposed the model of rolling resistance, based on Padé approximations of resultant friction force and moment. He used the special contact pressure distribution on a circular contact area. In [4, 5], authors presented the generalization of the models based on Padé approximants as the family of approximant models of friction forces. Application of the proposed models was considered in [6, 7].

This work is the implementation of the proposed models of friction force and moment in the case of a rigid body lying on the vibrating table. By manipulation of the table oscillations' parameters, we shape and control the behaviour of the moving body. Proposed models assume the fully developed sliding on the plane contact area with any pressure distribution. To reduce the computational cost of the equations we propose the simplifications of the model as well.

2 Modelling the Contact Forces

This part of the paper is thoroughly described in work [5] and for the purpose of this study, we present the most important parts which are necessary to understand the theoretical foundations of the problem. We consider the dimensionless form of plane, circular contact area F, with the Cartesian coordinate system Axyz., where x

and y axes lie in the contact plane. We define the dimensionless length as the quotient of the actual length and the radius of real contact $\hat{a}$. Point situated on the contact area F has the dimensionless coordinates $x = \hat{x}/\hat{a}$ and $y = \hat{y}/\hat{a}$. The following form of the non-dimensional contact pressure distribution is further assumed

$$\sigma(x,y) = \hat{\sigma}(x,y)\frac{\hat{a}^2}{\hat{N}} = \frac{3}{2\pi}\sqrt{1-x^2-y^2}(1+d_c x + d_s y), \tag{1}$$

where

$$d_c = d\cos\gamma = d\frac{v_{rx}}{\sqrt{v_{rx}^2+v_{ry}^2}} \text{ and } d_s = d\sin\gamma = d\frac{v_{ry}}{\sqrt{v_{rx}^2+v_{ry}^2}} \tag{2}$$

In above expressions (Eqs. 1 and 2) $\hat{\sigma}(x,y)$ is the real contact pressure, $\hat{N}$—normal component of the real resultant force, d—rolling resistance parameter, γ—angle describing direction of rolling. The variables v_{rx} and v_{ry} are the components of the non-dimensional "rolling velocity" $\mathbf{v}_r = \hat{\mathbf{v}}_r/\hat{a} = = v_{rx}\mathbf{e}_x + v_{ry}\mathbf{e}_y$ ($\hat{\mathbf{v}}_r$ is the corresponding real vector, $\mathbf{e}_i$ is unit vector of i axis). Proposed model of contact pressure distribution (Eq. 1) is the modification of Hertzian stress distribution, with the assumption that the centre of pressure distribution does not coincide with the geometrical centre A. Due to this assumption, we can implement the non-dimensional rolling resistance

$$\mathbf{M}_r = \mathbf{f}\times\mathbf{e}_z = y_S\mathbf{e}_x - x_S\mathbf{e}_y = M_{rx}\mathbf{e}_x + M_{ry}\mathbf{e}_y, \tag{3}$$

where

$$M_{rx} = \frac{1}{5}d_s,\ M_{ry} = -\frac{1}{5}d_c \tag{4}$$

In above expression (Eq. 3) $\mathbf{f} = \overrightarrow{AS} = x_S\mathbf{e}_x + y_S\mathbf{e}_y$ is a vector denoting the position of centre of non-dimensional pressure distribution S. The real counterpart of rolling resistance can be calculated as $\hat{\mathbf{M}}_r = \hat{a}\hat{N}\,\mathbf{M}_r$. The assumption of fully developed sliding on the contact area F is made. We consider that the deformations of moving bodies are small enough to describe the relative motion as a plane motion of rigid bodies. As the result the motion is described by the following dimensionless linear sliding velocity in centre A: $\mathbf{v}_s = \hat{\mathbf{v}}_s/\hat{a} = v_{sx}\mathbf{e}_x + v_{sy}\mathbf{e}_y$, and the angular sliding velocity: $\mathbf{v}_s = \hat{\mathbf{v}}_s/\hat{a} = v_{sx}\mathbf{e}_x + v_{sy}\mathbf{e}_y$, where $\hat{\mathbf{v}}_s$ and $\hat{\boldsymbol{\omega}}_s$ denote the corresponding real counterparts and $\mathbf{e}_x$, $\mathbf{e}_y$ and $\mathbf{e}_z$ are the unit vectors of the corresponding axes. We apply the Coulomb friction law on each element dF of the area F

$$d\mathbf{T}_s = d\hat{\mathbf{T}}_s/(\mu\hat{N}) = -\sigma(x,y)dF\,\mathbf{v}_P/\|\mathbf{v}_P\|, \tag{5}$$

where $d\mathbf{T}_s$ and $d\hat{\mathbf{T}}_s$ are elementary non-dimensional friction force and its real counterpart, respectively. $\mathbf{v}_P$ is the local dimensionless velocity of sliding and μ—dry friction coefficient. The moment of the friction force $d\mathbf{T}_s$ about the centre A of the contact is described as follows:

$$d\mathbf{M}_s = \boldsymbol{\rho} \times d\mathbf{T}_s = d\hat{\mathbf{M}}_s / (\hat{a}\mu\hat{N}), \tag{6}$$

where $d\hat{\mathbf{M}}_s$ is the corresponding real moment. Summing up the elementary friction forces $d\mathbf{T}$ and moments $d\mathbf{M}$, we get the total friction force $\mathbf{T}$ acting in the point A and moment $\mathbf{M}$. The resulting integral expressions may possess the singularities in the case of lack of the relative motion. Therefore, we use a small numerical parameter ε_t to the corresponding integral expressions to avoid above-mentioned singularities. Finally we obtain

$$\begin{aligned}
T_{sx} &= \iint_F \sigma(x,y) \frac{(v_{sx} - \omega_s y)}{\sqrt{(v_{sx} - \omega_s y)^2 + (v_{sy} + \omega_s x)^2 + \varepsilon_t^2}} dxdy, \\
T_{sy} &= \iint_F \sigma(x,y) \frac{(v_{sy} + \omega_s x)}{\sqrt{(v_{sx} - \omega_s y)^2 + (v_{sy} + \omega_s x)^2 + \varepsilon_t^2}} dxdy, \\
M_s &= \iint_F \sigma(x,y) \frac{\omega_s (x^2 + y^2) + v_{sy} x - v_{sx} y}{\sqrt{(v_{sx} - \omega_s y)^2 + (v_{sy} + \omega_s x)^2 + \varepsilon_t^2}} dxdy
\end{aligned} \tag{7}$$

The real counterparts of the friction force and moment can be found as $\hat{\mathbf{T}}_s = \mu\hat{N}\,\mathbf{T}_s$ and $\hat{\mathbf{M}}_s = \hat{a}\mu\hat{N}\mathbf{M}_s$, respectively. The above-mentioned expressions (Eq. 7) have the integrals over the contact area and for the numerical simulations they are very time consuming and may be inconvenient. Therefore, we propose the corresponding components of the integral model, basing on special modifications of Padé approximants

$$\begin{aligned}
T_{sx}^{(I)} &= \frac{v_{sx} - b_T c_{0,1,1}^{(x,y)} \omega_s}{\sqrt{\left(|v_s|^{m_T} + b_T^{m_T} |\omega_s|^{m_T}\right)^{2m_T^{-1}} + \varepsilon_t^2}}, \\
T_{sy}^{(I)} &= \frac{v_{sy} + b_T c_{1,0,1}^{(x,y)} \omega_s}{\sqrt{\left(|v_s|^{m_T} + b_T^{m_T} |\omega_s|^{m_T}\right)^{2m_T^{-1}} + \varepsilon_t^2}}, \\
M_s^{(I)} &= \frac{b_M c_{0,0,-1}^{(x,y)} \omega_s - c_{0,1,0}^{(x,y)} v_{sx} + c_{1,0,0}^{(x,y)} v_{sy}}{\sqrt{\left(b_M^{m_M} |\omega_s|^{m_M} + |v_s|^{m_M}\right)^{2m_M^{-1}} + \varepsilon_t^2}},
\end{aligned} \tag{8}$$

where

$$c_{i,j,k}^{(x,y)} = \iint\limits_F x^i y^j \left(x^2 + y^2\right)^{-\frac{k}{2}} \sigma(x,y)\, dxdy. \tag{9}$$

Full set of relations and expressions can be found in the work [5].

Using the proposed model of contact pressure distribution (Eq. 1) we get

$$c_{0,1,1}^{(x,y)} = \frac{3}{32}\pi d_s,\ c_{1,0,1}^{(x,y)} = \frac{3}{32}\pi d_c,\ c_{0,0,-1}^{(x,y)} = \frac{3}{16}\pi,\ c_{0,1,0}^{(x,y)} = \frac{1}{5}d_s,\ c_{1,0,0}^{(x,y)} = \frac{1}{5}d_c \tag{10}$$

Model presented in (Eq. 8) has the constant parameters: b_T, m_T, b_M and m_M, which can be found by the process of optimization of the approximate model to the integral components. Those parameters may be identified experimentally as well. For this work we propose the following objective functions:

$$F_T(b_T, m_T) = \int\limits_D \left(\left(T_{sx} - T_{sx}^{(I)}\right)^2 + \left(T_{sy} - T_{sy}^{(I)}\right)^2\right) dD,$$

$$F_M(b_M, m_M) = \int\limits_D \left(M_s - M_s^{(I)}\right)^2 dD. \tag{11}$$

where D is the representative area of model's kinematic parameters. Above expressions result in the following set of optimal parameters: $b_T = 0.771$, $m_T = 2.655$, $b_M = 0.419$ and $m_M = 3.073$.

Finally, using expressions (Eq. 10) and the simplified model (Eq. 8) adding a small parameter to avoid singularities, we get the following form of total friction force and moment:

$$T_{sx\varepsilon}^{(I)} = \frac{v_{sx} - \frac{3}{32}\pi b_T d_{s\varepsilon}\omega_s}{\sqrt{\left(|v_s|^{m_T} + b_T^{m_T}|\omega_s|^{m_T}\right)^{2m_T^{-1}} + \varepsilon_t^2}},$$

$$T_{sy\varepsilon}^{(I)} = \frac{v_{sy} + \frac{3}{32}\pi b_T d_{c\varepsilon}\omega_s}{\sqrt{\left(|v_s|^{m_T} + b_T^{m_T}|\omega_s|^{m_T}\right)^{2m_T^{-1}} + \varepsilon_t^2}}, \tag{12}$$

$$M_{s\varepsilon}^{(I)} = \frac{\frac{3}{16}\pi b_M \omega_s - \frac{1}{5}d_{s\varepsilon}v_{sx} + \frac{1}{5}d_{c\varepsilon}v_{sy}}{\sqrt{\left(b_M^{m_M}|\omega_s|^{m_M} + |v_s|^{m_M}\right)^{2m_M^{-1}} + \varepsilon_t^2}}.$$

3 Modelling the Rigid Body on the Vibration Table

In this paper, we propose the application of the friction model presented in (Eq. 12) as the rigid body lying on the vibration table. Rigid body is assumed to be a ball (for example the billiard ball), situated on the table, which is allowed to make vibrations in x and y direction. Those vibrations have influence on the movement of the ball. We assume that the table can be rotated around x or y axis with angle α, which result in the external force $\mathbf{F}_g$ acting on the body. Model is presented in Fig. 1, where the following notation is used: $\mathbf{v}$—velocity of the ball centre O; $\hat{\mathbf{v}}_\mathbf{r}$—linear rolling velocity; $\hat{\mathbf{v}}_\mathbf{s}$—linear sliding velocity at the point A; $\hat{\boldsymbol{\omega}}_s$—angular sliding velocity; $\hat{\mathbf{T}}_{s\varepsilon}$—the resultant friction force acting at the contact centre A; $\hat{\mathbf{N}} = \hat{N}\mathbf{e}_z$—the normal reaction acting on the ball; $\hat{\mathbf{M}}_{s\varepsilon}$—moment of friction forces; $\hat{\mathbf{M}}_{r\varepsilon}$—moment of rolling resistance. It is assumed that a rigid ball rolls and slides over the vibration table, then $\hat{\mathbf{v}}_\mathbf{r} = \mathbf{v}$.

The analyzed dynamical system has five degrees of freedom and is governed by the following set of differential equations:

$$m\frac{d\mathbf{v}}{dt} = \hat{\mathbf{T}}_{s\varepsilon} + \mathbf{F}_g,\ \mathbf{B}\frac{d\boldsymbol{\omega}}{dt} = \mathbf{r}\times\hat{\mathbf{T}}_{s\varepsilon} + \hat{\mathbf{M}}_{s\varepsilon} + \hat{\mathbf{M}}_{r\varepsilon}. \tag{13}$$

where $\mathbf{r} = \overrightarrow{OA}$, m is the mass of the ball, $\mathbf{B}$ is a tensor of inertia in the mass centre O. The matrix representation of the Eq. 13 can be presented as

$$\mathbf{v} = \begin{bmatrix} v_x \\ v_y \\ v_z \end{bmatrix},\ \boldsymbol{\omega} = \begin{bmatrix} \omega_x \\ \omega_y \\ \omega_z \end{bmatrix},\ \mathbf{r} = \begin{bmatrix} 0 \\ 0 \\ -r \end{bmatrix},\ \hat{\mathbf{T}}_{s\varepsilon} = \mu mg\cos(\alpha)\begin{bmatrix} T_{sx\varepsilon} \\ T_{sy\varepsilon} \\ 0 \end{bmatrix},\ \mathbf{F}_g = \begin{bmatrix} mg\sin(\alpha) \\ 0 \\ 0 \end{bmatrix},$$

$$\hat{\mathbf{M}}_{s\varepsilon} = \hat{a}\mu mg\cos(\alpha)\begin{bmatrix} 0 \\ 0 \\ M_{s\varepsilon} \end{bmatrix},\ \hat{\mathbf{M}}_{r\varepsilon} = \hat{a}mg\cos(\alpha)\begin{bmatrix} M_{rx\varepsilon} \\ M_{rx\varepsilon} \\ 0 \end{bmatrix},\ \mathbf{B} = \begin{bmatrix} B & 0 & 0 \\ 0 & B & 0 \\ 0 & 0 & B \end{bmatrix} \tag{14}$$

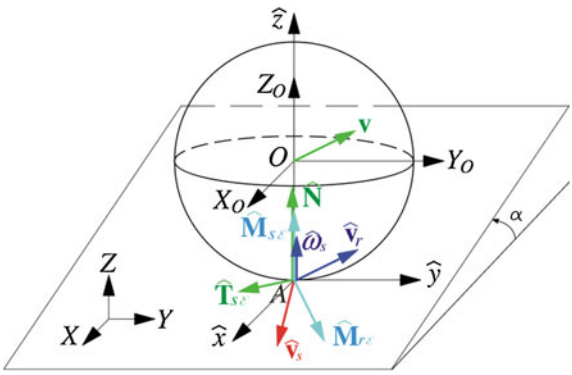

Fig. 1 Rigid body and the vibration table contact area

with the assumption that ball is homogenous and $B = 2/5mr^2$ is the central inertia moment of the body.

The dynamical system in the Cartesian coordinate system $Axyz$ is represented by the two scalar differential equations for the linear motion

$$\frac{dv_x}{dt} = -\mu g\cos(\alpha)T_{sx\varepsilon} + g\sin(\alpha),\ \frac{dv_y}{dt} = -\mu g\cos(\alpha)T_{sy\varepsilon}. \tag{15}$$

Since the permanent contact of the ball with the table is assumed, the third equation is $dv_z/dt = 0$. The angular motion of the billiard ball is governed by the following equations:

$$\frac{d\omega_x}{dt} = -\frac{5}{2}\frac{g\cos(\alpha)}{r}\left(\mu T_{sy\varepsilon} - \frac{1}{r}\hat{a}M_{rx\varepsilon}\right),$$

$$\frac{d\omega_y}{dt} = \frac{5}{2}\frac{g\cos(\alpha)}{r}\left(\mu T_{sx\varepsilon} + \frac{1}{r}\hat{a}M_{ry\varepsilon}\right),\ \frac{d\omega_z}{dt} = -\frac{5}{2}\frac{g\cos(\alpha)}{r^2}\hat{a}\mu M_{s\varepsilon}, \tag{16}$$

where r—radius of the ball; v_x, v_y—the corresponding components of velocity of the ball centre O; ω_x, ω_y, ω_z—components of angular velocity. In the global coordinate system XYZ presented in Fig. 2, X_O and Y_O denote the coordinates of the ball centre O. To compute the absolute position of the ball centre, we use the following expressions:

$$\frac{dX_O}{dt} = v_x,\ \frac{dY_O}{dt} = v_y. \tag{17}$$

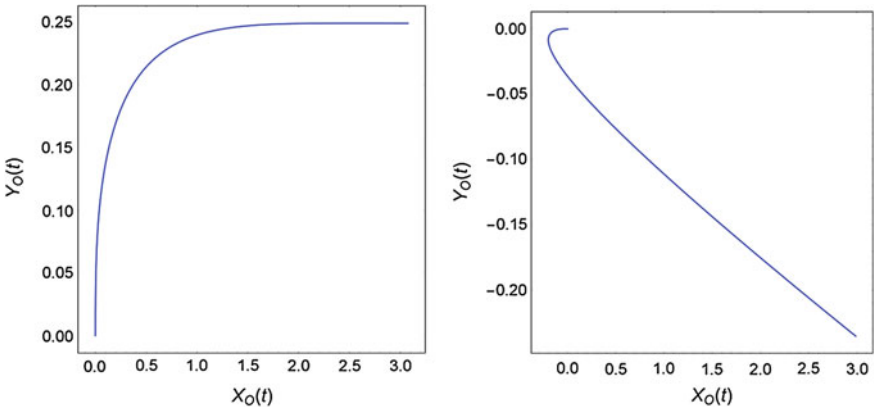

Fig. 2 Simulations of rigid body's movement

The following relations can be used for calculations of the arguments of the above-presented models of friction, in the case of no vibrations of the table:

$$v_{sx} = \frac{v_x - r\omega_y}{\hat{a}},\ v_{sy} = \frac{v_y + r\omega_x}{\hat{a}},\ v_{rx} = \frac{v_x}{\hat{a}},\ v_{ry} = \frac{v_y}{\hat{a}}. \tag{18}$$

Since, the rigid body is lying on the vibrating table, we apply the vibrations to the dynamical system by changing the expressions (18). We add the vibration parameters to the sliding and rolling velocities of the ball as follows:

$$v_{sx} = \frac{v_x - r\omega_y + A_x cos(\omega_a t)}{\hat{a}},\ v_{sy} = \frac{v_y + r\omega_x + A_y cos(\omega_b t + \varphi_y)}{\hat{a}}$$

$$v_{rx} = \frac{v_x + A_x cos(\omega_a t)}{\hat{a}},\ v_{ry} = \frac{v_y + A_y cos(\omega_b t + \varphi_y)}{\hat{a}}. \tag{19}$$

where A_x, A_y are the amplitudes of the vibrations, ω_a, ω_b are the angular frequencies and φ_y is the phase of the oscillations in y direction.

The results of the simulations of the ball's motion are presented in Fig. 3. We use the model of friction forces (Eq. 12), changing the sliding velocity (Eq. 19) with the following parameters and initial conditions: $\hat{a} = 0.003$ m, $\mu = 0.2$, $d = 1$, $\varepsilon_t = 0.01$, $\varepsilon_r = 0.01$, $g = 9.81$ m/s^2, $r = 0.02$ m, $m_T = 2.655$, $m_M = 3.073$, $b_T = 0.771$, $b_M = 0.419$, $X_O(0) = 0$, $Y_O(0) = 0$, $\alpha_x(0) = 20$, $\alpha_y(0) = 0$, $\alpha_z(0) = 0$, $v_x(0) = 0$, $v_y(0) = 0.4$. For the simulations presented in Fig. 2, the following other parameters were used for the graph on the left: $A_x = 1$, $A_y = 0.5$, $\omega_a = 1000$ rad/s, $\omega_b = 500$ rad/s, $\varphi_y = 0$; and for the right graph: $A_x = 1000$, $A_y = 800$, $\omega_a = 1500$ rad/s, $\omega_b = 1200$ rad/s, $\varphi_y = 1$. Table was rotated around y axis resulting.

For the simulations presented in Fig. 3, the following parameters were used for the top left graph: $A_x = 1$, $A_y = 1$, $\omega_a = 1000$ rad/s, $\omega_b = 500$ rad/s, $\varphi_y = 0$; for the top right graph: $A_x = 1$, $A_y = 3$, $\omega_a = 1200$ rad/s, $\omega_b = 1000$ rad/s, $\varphi_y = 1$; for the bottom left graph: $A_x = 1$, $A_y = 1$, $\omega_a = 2000$ rad/s, $\omega_b = 1000$ rad/s, $\varphi_y = 1$; finally for the bottom right graph: $A_x = 1$, $A_y = 1$, $\omega_a = 800$ rad/s, $\omega_b = 1500$ rad/s, $\varphi_y = 0.5$ and table was rotated around x axis.

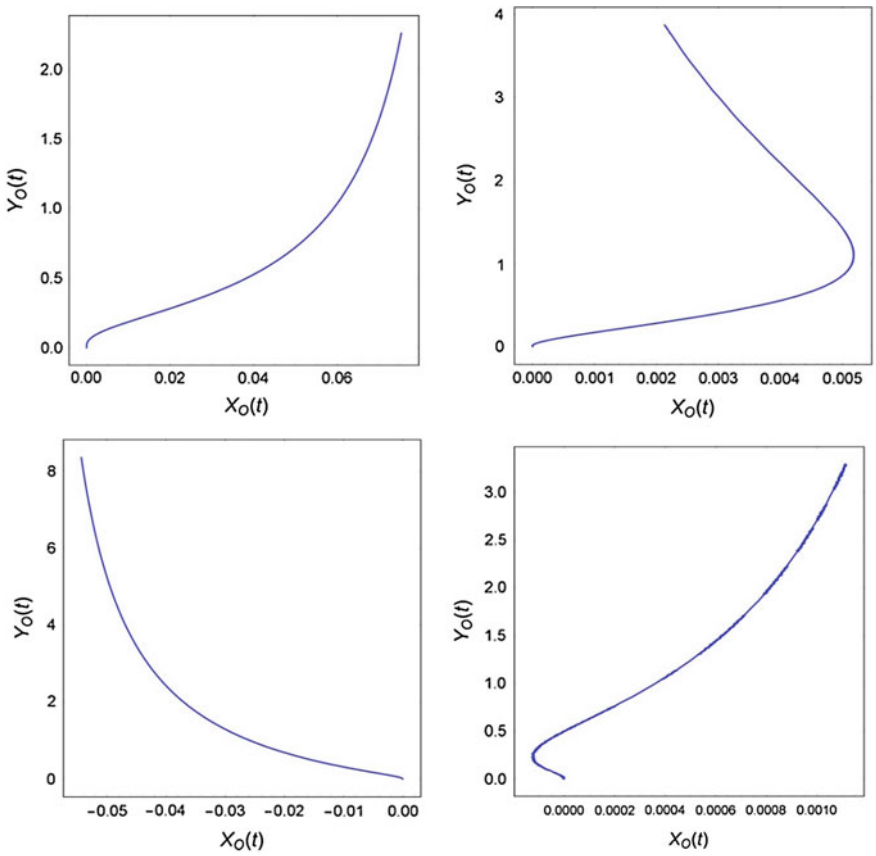

Fig. 3 Simulations of rigid body's movement

4 Conclusions

This work presents the possible implementation of the model of the resultant contact forces. Due to the complexity of computation of the integrals over the contact area, the authors proposed a model for the numerical simulations, which is based on Padè approximant. Possible application of the model is a dynamical system consisting of a rigid body (billiard's ball) lying on a vibrating table. By manipulating the oscillations of the vibrating table, different balls' movements have been achieved. Results presented in this paper may be a good starting point for the verification of the presented model not only by numerical simulations, but with the real object as well. Developing such a dynamical system and its technical implementation may be the authors' object of interest in future.

Acknowledgments The work has been supported by the Polish National Science Centre, MAESTRO 2, No. 2012/04/A/ST8/00738.

References

1. Macmillan W.D., *Dynamics of Rigid Bodies*. McGraw-Hill, New York, 1936.
2. Contensou P., *Couplage entre frottement de glissement et de pivotement dans la téorie de la toupe*, In: Ziegler H. (Ed.), Kreiselprobleme Gyrodynamic, IUTAM Symposium Celerina, Springer, Berlin, 1962, pp. 201–216.
3. Zhuravlev V.P., The model of dry friction in the problem of the rolling of rigid bodies, *Journal of Applied Mathematics and Mechanics*, 62(5), 1998, pp. 705–710.
4. Kudra G., Awrejcewicz J., "Application and experimental validation of new computational models of friction forces and rolling resistance", *Acta Mechanica*, 2015, pp. 2831–2848.
5. Kudra G., Awrejcewicz J., "Approximate modelling of resulting dry friction forces and rolling resistance for elliptic contact shape", *European Journal of Mechanics A/Solids*, 42, 2013, pp. 358–375.
6. Kudra G., Szewc M., Wojtunik I., Awrejcewicz J. "Shaping the trajectory of the billiard ball with approximations of the resultant contact forces", *3rd Int. Conference on Mechatronics—Ideas for Industrial Applications*, May 11–13, Gdansk, 2015.
7. Kudra G., Szewc M., Wojtunik I., Awrejcewicz J. "On some approximations of the resultant contact forces and their applications in rigid body dynamics", *International Conference on Structural Engineering Dynamics (ICEDyn 2015)*, June 22–24, Portugal, 2015.
8. Borisov A.V., Karavaev Y. L., Mamaev I.S., Erdakova N. N., Ivanova T. B., Tarasov V. V. "Experimental Investigation of the Motion of a Body with an Axisymmetric Base Sliding on a Rough Plane", *Regular and Chaotic Dynamics,* 2015, Vol. 20, No. 5, pp. 518–541.
9. A. A. Kireenkov, "Combined model of sliding and rolling friction in dynamics of bodies on a rough plane", *Mechanics of Solids*, 43, 3, 2008, pp. 412–425.
10. Szewc, M., Wojtunik, I., Kudra, G, Awrejcewicz J. "Dynamics simulations of a rigid body lying on a vibrating table with the use of special approximations of the resulting contact forces", *13th International Conference Dynamical Systems Theory and application*, December 7–10, 2015 Lodz, Poland.

Analysis of a Constrained Two-Body Problem

Wojciech Szumiński and Tomasz Stachowiak

Abstract We consider the system of two material points that interact by elastic forces according to Hooke's law and their motion is restricted to certain curves lying on the plane. The nonintegrability of this system and idea of the proof are communicated. Moreover, the analysis of global dynamics by means of Poincaré cross sections is given and local analysis in the neighborhood of an equilibrium is performed by applying the Birkhoff normal form. Conditions of linear stability are determined and some particular periodic solutions are identified.

1 Introduction

Seeking exact solutions of nonlinear dynamical systems is a task to which physicists, engineers and mathematicians have devoted much of their time over the centuries. But to date, only a few particular examples of real importance have been found. In a typical situation, nonlinear equations of motion are nonintegrable and hence we have little or no information about qualitative and quantitative behavior of their solutions. However, a very useful tool to overcome these difficulties is the so-called Birkhoff normalization. The idea of this treatment, which is used in Hamiltonian systems, goes back to Poincaré and it was broadly investigated by Birkhoff in [1]. It is mainly based on the simplification of the Hamiltonian expanded as a Taylor series in the neighborhood of an equilibrium position by means of successive canonical transformations. Using the Birkhoff normalization one can: determine stability of equilibrium solutions; find approximation of analytic solutions of Hamiltonian equations; and identify families of periodic solutions with given winding numbers.

W. Szumiński (✉)
Institute of Physics, University of Zielona Góra, Licealna 9, 65-407
Zielona Góra, Poland
e-mail: uz88szuminski@gmail.com

T. Stachowiak
Center for Theoretical Physics, Polish Academy of Sciences, Al. Lotników 32/46, 02-668
Warsaw, Poland
e-mail: stachowiak@cft.edu.pl

© Springer International Publishing Switzerland 2016

J. Awrejcewicz (ed.), *Dynamical Systems: Theoretical and Experimental Analysis*, Springer Proceedings in Mathematics & Statistics 182, DOI 10.1007/978-3-319-42408-8_29

The aim of this paper is the analysis of dynamics of the system of two material points that interact by elastic force and can only move on some curves lying on the plane. At first in order to get a quick insight into the global dynamics of the considered system, we make a few Poincaré cross sections for generic values of parameters. Moreover, we communicate the nonintegrability result and give the idea of their proof. Next, we look for equilibria of the system and we make the local analysis in their neighborhood by means of Birkhoff normal form. In particular we look for values of parameters for which equilibrium is linearly stable, we plot resonance curves and look for periodic solutions corresponding to them.

2 Description of the System and Its Dynamics

In Fig. 1 the geometry of the system is shown. It consists of two masses m_1 and m_2 connected by a spring with elasticity coefficient k. The first mass, m_1, moves on an ellipse parametrized by $\boldsymbol{r} = (a\cos\varphi, b\sin\varphi)^T$, while the second one, m_2, moves along the straight line parallel to the x-axis and shifted from it by the distance d. The Lagrange function corresponding to this model is as follows

$$L = \frac{1}{2}m_1\left(b^2\cos^2\varphi + a^2\sin^2\varphi\right)\dot{\varphi}^2 + \frac{1}{2}m_2\dot{x}^2 - \frac{1}{2}k\left[(x - a\cos\varphi)^2 + (d - b\sin\varphi)^2\right]. \quad (1)$$

In order to have invertible Legendre transformation, we assume that the condition $m_1 m_2 \neq 0$ is always satisfied. Thus, the Hamiltonian function can be written as

$$H = \frac{p_\varphi^2}{2m_1(b^2\cos^2\varphi + a^2\sin^2\varphi)} + \frac{p_x^2}{2m_2} + \frac{1}{2}k\left[(x - a\cos\varphi)^2 + (d - b\sin\varphi)^2\right], \quad (2)$$

and the equations of motion are given by

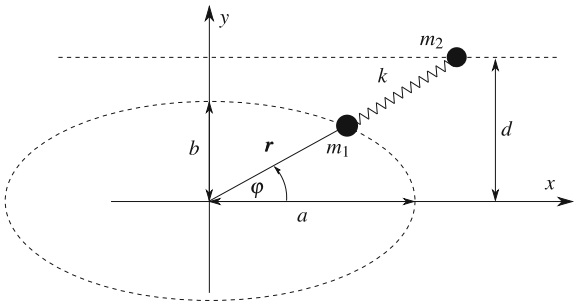

Fig. 1 Geometry of the system

$$\dot{x} = \frac{p_x}{m_2}, \quad \dot{p}_x = -kx + ak\cos\varphi, \quad \dot{\varphi} = \frac{p_\varphi}{m_1(b^2\cos^2\varphi + a^2\sin^2\varphi)},$$
$$\dot{p}_\varphi = \frac{(a^2 - b^2)\sin(2\varphi)p_\varphi^2}{2m_1(b^2\cos^2\varphi + a^2\sin^2\varphi)^2} + [bd + (a^2 - b^2)\sin\varphi]k\cos\varphi - akx\sin\varphi. \tag{3}$$

In order to present the dynamics of the considered model, we made several Poincaré cross sections which are presented in Figs. 2 and 3.

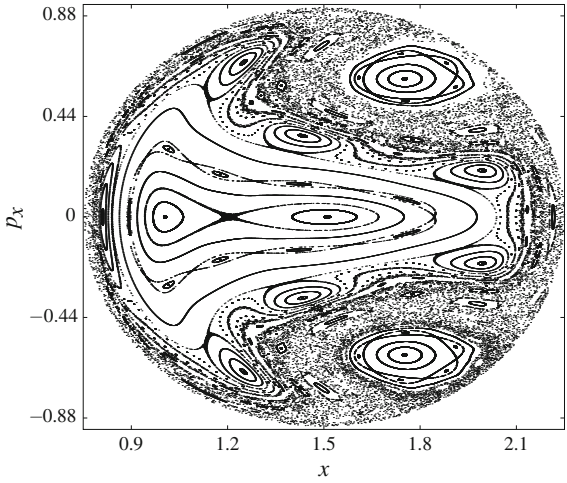

Fig. 2 Poincaré cross section on the surface $\varphi = 0$ with $p_\varphi > 0$ for the values of parameters: $E = 0.28$, $m_1 = 1$, $m_2 = 1.5$, $k = 1$, $a = 1.5$, $b = 1$, $d = 0$

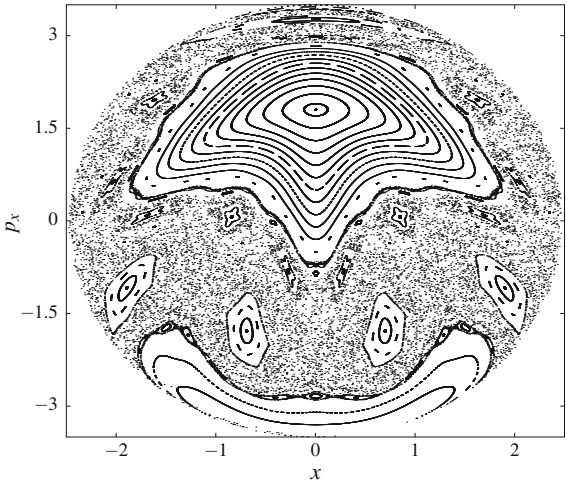

Fig. 3 Poincaré cross section on the surface $\varphi = 0$ with $p_\varphi > 0$ for the values of parameters: $E = 3.2$, $m_1 = 1$, $m_2 = 2$, $k = 1$, $a = 1$, $b = 1.5$, $d = 2$

As we can see, they show that for generic values of parameters and sufficiently large energies the system exhibits chaotic behavior. In fact we can prove the following theorem.

Theorem 1 *The system of two point masses m_1 and m_2, such that $ab(m_1 - m_2) \neq 0$, one moving on an ellipse and the other on the straight line containing a semi-axis of the ellipse, is not integrable in the class of functions meromorphic in coordinates and momenta.*

The proof of the above theorem consists in the direct application of the so-called Morales–Ramis theory that is based on analysis of the differential Galois group of variational equations. They are obtained by linearization of the equations of motion along a particular solution that is not an equilibrium position. For the precise formulation of the Morales–Ramis theory and the definition of the differential Galois group see e.g., [5, 8]. The main theorem of this theory states that if the system is integrable in the Liouville sense, then the identity component of the differential Galois group of variational equations is Abelian, so in particular it is solvable. The technical details of the proof of this theorem are given in [7], where the authors show that for this system these necessary integrability conditions are not satisfied.

3 Stability Analysis—Birkhoff Normalization

Although Hamiltonian (2) turned out to be not integrable, we can deduce some important information about the dynamics from its Birkhoff normal form. But first, in order to minimize the number of parameters and thus simplify our calculations as much as possible, we rescale the variables in H (2) in the following way

$$q_1 = \frac{\pi}{2} - \varphi, \quad p_1 = \frac{\tau}{b^2 m_2} p_\varphi, \quad q_2 = \frac{x}{b}, \quad p_2 = \frac{\tau}{b m_2} p_x, \quad e = \frac{\tau^2}{m_2 b^2} E. \tag{4}$$

Choosing $\tau = \omega_0^{-1}$, where $\omega_0 = \sqrt{k/m_2}$, the dimensionless Hamiltonian takes the form

$$H = \frac{1}{2}\left(\frac{p_1^2}{\alpha(\beta^2 \cos^2 q_1 + \sin^2 q_1)} + p_2^2 + \left(x - \beta \sin q_1\right)^2 + \left(\delta - \cos q_1\right)^2 \right). \tag{5}$$

The new dimensionless parameters (α, β, δ) are defined by

$$\alpha = \frac{m_1}{m_2}, \qquad \beta = \frac{a}{b}, \qquad \delta = \frac{d}{b} - 1. \tag{6}$$

Let us denote $\boldsymbol{x} = (q_1, q_2, p_1, p_2)^T$, and let $\dot{\boldsymbol{x}} = \boldsymbol{v}_H(\boldsymbol{x}) = \boldsymbol{J}\nabla H$ be the Hamiltonian vector field generated by the Hamiltonian (5), then it is easy to verify that the equilibrium

$\dot{\boldsymbol{x}} = 0$ is localized at the origin. Thus, if we assume that H is analytic in the neighborhood of $\boldsymbol{x} = 0$, then we can represent it as a Taylor series

$$H = H_2 + H_3 + H_4 + \cdots + H_j + \cdots, \tag{7}$$

where H_j is a homogeneous polynomial of order j with respect to variables $\boldsymbol{x}$. In our case the second term H_2 is as follows

$$H_2 = \frac{p_1^2}{2\alpha\beta^2} + \frac{p_2^2}{2} + \frac{1}{2}(\beta^2 + \delta)q_1^2 - \beta q_1 q_2 + \frac{q_2^2}{2}. \tag{8}$$

Since H_2 is quadratic form of $\boldsymbol{x}$ it can be written as

$$H_2 = \frac{1}{2}\boldsymbol{x}^T \hat{\boldsymbol{H}} \boldsymbol{x}, \tag{9}$$

where $\hat{\boldsymbol{H}}$ is the symmetric matrix

$$\hat{\boldsymbol{H}} = \begin{pmatrix} \beta^2 + \delta & -\beta & 0 & 0 \\ -\beta & 1 & 0 & 0 \\ 0 & 0 & (\alpha\beta^2)^{-1} & 0 \\ 0 & 0 & 0 & 1 \end{pmatrix}. \tag{10}$$

The Hamilton equations generated by H_2 are a linear system with constant coefficients of the following form

$$\dot{\boldsymbol{x}} = \boldsymbol{A}\boldsymbol{x}, \quad \text{where} \quad \boldsymbol{A} = \boldsymbol{J}\hat{\boldsymbol{H}}. \tag{11}$$

Here $\boldsymbol{J}$ is the standard symplectic form satisfying $\boldsymbol{J} = -\boldsymbol{J}^T$. Considering the eigenvalues of the matrix $\boldsymbol{A}$, we can obtain information about the stability of the linear system (11) near the equilibrium $\boldsymbol{x} = 0$. Following e.g., [3], the necessary and sufficient condition for stability of linear Hamiltonian system is that the matrix $\boldsymbol{A}$ has distinct and purely imaginary eigenvalues, i.e., $\lambda_i = \mathrm{i}\omega_i$, $\lambda_{j+i} = -\mathrm{i}\omega_i$, $i = 1, \ldots, j$, and $\omega_i \in \mathbb{R}$. In our case the characteristic polynomial of $\boldsymbol{A}$ takes the form

$$p(\lambda) = \det[\boldsymbol{A} - \lambda \boldsymbol{I}] = \lambda^4 + \frac{(\alpha + 1)\beta^2 + \delta}{\alpha\beta^2}\lambda^2 + \frac{\delta}{\alpha\beta^2}. \tag{12}$$

Because $p(\lambda)$ is an even function of λ we can substitute $\sigma = \omega^2 = -\lambda^2$, that gives

$$p(\sigma) = \sigma^2 - \frac{(\alpha + 1)\beta^2 + \delta}{\alpha\beta^2}\sigma + \frac{\delta}{\alpha\beta^2}. \tag{13}$$

It is easy to verify that the roots $\sigma_{1,2}$ of Eq. (13) are distinct real and positive only for $\delta > 0$. This implies that the equilibrium is linearly stable for $d > b$, and in this paper we restrict the value of δ to greater than zero.

Next, we want to make the canonical transformation

$$\boldsymbol{x} = \boldsymbol{M}\boldsymbol{X}, \qquad \boldsymbol{M}^T\boldsymbol{J}\boldsymbol{M} = \boldsymbol{J}, \tag{14}$$

such that the Hamiltonian H_2 in the new variables $\boldsymbol{X} = (Q_1, Q_2, P_1, P_2)^T$ takes the form of the sum of two Hamiltonians for two independent harmonic oscillators

$$\mathscr{H}_2 = \frac{1}{2}\omega_1\left(Q_1^2 + P_1^2\right) + \frac{1}{2}\omega_2\left(Q_2^2 + P_2^2\right) = \frac{1}{2}\boldsymbol{X}^T\hat{\boldsymbol{K}}\boldsymbol{X}, \quad \hat{\boldsymbol{K}} = \mathrm{diag}(\omega_1, \omega_2, \omega_1, \omega_2). \tag{15}$$

From Eqs. (11) and (14) we have the following condition for the matrix $\boldsymbol{M}$

$$\boldsymbol{M}\boldsymbol{J}\hat{\boldsymbol{K}} = \boldsymbol{J}\hat{\boldsymbol{H}}\boldsymbol{M}. \tag{16}$$

Then, we look for $\boldsymbol{M}$ as a product $\boldsymbol{M} = \boldsymbol{N}\boldsymbol{L}$, where $\boldsymbol{N}$ transforms $\boldsymbol{A} = \boldsymbol{J}\hat{\boldsymbol{H}}$ into its Jordan form, and $\boldsymbol{L}$ is given by

$$\boldsymbol{L} = \begin{pmatrix} \mathrm{i}\mathbb{I}_{2\times 2} & \mathbb{I}_{2\times 2} \\ -\mathrm{i}\mathbb{I}_{2\times 2} & \mathbb{I}_{2\times 2} \end{pmatrix}, \tag{17}$$

where $\mathbb{I}$ is the unit matrix. Matrix $\boldsymbol{N}$ is built from the eigenvectors of the matrix $\boldsymbol{A}$ corresponding to eigenvalues $\omega_{1,2}$. Choosing appropriate order of eigenvectors in $\boldsymbol{A}$ as well as its lengths we can obtain the real transformation $\boldsymbol{M} = \boldsymbol{N}\boldsymbol{L}$ satisfying the canonical condition $\boldsymbol{M}^T\boldsymbol{J}\boldsymbol{M} = \boldsymbol{J}$, see e.g., [3]. After such transformation H_2 takes the form (15) with characteristic frequencies

$$\begin{aligned} \omega_1 &= \frac{\sqrt{2}\sqrt{(\alpha+1)\beta^2 + \sqrt{(\alpha+1)^2\beta^4 - 2(\alpha-1)\beta^2\delta + \delta^2} + \delta}}{2\beta\sqrt{\alpha}}, \\ \omega_2 &= \frac{\sqrt{2}\sqrt{(\alpha+1)\beta^2 - \sqrt{(\alpha+1)^2\beta^4 - 2(\alpha-1)\beta^2\delta + \delta^2} + \delta}}{2\beta\sqrt{\alpha}}. \end{aligned} \tag{18}$$

As we can notice these frequencies are different in general. However, it is easy to verify that for some specific values of parameters (α, β, δ) they become linearly dependent over the rational numbers. We say that the eigenfrequences $\omega_{1,2}$ satisfy a resonance relation of order k if there exist integers (m, n) such that

$$m\omega_1 + n\omega_2 = 0, \qquad |m| + |n| = k. \tag{19}$$

Figure 4 presents examples of the resonance curves plotted on the parameter plane (δ, α) for the fixed $\beta = 1$. In this figure we use the notation

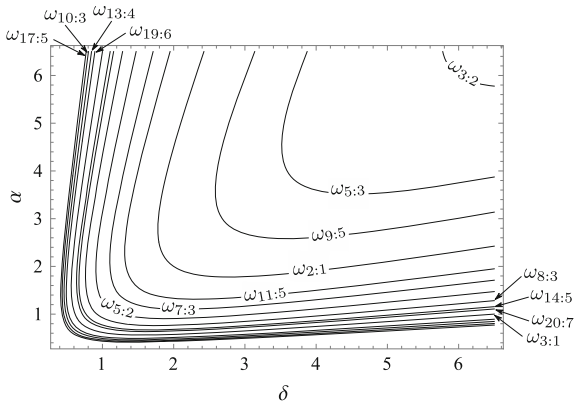

Fig. 4 Examples of resonance curves plotted on the parameter plane for fixed $\beta = 1$

$$\omega_{n:m} := \left\{ (\alpha, \beta, \delta) \in \mathbb{R} \;\middle|\; \frac{\omega_1}{\omega_2} = \frac{n}{m} \right\}. \tag{20}$$

In fact we can obtain the explicit formulae for the resonance. Namely, substituting (18) into (19) and solving with respect to δ, we obtain

$$\delta = \frac{\beta^2 \left(\alpha + \alpha l^4 - 2l^2 \pm \sqrt{\alpha} \left(l^2 + 1 \right) \sqrt{\alpha + \alpha l^4 - 2(\alpha + 2) l^2} \right)}{2l^2}, \quad l = \frac{n}{m}. \tag{21}$$

Limiting the normalization of the Hamiltonian H (5) only to the quadratic part $\mathscr{H}_2$, does not give in general sufficient accuracy of solutions of Hamilton's equations of the original untruncated H. Thus, in order to improve the accuracy we need to take into account the higher order terms of H, and normalize them so that the Hamiltonian and the dynamics become especially simple. We can do this by means of a sequence of nonlinear canonical transformations with some appropriately chosen generating function

$$S = \boldsymbol{P}^T \boldsymbol{q} + W(\boldsymbol{q}, \boldsymbol{P}), \qquad W = W_3 + \cdots + W_K, \tag{22}$$

where

$$W_K = \sum_{\nu_1 + \cdots + \mu_n = K} w_{\nu_1, \ldots \mu_n} q_1^{\nu_1} \cdots q_n^{\nu_n} P_1^{\mu_1} \cdots P_n^{\mu_n},$$

for details consult e.g., [2, 3]. Let

$$\boldsymbol{Q} = \frac{\partial S}{\partial \boldsymbol{P}} = \boldsymbol{q} + \frac{\partial W(\boldsymbol{q}, \boldsymbol{P})}{\partial \boldsymbol{P}}, \qquad \boldsymbol{p} = \frac{\partial S}{\partial \boldsymbol{q}} = \boldsymbol{P} + \frac{\partial W(\boldsymbol{q}, \boldsymbol{P})}{\partial \boldsymbol{q}} \tag{23}$$

be the canonical transformation generated by (22). Then, from the implicit function theorem, in the neighborhood on the equilibrium $\boldsymbol{X} = 0$ we can express $(\boldsymbol{q}, \boldsymbol{p})$ as a functions of $(\boldsymbol{Q}, \boldsymbol{P})$. Namely, one can solve (23) for $\boldsymbol{q}$ and $\boldsymbol{p}$, treating the derivatives as known, and then recursively substitute those expressions into themselves. Because W contains polynomials of degree 3 or higher, the Taylor series is recovered, with the first terms

$$\boldsymbol{q} = \boldsymbol{Q} - \frac{\partial W(\boldsymbol{Q}, \boldsymbol{P})}{\partial \boldsymbol{P}} + \cdots, \qquad \boldsymbol{p} = \boldsymbol{P} + \frac{\partial W(\boldsymbol{Q}, \boldsymbol{P})}{\partial \boldsymbol{Q}} + \cdots. \tag{24}$$

The Hamiltonian function in the new variables is reduced to the Birkhoff normal form $\mathscr{H}_K(\boldsymbol{X})$ of order K, i.e., with all homogeneous terms of degrees up to K normalized so that they Poisson commute with the quadratic part

$$H(\boldsymbol{x}) = \mathscr{H}_K(\boldsymbol{X}) + \mathscr{O}(\boldsymbol{X}^{K+1}), \quad \{\mathscr{H}_K, \mathscr{H}_2\} = 0. \tag{25}$$

Introducing the action-angle variables as the symplectic polar coordinates (I_i, ϕ_i) defined by

$$Q_i = \sqrt{2I_i}\sin\phi_i, \qquad P_i = \sqrt{2I_i}\cos\phi_i, \qquad i = 1, \ldots, n$$

and discarding the non-normalized terms in (25) we obtain the integrable system whose Hamiltonian $\mathscr{H}_K(\boldsymbol{I})$ depends only on actions and whose trajectories will round the tori $\boldsymbol{I} = \text{const}$ with frequencies $\boldsymbol{\Omega} = \partial_{\boldsymbol{I}}\mathscr{H}_K$. Since $\mathscr{H}_K(\boldsymbol{X})$ consist of homogeneous terms of degrees up to K, its Birkhoff normal form can be written in action-angle variables as a polynomial of degree $[K/2]$ in $\boldsymbol{I}$. We can transform H to such form by a sequence of canonical transformations provided eigenfrequences ω_i do not satisfy any resonance relation of order K or less.

The Birkhoff normal form of degree four is given by

$$\mathscr{H}_4 = \omega_1 I_1 + \omega_2 I_2 + h_{20} I_1^2 + h_{11} I_1 I_2 + h_{02} I_2^2, \tag{26}$$

where the coefficients h_{20}, h_{11}, h_{02} related to our system have the form

$$\begin{aligned}
h_{20} &= \frac{\omega_1^2\omega_2^4\left(\omega_1^2-1\right)\left(3\delta\left(\omega_1^2-1\right)\left(\omega_2^2-1\right)+\left(3\omega_2^2+1\right)\omega_1^2-3\omega_2^2+3\right)}{16\delta^2\left(\omega_1^2-\omega_2^2\right)^2\left(\omega_2^2-1\right)},\\
h_{11} &= \frac{\omega_1^3\omega_2^3\left(\left(1-3\omega_2^2\right)\omega_1^2+\omega_2^2-3-3\delta\left(\omega_1^2-1\right)\left(\omega_2^2-1\right)\right)}{4\delta^2\left(\omega_1^2-\omega_2^2\right)^2},\\
h_{02} &= \frac{\omega_1^4\omega_2^2\left(\omega_2^2-1\right)\left(3\delta\left(\omega_1^2-1\right)\left(\omega_2^2-1\right)+3\left(\omega_2^2-1\right)\omega_1^2+\omega_2^2+3\right)}{16\delta^2\left(\omega_1^2-1\right)\left(\omega_1^2-\omega_2^2\right)^2}.
\end{aligned} \tag{27}$$

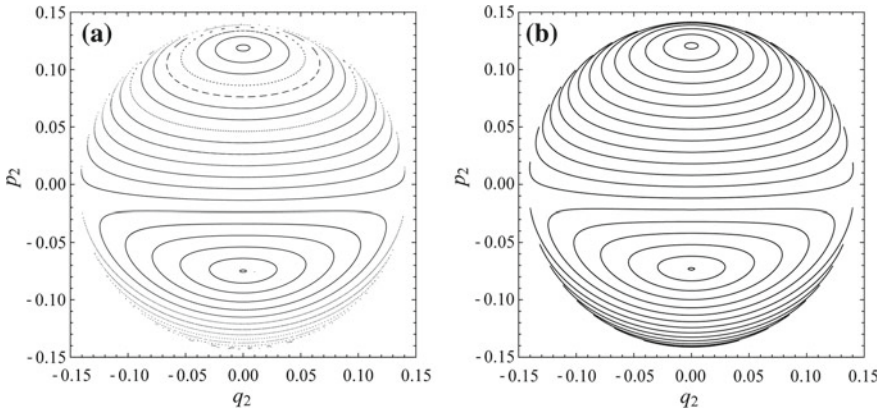

Fig. 5 Poincaré sections on the surface $q_1 = 0$, with $p_1 > 0$

Now let us try to deduce some interesting information from the normalized Hamiltonian (26). First of all, in order to check that the normalization up to order four gives sufficiently good accuracy, we have to compare solutions of Hamilton equations governed by Hamiltonian (26) with (5). We can do this easily for example by comparison of Poincaré cross sections for original Hamiltonian system and its normal form of degree four. Let us note that action variables (I_1, I_2) are the first integrals of the normalized Hamiltonian $\mathscr{H}_4$. We can chose one of them, for example I_1 and make the inverse canonical transformation in order to go back to the original variables $(q_1, q_2, p_1, p_2)^T$. Then for the chosen energy level, we make the contour plot of I_1 restricted to the plane (q_2, p_2) with $q_1 = 0$. Figure 5 presents numerical and analytical Poincaré cross sections constructed for chosen values of parameters belonging to the stability region, namely: $\omega_1 = \omega_1 = 1.75$, $\omega_2 = 0.5$, $\delta = 0.75$, with cross-section plane $q_1 = 0$ and $p_1 > 0$, on the energy level $E = E_{\min} + 0.01$. As expected, for E close to the energy minimum corresponding to an equilibrium both the images are very regular. In fact each of them can be divided into two regions filled by invariant tori around two stable particular periodic solutions. As we can notice, the differences between numerical and analytical computations are not visible. See especially the Fig. 6 showing the superposition of Fig. 5a, b, where for better readability the analytical loops have been plotted in bold gray lines.

As we mentioned previously, the Birkhoff normalization can be also very effective in finding families of periodic solutions. Figures 7, 8 and 9 present contour plots showing examples of such families

- on the (I_1, I_2) plane,
- on the (q_1, q_2) plane with $p_1 = p_2 = 0$,
- on the (q_2, p_2) plane with $q_1 = p_1 = 0$,

respectively, where (Ω_1, Ω_2) are defined by

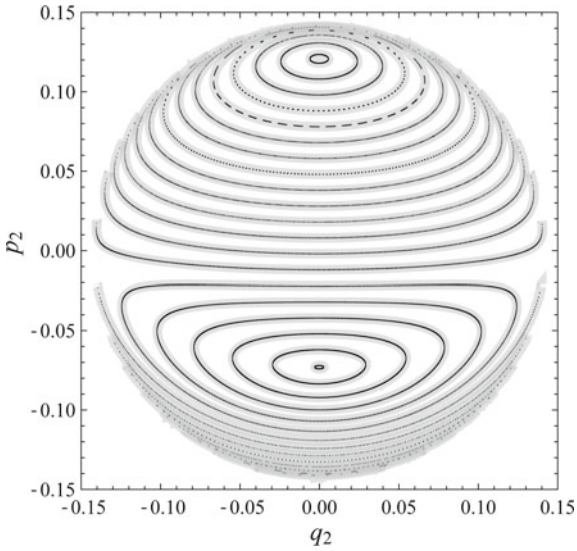

Fig. 6 Superposition of Fig. 5a, b

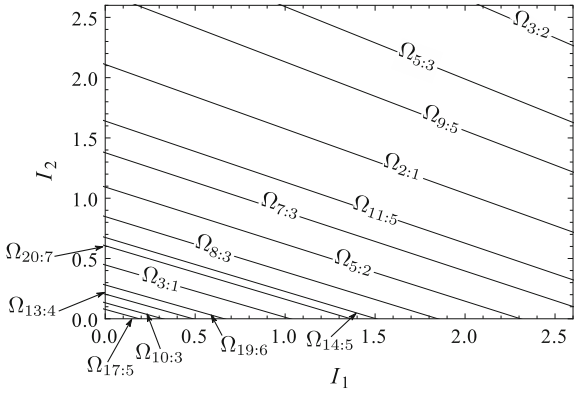

Fig. 7 Contour plot showing the resonance curves on the (I_1, I_2) plane for the fixed values of parameters: $\omega_1 = 1.75$, $\omega_2 = 0.5$, $\delta = 0.75$

$$\Omega_1 = \frac{\partial \mathscr{H}_4}{\partial I_1} = \omega_1 + 2h_{20}I_1 + h_{11}I_2, \quad \Omega_2 = \frac{\partial \mathscr{H}_4}{\partial I_2} = \omega_1 + 2h_{02}I_2 + h_{11}I_1,$$
$$\text{and} \quad \Omega_{n:m} := \left\{ (I_1, I_2) \in \mathbb{R}^2 \;\middle|\; \frac{\Omega_1}{\Omega_2} = \frac{n}{m} \right\}. \tag{28}$$

These figures are very helpful because from them we can read initial conditions for which the motion of the system is periodic. For example, Fig. 10 presents periodic orbits in the configuration space given by the numerical computations with the initial values related to resonances $\Omega_{17:5}$ and $\Omega_{10:3}$, respectively.

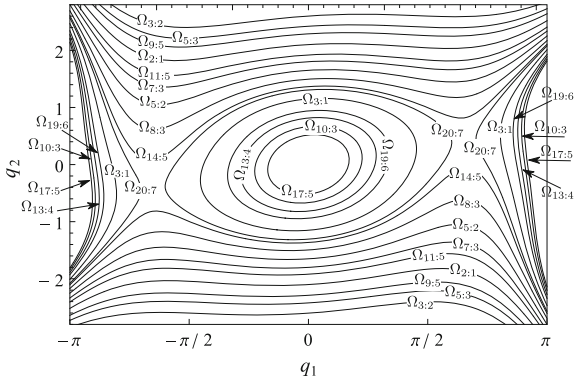

Fig. 8 Contour plot showing the resonance curves on the (q_1, q_2) plane with $p_1 = p_2 = 0$ for the fixed values of parameters: $\omega_1 = 1.75,\ \omega_2 = 0.5,\ \delta = 0.75$

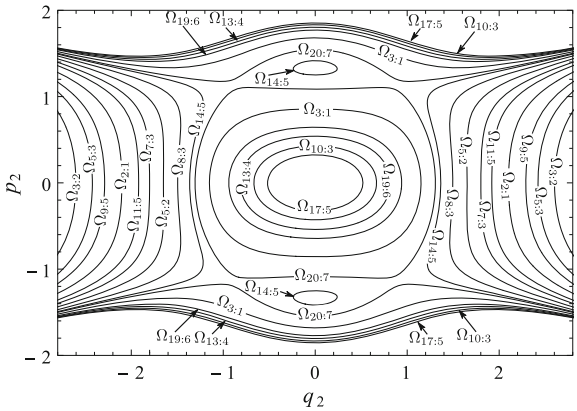

Fig. 9 Contour plot showing the resonance curves on the (q_2, p_2) plane with $q_1 = p_1 = 0$ for the fixed values of parameters: $\omega_1 = 1.75,\ \omega_2 = 0.5,\ \delta = 0.75$

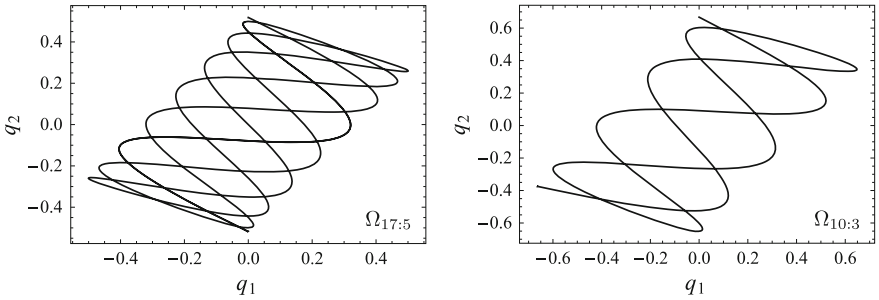

Fig. 10 Examples of trajectories in the configuration space given by the numerical computations with the initial values related to certain resonances presented in Figs. 8 and 9

4 Conclusions

As we have seen, in order to determine stability of equilibrium solution, detect families of periodic solutions as well as find approximation of analytic solutions of equations of motion the Birkhoff normalization proves very useful. However, it is worth mentioning certain inconveniences associated with this method. Namely, it gives us opportunity to investigate behavior of the system over large time intervals, with sufficiently good accuracy, only in the neighborhood of equilibrium. Furthermore, it should be emphasized that the linear stability of the equilibrium $\boldsymbol{x} = 0$ does not imply its stability in the Lyapunov sense. This is due to the fact that the discarded parts of the series can destroy the stability in the long timescale. It would seem that the higher degree normalization should gives us a better approximation of reality. However, in general there does not exist a convergent Birkhoff transformation, see e.g., [6], so the estimation of those terms is not straightforward. To check the nonlinear stability of equilibrium for Hamiltonian vector field $\boldsymbol{v}_H(\boldsymbol{x})$ more involved analysis is necessary, e.g., application of the second Lyapunov method or the Arnold–Moser theorem, which itself relies on normal form, see [4].

Despite these limitations, the Birkhoff normalization is still a very useful source of important information about dynamics and often the starting point of further analysis.

Acknowledgments The work has been supported by grants No. DEC-2013/09/B/ST1/ 04130 and DEC-2011/02/A/ST1/00208 of National Science Centre of Poland.

References

1. Birkhoff, G. D.: Dynamical Systems. American Math Society (1927)
2. Jorba, Á.: A Methodology for the Numerical Computation of Normal Forms, Centre Manifolds and First Integrals of Hamiltonian Systems. Experimental Mathematics. **8**, 155–195 (1999)
3. Markeev, A. P.: Libration Points in Celestial Mechanics and Cosmodynamics, Nauka, Moscow (1978), In Russian
4. Merkin, D. R.: Introduction to the Theory of Stability, Texts in Applied Mathematics, **24**, Springer-Verlag, New York (1997)
5. Morales-Ruiz, J. J.: Differential Galois Theory and Non-Integrability of Hamiltonian Systems, Progress in Mathematics, Birkhauser Verlag, Basel (1999)
6. Perez-Marco, R.: Convergence or generic divergence of the Birkhoff normal form. Ann. of Math. **157**, 557–574 (2003)
7. Szumiński, W., Przybylska, M.: Non-integrability of constrained n-body problems with Newton and Hooke interactions. Work in progress
8. Van der Put, M., Singer, M. F.: Galois theory of linear differential equations, Springer-Verlag, Berlin (2003)

Analysis of the Forces Generated in the Shock Absorber for Conditions Similar to the Excitation Caused by Road Roughness

Jan Warczek, Rafał Burdzik and Łukasz Konieczny

Abstract Damping vibrations occurring within the car's suspension is an indispensable phenomenon in suspension operation. The most common damping element used in the suspension is the hydraulic shock absorber. Modern shock absorbers used in the suspensions mostly have nonlinear characteristics and other complex functional properties. The chapter presents research on hydraulic shock absorbers for similar conditions of their operation. The main aim of the study is to determine the forces generated in the damper due to the impact of road roughness. Thus the simulation studies were carried out on a developed dynamic model of the damper. Defined random signals were used as the input functions, which correspond to the real spectral density of road inequalities. For the proper analysis result, signal processing in the time and frequency domains was conducted. A further objective of the work is to develop guidelines for test methods for the technical conditions under normal operation of shock absorbers built into vehicles.

1 Introduction

A vehicle travelling on the road is subjected to extortion derived from surface irregularities. Safe travelling of all kinds of transport depends on their design, matched on the basis of the criteria adopted in the design phase. In the case of motor vehicles the type of construction of the suspension that is used is influential. Antithetic are goals for car suspensions for maintaining high ride comfort and at the same time a large factor of safety. Large values of suspensions' damping force accordingly ensure the achievement of high security (ensuring a constant wheel

J. Warczek (✉) · R. Burdzik · Ł. Konieczny
Silesian University of Technology, Krasińskiego 8, 40-019 Katowice, Poland
e-mail: jan.warczek@polsl.pl

R. Burdzik
e-mail: rafal.burdzik@polsl.pl

Ł. Konieczny
e-mail: lukasz.konieczny@polsl.pl

© Springer International Publishing Switzerland 2016

J. Awrejcewicz (ed.), *Dynamical Systems: Theoretical and Experimental Analysis*, Springer Proceedings in Mathematics & Statistics 182, DOI 10.1007/978-3-319-42408-8_30

contact with the ground) but on the other hand, affect the deterioration of the ride comfort (i.e. the effect of "stiffening" of suspension fitted with shock absorbers with progressive damping characteristics).

Used in automotive vehicles, shock absorbers have complex functional features that are difficult to reproduce in the form of mathematical models [1–3]. For this reason, there is a need to develop models of car shock absorbers, so that you can reproduce the actual force generated in the silencer while driving on the road. This will allow for development of precise methods for diagnosis, even in the case of random excitations and thus implement such solutions directly to the vehicle.

The use of motor vehicles takes place on roads with different surface conditions, which are most conveniently characterized by spectral density [4–7]. It is assumed then that inequality creates a profile record stationary and ergodic process. Registration of a road profile at a linear speed equal to 1 [m/s] can provide spectral density of inequality as a function, for example, wavelength inequality L_n [m].

A car moving along a given road is subjected to extortion dependent on the state of its surface and the current speed. Power spectral density of roads can be represented as a function of frequency after taking into account an additional parameter which is speed. For this purpose, the scale of abscissae must be multiplied by the driving speed v. To maintain a constant value of the mean square irregularities' amplitude the ordinate scale shall be divided by the value of the speed.

The task of diagnosing a technical object often imposes the need for detection of a disability based on early symptoms of the condition. In practice, this often means the use of the vibroacoustic method for the analysis of low-energy disturbance signals. In this case, a necessary condition is the use of a detailed model which best reflects reality. The aim of the study was to determine the forces generated in the damper due to the impact of road roughness. As part of the work we carried out simulation studies for a developed, detailed, dynamic model of the damper. The appointment of the current and future state of technology allows the use of effective countermeasures. This allows avoiding crashes and motor vehicles with significantly improved safety.

2 Object and Research Method

In the simulation tests of suspension dynamics of motor vehicles a commonly used procedure is to model the shock absorber to a great extent by simplification. The greatest possible simplification of the model attenuation is in the form of a constant damping factor. Depending on the superior order to conduct simulation studies, this approach is often justified, for example, to test vibration control algorithms.

Characteristics of a real damper include being nonlinear and very often not symmetrical with respect to the origin of coordinates.

In the classical models of shock absorber damping characteristics is assumed the uniqueness of the instantaneous value of the force generated by the shock absorber to the instantaneous value of relative motion velocity of the piston and the housing

shock absorber. Thus the formulated assumption implies that the shock absorber is an element for suppressing viscous. When analysing the dynamic forces generated by the actual shock absorber for higher frequency vibrations there is an association between the frequency of extortion and the generated force. In addition, the shock absorber damping force is dependent upon the overall length of the spring force. Such dependence can be seen in the velocity charts obtained during damper tests on the position of the indicator [8]. Thus, the force generated by the shock absorber is the sum of two components: suppression and apparent modulus.

For this reason, it is appropriate to consider the damping characteristics of the shock absorber as a binary function. Based on previous work of the authors, a mathematical shock absorber model was developed which takes into account the apparent resilience of the shock absorber and defines the damping characteristics as a binary function [9, 10]. The achieved procedure allows for the recording of parametric absorber damping properties set within a certain range of variation extortion. The strong dependence of the damping characteristics for the working stroke length determines the need to take account of this phenomenon in computational models of automotive shock absorbers. The relationship describing this phenomenon in general is as follows,

$$F_D = f(v, w_s) \tag{1}$$

where v is the current velocity of extortion and w_s is the total length of the working stroke.

Characteristics of the seeming stiffness of the damper force are a function of frequency and displacement. Thus the seeming stiffness of the damper can be described as

$$F_{ss} = f(d,f) \tag{2}$$

where d is displacement and f is the frequency of extortion.

Consideration of the dependencies described in Eqs. (1) and (2) allows us to introduce the vibration damper model as the surface of a pair of graphs (Figs. 1 and 2). These can be likened to a map of operation of a shock absorber.

Determination of instantaneous values of damping forces and seeming stiffness may be based on such models set by interpolation. When needed determination of the approximate values of the function at points other than nodes and estimation error of the approximate values can be calculated. For this purpose function $F(x)$—called the interpolation function—should be found, which in the nodes of interpolation has the same values as the function $y = f(x)$.

Interpolation is in a sense opposite to the tabulation task of functions. According to the authors the best way to determine the values of the damping forces and seeming stiffness is a two-argument function interpolation using the theory of spline functions.

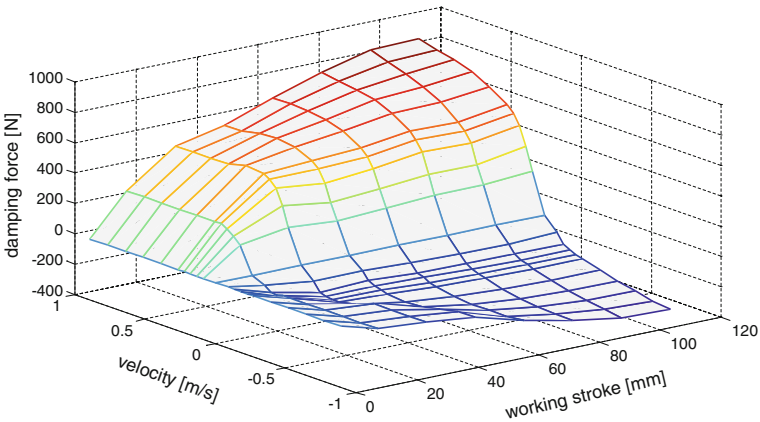

Fig. 1 The surface of damping force

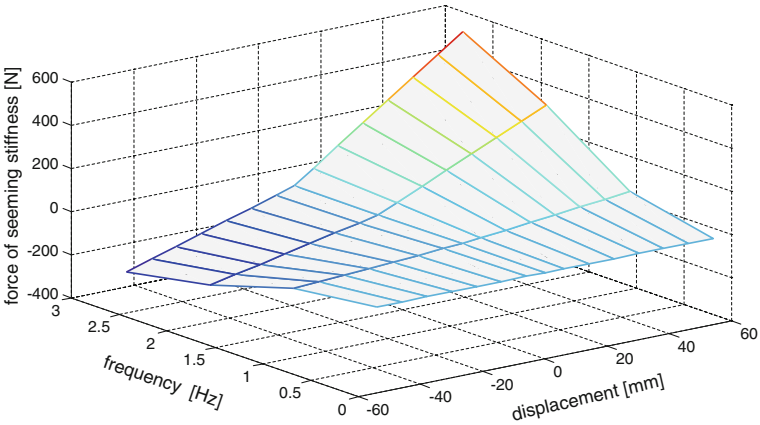

Fig. 2 The distribution of seeming stiffness force

The value of damping force F_D in the concept model of the shock absorber to be determined by interpolation is

$$F_D = f(v, w_s)\colon [a, b, c, d] \to R \tag{3}$$

where limits a, b, c, and d are determined empirically.

The approximation of function values F_D for any arguments

$$v \in [v_0, v_n] \subset [a, b] \text{ and } w_s \in [w_0, w_m] \subset [c, d]$$

It is made for the known values, interpolation nodes which are the results of measurements:

$$f(v, w_s) = \begin{bmatrix} f(v_0, w_0) & f(v_0, w_1) & \dots & f(v_0, w_m) \\ f(v_1, w_0) & \cdot & & \vdots \\ \vdots & & & \\ f(v_n, w_0) & \dots & & f(v_n, w_m) \end{bmatrix} \tag{4}$$

where

$$a \le v_0 \le v_1 \le v_2 \le \dots \le v_n \le b$$

$$c \le w_0 \le w_1 \le w_2 \le \dots \le w_m \le d$$

using a spline function. The force of seeming stiffness F_{ss} is interpolated as

$$F_{ss} = f(d,f)\colon [a, b, c, d] \to R \tag{5}$$

where limits a, b, c, and d are determined empirically.

The approximation of function F_{ss} for any arguments:

$$d \in [d_0, d_n] \subset [a, b] \text{ and } f \in [f_0, f_m] \subset [c, d]$$

for interpolation nodes is

$$f(d,f) = \begin{bmatrix} f(d_0,f_0) & f(d_0,f_1) & \dots & f(d_0,f_m) \\ f(d_1,f_0) & \cdot & & \vdots \\ \vdots & & & \\ f(d_n,f_0) & \dots & & f(d_n,f_m) \end{bmatrix} \tag{6}$$

where

$$a \le d_0 \le d_1 \le d_2 \le \dots \le d_n \le b$$

$$c \le f_0 \le f_1 \le f_2 \le \dots \le f_m \le d$$

using a spline function.

In part associated with the damping of the graphical model, the strong dependence of the damping characteristics of the two variables is clearly visible. This is a decisive prerequisite to the case of testing new solutions; not only velocity but also the working stroke length is important. Similarly, when in operation, examining the condition of the shock absorber, it can't be uniquely determined for changing the length of the working stroke.

The prepared mathematical model of a shock absorber was introduced as a damping element in the quadrant model of vehicle suspension. Simulation studies were carried out in a computing environment, MATLAB®/SIMULINK. The view of the shock absorber model was based on the mathematical description presented in Eqs. (1)–(6) and is shown in Fig. 3.

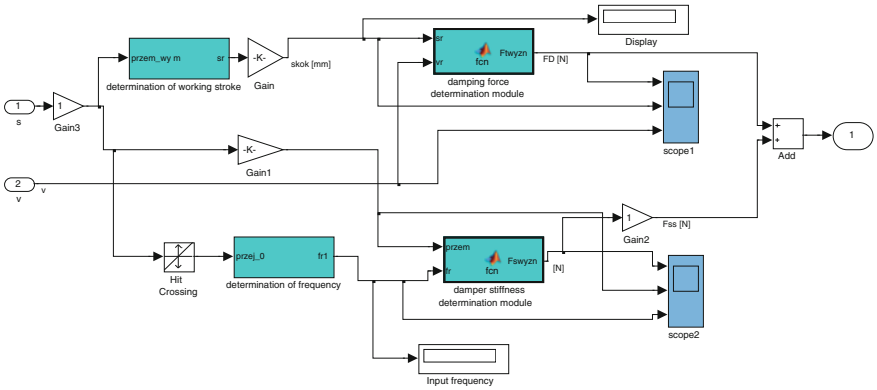

Fig. 3 Shock absorber model in MATLAB/SIMULINK

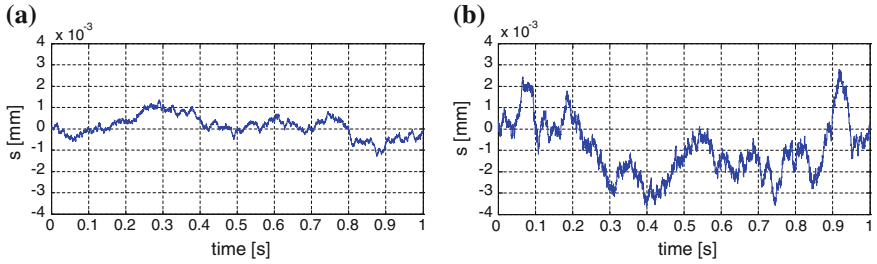

Fig. 4 Timing charts of random excitations used in simulations: **a** good road surface, **b** poor road surface

To determine the forces generated in the vibration damper random extortions were used whose spectral power density roughly corresponded to the actual spectral descriptions of the irregularities of road surfaces. Examples of extortions corresponding to the random inequalities of roads of different categories are shown in Fig. 4.

3 Analysis of the Results

The study simulation allowed us to determine the forces generated in the shock absorber divided into components of damping and resilience and total force. Sample results of simulation of power generated in the shock absorber are shown in Figs. 5 and 6.

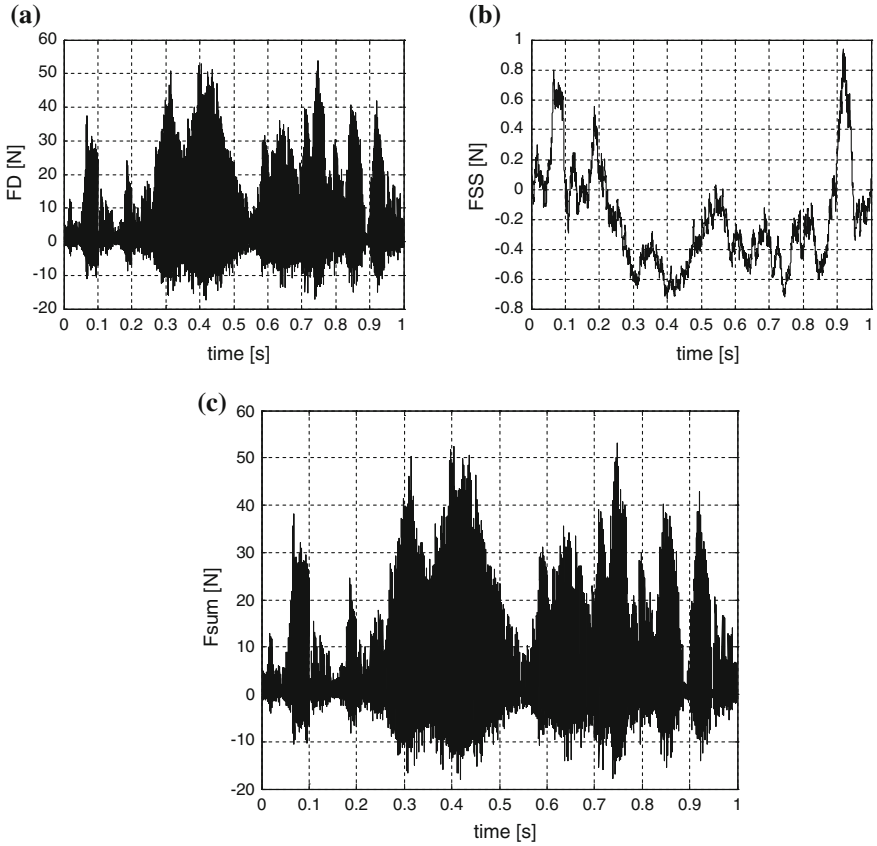

Fig. 5 The forces generated in the shock absorber to extortion corresponding to the road with good surface quality: **a** the damping component, **b** component of elasticity, **c** the resultant force

Analysis of the results in the time domain was due to the impeded high complexity [11, 12]. To emphasize: the useful information obtained from waveform forces arising in the shock absorber was subjected to time-frequency analysis.

Continuous wavelet transform was used to determine time-frequency distribution. The wavelet transformation helped obtain information about both the time and frequency structure of the analysed signal due to the fact that this transformation wavelet function can be either lengthened or shortened. Narrow wavelets enabled the analysis of high-frequency signal components and at the same time long-term base functions revealed slow change features of the signal.

Continuous wavelet transformation of the signal can be defined as

$$CWT_x(a,b) = \frac{1}{\sqrt{a}} \int_{-\infty}^{\infty} x(t) \Psi \left(\frac{t-b}{a} \right) \mathrm{d}t \tag{7}$$

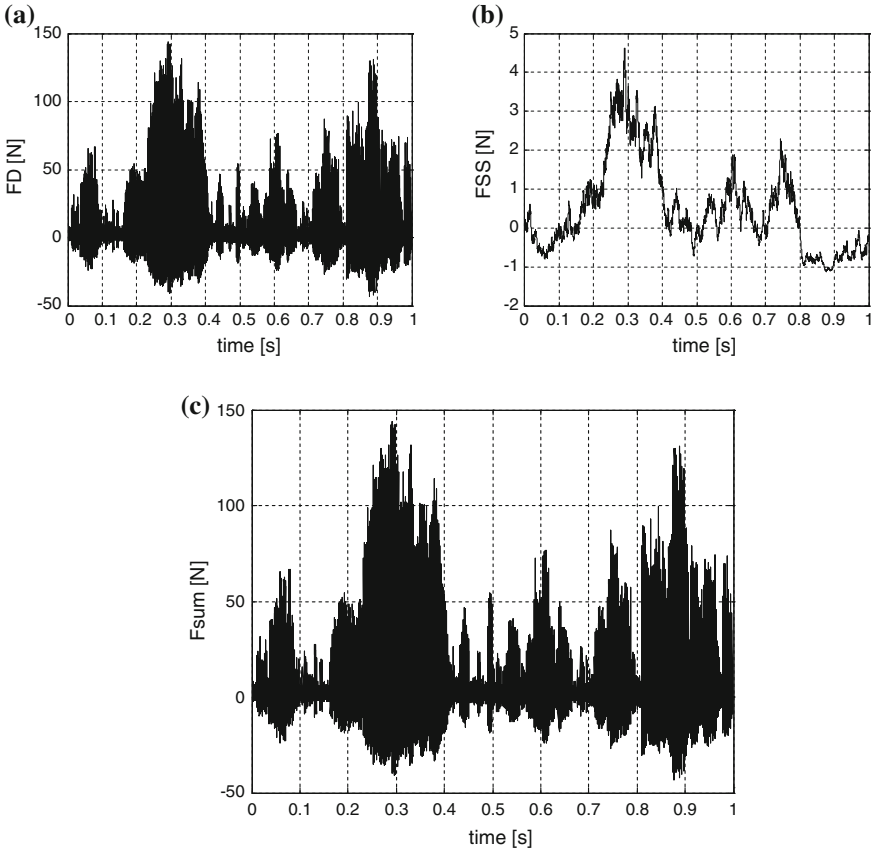

Fig. 6 The forces generated in the shock absorber to the extortion corresponding to the road on poor road surfaces: **a** the damping component, **b** component of elasticity, **c** the resultant force

where

$\Psi(t)$ is the wavelet family, a is the scale parameter $a \in R^+ / 0 \ \wedge \ a \sim \frac{1}{f}, \frac{1}{\sqrt{a}}$ is the scaling factor normalizing the wavelet energy, and b is the translation parameter in time domain $b \in R$.

The wavelet transform represents the correlation between the analysed signal and a scaled function $\Psi(t)$, respectively. The idea of wavelet transformation is to decompose a signal $x(t)$ into wavelet coefficients $WT_x(a, b)$ with the use of a wavelet function. As the result of such transformation wavelet coefficients that are functions of scale and time location are obtained. With the change of scale parameter a and time shift parameter b, respectively, the time-frequency distribution is obtained. The base function of the wavelet transformation is subjected to scaling and translation, which helps obtain wavelets of diverse lifetime and centre frequencies. When the current value of the wavelet centre frequency is considered then the frequencies

corresponding to the analysed scale ranges can be determined. The best results are obtained when wavelets the shape of which matches the primary signal features are used. Obtained distributions of the time-frequency are shown in Figs. 7 and 8.

The signal of forces generated by the shock absorber model working in the DOF model is complex because of the nature of the random force, and because it is the effect of nonlinearity of its characteristics. Furthermore it in the developed model (Eqs. 3–6) into account design features cause a large complexity of the dynamic response of the shock absorber (Figs. 7 and 8). Only the use of time-frequency

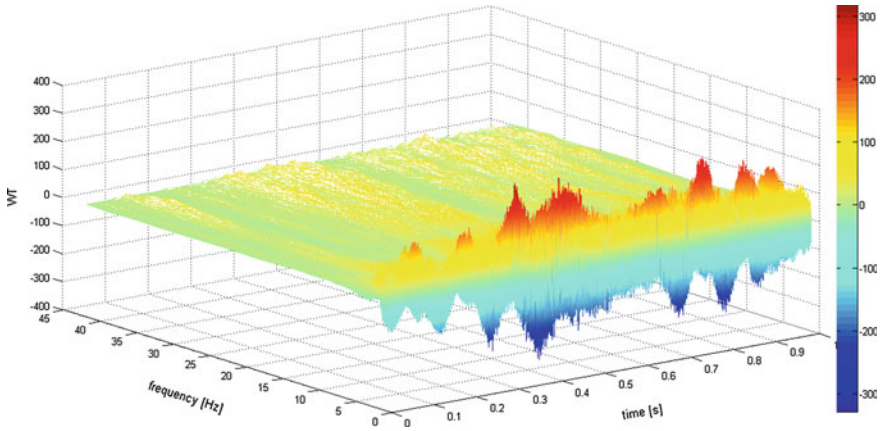

Fig. 7 The wavelet distribution of force for shock-absorber for good road surface

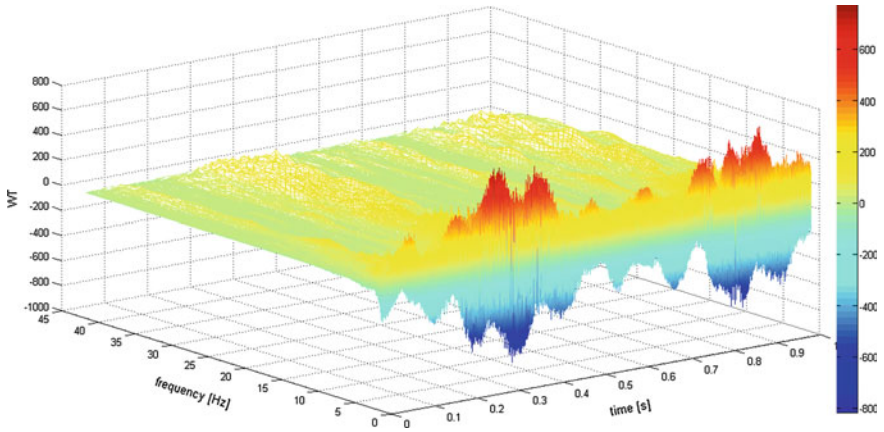

Fig. 8 The wavelet distribution of force for shock-absorber for poor road surface

analysis allows you to look at the nature of the interactions of the dynamic damper. For this reason, it seems appropriate to search for measures of technical conditions of the shock absorber that will take into consideration its complex traits.

4 Summary

Automobile shock absorber operation produces the entire range of dynamic forces affecting the operation of the suspension system. This results in the formation of a complex dynamic state, whose observation in the form of selected physical quantities enables acquisition of signals containing a large amount of information. Obtaining useful information about the technical conditions of the tested shock absorber requires the use of advanced methods of analysis signals. A further objective of the work is the development of guidelines for research methods for the technical conditions of vehicle shock absorbers under normal operating conditions.

References

1. Dixon C. J.: The Shock Absorber Handbook. John Wiley & Sons, Ltd., 2007.
2. Warczek J.: Application of time shift for nonlinear damping characteristic identification. Transport Problems, vol. 4 issue 3 part 2, Gliwice 2009, Poland.
3. Warczek J., Burdzik R., Peruń G.: The method for identification of damping coefficient of the trucks suspension. Smart diagnostics V. Selected, peer reviewed papers from the 5th International Congress of Technical Diagnostics, Krakow, Poland, September 3–5, 2012. Ed. by T. Uhl, Stafa-Zurich, Trans Tech Publications, 2014, s. 281-289, Key Engineering Materials; vol. 588 1662-9795.
4. Barbosa R. S.: Vehicle Vibration Response Subjected to Longwave Measured Pavement Irregularity. Journal of Mechanical Engineering and Automation 2012, 2(2): 17–24.
5. ISO 8608: Mechanical vibration-road surface profiles-Reporting of measured data, International Organization for Standardization, 1995.
6. Bogsjö K., Podgórski K., Rychlik I.: Models for road surface roughness.Vehicle System Dynamics, International Journal of Vehicle Mechanics and Mobility 2012 pp. 725–747.
7. Hartikainen L., Petry F., Westermann S.: Frequency-wise correlation of the power spectral density of asphalt surface roughness and tire wet friction. Wear no.317 (2014) pp. 111–119.
8. Warczek J., Burdzik R., Konieczny Ł.: The concept of multi-parametric diagnostic model of car shock absorber. Diagnostics of Machines. XXXVII Symposium, Wisla, 08.03–13.03.2010,. Faculty of Transport Silesian University of Technology, 2010.
9. Warczek J., Burdzik R.: Visco-elastic model of dynamic of hydraulic damper as a basis for determining the measurement condition. Scientific Papers of Transport. Silesian University of Technology 2010 issue 66.
10. Warczek J., Młyńczak J., Burdzik R., Konieczny Ł.: Simulation of a visco-elastic damper based on the model of the vehicle shock absorber. -Journal of Vibroengineering. 2015 vol. 17 no. 4, pp. 2040–2048.

11. Burdzik R. Research on structure and directional distribution of vibration generated by engine in the location where vibrations penetrate the human organism. Diagnostyka, Vol. 14, Issue 2, 2013, p. 57–61.
12. Burdzik R. Implementation of multidimensional identification of signal characteristics in the analysis of vibration properties of an automotive vehicle's floor panel. Eksploatacja i Niezawodność—Maintenance and Reliability, Vol. 16, Issue 3, 2014, p. 439–445.

A Pendulum Driven by a Crank-Shaft-Slider Mechanism and a DC Motor—Mathematical Modeling, Parameter Identification, and Experimental Validation of Bifurcational Dynamics

Grzegorz Wasilewski, Grzegorz Kudra, Jan Awrejcewicz, Maciej Kaźmierczak, Mateusz Tyborowski and Marek Kaźmierczak

Abstract In this work, we investigate numerically and experimentally the dynamics of a pendulum vertically excited by a crank-shaft-slider mechanism driven by a DC motor. The power supplied to the DC is small enough to observe return influence of the pendulum dynamics on the motor angular velocity. In the performed experiments, the motor is supplied with constant time voltages. A series of experimental periodic solutions allowed to estimate the model parameters and, in the further step, predict bifurcation phenomena observed in the real object.

G. Wasilewski · G. Kudra (✉) · J. Awrejcewicz · M. Kaźmierczak · M. Tyborowski · M. Kaźmierczak
Department of Automation, Biomechanics and Mechatronics,
Lodz University of Technology, 1/15 Stefanowski St., 90-924 Łódź, Poland
e-mail: grzegorz.kudra@p.lodz.pl

G. Wasilewski
e-mail: grzegorz.wasilewski@p.lodz.pl

J. Awrejcewicz
e-mail: jan.awrejcewicz@p.lodz.pl

M. Kaźmierczak
e-mail: 182720@edu.p.lodz.pl

M. Tyborowski
e-mail: 82777@edu.p.lodz.pl

M. Kaźmierczak
e-mail: marek.kazmierczak.1@p.lodz.pl

© Springer International Publishing Switzerland 2016

J. Awrejcewicz (ed.), *Dynamical Systems: Theoretical and Experimental Analysis*, Springer Proceedings in Mathematics & Statistics 182, DOI 10.1007/978-3-319-42408-8_31

1 Introduction

There exist a lot of studies on nonlinear dynamics of mechanical systems composed of pendulums in different configurations, including plane or spatial, single or multiple, and sometimes parametrically excited pendulums. Physicians are particularly interested in those kinds of the dynamical systems, since they are relatively simple but can exhibit almost all aspects and phenomena of nonlinear dynamics. In some cases, an experiment is performed in order to confirm analytical or numerical investigations [1–3]. Sometimes, in order to achieve a good agreement between the model's predictions and experimental data, one must take into account many details concerning physical modeling of the real process [3].

When considering behavior of the real dynamical systems, one can encounter a problem of mutual interactions between the oscillatory system and the energy source of limited power, i.e., nonideal energy source. Belato et al. [4] investigated numerically, the electromechanical system composed of a pendulum excited by a crank-shaft-slider mechanism driven by a DC motor considered as a limited power source. A comprehensive numerical analysis of bifurcational dynamics of a similar mechanical system is presented in [5]. An extensive review on the nonideal vibrating systems one can find in [6].

In the work [7], the authors investigated both numerically and experimentally an electromechanical system consisting of a pendulum suspended on the slider of a crank-slider mechanism driven by a DC motor. Since the power of the motor was relatively high, the angular velocity of the shaft was almost constant. Mathematical modeling of the same system under simplifying assumption of a constant angular velocity of the crank, together with the improved algorithm of the parameters' estimation, is presented in [8].

In the present work, the same structure of the mathematical model as in [7] is used in the analysis of the similar real electromechanical system, but in the case of relatively low power supplied to the DC motor, resulting in more variable angular velocity of the crank. This work is also an extended version of the conference publication [9]. In comparison to the work [9], the identification process has been repeated because of small changes in the experimental rig resulting from certain technical reasons. Moreover some additional parameters (previously assumed as known) have been added to the set of identified parameters (for details see Sect. 4). Further bifurcation analysis and model validation in Sect. 5 have also been extended by additional analysis of some irregular attractors and more detailed analysis of the threshold of chaos near the $u_0 = -8.4$ V.

2 Experimental Rig

Figure 1 presents the experimental setup of mathematical model that will be described in next part of the paper. A voltage generator 1 supplies the low-power DC motor 3. Output shaft of the motor is connected with steel shaft 5 by aluminium

coupling 4. Shaft 5 is embedded in pair of ball bearings 6 that provides alignment of shafts. Ball bearings are mounted on 'L' bracket 7a with additional two brackets in 'C' 7b and 'L' 7c shape that support first one to be more stable. Two aluminium strips 7d act as rails to set 'L' bracket both with ball bearings and with DC motor to set them in right position.

There is also the possibility to change low-power DC motor into other one with higher power. On the other end of shaft 5 there is mounted disk 8. Angular position of disk is measured by the use of encoder 9 (type MHK, 360 steps) supplied by wire 10. Rotational motion of disk is transformed thanks to joint 11 (connecting bar) into linear motion of the slider 12 moving on two horizontal guides 13. To the slider there is mounted bracket with two ball bearings 14 (same type as 5) and shaft 15 inserted into them. On this part there is seated physical pendulum 16. In identical way like disk, angular position of pendulum is measured by two types of encoders. 17 is the same type like in case of measuring position of disk. Encoder 18 (type MAB-analog out, supplied by to batteries 19) is used to perform longer measurement, because encoder 17 (type MHK, 3600 steps) have a high resolution what really quickly fills up available space on PC hard disk. All data from encoders are collected by data acquisition devices 2.

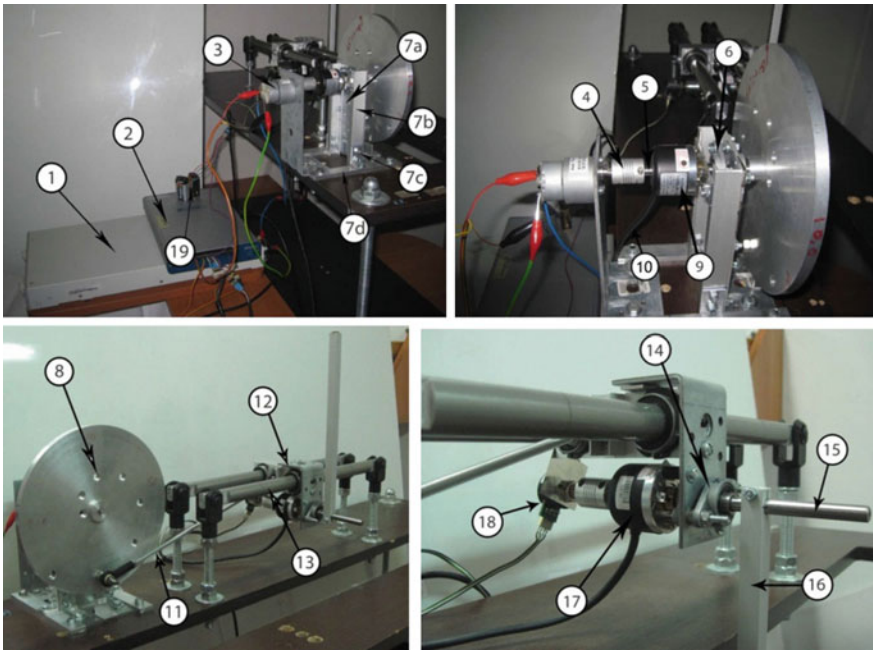

Fig. 1 Experimental setup

3 Mathematical Modeling

In this section, there is presented the mathematical model of the experimental rig presented in Sect. 2. It is based on the results published in the work [7]. Figure 2a exhibits a block diagram presenting the general structure of the system. It is composed of two main subsystems: (i) DC motor (understood as a pure electrical object converting the electrical energy to the mechanical torque; (ii) a two-degree-of-freedom mechanical system including all mechanical elements of the system. The input signal (being under control) is the voltage $u(t)$ supplied to the DC motor. The two coordinates $\theta(t)$ and $\varphi(t)$ determining the position of the mechanical system are assumed to be outputs.

For an armature-controlled DC motor equipped with a gear transmission and assuming that the armature inductance is negligible, one gets the following equation

$$M = \frac{K_T}{R} i_g u - \frac{K_E K_T}{R} i_g^2 \frac{d\theta}{dt}, \tag{1}$$

where M is the torque on the output shaft of the gear transmission, u—input voltage, θ—angular position of the output shaft of the gear transmission, i_g—reduction ratio of the gear transmission, R—armature resistance, K_T—the proportionality constant between the torque generated on the output shaft of the DC motor and the armature current, and K_E—the proportionality constant between the back electromotive force and the angular velocity of the DC motor.

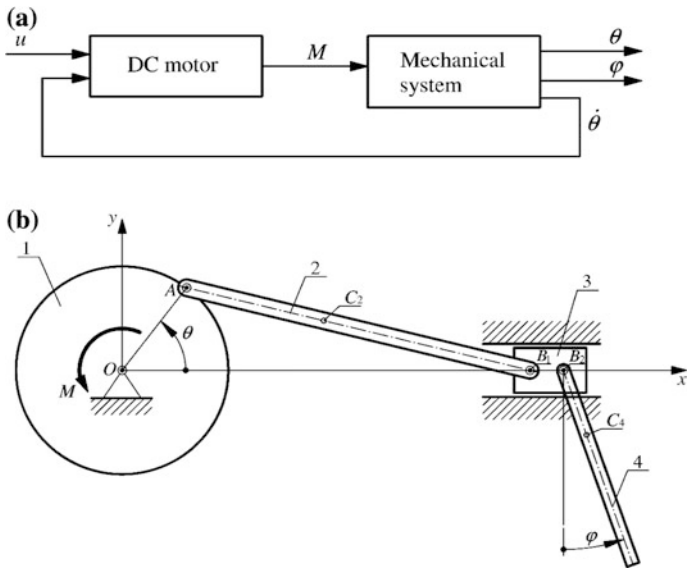

Fig. 2 Physical model of the system

A sketch of a physical model of the mechanical section of the system is depicted in Fig. 2b. This plane two-degree-of-freedom mechanical system is composed of four rigid bodies (1—disk, 2—connecting bar, 3—slider, 4—pendulum) connected by the use of four rotational joints (O, A, B_1, and B_2). Masses of the links 2–4 are denoted as m_b, m_S, and m, respectively. Moments of inertia of the bodies 1, 2, and 4, with respect to their mass centers (located in the points O, C_2, and C_4), are represented by the symbols I_O, I_b, and I, respectively. The corresponding lengths of the mechanical system are denoted as follows: $a = OA$, $b = AB$, $b_1 = AC_2$, and $r = BC_4$. The position of the system is determined by two angles: θ—angular position of the disk (equal to the angular position of the gear transmission output shaft) and φ—angular position of the pendulum. The disk 1 represents all rotating elements of the DC motor, gear transmission, and real disk of the experimental rig.

The governing equations of the investigated system read

$$\mathbf{M}(\mathbf{q})\,\ddot{\mathbf{q}} + \mathbf{N}(\mathbf{q})\dot{\mathbf{q}}^2 + \mathbf{w}(\mathbf{q}) = \mathbf{f}(t) - \mathbf{r}(\mathbf{q},\,\dot{\mathbf{q}}), \tag{2}$$

where

$$\begin{aligned}
&\mathbf{q} = \begin{Bmatrix} \theta \\ \varphi \end{Bmatrix},\ \dot{\mathbf{q}} = \begin{Bmatrix} \dot{\theta} \\ \dot{\varphi} \end{Bmatrix},\ \ddot{\mathbf{q}} = \begin{Bmatrix} \ddot{\theta} \\ \ddot{\varphi} \end{Bmatrix},\ \dot{\mathbf{q}}^2 = \begin{Bmatrix} \dot{\theta}^2 \\ \dot{\varphi}^2 \end{Bmatrix},\\
&\mathbf{M}(\mathbf{q}) = \begin{bmatrix} I_O + a^2\left(F^2(m+m_S) + F_1^2 m_b\right) + \frac{a^2}{b^2}\cos^2\theta\left((b-b_1)^2 m_b + G^2 I_b\right) & -amrF\cos\varphi \\ -amrF\cos\varphi & I + mr^2 \end{bmatrix},\\
&\mathbf{N}(\mathbf{q}) = = \begin{bmatrix} aFH\left(1+\frac{m_S}{m}\right) + aF_1H_1 - \frac{a^2}{2b^2}\,\mathbf{sin2\theta}\left((b-b_1)^2 m_b + G^2 I_b\left(1 - \frac{a^2}{b^2}G^2\,\mathbf{cos^2\theta}\right)\right) & amrF\,\mathbf{sin\varphi} \\ -rH\,\mathbf{cos\varphi} & 0 \end{bmatrix},\\
&\mathbf{w}(\mathbf{q}) = \begin{Bmatrix} \frac{a}{b}(b-b_1)m_b g\cos\theta \\ mgr\sin\varphi \end{Bmatrix},\ \mathbf{f}(t) = \begin{Bmatrix} M(t) \\ 0 \end{Bmatrix},\ \mathbf{r}(\mathbf{q},\dot{\mathbf{q}}) = \begin{Bmatrix} M_{R\theta}(\theta,\dot{\theta}) \\ M_{R\varphi}(\dot{\varphi}) \end{Bmatrix},
\end{aligned} \tag{3}$$

and where one has used the following notation

$$G = \frac{1}{\sqrt{1 - \frac{a^2}{b^2}\sin^2\theta}},\ F = \left(1 + \frac{a}{b}G\cos\theta\right)\sin\theta,\ F_1 = \left(1 + \frac{ab_1}{b^2}G\cos\theta\right)\sin\theta,$$

$$H = am\left(\cos\theta + \frac{a}{b}G\cos 2\theta + \frac{1}{4}\frac{a^3}{b^3}G^3\sin^2 2\theta\right),$$

$$H_1 = am_b\left(\cos\theta + \frac{ab_1}{b^2}G\cos 2\theta + \frac{1}{4}\frac{a^3 b_1}{b^4}G^3\sin^2 2\theta\right). \tag{4}$$

The vector $\mathbf{r}(\mathbf{q}, \dot{\mathbf{q}})$ contains all resistance forces and their components

$$M_{R\theta}(\theta, \dot{\theta}) = c_O\dot{\theta} + \frac{2}{\pi}M_O \arctan(\varepsilon_O\dot{\theta}) + a^2F^2c_S\dot{\theta} - \frac{2}{\pi}aFT_S \arctan(-\varepsilon_S aF\dot{\theta}),$$

$$M_{R\varphi}(\dot{\varphi}) = c_B\dot{\varphi} + \frac{2}{\pi}M_B \arctan(\varepsilon_B\dot{\varphi}), \tag{5}$$

The terms $c_O\dot{\theta}$ and $\frac{2}{\pi}M_O \arctan(\varepsilon_O\dot{\theta})$ represent the viscous damping and dry friction components of the resistance in the joint O, where c_O is viscous damping coefficient, M_O—magnitude of dry friction torque. One assumes that M_O is a constant parameter, independent from the loading of the joint O. The expressions $a^2F^2c_S\dot{\theta}$ and $-\frac{2}{\pi}aFT_S \arctan(-\varepsilon_S aF\dot{\theta})$ represent the viscous damping and dry friction components of resistance between the slider and guide, reduced to the coordinate θ, where c_S and T_S are the corresponding constant parameters. Similarly, the terms $c_B\dot{\varphi}$ and $\frac{2}{\pi}M_B \arctan(\varepsilon_B\dot{\varphi})$ are viscous damping and dry friction components in the joint B_2. The quantities ε_O, ε_S and ε_B are numerical parameters used in the dry friction model regularization. Usually they are relatively large since one wants to approximate accurately the sign function. However it occurs that sometimes the smaller values of these parameters lead to the better results (in the sense of fitting of the simulation results to the experimental data)—one can find an example in the work [8]. In comparison to the work [9], we assume three different parameters ε_O, ε_S, and ε_B (previously they were substituted by one parameter ε). Resistances in the joints A and B_1 are not taken into account.

Finally one gathers the right-hand side of Eq. (6) into one vector

$$\mathbf{f}_r(t, \mathbf{q}, \dot{\mathbf{q}}) = \mathbf{f}(t) - (\mathbf{q}, \dot{\mathbf{q}}) = \\ = \left\{ \begin{array}{c} K_M u(t) - C_O\dot{\theta} - \frac{2}{\pi}M_O \arctan(\varepsilon_O\dot{\theta}) - a^2F^2c_S\dot{\theta} + \frac{2}{\pi}aFT_S \arctan(-\varepsilon_S aF\dot{\theta}) \\ -c_B\dot{\varphi} - \frac{2}{\pi}M_B \arctan(\varepsilon_B\dot{\varphi}) \end{array} \right\}, \tag{6}$$

where

$$K_M = \frac{K_T}{R}i_g,\ C_O = \frac{K_E K_T}{R}i_g^2 + c_O.$$

Let us note, that the mechanical viscous damping in the joint O and the back electromotive force (multiplied by some other constants) have mathematically the same influence on the final torque on the output shaft of the gear transmission. They are mathematically indistinguishable and unidentifiable in the developed model. Their aggregate action is defined by the coefficient C_O.

4 Parameter Estimation

In the process of identification, one has used three experimental solutions, with the input signal $u(t)$ in a form of step function with zero initial value, and constant final value u0, equal to −10.8, −8.0 and −6.5 V, respectively. The initial conditions are the same for all experiments: $\theta(0) = -\frac{\pi}{2}$ rad, $\varphi(0) = 0$ rad, $\dot{\theta}(0) = 0$ rad/s, and $\dot{\varphi}(0) = 0$ rad/s. The solutions tend to periodic attractors, which allows to avoid problems of identification related to high sensitivity to initial conditions. The angles $\varphi(t)$ and $\theta(t)$ were recorded on the time interval [0, 60] s.

Because of nonideal behavior of resistances in the system (small random fluctuations of friction), the angular velocity of the disk undergoes some random changes, which cannot be described by the use of deterministic equations. These changes are not big, but after some time they can lead to significant time shift in the angular position of the disk. It may cause problems in fitting of the simulated signals to those obtained experimentally, if we express them in the time domain. This is the reason of the idea to compare the corresponding signals expressed as functions of angular position of the disk θ.

Since we plan to use in the estimation process two different signals (angular position of the pendulum and angular velocity of the disk), we construct the objective function F_o in the form of weighted sum of two different parts

$$F_O(\boldsymbol{\mu}) = w_\varphi F_{O\varphi}(\boldsymbol{\mu}) + w_\omega F_{O\omega}(\boldsymbol{\mu}), \tag{7}$$

where $\boldsymbol{\mu}$ is vector of the estimated parameters, w_φ and w_ω are the corresponding weights, and where

$$F_{O\varphi}(\boldsymbol{\mu}) = \frac{1}{\sum_{i=1}^{N}\left(\theta_{fi} - \theta_0\right)} \sum_{i=1}^{N} \int_{\theta_0}^{\theta_{fi}} \left(\varphi_{si}(\theta, \boldsymbol{\mu}) - \varphi_{ei}(\theta, \boldsymbol{\mu})\right)^2 d\theta,$$

$$F_{O\omega}(\boldsymbol{\mu}) = \frac{1}{\sum_{i=1}^{N}\left(\theta_{fi} - \theta_0\right)} \sum_{i=1}^{N} \int_{\theta_0}^{\theta_{fi}} \left(\omega_{fsi}(\theta, \boldsymbol{\mu}) - \omega_{fei}(\theta, \boldsymbol{\mu})\right)^2 d\theta. \tag{8}$$

In the expressions (8) N denotes number of the compared pairs of solutions, θ_0 is common initial angle θ, θ_{fi} ($i = 1, 2, \ldots, N$) are final angular positions of the disk, φ_{si} and φ_{ei} are angular positions of the pendulum obtained by the use of i-th numerical simulation and experiment, correspondingly. Since we measure the angular position of the disk, we differentiate this signal with respect to time in order to obtain the corresponding angular velocity. We do it numerically, by passing the signal $\theta_{ei}(t)$ (obtained by the linear interpolation of the experimental data) through the filter of the transfer function $G_f(s) = \frac{s}{\left(T_f s + 1\right)^2}$. As an output we obtain the signal $\omega_{fei}(t)$, which appears in the expressions (8), but as a function of the angle θ. In

order to have the proper simulation signal, which could be compared with the signal ω_{fei}, we also pass through the filter $G_f(s)$ the numerical signal $\theta_{si}(t)$, obtaining $\omega_{fsi}(t)$.

Using the functions (8), one assumes that initial conditions and input signals $u(t)$ are known and they are the same for both the experiment and simulation. Moreover, some parameters' values are easy to obtain by the direct measurements of masses and lengths. They are assumed to be constant during the identification process: $m_b = 0.057\,\text{kg}$, $m_S = 0.777\,\text{kg}$, $m = 0.226\,\text{kg}$, $a = 0.080\,\text{m}$, and $b = 0.300\,\text{m}$. Other parameters assumed to be constant are: $\varepsilon_O = 10^3$, $g = 9.81\,\text{m}\,\text{s}^{-2}$. The remaining parameters (as the elements of the vector $\boldsymbol{\mu}$) will be obtained by minimization of the objective function F_o, using the Nelder–Mead method [10, 11], also known as downhill simplex method. This is commonly used optimization algorithm, implemented in MATLAB and Scilab functions *fminsearch*. One also assumes the following values of the weights and the time constant of the filter: $w_\varphi = 1\,\text{rad}^{-2}$, $w_\omega = 1\,\text{s}^2\,\text{rad}^{-2}$, and $T_f = 0.1\,\text{s}$.

In the estimation process one obtained the following values of the model parameters: $K_M = 3.066 \times 10^{-2}\,\text{N m/V}$, $C_O = 3.003 \times 10^{-2}\,\text{N m s}$, $M_O = 1.937 \times 10^{-2}\,\text{N m}$, $I_O = 5.252 \times 10^{-3}\,\text{kg m}^2$, $I_b = 2.373 \times 10^{-6}\,\text{kg m}^2$, $b_1 = 8.801 \times 10^{-2}\,\text{m}$, $c_S = 2.171 \times 10^{-1}\,\text{N s}$, $T_s = 6.583 \times 10^{-1}\,\text{N}$, $I = 1.426 \times 10^{-3}\,\text{kg m}^2$, $r = 5.417 \times 10^{-2}\,\text{m}$, $c_B = 2.486 \times 10^{-4}\,\text{N m s}$, $M_B = 2.162 \times 10^{-3}\,\text{N m}$, $\varepsilon_S = 27.68$ and $\varepsilon_B = 3.193$. Figure 3 exhibits comparison of four numerical solutions $\varphi(\theta)$ to the model with the corresponding experimental data used during the identification process (only the final parts of the solutions are presented). In Fig. 4, there are presented the comparison of the corresponding solutions $\omega_f(\theta)$. The optimal value of the objective function (7) is 2.298×10^{-3}. Note that in comparison to the work [9] the parameters ε_S and ε_B have been added to the set of the identified parameters, which allow to obtain better modeling results (see the comments in Sect. 1 and the work [8]).

5 Bifurcation Dynamics

Further experimental investigations of the systems showed that it can also exhibit irregular behavior. For example the constant input voltage of −8.51 V leads to irregular dynamics, with full rotations of the pendulum, presented in Fig. 5. These solutions were not used in the identification process because of potential problems related to high sensitivity to initial conditions. However, they are confirmed qualitatively very well by the developed mathematical model and its numerical simulations, as shown in Fig. 5.

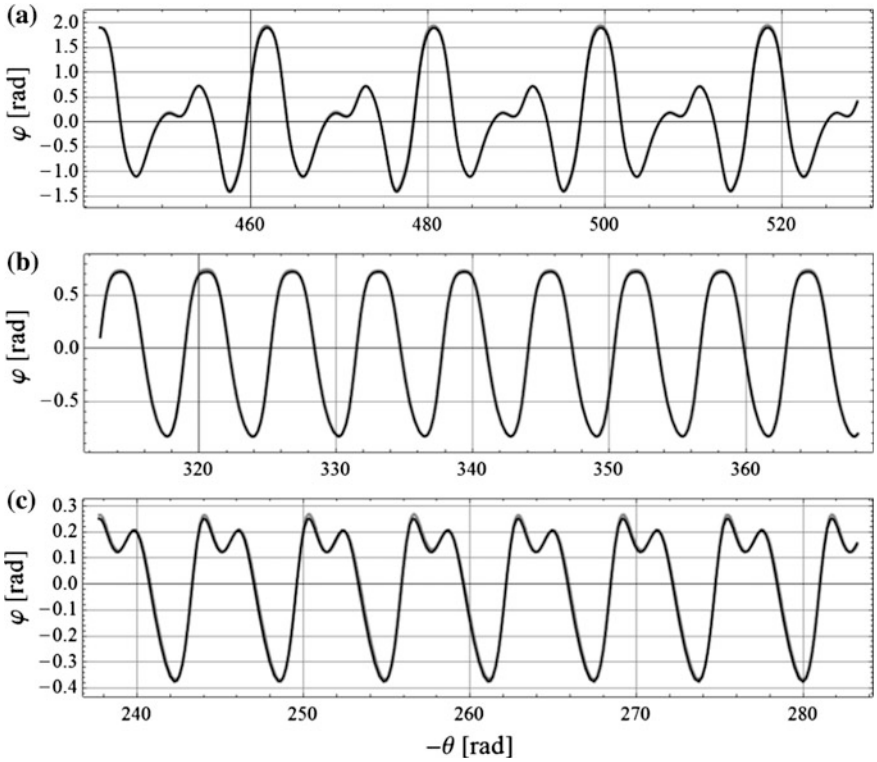

Fig. 3 Three numerical solutions $\varphi(\theta)$ (*black line*) compared with the corresponding experimental data (*gray line*) ($u_0 = -10.8$, -8.0, and -6.5 V, for subfigures **a**, **b**, and **c**, respectively)

In Fig. 6, there are presented the Poincaré sections of exemplary irregular attractors (they are constructed by sampling of the system state at the instances, when the angular position $\theta(t)$ of the disk crosses the zero position) exhibited by mathematical model for $u_0 = -11.3$ V (a), -10.3 V (b), -9.01 V (c), and -8.51 V (d). The examples (a–b) correspond to quasiperiodic behavior of the system, while the sections (c–d) indicate the chaotic character of the attractor. Figure 7 exhibits bifurcation diagrams of the mathematical model—for quasi-statically changing the bifurcation parameter u_0 from -13 to -5 V (a) and from -5 to -13 V (b), confirming the chaotic window around the value $u_0 = -8.51$ V and many other zones of interesting bifurcational dynamics. In Fig. 8 one can observe results of numerical (a) and experimental (b) investigations of the threshold of the chaotic behavior of the system (for decreasing control parameter) near the $u_0 = -8.4$ V seen in Fig. 7. In the experimental investigations, the control parameter has been changed from -8.3 V to -8.48 with the speed of -0.0015 V/s (the investigation lasted 120 s).

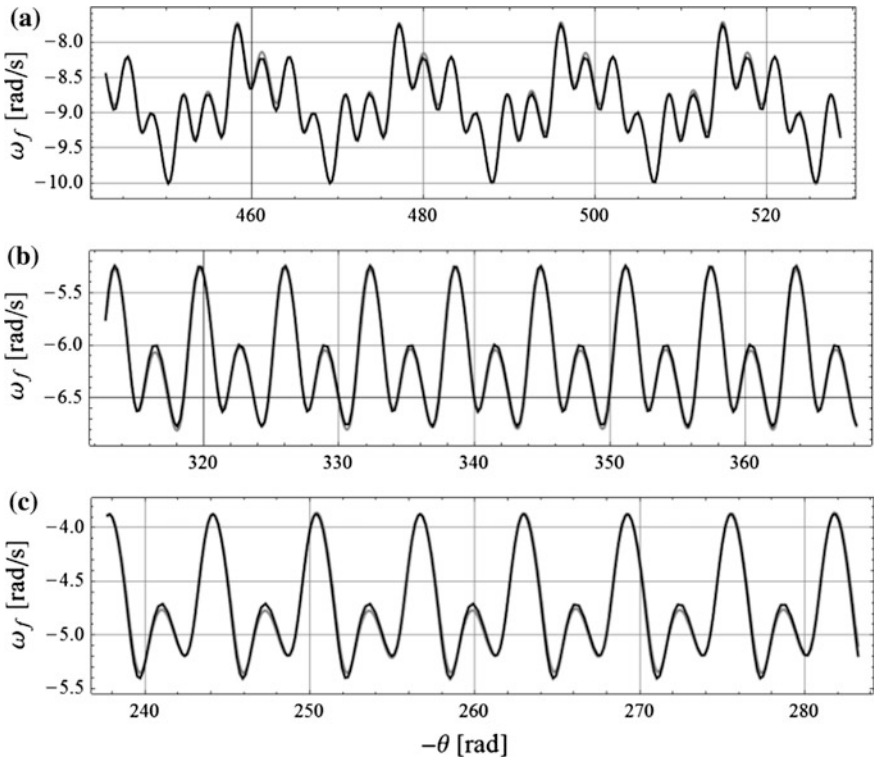

Fig. 4 Three numerical solutions $\omega_f(\theta)$ (*black line*) compared with the corresponding experimental data (*gray line*) ($u_0 = -10.8$, -8.0, and -6.5 V, for subfigures **a**, **b** and **c**, respectively)

Then the same condition was reconstructed during numerical simulations. One can notice 0.05 V of difference between the borders of the chaotic window observed numerically and experimentally.

6 Concluding Remarks

In the paper, there have been presented the results of the preliminary phase of the larger project aimed in numerical and experimental analysis of different configurations of a pendulum driven by an electric motor. In the current stage, one developed a mathematical and simulation model of real physical object being a physical pendulum excited vertically by a crank-shaft-slider mechanism, which is driven by a DC motor.

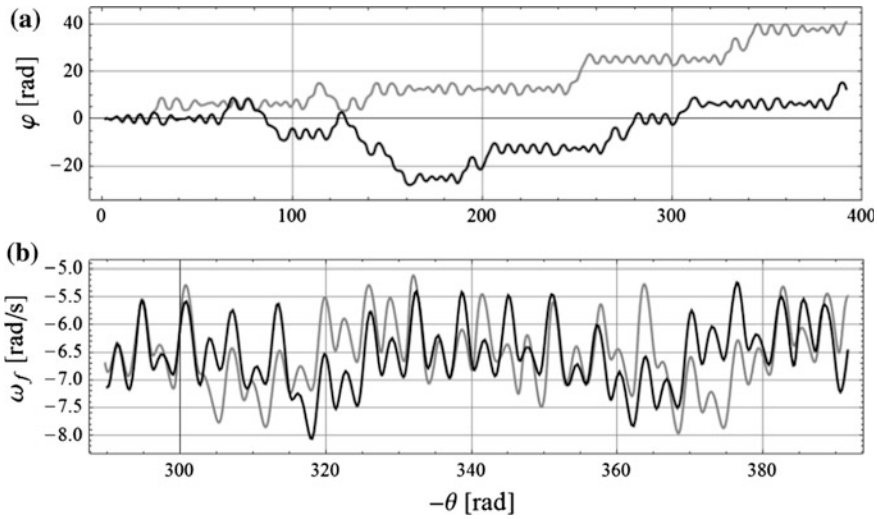

Fig. 5 The chaotic numerical solutions (*black lines*) $\varphi(\theta)$ (**a**) and $\omega_f(\theta)$ (**b**) compared with the corresponding experimental data (*gray lines*) for $u_0 = -8.51$ V

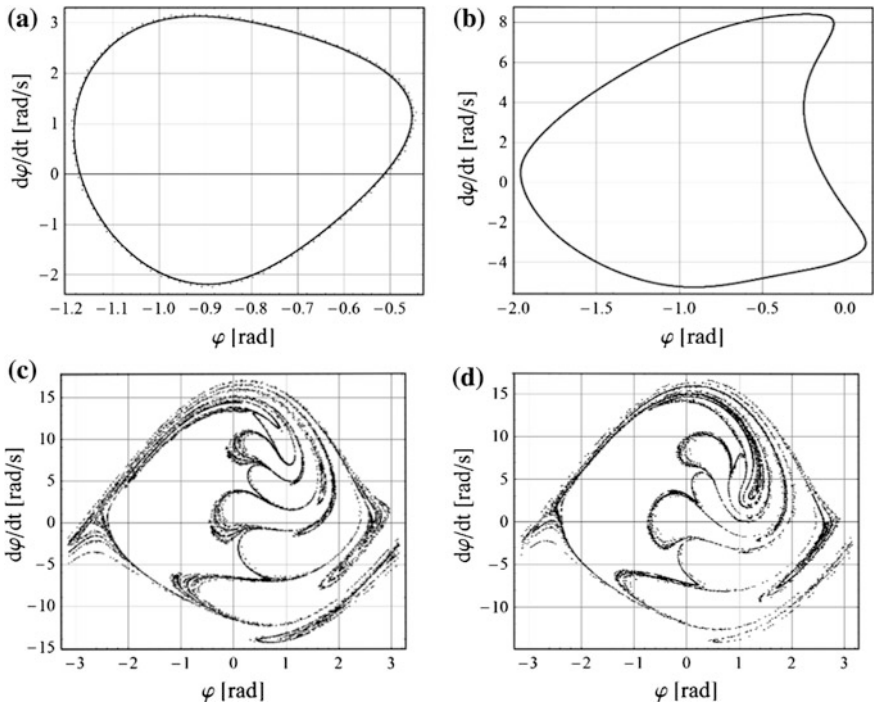

Fig. 6 Poincaré sections of the attractors obtained numerically for $u_0 = -11.3$ V (**a**), -10.3 V (**b**), -9.01 V (**c**), and -8.51 V (**d**)

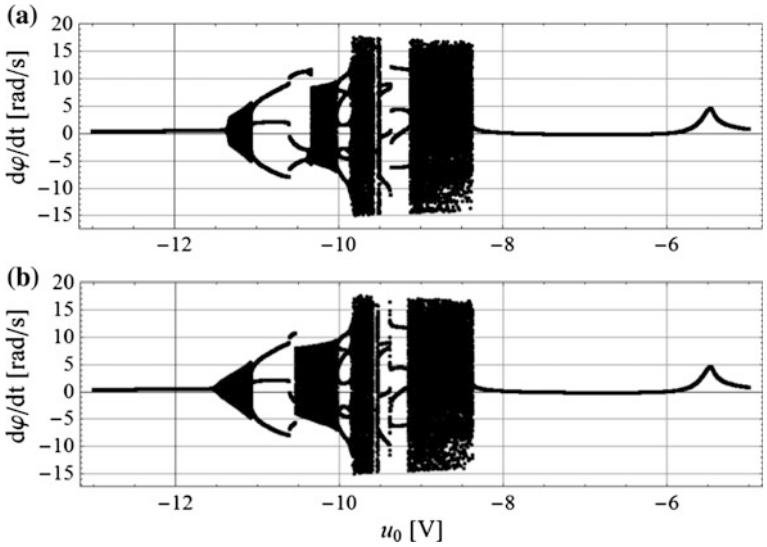

Fig. 7 Bifurcation diagram with constant in time input voltage u_0 as a control parameter—for growing (**a**) and decreasing (**b**) bifurcation parameter

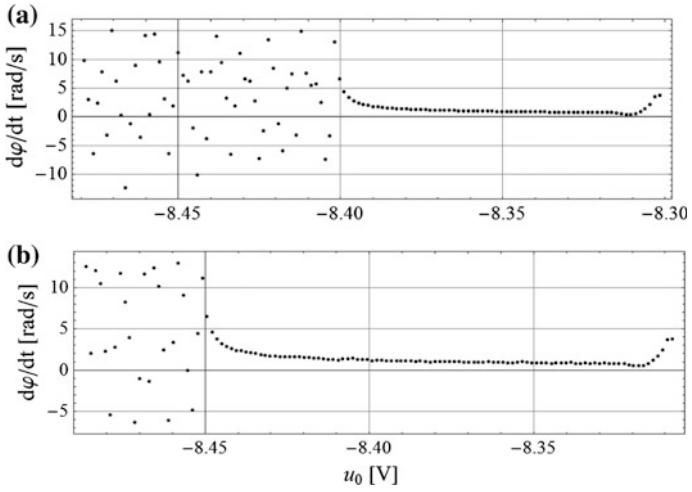

Fig. 8 Numerical (**a**) and experimental (**b**) investigations of the threshold of the chaotic behavior of the system (for decreasing control parameter)

Since the initial goal of the project is to develop exact and reliable mathematical and simulation model of the system, we take into account many details of friction and damping. We have also treated the parameters controlling the functions approximating the sign functions in the dry friction model as the parameters to be

identified from the experimental data. It resulted in a new resistance model rather than in a smooth approximation of the sign function. But this new model leads to better simulation results both in the sense of accuracy and speed of simulation. The second aspect results from the avoidance of stiffness of the differential equation of motion typical for smooth approximation of the sign function.

It should be noted that the a priori knowledge about the system was very poor including the knowledge about the DC motor and the gear transmission. But only three experimental periodic solutions were sufficient for developing a mathematical model mapping the dynamics of real system very well and allowing for reliable numerical simulations.

Acknowledgments The work has been supported by the Polish National Science Centre, MAESTRO 2, No. 2012/04/A/ST8/00738.

This is an extended version of the work [9] presented at the 13th Conference on Dynamical Systems—Theory and Applications, December 7–10, 2015, Łódź, Poland.

References

1. Blackburn, J.A., Zhou-Jing, Y., Vik, S., Smith, H.J.T., and Nerenberg, M.A.H. Experimental study of chaos in a driven pendulum. *Physica D* 26, 1–3 (1987), pp. 385–395.
2. Zhu, Q., and Ishitobi, M. Experimental study of chaos in a driven triple pendulum. *Journal of Sound and Vibration*, 227, 1 (1999), pp. 230–238.
3. Awrejcewicz, J., Supeł, B., Kudra, G., Wasilewski, G., and Olejnik, P. Numerical and experimental study of regular and chaotic motion of triple physical pendulum. *International Journal of Bifurcation and Chaos* 18, 10 (2008), pp. 2883–2915.
4. Belato, D., Weber, H.I., Balthazar, J.M., and Mook, D.T. Chaotic vibrations of a nonideal electro-mechanical system. *International Journal of Solids and Structures*, 38 (2001), pp. 1699–1706.
5. Avanço, R.H., Navarro, H.A., Brasil, R.M.L.R.F., and Balthazar, J.M. Nonlinear Dynamics of a Pendulum Excited by a Crank-Shaft-Slider Mechanism, *ASME 2014 International Mechanical Engineering Congress and Exposition*, *Volume 4B: Dynamics, Vibration, and Control*, Montreal, Quebec, Canada, 2014.
6. Cveticanin, L. Dynamics of the non-ideal mechanical systems: A review. *Journal of the Serbian Society for Computational Mechanics* 4, 2 (2010), pp. 75–86.
7. Kaźmierczak, M., Kudra, G., Awrejcewicz, J., and Wasilewski, G. Numerical and experimental investigation of bifurcational dynamics of an electromechanical system consisting of a physical pendulum and DC motor, in: Awrejcewicz J., Kaźmierczak M., Olejnik P. and Mrozowski J. (eds.) *Dynamical Systems – Applications.* TU of Lodz Press, Lodz, 2013, pp. 49–58.
8. Kaźmierczak, M., Kudra, G., Awrejcewicz, J., and Wasilewski, G. Mathematical modelling, numerical simulations and experimental verification of bifurcation dynamics of a pendulum driven by a dc motor. *European Journal of Physics* 36, 5 (2015), 13 pages.
9. Wasilewski G., Kudra G., Awrejcewicz J., Kaźmierczak M., Tyborowski M., and Kaźmierczak M. Experimental and numerical investigations of a pendulum driven by a low-powered DC motor, in: Awrejcewicz J., Kaźmierczak M., Olejnik P. and Mrozowski J. (eds.) *Dynamical Systems—Mathematical and Numerical Approaches*, TU of Lodz, Lodz, 2015, pp. 579–590.

10. Gershenfeld, N. *The Nature of Mathematical Modelling*. Cambridge University Press, 2011.
11. Nelder, J.A., and Mead, R. A simplex method for function minimization. Computer Journal 7, 4 (1965), pp. 308–313.

Bio-Inspired Tactile Sensors for Contour Detection Using an FEM Based Approach

Christoph Will

Abstract Various mammals, like mice, cats, and rats, have long hairs in the snout region, called mystacial vibrissae. These vibrissae allow the animal to determine a mechanical contact to obstacles and even to get information about the obstacles contour. Thereby, the vibrissa itself can be seen as conductor for mechanical forces and moments. From a mechanical perspective, the only information (the animal relies on) are governed at the support of the hair: the follicle sinus complex (FSC). Here, a lot of different mechanoreceptors detect several mechanical properties to recognize deformation. The vibrissa itself is a hair of conical shape, which is precurved and consists of multiple materials of different properties. In order to use the biological principle for technical sensory system, the reason for this design of the hair needs to be analyzed. Beam models incorporating all these facts (conical shape, hollow, multiple layers, precurvature, visco-elastic support) boundary-value problems, which are hard to handle using numerics. For this, we develop a mechanical model using an FEM-based approach to match all facts from biology and transfer them into a mechanical model for investigations. This work shall serve as a first attempt.

1 Introduction

Many rodents, e.g. mice and rats, have long hairs, called vibrissae, in their snout region. Those hairs are used by the animal to get information about the environment either by actively rotating them or passively using deformation information. In both cases, the information about mechanical deflection is gathered at the base of the vibrissa, namely the follicle sinus complex (FSC). At it, as seen in Fig. 1, different kind of cells convert mechanical strain into nerve signal for further processing.

C. Will (✉)
Department of Technical Mechanics, Ilmenau University of Technology,
Max-Planck-Ring 12 (Building F), 98693 Ilmenau, Germany
e-mail: christoph.will@tu-ilmenau.de

© Springer International Publishing Switzerland 2016

J. Awrejcewicz (ed.), *Dynamical Systems: Theoretical and Experimental Analysis*, Springer Proceedings in Mathematics & Statistics 182, DOI 10.1007/978-3-319-42408-8_32

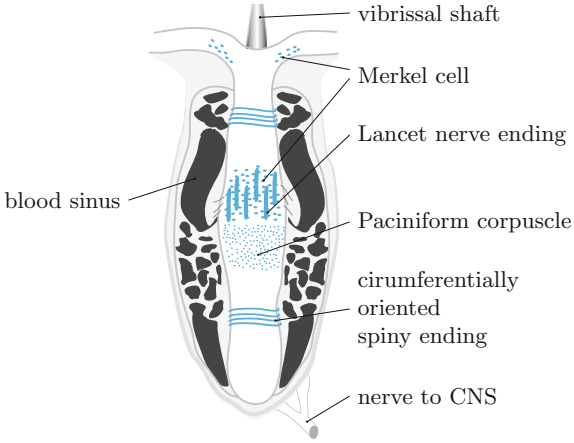

Fig. 1 Follicle sinus complex [1]

The animal seems to recognize obstacles by touching them with an arbitrary point of its vibrissae, while the only information it can get is at the FSC. This interesting observation is analyzed in this paper from a mechanical point of view, concentrating on the passive mode of vibrissa usage.

2 State of the Art

In the last decades, various approaches have been taken to transfer the biological paragon into a tactile sensor for application in technics. A first example of a "whisker-like" digital sensor, presented in [3], uses the deformation of a beam to detect obstacle contact. Unlike the biological paragon, this sensor is only capable of signalizing the presence or absence of an obstacle contact and no information about the objects shape or distance during the contact. For the purpose of this sensor, trajectory planing of mobile robots, this may seem sufficient, but for detailed information another principle is necessary.

Another approach is given in [4], in which linear beam theory is used to approximate large deflections of beams. As a matter of principle, the suggested method cannot give an exact object contour, but can approximate the object distance if the slope angle at the support is known.

An example on how the precurvature is used in models is given in [2]. In it, a superposition of the natural curvature of a vibrissa and a deflection based on linear beam theory is suggested. The authors indicate that this approach is only useful if a force is applied near the support of the vibrissa (clamping). This inevitably results in small deformation, which is the scope of linear theory of beams.

Recent works, e.g. [5], use a finite difference approximation of the curvature of the beam. In contrast to the methods mentioned above, this allows large deflections with manageable errors (spacial discretization). In [7], only the reconstruction of different shaped objects is analyzed, relinquishing any simulation on how an artificial vibrissa bends.

As an approach to have both, models for sensor design and reconstruction methods, the problem was analyzed analytically in [8] and [9] to the largest attempt. Assuming a straight beam, no precurvature and an ideal contact, it is shown, that an a priori contact point approximation is possible with only force and moment information at the base of the artificial vibrissa. The model also allows a force- and moment-sensor choice, based on typical scenarios at which the tactile sensor will be used. The presented reconstruction method is only applicable, if there is only a single contact point.

This paper aims to improve the model with respect to its capabilities to model more properties of biological vibrissa and contact scenarios, to allow an artificial vibrissa design for low error reconstruction.

3 Analytical Approach

As described in [8], an analytical treatment of the vibrissa-like scan process and the object contour reconstruction is possible. Assuming an animal moving at a straight line, w.l.o.g. the *xy*-plane, with an object in range of its vibrissae, the problem can be visualized as seen in Fig. 2.

In order to model the problem, the following assumptions are made [8]:

- The problem is modeled in the *xy*-plane. The obstacle is kept at a fixed position, while the vibrissa base is moving from the right to the left.
- Only static deformation is considered, so the problem is modeled quasi-statically.
- The vibrissa is a single, long, straight, and slim beam, which allows to use Euler-Bernoulli theory.

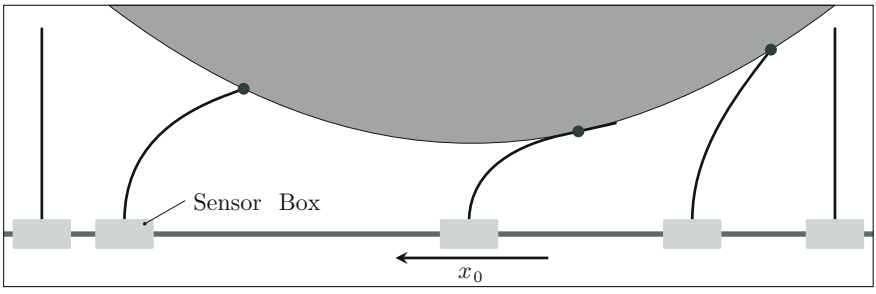

Fig. 2 Scheme of profile scanning. • Contact point

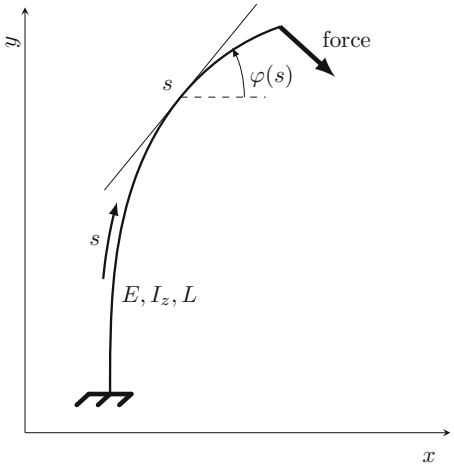

Fig. 3 Large deflection of an Euler-Bernoulli beam, [8]

- The support of the vibrissa is a clamp.
- Stress and strain are sufficiently small to use linear material behavior with Young's modulus E.
- The object has a strictly convex contour and is modeled as rigid body.
- The object contact is ideal, e.g., the beam deformation is caused by a single contact force.

Additionally, all lengths are measured in the beams length L, all moments in EI_zL^{-1} and forces in EI_zL^{-2}, with I_z being the second moment of area. The beams parametrization is shown in Fig. 3 with deflection angle φ and arc length coordinate $s \in [0, 1]$.

For better handling of the equations, the initial equation $\kappa(s) = M_{bz}(s)$ is differentiated with respect to s. This results in decoupled equations for curvature κ, and the slope angle of the beam φ and position x resp. y. Thus, the ODE system for the scan process with profile slope angle α is

$$\begin{array}{llll} \text{(a)} & \kappa'(s) = f\cos(\varphi(s) - \alpha) & \text{(c)} & x'(s) = \cos(\varphi(s)) \\ \text{(b)} & \varphi'(s) = \kappa(s) & \text{(d)} & y'(s) = \sin(\varphi(s)) \end{array} \tag{1}$$

During the scan process of an arbitrary strictly convex profile, two contact situations must be considered: tip contact of beam with the profile (Phase A) and tangential contact of beam and profile (Phase B). Both phases share the same ODE system, but have different boundary conditions. With given profile slope angle α and, therefore, given contact point of beam and profile $(\xi(\alpha), \eta(\alpha))$ in the xy-plane, the boundary-value problems (BVPs) are for

$$\begin{array}{llll} \text{(a)} & \varphi(0) = \frac{\pi}{2} & \text{(c)} \quad \kappa(1) = 0 & \text{(d)} \quad x(1) = \xi(\alpha) \\ \text{(b)} & y(0) = 0 & & \text{(e)} \quad y(1) = \eta(\alpha) \end{array} \tag{2}$$

Phase B (tangential contact at $s = s_1$):

$$\begin{array}{llllll} \text{(a)} & \varphi(0) = \frac{\pi}{2} & \text{(c)} & \kappa(s_1) = 0 & \text{(e)} & x(s_1) = \xi(\alpha) \\ \text{(b)} & y(0) = 0 & \text{(d)} & \varphi(s_1) = \alpha & \text{(f)} & y(s_1) = \eta(\alpha) \end{array} \tag{3}$$

A detailed solution with analytical treatment to the largest extent can be found in [8, 9].

4 Profile Reconstruction

While the generation of the observables during the design process is a BVP and later sensor data from an experimental setup, the reconstruction is a much easier problem: an initial value problem (IVP) of the ODE system (1). In contrast to Sect. 3, all equations necessary to solve the problem are formulated at the point $s = 0$:

$$\begin{aligned} \kappa(0) &= -M_z\,, \\ \varphi(0) &= \frac{\pi}{2}\,, \\ x(0) &= x_0\,, \\ y(0) &= 0\,, \end{aligned}$$

with M_z the clamp reaction moment in z direction and x_0 the position of the beam's support. Necessary parameters to formulate the ODE system (1) can be obtained using the observables, the force at the support in x (resp. y) direction F_x (resp. F_y),

$$\begin{aligned} \alpha &= -\arctan\left(\frac{F_x}{F_y}\right)\,, \\ f &= \sqrt{F_x^2 + F_y^2}\,. \end{aligned}$$

As presented in [8, 9], the contact point with respect to the current set of observables can be determined. Using multiple observables at different locations of the beam (during a scan process), a sequence of contact points can be computed, which approximate the profile contour.

5 Critical Discussion

For real-world applications, it cannot be guaranteed that the tactile sensor gets only in contact with strictly convex objects. For convex objects, no problem arises, because the assumption of only one contact force holds. For an object with concave sections,

there might certainly be contact situations at which the contact force must be seen as distributed load. In this case, only the net force can be sensed at the base, which will lead, analog to linear problems, to a false deformation and, therefore, to a contact point estimation with unpleasant error.

The prevention of a distributed load as a contact area is an objective, which needs to be considered in the design of tactile sensors. Animal vibrissae are precurved of conical shape and piecewise hollow, which all may or may not influence the bending behavior of the tactile sensor with respect to contact scenarios. To analyze the influence of these properties, the model needs to be reconsidered. An analytical solution has only been found, if the beam is straight and of constant diameter, see [8]. To solve the BVP for other beams, e.g., conical shaped ones, the use of numerics is unavoidable. Furthermore, in case of obstacle with concave sections, the ODE system would change, due to the fact that the contact force must be replaced by an unknown function describing the distributed load. A more elegant solution to obtain a model is to discretize the beam with local functions and allow contact forces only at their boundaries. With an sufficient amount of functions and, therefore, a high density of boundaries, an approximation of the distributed load can be found.

The present paper serves as a first step in focussing the problems described above. To verify the FEM approach, a comparison of the FE model and the analytical model is done.

6 FEM Approach

In the following, the total Lagrange formulation of a plane geometrically exact C^0 beam, like the one presented in [6, 10], is derived in short. This shall be seen as a first step in developing a FE model, which exhibits the properties of Sect. 5 neglected until now. The element is capable of performing large rotations, and, therefore, large deflections, but uses linear material behavior (small strains). The stain-deflection relations are, with axial strain ε, shear strain γ, and curvature κ:

$$\varepsilon = \left(1 + \frac{\mathrm{d}u_x}{\mathrm{d}x}\right)\cos(\theta) + \frac{\mathrm{d}u_y}{\mathrm{d}x}\sin(\theta) - 1\,, \tag{4}$$

$$\gamma = \frac{\mathrm{d}u_y}{\mathrm{d}x}\cos(\theta) - \left(1 + \frac{\mathrm{d}u_x}{\mathrm{d}x}\right)\sin(\theta)\,, \tag{5}$$

$$\kappa = \frac{\mathrm{d}\theta}{\mathrm{d}x}\,, \tag{6}$$

where u_x is the displacement in axial direction, u_y the deflection, and θ the rotation, as seen in Fig. 4.

Assuming only one element with its first node on the left side and second one on the right, the displacement can be noted using linear shape functions with $\chi = \frac{2x}{L_0} - 1$, while L_0 is the length of the undeformed element

Fig. 4 C^0 beam kinematics

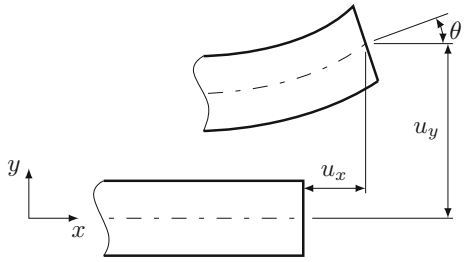

$$\begin{pmatrix} u_x(x) \\ u_y(x) \\ \theta(x) \end{pmatrix} = \frac{1}{2} \begin{pmatrix} 1-\chi & 0 & 0 & 1+\chi & 0 & 0 \\ 0 & 1-\chi & 0 & 0 & 1+\chi & 0 \\ 0 & 0 & 1-\chi & 0 & 0 & 1+\chi \end{pmatrix} \begin{pmatrix} u_{x1} \\ u_{y1} \\ \theta_1 \\ u_{x2} \\ u_{y2} \\ \theta_2 \end{pmatrix}. \tag{7}$$

The strain energy U is then given by

$$U = \int_{(L_0)} \frac{1}{2} E A_0 \varepsilon^2 \, \mathrm{d}x + \int_{(L_0)} \frac{1}{2} G A_0 \gamma^2 \, \mathrm{d}x + \int_{(L_0)} \frac{1}{2} E I_z \kappa^2 \, \mathrm{d}x \,, \tag{8}$$

with cross section area at undeformed state A_0 and shear modulus G. The appearing integrals are evaluated by a one-point Gauss integration rule with the sample point at $\chi = 0$. For an arbitrary orientation in the xy-plane, the C^0 element is not aligned with x. In the present paper, this is deliberately omitted for brevity.

A property of the C^0 beam to be well aware of is shear locking. A phenomenon which is caused by too much strain energy taken by shear and resulting in a very stiff behavior of the beam. A common way to eliminate this effect is the residual bending flexibility (RBF) correction. The term GA_0 is replaced by $(12EI_z)/(L_0^2)$. The strain due to axial load, which is considered in the FE model but not in the analytical model, is negligible due to a large factor of the product EA.

Since the snap-off of the beam is a critical part of the scanning process, which is not yet fully understood, a simple formulation of the contact based on penetration of beam and profile was discarded. Instead, a more exact contact formulation is used: Lagrangian multipliers. With the assumption of a rigid profile with f as a function describing its boundary, the following optimization problem can be stated:

$$\min U(u_{xi}, u_{yi}, \theta_i) \qquad \text{w.r.t} \quad Y_i + u_{yi} \leq f(X_i + u_{xi}),\ i = 1, \ldots, n+1 \,, \tag{9}$$

with

- n the number of finite elements
- u_{xi} resp. u_{yi} the node deflection of the i-th node in x-direction resp. y-direction
- X_i resp. Y_i the i-th node position in x resp. y direction.

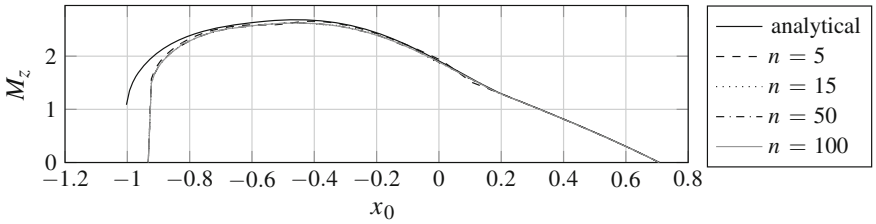

Fig. 5 Clamping moment

The gradient (force vector) of U is computed element wise by symbolic differentiation. To solve this optimization problem, Matlab's *fmincon* (*SQP* algorithm) is used. By starting from the undeformed state, moving the beam from the right to left and using the last result as initial point for the next step, a (numerically) solution of the optimization problem computed.

With respect to future application scenarios, a profile is chosen at which both phases (tip and tangential contact) occur: $f(x) \mapsto x^2 + \frac{1}{2}$.

As shown in Fig. 5, at the beginning of the scan process ($x_0 \in (0.2, 0.7)$), the analytical and the FE solution, even with a small amount of elements, nearly give the same observables. Beginning from that point at the scan process, the FE solution with five elements starts to show differences, during the inability to perform a tangential contact near the tip. The special discretization also is clearly to see in the ongoing scan process, resulting in oscillation-like graph. More elements smoothen the graph, where with 100 elements, the discretization is so accurate, no oscillation of the graph is noticeable. Although another effect can be noticed; even with 100 elements, the clamping moment of the FE solution is smaller than the analytical one. The difference is most likely be caused by the C^0 beam and its necessity to use a concept like the RBF correction.

The clamping forces F_x, shown in Fig. 6, and F_y, shown in Fig. 7, show a similar behavior. At the beginning of the scan process, the graphs are nearly inseparable, while beginning with $x_0 = 0.2$ to the snap-off of the beam at $x_0 = -1.0$, the spacial discretization of the FE method becomes visible. In contrast to the clamping moment, especially F_y shows a more distinct oscillation-like behavior. During the tangential

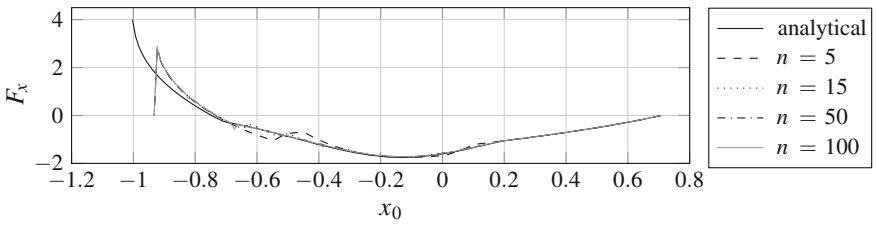

Fig. 6 Clamping force in x-direction

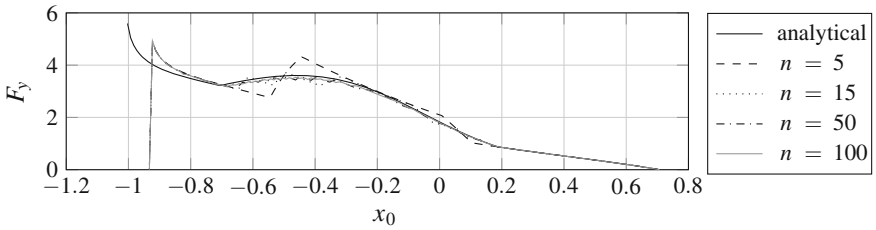

Fig. 7 Clamping force in y-direction

contact phase ($x_0 \in (-0.7, -0.3)$) the discretization is clearly noticeable even for the 100 element scan.

The snap-off of the beam, a part of the scan process which is not yet fully understood, shows the major difference of the two approaches. While the scan process of the analytical approach is terminated by the condition of a steady shrinking x_0 during a scan from the right to the left, the optimization algorithm used to determine a solution of (9) yields an undeformed beam at the end of the scan process, i.e., the potential energy of the beam is at its minimum. Although it is possible for the optimization algorithm to find a false local minimum, not representing the correction solution, this is rated unlikely due to a translation of the beams support of 10^{-2}.

7 Conclusion

The FE Method, i.e., the Total Lagrange C^0 beam element allows for an easy, yet efficient way to model the scanning procedure of tactile sensors. Although not covered in the present paper, a precurved and conical shape of the beam is possible by choosing geometric parameters element wise. With sufficiently small spacial discretization of the beam, tangential contact among beam tip and support can be represented and easily detected by an evaluation of the Lagrange multipliers. These also allow for a detection of contact situation, where multiple nodes are in contact with the profile, which is a main requirement to avoid, if the use of the reconstruction method mentioned in Sect. 4 is desired. Yet, to generate observables for the reconstruction algorithm by computation, the C^0 beam may not be the best choice. As mentioned in Sect. 6, deviations of analytical and FE approach in the computed observables may be caused by the fundamental properties of the C^0 beam. For buckling problems, which should not arise with the chosen profile during a scan process, the C^0 beam is known for disadvantages compared to the C^1 beam in the tangent stiffness matrix. Yet, also considering the RBF correction, this can not expelled to affect the scanning process. In future works, a comparison of both elements should be targeted.

The end of the scanning process, a snap-off of the beam from the profile, is still not fully understood. While both approaches lead to correct solutions in their scope, i.e., the analytical solution fulfilling the BVP and the FE solution (numerically) providing

a local minimum of the optimization problem, the difference in the observables is unlikely to be caused by the spatial discretization of the FE method. Experiments, using the setup shown in Fig. 2, are planned and may provide further insights if the snap-off can be treated quasi-statically and if so, which approach results in a better approximation.

References

1. Behn, C.: Modeling the behavior of hair follicle receptors as technical sensors using adaptive control. In: J.L. Ferrier, J. Sasiadek, K. Madani, O. Gusikhin (eds.) Proceedings of the 10th International Conference on Informatics in Control, Automation and Robotics, pp. 336–345 (2013). http://dx.doi.org/10.5220/0004488003360345
2. Birdwell, J.A., Solomon, J.H., Thajchayapong, M., Taylor, M.A., Cheely, M., Towal, R.B., Conradt, J., Hartmann, M.J.Z.: Biomechanical Models for Radial Distance Determination by the Rat Vibrissal System. Journal of Neurophysiology **98**(4), 2439–2455 (2007). doi:10.1152/jn.00707.2006
3. Hirose, S., Inoue, S., Yoneda, K.: The whisker sensor and the transmission of multiple sensor signals. Advanced Robotics **4**(2), 105–117 (1989). doi:10.1163/156855390X00099
4. Kim, D., Möller, R.: Biomimetic whiskers for shape recognition. Robotics and Autonomous Systems **55**(3), 229–243 (2007). doi:10.1016/j.robot.2006.08.001
5. Pammer, L., O'Connor, D.H., Hires, S.A., Clack, N.G., Huber, D., Myers, E.W., Svoboda, K.: The mechanical variables underlying object localization along the axis of the whisker. The Journal of neuroscience : the official journal of the Society for Neuroscience **33**(16), 6726–6741 (2013). doi:10.1523/JNEUROSCI.4316-12.2013
6. Reissner, E.: On one-dimensional finite-strain beam theory: The plane problem. Zeitschrift für angewandte Mathematik und Physik ZAMP **23**(5), 795–804 (1972). doi:10.1007/BF01602645.
7. Scholz, G.R., Rahn, C.D.: Profile Sensing With an Actuated Whisker. IEEE Transactions on Robotics and Automation **20**(1), 124–127 (2004). doi:10.1109/TRA.2003.820864
8. Will, C., Steigenberger, J., Behn, C.: Object Contour Reconstruction using Bio-inspired Sensors. In: J. Filipe, J. Sasiadek, K. Madani, O. Gusikhin (eds.) Proceedings of the 11th International Conference on Informatics in Control, Automation and Robotics, pp. 459–467. SCITEPRESS (2014). doi:10.5220/0005018004590467
9. Will, C., Steigenberger, J., Behn, C.: Quasi-static object scanning using technical vibrissae. In: P. Scharff, A. Schneider (eds.) Shaping the future by engineering: 58th IWK, Ilmenau Scientific Colloquium, Technische Universität Ilmenau. Univ.-Verl. Ilmenau, Ilmenau, Germany (2014)
10. Wriggers, P.: Nonlinear Finite Element Methods. Springer, Berlin and Heidelberg (2008)

Kinematics and Dynamics of the Drum Cutting Units

Marcin Zastempowski and Andrzej Bochat

Abstract The drum cutting assembly is the basic working assembly of self-propelled and fastened chaff cutters. The task of the drum cutting assembly is to cut plant material into parts of specified length—into chaff. Within the frames of the study's realization, mathematical dependencies are making it possible to determine the relationships between the basic parameters and construction features of cutting drums in the aspects of kinematics, and dynamics of their movement in the phase of the cutting process have been drawn up. The developed dependencies may be used at the time of simulation calculations on new drum constructions of cutting assemblies and in the process of their operation process' automation.

1 Introduction

The drum cutting assembly constitutes the basic operating assembly of self-propelled, fastened, and stationary chaff cutters. The task of the drum cutting assembly is to cut plant material (stalks or blades) into parts of specified length—into chaff.

Application of that type of assembly in chaff cutters makes it possible to obtain the required degree of material's size reduction. However, in order to obtain the required nutrition effects, there shall be required chaff of uniform length; however its length depends on the individual features of animals and the manner of their feeding [3].

In Figs. 1 and 2, there are presented the selected examples of agrarian machines, the basic operating assembly of which is the drum cutting assembly.

M. Zastempowski (✉) · A. Bochat
UTP University of Science and Technology, Bydgoszcz, Poland
e-mail: zastemp@utp.edu.pl

A. Bochat
e-mail: bochat@utp.edu.pl

© Springer International Publishing Switzerland 2016

J. Awrejcewicz (ed.), *Dynamical Systems: Theoretical and Experimental Analysis*, Springer Proceedings in Mathematics & Statistics 182, DOI 10.1007/978-3-319-42408-8_33

Fig. 1 Self-propelled chaff cutter make Claas [7]

Fig. 2 Fastened chaff cutter make Pöttinger [7]

2 Construction and the Principles of Operation of the Drum Cutting Assemblies

The exemplary construction of the drum cutting assembly is presented in Fig. 3. Cutting drums may be of open or closed construction [1–7]. A drum of an open construction is composed of a shaft on which there are mounted shields with openings. Cutter holders are fastened to the shields. Cutting knives are mounted in grippers. The knives, depending on the drum's construction may be straight or bended along the screw line.

Moreover, there may be distinguished uniform or sectional knives. A cutting drum is positioned in side boards of a chaff cutter.

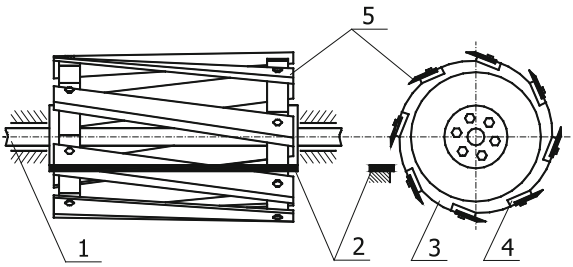

Fig. 3 Cutting drum of the chaff cutter: *1*—shaft of the cutting drum, *2*—crosscut edge called shear bar, *3*—cutting drum's shield, *4*—cutter holder, *5*—cutting knife

On the other hand in a drum of a closed construction on a shaft, instead of several shields there is mounted a construction in the form of a closed drum, on side surface of which there are located brackets with cutting knives attached to them.

Rotational motion of a cutting knife drum is in simultaneous translocation of cutting knives. The knives moving relative to the immovable shear bar at the first stage cause deformation and compression of the layer of plant material and then its cutting through.

Supply of material between the knife's blade and counter cutter takes place thanks to the rotational motion of the pulling and crushing shafts which preliminarily form and compact the material.

The essence of the process of plant material's supply to the cutting drum is presented in Fig. 4.

In the drum cutting assemblies, cutting takes place most often with the slide of knife towards the cut layer of the plant material, where the angle of the slide cutting assumes the constant value at the time of the knife edges' relocation with respect to that layer.

In Figs. 5 and 6 the constructions of cutting drums which are manufactured by the leading chaff cutters' producers are presented.

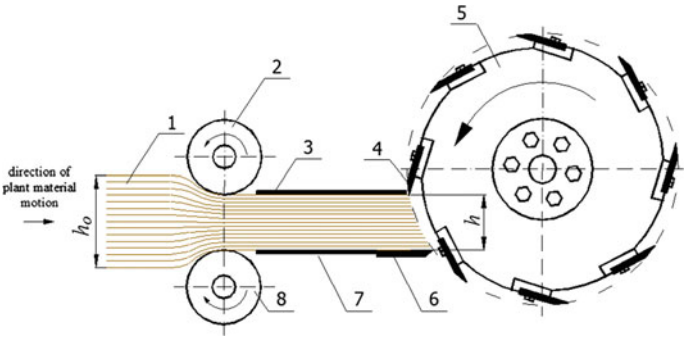

Fig. 4 Process of plant material's supply to the cutting drum: *1*—material layer, *2*—upper pulling and crushing shaft, *3*—pressure plate, *4*—cutting knife, *5*—cutting drum, *6*—shear bar, *7*—lower pulling and crushing shaft, h_0—height of the material's layer before compaction, h—height of the material's layer after compaction

Fig. 5 Cutting knife of the chaff cutter make New Holland [7]

Fig. 6 Cutting drum of the chaff cutter make Krone [7]

New Holland company has been using uniform knives, bended along the screw line in its constructions.

Chaff cutters make Claas and Krone use cutting drums with knives mounted in "V" configuration are used.

The exemplary construction of a cutting drum made by Krone is presented in Fig. 6.

In the opinion of producers, such a solution reduces the cutting resistance in connection with the decreased friction of plant material against the chaff cutter's casting and results in chaff's concentration inside a drum that facilitates the operation of pulling and crushing shafts [7].

The company John Deere has been using in its chaff cutters' constructions a cutting drum equipped with short knives (most often four knives in a row). The knife edges are parallel to the crosscut edge.

The effect of that is cutting of plant material into equal parts. Moreover, the knives may be replaced one by one that, in case of their damage, considerably decreases the cost of their replacement (Fig. 7).

Fig. 7 Cutting drum of the chaff cutter make John Deere [7]

3 Purpose of the Study

The purpose of the study is drawing mathematical dependencies making it possible to establish the relationships between the basic parameters and the design features of drum cutting assemblies in the aspect of kinematics and dynamics of their movement at the stage of the cutting process of plant material's cutting. Moreover, selected simulation calculations on the drawn up mathematical dependencies are conducted.

4 Kinematics of the Movement of the Drum Cutting Assembly

The operational quality of the cutting drum depends not only on the quality of the cutting edge (degree of its sharpening), but also setting of the axis of rotation of the drum towards the crosscut edge (shear bar) and thickness of the layer of the fed plant material.

Analyzing the complex movement of knife edge's movement, it may be noticed that the cutting speed ϑ_c is the variable value and precisely determined peripheral speed of knives ϑ_b (speed equivalent to the drum's linear velocity on the radius R) and the speed of feeding of material ϑ_m to be cut. The direction and the speed value ϑ_c, change together with the value of the drum's angular displacement φ. For any position of the knife's blade, according to the Fig. 8, speed ϑ_c may be calculated from dependence

$$\vartheta_c = \sqrt{\vartheta_b^2 + \vartheta_m^2 + 2\,\vartheta_b\,\vartheta_m \cos\psi}. \tag{1}$$

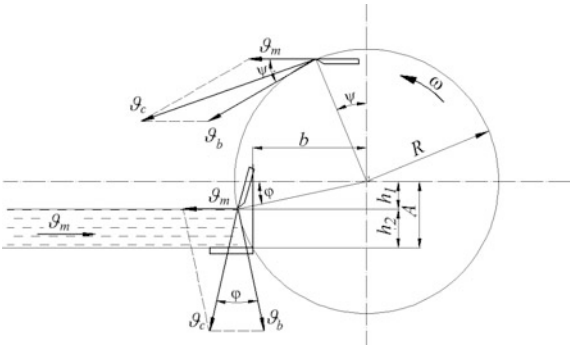

Fig. 8 Placement of drum's rotation axis with regards to the crosscut edge

In case of correct positioning of shear bar towards the axis of a drum, the knife shall cause the material's pushing away that shall result in the increase of cutting resistance and the increase of chaff's cutting non-uniformity.

The border position of the shear bar, at the constant thickness of the fed layer, ensures correct cutting when the constituent horizontal knife's linear velocity shall be equal to the material feeding speed that takes place when

$$\sin\varphi = \frac{\vartheta_m}{\vartheta_b}. \tag{2}$$

From the analysis of the Fig. 8 it results in

$$h_1 = R\sin\varphi = R\frac{\vartheta_m}{\vartheta_b} = R\frac{1}{\lambda}, \tag{3}$$

where

R—drum's radius,
λ—kinematic index of the drum cutting assembly determined as the proportion of the peripheral speed ϑ_b of the cutting knife to the speed of feeding ϑ_m of material to be cut.

So, the distance of the shear bar's cutting edge from the drum's axis in the vertical plane may be calculated with the formula

$$A = h_2 + \frac{R}{\lambda}. \tag{4}$$

On the other hand, the distance of the drum's rotation axis in the horizontal plane may be calculated from the relationship

$$b = \sqrt{R^2 - A^2} = \sqrt{R^2 - \left(h_1 - \frac{R}{\lambda}\right)^2}. \tag{5}$$

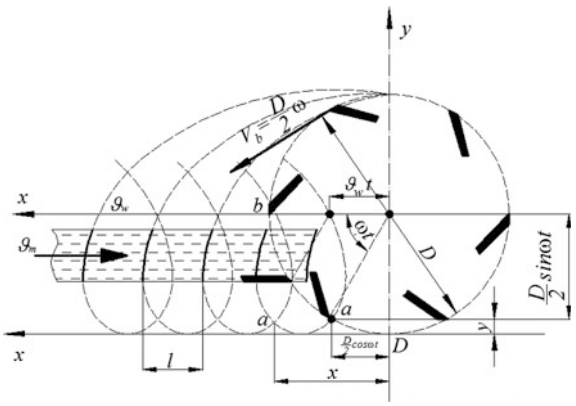

Fig. 9 Drums' blades track in relations to the cut material's layer

From the analysis of the formulae (4) and (5), it results that positioning of the crosscut edge (shear bar) towards the cutting drum's rotation axis depends on the drum's radius, thickness of the cut material's layer, and the kinematic rate.

Due to the fact that the cutting drum makes rotational motions and the material moves in an uniform linear motion in its direction, the motion track of knives has the form of trochoid which, according to Fig. 9 is described with the parametric equation

$$x_a = \vartheta_m t + R\cos\omega t, \tag{6}$$

$$y_a = R(1 - \sin\omega t). \tag{7}$$

In order to establish the resultant cutting speed ϑ and acceleration speed a of the knife, the Eqs. (6) and (7) are to be appropriately differentiated and carry out appropriate mathematical operations.

Differentiating the Eqs. (6) and (7) one time, the result was

$$\vartheta_{xa} = \frac{\mathrm{d}x_a}{\mathrm{d}t} = \vartheta_m - R\omega\sin\omega t, \tag{8}$$

$$\vartheta_{ya} = \frac{\mathrm{d}y_a}{\mathrm{d}t} = -R\omega\cos\omega t. \tag{9}$$

Taking into account that resultant speed of the beater is described by dependence

$$\vartheta = \sqrt{\vartheta_{xa}^2 + \vartheta_{ya}^2}, \tag{10}$$

after transformations we received

$$\vartheta = \sqrt{\vartheta_m^2 - 2\,\vartheta_m R\omega \sin \omega t + R^2\,\omega^2}. \tag{11}$$

While differentiating the Eqs. (6) and (7) two times we received

$$a_{xa} = \frac{\mathrm{d}\vartheta_{xa}}{\mathrm{d}t} = -R\,\omega^2 \cos \omega t, \tag{12}$$

$$a_{ya} = \frac{\mathrm{d}\vartheta_{ya}}{\mathrm{d}t} = R\,\omega^2 \sin \omega t. \tag{13}$$

Taking into account that resultant speed of the knife is described by dependence

$$a = \sqrt{a_{xa}^2 + a_{ya}^2}, \tag{14}$$

after transformations we received

$$a = \sqrt{(-R\,\omega^2 \cos \omega t)^2 + (R\,\omega^2 \sin \omega t)^2} = R\,\omega^2\,. \tag{15}$$

The distances between the adjacent trochoid loops accumulated on the layer of the cut material are equal to each other and constitute the so-called computational cutting length corresponding to the chaff's length.

The theoretical chaff's length l with sufficient approximation may be calculated from the dependence

$$l = \frac{\vartheta_m}{n \cdot z}, \tag{16}$$

where

ϑ_m—material feeding speed,
n—rotational speed of the cutting drum,
z—number of knives.

5 Dynamics of the Drum Motion of Cutting Assembly

Dynamic alignment of rotational speed of the drum cutting assembly may be described with equation

$$M = J \cdot \varepsilon, \tag{17}$$

where

M—turning moment on the shaft driving the drum cutting assembly,
J—mass moment of inertia of the cutting drum,
ε—angular acceleration of the cutting assembly.

Turning moment on the driving shaft M should be selected in such a manner, so as to make the transfer of power from the motor in an uniform manner; and the changes of the cutting resistance moments do not cause fluctuations of the angle speed of the powered motor. Such a condition is fulfilled when the turning moment M is high enough to impart the rotor with the necessary angle acceleration ε. It results from the literature data that is should amount at least to 1.5–5.0 rad/s^2 [2, 3].

The angle acceleration of the drum cutting assembly may be calculated from the dependence

$$\varepsilon = \frac{a}{R}, \tag{18}$$

or

$$\varepsilon = \frac{\Delta\omega}{t}, \tag{19}$$

where

a—knife's linear acceleration,
R—cutting drum's radius,
$\Delta\omega$—increment of the angle speed of the drum cutting assembly
t—time.

Designing the power transmission system for a given type of a chaff cutter, one should consider the starting power of rotating mass. It is the mass necessary to put the cutting drum into motion from the standstill. Usually it is assumed that the start-up is the uniformly accelerated motion. First, the moment of inertia of the cutting drum J and the angle acceleration of the start-up ε are calculated. Then, from the formula (20) the power needed for the start-up may be calculated

$$P_r = M \cdot \omega \tag{20}$$

where

P_r—starting power of the cutting drum,
M—turning moment on the cutting drum's shaft,
ω—shaft's rotary speed.

6 Selected Simulation Calculations of the Drum Cutting Assemblies

The introduced mathematical dependencies between the basic parameters and design features of cutting drums may be applied on the stage of simulation calculations in the process of designing or exploitation of the drum cutting assemblies.

In Table 1 there is presented specification of the basic results of simulation calculations of the cutting speed ϑ_c for the cutting drum having the radius $R = 0.20$ m and its angle speeds ω respectively equal to: 50, 75; 100 rad/s. The speed of material feeding ϑ_m was assumed as equal to 0.04 m/s. Assuming the correct cutting speed ϑ_c has a crucial importance for the cutting process's quality; depending on the type of the cut plant material, it should amount from 5 to 25 m/s [2, 3]. On the basis of the derived dependencies, one may establish appropriate parameters and design features of the cutting drum, which shall make it possible to obtain an appropriate cutting speed ϑ_c.

However, in Table 2 there are presented the selected simulation calculations of the speed ϑ and acceleration a of a single knife of a cutting drum in the time t from 1 to 10 s. The simulation calculations have been made for a cutting drum having the radius $R = 0.20$ m and its angular speed ω equal to 75 rad/s. The speed of material feeding ϑ_m was assumed to be equal to 0.04 m/s. The detailed values of parameters ϑ and a are necessary to conduct design calculations of the drum cutting assemblies.

However, dependencies derived in Sect. 5 make it possible to calculate the moment and power of the cutting drum's start-up. It results from the literature data that the drum's start-up power constitutes from 10 to 11 % of the total power necessary to perform the cutting process with the drum cutting assembly [3]. Due to that, as an example for a construction of the drum of the mass inertia moment.

$J = 4$ kg m^2 and its acceleration $\varepsilon = 5$ rad/s^2 and the angle speed $\omega = 100$ rad/s we have the start-up moment $M = 20$ Nm and the start-up power correspondingly.

$P = 2.0$ kW. So, the power necessary for the drum cutting assembly's power transmission should amount to at least $P = 20$ kW.

7 Final Conclusions

Within the frames of the study's conducting, there have been drawn up mathematical dependencies making it possible to establish relations between the basic parameters and design features of the drum cutting assemblies in the aspect of kinematics and dynamics of their movement on the stage of the process of the plant material layer's cutting.

Table 1 Exemplary results of simulation calculations of the cutting speed ϑ_c

R (m)	0.20	0.20	0.20	0.20	0.20	0.20	0.20	0.20	0.20	0.20	0.20	0.20
$\boldsymbol{\omega}$ (rad/s)	100	100	100	100	75	75	75	75	50	50	50	50
ϑ_b (m/s)	20	20	20	20	15	15	15	15	10	10	10	10
ϑ_m (m/s)	0.04	0.04	0.04	0.04	0.04	0.04	0.04	0.04	0.04	0.04	0.04	0.04
$\boldsymbol{\Psi}$ ($\ldots^0$)	0	55	110	165	0	55	110	165	0	55	110	165
$\boldsymbol{\vartheta}_c$ (m/s)	20.04	20.02	19.98	19.96	15.04	15.02	14.99	14.96	10.04	10.02	10.02	9.96

Table 2 Exemplary results of simulation calculations of speed ϑ and acceleration a of a cutting drum's knife

R (m)	0.20	0.20	0.20	0.20	0.20	0.20	0.20	0.20	0.20	0.20
$\boldsymbol{\omega}$ (rad/s)	75	75	75	75	75	75	75	75	75	75
$\boldsymbol{\vartheta}_b$ (m/s)	15	15	15	15	15	15	15	15	15	15
$\boldsymbol{\vartheta}_m$ (m/s)	0.04	0.04	0.04	0.04	0.04	0.04	0.04	0.04	0.04	0.04
t (s)	1	2	3	4	5	6	7	8	9	10
$\boldsymbol{\vartheta}$ (m/s)	15.06	15.04	15.03	15.00	14.97	14.96	14.97	15.00	15.03	15.04
$\boldsymbol{a}$ (m s^{-2})	1125	1125	1125	1125	1125	1125	1125	1125	1125	1125

The drawn up mathematical dependencies may be applied on the stage of simulation calculations while designing new constructions of the drum cutting assemblies for chaff cutters.

The drawn up mathematical dependencies may be applied on the stage of selection of appropriate operating parameters of drum cutting assemblies in the course of their use in chaff cutters while cutting different materials of plant origin.

References

1. Bochat A., Zastempowski M.: Analiza badań cięcia źdźbeł roślin zbożowych i nowy bębnowy zespół tnący. (The analysis of studies on cutting of stalks of grain crops and a new drum cutting assembly). *Chemical Engineering and Equipment* 1-2/2005, pp. 31–33.
2. Bochat A.: *Teoria i konstrukcja zespołów tnących maszyn rolniczych. (Theory and construction of cutting assemblies of agrarian machines).* Publishing company - UTP University of Science and Technology, Bydgoszcz, 2010.
3. Dmitrewski J.: *Teoria i konstrukcja maszyn rolniczych. Tom 3, (Theory and construction of agrarian machines, vol. 3).* PWRiL, Warszawa, 1978.
4. Haffert A. Harms H.H.: Schnittvorgang im Feldhäckslern. *Landtechnik* 2/2002, pp. 106–107.
5. O'Dogherty M.J., Gale G.: Laboratory studies of the cutting of grass systems. *Journal of Agricultural Engineering Research* 35/1986, pp. 115–129.
6. O'Dogherty M.J., Huber J.A., Dyson J., Marshall C.J.: A study of the physical and mechanical properties of wheat straw. *Journal of Agricultural Engineering Research* 62/1995, pp. 133–142.
7. Company's materials: Claas, John Deere, New Holland, Krone, Pöttinger.